Nucleosynthesis and Chemical Evolution of Galaxies

Bernard E. J. Pagel

This page intentionally left blank

NUCLEOSYNTHESIS AND
CHEMICAL EVOLUTION OF GALAXIES

Second Edition

The distribution of elements in the cosmos is the result of many processes, and it provides a powerful tool to study the Big Bang, the density of baryonic matter, nucleosynthesis and the formation and evolution of stars and galaxies. This textbook, by a pioneer of the field, provides a lucid and wide-ranging introduction to the interdisciplinary subject of galactic chemical evolution for advanced undergraduates and graduate students. It is also an authoritative overview for researchers and professional scientists.

In this textbook many exciting topics in astrophysics and cosmology are covered, from abundance measurements in astronomical sources, to light element production by cosmic rays and the effects of galactic processes on the evolution of the elements. Simple derivations for key results are provided, together with problems and helpful solution hints, enabling the student to develop an understanding of results from numerical models and real observations.

This new edition includes results from recent space missions, including WMAP and FUSE, new material on abundances from stellar populations, nebular analysis and meteoric isotopic anomalies, and abundance analysis of X-ray gas, and several extra problems at the end of chapters.

NUCLEOSYNTHESIS AND CHEMICAL EVOLUTION OF GALAXIES

Second Edition

BERNARD PAGEL

Visiting Professor of Astronomy
University of Sussex
Emeritus Professor of Astrophysics at NORDITA
Copenhagen

Bernard E. J. Pagel

Bernard Ephraim Julius Pagel was born in Berlin on 4 January 1930, but when his father was dismissed from his post as Jewish persecution increased, the family moved to Britain in 1933. From Merchant Taylors' School he won an open scholarship in Natural Sciences at Sidney Sussex College, Cambridge, graduating with First-class honours in Physics in 1950. His early research at Cambridge (Ph.D. 1955) centred on the solar atmosphere. Inspired by Willy Fowler, a future Nobel Prize winner who was visiting from California, he started a life-long interest in the abundances of the chemical elements.

In 1956 he moved to the Royal Greenwich Observatory at Herstmonceux Castle, Sussex. A search for more accurate estimates of chemical abundances led him to develop new analytic methods of analyzing the spectra of stars. By 1967, Sussex University had established an M.Sc. programme in astronomy, where Bernard lectured. During the early 1970s he began to develop the simple but elegant theoretical models to describe the chemical evolution of galaxies that have served as a foundation for the subject.

In 1975, using the new Anglo-Australian Telescope, Bernard started a long series of collaborations on the abundance analysis of H II regions in external galaxies, starting with the Magellanic Clouds. This led to the development of a method of estimating rough values for chemical abundances when observational data were sparse and only the strongest lines could be seen. Despite the method's acknowledged limitations, it had enormous influence as modern detectors allowed spectroscopic observation of faint galaxies. Variants of the method are still extensively used today. Further collaboration through observatories in the Canary Islands resulted in his fruitful influence on a generation of Spanish research students.

Retirement at 60 from his happy years at Herstmonceux was compulsory, so he moved in 1990 to a Chair at the Nordic Institute for Theoretical Astrophysics in Copenhagen. He became respected throughout Scandinavian astronomy, aided by his extraordinary facility for languages. A major programme was completed on the

determination of the primordial helium abundance, and he started new joint work on the chemical evolution of our own Galaxy. By the time he had 'retired' again in 1998, this time from Copenhagen back to Sussex, he had written the first edition of *Nucleosynthesis and Chemical Evolution of Galaxies*, the revisions for the second edition of which he had virtually completed just before his death on 14 July 2007.

He could be a formidable, but always fair, critic, and gave freely of his time to those who asked for help and advice. The Pagel family household in Ring-mer, Sussex, will be warmly remembered by many visiting astronomers. Bernard loved classical music – often playing the piano with great enthusiasm, if not with quite the accuracy of his abundance determinations! He will be remembered with great affection, particularly for the beady-eyed look over his pipe and a quick and brilliant intelligence which would even put one of his heroes, Sherlock Holmes, to shame.

To Annabel

Contents

List of abbreviations

A & A	*Astronomy & Astrophysics*
ABB	after the Big Bang
AGB	asymptotic giant branch
AGN	active galactic nucleus
AMR	age–metallicity relation
amu	atomic mass unit
Ap. J.	*Astrophysical Journal*
AQ	Astrophysical Quantities, by C. W. Allen
Astr. J.	*Astronomical Journal*
B^2FH	E. M. and G. R. Burbidge, Fowler and Hoyle
BABI	basaltic achondrite
BBNS	Big Bang nucleosynthesis
BCG	blue compact galaxy
BDM	baryonic dark matter
B.E.	binding energy
BSG	blue supergiant
CAI	calcium-aluminium-rich inclusion
CC1	carbonaceous chondrite type 1
CDM	cold dark matter
CERN	European Council for Nuclear Research (Geneva)
CM	centre of mass
CNO	carbon, nitrogen and oxygen
CO	CO molecule, or carbon and oxygen
CP	chemically peculiar
DDO	David Dunlap Observatory, Toronto, intermediate-band system
2DF	two-degree field
3DHO	three-dimensional harmonic oscillator
E-AGB	early AGB

ELS	Eggen, Lynden-Bell and Sandage
EW	equivalent width
FIP	first ionization potential
FUN	fractionation and unknown nuclear
FUSE	Far Ultraviolet Spectroscopic Explorer
GCE	Galactic chemical evolution
GCR	Galactic cosmic ray
GT	Gamow–Teller
GUT	grand unification theory
HB	horizontal branch
HR	Hertzsprung–Russell
HST	Hubble Space Telescope
IGM	intergalactic medium
IMF	initial mass function
IMS	intermediate-mass stars
IR	infrared
IRAS	Infra-Red Astronomy Satellite
ISM	interstellar medium
ISW	infinite square well
IUE	International Ultraviolet Explorer
KBH	Kulkarni, Blitz and Heiles
K.E.	kinetic energy
LBG	Lyman-break galaxy
LEP	Large Electron–Positron Collider
LINER	low-ionization nuclear emission line region
LMC	Large Magellanic Cloud
LTE	local thermodynamic equilibrium
MEMMU	Milne, Eddington, Minnaert, Menzel and Unsöld
MNRAS	*Monthly Notices of the Royal Astronomical Society*
MS	main sequence
MWB	microwave background radiation
NDM	non-baryonic dark matter
ORS	Oliver, Rowan-Robinson and Saunders
PDMF	present-day mass function
PN	planetary nebula
PP	Partridge and Peebles
QM	quantum mechanics
QSO	quasi-stellar object
RGB	red-giant branch
RSG	red supergiant

SBBN	standard Big Bang nucleosynthesis
SDSS	Sloan Digital Sky Survey
SFR	star formation rate
SGB	subgiant branch
SMC	Small Magellanic Cloud
SN	supernova
SN Ia	Type Ia supernova
SN II	Type II supernova
SNR	supernova remnant
snu	solar neutrino unit
SSP	single stellar population
SZ	Searle and Zinn
TAMS	terminal main sequence
TP-AGB	thermal pulse AGB
UBV	Johnson UBV broad-band system
UV	ultraviolet
WMAP	Wilkinson Microwave Anisotropy Probe
WIMPS	weakly interacting massive particles
WR	Wolf–Rayet
ZAHB	zero-age horizontal branch
ZAMS	zero-age main sequence

Preface to the first edition

This book is based on a lecture course given at Copenhagen University in the past few years to a mixed audience of advanced undergraduates, graduate students and some senior colleagues with backgrounds in either physics or astronomy. It is intended to cover a wide range of interconnected topics including thermonuclear reactions, cosmic abundances, primordial synthesis of elements in the Big Bang, stellar evolution and nucleosynthesis. There is also a (mainly analytical) treatment of factors governing the distribution of element abundances in stars, gas clouds and galaxies and related observational data are presented.

Some of the content of the course is a concise summary of fairly standard material concerning abundance determinations in stars, cold gas and ionized nebulae, cosmology, stellar evolution and nucleosynthesis that is available in much more detail elsewhere, notably in the books cited in the reading list or in review articles; here I have attempted to concentrate on giving up-to-date information, often in graphical form, and to give the simplest possible derivations of well-known results (e.g. exponential distribution of exposures in the main s-process). The section on Chemical Evolution of Galaxies deals with a rapidly growing subject in a more distinctive way, based on work in which I and some colleagues have been engaged over the years. The problem in this field is that uncertainties arising from problems in stellar and galactic evolution are compounded. Observational results are accumulating at a rapid rate and numerical models making a variety of often arbitrary assumptions are proliferating, leading to a jungle of more or less justifiable inferences that are often forgotten in the next instant paper. The analytical formalism on which I have been working on and off since my paper with the late B. E. Patchett in 1975, and to which very significant contributions have also been made by D. D. Clayton, M. G. Edmunds, F. G. A. Hartwick, R. B. Larson, D. Lynden-Bell, W. L. W. Sargent, L. Searle, B. M. Tinsley and others, is designed not only to keep the computations simple but also to introduce some order into the subject and provide the reader with an insight into what actually are the important factors

in chemical evolution models, whether analytical or numerical, and which are the major uncertainties.

The book should be considered basically as a textbook suitable for beginning graduate students with a background in either physics or astronomy, but it is hoped that parts of it will also be useful to professional scientists. For this purpose, I have tried to keep the text as expository as possible with a minimum of references, but added notes at the ends of some chapters to provide a guide to the literature.

I should like to take this opportunity to thank Donald Lynden-Bell for arousing my interest in this subject and for his continued encouragement and stimulation over the years; and likewise Michael Edmunds, whose collaboration in both observational and theoretical projects has been a source of pleasure as well as (one hopes) insight. Thanks are due to them, and also to Sven Åberg, Chris Pethick and the late Roger Tayler, for helpful comments on successive versions. Finally, I warmly thank Elisabeth Grothe for her willing and expert work on the diagrams.

Bernard Pagel

Preface to the second edition

Much has happened since the book first came out in 1997. Cosmology has been transformed by balloon and satellite studies of the microwave background and by studies of distant supernovae. Host galaxies of γ-ray burst sources have been identified and some of their properties revealed. Cosmological simulations have been very successful in accounting for the large-scale structure of the Universe, although they are still challenged by observed element:element ratios suggesting that the largest galaxies were formed rapidly a long time ago, limiting the time available for their formation by mergers. The coming of 10-metre class telescopes, supplementing the Hubble Space Telescope, has led to enormous advances in abundance determinations in stars of all kinds and in galaxies, notably at high redshifts. Some stellar atmospheres can now be modelled by *ab initio* hydrodynamical simulations which account for granulation and eliminate the need for ad hoc parameters describing 'macro-turbulence' and 'micro-turbulence', leading to increasingly sophisticated abundance determinations. Nevertheless, simple analytical treatments retain their usefulness because of the insight they provide into the essential ingredients of more elaborate numerical models, whether of stellar atmospheres or of galactic chemical evolution.

I thank Monica Grady, Chris Tout and Max Pettini for critically reading through the revised Chapters 3, 5 and 12 respectively, and Mike Edmunds for continued cooperation and enlightening discussions. I owe particular thanks to my wife Annabel Tuby Pagel for her loving care during difficult times.

Bernard Pagel

1
Introduction and overview

I believe that a leaf of grass is no less than the journey work of the stars.
Walt Whitman, *Song of Myself*

1.1 General introduction

The existence and distribution of the chemical elements and their isotopes is a consequence of nuclear processes that have taken place in the past in the Big Bang and subsequently in stars and in the interstellar medium (ISM) where they are still ongoing. These processes are studied theoretically, experimentally and observationally. Theories of cosmology, stellar evolution and interstellar processes are involved, as are laboratory investigations of nuclear and particle physics, cosmochemical studies of elemental and isotopic abundances in the Earth and meteorites and astronomical observations of the physical nature and chemical composition of stars, galaxies and the interstellar medium.

Figure 1.1 shows a general scheme or 'creation myth' which summarizes our general ideas of how the different nuclear species (loosely referred to hereinafter as 'elements') came to be created and distributed in the observable Universe. Initially – in the first few minutes after the Big Bang – universal cosmological nucleosynthesis at a temperature of the order of 10^9 K created all the hydrogen and deuterium, some ^{3}He, the major part of ^{4}He and some ^{7}Li, leading to primordial mass fractions $X \simeq 0.75$ for hydrogen, $Y \simeq 0.25$ for helium and $Z = 0.00$ for all heavier elements (often loosely referred to by astronomers as 'metals'!). The existence of the latter in our present-day world is the result of nuclear reactions in stars followed by more or less violent expulsion of the products when the stars die, as first set out in plausible detail by E. M. and G. R. Burbidge, W. A. Fowler and F. Hoyle (usually abbreviated to B^{2}FH) in a classic article in *Reviews of Modern Physics* in 1957 and independently by A. G. W. Cameron in an Atomic Energy of Canada report in the same year (B^{2}FH 1957; Cameron 1957).
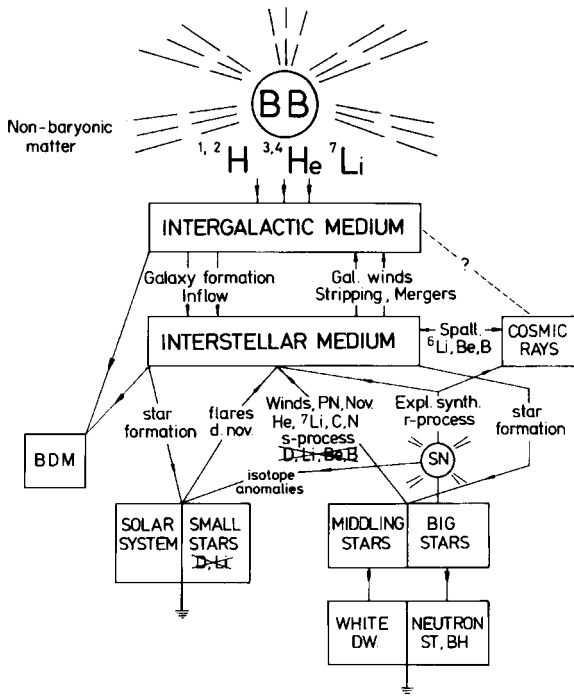
Fig. 1.1. A scenario for cosmic chemical evolution, adapted from Pagel (1981).

Estimates of primordial abundances from the Big Bang, based on astrophysical and cosmochemical observations and arguments, lead to a number of interesting deductions which will be described in Chapter 4. In particular, there are reasons to believe that, besides the luminous matter that we observe in the form of stars, gas and dust, there is dark matter detectable from its gravitational effects (including gravitational lensing). This dark matter, in turn, has two quite distinct components: one is ordinary baryonic matter, consisting of protons, neutrons and electrons, which happens not to shine detectably at accessible wavelengths. There is evidence for such baryonic dark matter (BDM) in the form of rarefied ionized intergalactic gas producing absorption lines – notably at high redshifts – and also possibly in the form of 'MACHOs' (massive compact halo objects) – stellar-mass dark objects arguably in the halo of our Galaxy detected from their gravitational micro-lensing of background sources in the Magellanic Clouds (but at least some of them are possibly normal stars in the Magellanic Clouds themselves). There could also be contributions from cold molecular hydrogen and from low surface brightness galaxies not picked up in redshift surveys.

The other kind of dark matter must be non-baryonic (NDM) and is thought to consist of some kind of particles envisaged in extensions of the 'Standard Model'

of particle physics. The most popular candidates are so-called cold dark matter (CDM) particles that decoupled from radiation very early on in the history of the Universe and now have an exceedingly low kinetic temperature which favours the formation of structures on the sort of scales that are observed in galaxy red-shift surveys. The seeds of those structures would have been quantum fluctuations imprinted very early (maybe $\sim 10^{-35}$ s) after the Big Bang during a so-called inflationary era of super-rapid expansion preceding the kind of expanding Universe that we experience now, which later enabled pockets of mainly dark matter slightly denser than the average to separate out from the general expansion by their own gravity. A small contribution to NDM also comes from neutrinos, since evidence for their flavour oscillations implies that they have a small mass, but this mass is estimated from microwave background data to be ≤ 0.2 eV (averaged over the three flavours) and their contribution to NDM ≤ 5 per cent.

The first few minutes are followed by a plasma phase lasting of the order of 10^5 years during which the Universe was radiation-dominated and the baryonic gas, consisting almost entirely of hydrogen and helium, was ionized and consequently opaque to radiation through electron scattering. But expansion was accompanied by cooling, and when the temperature was down to about 10^4 K (at a redshift of about 3450), matter began to dominate and at redshifts around 1100, some 370 000 years after the Big Bang (ABB), first helium and then hydrogen became neutral by recombination.[1] The Universe became transparent and background radiation was scattered for the last time (and is now received as black-body radiation with a temperature of 2.7 K) leading to a period commonly known as the 'dark ages'.[2] Eventually gas began to settle in the interiors of the pre-existing dark-matter halos, resulting in the formation of stars, galaxies and groups and clusters of galaxies, and in re-ionization of the intergalactic medium by newly formed massive stars and/or the compact ultra-luminous objects known as quasars or quasi-stellar objects (QSOs) associated with galactic nuclei.

The epoch and mode of galaxy formation are not well known, but both quasars and star-forming galaxies are known with redshifts up to about 7, corresponding to an era when the expanding Universe was only 1/8 of its present size, and the emission-line spectra of quasars indicate a large heavy-element abundance (solar or more; Hamann & Ferland 1999), suggesting prior stellar activity. The first stars, on the other hand, known as 'Population III', would have been devoid of 'metals'; whether they differed from normal stars in other basic characteristics, notably their mass distribution, is not known, since no completely metal-free stars have been

---

[1] Since this was the first time electrons were captured by protons and α-particles it might be more appropriate to talk about 'combination' rather than 'recombination'!

[2] 'Infrared ages' might be a more appropriate term.

found. Data from the WMAP[3] polarization measurements published in 2003 suggest that re-ionization took place over an extended period between redshifts of 30 and 10, corresponding to ages of the Universe between about 100 and 400 Myr.[4] In the most popular models, galaxies form by cooling and collapse of baryonic gas contained in non-gaseous (and consequently non-dissipative) dark-matter halos that build up from hierarchical clustering, with complications caused by mergers that may take place both in early stages and much later; these mergers (or tidal interactions) may play a significant role in triggering star formation at the corresponding times.

Galaxies thus have a mixture of stars and diffuse interstellar medium. (The diffuse ISM generally consists of gas and dust, but will often be loosely referred to hereinafter as 'gas'.) Most observed galaxies belong to a sequence first established in the 1920s and 30s by Edwin Hubble. So-called early-type galaxies according to this classification are the ellipticals, which are ellipsoidal systems consisting of old stars and relatively little gas or dust detectable at optical, infrared or radio wavelengths; they do, however, contain substantial amounts of very hot X-ray emitting gas. Later-type galaxies have a rotating disk-like component surrounding an elliptical-like central bulge, with the relative brightness of the disk increasing along the sequence. The disks display a spiral structure, typical of spiral galaxies such as our own Milky Way system, and the proportion of cool gas relative to stars increases along the sequence, together with the relative rate of formation of new stars from the gas, so that their colours become increasingly blue. At the end of the Hubble sequence are irregular galaxies, such as the Magellanic Clouds (the nearest major galaxies outside our own), and outside the sequence there is a variety of small systems known as dwarf spheroidals, dwarf irregulars and blue compact and H II (i.e. ionized hydrogen) galaxies. The last three classes actually overlap (being partly classified by the method of discovery) and they are dominated by the light of young stars and (in the case of H II and some blue compact galaxies) the gas ionized by those young stars (see Chapter 3). There are also radio galaxies and so-called Seyfert galaxies with bright nuclei that have spectra resembling those of quasars; these are collectively known as active galactic nuclei (AGNs), and are associated with large ellipticals and early-type spirals. The increase in the proportion of cool gas along the Hubble sequence could be due to differences in age, the most gas-poor galaxies being the oldest, or to differences in the rates at which gas has been converted into stars in the past or added or removed by interaction with other galaxies and the intergalactic medium (IGM), or perhaps some combination of all of these.

---

[3] Wilkinson Microwave Anisotropy Probe, launched in 2001.

[4] Assuming the currently favoured flat Λ-CDM cosmology with $\Omega_m = 0.24$, $H_0 = 73 \, \text{km} \, \text{s}^{-1} \, \text{Mpc}^{-1}$.

The figure illustrates very schematically some possible interactions between galaxies and the intergalactic medium. The IGM can be roughly considered as a combination of a diffuse medium and discrete clouds, the latter being manifested in the local Universe by absorption lines of H I Lyman-α λ 1216 and O VI $\lambda\lambda$ 1032, 1038 detected in the far ultraviolet,[5] by high-velocity H I clouds detected from the hyperfine 21-cm transition of neutral atomic hydrogen at high Galactic latitudes (which may be of extragalactic origin in some cases, although this is quite controversial) and by hot X-ray emitting gas in clusters and groups of galaxies. H I gas is detected in disk and blue compact galaxies but no isolated intergalactic H I clouds have been found. At high redshifts, Gunn and Peterson (1965) predicted[6] that, as one looks through to the re-ionization epoch, one should see a broad absorption trough shortward of the Lyman-α emission line from a quasar, due to diffuse neutral hydrogen at a range of redshifts in the foreground. This effect was first found for the corresponding line of He$^+$, λ 304 (redshifted to wavelengths near 1200 Å accessible to HST[7] and FUSE), accompanied by discrete absorption lines from the knots and filaments in which most of the CDM (and associated gas) has gathered by the corresponding epoch in accordance with numerical simulations of gravitational clustering. In the case of H I, which is much less abundant owing to the ionizing radiation field at those epochs, one only sees discrete lines, called the 'Lyman-α forest', resulting from the knots and filaments, at redshifts up to 4 or so (see Figs. 4.5, 12.5), but the classical Gunn–Peterson effect of diffuse intergalactic hydrogen does appear at redshifts greater than about 6, deeper into the re-ionization epoch.

The interactions between the ISM and IGM include expulsion of diffuse material from galaxies in the form of galactic winds driven by supernova energy ('feedback'), stripping of (especially the outer) layers of the gas content of galaxies by tidal forces or by ram pressure in an intra-cluster medium when the galaxy is a member of a cluster; and/or inflow of intergalactic gas into galaxies, which latter may be manifested by some of the high-velocity H I clouds in our own Milky Way system.

Figure 1.1 also gives a schematic illustration of the complex interactions between the ISM and stars. Stars inject energy, recycled gas and nuclear reaction products ('ashes of nuclear burning') enriching the ISM from which other generations of stars form later. This leads to an increase in the heavy-element content of both the ISM and newly formed stars; the subject of 'galactic chemical evolution' (GCE) is really all about these processes. On the other hand, nuclear products may

---

[5] Notably by the FUSE (Far UV Spectroscopic Explorer) mission launched in 1999.
[6] Similar considerations were put forward independently by Shklovsky (1964) and Scheuer (1965).
[7] Hubble Space Telescope.

be lost from the ISM by galactic winds or diluted by inflow of relatively unpro-
cessed material. The heavy-element content of the intra-cluster X-ray gas in rich
clusters like Coma,[8] amounting to about 1/3 of solar, may have resulted from winds
from the constituent galaxies (see Chapter 11), or possibly from the destruction of
dwarf galaxies in the cluster.

The effects of different sorts of stars on the ISM depend on their (initial) mass
and on whether they are effectively single stars or interacting binaries; some of the
latter are believed to be the progenitors of Type Ia supernovae (SN Ia) which are
important contributors to iron-group elements in the Galaxy. Big stars, with initial
mass above about $10\,M_\odot$ ($M_\odot$ is the mass of the Sun), have short lives ($\sim 10\,\text{Myr}$),
they emit partially burned material in the form of stellar winds and those that are
not too massive eventually explode as Type II (or related Types Ib and Ic) super-
novae, ejecting elements up to the iron group with a sprinkling of heavier elements.
(Supernovae are classed as Type I or II according to whether they respectively lack,
or have, lines of hydrogen in their spectra, but all except Type Ia seem to be associ-
ated with massive stars of short lifetime which undergo core collapse leading to a
compact remnant.) The most massive stars of all are expected to collapse into black
holes, with or without a prior supernova explosion; the upper limit for core collapse
supernovae is uncertain, but it could be somewhere in the region of $50\,M_\odot$.

Middle-sized stars, between about 1 and $8\,M_\odot$, undergo complicated mixing pro-
cesses and mass loss in advanced stages of evolution, culminating in the ejection of
a planetary nebula while the core becomes a white dwarf. Such stars are important
sources of fresh carbon, nitrogen and heavy elements formed by the slow neutron
capture (s-) process (see Chapter 6). Finally, small stars below $1\,M_\odot$ have lifetimes
comparable to the age of the Universe and contribute little to chemical enrichment
or gas recycling and merely serve to lock up material.

The result of all these processes is that the Sun was born 4.6 Gyr ago with mass
fractions $X \simeq 0.70,\ Y \simeq 0.28,\ Z \simeq 0.02$. These abundances (with perhaps a
slightly lower value of Z) are also characteristic of the local ISM and young stars.
The material in the solar neighbourhood is about 15 per cent 'gas' (including dust
which is about 1 per cent by mass of the gas) and about 85 per cent stars or compact
remnants thereof; these are white dwarfs (mainly), neutron stars and black holes.

1.2 Some basic facts of nuclear physics

(i) An atomic nucleus consists of Z protons and N neutrons, where Z is the *atomic number*
defining the charge of the nucleus, the number of electrons in the neutral atom and
hence the chemical element, and $Z + N = A$, the *mass number* of the nuclear species.

---

[8] The nearest rich cluster of galaxies, in the constellation Coma Berenices.
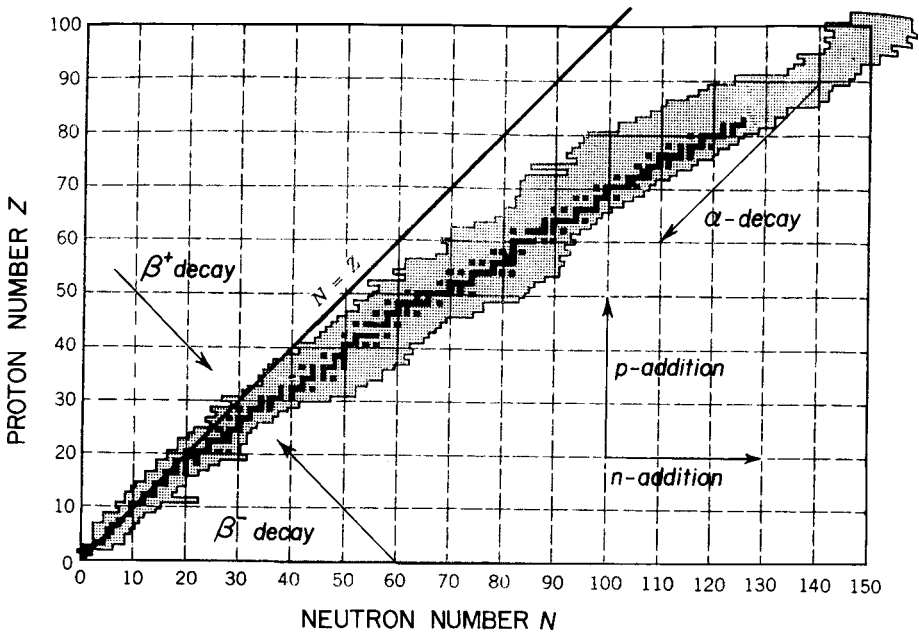
Fig. 1.2. Chart of the nuclides, in which Z is plotted against N. Stable nuclei are shown in dark shading and known radioactive nuclei in light shading. Arrows indicate directions of some simple nuclear transformations. After Krane (1987). Reproduced by permission of John Wiley & Sons, Inc.

Protons and neutrons are referred to collectively as *nucleons*. Different values of A and N for a given element lead to different *isotopes*, while nuclei with the same A and different Z are referred to as *isobars*. A given nuclear species is usually symbolized by the chemical symbol with Z as an (optional) lower and A as an upper prefix, e.g. $^{56}_{26}$Fe.

Stable nuclei occupy a 'β-stability valley' in the Z, N plane (see Fig. 1.2), where one can imagine energy (or mass) being plotted along a third axis perpendicular to the paper. Various processes, some of which are shown in the figure, transform one nucleus into another. Thus, under normal conditions, a nucleus outside the valley undergoes spontaneous decays, while in accelerators, stars and the early Universe nuclei are transformed into one another by various reactions.

(ii) The binding energy per nucleon varies with A along the stability valley as shown in Fig. 1.3, and this has the following consequences:

(a) Since the maximum binding energy per nucleon is possessed by ^{62}Ni, followed closely by ^{56}Fe, energy is released by either fission of heavier or fusion of lighter nuclei. The latter process is the main source of stellar energy, with the biggest contribution (7 MeV per nucleon) coming from the conversion of hydrogen into helium (H-burning).

(b) Some nuclei are more stable than others, e.g. the α-particle nuclei ^{4}He, ^{12}C, ^{16}O, ^{20}Ne, ^{24}Mg, ^{28}Si, ^{32}S, ^{36}Ar, ^{40}Ca. Nuclei with a couple of A-values (5 and 8) are
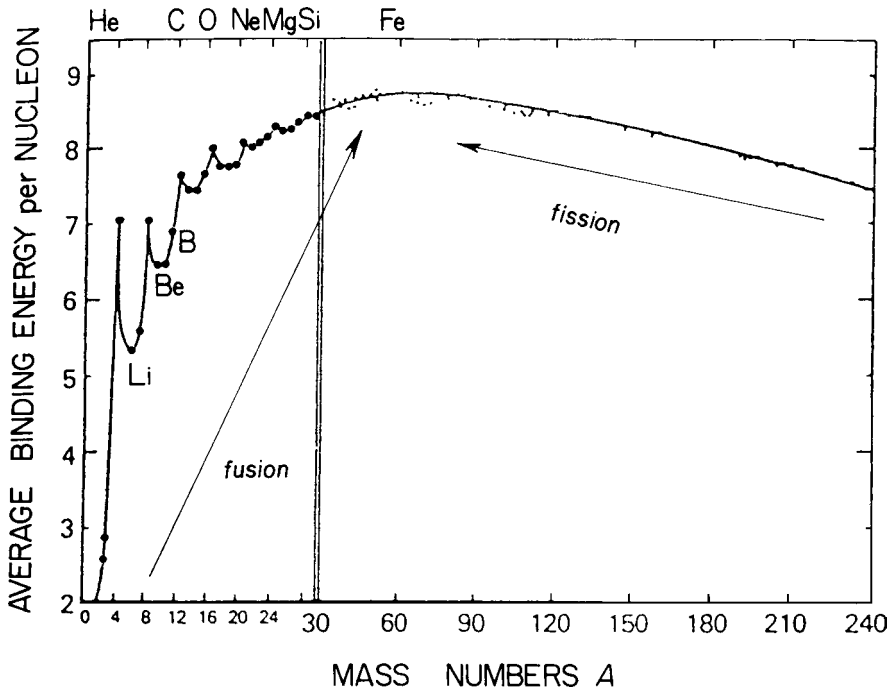
Fig. 1.3. Binding energy per nucleon as a function of mass number. Adapted from Rolfs and Rodney (1988).

violently unstable, owing to the nearby helium peak. Others are stable but only just: examples are D, ^{6,7}Li, ^{9}Be and ^{10,11}B, which are destroyed by thermonuclear reactions at relatively low temperatures.

(iii) Nuclear reactions involving charged particles (p, α etc.) require them to have enough kinetic energy to get through in spite of the electrostatic repulsion of the target nucleus (the 'Coulomb barrier'); the greater the charges, the greater the energy required. In the laboratory, the energy is supplied by accelerators, and analogous processes are believed to occur in reactions induced in the ISM by cosmic rays (see Chapter 9). In the interiors of stars, the kinetic energy exists by virtue of high temperatures (leading to *thermonuclear* reactions) and when one fuel (e.g. hydrogen) runs out, the star contracts and becomes hotter, eventually allowing a more highly charged fuel such as helium to 'burn'.

There is no Coulomb barrier for neutrons, but free neutrons are unstable so that they have to be generated *in situ*, which again demands high temperatures.

1.3 The local abundance distribution

Figure 1.4 shows the 'local Galactic' abundances of isobars, based on a combination of elemental and isotopic determinations in the Solar System with data from
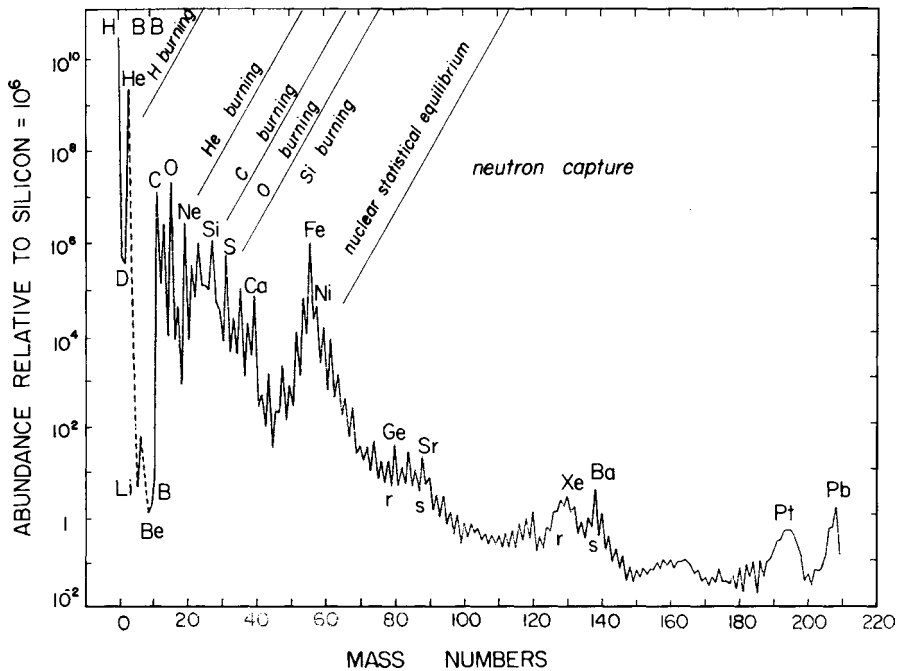
Fig. 1.4. The 'local Galactic' abundance distribution of nuclear species, normalized to 10^6 ^{28}Si atoms, adapted from Cameron (1982).

nearby stars and emission nebulae. These are sometimes referred to as 'cosmic abundances', but because there are significant variations among stars and between and across galaxies this term is best avoided. The curve shows a number of features that give clues to the origin of the various elements:

(i) Hydrogen is by far the most abundant element, followed fairly closely by helium. This is mainly formed in the Big Bang, with some topping up of the primordial helium abundance ($Y_P \simeq 0.25$) by subsequent H-burning in stars ($Y \simeq 0.28$ here and now). Only a small fraction ($Z \simeq 0.02$) of material in the ISM and in newly formed stars has been subjected to high enough temperatures and densities to burn helium.

(ii) The fragile nuclei Li, Be and B are very scarce, being destroyed in the harsh environment of stellar interiors, although some of them may also be created there. (The lithium abundance comes from measurements in meteorites; it is still lower in the solar photosphere because of destruction by mixing with hotter layers below.) On the other hand, they are much more abundant in primary cosmic rays as a result of $\alpha - \alpha$ fusion and spallation reactions between p, α and (mainly) CNO nuclei at high energies. The latter may also account for the production of some of these species in the ISM. Some ^{7}Li (about 10 per cent) is also produced in the Big Bang.

(iii) Although still more fragile than Li, Be and B, deuterium is vastly more abundant (comparable to Si and S). D is virtually completely destroyed in gas recycled through

stars and there are no plausible mechanisms for creating it there in such quantities, but it is nicely accounted for by the Big Bang. The observed abundance is a lower limit to the primordial abundance. The light helium isotope ^{3}He is the main product when deuterium is destroyed and can also be freshly produced in stars as well as destroyed. It has comparable abundance to D and some is made in the Big Bang, but in this case the interpretation of the observed abundance is more complicated.

(iv) Nuclei from carbon to calcium show a fairly regular downward progression modulated by odd:even and shell effects in nuclei which affect their binding energy (see Chapter 2). These are produced in successive stages of stellar evolution when the exhaustion of one fuel is followed by gravitational contraction and heating enabling the previous ashes to 'burn'. The onset of carbon burning, which leads to Mg and nearby elements, is accompanied by a drastic acceleration of stellar evolution due to neutrino emission caused by lepton and plasma processes at the high densities and temperatures required for such burning. The neutrinos directly escape from the interior of the star, in contrast to photons for which it takes of the order of 10^5 yr for their energy to reach the surface, and they eventually carry away energy almost as fast as it is generated by nuclear reactions; it is this rapid loss of energy[9] that speeds up the stellar evolution (see Chapter 5).[10]

(v) The iron-group elements show an approximation to nuclear statistical equilibrium at a temperature of several $\times 10^9$ K or several tenths of an MeV leading to the iron peak. This was referred to by B^{2}FH as the 'e-process' referring to thermodynamic equilibrium. Because the reactions are fast compared to β-decay lifetimes, the overall proton:neutron ratio remains fixed so that complete thermodynamic equilibrium does not apply here, but one has an approach to statistical equilibrium in which forward and reverse nuclear reactions balance. The iron peak in the abundance distribution is thought to result from explosive nucleosynthesis which may occur in one or other of two typical situations. One of these involves the shock that emerges from the core of a massive star that has collapsed into a neutron star; heat from the shock ignites the overlying silicon and oxygen layers in a Type II (or related) supernova outburst, and they are expelled with the aid of energetic neutrinos from the collapsed object ('neutrino heating' or 'drag'). Another possible cause is the sudden ignition of carbon in a white dwarf that has accreted enough material from a companion to bring it close to or over the Chandrasekhar mass limit (supernova Type Ia, often referred to as 'thermonuclear'). In either case, the quasi-equilibrium is frozen at a distribution characteristic of the highest temperature reached in the shock before the material is cooled by expansion, but the initial proton:neutron ratio is another important parameter. Calculations and observations both indicate that the dominant product is actually

---

[9] Sometimes referred to as 'neutrino cooling', although it does not in general lead to lower temperatures.

[10] Neutrinos are also generated by purely nuclear processes involving weak interactions, e.g. in the Sun. Such neutrinos can be an important cause of energy losses in compact stars through the 'Urca' process, in which an inverse β-decay is followed by a normal β-decay resulting in a neutrino–antineutrino pair.

^{56}Ni, the 'doubly magic' nucleus with equal numbers of protons and neutrons, which later decays via ^{56}Co into ^{56}Fe.

(vi) Once iron-group elements have been produced, all nuclear binding energy has been extracted and further gravitational contraction merely leads to photo-disintegration of nuclei with a catastrophic consumption of energy. This is one of several mechanisms that either drive or accelerate core collapse. By contrast, the thermonuclear explosion of a white dwarf simply leads to disintegration of the entire star.

Consequently, charged-particle reactions do not lead to significant nucleosynthesis beyond the iron group and the majority of heavier nuclei result from neutron captures. One or more such captures on a seed nucleus (in practice mostly ^{56}Fe) lead to the production of a β-unstable nucleus (e.g. ^{59}Fe) and the eventual outcome then depends on the relative timescales for neutron addition and β-decay. In the slow or s-process, neutrons are added so slowly that most unstable nuclei have time to undergo β-decay and nuclei are built up along the stability valley in Fig. 1.2 up to ^{209}Bi, whereafter α-decay terminates the process. In the rapid or r-process, the opposite is the case and many neutrons are added under conditions of very high temperature and neutron density, building unstable nuclei up to the point where (n, γ) captures are balanced by (γ, n) photo-disintegrations leading to a kind of statistical equilibrium modified by (relatively slow) β-decays. Eventually (e.g. after a SN explosion), the neutron supply is switched off and the products then undergo a further series of β-decays ending up at the nearest stable isobar, which will be on the neutron-rich side of the β-stability valley (Fig. 1.5). Some species have contributions from both r- and s-processes, while others are pure r (if by-passed by the s-process) or pure s (if shielded by a more neutron-rich stable isobar); the actinides (U, Th etc.) are pure r-process

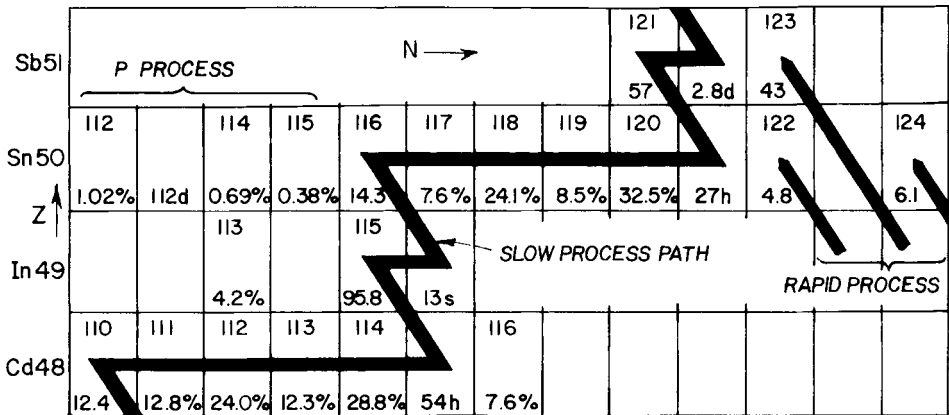**Fig. 1.5.** Paths of the r-, s- and p-processes in the neighbourhood of the tin isotopes. Numbers in the boxes give mass numbers and percentage abundance of the isotope for stable species, and β-decay lifetimes for unstable ones. ^{116}Sn is an s-only isotope, shielded from the r-process by ^{116}Cd. After Clayton *et al.* (1961). Copyright by Academic Press, Inc. Courtesy Don Clayton.

products. A few species on the proton-rich side of the stability valley are not produced by neutron captures at all and are attributed to what B^2FH called the 'p-process'; these all have very low abundances and are believed to arise predominantly from (γ, n) photo-disintegrations of neighbouring nuclei.

Neutron capture processes give rise to the so-called magic-number peaks in the abundance curve, corresponding to closed shells with 50, 82 or 126 neutrons (see Chapter 2). In the case of the s-process, the closed shells lead to low neutron-capture cross-sections and hence to abundance peaks in the neighbourhood of Sr, Ba and Pb (see Fig. 1.4), since such nuclei will predominate after exposure to a chain of neutron captures. In the r-process, radioactive progenitors with closed shells are more stable and hence more abundant than their neighbours and their subsequent decay leads to the peaks around Ge, Xe and Pt on the low-A side of the corresponding s-process peak.

1.4 Brief outline of stellar evolution

(i) An interstellar cloud collapses forming a generation of stars. The masses of the stars are spread over a range from maybe $0.01\,M_\odot$ or less to maybe $100\,M_\odot$ or so. The distribution function of stellar masses at birth, known as the 'initial mass function' (IMF), has more small stars than big ones.

(ii) The young stars, which appear as variable stars with emission lines known as T Tauri stars and related classes, initially derive their energy from gravitational contraction, which leads to a steady increase in their internal temperature (see Chapter 5). Eventually the central temperature becomes high enough ($\sim10^7\,$K or $1\,$keV) to switch on hydrogen burning and the star lies on the 'zero-age main sequence' (ZAMS) of the Hertzsprung–Russell (HR) diagram in which luminosity is plotted against surface temperature (Fig. 1.6). Stars spend most of their lives (about 80 per cent) in a main-sequence band stretching slightly upwards from the ZAMS; the corresponding time is short (a few $\times\ 10^6$ years) for the most massive and luminous stars and very long ($>10^{10}$ years) for stars smaller than the Sun, because the luminosity varies as a high power of the mass and so bigger stars use up their nuclear fuel supplies faster.

(iii) When hydrogen in a central core occupying about 10 per cent of the total mass is exhausted, there is an energy crisis. The core, now consisting of helium, contracts gravitationally, heating a surrounding hydrogen shell, which consequently ignites to form helium and gradually eats its way outwards (speaking in terms of the mass coordinate). At the same time, the envelope expands, making the star a red giant in the upper right part of the diagram.

(iv) Eventually, the contracting core becomes hot enough to ignite helium ($3\alpha \rightarrow {}^{12}C$; ${}^{12}C + {}^4He \rightarrow {}^{16}O$) and the core contraction is halted.

(v) In sufficiently big stars ($>\sim 10\,M_\odot$) this process repeats; successive stages of gravitational contraction and heating permit the ashes of the previous burning stage to be
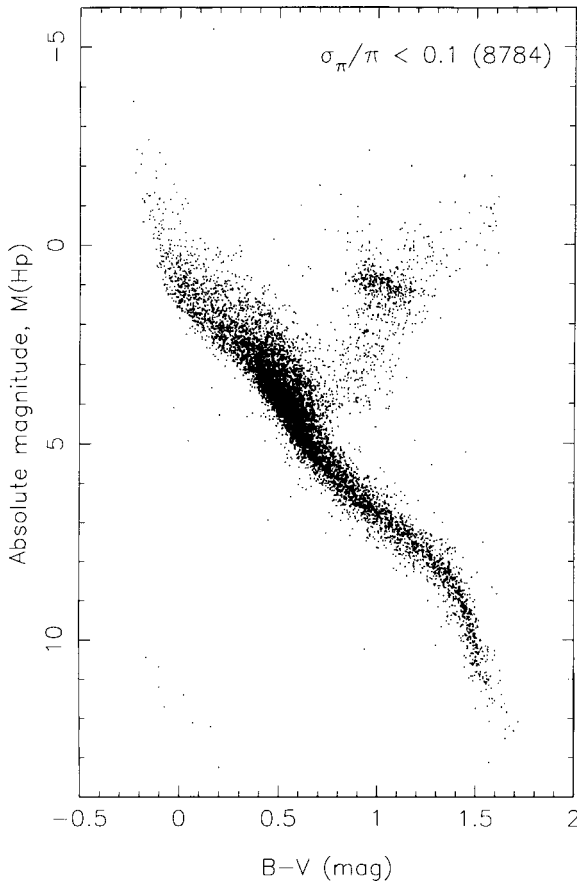
Fig. 1.6. HR diagram for nearby stars with well-known parallaxes (i.e. distances) from the HIPPARCOS astrometric satellite mission, after Perryman *et al.* (1995). The abscissa, B (blue)−V (visual) magnitude is a measure of 'redness' or inverse surface temperature ranging from about 2×10^4 K on the left to about 3000 K on the right, while the ordinate measures luminosity in the visual band expressed by absolute magnitude M_{Hp} in the HIPPARCOS photometric system. Luminosity decreases by a factor of 100 for every 5 units increase in M and the Sun's $M_V \simeq M_{Hp}$ is 4.8. The main sequence forms a band going from top left to bottom right in the diagram, with the ZAMS forming a lower boundary. Subgiants and red giants go upward and to the right from the MS and a few white dwarfs can be seen at the lower left. Courtesy Michael Perryman.

ignited leading to C, Ne, O and Si burning in the centre with less advanced burning stages in surrounding shells leading to an onion-like structure with hydrogen-rich material on the outside. Silicon burning leads to a core rich in iron-group elements and with a temperature of the order of 10^9 K, i.e. about 100 keV.

(vi) The next stage of contraction is catastrophic, partly because all nuclear energy supplies have been used up when the iron group is reached, and partly because the core, having

reached nearly the Chandrasekhar limiting mass for a white dwarf supported by electron degeneracy pressure, is close to instability and also suffers loss of pressure due to neutronization by inverse β-decays. Further contraction leads to photo-disintegration, which absorbs energy, and this leads to dynamical collapse of the core which continues until it reaches nuclear density and forms a neutron star. (If the mass of collapsing material is too large, then a black hole will probably form instead.) The stiff equation of state of nuclear matter leads to a bounce which sends a shock out into the surrounding layers. This heats them momentarily to high temperatures, maybe 5×10^9 K in the silicon layer, leading to explosive nucleosynthesis of iron-peak elements, mainly ^{56}Ni
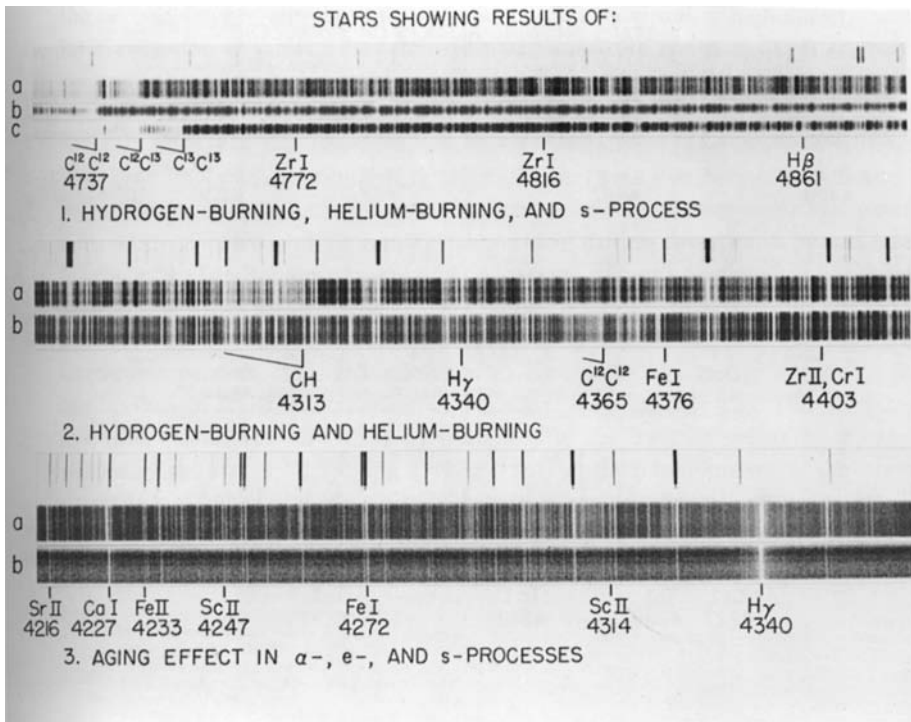
Fig. 1.7. Photographic (negative) spectra of stars showing various aspects of nucleosynthesis. Top: (a) carbon star X Cancri with ^{12}C/^{13}C $\simeq 4$ from H-burning by the CNO cycle and a suggestion of enhanced Zr; (b) peculiar carbon star HD 137613 without ^{13}C bands in which hydrogen is apparently weak (H-deficient carbon star); (c) carbon star HD 52432, with ^{12}C/^{13}C ~ 4. Middle: (a) normal carbon star HD 156074, showing the CH band and Hγ; (b) peculiar (H-poor) carbon star HD 182040 showing C_2 but weak Hγ and CH. Bottom: (a) normal F-type star ξ Pegasi (slightly hotter than the Sun); (b) old Galactic halo population star HD 19445 with similar temperature (shown by Hγ) but very low metal abundance (about 1/100 solar). After Burbidge, Burbidge, Fowler and Hoyle (B^{2}FH 1957). Courtesy Margaret and Geoffrey Burbidge.

(which later decays by electron capture and β^+ to ^{56}Fe); more external layers are heated to lower temperatures resulting in milder changes. Assisted by high-energy neutrinos, the shock expels the outer layers in a supernova explosion (Type II and related classes); the ejecta eventually feed the products into the ISM which thus becomes enriched in 'metals' in course of time. This scenario was first put forward in essentials by Hoyle (1946), and modern versions give a fairly good fit to the local abundances of elements from oxygen to calcium. The iron yield is uncertain because it depends on the mass cut between expelled and infalling material in the silicon layer, but can be parameterized to fit observational data, e.g. for SN 1987A in the Large Magellanic Cloud (LMC). The upshot is that iron-group elements are probably underproduced relative to local abundances, but the deficit is plausibly made up by contributions from supernovae of Type Ia. A subset of Type II supernovae may also be the site of the r-process (see Chapter 6).
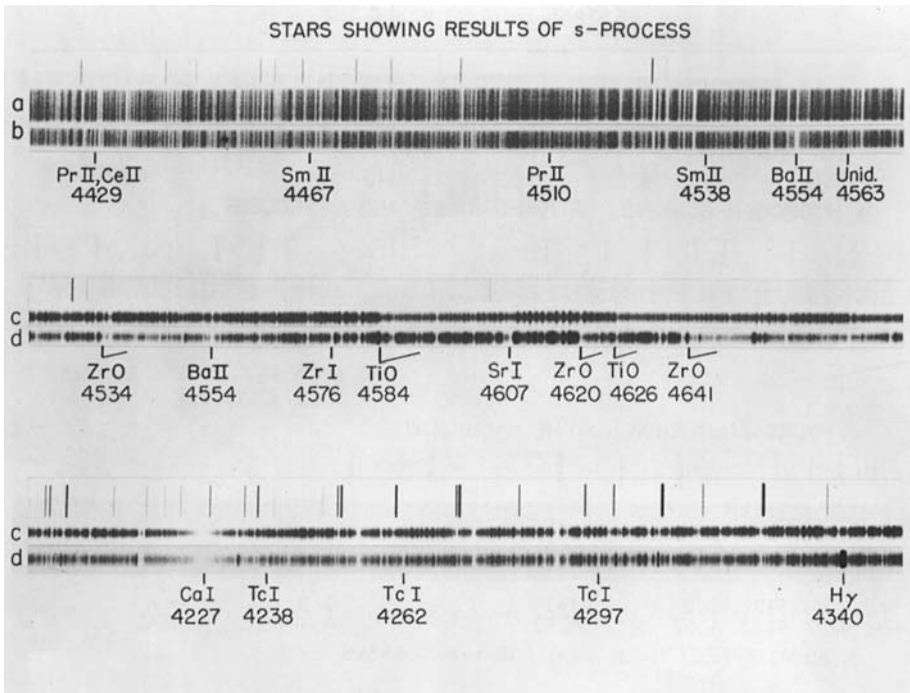
Fig. 1.8. Spectra showing effects of s-process. Top: (a) normal G-type giant κ Gem (similar temperature to the Sun); (b) Ba II star HD 46407, probably not an AGB star but affected by a companion which was. Middle: (c) M-type giant 56 Leo, showing TiO bands; (d) S-type AGB star R Andromedae showing ZrO bands, partly due to enhanced Zr abundance. Bottom: another spectral region of the same two stars showing Tc features in R And which indicate s-processing and dredge-up within a few half-lives of technetium 99 (2×10^5 yr) before the present. After B^{2}FH (1957). Courtesy Margaret and Geoffrey Burbidge.

(vii) For intermediate-mass stars (IMS), $\sim 1\,M_\odot \leq M \leq \sim 8\,M_\odot$, stages (i) to (iii) are much as before, but these never reach the stage of carbon burning because the carbon–oxygen core becomes degenerate first by virtue of high density, and later evolution is limited by extensive mass loss from the surface. After core helium exhaustion, these stars re-ascend the giant branch along the so-called asymptotic giant branch (AGB) track (see Fig. 5.15) with a double shell source: helium-burning outside the CO core and hydrogen-burning outside the He core. This is an unstable situation giving rise to thermal pulses or 'helium shell flashes' in which the two sources alternately switch on and off driving inner and outer convection zones (in which mixing takes place) during their active phases (see Chapter 5). The helium-burning shell generates ^{12}C and neutrons, either from ^{22}Ne$(\alpha, \text{n})^{25}$Mg or from ^{13}C$(\alpha, \text{n})^{16}$O, leading to s-processing, and the products are subsequently brought up to the surface in what is known as the third dredge-up process. This process leads to observable abundance anomalies in the spectra of AGB stars: carbon and S stars; see Figs. 1.7, 1.8. The products are then ejected into the ISM by mass loss in the form of stellar winds and planetary nebulae (PN), leaving a white dwarf as the final remnant. If the white dwarf is a member of a close binary system, it can occasionally be 'rejuvenated' by accreting material from its companion, giving rise to cataclysmic variables, novae and supernovae of Type Ia (see Chapter 5).

2

Thermonuclear reactions

Wie kann man einen Helium-Kern im Potenzial-Topf kochen?
R. d'E. Atkinson and F. G. Houtermans (1928),
paraphrased in Gamow and Critchfield (1949).

2.1 General properties of nuclei

Nuclear matter has an approximately constant density, the nuclear radius being about $R_0 A^{1/3}$ where $R_0 \simeq 1.2\,\mathrm{fm}$ (1 fm, Fermi or femtometre $= 10^{-13}\,\mathrm{cm}$) and the density $2.3 \times 10^{14}\,\mathrm{gm\,cm^{-3}}$ or $0.14\,\mathrm{amu\,fm^{-3}}$ (the atomic mass unit, amu, is defined as 1/12 of the mass of a neutral $^{12}\mathrm{C}$ atom). R_0 is of the order of the Compton wavelength of the π meson, $\hbar/m_\pi c = 1.4\,\mathrm{fm}$. Some properties of nuclei can be explained on the basis of Niels Bohr's 'liquid drop' model, but others depend on the very complicated many-body effects of interactions among the constituent nucleons. These, in turn, are partially explained by the shell model, in which each nucleon is assumed to move in the mean field caused by all the others and has quantum numbers analogous to those of electrons in an atom. Gross features of the β-stability valley (Fig. 1.2) and the binding-energy curve (Fig. 1.3) are summarized in the semi-empirical mass formula originally due to C. F. von Weizsäcker

$$M(A, Z) = Zm(^1\mathrm{H}) + (A - Z)m_n - \mathrm{B.E.}/c^2, \tag{2.1}$$

where M is the mass of the neutral atom, B.E. is the total binding energy, $c^2 = 931.5\,\mathrm{MeV\,amu^{-1}}$, and

$$\mathrm{B.E.} \simeq a_v A - a_s A^{2/3} - a_c Z(Z - 1)A^{-1/3} - a_{sym}\frac{(A - 2Z)^2}{A}$$

$$+ \frac{1 + (-1)^A}{2}(-1)^Z a_p A^{-3/4}. \tag{2.2}$$

Here $a_v \simeq 15.5\,\mathrm{MeV}$ represents a constant term in B.E. per nucleon, $a_s \simeq 16.8\,\mathrm{MeV}$ provides a surface term allowing for a reduced contribution to B.E. from

nucleons at the surface and $a_c \simeq 0.72\,\text{MeV} \simeq 0.6e^2/R_0$ allows for the electrostatic repulsion of the protons. $a_{sym} \simeq 23\,\text{MeV}$ gives a term favouring equal numbers of protons and neutrons, especially at low A, which arises in part from the Pauli Exclusion Principle and in part from symmetry effects in the interaction between nucleons. The last term, with $a_p \simeq 34\,\text{MeV}$, comes from a 'pairing force' due to the propensity of identical particles to form pairs with opposite spins. This last term permits several stable isobars to exist for even A.

To the extent that the nuclear potential is central, each nucleon has an orbital angular momentum ℓ as well as a spin $\mathbf{s}$, where $s = 1/2$, and total angular momentum $\mathbf{j}$. These combine by $j - j$ coupling to form the total nuclear 'spin' $\mathbf{I}$. Nuclear states are specified by their energy (relative to the ground state), and their spin and parity I^π, e.g. 0^+, where $\pi = (-1)^{\Sigma \ell}$. Because the individual j's of nucleons are half-integral, I is always an integer for even A and half-integral for odd A. The nuclear force is almost charge-independent, but depends on the relative orientation of particle spins and has a small non-central or tensor component. The force is of short range, overcoming the Coulomb repulsion of protons at distances $\sim R_0$, but becomes highly repulsive at shorter distances $< 0.5\,\text{fm}$ maintaining a nearly constant nuclear density.

Many significant properties of nuclear states are explained by the shell model, for which Maria G. Mayer and Hans Jensen shared the 1963 Nobel prize. This is patterned after the shell model of the atom, in which electrons fill consecutively the lowest lying available bound states and it is assumed that each nucleon effectively moves in a spherically symmetrical mean potential $V(r)$, giving it a definite orbital angular momentum quantum number ℓ and a quantum number n related to the number of nodes in the radial wave function. For the Coulomb potential, which does not apply here, the energy depends uniquely on the principal quantum number $N = n + \ell$. In the more general case, the energy depends on both n and ℓ, and n is simply used as a label to indicate successively higher energy states (starting with $n = 1$) for given ℓ, so we can have (using atomic notation) $1s, 2s \ldots, 1p,$ $2p \ldots$ etc.

Some simple models for $V(r)$ are shown in Fig. 2.1. Two crude approximations, the infinite square well (ISW) and the 3-dimensional harmonic oscillator (3DHO), have the advantage of leading to analytical solutions of the Schrödinger equation which lead to the following energy levels:

For ISW ($V = -V_0$ for $r < R$; $V = \infty$ for $r > R$), Clayton (1968) has given the approximation

$$E(n, \ell) \simeq -V_0 + \frac{\hbar^2}{2mR^2} \left[\pi^2 \left(n + \frac{\ell}{2} \right)^2 - \ell(\ell + 1) \right], \qquad (2.3)$$
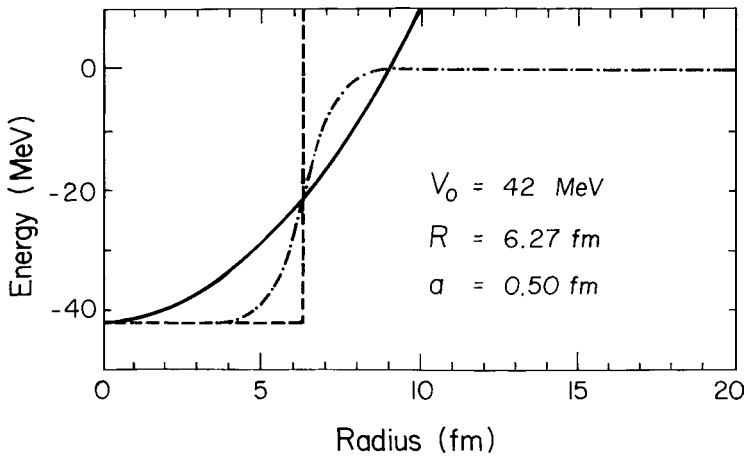
Fig. 2.1. Approximate potentials for the nuclear shell model. The solid curve represents the 3-dimensional harmonic oscillator potential, the dashed curve the infinite square well and the dot-dashed curve a more nearly realistic Woods–Saxon potential, $V(r) = -V_0/[1 + \exp\{(r - R)/a\}]$ (Woods & Saxon 1954). Adapted from Cowley (1995).

whereas for 3DHO ($V = -V_0 + \frac{1}{2}m\omega^2 r^2$),

$$E(n, \ell) = -V_0 + \hbar\omega\left(2n + \ell - \frac{1}{2}\right) \tag{2.4}$$

and the levels are highly degenerate. Figure 2.2 shows the resulting energy levels for the two cases, in which distinct energy gaps appear corresponding to closed shells of either protons or neutrons, each of which separately obey the Pauli principle. A more realistic form for $V(r)$ leads to energy levels intermediate between the two, shown on the left side of Fig. 2.3, but the higher cumulative occupation numbers above 20 do not correspond to reality. The solution to this problem came from the inclusion of a spin–orbit potential, analogous to the spin–orbit interaction that causes fine structure in atomic spectra, but in this case not of electromagnetic origin. Thus each (n, ℓ) level is split into two, with $j = \ell + s$ and $j = \ell - s$ respectively, and the splitting is proportional to $\boldsymbol{\ell}.\mathbf{s}$, for which the expectation value can be calculated by an elementary argument:

Since

$$\mathbf{j}^2 = (\boldsymbol{\ell} + \mathbf{s})^2 = \boldsymbol{\ell}^2 + 2\boldsymbol{\ell}.\mathbf{s} + \mathbf{s}^2, \tag{2.5}$$

$$\boldsymbol{\ell}.\mathbf{s} = \frac{1}{2}(\mathbf{j}^2 - \boldsymbol{\ell}^2 - \mathbf{s}^2) \tag{2.6}$$
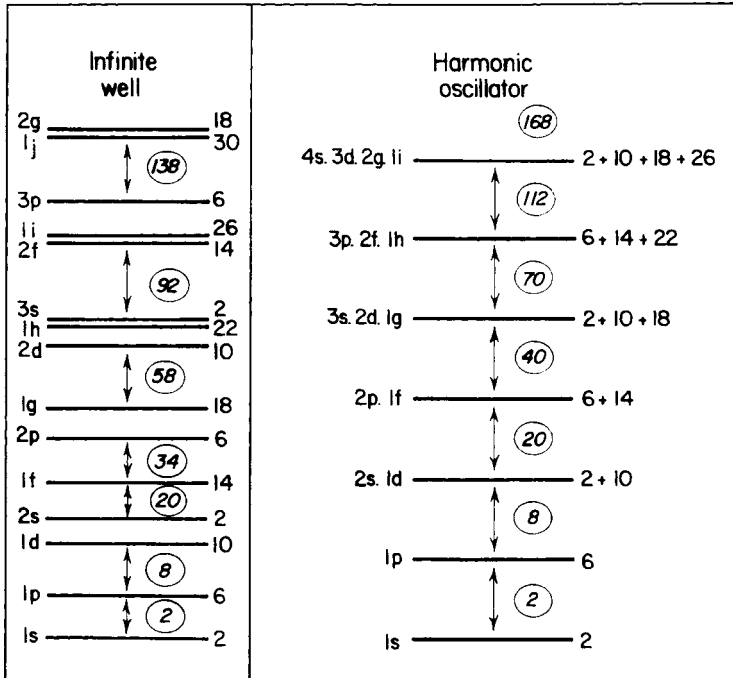
Fig. 2.2. Energy levels for ISW and 3DHO potentials. Each shows major gaps corresponding to closed shells and the numbers in circles give the cumulative number of protons or neutrons allowed by the Pauli principle. In a more realistic potential, the levels for given (n, ℓ) are intermediate between these extremes, in which the lower magic numbers 2, 8 and 20 are already apparent. Adapted from Krane (1987).

and its expectation value (in units of $\hbar^2$) is

$$\langle \boldsymbol{\ell}.\mathbf{s} \rangle = \frac{1}{2}[j(j+1) - \ell(\ell+1) - s(s+1)], \tag{2.7}$$

whence

$$\langle \boldsymbol{\ell}.\mathbf{s} \rangle_{\ell+1/2} - \langle \boldsymbol{\ell}.\mathbf{s} \rangle_{\ell-1/2} = \frac{1}{2}(2\ell+1) \tag{2.8}$$

so that the splitting increases with ℓ. Taking the higher j value to correspond to the lower energy (i.e. a negative coefficient of $\boldsymbol{\ell}.\mathbf{s}$ in the energy term, specifically $-13A^{-2/3}$ MeV) gives the correct magic numbers for shell closures shown on the right side of Fig. 2.3.

These shell closures have a profound influence on nuclear properties, in particular the binding energy (adding terms not accounted for in Eq. 2.2), particle separation energies and neutron capture cross-sections. The shell model also forms a basis for predicting the properties of nuclear energy levels, especially the ground

Intermediate form

Intermediate form with spin orbit
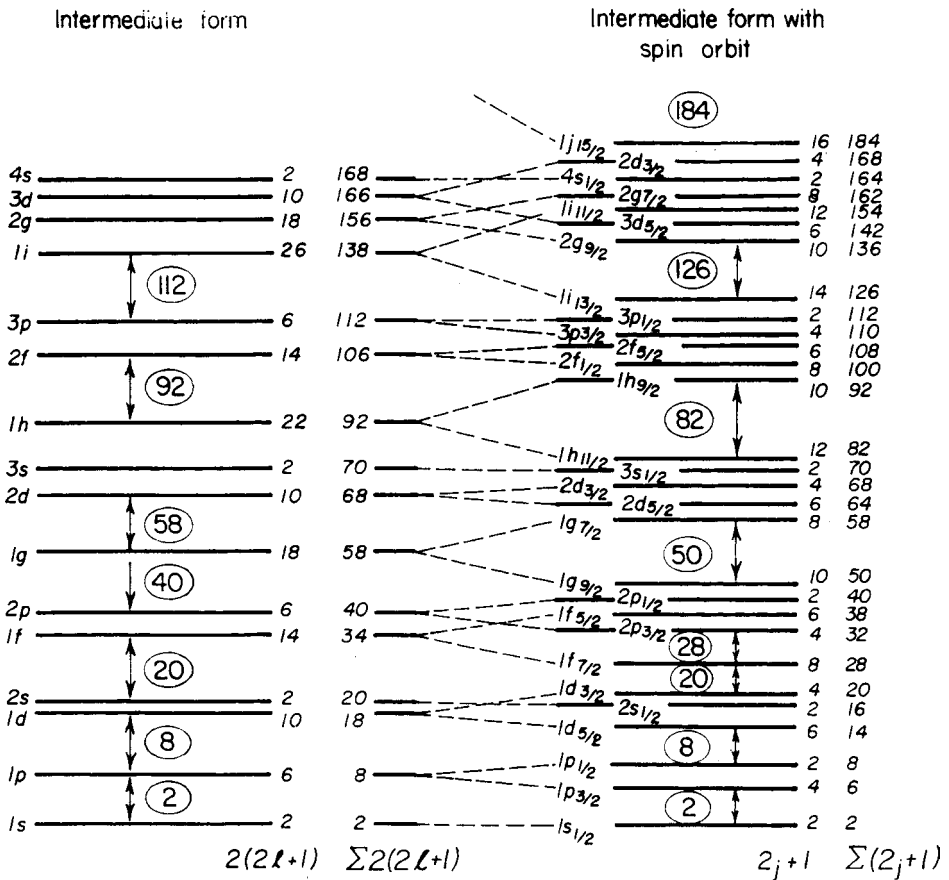
(84)

4s	2	168
3d	10	166
2g	18	156
1i	26	138

(112)

| 3p | 6 | 112 |
| 2f | 14 | 106 |

(92)

| 1h | 22 | 92 |

| 3s | 2 | 70 |
| 2d | 10 | 68 |

(58)

| 1g | 18 | 58 |

(40)

| 2p | 6 | 40 |
| 1f | 14 | 34 |

(20)

| 2s | 2 | 20 |
| 1d | 10 | 18 |

(8)

| 1p | 6 | 8 |

(2)

| 1s | 2 | 2 |

$2(2\ell+1)$ $\Sigma 2(2\ell+1)$

Right side (Intermediate form with spin orbit):

$1j_{15/2}$ — 16 184
$2d_{3/2}$ — 4 168
$4s_{1/2}$ — 2 164
$2g_{7/2}$ — 8 162
$1i_{11/2}$ — 12 154
$3d_{5/2}$ — 6 142
$2g_{9/2}$ — 10 136

(126)

$1i_{13/2}$ — 14 126
$3p_{1/2}$ — 2 112
$3p_{3/2}$ — 4 110
$2f_{5/2}$ — 6 108
$2f_{7/2}$ — 8 100
$1h_{9/2}$ — 10 92

(82)

$1h_{11/2}$ — 12 82
$3s_{1/2}$ — 2 70
$2d_{3/2}$ — 4 68
$2d_{5/2}$ — 6 64
$1g_{7/2}$ — 8 58

(50)

$1g_{9/2}$ — 10 50
$2p_{1/2}$ — 2 40
$1f_{5/2}$ — 6 38
$2p_{3/2}$ — 4 32

(28)

$1f_{7/2}$ — 8 28

(20)

$1d_{3/2}$ — 4 20
$2s_{1/2}$ — 2 16
$1d_{5/2}$ — 6 14

(8)

$1p_{1/2}$ — 2 8
$1p_{3/2}$ — 4 6

(2)

$1s_{1/2}$ — 2 2

$2j+1$ $\Sigma(2j+1)$

Fig. 2.3. At left, energy levels for a Woods–Saxon potential with $V_0 \simeq 50\,\text{MeV}$, $R = 1.25A^{1/3}$ fm and $a = 0.524$ fm, neglecting spin–orbit interaction. At right, the same with spin–orbit term included. Adapted from Krane (1987).

states. For even-A, even-Z nuclei, the pairing effect expressed by the a_{sym} term in Eq. (2.2) combines with the j-dependence of the energy levels to make all their ground states 0^+. For even-A, odd-Z nuclei, on the other hand, the extra proton and neutron have an overall symmetrical wave function in their respective coordinates (leading to a more compact wave function and hence lower energy than an anti-symmetrical one), with parallel spins. Thus among the few stable even-A, odd-Z nuclei (^{2}H, ^{6}Li, ^{10}B, ^{14}N), three have 1^+ ground states, while ^{10}B has 3^+.

In the case of odd-A nuclei, I^π in the ground state is fixed by the single 'valency' nucleon in the lowest vacant level shown in Fig. 2.3. In ^{15}O, for example, 8 protons fill closed shells up to $1p_{1/2}$, 6 neutrons fill closed shells up to $1p_{3/2}$ and the last neutron occupies $1p_{1/2}$ making the state $\frac{1}{2}^-$. In ^{17}O, on the other hand, all states up to $1p_{1/2}$ are filled by both protons and neutrons and the extra neutron occupies

$1d_{5/2}$, making the state $\frac{5}{2}^+$. These rules are generally valid for $A < 150$ and $190 < A < 220$; outside these ranges, cooperative effects of many single-particle shell-model states may combine to produce a permanent nuclear deformation, and even within them the single-particle shell model does not account for all excited states. A more general classification uses the concept of isospin which treats protons and neutrons as states of a single nucleon with $+1/2$ and $-1/2$ components along the z-axis of a spin-like vector in an abstract space.

2.2 Nuclear reaction physics

Typical reactions relevant to astrophysics are

- H-burning in the Big Bang ($T \simeq 10^9$ K, $kT \simeq 0.1$ MeV) and in stars (10^7 K $< T < 10^8$ K, 1 keV $< kT < 10$ keV).
- He-burning in stars ($T \simeq 10^8$ K, $kT \simeq 10$ keV).
- C-, Ne-, O-burning in stars (10^8 K $< T < 10^9$ K, 10 keV $< kT < 0.1$ MeV).
- Si-burning, hydrostatically near 10^9 K (0.1 MeV) and explosively at several times 10^9 K.
- Neutron capture in the Big Bang, s-process (a few $\times 10^8$ K) and r-process (a few $\times 10^9$ K).
- Spallation reactions, especially those involving cosmic rays in the ISM (non-thermal, with MeV to GeV energies). Spallation reactions are those in which one or a few nucleons are split off from a nucleus (see Chapter 9).

Figure 2.4 illustrates two kinds of generic nuclear reaction. A target labelled '1', which is in its ground state, is impacted by a projectile '2' with initial kinetic energy E in the centre-of-mass (CM) coordinate system, leading to a product '3' and ejecta '4' with energy E'. The reaction is summarized in compact notation as $1(2,4)3$, e.g. $^{15}\text{N}(p,\alpha)^{12}\text{C}$. The energy released, $E' - E$, is usually called Q, and

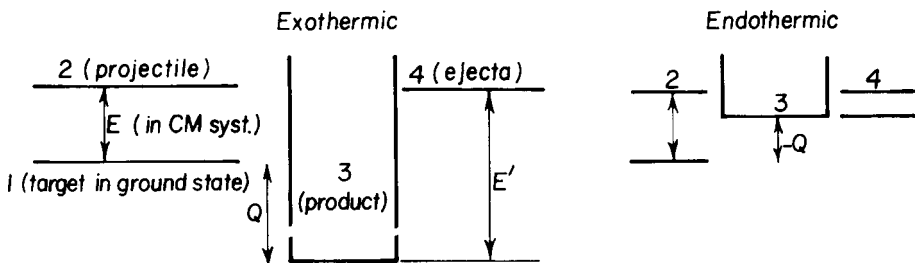$$Q = c^2(M_1 + M_2 - M_3 - M_4), \tag{2.9}$$

Fig. 2.4. Schematic illustration of a generic nuclear reaction.

where $c^2 = 931.5\,\text{MeV amu}^{-1}$ and the reaction is said to be exothermic or endothermic according to whether Q is positive or negative. The value of Q can be deduced from tables of nuclear masses, and the CM kinetic energy is $\frac{1}{2}mv^2$, where m is the reduced mass $M_1 M_2/(M_1 + M_2)$ and v the relative velocity, since relativistic effects are negligible for nuclear particles at the relevant energies. Nuclear reactions are subject to the standard conservation laws in addition to that of mass–energy, i.e. conservation of linear and angular momentum, parity, baryon and lepton numbers and isospin, except that parity and isospin are not always conserved in weak interactions.

The probability of a particular reaction (or scattering) taking place is measured by the relevant cross-section, which can be thought of in classical terms as the cross-sectional area of a sphere that has the same probability of being hit. The corresponding nuclear dimensions would be of order

$$
\begin{aligned}
\pi (R_1 + R_2)^2 &= \pi [1.2 \times 10^{-13}(A_1^{1/3} + A_2^{1/3})\,\text{cm}]^2 \\
&= 4.5 \times 10^{-26}(A_1^{1/3} + A_2^{1/3})^2\,\text{cm}^2 \\
&\sim 10^{-24}\,\text{cm}^2 \equiv 1\,\text{barn},
\end{aligned}
\tag{2.10}
$$

but at relevant energies the cross-section is in fact related to the de Broglie wavelength and mutual orbital angular momentum of the particles. The incoming particle is represented quantum-mechanically as a plane wave which in turn can be decomposed into a series of spherical waves characterized by their angular momentum quantum number ℓ, corresponding to an impact parameter r_ℓ where

$$
mv\,r_\ell = \ell\hbar,
\tag{2.11}
$$

i.e. the impact parameters are quantized in units of the reduced de Broglie wavelength $\bar{\lambda} = \hbar/mv$. A semi-classical interpretation is that the plane of impact parameters is divided into zones of differing values of ℓ as shown in Fig. 2.5. The area of the ℓth zone, which is the total cross-section for given ℓ, is then

$$
\pi (\hbar/mv)^2 [(\ell + 1)^2 - \ell^2] = \pi (\hbar/mv)^2 (2\ell + 1).
\tag{2.12}
$$

Thus for an s-wave ($\ell = 0$), which corresponds to hitting the bull's eye and so usually dominates unless forbidden by selection rules or upstaged by a resonance, the total cross-section (of which the major component is normally elastic scattering) is given by

$$
\sigma_{1,2\,tot} = (1 + \delta_{12})\pi \bar{\lambda}^2 = (1 + \delta_{12})\frac{65.7}{AE}\,\text{barn},
\tag{2.13}
$$

where A is the reduced mass in amu and E in keV. The factor $(1+\delta_{12})$ comes from the fact that, when two identical particles interact, the cross-section is doubled because either of them can be identified as the projectile or as the target. Actual
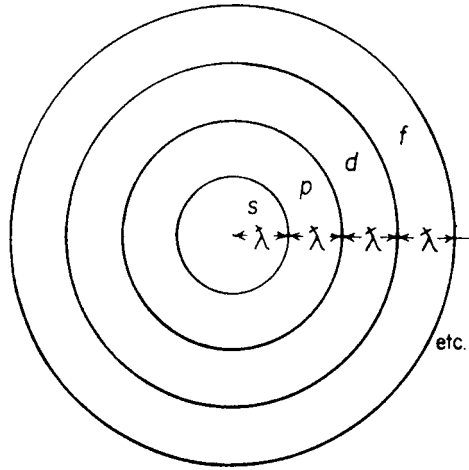
Fig. 2.5. Dependence of total reaction cross-section on the angular momentum quantum number.

cross-sections vary widely according to the nature of the interaction involved, e.g. for $E = 2\,\mathrm{MeV}$ some characteristic cross-sections are as follows:

- for $^{15}\mathrm{N}(p, \alpha)^{12}\mathrm{C}$, $\sigma = 0.5\,\mathrm{b}$ (strong nuclear force);
- for $^{3}\mathrm{He}(\alpha, \gamma)^{7}\mathrm{Be}$, $\sigma \simeq 10^{-6}\,\mathrm{b}$ (electromagnetic interaction);
- for $p(p, e^{+}\nu)d$, $\sigma \simeq 10^{-20}\,\mathrm{b}$ (weak force, based on theoretical calculations, since the rate is too small to be measured).

2.3 Non-resonant reactions

Reactions may be either 'direct', where an energetic particle has such a small wavelength that it only 'sees' one nucleon of the target, or 'compound nucleus' reactions, where the projectile's energy is shared among many nucleons in successive collisions within a compound nucleus which can then decay into one of a number of 'exit channels' (Fig. 2.6). The first case is the more common one in reactions between light nuclei, whereas the second dominates for heavier ones.

A compound-nucleus reaction can be described as

$$1 + 2 \rightarrow C \rightarrow 3 + 4 + Q \tag{2.14}$$

and the cross-section results from the joint probability that the compound nucleus is formed from $1 + 2$ and that it then decays into the channel $3 + 4$, i.e.

$$\sigma = \sigma_{tot}\, \omega \mid \langle 3, 4 \mid H_{II} \mid C \rangle \langle C \mid H_{I} \mid 1, 2 \rangle \mid^{2}, \tag{2.15}$$

where $\omega = (2I_3 + 1)(2I_4 + 1)/[(2I_1 + 1)(2I_2 + 1)]$ is the statistical-weight factor (obtained by averaging over initial states and summing over final states).
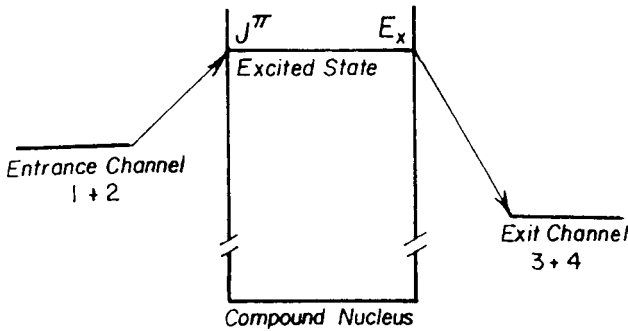
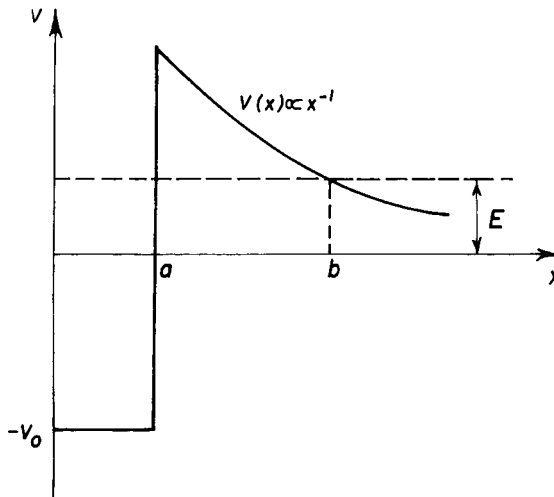**Fig. 2.6.** Schematic of a compound-nucleus reaction.

Fig. 2.7. Coulomb barrier penetration by a charged particle. a is the range of the nuclear force and b the classical turning point.

The matrix elements in angle brackets contain nuclear factors and (in the case of charged particles) the Coulomb barrier penetration probabilities or Gamow factors, originally calculated in the theory of α-decay, which can be roughly estimated as follows (Fig. 2.7).

A particle with energy E moving one-dimensionally along the negative x-axis in a potential $V(x)$ is described quantum-mechanically by a plane wave

$$\Psi = A\,e^{i(\omega t + kx)} = A\,e^{\frac{i}{\hbar}(Et + \sqrt{[2m(E-V)]}x)}. \tag{2.16}$$

The probability current is conserved for $E > V$. When penetrating the barrier, $E - V$ becomes negative and $\Psi^*\Psi$ decays as $e^{-(2/\hbar)\sqrt{[2m(V(x)-E)]}\delta x}$ as the particle moves from position $x + \delta x$ to position x. The total probability of

barrier penetration (neglecting angular momentum which supplies an additional 'centrifugal' barrier) then includes a factor e^{-G}, where

$$G = \frac{2}{\hbar} \int_a^b \sqrt{[2m(V(x) - E)]} \, dx = \frac{2(2mE)^{1/2}}{\hbar} \int_a^b \sqrt{\left(\frac{b}{x} - 1\right)} \, dx \quad (2.17)$$

and

$$b = \frac{Z_1 Z_2 e^2}{E} = \frac{2Z_1 Z_2 e^2}{mv^2} \quad (2.18)$$

is the classical turning point. The integral can be evaluated by an elementary trigonometric substitution, giving

$$G = \frac{4Z_1 Z_2 e^2}{\hbar v} [\arccos \sqrt{(a/b)} - \sqrt{(a/b)}\sqrt{(1 - a/b)}]. \quad (2.19)$$

Since $a \ll b$ (typically by a factor of order 100), the factor in brackets is nearly $\pi/2$ and is quite insensitive to the value of a. Numerically, the barrier penetration probability for s-waves is thus

$$P \propto e^{-2\pi Z_1 Z_2 e^2/(hv)} \equiv e^{-2\pi \eta} = e^{-BE^{-1/2}} \quad (2.20)$$

where

$$B = (2m)^{\frac{1}{2}} \pi Z_1 Z_2 e^2/\hbar = 31.3 \, Z_1 Z_2 A^{\frac{1}{2}}; \quad (2.21)$$

A is the reduced mass in amu and E is in keV. For example, for 1 keV protons, $P \sim 10^{-9}$, but the penetration probability is enhanced at high densities by electron screening effects. At very high densities, so-called pycnonuclear reactions occur, even at low temperatures, owing to quantum tunnelling and kinetic energy from vibrations in a solid lattice. Pycnonuclear reactions set in quite suddenly above a certain critical density, which (in gm cm^{-3}) is of the order of 10^6 for hydrogen, 10^9 for He and 10^{10} for C; such densities can be reached in accreting white dwarfs and advanced burning stages of massive stars.

The steep dependence of P on energy leads to the use of the 'astrophysical S-factor' defined by

$$\sigma(E) = \frac{1}{E} e^{-2\pi \eta} S(E), \quad (2.22)$$

which contains the purely nuclear part of the cross-section, plus factors of a few in the barrier penetration probability, and varies only slowly with E in the absence of resonances. Laboratory measurements of cross-sections, which usually have to be carried out at higher energies than those mostly relevant in stars, are converted into $S(E)$ to facilitate extrapolation to these lower energies (Fig. 2.8).
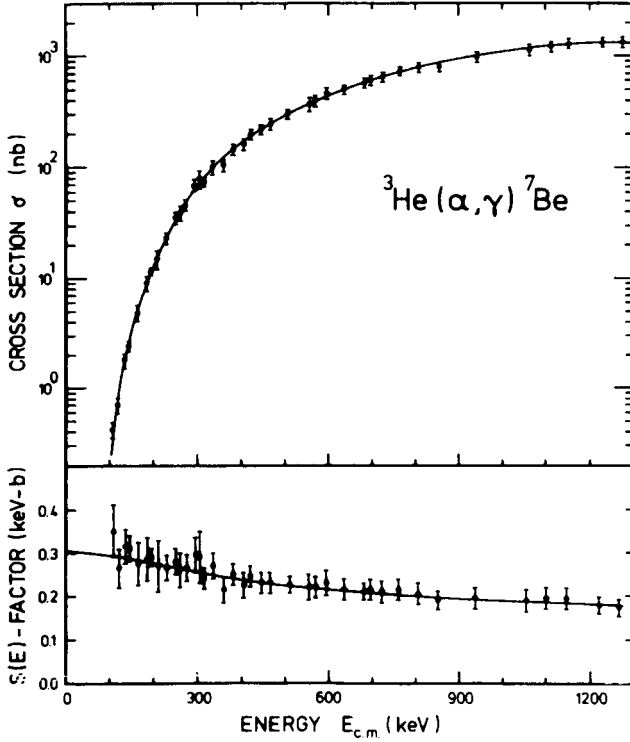
Fig. 2.8. Energy dependence of the cross-section and of $S(E)$ for a typical nuclear reaction. The extrapolation of $S(E)$ to zero energy is carried out with the aid of theory. After Rolfs and Rodney (1988). Copyright by the University of Chicago. Courtesy Claus Rolfs.

A more exact expression for the barrier penetration factor, derived for example by Clayton (1968), is

$$P_\ell(E) = \left(\frac{E_c}{E}\right)^{1/2} \exp\left[-BE^{-1/2} + 4\left(\frac{E_c}{\hbar^2/2mR^2}\right)^{1/2} - 2\left(\ell + \frac{1}{2}\right)^2 \left(\frac{\hbar^2/2mR^2}{E_c}\right)^{1/2} \right] \tag{2.23}$$

or numerically

$$P_\ell(E) = \left(\frac{E_c}{E}\right)^{1/2} \exp[-BE^{-1/2} + 1.05(ARZ_1Z_2)^{1/2}$$
$$- 7.62\left(\ell + \frac{1}{2}\right)^2 (ARZ_1Z_2)^{-1/2}] \tag{2.24}$$

where

$$E_c = \frac{Z_1Z_2e^2}{R} = 1.0\frac{Z_1Z_2}{A_1^{1/3} + A_2^{1/3}} \text{ MeV} \tag{2.25}$$

is the height of the Coulomb barrier and R is in fm.

2.4 Sketch of statistical mechanics

Many situations in both nuclear and other parts of astrophysics can be treated to a greater or lesser degree of approximation using concepts of thermodynamic equilibrium. An obvious example is the velocity distribution in classical plasmas, which is Maxwellian to a high degree of approximation under a very wide range of conditions because of the high frequency of elastic collisions, but there are many others. In nuclear reactions at very high temperatures, many reverse reactions proceed with almost the same frequency as forward reactions, leading to a situation of quasi-equilibrium between abundances of the relevant nuclei. Excitation and ionization of atoms, and the dissociation of molecules, follow very precisely thermal equilibrium relations in stellar interiors, and these relations also provide a more or less usable first approximation in stellar atmospheres which is known as local thermodynamic equilibrium. This section therefore gives a brief sketch of relevant parts of statistical thermodynamics, which will have many applications in what follows.

Consider N fermions in a box with fixed energy levels $\tilde{E}_i$ (including rest-mass which itself includes internal excitation energy). To each $\tilde{E}_i$ there correspond ω_i distinct (degenerate) states, made up of g_i internal states and $4\pi V p^2 dp / h^3$ kinetic degrees of freedom, where p is momentum and V is the volume.

Because fermions are indistinguishable and satisfy the Pauli Exclusion Principle, the number of different ways in which each set of ω_i states with energy $\tilde{E}_i$ can have N_i of them occupied is

$$W(N_i, \tilde{E}_i) = \prod_i C_{N_i}^{\omega_i} = \prod_i \frac{\omega_i!}{N_i!\,(\omega_i - N_i)!}. \tag{2.26}$$

Stirling's formula for huge numbers is

$$n! \simeq n^n e^{-n} \tag{2.27}$$

so

$$\ln W = \sum_i [\omega_i \ln \omega_i - N_i \ln N_i - (\omega_i - N_i)\ln(\omega_i - N_i)]. \tag{2.28}$$

Thermal equilibrium implies that, under fixed conditions, W takes on its maximum possible value, i.e.

$$0 = \delta \ln W = \sum_i \delta N_i \, \ln\left(\frac{\omega_i}{N_i} - 1\right) \tag{2.29}$$

subject to overall conditions

$$\sum_i N_i = N, \tag{2.30}$$

the total number (which becomes irrelevant in cases where particles are easily created and destroyed), and

$$\sum_i N_i \tilde{E}_i = \tilde{E}, \tag{2.31}$$

the total energy.

These conditions are incorporated into the stationary condition (2.29) using Lagrange multipliers

$$\sum_i \delta N_i \left[\ln \left(\frac{\omega_i}{N_i} - 1 \right) - \alpha - \beta \tilde{E}_i \right] = 0 \quad \forall \, \delta N_i, \tag{2.32}$$

whence

$$N_i = \frac{\omega_i}{e^{\alpha + \beta \tilde{E}_i} + 1}. \tag{2.33}$$

We now appeal to Boltzmann's entropy postulate

$$S = k \ln W \tag{2.34}$$

and let a small reversible change take place. Specifically, we allow some heat and particles to enter a cylinder containing perfect gas at a fixed temperature and pressure. This will lead to a variation in the ω_i's by virtue of the volume change, and

$$\begin{aligned} \delta S &= k \sum_i \delta N_i \, \ln \left(\frac{\omega_i}{N_i} - 1 \right) - k \sum_i \delta \omega_i \, \ln \left(1 - \frac{N_i}{\omega_i} \right) \\ &= k(\alpha \delta N + \beta \delta \tilde{E} + \frac{N}{V} \delta V - \cdots). \end{aligned} \tag{2.35}$$

Considering this thought-experiment from the point of view of thermodynamics, the additional particles add enthalpy,

$$dH \equiv d(G + TS) = d\tilde{E} + PdV, \tag{2.36}$$

where G is the Gibbs free energy, i.e.

$$T \, dS = d\tilde{E} + PdV - \sum_j \mu_j dN_j. \tag{2.37}$$

μ_j is the *chemical potential* of particle species j which is just the specific Gibbs free energy per particle dG/dN_j.[1] Carrying out some divisions in Eq. (2.37),

$$\left(\frac{\partial S}{\partial \tilde{E}} \right)_{V,N_j} = k\beta = \frac{1}{T}; \quad \left(\frac{\partial S}{\partial N_j} \right)_{\tilde{E},V} = k\alpha = -\frac{\mu_j}{T}. \tag{2.38}$$

---

[1] This case is more rigorously treated in the theory of the 'Grand Canonical Ensemble', which consists of a number of identical systems that are able to exchange heat and particles with a common thermal bath.

Therefore

$$\beta = \frac{1}{kT}, \quad \alpha = -\frac{\mu}{kT} \tag{2.39}$$

for a particular species, leading to the Fermi–Dirac distribution (per unit volume)

$$n_i(\tilde{E}) d\tilde{E} = \frac{g_i}{h^3} \frac{4\pi p^2 dp}{e^{(\tilde{E}-\mu)/kT} + 1} \tag{2.40}$$

$$= \frac{4\pi g_i}{(hc)^3} \frac{\tilde{E}(\tilde{E}^2 - m^2 c^4)^{1/2} d\tilde{E}}{e^{(\tilde{E}-\mu)/kT} + 1}, \tag{2.41}$$

where we have used the exact relativistic expression $\tilde{E}^2 = m^2 c^4 + p^2 c^2$. $g_i = 2$ for free electrons etc. and in general g_i is the statistical weight of some internal energy level for nuclei, atoms and molecules. A similar expression can be derived for bosons (particles with integral spin), but with -1 in the denominator instead of $+1$;[2] for photons, $\mu = m = 0$.

Consider a non-degenerate ($\mu \ll mc^2$), non-relativistic ($\tilde{E} = mc^2 + p^2/2m$) gas. The total number density is

$$n = \frac{4\pi u}{h^3} e^{(\mu - mc^2)/kT} \int_0^\infty p^2 e^{-p^2/2mkT} dp \tag{2.42}$$

$$= \left(\frac{mkT}{2\pi\hbar^2}\right)^{3/2} u\, e^{(\mu - mc^2)/kT} \tag{2.43}$$

where u is the internal partition function $\sum_i g_i e^{-(\tilde{E}_i - \tilde{E}_1)/kT}$, or

$$\mu = kT \ln\left[n \Big/ \left\{ u\, e^{-mc^2/kT} \left(\frac{mkT}{2\pi\hbar^2}\right)^{3/2} \right\} \right] \equiv mc^2 + kT \ln[n/(un_Q)]. \tag{2.44}$$

$n_Q \equiv (mkT/2\pi\hbar^2)^{3/2}$ is called the *quantum concentration*. Replacing g_i by u in Eq. (2.40) and dividing by Eq. (2.43) gives the Maxwellian velocity distribution function

$$\frac{n(v)dv}{n} = \left(\frac{m}{2\pi kT}\right)^{3/2} 4\pi v^2 e^{-\frac{1}{2}mv^2/kT} dv. \tag{2.45}$$

For two particles having masses m_1, m_2, the distribution function of relative velocity is obtained by substituting for m the reduced mass $m_1 m_2/(m_1 + m_2)$ (see Problem 6 at the end of this chapter).

In the application to chemical equilibrium, we consider a generic reaction of the form

$$AB \rightleftharpoons A + B \tag{2.46}$$

---

[2] As can readily be derived by substituting in Eq. (2.26) $W(N_i, \tilde{E}_i) = \prod_i C_{N_i}^{\omega_i + N_i}$.

(nuclear disintegration, atomic ionization, molecular dissociation). This is in equilibrium when the (Gibbs) free energy is a global minimum with respect to the numbers on each side, i.e. the total chemical potentials are the same on both sides:

$$\delta G = \mu_A \delta N_A + \mu_B \delta N_B + \mu_{AB} \delta N_{AB} = \delta N_A (\mu_A + \mu_B - \mu_{AB}) = 0 \quad \forall \, \delta N_A. \tag{2.47}$$

In combination with expression (2.44) for μ, this leads to Saha's equation (aka the Law of Mass Action) in the form

$$\frac{n_A n_B}{n_{AB}} = \frac{u_A u_B}{u_{AB}} \left(\frac{m_A m_B}{m_{AB}} \frac{kT}{2\pi\hbar^2} \right)^{3/2} e^{(m_{AB} - m_A - m_B)c^2/kT}. \tag{2.48}$$

2.5 Thermonuclear reaction rates

In a hot plasma, the reaction rate per unit volume between particles of types i and j is

$$r_{ij} = n_i n_j (1 + \delta_{ij})^{-1} <\sigma v>_{ij} \tag{2.49}$$

where n_i, n_j are the respective number densities and $<\sigma v>$ is the velocity-averaged product of cross-section and relative velocity, also known as the rate coefficient. The factor $(1 + \delta_{ij})^{-1}$ comes from the fact that, if i and j are identical, the number density of particle pairs is $n(n-1)/2 \simeq n^2/2$. Nucleus i has a corresponding mean life

$$\tau_i = \left(\sum_j n_j <\sigma v>_{ij} \right)^{-1} \tag{2.50}$$

without the $(1 + \delta_{ij})$ factor. Number densities are related to the total mass density ρ by

$$n_i = 6.02 \times 10^{23} \rho X_i / A_i \equiv 6.02 \times 10^{23} \rho Y_i, \tag{2.51}$$

where ρ is in gm cm^{-3} and X_i is the abundance by mass fraction of nucleus i with atomic mass number A_i. The net energy production per unit mass is

$$\epsilon = (r_{ij} - r_{ji}) Q / \rho - \text{neutrino losses}. \tag{2.52}$$

Averaging over the Maxwell distribution,

$$<\sigma v> = (8/\pi m)^{1/2} (kT)^{-3/2} \int_0^\infty E\sigma(E) e^{-E/kT} dE. \tag{2.53}$$

For non-resonant reactions, the *S*-factor defined in Eq. (2.22) is a slowly varying quantity which can be replaced by an appropriate mean value, i.e.

$$<\sigma v> = (8/\pi m)^{1/2} (kT)^{-3/2} <S(E)> \int_0^\infty e^{-\frac{E}{kT}-2\pi\eta} dE. \qquad (2.54)$$

(For endothermic reactions, the lower limit of integration is $-Q$.) Now from Eq. (2.20) it is easily derived that the integrand of Eq. (2.54), expressed as

$$f(E) = e^{-(\frac{E}{kT}+BE^{-1/2})} \qquad (2.55)$$

(where *B* is given by Eq. 2.21) has a maximum for an energy

$$E_0 = (BkT/2)^{2/3} \qquad (2.56)$$

where its value is

$$f(E_0) = e^{-(B^2/kT)^{1/3}(2^{1/3}+2^{-2/3})} = e^{-3E_0/kT} \equiv e^{-\tau}, \qquad (2.57)$$

and

$$\tau \equiv 3 (B/2kT)^{2/3}. \qquad (2.58)$$

This is known as the 'Gamow peak'. Owing to the two contrary exponential dependences on energy in Eq. (2.55), reaction rates are significant only for particles in a more or less narrow range of energy around E_0, which is much larger than kT (see Fig. 2.9), but still usually small compared to energies at which cross-sections can be measured in the laboratory. The integral can be approximated by the 'method of steepest descents' in which $f(E)$ is approximated by a Gaussian with the same peak value and the same second derivative at that peak, i.e.

$$\int_0^\infty f(E)\, dE \simeq f(E_0)\sqrt{[2\pi f(E_0)/ - f''(E_0)]} = \frac{2}{3}\pi^{1/2} kT\, \tau^{1/2}\, e^{-\tau}. \qquad (2.59)$$

Owing to the asymmetry in $f(E)$, the best value to take for $<S(E)>$ turns out to be $S(E_0' \simeq E_0 + \frac{5}{6}kT)$ rather than $S(E_0)$. Making all the substitutions in Eq. (2.54) one finds

$$<\sigma v> \simeq \frac{8}{81} \frac{\hbar}{\pi Z_1 Z_2 e^2 m} \tau^2 e^{-\tau} S(E_0') = \frac{7.2\times10^{-19}}{AZ_1Z_2} \tau^2 e^{-\tau} S(E_0')\ \text{cm}^3\ \text{s}^{-1},$$
$$(2.60)$$

where $S(E_0')$ is in keV barns, and

$$\tau = 3E_0/kT = 19.7\,(Z_1^2 Z_2^2 A/T_7)^{1/3} \qquad (2.61)$$

where T_7 is in units of 10^7 K.

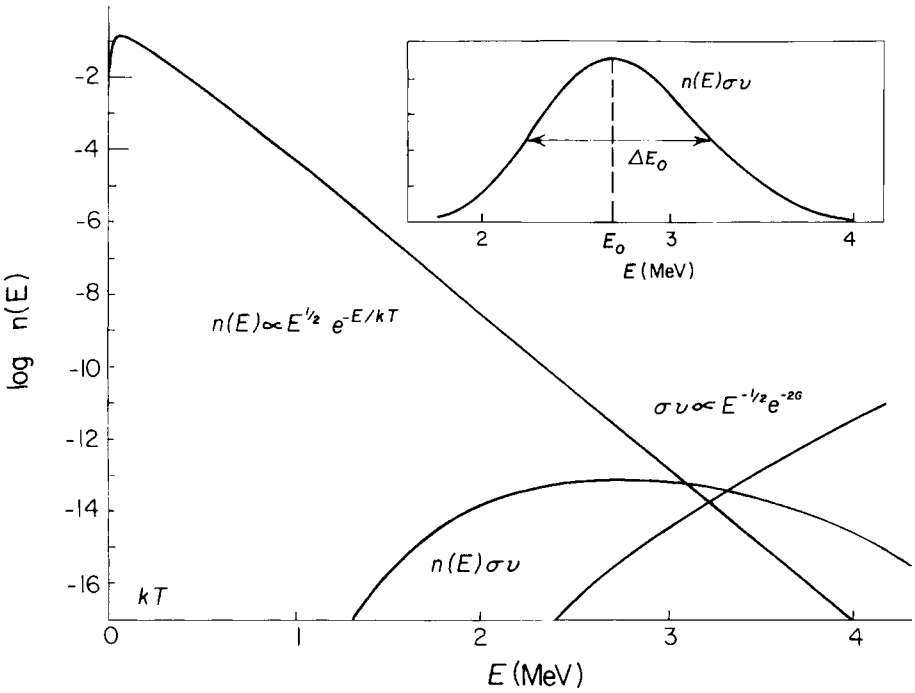From Eqs. (2.60), (2.61), one can deduce an approximate power-law dependence of specific reaction rates on temperature, T^ν, since

Fig. 2.9. Dependence of particle number and barrier penetration probability on energy for $^{12}C + {}^{12}C$ at a temperature $kT = 100\,\text{keV}$. In this case, the energy at the Gamow peak, shown on a linear scale in the inset, is well within the range of typical laboratory energies. Adapted from Krane (1987).

$$\nu \equiv \frac{\partial \log <\sigma v>}{\partial \log T} = \frac{\tau - 2}{3}. \tag{2.62}$$

For example, in the interior of the Sun ($T_7 = 1.5$; $kT = 1.3\,\text{keV}$), one has the following:

Reaction	$E_0(\text{keV})$	τ	ν
$p + p$	5.9	13.7	3.9
$p + {}^{14}N$	27	63	20

These temperature dependences are illustrated in Fig. 5.5.

2.6 Resonant reactions

When the compound nucleus has an excited level coinciding in energy with that of the projectile in the CM system, i.e. the projectile energy E is close to E_P where
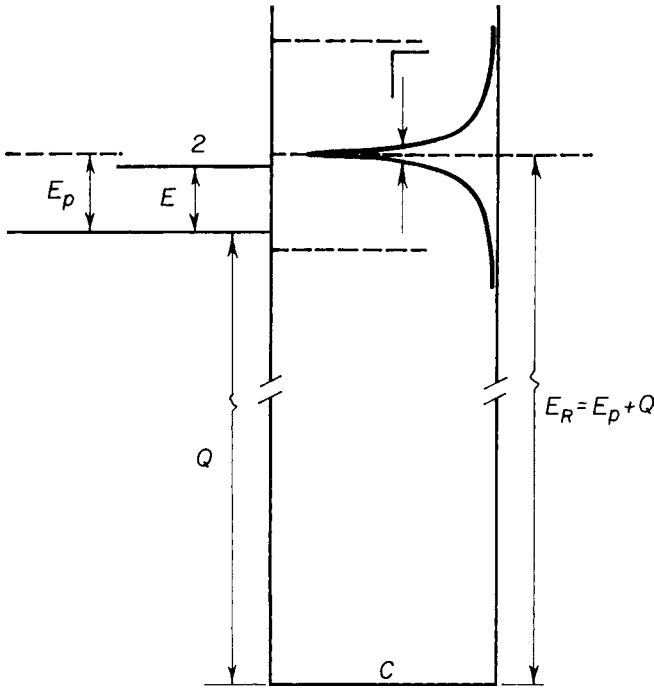
$$E_P + Q = E_R, \tag{2.63}$$

Fig. 2.10. Schematic of input channel for a resonant reaction.

the energy of the level above the ground state (see Fig. 2.10), the reaction cross-section is greatly enhanced by resonance effects, subject to the standard selection (or conservation) rules. In these cases, Q is often referred to as the threshold. The excited level is broadened owing to its finite lifetime τ and thus has (in the system of the compound nucleus) a probability distribution

$$P(E)dE = \frac{\Gamma/2\pi}{(E - E_R)^2 + (\Gamma/2)^2} dE \qquad (2.64)$$

where

$$\Gamma = \hbar/\tau = \Gamma_p + \Gamma_n + \Gamma_\alpha + \Gamma_\beta + \Gamma_\gamma + \cdots \qquad (2.65)$$

is the total width, and is the sum of partial widths for the various possible decay channels. The rate at which the excited compound nucleus decays into any channel is proportional to its partial width. The rate at which the excited state is formed by incoming particles with energy E is proportional to $P(E)$. If the reaction is to be initiated by a particle of type a, say, the cross-section must also be proportional to Γ_a. A reaction occurs if the excited state breaks up into any other channel, i.e. with a probability proportional to $\Gamma - \Gamma_a$, and the probability of ejecting particles of type b, say, is proportional to Γ_b. Putting all these factors together and normalizing
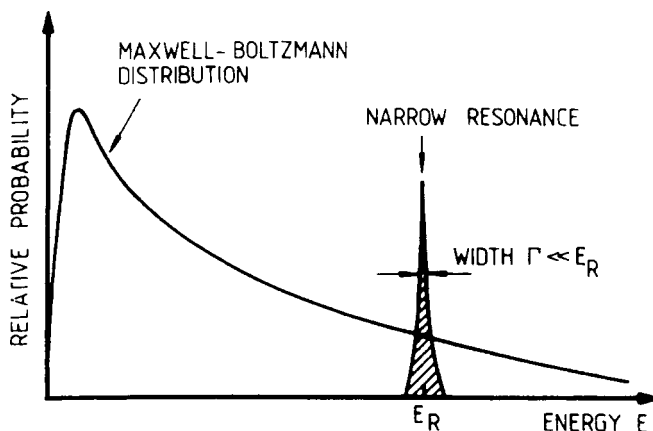
Fig. 2.11. A narrow resonance near or not too far above the Gamow peak. After Rolfs and Rodney (1988). Copyright by the University of Chicago. Courtesy Claus Rolfs.

to the maximum cross-section at $E = E_P$, one obtains the Breit–Wigner formula for a single-level resonance

$$\sigma(E) = \pi \bar{\lambda}^2(E_P)\,(1 + \delta_{12})\,\omega\,\frac{\Gamma_a \Gamma_b}{(E - E_P)^2 + (\Gamma/2)^2} \qquad (2.66)$$

with

$$\omega = \frac{2I + 1}{(2I_1 + 1)(2I_2 + 1)}, \qquad (2.67)$$

where I is the angular momentum of the excited state in the compound nucleus: $\mathbf{I} = \mathbf{I_1} + \mathbf{I_2} + \boldsymbol{\ell}$. Here Γ_a is the width for elastic resonant scattering and the reaction cross-section is a maximum for $\Gamma_a = \Gamma_b = \Gamma/2$, i.e. any reaction is accompanied by elastic resonant scattering. The Γ's for charged particle interactions are generally energy-dependent, owing to the penetration factor, whereas Γ_γ is constant and small, of the order of 1 eV or less, depending on the energy and order (electric or magnetic dipole, quadrupole etc.) of the transition. A Γ of 1 eV corresponds to a mean lifetime of 6.6×10^{-16} s.

A narrow resonance not too far from the Gamow peak may supplant the latter (see Fig. 2.11). The reaction rate coefficient is then given in analogy to Eq. (2.53) by

$$<\sigma v> = (8/\pi m)^{1/2}(kT)^{-3/2} E_P\, e^{-E_P/kT} \int_0^\infty \sigma(E)\,dE, \qquad (2.68)$$

where

$$\int \sigma(E)\,dE = 2\pi^2\,\bar{\lambda}_P^2\,\omega\,\frac{\Gamma_a \Gamma_b}{\Gamma} \equiv 2\pi^2\,\bar{\lambda}_P^2\,\omega\,\gamma. \qquad (2.69)$$

$\gamma \equiv \Gamma_a\Gamma_b/\Gamma$ is referred to as the strength of the resonance and the reaction rate coefficient finally becomes

$$<\sigma v> = \left(\frac{2\pi}{mkT}\right)^{3/2} \hbar^2 (\omega\gamma)_P f \, e^{-E_P/kT} \tag{2.70}$$

$$= 2.6 \times 10^{-13}(AT_7)^{-3/2} f\omega\gamma \, e^{-1.16E_P/T_7} \text{ cm}^3 \text{ s}^{-1}, \tag{2.71}$$

where f is a correction factor ≥ 1 for electron screening and E_P and γ are in keV. For several narrow resonances that are well separated, the rate coeffients are simply summed; in heavier nuclei these become numerous and can be treated by statistical methods. When resonances overlap, however, interference effects can occur.

The dependence of Γ on energy for charged-particle decay can be found as follows. The decay rate is the probability density flux integrated over surface area at infinity, i.e.

$$\Gamma/\hbar = \lim_{r\to\infty} v \int_\Omega |\psi(r,\theta,\phi)|^2 \, r^2 d\Omega. \tag{2.72}$$

For a spherical potential, the wave function has the form

$$\psi(r,\theta,\phi) = \frac{\chi_\ell(r)}{r} Y_{\ell m}(\theta,\phi), \tag{2.73}$$

where the spherical harmonics $Y_{\ell m}$ have the normalization

$$\int_\Omega |Y_{\ell m}(\theta,\phi)|^2 \, d\Omega = 1, \tag{2.74}$$

so that

$$\Gamma/\hbar = v \, |\chi_\ell(\infty)|^2 = v P_\ell(v) \, |\chi_\ell(R)|^2, \tag{2.75}$$

where v is the speed at infinity, R the nuclear radius and $P_\ell(v)$ the barrier penetration probability given by Eq. (2.24). $|\chi_\ell(R)|^2$ is the probability per unit dr of finding the particle within dr of the nuclear surface, which for a uniform nuclear density is given by

$$|\chi_\ell(R)|^2 = 3/R, \tag{2.76}$$

so that one may write

$$\Gamma_\ell = \frac{3\hbar v}{R} P_\ell(v) \theta_\ell^{\,2}, \tag{2.77}$$

where the dimensionless quantity $\theta_\ell^{\,2}$, called the reduced width, is a constant between 0 and 1 depending on details of the nucleus. This is especially useful when $\theta_\ell^{\,2}$ can be estimated from laboratory measurements around E_P and the resonance is broad enough to affect the S-factor at much lower energies. Allowance for these effects is often straightforward, but the case of $^{12}\text{C}(\alpha,\gamma)^{16}\text{O}$ presents some
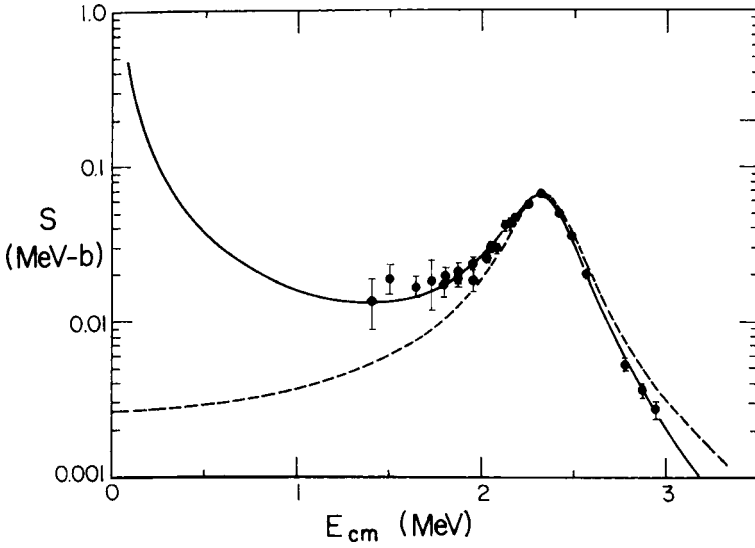
Fig. 2.12. S-factor for $^{12}C(\alpha, \gamma)^{16}O$. The dashed curve ignores the sub-threshold resonances, while the continuous curve allows for them, but the uncertainties are still significant at low energies. Koonin, Tombrello and Fox (1974). Reproduced with kind permission of Elsevier Science. Courtesy S. E. Koonin.

difficulties (Fig. 2.12) because the main ^{16}O resonance at 2.5 MeV above threshold is accompanied by two sub-threshold resonances (see Fig. 5.8).

When there are only two possible decay channels for the excited state of the compound nucleus, i.e. $\Gamma = \Gamma_a + \Gamma_b$, two simple limiting cases arise:

(i) $\Gamma_b \gg \Gamma_a$; $\gamma \simeq \Gamma_a$. This could be the case for a (p, α) reaction, or for (p, γ) or (α, γ) when the energy of the incident particle is so low that Γ_a falls below 1 eV or so. In this case, $\gamma \simeq \Gamma_a$ and is independent of Γ_b. The reaction occurs virtually every time the resonant state is formed.

(ii) $\Gamma_a \gg \Gamma_b$; $\gamma \simeq \Gamma_b$. This could be the case for resonances of energy sufficiently high that the state decays predominantly by re-emission of the incident particle and the reaction rate coefficient is given by Eq. (2.69) with γ replaced by Γ_b. If the number density of excited nuclei is n^*, say, then we now have for the reaction rate

$$r_{12} = n_1 n_2 <\sigma v> = n^* \Gamma_b / \hbar, \tag{2.78}$$

whence

$$\frac{n^*}{n_1 n_2} = \left(\frac{2\pi \hbar^2}{mkT}\right)^{3/2} \omega f e^{-E_P/kT}, \tag{2.79}$$

equivalent to the Saha equation (2.48) apart from the factor f which represents modification of the laboratory dissociation energy by the same plasma effects as give rise to electron screening. This is an example of statistical equilibrium brought about by the balancing of forward and backward reactions, and it applies in particular to helium

burning by the 3α reaction. In such cases, many reaction cross-sections can be replaced in calculations by simpler statistical properties.

2.7 Neutron capture reactions

Neutron captures have no Coulomb barrier (there is a centrifugal barrrier for $\ell > 0$) and generally take place through a series of broad and overlapping resonances, the breadth of the levels reflecting the ease with which a neutron can escape from an excited nucleus. For magic-number nuclei with closed neutron shells, the resonances have much higher energies and the neutron capture cross-sections are then particularly small (see Fig. 6.2).

The capture rate is dominated at thermal energies around 30 keV by s-waves for which the Breit–Wigner formula gives

$$\sigma_n(E_n) \propto \bar{\lambda}^2 \, \Gamma_n(E_n) \, \Gamma_X(E_n + Q). \tag{2.80}$$

The last factor is essentially $\Gamma_X(Q)$, since $Q \gg E_n$, and is virtually independent of energy; X may refer to γ, which is the normal exit channel in the s- and r-processes, or to p etc. Γ_n, on the other hand, is proportional to v by virtue of Eq. (2.77). This combines with the v^{-2} dependence of $\bar{\lambda}^2$ to make σ_n approximately proportional to $1/v$ (see Fig. 2.13), i.e.

$$\sigma_n v \simeq \text{const.} \simeq <\sigma_n v>, \tag{2.81}$$

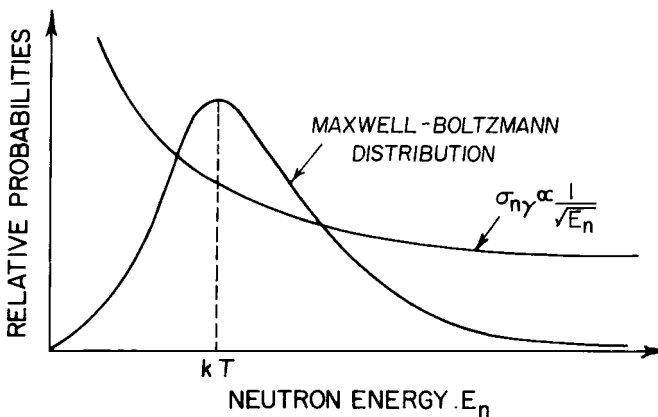so the reaction rate follows directly from Eq. (2.49).

Fig. 2.13. Schematic superposition of the Maxwell energy distribution and neutron capture cross-section. The most probable energy for the capture process in stars is near kT. After Rolfs and Rodney (1988). Copyright by the University of Chicago. Courtesy Claus Rolfs.

2.8 Inverse reactions

At low stellar temperatures, nuclear reactions occur predominantly in the direction leading to positive values of Q, but at higher temperatures the inverse reactions become increasingly significant. In Eq. (2.15), owing to time-reversal invariance, the matrix elements are the same for both forward and reverse reactions, so that the ratio of the two cross-sections is

$$\frac{\sigma_{12}}{\sigma_{34}} = \frac{m_3 m_4 E_{34}(2I_3 + 1)(2I_4 + 1)(1 + \delta_{12})}{m_1 m_2 E_{12}(2I_1 + 1)(2I_2 + 1)(1 + \delta_{34})}, \tag{2.82}$$

where $\bar{\lambda}_{ik}^{-2}$ has been replaced by the equivalent quantity $\hbar^2/2mE$. This means that, by measuring a reaction cross-section in one direction, one can infer the cross-section in the opposite direction provided that the same specific nuclear states are involved. This is particularly useful in predicting photo-disintegration rates, which are important at high temperatures in the Big Bang and in advanced stages of stellar evolution, and are not easy to measure.

When four particles are involved, e.g. for $^{15}N(p, \alpha)^{12}C$ and its reverse, averaging over the Maxwell distribution as in Eq. (2.53) and using Eq. (2.82) above, one finds

$$\frac{<\sigma v >_{34}}{<\sigma v >_{12}} = \frac{(2I_1 + 1)(2I_2 + 1)(1 + \delta_{34})}{(2I_3 + 1)(2I_4 + 1)(1 + \delta_{12})} \left(\frac{m_{12}}{m_{34}}\right)^{3/2} e^{-Q/kT} \tag{2.83}$$

provided only single states of each nucleus are involved; the same result can be found from Saha's equation (2.48) using the principle of detailed balancing. For photo-disintegration, e.g. $^{14}N(\gamma, p)^{13}C$, an analogous expression can be derived by calculating the lifetime τ_3 from Saha's equation:

$$\frac{n_3}{n_1 n_2} = \tau_3 <\sigma v >_{12} \tag{2.84}$$

$$= \frac{2I_3 + 1}{(2I_1 + 1)(2I_2 + 1)} \left(\frac{2\pi \hbar^2}{m_{12} kT}\right)^{3/2} e^{Q/kT}, \tag{2.85}$$

whence

$$n_\gamma <\sigma v >_\gamma = \tau_3^{-1} = <\sigma v >_{12} \left(\frac{m_{12} kT}{2\pi \hbar^2}\right)^{3/2} \frac{(2I_1 + 1)(2I_2 + 1)}{2I_3 + 1} e^{-Q/kT}. \tag{2.86}$$

At high temperatures, the rates have to be summed over relevant nuclear states and the $(2I + 1)$-factors in Saha's equation replaced by partition functions.

2.9 α-decay and fission

From the binding-energy curve, Fig. 1.3, it appears that it is energetically favourable for many of the heavier nuclei to split into lighter ones. Considering

the nucleus as a vibrating liquid drop, this could occur as a result of its changing shape from a nearly spherical to an elongated one from which a piece could break off, resulting in a gain in binding energy which would initially appear as kinetic energy of the nucleons. However, escape of the resulting fragment from the nucleus is strongly inhibited by the height of the Coulomb barrier.

One of the easiest ways for a heavy nucleus to split is by α-decay, because α-particles retain some of their identity within the nucleus, they are highly favoured energetically compared to any lighter particles (protons, neutrons or deuterons) and the Coulomb barrier is still relatively low: for an energy gain $\Delta Q = 1\,\mathrm{MeV}$, $2\pi\eta \simeq 3Z$ from Eq. (2.21). (For $^{238}\mathrm{U} \to {}^{234}\mathrm{Th} + \alpha$, $\Delta Q \simeq 4\,\mathrm{MeV}$.) Much higher values of ΔQ are available from fission into two nearly equal fragments, but this occurs at the expense of much higher Coulomb barriers, which explains why fission is less common than α-decay.

From the semi-empirical mass formula Eq. (2.2), neglecting the last two terms, the gain in B.E. for a nucleus splitting into two equal fragments is

$$\Delta Q = a_s A^{2/3} + a_c Z^2 A^{-1/3} - 2a_s \left(\frac{A}{2}\right)^{2/3} - 2a_c \left(\frac{Z}{2}\right)^2 \left(\frac{A}{2}\right)^{-1/3} \tag{2.87}$$

$$= a_c Z^2 A^{-1/3}(1 - 2^{-2/3}) - a_s A^{2/3}(2^{1/3} - 1) \simeq 250\,\mathrm{MeV} \tag{2.88}$$

if $Z \simeq 100$ and $A \simeq 250$. The first term in Eq. (2.88) is a gain due to reduced Coulomb repulsion and the second is a loss due to increased surface area. In practice, the fission fragments are not usually equal in mass, but the above calculation is adequate to get a general idea.

The Coulomb barrier is roughly given by

$$E_{\mathrm{Coul}} \simeq \left(\frac{Ze}{2}\right)^2 \Big/ 2R_0 \left(\frac{A}{2}\right)^{1/3} \simeq 0.28 a_c Z^2 A^{-1/3} \simeq 320\,\mathrm{MeV} \tag{2.89}$$

for the same parameters, leaving a substantial barrier or threshold to spontaneous fission; $2\pi\eta \simeq 1200$. The barrier can be overcome or penetrated if the nucleus is excited by capturing a particle, say a neutron, leading to induced fission. Spontaneous fission will only occur if ΔQ is comparable to, or greater than, E_{Coul}, i.e. if

$$\frac{Z^2}{A} \geq\sim 3\frac{a_s}{a_c} \simeq 67 \tag{2.90}$$

according to the constants adopted in Eq. (2.2), but this number is quite inaccurate because no account has been taken of ellipticity. A better value for the fission parameter Z^2/A would be in the neighbourhood of 45. One consequence of the form of this parameter is that a nucleus can become liable to spontaneous fission as a result of β-decay, an effect known as β-delayed fission. All three kinds of fission

play a role in the r-process, where successive neutron captures lead to very heavy unstable nuclei (see Chapter 6). Each fission can be followed by more neutron captures leading to a cyclic process in which the fission fragments and heavier nuclei are doubled in abundance every time the cycle operates.

2.10 Weak interactions

Unstable nuclei decay to an isobar in the β stability valley by β^- or β^+ emission or electron capture:

$$n \rightarrow p + e^- + \overline{\nu}_e; \quad p \rightarrow n + e^+ + \nu_e; \quad p + e^- \rightarrow n + \nu_e. \tag{2.91}$$

The (electron) neutrino ν_e and antineutrino $\overline{\nu}_e$ ensure conservation of energy, momentum, angular momentum and (electron) lepton number. (The lepton numbers are +1 for electrons and ν_e, and -1 for their antiparticles.) In the Standard Model of particle physics, there are three families each consisting of two quarks and two leptons, together with their antiparticles. Ordinary matter is made up from the first family: up and down quarks constitute protons and neutrons and the associated leptons are $e^\pm$ and ν_e, $\overline{\nu}_e$. The second family has strange and charm quarks and its leptons are the $\mu^\pm$ and the muon neutrinos ν_μ, $\overline{\nu}_\mu$; the third has bottom (or beauty) and top quarks and its leptons are the $\tau^\pm$ and ν_τ, $\overline{\nu}_\tau$. The muon and tauon are massive and unstable, and their decay is accompanied by the emission of the corresponding neutrino or antineutrino, which play an analogous role to electron neutrinos in preserving lepton number separately for each family. The idea of conserved lepton numbers means that emission of a neutrino can be treated as absorption of an antineutrino and vice versa.

ν_μ and ν_τ and their antineutrinos are produced along with ν_e, $\overline{\nu}_e$ in the early Universe and in collapsing cores of massive stars at the end of their evolution. Rest masses of neutrinos are non-zero, but small, averaging 0.2 eV or less, as judged from flavour oscillations and cosmological data. This is much less than the upper limits of order 5 eV, 160 keV and 24 MeV for ν_e, ν_μ and ν_τ respectively deduced from direct measurements. Neutrinos are fermions with spin 1/2, but they differ from protons, neutrons and electrons (apart from those emitted in β-decay) in having a fixed helicity; the spin vector of neutrinos points in the opposite direction to their velocity vector, while that of antineutrinos points in the same direction. Thus they are sometimes referred to as 'left-handed'. Right-handed neutrinos, if they exist at all, do not take part in the regular weak interaction and are referred to as 'sterile'. This effect is an example of the non-conservation of parity in weak interactions.

Unlike α-decay (and the related nuclear processes involving strong and electromagnetic interactions), β-decay involves creation of new particles and relativistic

mechanics. Basic understanding of the process was provided by Enrico Fermi, who postulated the existence of a weak interaction, analogous to the electromagnetic interaction responsible for radiation. Time-dependent perturbation theory (see Appendix 3) leads to the Golden Rule:[3]

$$\lambda(E_f) = \frac{2\pi}{\hbar} |V_{fi}|^2 \rho(E_f), \tag{2.92}$$

where $\lambda \equiv \ln 2/t$ is the decay constant, and

$$V_{fi} = g \int [\psi_f^* \phi_e^* \phi_\nu] O_X \psi_i \, dv \tag{2.93}$$

is a matrix element involving a coupling constant g and an overlap integral between the perturbing potential assumed to act like some operator O_X on the initial nuclear wave function ψ_i and the final wave functions of the daughter nucleus ψ_f, the electron ϕ_e and the neutrino ϕ_ν. (Strictly one should speak of an electron and antineutrino, or positron and neutrino, but the distinction is not important for the present purpose. The wave functions are actually 4-component spinors and the operator a 4×4 matrix.) The operator O_X can in principle behave under coordinate transformations in one of five different ways all consistent with Special Relativity: like a (polar) 4-vector (as in electric dipole radiation), like an axial vector, like a scalar, pseudo-scalar or tensor; in practice only the first two are found in nature and they are referred to as Fermi and Gamow–Teller decays respectively. Finally, the phase-space factor $\rho(E_f)$ is the density of states (i.e. the number of states per unit energy interval) available to the outgoing leptons within the range of final energies E_f allowed by the Uncertainty Principle as a result of the finite lifetime of the initial state. For an electron momentum p to $p + dp$ and a neutrino momentum q to $q + dq$ in a volume V, the number of states (bearing in mind the fixed helicity) is

$$d^2n = (4\pi)^2 \, V^2 p^2 dp \, q^2 dq / h^6. \tag{2.94}$$

For typical lepton energies of a few MeV, the de Broglie wavelength is of order 100 times the nuclear radius and when orbital angular momentum is zero, one can use the 'allowed' approximation for their wave functions

$$\phi_{e,\nu} = \text{const.} = V^{-1/2}. \tag{2.95}$$

The partial decay constant then becomes

$$d\lambda = \frac{2\pi}{\hbar} g^2 |M_{fi}|^2 (4\pi)^2 \frac{p^2 dp \, q^2}{h^6} \frac{dq}{dE_f}, \tag{2.96}$$

---

[3] Sometimes referred to as Fermi's Golden Rule, although it was originally derived by Dirac. Mandl (1992) has remarked that 'Fermi is not in need of "borrowed feathers".'

where $M_{fi} \equiv \int \psi_f^* O_X \psi_i \, dv$ is the nuclear matrix element. It then readily follows that the kinetic-energy spectrum of the electron (neglecting the small amount of energy taken up by recoil of the nucleus) is given by

$$N(T_e) \, dT_e = N(p) \, dp \propto p^2 dp \, (Q - T_e)^2, \qquad (2.97)$$

a function which vanishes at $T_e = 0$, Q and has a single maximum.[4]

The actual curve, however, is somewhat modified by Coulomb interaction between the electron or positron and the nucleus. This is allowed for by multiplication with a dimensionless function $F(Z', p)$, which leads to a correction factor f for the total decay rate, and it is the product ft that is used for purposes of comparing measured lifetimes with theory. The most rapid decays, with $ft = 10^3$ to 10^4 s, are known as 'superallowed'. These include 0^+ to 0^+ decays having $|M_{fi}|^2 = 2$ and ft is found experimentally to be close to 3000 s, giving the coupling constant for the Fermi interaction

$$g_F = 0.88 \times 10^{-4} \text{ MeV fm}^3 = 1.44 \times 10^{-49} \text{ erg cm}^3 \qquad (2.98)$$

and its dimensionless equivalent (analogous to the fine structure constant $\alpha \sim 10^{-2}$)

$$G_F \equiv \frac{g_F}{m_p c^2 \, (\hbar/m_p c)^3} = g_F \, m_p^2 c/\hbar^3 = 1.02 \times 10^{-5}. \qquad (2.99)$$

Allowed decays are those in which the leptons can be treated as originating at the origin in the nucleus, so that they cannot carry orbital angular momentum or a change in parity. Their spins may be anti-parallel, leading to a Fermi decay, or parallel, leading to a Gamow–Teller decay. In the first case, the nuclear spin is unchanged; in the second, it changes by one vector unit, i.e. $\Delta I = 0$ or ± 1, except that $I = 0 \rightarrow I = 0$ is forbidden. Thus $0^+ \rightarrow 0^+$ transitions are purely of the Fermi type, whereas free neutron decay ($\frac{1}{2}^+ \rightarrow \frac{1}{2}^+$) has contributions from both types, involving different coupling constants and matrix elements. In cases where the nuclear parity changes, the leptons carry orbital angular momentum; such transitions are 'forbidden' and accordingly slower.

The modern theory of weak interactions treats them as mediated by virtual weak-interaction quanta (known as intermediate vector bosons) acting between fermion currents, the fermions being endowed with a 'weak charge' g in analogy with electric charge (Fig. 2.14). Experiments show that, in addition to charge-changing (called 'charged-current') interactions mediated by $W^\pm$ bosons, there are also 'neutral-current' interactions mediated by a neutral particle, the Z^0. The electroweak theory of S. Weinberg, A. Salam and S. Glashow, which unifies electromagnetic and weak interactions at high energies, predicted masses of order 80

---

[4] For β^+-decay, since Q is calculated from atomic masses, the last factor has $Q - 2m_e c^2$ instead of Q.
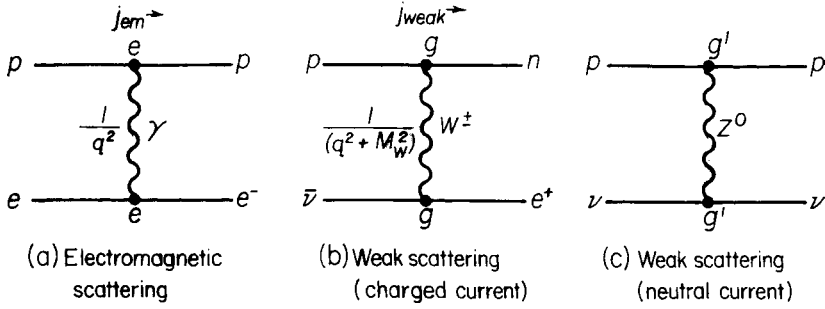
Fig. 2.14. Electromagnetic and weak interactions mediated by virtual boson exchange. q is the 4-momentum transferred in the interaction. Adapted from Perkins (1982).

and 90 GeV for the $W^\pm$ and Z^0 respectively, which were confirmed experimentally at CERN in 1983, and subsequent measurements of the width (i.e. lifetime) of the Z^0 resonance show that there cannot be any additional neutrinos (above the three pairs in the Standard Model) coupling to the Z^0 and having a mass below $m_Z/2$. In accordance with the hypothesis of a 'universal Fermi interaction', supported by many experiments, the ν_μ and ν_τ, as well as the ν_e, interact with matter through the neutral current mechanism, which can give rise to elastic and inelastic scattering events, but at typical stellar energies (below many MeV) only the ν_e and $\bar{\nu}_e$ have charged-current interactions (corresponding to absorption), since these require creation of the corresponding charged lepton.

Inverse β-decays, e.g.

$$p + e^- \rightarrow n + \nu_e, \tag{2.100}$$

$$\bar{\nu}_e + p \rightarrow n + e^+, \tag{2.101}$$

$$\nu_e + {}^{37}\text{Cl} \rightarrow {}^{37}\text{Ar} + e^-, \tag{2.102}$$

are important in primordial nucleosynthesis and advanced stages of stellar evolution, as well as in the experimental detection of neutrinos (from the Sun) and antineutrinos (from reactors and from Supernova 1987A). Experimental detection is difficult because the interaction with matter is so weak. The cross-section for neutrino interactions can be estimated from Eqs. (2.92), (2.93) and (2.95) with a fixed neutrino momentum q:

$$n_\nu \sigma c \equiv \lambda = \frac{2\pi}{\hbar} g^2 \frac{|M_{fi}|^2}{V^2} \frac{4\pi p^2}{h^3} \frac{dp}{dE} V, \tag{2.103}$$

where $n_\nu = 1/V$ is the number density of neutrinos, σ the cross-section and $E = T_e = pc$ for relativistic electrons, whence

$$\sigma = \frac{2\pi}{\hbar c} g^2 |M_{fi}|^2 \frac{4\pi p E}{c^2 h^3} = 1.6 \times 10^{-20} |M_{fi}|^2 \left(\frac{E}{1\,\text{MeV}}\right)^2 \text{ barn.} \qquad (2.104)$$

Thus the mean free path of a 10 MeV neutrino (not counting scattering processes) is of the order of 10^{42} nucleons cm^{-2} or 10^{18} gm cm^{-2}, around 1 light-year through water density. ν_μ and ν_τ interact still more weakly. In very dense matter, however, as in the collapsing core of a supernova, high-energy neutrinos are effectively trapped, mostly by scattering processes, ν_μ and ν_τ at somewhat deeper and hotter levels than ν_e.

Notes to Chapter 2

More information about the topics discussed in this chapter can be found in the following textbooks:

D. D. Clayton, *Principles of Stellar Evolution and Nucleosynthesis*, McGraw-Hill 1968, University of Chicago Press 1984. This classic text is particularly well written and gives more accurate and rigorous arguments for results derived here often in a somewhat heuristic manner. A more up-to-date (though in some ways less complete) description of nuclear astrophysics is given in

David Arnett, *Supernovae and Nucleosynthesis*, Princeton University Press 1996.

K. S. Krane, *Introductory Nuclear Physics*, John Wiley & Sons 1987, is an excellent account of nuclear physics at a fairly simple level.

D. H. Perkins, *Introduction to High Energy Physics*, Addison-Wesley Publishing Co. 1987, is also strongly recommended.

C. E. Rolfs and W. S. Rodney, *Cauldrons in the Cosmos*, University of Chicago Press 1988. This book gives a good overview of modern astrophysics as well as a detailed account of how reaction rates are measured in the laboratory.

G. W. C. Kaye and T. H. Laby, *Tables of Physical and Chemical Constants*, Longman 1995, gives a table of properties of the nuclides including isotopic abundance or half-life, decay modes, mass excess, neutron capture cross-section and ground-state spin and parity. This publication, with a prospect of regular updates, is available on the website **http://www.kayelaby.npl.co.uk/**.

Detailed formulae and tables for nuclear reaction rates are given by

Caughlan and Fowler (1988), for light nuclei. Rates for unstable light nuclei are given by Malaney and Fowler (1988, 1989a) and van Wormer *et al.* (1994). Rates for medium and heavy nuclei which exhibit a high density of excited states at capture energies, calculated using the Hauser–Feshbach statistical model, are given by Woosley *et al.* (1978). Experimental neutron capture cross-sections are summarized by Bao and Käppeler (1987) and Maxwell-averaged cross-sections given by Beer *et al.* (1992). Neutron capture cross-sections and other properties of

heavy unstable nuclei are discussed by Cowan, Thielemann and Truran (1991a). Updated rates for nuclear reactions are provided in the NACRE compilation (Angulo *et al.* 1999) and on the Lawrence-Livermore National Laboratory website **http://www-phys.llnl.gov/Research/RRSN/**.

An introduction to chemical thermodynamics (which is outside the scope of this book) as well as many relevant aspects of elementary nuclear physics can be found in:

C. R. Cowley, *An Introduction to Cosmochemistry*, Cambridge University Press 1995.

Problems

1. Show that the zero-order energies E_0 of nuclear energy states with quantum numbers ℓ, s, where $s = 1/2$, are shifted respectively by the spin–orbit interaction $-a\ell.s$ to

$$E_1 = E_0 - \frac{a}{2}\ell; \qquad j = \ell + \frac{1}{2}; \tag{2.105}$$

$$E_2 = E_0 + \frac{a}{2}(\ell + 1); \quad j = \ell - \frac{1}{2}; \tag{2.106}$$

and that the average energy is still E_0.

2. Use the shell model (Fig. 2.3) to find the ground-state spins and parities of the following nuclei: ^{3}He, ^{7}Li, ^{9}Be, ^{11}B, ^{13}C, ^{15}N.

3. Given that the tabulated masses refer to the neutral atom, verify that,
- for β^--decay, $\qquad M(A, Z) = M(A, Z + 1) + Q$;
- for β^+-decay, $\qquad M(A, Z) = M(A, Z - 1) + Q + 2m_e$;
- for K-electron capture, $\quad M(A, Z) = M(A, Z - 1) + Q$,

where $m_e = 5.5 \times 10^{-4}$ amu is the electron rest-mass.

4. Given the atomic masses tabulated below, find the Q-values and the changes in B.E. per nucleon (both in MeV) for the following reactions:
- 4^1H$\rightarrow^4$He;
- 3^4He$\rightarrow^{12}$C;
- ^{12}C$+^4$He$\rightarrow^{16}$O;
- ^{13}C$(\alpha, n)^{16}$O;
- ^{116}Sn$(n, \gamma)^{117}$Sn.

Neutron	1.008 665	^{13}C	13.003 355
^{1}H	1.007 825	^{16}O	15.994 915
^{4}He	4.002 603	^{116}Sn	115.901 747
^{12}C	12.000 000	^{117}Sn	116.902 956

(Remember that two electrons are annihilated in the first reaction above.)

5. Verify that the kinetic energy of two (non-relativistic) particles with masses m_1, m_2 and velocities $\mathbf{v_1}, \mathbf{v_2}$ can be written

$$E = \frac{1}{2}(m_1 + m_2)V^2 + \frac{1}{2}mv^2 \tag{2.107}$$

where

$$\mathbf{V} = \frac{m_1\mathbf{v_1} + m_2\mathbf{v_2}}{m_1 + m_2}, \tag{2.108}$$

$$m = \frac{m_1 m_2}{m_1 + m_2} \tag{2.109}$$

(the reduced mass) and

$$\mathbf{v} = \mathbf{v_2} - \mathbf{v_1}. \tag{2.110}$$

The first term in E is the K.E. of the centre of mass, which conserves its momentum and hence its velocity (almost, as the change in mass from Q is relatively very small), and the second term is the K.E. in the CM system which is available for penetrating the Coulomb barrier.

What are the momenta of each of the two particles in the CM system?

6. Prove the assertion in the text that the relative velocity of two sets of particles having individual Maxwellian velocity distribution functions also has a Maxwellian distribution with the masses replaced by the reduced mass.

Hint: this is most easily done by projecting each distribution into one dimension, where it becomes a Gaussian, and using the theorem from statistics that the variance of the difference (or sum) of two random variables is the sum of the individual variances.

What is the distribution function for the velocity of the centre of gravity?

7. Use Lagrange's method of multipliers to derive the law of refraction of light from Fermat's principle of least time between two fixed points.

8. Use the expression (2.28) with the approximations $\omega_i \gg N_i$, $\omega_i/N_i = \exp[(\tilde{E}_i - \mu)/kT]$, $\tilde{E} = mc^2 + p^2/2m$ to derive the Sackur–Tetrode equation for the entropy of an ideal gas

$$S = kN\left[\frac{5}{2} + \ln\left(\frac{un_Q}{n}\right)\right] \tag{2.111}$$

and verify that this is consistent with the Second Law Eq. (2.37) and the chemical potential from Eq. (2.44).

9. Find the number density of positrons resulting from pair production by γ-rays in thermal equilibrium in oxygen at a temperature of 10^9 K and a density of 1000 gm cm^{-3}, using the twin conditions that the gas is electrically neutral and that the chemical potentials of positrons and electrons are equal and opposite. (At this temperature, the electrons can be taken as non-relativistic.) The quantum concentration for positrons and electrons is $8.1 \times 10^{28} T_9^{3/2}$ cm^{-3}, the electron mass is 511 keV and $kT = 86.2 T_9$ keV.

10. Verify Eq. (2.62) for the power-law dependence of reaction rate on temperature.

11. At what centre-of-mass energy should one study the reaction ^{28}Si $(\alpha, \gamma)^{32}$S to duplicate stellar conditions at a temperature of the order of 10^9 K? If α-particles are incident on a Si target at rest in the laboratory, what energy should be chosen?

12. Show that the integration procedure over the Gamow peak implies for that peak a $1/e$ full width of $\Delta = (4/\sqrt{3})\sqrt{(E_0 kT)}$, i.e. essentially twice the geometric mean of E_0 and kT.

   Evaluate E_0 and Δ for ^{12}C$(p, \gamma)^{13}$N as functions of T_7.

13. Find the range of neutrino energies resulting from the reaction

$$p + p \to d + e^+ + \nu, \qquad (2.112)$$

given the following mass excesses:
H 7.289 MeV
D 13.136 MeV.
(The electron mass is 0.511 MeV.)
   Which of the following reactions might be used to detect such neutrinos from the Sun?
^{37}Cl$(\nu, e^-)^{37}$Ar $(Q = -0.81$ MeV$)$; ^{71}Ga$(\nu, e^-)^{71}$Ge $(Q = -0.23$ MeV$)$; ^{115}In$(\nu, e^-)^{115}$Sn $(Q = 0.49$ MeV$)$.
   Estimate the kinetic energy of the D nucleus when all the available energy is taken up (a) by the positron, (b) by the neutrino.

14. Show that the slope of the electron energy spectrum for allowed β-decays is zero near $T_e = Q$ if the neutrino has zero rest-mass, but becomes infinite if it has a finite rest-mass.

15. If a supernova emits gravitational waves as well as neutrinos, the gravitational waves will reach Earth-bound detectors slightly earlier because of the finite neutrino rest-mass. Assuming a supernova goes off at a distance of 100 Mpc, and a neutrino rest-mass of 0.1 eV, find the time delay for neutrino energies of 1 MeV and 10 MeV respectively.

3

Cosmic abundances of elements and isotopes

Science can be divided into two parts: physics and stamp-collecting.

Lord Rutherford[1]

3.1 Introduction: data sources

The data sources can be classified into 'tangible', for which samples can be directly handled and analyzed by chemical and other laboratory methods, and 'intangible' requiring spectroscopy, remote sensing or considerations from theoretical astrophysics. Table 3.1 lists some typical objects and methods relating to each class.

Our discussion will concentrate on astrophysical spectroscopy.

3.2 Analysis of absorption lines

3.2.1 Physical basis

The bulk of stellar radiation comes from the surface layers or 'atmosphere' of a star, more particularly the 'photosphere', which is defined as the region having optical depths for continuum radiation between about 0.01 and a few. The optical depth τ_λ is measured inwards from the surface and represents the number of mean free paths of radiation travelling vertically outwards before it escapes from the star. It is related to the geometrical height z above some arbitrary layer by

$$\tau_\lambda(z) = \int_z^\infty \kappa_\lambda(z')\rho(z')dz', \tag{3.1}$$

where ρ is the mass density and κ the mass absorption coefficient or opacity, measured in, e.g., $cm^2\,gm^{-1}$. One of the more important parameters governing

---

[1] Quoted in Birks (1962).

Table 3.1. *Data sources and methods for cosmic abundances*

Data sources		
Tangible:		**Intangible:**
Earth:	atmosphere oceans crust	Earth: mantle core
	Astrophysical objects:	
Moon (Apollo meteorites) Mars (meteorites) Asteroids (meteorites) Comets (dust) Circum-/interstellar dust (meteorites).		Sun, planets, comets, stars, PN, SNR, H II regions, ISM, galaxies, intra-cluster gas (X-r), QSOs, intervening gas.
Space plasmas:	Ionosphere, magnetosphere Solar wind Cosmic rays	

Methods		

Chem. analysis
Mass spectrometry
Electron microscopy
Optical microscopy
X-ray diffraction
  Neutron activation,
  X-r fluorescence spectr.,
Ion + electron microprobe
  ICP-MS
  Proton probe (PIXE)
 	
Balloon and space-borne
	
	for
	trace
	species
	
	nucl. em./plastic
	
	ion counters
		Seismic methods
		Radar mapping
		Thermal mapping
		
		Spectrum analysis
		(abs. or em. lines)
		from γ-r to radio.
		
		Deductions from
		stellar structure
		and evolution.

the structure of the photosphere is the effective temperature T_{eff}, defined as the temperature of a black body having the same emissivity (integrated over all wavelengths) as the stellar surface. T_{eff} is equal to the actual (kinetic) temperature at $\bar{\tau} \simeq 2/3$. In hotter stars ($T_{\text{eff}} > \sim 10^4$ K), the atmospheric opacity comes mainly from photo-ionization of hydrogen atoms in different excitation levels

$$\text{H}^* + h\nu \rightarrow \text{H}^+ + \text{e}^-. \tag{3.2}$$

This gives rise to absorption in the Lyman ($\lambda \leq 912\,\text{Å}$), Balmer ($\lambda \leq 3646\,\text{Å}$), Paschen ($\lambda \leq 8208\,\text{Å}$) etc. continua, together with free–free transitions of electrons passing by protons, which dominate in the infrared. In cooler stars like the Sun

($T_{\text{eff}} = 5780$ K), the main opacity source in the optical region is photo-detachment of negative hydrogen ions (for $\lambda < 1.66\,\mu$m),

$$\mathrm{H}^- + h\nu\ (\geq 0.75\,\mathrm{eV}) \rightarrow \mathrm{H} + \mathrm{e}^-, \tag{3.3}$$

again dominated in the infrared by free–free transitions, this time in the fields of neutral hydrogen atoms which now dominate the population. Emission is due to the same processes in reverse and in many cases there is a good approximation to local thermodynamic equilibrium (LTE). In LTE, the relative populations of protons, neutral hydrogen atoms and H^- ions are as predicted by the Boltzmann and Saha equations (see Eq. 2.48):

$$\frac{n_i}{n_j} = \frac{g_i}{g_j} e^{-(E_i - E_j)/kT} = \frac{g_i}{g_j} 10^{-\theta \chi_{ij}} \tag{3.4}$$

where g_i, g_j are the statistical weights ($2J + 1$) of two atomic levels, χ_{ij} is the difference in excitation potential in volts and

$$\theta \equiv \frac{5040}{T}; \tag{3.5}$$

and

$$\frac{n_+ n_e}{n_0} = 2\frac{u_+}{u_0}\left(\frac{m_e kT}{2\pi\hbar^2}\right)^{3/2} e^{-E_I/kT} \tag{3.6}$$

or

$$\log\frac{n_+}{n_0} = \log\left(\frac{u_+}{u_0}\right) + 9.08 - 2.5\log\theta - \theta I - \log P_e, \tag{3.7}$$

where I is the ionization potential in volts to detach an electron from a species labelled with 0 and the u's are partition functions defined in Section 2.4. Broadly speaking, the temperature is fixed as a function of optical depth by considerations of radiative transfer, and the pressure P or density by hydrostatic equilibrium at a mass column density governed by the opacity which itself depends mainly on the electron pressure P_e:

$$dP = -g\rho dz \quad \text{and} \quad d\tau_\lambda = -\kappa_\lambda \rho dz, \tag{3.8}$$

whence

$$P(\tau_\lambda) = g\int_0^{\tau_\lambda} \frac{d\tau_\lambda'}{\kappa_\lambda(T, P_e[P, T])}. \tag{3.9}$$

At solar-like temperatures, most of the free electrons come from easily ionized metals (Na, Mg, Al, Si, Ca, Fe) which for solar chemical composition total about 10^{-4} of the hydrogen number density leading to an electron pressure that is about

10^{-4} times the gas pressure. The processes of absorption and emission in LTE, which lead to an emissivity governed by Planck's law for specific intensity,

$$I_\nu d\nu = B_\nu(T)d\nu \equiv \frac{2h\nu^3}{c^2}\frac{d\nu}{\exp(h\nu/kT)-1}, \tag{3.10}$$

are often referred to as 'pure absorption'. Large departures from LTE occur in stellar chromospheres (rarefied hotter layers above the photosphere which dominate the continuum in the far IR and UV, but contribute little at optical and near IR wavelengths) and at extreme temperatures and low densities. The result of these processes is that stars emit a black-body-like continuum modulated by the dependence of κ_λ on wavelength. Neutral hydrogen in hotter stars causes a discontinuous decrease in intensity as one moves shortward in wavelength across the Paschen, Balmer and especially the Lyman limit (see Fig. 3.20), whereas H^- opacity varies smoothly with wavelength and does not lead to very notable departures from a black-body-like continuum in the visible and near IR. At very high temperatures, electron scattering dominates the opacity and leads again to a more black-body-like spectrum because it is independent of wavelength. Table 3.2 gives a rough overview

Table 3.2. *Logarithm of opacity $\kappa_{0.5\mu m}$ in stellar photospheres as a function of θ and $\log P_e$*

Spec. type (I)	θ	$\log P_e$						θ	Spec. type (V)
		-2	-1	0	1	2	3		
	0.1		Thomson scat.				-0.1	0.1	O5
B0	0.2		$\log\sigma =$			-0.3	0.4	0.2	B0
B3	0.3		$\log x_H - 0.5$			0.0	0.9	0.3	B3
A0	0.5				-0.2	0.6	1.2	0.5	A0
A5	0.7			-0.8	-0.8	0.0	0.9	0.7	A5
F2	0.8			-1.4	-0.9	0.1		0.8	F8
F8	0.9		-2.4	-1.7	-0.7			0.9	G2
G3	1.0	Rayl.	-2.4	-1.5	-0.5			1.0	G8
G8	1.2	-3.3	-2.1	-1.2				1.2	K3
K5	1.5	-2.6	-1.6	-0.6				1.5	M0
	$\log P_e$:	-2	-1	0	1	2	3		

Letters OBAFGKM define spectral types in a sequence of decreasing effective temperature, with decimal subdivisions, while I to V indicate declining luminosity, corresponding to increasing gravity, main-sequence stars being of luminosity class V and normal giants class III; the Sun is classified as G2V. x_H is the fraction of hydrogen ionized to H^+. The solid lines represent boundaries between different opacity regimes; Rayl. stands for Rayleigh scattering which varies as λ^{-4}.

of stellar atmospheric opacities, $\log(\kappa_{0.5\,\mu m} + \sigma)$, in $cm^2\,gm^{-1}$, as a function of θ and $\log P_e$, with a rough indication of corresponding spectral types where these parameters are typical of photospheric conditions.

Some insight into the structure of stellar atmospheres can be obtained by considering the simple case of a plane parallel grey atmosphere ($\kappa + \sigma$ independent of wavelength) in radiative equilibrium.

Figure 3.1 shows a ray with specific intensity $I(\tau, \theta)$ (integrated over all wavelengths) travelling outwards at an angle θ to the normal. On passing through a layer with vertical thickness dz, it loses $I\,d\tau/\mu$ from absorption (where $\mu \equiv \cos\theta$) and gains $j\,dz/\mu \equiv S\,d\tau/\mu$ from emission, where $j(\tau)$ is the emission per unit solid angle per unit volume and $S(\tau) \equiv j/\kappa\rho$ is known as the source function. The transfer equation then reads

$$\mu\frac{\partial I}{\partial \tau} = I - S. \tag{3.11}$$

Integrating Eq. (3.11) over solid angles and dividing by 4π, one obtains

$$\frac{dH}{d\tau} = J - S, \tag{3.12}$$

where $J(\tau) \equiv \int I\,d\omega/4\pi \equiv \frac{1}{2}\int_{-1}^{1} I\,d\mu$ is the (angle-averaged) mean intensity and $H \equiv \int I\mu\,d\omega/4\pi \equiv \frac{1}{2}\int_{-1}^{1} I\mu\,d\mu$ is known as the 'Eddington flux'; the actual flux is $\sigma T_{\text{eff}}^4 \equiv \pi F \equiv 4\pi H$. In radiative equilibrium, the flux is constant, so

$$S = J, \tag{3.13}$$
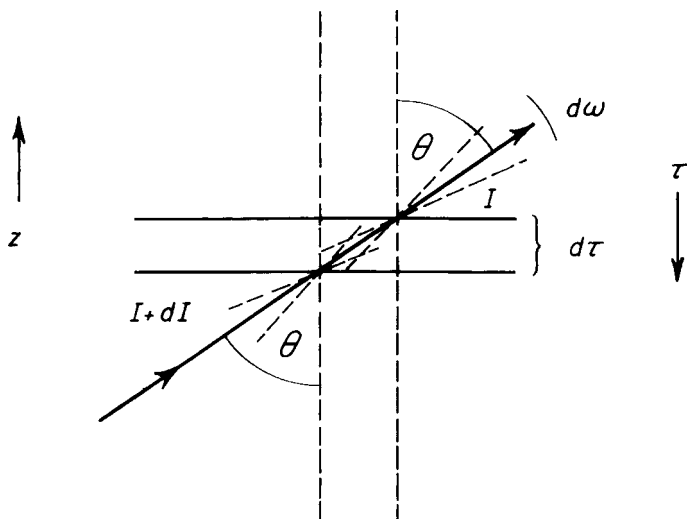
Fig. 3.1. Derivation of the equation of radiative transfer.

and in LTE the source function comes from Planck's law,

$$S = B(T) = \sigma T^4/\pi \tag{3.14}$$

(Stefan's law). Multiplying Eq. (3.11) by μ and integrating over solid angles again, one has

$$\frac{dK}{d\tau} = H \tag{3.15}$$

where $K \equiv \frac{1}{2}\int_{-1}^{1} I\mu^2 d\mu$ is $(c/4\pi)\times$ the radiation pressure. Eddington's approximation consists in setting

$$K = \frac{1}{3}J \tag{3.16}$$

(which is exact if $I(\tau, \mu)$ can be expanded in odd powers of μ, plus a constant), so from Eqs. (3.13) to (3.16)

$$J = S = B = 3H\tau + \text{const.} \tag{3.17}$$

A simple boundary condition at the surface is obtained by assuming $I(\tau = 0, \mu > 0) = \text{const.}$ (i.e. limb-darkening is neglected), $I(\tau = 0, \mu < 0) = 0$. Then $J(\tau = 0) = 2H$ and we have

$$S = J = H(2 + 3\tau) \tag{3.18}$$

and in LTE using $\pi F = 4\pi H = \sigma T_{\text{eff}}^4$

$$T^4 = T_{\text{eff}}^4 \left(\frac{1}{2} + \frac{3}{4}\tau\right). \tag{3.19}$$

Equation (3.19) gives a first approximation to the temperature structure of an atmosphere in radiative equilibrium, and departures from greyness can also be treated approximately by defining a suitable mean absorption coefficient (see Chapter 5). The emergent monochromatic intensity at an angle θ to the normal (relevant to some point on the solar disk) is also found by integrating the equation of transfer (3.11):

$$I_\lambda(0, \mu) = \int_0^\infty B_\lambda[T(\tau_\lambda)]e^{-\tau_\lambda/\mu}d\tau_\lambda/\mu \tag{3.20}$$

and the flux (relevant to radiation from an unresolved stellar surface) from $F_\lambda(0) = 2\int_0^1 I_\lambda(0, \mu)\mu d\mu$. In the Eddington–Barbier approximation, $B_\lambda(\tau_\lambda)$ is treated as a linear function and then one has simply

$$I_\lambda(0, \mu) \simeq B_\lambda(\tau_\lambda = \mu) \tag{3.21}$$

and

$$F_\lambda(0) \simeq B_\lambda(\tau_\lambda = 2/3). \tag{3.22}$$
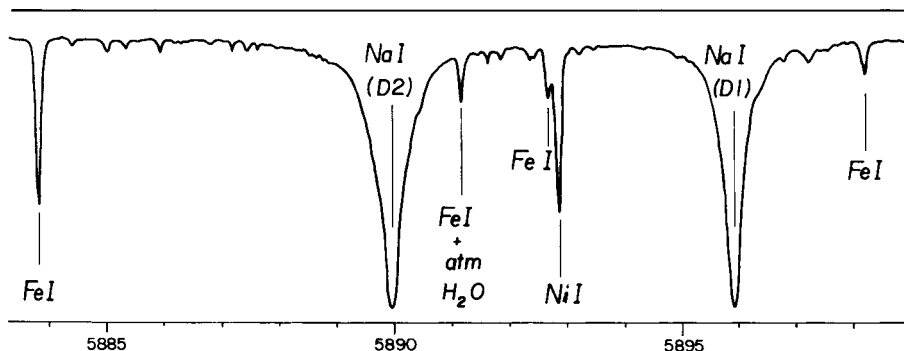
Fig. 3.2. Portion of the solar spectrum in the neighbourhood of the sodium D-lines. Adapted from Delbouille, Roland and Neven (1973).

Atoms, ions and molecules present in the stars provide additional opacity at wavelengths corresponding to specific atomic transitions; these give rise to comparatively narrow absorption lines (see Fig. 3.2) with intensities related to the abundances of the relevant elements (and much else). Despite the name, processes other than pure absorption (e.g. scattering and fluorescence) are involved in the production of these lines and, while they are often treated in LTE, this is now only a simplifying approximation which often works fairly well, but needs to be checked by more detailed calculations for each particular case. (In some cases, there are even emission lines or emission components, e.g. the solar Ca^+ H and K lines in the near UV, which are so strong that the chromosphere affects their central parts.)

Accurate abundance analysis of stellar absorption lines is an elaborate physical and numerical exercise involving the following steps (see Fig. 3.3):

- Calculate a model atmosphere, normally based on principles of radiative and (where necessary) convective equilibrium, together with hydrostatic equilibrium. This gives the run of physical parameters (temperature T, P_g, P_e, κ_λ) with optical depth $\tau_{\lambda 1}$ at some chosen wavelength, using as input parameters T_{eff}, the surface gravity g and relevant parameters relating to chemical composition, e.g. He/H and m/H, where m represents easily ionized metals. Effects of line opacity ('line blanketing') on the structure of the atmosphere need to be allowed for, raising a major computational problem. A further parameter affecting line profiles and intensities is the so-called micro-turbulent velocity, which usually has to be found empirically for each star, although in some more recent work this has been replaced by *ab initio* hydrodynamical simulations which also account for granulation and the associated temperature inhomogeneities (e.g. Asplund *et al.* 2000ab; Asplund 2000).
- Deduce atomic level populations at each depth point, using LTE or preferably something better.
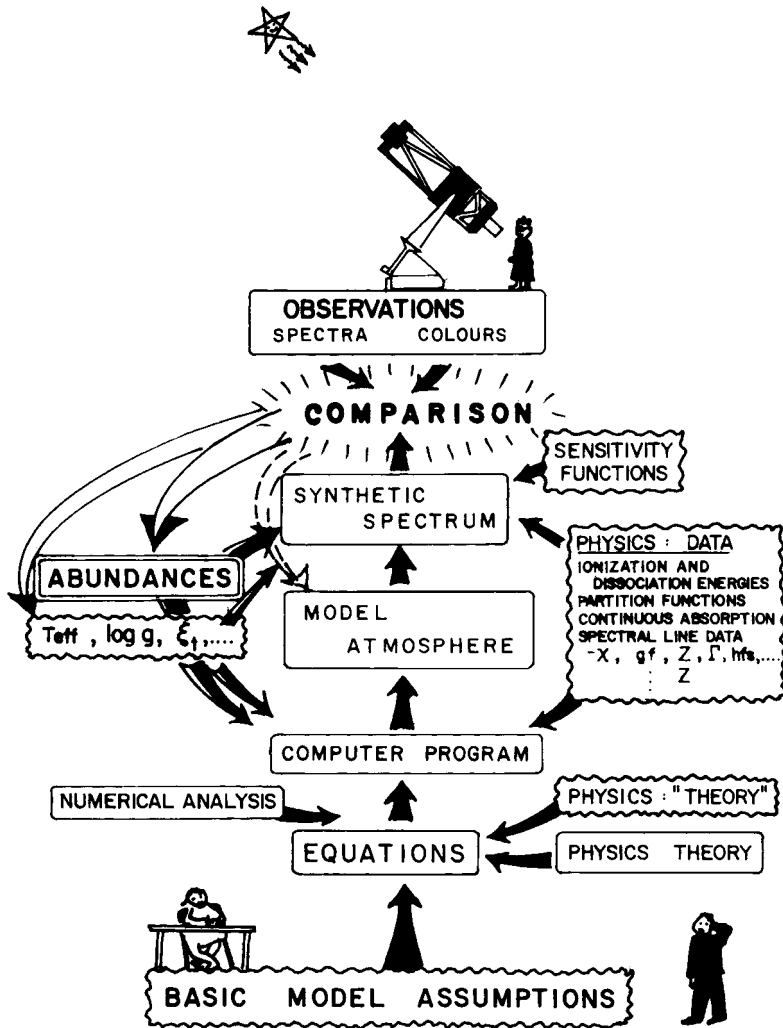
Fig. 3.3. Cartoon indicating steps in abundance analysis using model atmospheres. After Gustafsson (1980).

- Deduce the selective absorption coefficients $\kappa_l(\Delta\nu, \tau_\lambda)$ as functions of depth and distance from the line centre.
- Integrate the equation of radiative transfer to produce a synthetic spectrum as a function of assumed abundances of each element of interest.
- Convolve the synthetic spectrum with the surface velocity field (rotation, granulation) and with the instrumental profile.
- Compare the convolved synthetic spectrum with the observed spectrum, line profiles or equivalent widths.

The precision that can be achieved depends on having an accurate model with the right T_{eff}, good control over non-LTE effects and the availability of suitable lines with known atomic parameters, especially oscillator strengths (defined in Appendix 3). Various consistency checks can be made, in particular the model should fit the continuum energy distribution and hydrogen line profiles, and in some cases (e.g. CNO in the Sun), one may check that the same set of abundances fits a variety of atomic and molecular lines (C I, [C I], N I, [N I], O I, [O I], CO, CH, CN, OH). Some solar abundance determinations are even based on a semi-empirical model (Holweger & Müller 1974) which takes into account observable centre-limb effects, rather than on a purely theoretical model, and scaled versions of this or other solar models have sometimes been applied to stars having similar characteristics to the Sun. Special difficulties arise when the star is either very hot ($T_{\text{eff}} > 30\,000\,\text{K}$) or very cool ($T_{\text{eff}} < 4000\,\text{K}$) or has a very low gravity ($\log g < 0$; cf. $\log g_{\odot} = 4.4$ in cgs units). In favourable cases, an accuracy of perhaps ± 0.1 dex can be achieved, although abundances are often quoted to two decimal places in the logarithm.[2]

3.2.2 Equivalent widths and curves of growth

We now consider in somewhat more detail a simplified approach based on the 'curve of growth'. For this, we ignore fine details of the observed line profile and use the equivalent width (EW) defined in Fig. 3.4, $W_{\lambda} \equiv \int R \, d\lambda$ or $W_{\nu} \equiv \int R \, d\nu$, where $R(\Delta\lambda)$ or $R(\Delta\nu)$ is the relative depression below the continuum at some part of the line. The curve of growth is a relationship between the equivalent width of a line and some measure of the effective number of absorbing atoms. Equivalent
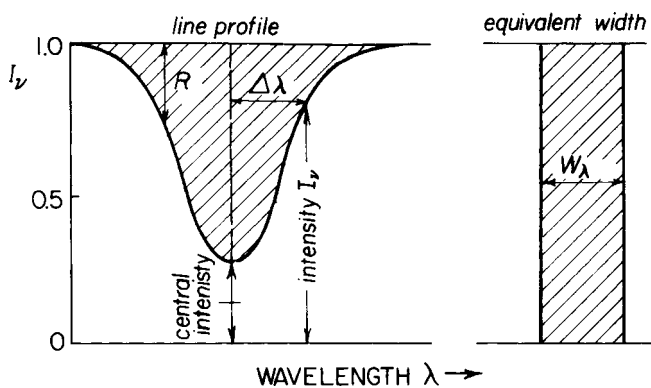
Fig. 3.4. Definition of equivalent width.

---

[2] I have described this practice as being like a second marriage – a triumph of hope over experience!

widths are useful (also in model-atmosphere analyses) as long as the line is isolated and has a well-defined continuum; this is not always the case, especially for rare elements represented by few lines, but when it is, the curve of growth is still a very useful tool for the analysis of many lines of one element, especially Fe I, and its theory offers good insights into the factors involved in the production of absorption lines. Under ideal conditions, the equivalent width is independent of instrumental broadening and velocity fields on the stellar surface.

The exponential curve of growth

The exponential curve of growth (van der Held 1931) is derived by caricaturing line formation as the result of an incident smooth continuum passing through a uniform gaseous column that absorbs only in the lines (Fig. 3.5). When applied to stars, it is based on an old and crude picture in which there is a gaseous 'reversing layer' that imprints absorption lines on continuous radiation coming from the photosphere below,[3] but it can give an exact picture of the formation of interstellar lines.

Consider continuous radiation with specific intensity I_1 incident normally on a uniform slab with a source function $S \equiv B_\nu(T_{ex}) \ll I_1$ (Fig. 3.6). S is the ratio of emission per unit volume per unit solid angle to the volume absorption coefficient $\kappa\rho$ and is equal to the Planck function B_ν of an 'excitation temperature' T_{ex} obtained by force-fitting the ratio of upper to lower state atomic level populations to the Boltzmann formula, Eq. (3.4). For the interstellar medium at optical and UV wavelengths, effectively $S = 0$.

The intensity emerging from the slab is

$$I = I_1 e^{-\tau_\nu} + S(1 - e^{-\tau_\nu}) \tag{3.23}$$
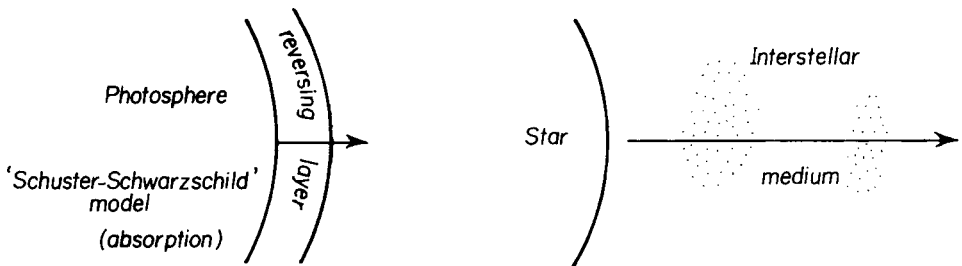
Fig. 3.5. Path of radiation through a stellar atmosphere (left) and through the interstellar medium (right).

---

[3] The reversing-layer picture is sometimes referred to as the 'Schuster–Schwarzschild model', but Arthur Schuster and Karl Schwarzschild considered more sophisticated models of radiative transfer (including scattering) than the one used here.
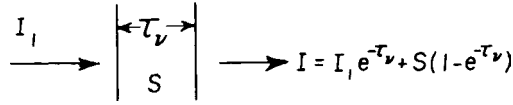
Fig. 3.6. The slab model.

where τ_v is the optical thickness of the slab at the appropriate distance in frequency from the line centre. Hence

$$R = 1 - \frac{I}{I_1} = \left(1 - \frac{S}{I_1}\right)(1 - e^{-\tau_v}) = R_\infty(1 - e^{-\tau_v}) \tag{3.24}$$

and

$$\frac{W_\lambda}{\lambda} = \frac{W_v}{v} = R_\infty \int_0^\infty (1 - e^{-\tau_v}) dv/v. \tag{3.25}$$

When the absorbing slab is effectively very cold compared to the brightness temperature of I, notably in the interstellar case, $R_\infty = 1$.

The optical depth τ_v is given – apart from a stimulated emission factor $(1 - e^{-hv/kT_{ex}})$ explained in Appendix 3 – by a product of the column density N of absorbing atoms in the appropriate state and the atomic absorption cross-section α_v. The latter depends on atomic constants and on a convolution of two line-broadening mechanisms: Doppler effect from a Gaussian distribution of velocities in the line of sight and damping from finite lifetimes of the atomic energy states, which latter usually leads to a Lorentzian distribution similar to Eq. (2.64); the effect of these two mechanisms is illustrated in Fig. 3.7.

$$\tau_v = N \frac{\pi e^2 f}{m_e c} \frac{\lambda e^{-v^2}}{b\sqrt{\pi}} \otimes \frac{\gamma}{\Delta\omega^2 + (\gamma/2)^2} \tag{3.26}$$

$$= N\alpha_0 H(a, v) \equiv \tau_0 H(a, v). \tag{3.27}$$

τ_0 is the (nominal) optical depth at the line centre, given by

$$\tau_0 = \frac{\pi^{1/2} e^2 f \lambda}{m_e c b} N \simeq 10^{-11} f \left(\frac{1 \,\text{km s}^{-1}}{b}\right) \left(\frac{\lambda}{0.5 \,\mu\text{m}}\right) N_{\text{cm}^{-2}}. \tag{3.28}$$

Here

- $\pi e^2 f/(m_e c) = \int \alpha(v) dv$ (in cgs units) from classical electromagnetic theory modified by quantum mechanics (e.g. time-dependent perturbation theory; see Appendix 3) which introduces the dimensionless oscillator strength f. f may be calculated theoretically or measured experimentally. Under certain circumstances it can also be cancelled out in a differential abundance analysis of one star relative to a standard (often the Sun) giving directly a logarithmic abundance change usually symbolized by [M/H] where M stands for some element.
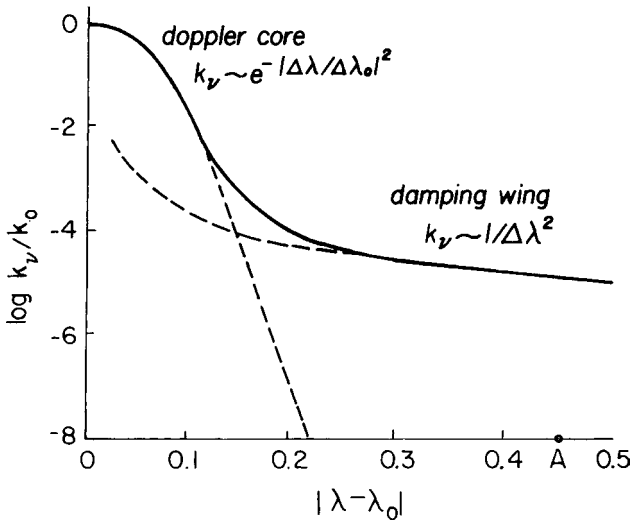
Fig. 3.7. Dependence of the line absorption coefficient on distance from the line centre, for the particular case of the Na I D-lines in the outer solar atmosphere. After Unsöld (1977). Copyright by Springer-Verlag New York Inc.

This method has become less important in recent years owing to advances in knowledge of f-values.

- $\pm b$ is the 'typical' line-of-sight velocity in a Gaussian distribution, specifically $\sqrt{2} \times$ the rms velocity, so that the probability of a velocity between V and $V + dV$ is $\exp(-V^2/b^2)dV/b\sqrt{\pi} \equiv \exp(-v^2)dv/\sqrt{\pi}$. The dimensionless velocity variable v has the equivalent definitions

$$v \equiv \frac{V}{b} \equiv \frac{\Delta\lambda}{\Delta\lambda_D} \equiv \frac{\Delta v}{\Delta v_D} \equiv \frac{\Delta\omega}{\Delta\omega_D}. \tag{3.29}$$

- $b^2 = b_{\text{th}}^2 + \xi^2$, where

$$b_{\text{th}} = \sqrt{\left(\frac{2kT}{Am_{\text{H}}}\right)} = 12.9 \left(\frac{T_4}{A}\right)^{1/2} \text{ km s}^{-1} \tag{3.30}$$

(with A the atomic mass number and T_4 the temperature in units of 10^4 K) is the thermal velocity, and ξ is an empirical parameter independent of A known as 'micro-turbulence' which is needed to account for the Doppler width of the absorption coefficient and amounts in most cases to between about 0.5 and a few km s^{-1}. In some more advanced stellar model-atmosphere analyses since 2000 or so, this empirical parameter is replaced by full hydrodynamical simulations.

- γ is the damping parameter or inverse mean lifetime of an excited level involved in the transition, made up of three components:

$$\gamma = \gamma_{\text{nat}} + \gamma_{\text{Stark}} + \gamma_{\text{coll}}. \tag{3.31}$$

Natural damping dominates in the interstellar medium. It is given for resonance lines (those involving the ground state) by $\gamma_{\text{nat},i} = \sum_j A_{ij}$, where A_{ij} is the Einstein spontaneous transition probability from an excited state i to any lower state j. On the other hand, pressure broadening from $\gamma_{\text{Stark}} + \gamma_{\text{coll}}$ dominates in main-sequence stars. (The Lorentzian broadening profile in Eq. (3.26) does not apply to stellar hydrogen lines, which have a linear Stark effect; it does apply, however, to interstellar lines because they just have natural damping.) An approximation to γ_{nat} for intrinsically strong lines is the classical damping constant

$$\gamma_{\text{cl}} = \frac{2e^2\omega^2}{3m_ec^3} = 8.9 \times 10^7 \left(\frac{0.5\,\mu\text{m}}{\lambda}\right)^2 \text{s}^{-1}. \tag{3.32}$$

- $\otimes$ denotes a convolution of the Doppler broadening due to a Gaussian velocity field with the Lorentzian from damping, expressed in the Voigt function

$$\frac{\alpha(v)}{\alpha_0} = H(a, v) \equiv \frac{a}{\pi} \int_{-\infty}^{\infty} \frac{e^{-x^2}dx}{a^2 + (v - x)^2} \tag{3.33}$$

where

$$a \equiv \frac{\gamma}{2\Delta\omega_D} = \frac{\gamma\lambda}{4\pi b} = 3.53 \times 10^{-3} \left(\frac{\gamma}{\gamma_{\text{cl}}}\right)\left(\frac{0.5\,\mu\text{m}}{\lambda}\right)\left(\frac{1\,\text{km s}^{-1}}{b}\right) \tag{3.34}$$

is the dimensionless damping parameter.

To develop the curve of growth, we shall roughly approximate the convolution integral in Eq. (3.33) by treating the two broadenings separately, i.e. we take

$$\alpha(v) \simeq \alpha_0 e^{-v^2} \tag{3.35}$$

for $v < 3$, and

$$\alpha(v) \simeq \frac{\pi e^2 f}{m_e c} \frac{\gamma}{\Delta\omega^2 + (\gamma/2)^2} = \alpha_0 \frac{a}{\sqrt{\pi}(a^2 + v^2)} \simeq \frac{\alpha_0 a}{\sqrt{\pi}v^2} \tag{3.36}$$

for $v > 3$.

At moderate optical depths, only the Gaussian part of the profile is significant:

$$\frac{W_\lambda}{\lambda R_\infty} = \int_{-\infty}^{\infty} [1 - \exp(-\tau_0 e^{-v^2})] \frac{b}{c} dv. \tag{3.37}$$

For $\tau_0 \ll 1$, this tends to

$$\frac{b}{c}\tau_0\sqrt{\pi} = \frac{\pi e^2}{m_e c^2} Nf\lambda \propto N \tag{3.38}$$

and we have the linear régime in which the EW is proportional to Nf and independent of line broadening. For $\tau_0 \gg 1$, the factor in brackets in Eq. (3.37) is
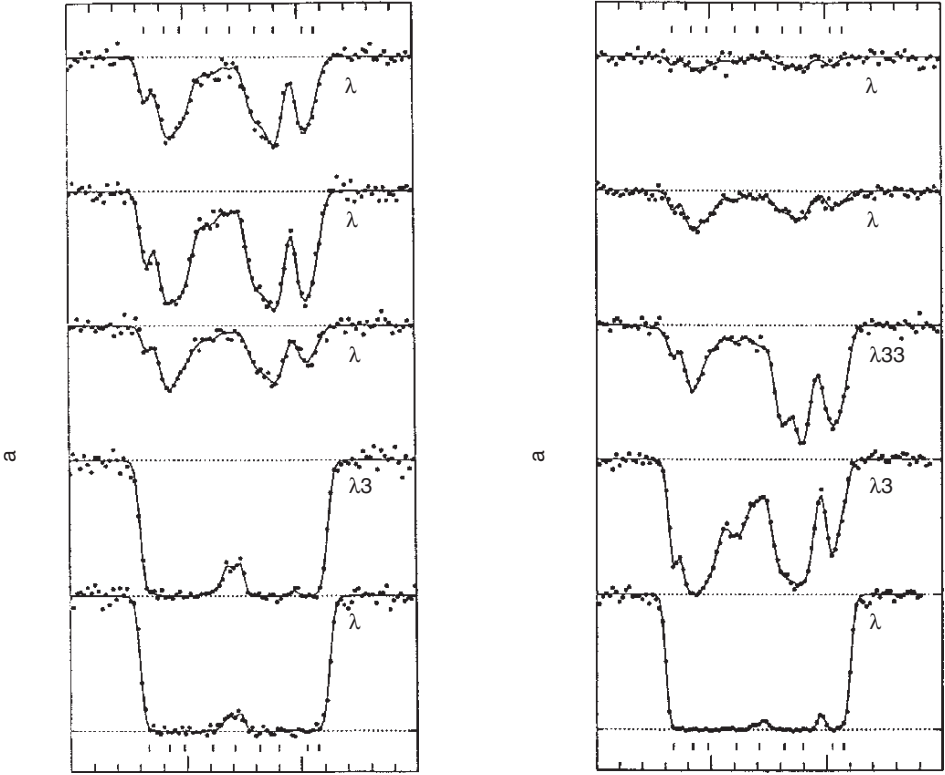
Fig. 3.8. Profiles of interstellar absorption lines observed in the line of sight to the star HD 93521 with the Goddard high resolution spectrograph at the Hubble Space Telescope. Solid lines are theoretical profiles based on cloud velocities indicated by the tick marks at the top; dots indicate the data points. After Spitzer and Fitzpatrick (1993). Courtesy Ed Fitzpatrick.

effectively 1 for $v^2 < \ln \tau_0$ and 0 for $v^2 > \ln \tau_0$, leading to a flat-bottomed profile (see Fig. 3.8) and the EW is given by

$$\frac{W_\lambda}{\lambda R_\infty} \simeq 2\frac{b}{c}\sqrt{\ln \tau_0} \propto b; \tag{3.39}$$

this is the saturated régime in which the EW depends mainly on b and increases only very slowly with the column density, leading to a flat portion of the curve of growth (Fig. 3.10). The flat portion can also be raised by line broadening due to hyperfine structure, when present.

For still larger column densities, the damping wings completely overcome the contribution of the Doppler core to the EW (see Fig. 3.9) and we can take for the whole line profile $\Delta\omega \gg \Delta\omega_D \gg \gamma$. Then
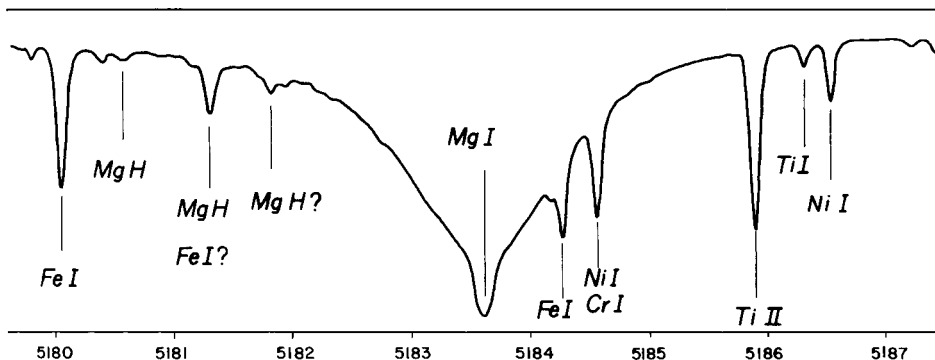
Fig. 3.9. A very strong absorption line of Mg I in the solar spectrum, dominated by damping wings. Adapted from the Liège Atlas (Delbouille *et al.* 1973).

$$\frac{1}{R_\infty} \frac{W_\lambda}{\lambda} = \int_{-\infty}^{\infty} \left\{ 1 - \exp\left(-\frac{N\pi e^2 f\gamma}{m_e c} \frac{1}{\Delta\omega^2} \right) \right\} d\,\Delta\omega/(2\pi v) \tag{3.40}$$

$$= \frac{\lambda}{c} \left(\frac{e^2}{m_e c} Nf\gamma \right)^{1/2} = \frac{2\pi e^2}{m_e c^2} \left(\frac{2}{3} Nf \frac{\gamma}{\gamma_{cl}} \right)^{1/2} \tag{3.41}$$

$$= 1.45 \times 10^{-12} \left(N_{cm^{-2}} f \frac{\gamma}{\gamma_{cl}} \right)^{1/2}, \tag{3.42}$$

the square-root law. In this case, the EW is once again independent of b. A generic set of exponential curves of growth is shown in Fig. 3.10 and tabulated in Table 3.3, while Fig. 3.11 shows a pair of curves fitted to interstellar lines for two different values of the Doppler width b. By the use of two or more lines from the same multiplet or ground state with different f-values, it is possible to sort out both the column density and the Doppler width, provided that at least one sufficiently weak line is available, e.g. in the doublet ratio method applied to the sodium D-lines. When several lines from the same lower atomic state or term are available, one can plot an empirical curve of growth, $\log(W/\lambda)$ against $\log f\lambda$ or $\log gf\lambda$ as appropriate and slide it over the theoretical one to deduce N and $\Delta\lambda_D$. However, complications can arise if there is more than one cloud in the line of sight. In such cases one may try to fit the spectrum with a superposition of individual Voigt profiles. An alternative that can sometimes be used is the 'optical depth method' (Hobbs 1974; Savage & Sembach 1991) in which the line profile as a function of line-of-sight velocity, V, say, is translated into a plot of $\tau(V) = -\ln\{1 - R(V)\}$ against V and the column density then follows from $\int \tau(V)dV = Nf\pi e^2/(m_e c)dV/dv = Nf\lambda\pi e^2/(m_e c)$. Conditions for the applicability of this method are (i) that instrumental broadening must be negligible,

Table 3.3. *Exponential curves of growth*

	$\log(W_\lambda/R_\infty\Delta\lambda_D)$		
$\log N\alpha_0\sqrt{\pi}$	$a = 0.001$	$a = 0.01$	$a = 0.1$
-0.75	-0.76	-0.76	-0.76
-0.50	-0.53	-0.52	-0.52
-0.25	-0.30	-0.29	-0.29
0.00	-0.08	-0.08	-0.07
0.50	0.27	0.27	0.30
1.00	0.47	0.47	0.54
1.50	0.56	0.58	0.69
2.00	0.65	0.68	0.87
2.50	0.70	0.74	1.07
3.00	0.73	0.88	1.31
3.50	0.79	1.07	1.55
4.00	0.92	1.31	1.80

After Powell (1969).
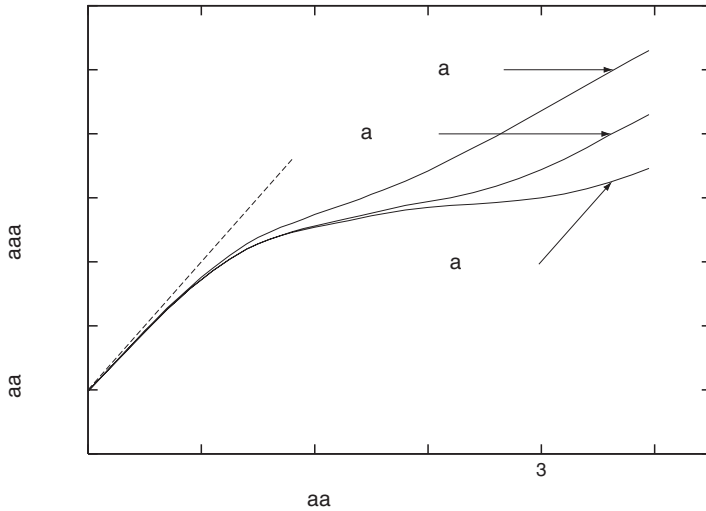
Fig. 3.10. Generic exponential curves of growth, normalized so that abscissa and ordinate are the same in the linear régime.

(ii) that the optical depth should not be so large at any velocity that the line goes black, making τ indeterminate, and (iii) that all the velocity components are in the same line of sight. If these conditions are fulfilled, no assumptions as to the velocity distribution need to be made.
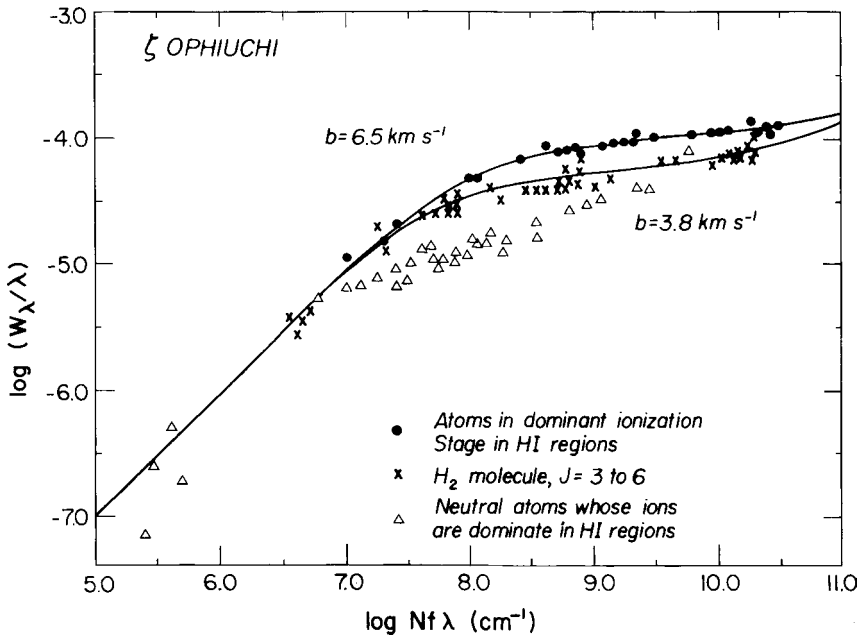
Fig. 3.11. Curves of growth for interstellar lines towards ζ Oph, observed with the Copernicus satellite. This method of plotting shows the dependence on *b* along the flat portion and its disappearance as the square-root portion is approached (provided all lines have the same value of $\gamma \lambda^2$). After Spitzer and Jenkins (1975). Copyright by Annual Reviews, Inc.

The MEMMU curve of growth

A form of the curve of growth more relevant to stellar (as opposed to interstellar) absorption lines is derived from work by E. A. Milne, A. S. Eddington, M. Minnaert, D. H. Menzel and A. Unsöld. In the 'Milne–Eddington' model of a stellar photosphere, the continuum source function (equated to the Planck function in the LTE approximation) increases linearly with continuum optical depth τ_λ and there is a selective absorption $\eta \kappa_\lambda$ in the line, where $\eta(\Delta v)$, the ratio of selective to continuous absorption, is a constant independent of depth given by

$$\eta(\Delta v) = \left(\frac{M}{H} \right) \left(\frac{M_{ij}}{M} \right) \left(\frac{\alpha(\Delta v)}{\alpha_\lambda} \right). \tag{3.43}$$

Here M/H is the atomic abundance, M_{ij}/M is the proportion of M atoms in the appropriate state of excitation and ionization to absorb the line, $\alpha(\Delta v)$ is the selective absorption cross-section implied by Eq. (3.27) and α_λ the continuous absorption cross-section per hydrogen atom; this latter is related to κ_λ (e.g. as in Table 3.2) by the number of H atoms per gram.

Expressing the source function by

$$B(\tau) = A\left(1 + \frac{3}{2}\beta\tau\right) \tag{3.44}$$

(where β is an increasing function of $h\nu/kT$ by virtue of Planck's law and a fixed $T(\tau)$ relation as in Eq. 3.19), the continuum flux obtained by solving the equation of radiative transfer for a typical angle of emergence of a ray, $\arccos 2/3$, is

$$F_1 \simeq A(1 + \beta), \tag{3.45}$$

while the line flux is

$$F \simeq A\left(1 + \frac{\beta}{1 + \eta}\right) \tag{3.46}$$

which basically expresses the fact that one sees less far down at the line frequency (see the Eddington–Barbier approximation, Eq. 3.22). Hence

$$R \equiv \frac{F_1 - F}{F_1} = \frac{\beta}{1 + \beta}\frac{\eta}{1 + \eta} = R_\infty\frac{\eta}{1 + \eta}, \tag{3.47}$$

or

$$\frac{1}{R} = \frac{1}{R_\infty} + \frac{1}{x(\Delta\nu)}, \tag{3.48}$$

where

$$x = \eta R_\infty = \frac{\eta\beta}{1 + \beta}. \tag{3.49}$$

This is the Menzel–Minnaert–Unsöld interpolation formula (often used assuming $R_\infty = 1$). It gives a better approximation to stellar absorption-line profiles (which are definitely not flat-bottomed) than does the exponential formula; the shape of the corresponding curve of growth is much the same, but its use leads to a b-parameter that is about 25 per cent higher for the same observational data. Denoting the central value of η by η_0, the Doppler part of the curve is given by

$$\frac{1}{R_\infty}\frac{W_\lambda}{\Delta\lambda_{\mathrm{D}}} = \int_{-\infty}^{\infty}\frac{\eta d\upsilon}{1 + \eta} = \eta_0\int_{-\infty}^{\infty}\frac{\exp(-\upsilon^2)d\upsilon}{1 + \eta_0\exp(-\upsilon^2)}. \tag{3.50}$$

As before, there are three régimes:

For $\eta_0 \ll 1$,

$$\frac{W_\lambda}{\lambda} = R_\infty\frac{\eta_0 b}{c}\sqrt{\pi} \tag{3.51}$$

independent of b. Here η_0 plays the same role as does $N\alpha_0$ in the exponential curve of growth.

For a mild degree of saturation ($\eta_0 < 1$), the denominator of Eq. (3.50) can be expanded as a power series

$$\frac{1}{R_\infty}\frac{W_\lambda}{\Delta\lambda_\mathrm{D}} = \eta_0 \int_{-\infty}^{\infty} e^{-v^2}(1 - \eta_0 e^{-v^2} + \eta_0^2 e^{-2v^2} - \cdots)dv \tag{3.52}$$

$$= \eta_0\sqrt{\pi}\left(1 - \frac{\eta_0}{\sqrt{2}} + \frac{\eta_0^2}{\sqrt{3}} - \cdots\right), \tag{3.53}$$

where the expression in brackets represents the saturation factor.

On the damping branch ($\eta_0 a \gg 1$), we have

$$\frac{1}{R_\infty}\frac{W_\lambda}{\Delta\lambda_\mathrm{D}} = \eta_0 \int_{-\infty}^{\infty} \frac{dv}{\eta_0 + \frac{\sqrt{\pi}}{a}v^2} = \sqrt{(\pi^{3/2}a\eta_0)} \tag{3.54}$$

or

$$\frac{1}{R_\infty}\frac{W_\lambda}{\lambda} = \frac{1}{2c}\sqrt{(\pi^{1/2}\eta_0 b\gamma\lambda)}, \tag{3.55}$$

again independent of b.

These approximations relate to model-atmosphere analysis like a one-point integration formula. $\eta_0 b R_\infty$ can be replaced by an exact integral through the atmosphere representing the equivalent width in the weak-line (unsaturated) limit, providing the abscissa for a curve of growth which then simply takes on the role of a saturation curve. This is sometimes known as the 'method of weighting functions', after a certain way of formulating the integral.

Curve-of-growth fitting procedures

In a simple-minded application known as 'coarse analysis', one simply assumes the lines to be formed in a single layer in quasi-LTE with a fixed excitation temperature θ_ex, a fixed ionization temperature θ_ion and a fixed electron pressure P_e. The logarithmic equivalent column density is then $\log gf - \theta_\mathrm{ex}\chi + \mathrm{const.}$, using gf rather than $gf\lambda$ mainly because the H^- opacity is more or less proportional to λ throughout the optical region and θ_ex is chosen to give the best fit between lines with differing lower excitation potential (see Fig. 3.12). θ_ion and $\log P_e$ are best determined from model-atmosphere considerations based on effective temperature (e.g. for the Sun, $\theta_\mathrm{ion} \simeq 0.9$ for $\theta_\mathrm{eff} = 0.87$) and gravity; $\log P_e$ can be taken from Table 3.2 for the relevant spectral type and luminosity class. Deducing $\eta_0 b/gf$ for ground-state lines by comparing the linear portion of the curve with Eq. (3.51), we then have from Eq. (3.28)

$$Agf = \eta_0\frac{b}{c}\sqrt{\pi} = \frac{\pi e^2}{m_e c^2}\frac{\mathrm{M}_1/g_1}{\mathrm{H}}\frac{gf\lambda}{\alpha_\lambda(\mathrm{H})} \tag{3.56}$$
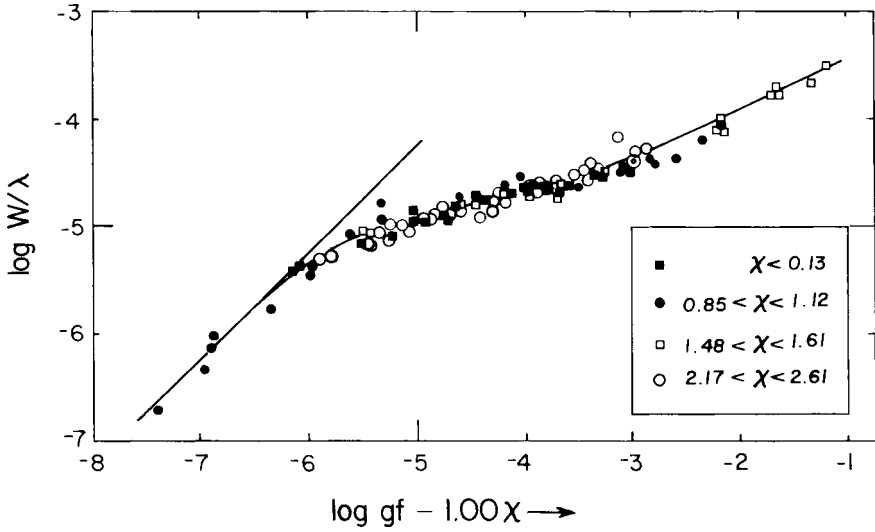
Fig. 3.12. Simple (exponential) curve of growth for low-excitation Fe I lines with wavelengths between 4000 and 8700 Å at the centre of the solar disk, with $\theta_{ex} = 1.00$, $b = 1\,\mathrm{km\,s^{-1}}$ (assuming $R_\infty = 1$), $a = 0.02$. Equivalent widths are from Moore, Minnaert and Houtgast (1966). gf-values are from furnace measurements by the Oxford group (Blackwell *et al.* 1986 and references therein).

where $\log A$ is the constant from the curve-of-growth shift, M_1/H is the abundance of the ground-state neutral atom relative to hydrogen and $\alpha_\lambda(H)$ the absorption cross-section per H atom, related to $\kappa_{0.5\,\mu m}$ given in Table 3.2 by

$$\alpha_{0.5\mu m} = 1.4\kappa_{0.5\mu m}m_H. \tag{3.57}$$

(The factor 1.4 comes from the assumption that the He/H ratio is 0.1.) We thus have

$$\frac{M_1/g_1}{H} = A\frac{1.4m_H\,\kappa_{0.5\mu m}}{\pi e^2\lambda/m_ec^2} = 5.2\times10^{-8}A\,\kappa_{0.5\mu m}. \tag{3.58}$$

Correcting $g_1^{-1}M_1/H$ to the total abundance (mostly the first ion) using Saha's equation (Eq. 3.7), one can obtain an estimate of a metallic abundance M/H good to about 0.2 dex, provided that the linear part of the curve of growth is well defined and the value of θ_{ion} judiciously chosen.

In a more sophisticated application, one calculates an abscissa $\log X$, which is a theoretical value of $\log W/\lambda$ taking into account all atmospheric effects except saturation, as a function of the desired abundance ratio M/H; $\log X = \log(M/H) + \log gf + \log\Gamma$, where Γ is calculated for given excitation and ionization potentials, ionic partition functions and the model atmosphere. The abundance is then chosen to give the optimal fit for weak lines. The same curve can also be used (with due

precautions) to predict saturation effects for elements represented by only a few lines that may not be weak.

Differential curve-of-growth analysis

Differential curve-of-growth analysis is a method of comparing stars with a standard (often the Sun) that was pioneered by L. H. Aller and J. L. Greenstein in the 1950s and developed further by G. Wallerstein, R. Cayrel, J. Jugaku, B. E. J. Pagel and others in the 1960s. The method can be quite accurate and it is described here in some detail both because it gives a good insight into the issues arising in abundance analysis and because it has provided some graphic illustrations of how abundance differences translate into visible curve-of-growth shifts. The idea is to find $\log X_\odot$ for a given solar line from an assumed normalized solar curve of growth and predict the corresponding $\log X$ for a stellar spectrum, as a function of differential abundance $[M/H] \equiv \log(M/H) - \log(M/H)_\odot$ for some element M using either detailed calculations of Γ from model atmospheres (e.g. Cayrel & Jugaku 1963) or simple considerations of the effect of temperature differences $\Delta\theta$ and electron pressure differences $[P_e] \equiv \Delta \log P_e$ between the star and the standard; these differences are a better approximation to the effects of stratification in the stellar atmosphere than is the use of single values of θ, $\log P_e$ in the simple curve-of-growth analysis. A further advantage, less important now than it was then, is that unknown oscillator strengths cancel out (or one can use 'solar oscillator strengths' designed to give accepted solar abundances from the given line in the solar spectrum), and it is still customary and useful to express stellar abundances in the relative [M/H] form.

A particularly simple case is that of neutral metals in F- to early K-type stars where these metals are predominantly singly ionized. Applying Saha's equation (Eq. 3.7) to such metals and also to H^-, which is itself predominantly 'ionized' to neutral H, one finds

$$[X] = [M/H] + [\Gamma] \simeq [\eta_0 b] \simeq [M^+/H] + \Delta\theta(I - \chi - 0.75). \qquad (3.59)$$

$\Delta\chi \equiv I - \chi$ is the ionization potential from the lower state of the line and 0.75 eV is the electron detachment potential of H^-. $[M^+/H] = [M/H] + [x]$, where x is the degree of ionization which changes negligibly while it is close to one, and the electron pressure cancels out. $\Delta\theta$ can be identified with $\Delta\theta_{\mathrm{ex}}^I$ obtained by optimally fitting neutral lines with different excitation potentials to one curve of growth (see Fig. 3.13), or deduced from red–infrared colours. As a refinement, a small term $[\theta]$ should be added to the rhs of Eq. (3.59) to allow for an increase of the weighting function integral towards lower effective temperatures.
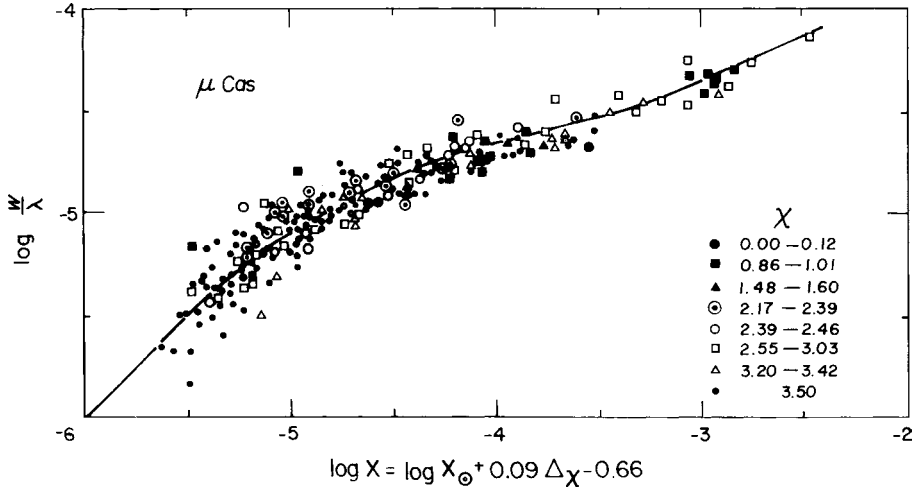
Fig. 3.13. Differential curve of growth for Fe I in μ Cas relative to the Sun, after Catchpole, Pagel and Powell (1967).

Figure 3.14 shows horizontal curve-of-growth offsets for different elements in the mild 'subdwarf' star μ Cassiopeiae, relative to those for Fe I at the same $I - \chi$. Several elements maintain a nearly constant abundance ratio relative to iron, so that [Fe/H], often known as the 'metallicity', is sometimes taken as representing the abundance change in the heavy-element mass fraction Z, which is made up of all the elements from carbon upwards; these are also often loosely referred to as 'metals' although they include nitrogen, oxygen etc. However, Fig. 3.14 shows some abundance differences characteristic of stars with significantly lower metallicity than the Sun: elements with α-particle nuclei (Mg, Si, Ca) and Ti are slightly overabundant compared to iron, and manganese slightly underabundant, although in this latter case the interpretation is complicated by hyperfine structure effects on the saturated portion of the curve of growth.

The curve-of-growth shift for singly ionized lines (or for neutral lines of elements with large ionization potentials like C, N, O) is given by

$$[X]^{\mathrm{II}} = [M^+/H] - \Delta\theta_{\mathrm{ex}}^{\mathrm{II}}(\chi + 0.75) - \frac{3}{2}[\theta] - [P_e]. \qquad (3.60)$$

$\Delta\theta_{\mathrm{ex}}^{\mathrm{II}}$ is generally numerically less than $\Delta\theta$ because excited lines of dominant species tend to be formed deeper in cooler atmospheres, and the $[P_e]$ term introduces further depth dependence, but accurate offsets between dominant species can be obtained by comparing plots of $[X]$ against χ among themselves. Figure 3.15 gives such a plot for the red giant Arcturus ([Fe/H] $\simeq -0.5$), which shows that oxygen shares the relative overabundance of the α-elements, while carbon does
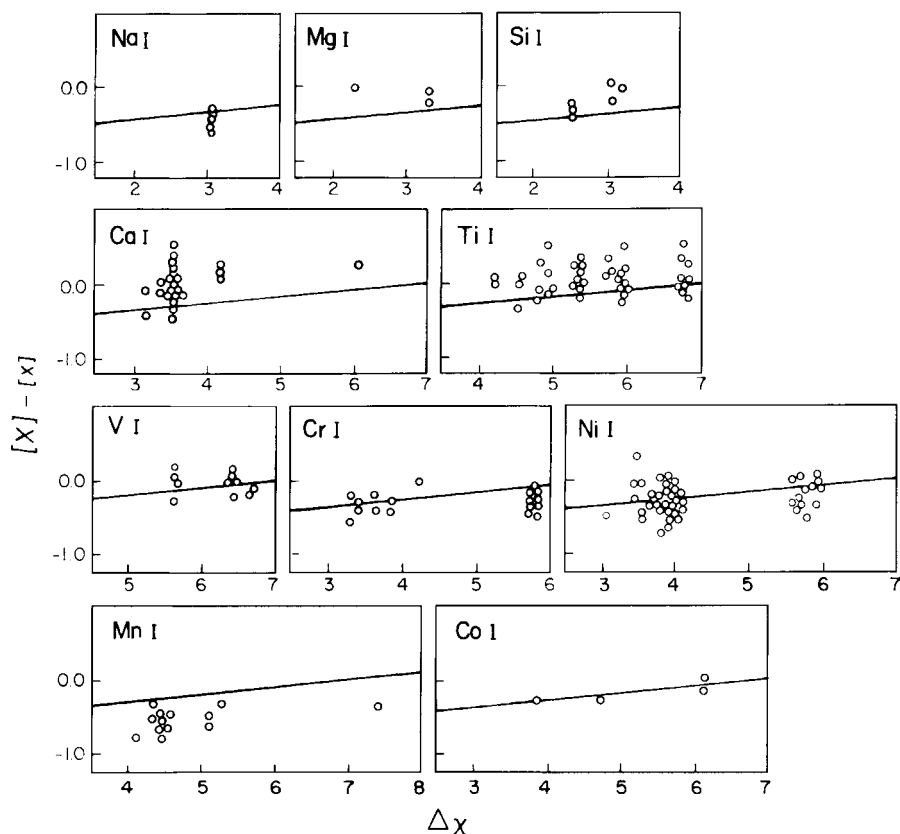
Fig. 3.14. Curve-of-growth shifts for individual lines of individual neutral elements in μ Cas, plotted against $\Delta\chi$. The solid line shows the corresponding relation for Fe I, so that the offsets give directly the differential abundance changes [M/Fe]. Adapted from Catchpole, Pagel and Powell (1967).

not. (The position of Fe II in this plot is ambiguous, because it is not the dominant species throughout the atmosphere of Arcturus, whereas it is so in the Sun, but the other metals are predominantly ionized in both stars, while C and O are predominantly neutral.)

Complications arise in differential curve-of-growth analysis when the star to be analyzed is extremely metal-deficient, making it necessary to use strong lines on the damping branch of the curve of growth for the Sun which reappear as weak lines in the star, and of high luminosity (low gravity) leading to near or complete absence of pressure broadening. In such cases one has to be cautious in using solar X or gf values, especially for neutral lines (although a reasonable result can still be obtained from ionized metal lines; see Fig. 3.16) and in modern work, direct analyses using oscillator strengths measured in the laboratory are preferred.

3

aa
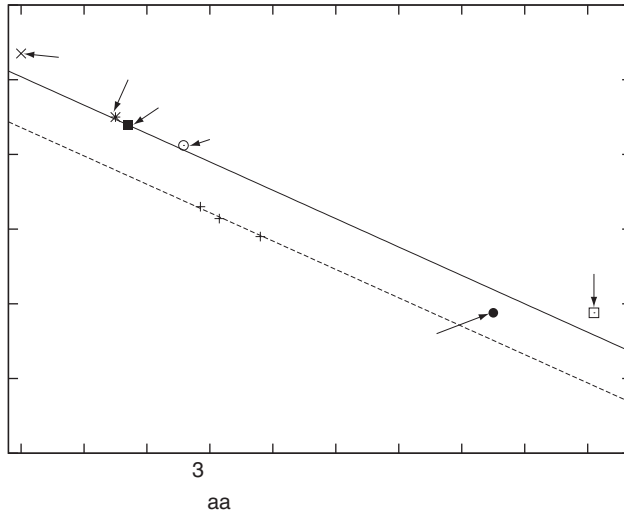
Fig. 3.15. Curve-of-growth shifts (relative to the Sun) for forbidden [O I], permitted O I and C I and singly ionized metals in the spectrum of Arcturus, adapted from Gasson and Pagel (1966).

3.2.3 *Quick methods for metallicity estimation*

A quick impression of a star's metallicity can often be derived from inspection – either qualitative or quantitative – of strong spectral features such as the CN band λ 4215 in giants or comparison of hydrogen and Ca^+ K-line (λ 3933) intensities, which has been particularly useful in the discovery of extremely metal-deficient stars (Beers, Preston & Shectman 1992). Numerical comparisons of digital spectra with low signal:noise ratio can also be carried out for this purpose (Carney *et al*. 1987).

3.2.4 *Integrated spectra of stellar populations*

While it is possible to obtain colours and spectra for the most luminous stars in the nearest galaxies – the Magellanic Clouds and other galaxies of the Local Group – this cannot be done for more distant galaxies. In gas-poor systems such as elliptical galaxies and the bulges of spirals one can only measure the integrated spectra and colours of an entire stellar population, either a cluster or a region in the field, such as the spectrum shown in Fig. 3.17. Several line features in the integrated spectrum are sensitive to metallicity, but their interpretation is far from straightforward.

The problem of interpreting integrated spectra has been studied by many investigators starting with Whipple (1935). One approach, known as 'stellar population
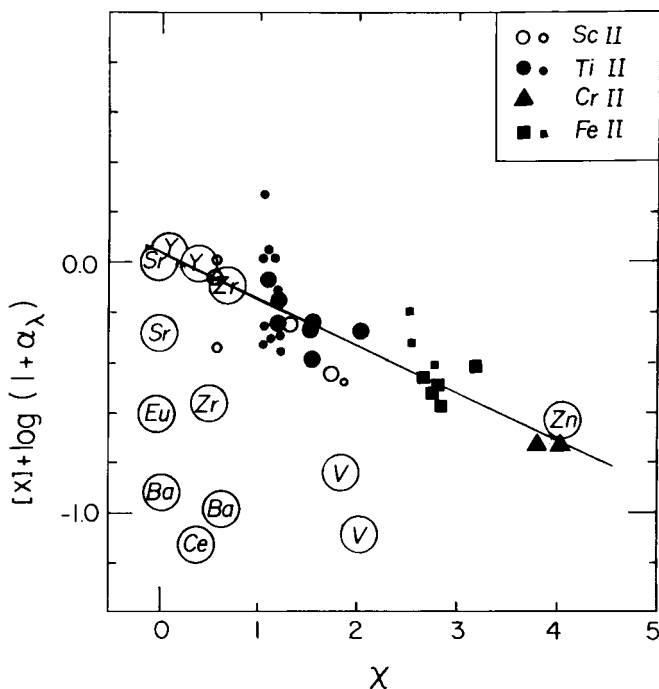
Fig. 3.16. Curve-of-growth shifts (corrected by a factor $(1 + \alpha_\lambda)$ for Rayleigh scattering opacity) for singly ionized metals in the giant HD 122563 ([Fe/H] = -2.6), against excitation potential. The line joining plotted points for Ti II, Fe II and Cr II defines a locus from which one can judge the presence or absence of additional deficiencies in the heavier elements. Adapted from Pagel (1965).

synthesis', has been to use a library of standard stellar spectra in some sort of optimized fitting procedure, subject to reasonable consistency with evolution from a smooth distribution of initial stellar masses (e.g. O'Connell 1976; Pickles 1985). A refinement of the empirical approach is to replace the stellar library with a library of globular clusters, taking old ones with a variety of known metallicities from our own Galaxy and rich clusters with a variety of ages from the Magellanic Clouds, so that stellar evolution and the initial mass function are automatically built in (Bica & Alloin 1986). Optimized fitting is then carried out subject to a reasonable evolutionary scenario, i.e. with metallicity not decreasing with time. Generally one or two cluster types dominate the fitting and it has become clear that the nuclei of large galaxies have stronger metal lines than known Galactic globular clusters, which themselves stop slightly short of solar metallicity.

In the last few years, there has been great progress in the more a-priori method of 'evolutionary population synthesis', pioneered by Tinsley (1968), using the same stellar libraries as in the empirical fitting, and calculating the spectral evolution of single stellar populations (SSP) as a function of age and metallicity. One problem
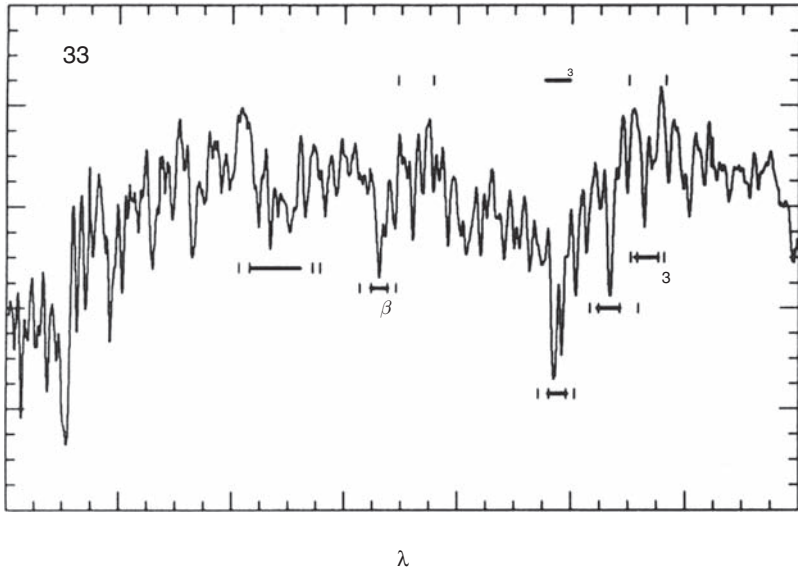
Fig. 3.17. Spectrum of the central region of an S0 galaxy, NGC 3384, showing hydrogen, magnesium and iron spectral features used in the Lick system. The resolution is $3.1\,\text{Å}$ ($\sim 75\,\text{km}\,\text{s}^{-1}$), compared to a line-of-sight velocity dispersion $\sim 140\,\text{km}\,\text{s}^{-1}$. After Fisher, Franx and Illingworth (1996). Courtesy Garth Illingworth.

arising in both methods is the so-called age–metallicity degeneracy (see Eq. 3.61 below), due to the fact that increasing age causes the red giants to become cooler with a consequent strengthening of metallic line features that mimics higher metallicity. This is usually overcome by reference to hydrogen lines (Gunn, Stryker & Tinsley 1981; Rabin 1982; Worthey 1994), which are sensitive to the temperature of dwarf stars at the turn-off from the main sequence. For the method to work, four major ingredients are required (Trager 2004):

- Accurate isochrones from stellar evolution modelling.
- An initial mass function; usually (but not always) the Salpeter function (see Chapter 7) is assumed.
- Stellar fluxes, derived either observationally or theoretically as a function of stellar effective temperature, gravity and chemical composition.
- A library of stellar spectra or absorption-line strengths, taking into account differences in α-element:iron and possibly other element abundance ratios. The spectra may be either observational or synthetic, i.e. theoretically computed.

Recent work in the field of integrated spectroscopy has been largely based on the Lick system (Burstein *et al.* 1984; Faber *et al.* 1985), using pseudo-equivalent
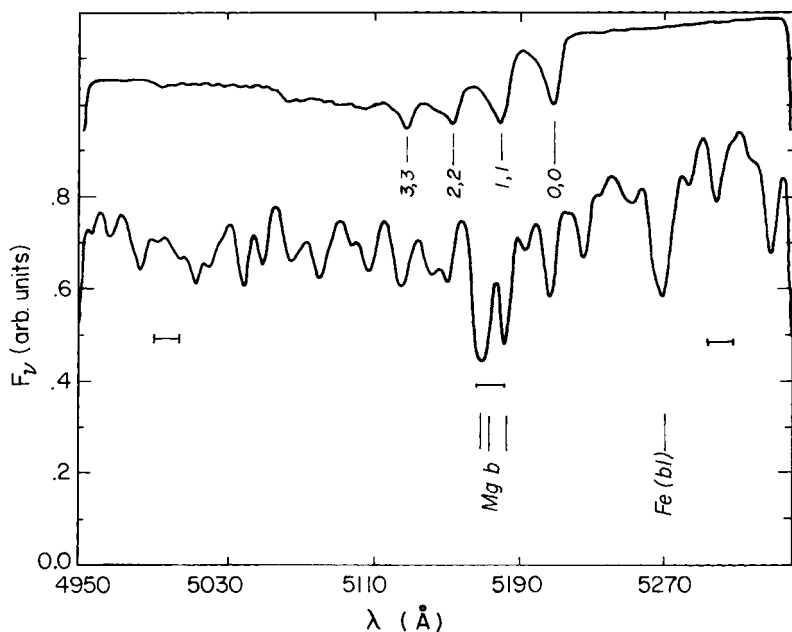
Fig. 3.18. Synthetic spectrum of a red giant, $T_{\text{eff}} = 4500\,\text{K}$, $\log g = 2.25$ in the region of the strong Mg I b lines (see Fig. 3.9). The upper spectrum is the same with atomic lines 'switched off' and shows molecular bands of MgH. The horizontal lines show the central and side bands of the Lick Mg_2 index. Adapted from Mould (1978).

widths of prominent spectral features, some of which are illustrated in Fig. 3.17. In earlier work, following previous studies of strong stellar features by Spinrad and Taylor (1969, 1971), Faber, Burstein and Dressler (1977) defined the Mg_2 index, centred on the Mg b triplet, accompanied by MgH molecular bands, which can be measured using interference filters centred on the region and continuum side bands (see Fig. 3.18) and expressed in stellar magnitude units, while the strengths of the other features are quoted in Å. Assuming an SSP and allowing for age differences on the basis of theoretical models, the feature has been calibrated using Galactic globular clusters for which the metallicity is known from individual stars, by Bender, Burstein and Faber (1993) who gave the calibration

$$\text{Mg}_2 \simeq 0.1 \left[\frac{Z}{Z_\odot} t(\text{Gyr}) \right]^{0.41} \tag{3.61}$$

where $\log(Z/Z_\odot)$ is more or less equivalent to [Mg/H]. A problem with this method (and others) is the lack of well-observed globular clusters with solar metallicity and above, but it undoubtedly gives a good ranking. A second problem is that the Mg/Fe ratio is not universal, so that it is important to measure other features as
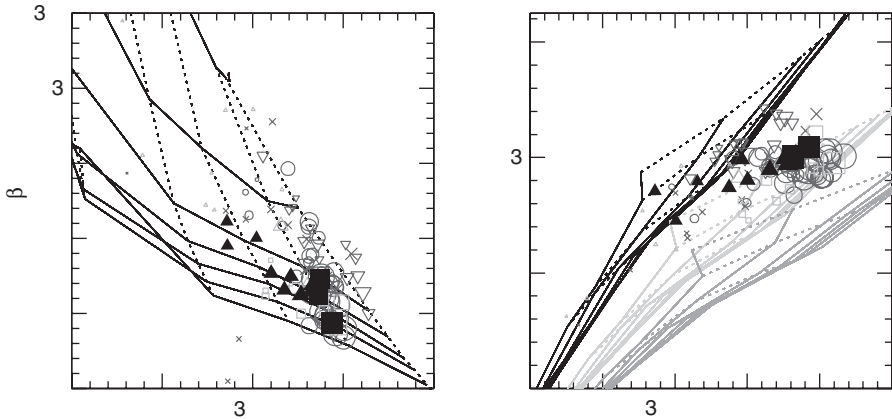
Fig. 3.19. Lick indices as indicators of age, metallicity and Mg/Fe ratio, according to models by Thomas, Maraston and Bender (2003). Left panel: solid lines are isochrones with ages 1, 2, 6, 8, 10, 12 and 15 Gyr (going down from the top) and with Fe/H increasing to the right, while dotted lines are loci of metallicity [Fe/H] = −1.35, −0.33, 0.0, 0.35 and 0.67 (going from left to right) with age increasing downwards. The abscissa is a geometric mean of Mg b and a combination of two iron features which is independent of α/Fe for given Z. Right panel: line bundles are loci of constant [Mg/Fe] = 0.0, 0.3 and 0.5. Data points: circles represent elliptical galaxies, black squares and triangles ellipticals and S0s in the Coma cluster, inverted triangles are S0s in groups and in the Virgo cluster and crosses are bulges of early-type spirals. Sizes of symbols are proportional to the central velocity dispersions, related to total mass. After Trager (2004).

well (see Chapter 11), and a third one is the age–metallicity degeneracy expressed by Eq. (3.61).

In recent years, efforts in this field have reached a high degree of sophistication, breaking the age–metallicity degeneracy by reference to hydrogen lines and allowing for variable element:element abundance ratios, notably Mg/Fe (see Fig. 3.19); other element ratio variations in such abundant species as C, N and Ca can be investigated using these models. Remaining concerns relate to the completeness of the evolutionary tracks – especially if the hydrogen lines are affected by very blue horizontal-branch stars or blue stragglers – and in the case of integrated spectra of field stars as opposed to extragalactic globular clusters (in which the assumption of an SSP is usually valid) to effects of a distribution in metallicity or age. In a composite population, the integrated spectrum gives a light-weighted mean metallicity, which differs from, and is normally less than, the corresponding mass-weighted number, because lower metallicity stars have a brighter red-giant branch. Similarly, young populations tend to dominate the light, even if their relative mass is quite small.

3.3 Photometric methods

Photoelectric or CCD photometry through colour filters is widely used for 'quantitative classification', i.e. to measure major spectral features with low wavelength resolution but rapidly and precisely to obtain major properties of large numbers of stars, such as

- T_{eff}, from continuum slope, Balmer jump in hotter stars and hydrogen-line strengths in F–G stars.
- Luminosity or gravity from H-line strengths in hotter stars, Balmer jump and molecular features in F–K stars.
- Reddening of the continuum by interstellar dust (which leads to excess redness, known as colour excess, relative to the spectral type from H or other line features).
- Metallicity, from integrated strength of metal lines, mostly due to Fe I, giving essentially [Fe/H].

These methods are a development from older photographic spectral methods developed by D. Barbier, D. Chalonge and others in the 1930s and 40s.

Some of the most widely used systems are

- The Johnson UBV(RIJKLMNO) broad-band system, $\lambda/\Delta\lambda \simeq 5$ (see Figs. 3.20, 3.21).
- The Strömgren $uvby\beta$ intermediate-band system, $\lambda/\Delta\lambda \simeq 40$ (see Fig. 3.20) using interference filters.
- The Geneva $UBB_1B_2VV_1G$ broad-band system, $\lambda/\Delta\lambda \simeq 10$.
- The DDO[4] (Toronto) (38)(41)(45)(48) intermediate-band system, designed for the study of cooler stars, mainly giants, on the basis of metallic and molecular features.

The Balmer jump causes strong non-linearity in the (U−B), (B−V) relation (see Fig. 3.21), which is useful in sorting out reddening effects for the hotter stars (in which metal lines are weak) and metallicity effects in F–G stars, where lowered metallicity causes a bluer colour for given T_{eff} due to reduced blocking of radiation by metal lines, which increase in number and strength towards shorter wavelengths. (There is also a reduction in the 'blanketing' or 'backwarming' effect, which is a raising of photospheric temperatures by radiation thrown back by the lines and works in the opposite direction.) This leads to an ultraviolet excess $\delta(U-B)$ relative to the relation for the Hyades, which are among the most metal-rich stars in the solar neighbourhood, having solar or slightly higher metallicity, and are commonly used as a standard. For metallicities that are not too low,

$$\delta(U-B) \simeq 0.03 - 0.2\,[\mathrm{Fe/H}], \tag{3.62}$$

---

[4] David Dunlap Observatory.
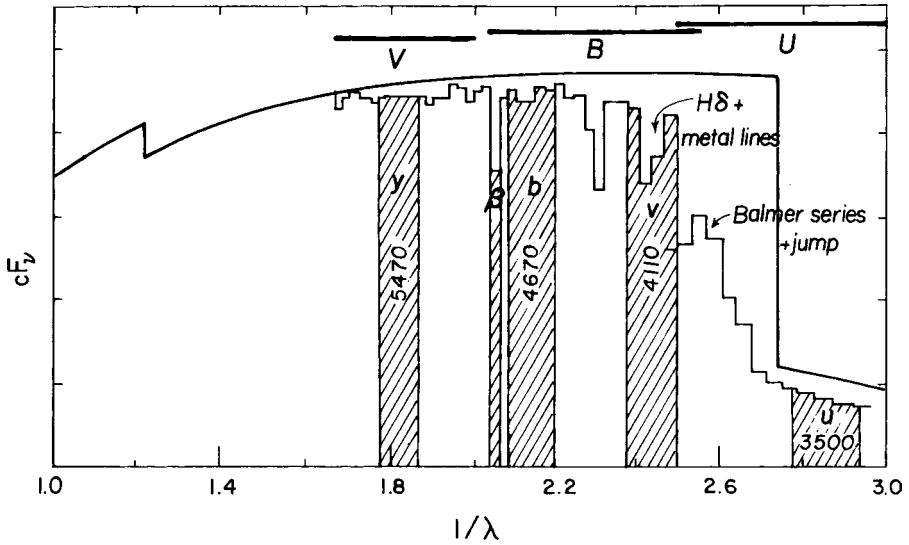
Fig. 3.20. Idealized continuum and actual fluxes measured in 50-Å-wide bands of A7 stars in the Hyades open cluster with $T_{\mathrm{eff}} = 8000\,\mathrm{K}$, plotted against inverse wavelength in $\mu\mathrm{m}^{-1}$. Horizontal lines above the spectrum show the locations of the Johnson U, B, V pass bands and the vertical boxes show schematically the corresponding properties of the Strömgren system with central wavelengths in Å. (In that system, there are actually two Hβ pass bands, one narrow and one broad, so that comparison of the two gives a measure of the strength of the line.) Some prominent spectral features are marked.

where $\delta(\mathrm{U-B})$ is measured in stellar magnitudes. Weaknesses in the U, B, V system for measuring metallicities arise from the dependence of $(\mathrm{U-B})$ on luminosity among F stars and from a loss of sensitivity when metallicities are very low.

The Strömgren system is a very elegant and precise method of quantitative classification (see Fig. 3.20), in which

- $(b-y)$ and β together indicate T_{eff} and reddening; differential blanketing effects on $(b-y)$ are rather small for stars warmer than the Sun;
- $m_1 \equiv (v-b) - (b-y)$ measures line blanketing: $[\mathrm{Fe/H}] \simeq -14\Delta m_1$ for given (intrinsic) $b-y$;
- $c_1 \equiv (u-v) - (v-b)$ measures the Balmer jump, a measure of gravity in F and G stars from which luminosities and ages can be deduced.

Because the continuum bands are equally spaced in $1/\lambda$, these double indices are relatively insensitive to T_{eff} and reddening, for which small corrections are applied.

The Geneva system makes use of some of the ideas of both broad- and intermediate-band systems, being similar to UBV but with the B and V each
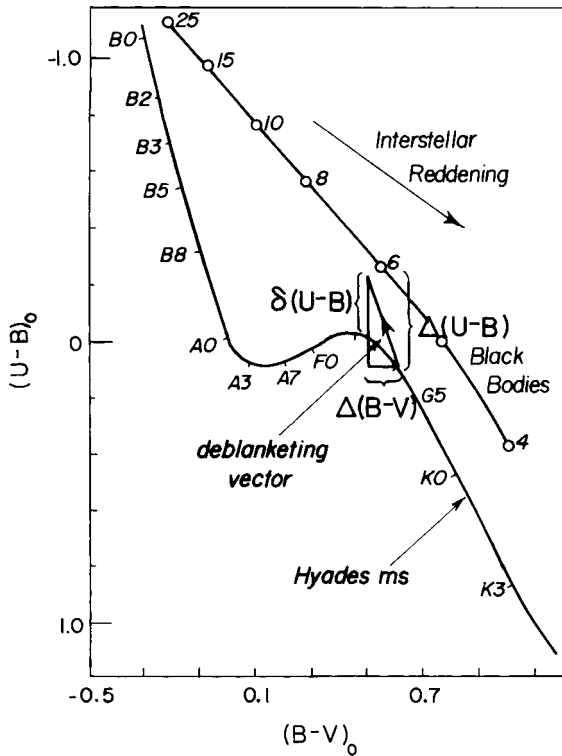
Fig. 3.21. Two-colour plot of (U−B) against (B−V). The curve shows the main sequence for stars with the metallicity of the Hyades, loci of black bodies (with temperatures marked in units of 1000 K) and a deblanketing vector illustrating schematically the effect of metal deficiency in F and G stars. Adapted from Unsöld (1977).

divided into two non-overlapping bands. The DDO system measures metallic, CH and CN features for luminosity and metallicity classification of red giants.

These methods, using well-defined band passes, are capable of a better internal precision than high-resolution spectroscopy (as well as being vastly quicker), but they give (in general) only one abundance parameter and they need high-resolution spectroscopy for calibration.

3.4 Emission lines from nebulae

3.4.1 Introduction

In gas clouds containing one or more hot stars ($T_{\rm eff} > 30\,000$ K), hydrogen atoms are ionized by the stellar UV radiation in the Lyman continuum and recombine to excited levels; their decay gives rise to observable emission lines such as the Balmer series (see, for example, Fig. 3.22). Examples are planetary nebulae (PN), which are envelopes of evolved intermediate-mass stars in process of ejection and
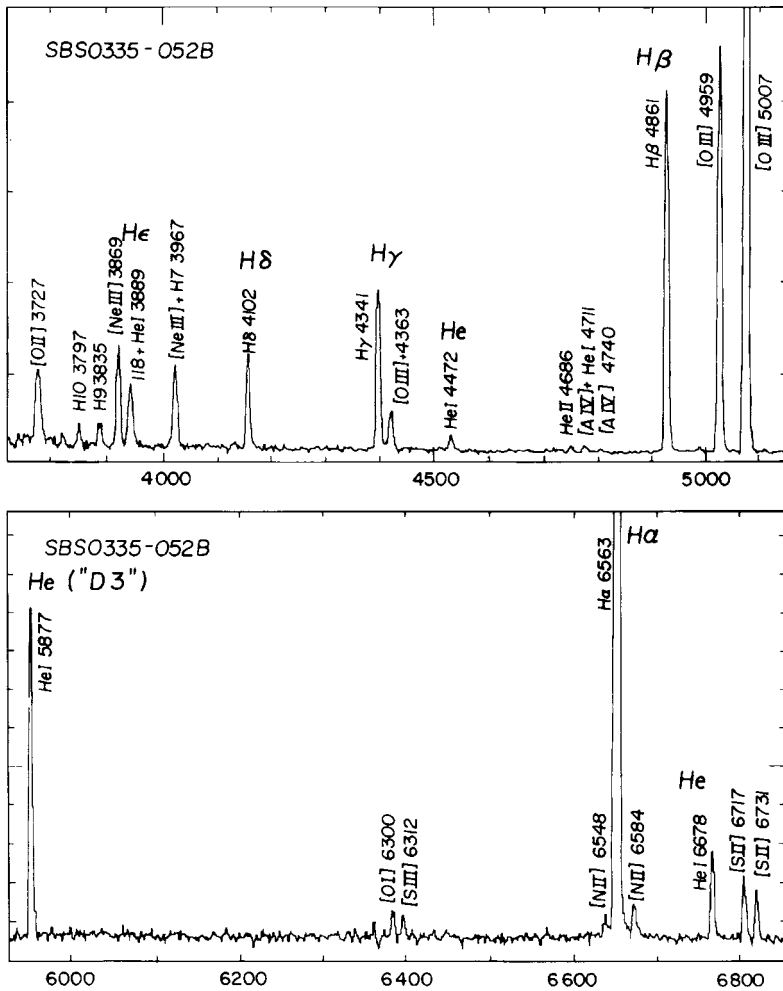
Fig. 3.22. Spectrum of an extragalactic H II region with low abundances, SBS 0335-0520 from the Second Byurakan Survey. Adapted from Melnick *et al.* (1992).

are ionized by the hot, exposed stellar core, and H II regions or 'diffuse nebulae' such as the Orion nebula, which are portions of molecular clouds in which new star formation has taken place within the last few million years and the most massive stars (spectral type O, mass $> \sim 15 \, M_\odot$) are still in the hot main-sequence stage. Giant H II regions, thousands of times larger than Orion, can be studied in distant galaxies and give important information about abundances in those systems, while Galactic H II regions like Orion provide local and more remote Galactic data on light elements (He, Ne, Ar) that do not appear in the solar photospheric spectrum, as well as others, notably N, O and S. Somewhat similar data are provided by PN, but with some modifications (particularly among the CNO elements)

due to previous internal nuclear evolution. Other emission nebulae giving interesting abundance information are Wolf–Rayet and nova shells, in which the cause of ionization is similar, supernova remnants (SNR, excited by radiative shocks) and active galactic nuclei (AGNs, excited by some combination of shocks, non-thermal radiation and thermal radiation from very hot stars).

3.4.2 Sketch of H II region physics

We consider a single hot star or compact cluster containing hot stars surrounded by a cloud of hydrogen and minority elements. If there is enough hydrogen to soak up all the UV photons, the region is said to be 'ionization bounded'; the opposite case is called 'matter bounded'. In the ionization-bounded case, all Lyman photons (continuum and lines) are eventually degraded into Lyman-α and recombination lines or continua of higher series which eventually escape, or may be absorbed by dust if the optical depth is large; this is often the case for Lyman-α. Long ago, Baker and Menzel (1938) identified two extreme cases of optical depth: Case A in which all optical depths are small and all photons escape; and Case B in which Lyman line and continuum photons are absorbed 'on the spot'. In practice, Case B is almost always a better approximation, and in this approximation one can treat the hydrogen atom as though its ground state did not exist, since every emission of a Lyman photon (apart from Ly-α which is multiply scattered) is cancelled by an absorption. In particular, the total recombination rate of protons and electrons is effectively the sum of the rates to the second and higher quantum levels.

The size of a spherically symmetrical ionization-bounded nebula (known as a 'Strömgren sphere') can be found by equating the total number of recombinations in Case B to the total emission rate of ionizing photons from the central star(s):

$$\frac{4}{3}\pi R^3 \epsilon\, n_e n_p \alpha_B(T_e) = Q(N, T_{\text{eff}}, L) \tag{3.63}$$

where we suppose a fraction ϵ of the volume (the 'filling factor') to have uniform electron density n_e and proton density $n_p \simeq n_e$. α_B is the Case B total recombination coefficient, which is a slowly varying function of the electron temperature T_e and the rate Q of ionizing photon production by the embedded star(s) is a function of their number N, effective temperature and luminosity L. The radius of the Orion nebula is a few pc (1 pc or parsec is 3.3 light-years), while that of a giant H II region like 30 Doradus in the Large Magellanic Cloud is of the order of 100 pc; still larger giant H II regions are seen in gas-rich spiral galaxies (especially Scd in the Hubble classification) and in star-forming dwarf galaxies, usually classified as 'blue compact' or 'H II' galaxies or both, according to the method of discovery.

The excess energy ($h\nu - 13.6\,\text{eV}$) of the ionizing photons supplies heat to the ionized gas, which is cooled chiefly by the emission of collisionally excited lines

from ions such as O^{++}, O^+, N^+ etc. This leads to a thermal balance at an elec-
tron temperature of the order of 10^4 K, depending on the stellar temperatures,
the chemical composition (T_e increases with a lowering of abundances because
there are then fewer coolants) and the ionization parameter $u = Q/(4\pi R^2 n_e c)$.
Most of these collisionally excited lines are from 'forbidden' transitions, i.e. tran-
sitions within the ground configuration of the atom or ion having no electric dipole
($\Delta\ell = 0$), and hence a very low transition probability, from magnetic dipole or
electric quadrupole interaction, so that they are not seen in the laboratory and have
to be identified from spectroscopic term analysis. But at the low densities of neb-
ulae (typically 10 to 10^4 cm^{-3}), collisional de-excitation is so slow that a photon
is eventually emitted after a time of the order of seconds. The green [O III] lines
(forbidden lines of O^{++}) $\lambda\lambda$ 4959, 5007 are sometimes the strongest in the entire
optical spectrum (and were once attributed to an unknown element, 'nebulium',
before they were identified by Ira S. Bowen in 1928).

3.4.3 Nebular spectrum analysis

Helium and hydrogen lines are formed by similar recombination processes, so
that their intensity ratios, with effective recombination coefficients calculated from
atomic physics, give the helium abundance subject to corrections for unseen neu-
tral helium and some other effects (see Chapter 4). (The effective recombination
coefficient for a given line, e.g. α_{42} for Hβ, is the sum of all direct recombination
coefficients to its upper level and all higher levels, multiplied by the probability
that a hydrogen atom in each of these levels will eventually emit an Hβ photon.)
To obtain intrinsic line ratios one has to correct the measured ratios for interstellar
reddening, which is usually done by comparing measured ratios of Balmer lines
(the 'Balmer decrement', going down from Hα in the red to higher series members
in the blue) with theoretical values for Case B, using an assumed law for reddening
as a function of wavelength.

Intensities of collisionally excited lines relative to hydrogen lines depend on the
ionic abundance and on the balance between excitation by electron collisions and
de-excitation by both electron collisions and radiation. The emission rates per unit
volume are given respectively by:

$$j(H_{nn'}) = n_e n_p \alpha_{nn'} h\nu_{nn'} \tag{3.64}$$

and

$$j(4959 + 5007) = n_{O^{++}}(N_2/N_{O^{++}})A_{21}h\nu(4959), \tag{3.65}$$

where N_2 represents the population in the appropriate excited state. In the low-
density limit (collisional de-excitation negligible), one 4959 or 5007 photon is
emitted for each collisional excitation (see Fig. 3.23), so
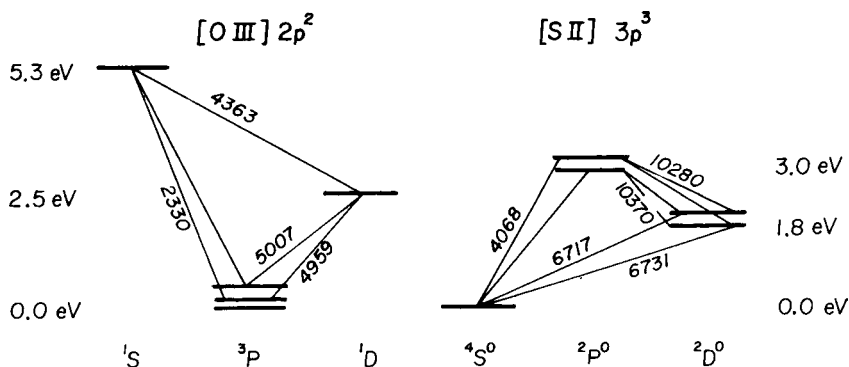
Fig. 3.23. Energy levels of O^{++} and S^+ relevant to the determination of t and n_e.

$$j(4959 + 5007) = n_{O^{++}}n_e h\nu[(g_2/g_1)q_{21}(T_e)e^{-E/kT_e}], \qquad (3.66)$$

where g_2/g_1 is a statistical weight factor, E the excitation energy ($E = h\nu$ in this case) and $q_{21}(T_e)$ is the collisional de-excitation rate coefficient, given by

$$g_2\, q_{21} = \pi\langle\bar{\lambda}^{-2}V\rangle\Omega_{12} = 8.63 \times 10^{-8}\, t^{-1/2}\Omega_{12}\ \mathrm{cm^3 s^{-1}}; \qquad (3.67)$$

t is the electron temperature in units of 10^4 K and $\Omega_{12} = \Omega_{21}$ a dimensionless constant, often of order 1, calculable from quantum mechanics and known as the 'collision strength' (analogous to oscillator strength, or, more precisely, gf).[5] Hence

$$\frac{n_{O^{++}}}{n_p} = \frac{I(5007)}{I(H\beta)} \times f(T_e) \qquad (3.68)$$

where $f(T_e)$ is a strong function driven by the exponential in Eq. (3.66), and similar relations exist for other ions. The total oxygen abundance can usually be found by adding those of O^{++} and O^+ which latter produces a strong doublet at λ 3727; in some planetary nebulae, novae and AGNs, higher ionization states of oxygen (detectable in the UV) may need to be considered. For most other elements, only one ionization state is visible in the optical and ionization correction factors need to be estimated, or found from observations in the UV and/or IR.

At higher densities, the population factor in Eq. (3.65) ceases to be proportional to the collisional excitation rate, but is rather given (in a two-level approximation) by

$$\frac{N_2}{N_1} = \frac{q_{12}n_e}{q_{21}n_e + A_{21}} = \frac{g_2}{g_1}\frac{e^{-E/kT_e}}{1 + A_{21}/(q_{21}n_e)}. \qquad (3.69)$$

[5] In more refined calculations, Ω is replaced by its average over the Maxwellian velocity distribution and is a slowly varying function of t.

Thus, above a certain critical density

$$n_{\text{crit}} = A_{21}/q_{21}, \qquad (3.70)$$

the relative population of the excited state ceases to increase with n_e and the forbidden line is 'suppressed'; when the density approaches within an order of magnitude of n_{crit}, collisional de-excitation has to be allowed for.

3.4.4 Determination of electron temperatures and densities

The left panel of Fig. 3.23 shows the energy levels of the ground configuration $2p^2$ of O^{++} and transitions between them. Direct transitions from the first excited level to the ground term, which in this case produce the famous 'nebulium' lines, are referred to as 'nebular', while the transition at λ 4363 is called 'auroral', by analogy with the similar transition of [O I] λ 5577 that is prominent in aurorae and the night sky in general. The third transition, from the upper state of λ 4363 to the ground state, occurs (in this case) in the UV and is called 'transauroral'. The ratio of the auroral line λ 4363 to the nebular lines $\lambda\lambda$ 4959, 5007 is a sensitive measure of electron temperature by virtue of an exponential factor analogous to that in Eq. (3.66). Similar configurations occur for N^+ and S^{++} and these can also be used in favourable cases, mainly PN and H II regions where the heavy-element abundance is below solar; in high-abundance H II regions t becomes so low that auroral lines become unmeasurably weak, but the situation is better for PN because they can have very hot ionizing stars and high surface brightness.

The right panel of Fig. 3.23 shows energy levels of a p^3 electron configuration, exemplified by O^+ and S^+. The nebular lines form a close doublet ([O II] $\lambda\lambda$ 3729, 3726; [S II] $\lambda\lambda$ 6717, 6731) with an intensity ratio that depends on n_e because at low density it is just the ratio of collisional excitation rates from the ground state, while at high density the upper states are relatively near thermal equilibrium and the line intensities are governed by statistical weights and radiative transition probabilities. The critical density is around $10^3 \, \text{cm}^{-3}$ (see Fig. 3.24), whereas for [O III] nebular lines it is much higher. In practice, [S II] is used more commonly than [O II] because it does not demand such a high spectral resolution.

The first of two limitations of the use of auroral:nebular line ratios to obtain t is the possibility that there may be temperature fluctuations (Peimbert 1967) or gradients in the nebula, which would cause a bias towards overestimating t and therefore underestimating abundances. The extent of this effect in H II regions is still not well known, but it could be of the order of 0.1 or 0.2 dex, judging from recombination lines of C II and O II, which are much less temperature-sensitive, but very weak and consequently available only for the brightest regions (e.g. Peimbert & Peimbert 2006). The gradients lead to a requirement to use different electron temperatures for different ions. The second limitation is the disappearance of auroral lines when
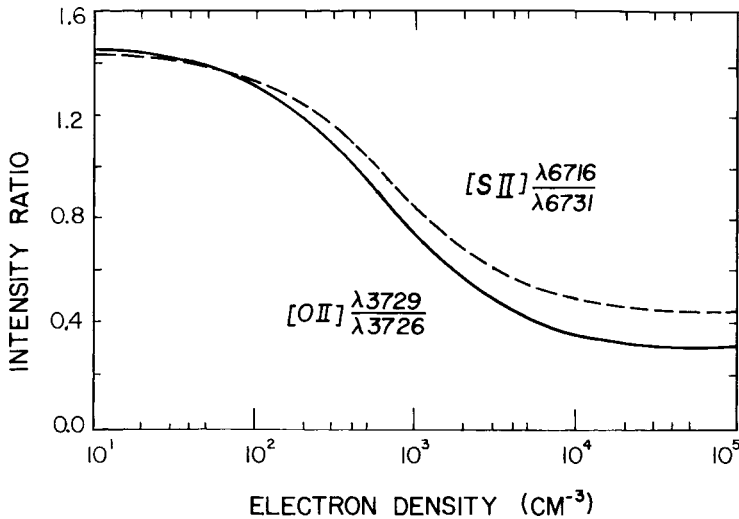
Fig. 3.24. Dependence of [O II] and [S II] doublet ratios on electron density when $t = 1$. The [S II] line at λ 6716 is often referred to as λ 6717. Reproduced with permission from Osterbrock (1988). Copyright by Astronomical Society of the Pacific.

$t < 0.75$ or so, depending on the surface brightness. To overcome the latter problem, so-called 'empirical' methods have been developed that can give a rough idea of t and abundances from nebular lines alone, inspired partly by photo-ionization models and partly by observational trends of line strengths with galactocentric distance in gas-rich spirals which, following Searle (1971), are believed to be due to a radial abundance gradient with abundances decreasing outwards (Figs. 3.25, 3.26), and much use has been made of the line ratio, which is defined as (Pagel *et al.* 1979)

$$R_{23} \equiv ([\text{O II}]3727 + [\text{O III}]4959, 5007)/\text{H}\beta$$

As abundances of cooling ions such as O^{++} decrease from near-solar values (shown by the horizontal line in Fig. 3.26), the intensity of the [O III] nebular lines relative to hydrogen lines paradoxically increases because of the rise in t, which itself is largely controlled by emission of [O III] fine-structure transitions in the far infrared. This goes on up to a certain point where the nebular lines take over a significant cooling role themselves and reach a maximum around $12 + \log(\text{O/H}) = 8.1$; for still lower abundances, the cooling is dominated by hydrogen free–free emission, and the lines revert to the more intuitively natural behaviour of decreasing with diminishing abundance.[6] The resulting ambiguity is resolved by reference to the

---

[6] The analogous ratio $S_{23} \equiv ([\text{S II}]$ 6717-31 + [S III] 9069-9532)/Hβ behaves similarly to R_{23}, but with the turnover at a somewhat higher abundance (Vílchez & Esteban 1996, Christensen, Petersen & Gammelgaard 1997, Díaz & Pérez-Montero 2000).
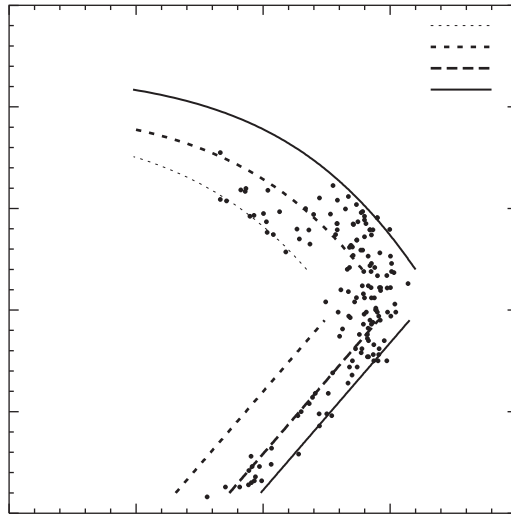
Fig. 3.25. Trends of nebular line strengths in H II regions with oxygen abundance. This figure shows oxygen abundance in H II regions of the Milky Way and spiral and irregular galaxies (determined using measured electron temperatures) vs. log R_{23}, after Pilyugin (2003); the p parameter is the line ratio [O III]/([O II] + [O III]).
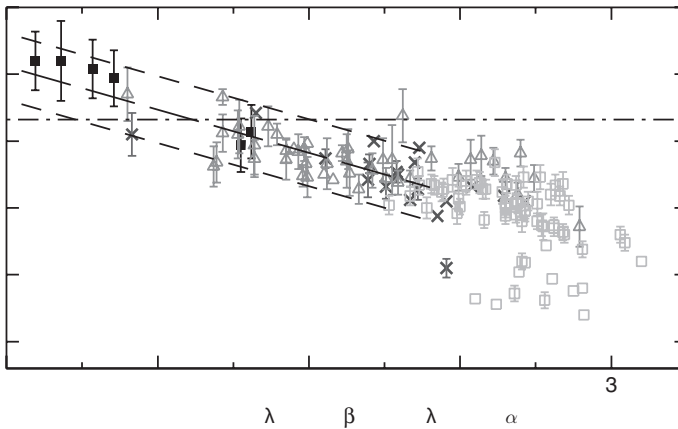
Fig. 3.26. Trends of nebular line strengths in H II regions with oxygen abundance. This figure shows oxygen abundance in H II regions of spiral and irregular galaxies (determined using measured electron temperatures or – for the filled squares – photo-ionization models) vs. log [O III] λ 5007/[N II] λ 6584. Solar oxygen abundance is shown by the horizontal line. After Pettini and Pagel (2004).

line ratio [O III]/[N II], which varies very much more than the abundance ratio N/O (Alloin *et al.* 1979; Pettini & Pagel 2004), or [N II]/Hα (Denicoló, Terlevich & Terlevich 2002).

3.4.5 Other kinds of emission nebulae

Apart from H II regions and PNs, interesting abundance data can be derived from a number of other nebular-type objects:

- Novae and symbiotic stars have shells which are excited by extremely hot stars (several $\times 10^5$ K) like some PNs, but denser, and display overabundances of elements up to Ne or beyond due to thermonuclear processes affecting matter accreted from a companion by a white dwarf.
- Supernova remnants (SNR) in early stages of expansion display results of advanced (explosive) nucleosynthesis, but in later stages light up the interstellar medium by shock excitation and give information about the ISM in external galaxies complementary to that derived from H II regions.
- AGNs range from their most extreme form in quasi-stellar objects (QSOs) and radio galaxies to milder forms in Seyfert galaxies, low-ionization emission line regions (LINERs) and starburst galaxies. The latter are essentially giant H II regions, usually rich in dust, in nuclei of Sc galaxies, and perhaps should not be classified as 'active' at all, but they can have very high luminosities in the infrared and may be relevant to luminous distant galaxies discovered by IRAS[7], which are among the most luminous objects known.

  QSOs[8] have high-excitation spectra with very broad lines, while Seyfert galaxies are early-type spirals (Sa to Sc) with nuclear emission-line spectra displaying differing proportions of a broad-line component similar to a QSO (Sy 1) and a narrow-line component (Sy 2) somewhat like the spectrum of a PN, but with very strong forbidden lines. The broad- and narrow-line components appear to come respectively from an inner, high-density region and an outer relatively low-density region, surrounding a 'central engine' (usually believed to be a black hole swallowing material from an accretion disk). The 'engine' emits a non-thermal spectrum with a component given by a power law, $F_\nu \propto \nu^{-n}$ where $n \sim 1$; and there is a more black-body-like component from the accretion disk. There may also be contributions to the ionizing continuum from radiative shocks and from very hot stars that have evolved by extensive mass loss to an extreme Wolf–Rayet (WR) stage, since fresh star formation is usually observed around Seyfert nuclei.

---

[7] Infrared Astronomy Satellite, launched in 1983.

[8] The term 'QSOs' is used to cover both radio-loud quasi-stellar objects, commonly known as 'quasars', and radio-quiet objects that otherwise have similar characteristics.
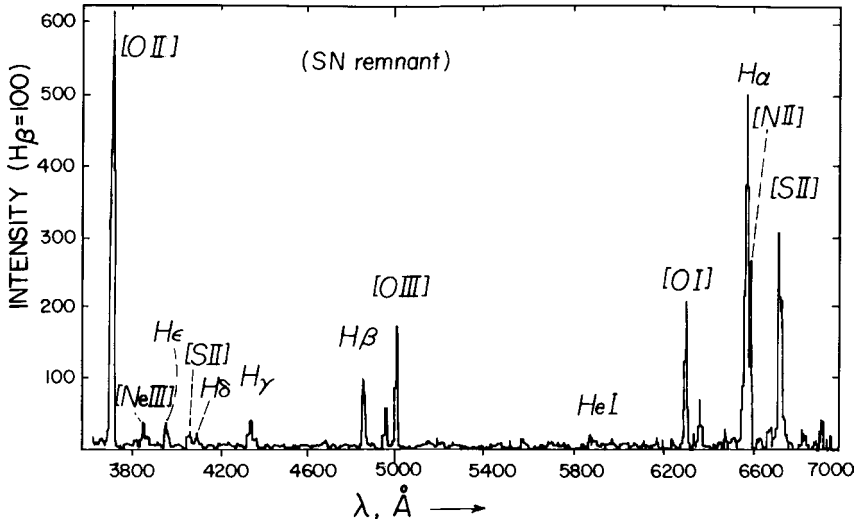
Fig. 3.27. Spectrum of a supernova remnant in the Scd spiral M33. Adapted from
Dopita, D'Odorico and Benvenuti (1980).

LINERs are weaker emission-line regions in certain elliptical and early-type
spiral galaxies (e.g. M51 and M81) showing relatively strong lines of [O I],
[N II] and [S II], similar to SNR. It is not clear whether they are excited by
shocks like SNR or by a very dilute (i.e. low u) non-thermal spectrum.

The analysis of SNR spectra (see Fig. 3.27) is more complicated than that of
ordinary H II regions because there are strong gradients in ionization and electron
temperature in the shocked gas which also photo-ionizes the pre-shock gas. Thus a
typical SNR, like the Cygnus Loop or N159 in the Large Magellanic Cloud (LMC),
is an X-ray source and shows a wide range of excitation conditions in its optical
spectrum, going from Mg I to [Ne V]. Electron temperatures range from $t \simeq 2$
for [O III] to $t \simeq 1.2$ for [N II] and $t \simeq 0.9$ for [S II] and analysis requires a
stratified model.

The evolution of a supernova remnant is believed to involve three main stages:

(i) Free expansion of the ejecta until they have swept up a mass of ISM comparable to their
     own mass, $\sim 10\,M_\odot$ in the case of a Type II; this would be the mass within a radius
     $\sim 1\,\mathrm{pc}$ that would be covered in a time of the order of 50 years. However, the SN is
     likely to be surrounded by one or more lumpy circumstellar shells due to previous mass
     ejection, which would make the time shorter; the impact of ejecta from SN 1987A in
     the LMC on such a shell began after some 15 years. The free expansion of the shell is
     decelerated by compressed material between it and the preceding shock front, resulting
     in a reverse shock which creates a hot X-ray emitting bubble on the inside of the shell.
(ii) The Sedov (self-similar) expansion phase, driven by thermal pressure. In this phase,
     which covers a distance $\sim 15\,\mathrm{pc}$ over a period $\sim 2 \times 10^4\,\mathrm{yr}$, the swept material cools
     adiabatically and accumulates in a shell behind the shock front.

JUMP CONDITIONS
STRONG SHOCK M>>1, B→O

UPSTREAM/PRE-SH | DOWN STREAM/POST SH

$\rho \rightarrow \rho \quad \rho' \rightarrow \quad \rho \sim \quad \rho$

$\xrightarrow{sh}$
$T \quad \rho$

$\xrightarrow{U} \quad \xrightarrow{U'}$
$T \quad \rho \cdots T'\rho'$ $\cdots\cdots\cdots\cdots$ to SN

$\rightarrow \qquad ' \rightarrow O$

$\rightarrow 3 \qquad ' \rightarrow$

'ADIABATIC' $\dfrac{cool}{recombine}$ ISOTHERMAL

$pc \qquad yrs$
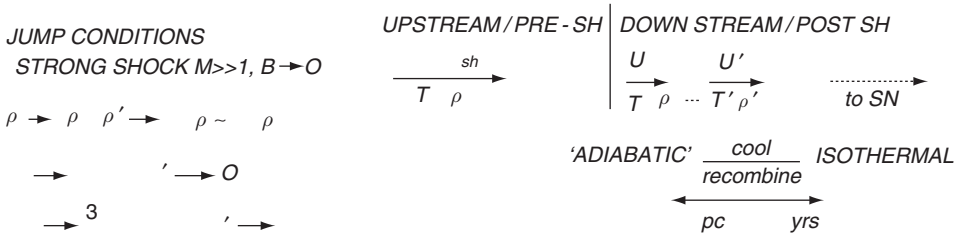
Fig. 3.28. Schematic picture of conditions surrounding a supernova shock. *M* is the Mach number, *B* the magnetic field and velocities are relative to the shock front.
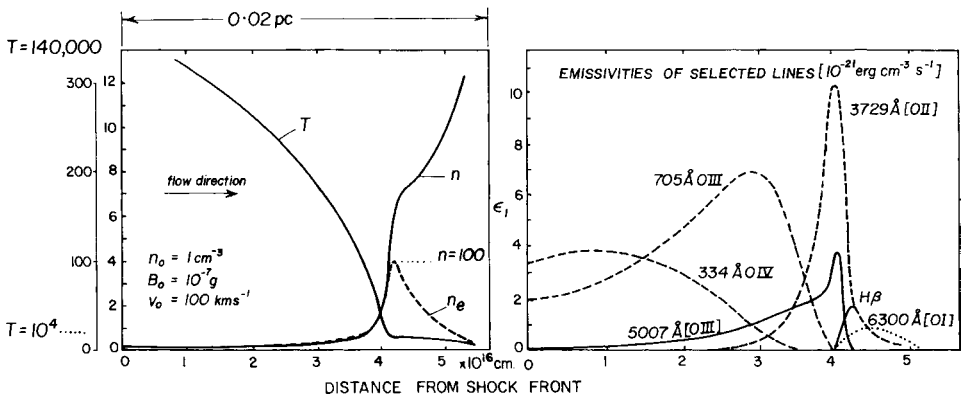
Fig. 3.29. Physical parameters and line emissivities in the post-shock gas according to a model of the Cygnus Loop SNR. Adapted from Cox (1972).

(iii) The snowplough phase in which the swept-up material cools radiatively for up to about 10^5 yr.

In a steady state, the shock velocity $\simeq 100 \, \text{km s}^{-1}$ and the pre-shock number density $\simeq 1 \, \text{cm}^{-3}$. The jump conditions are crudely illustrated in Fig. 3.28 and results of a specific model calculation in Fig. 3.29.

Useful line ratios to pin down the basic parameters of a model for the optical lines are (Dopita 1977):

- The [O II] or [S II] doublet ratio gives the ambient ISM density ρ_1 or n_1, normally after division by 4 in accordance with the jump condition for a strong shock.
- The ratio of [O III] λ 5007 to [O II] λ 3727 or [O I] λ 6300 is a diagnostic of the post-shock temperature T_2, and hence of the shock velocity.

Because of the ions' role in cooling, the intensities of [O II] and [S II] lines are affected by other elements, notably carbon, which is not accessible in the visible

region, and do not increase linearly with abundance, but when the abundances are not too high, as in the Magellanic Clouds, for example, the resulting uncertainties are small, subject to the models being realistic (plane-parallel, ionization-bounded, negligible magnetic pressure etc.), so that N, O and S abundances can be found from the singly charged ions.

Ionization by a power-law continuum also leads to a much greater range in *t* and ionization than exists in H II regions ionized by O-stars, because while in the latter case there is a sharp boundary between the hot H II region and a surrounding cool H I region, high-energy photons from the power-law continuum produce an extended boundary region with declining ionization and residual heating.

3.4.6 Abundances from X-ray spectra

Advances in X-ray astronomy have led to good spectra of energetic objects like supernova remnants (see Fig. 3.30) and the hot gas in clusters of galaxies (see Fig. 3.31), from which some deductions about abundances can be made subject to realistic modelling, which is not always straightforward. The SNR shown in
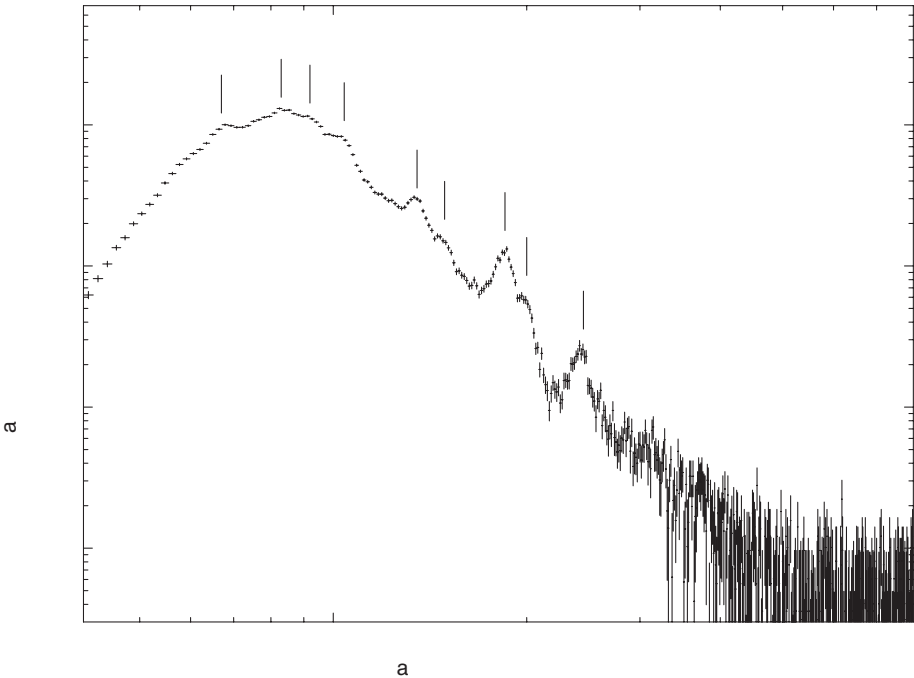
Fig. 3.30. X-ray spectrum of the supernova remnant N49 in the LMC, aged between 5000 and 10 000 yr, taken with the Advanced CCD Imaging Spectrometer on board the Chandra X-ray Observatory, showing H-like and He-like K-shell lines of abundant light elements and some L-shell lines of iron, after Park *et al.* (2003).
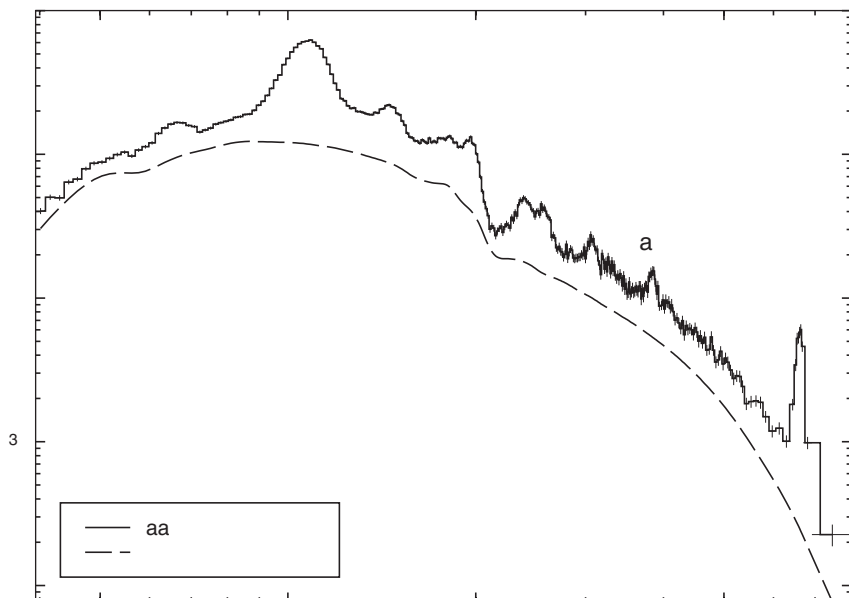
Fig. 3.31. X-ray spectrum taken from the XMM-Newton and Chandra X-ray observatories of the inner part of the Centaurus cluster of galaxies, where the metallicity is roughly twice solar, showing the iron L- and K-shell features at energies of 1.2 and 6.8 keV repectively. The curve is a two-component fit to the continuum with temperatures of 0.7 and 1.5 keV. After Sanders and Fabian (2006). Courtesy Andy Fabian.

Fig. 3.30 is believed to be in the Sedov phase, with the shock propagating at a high velocity ($730\,\mathrm{km\,s^{-1}}$) in the rarefied intercloud ISM ($n_\mathrm{H} \sim 0.9\,\mathrm{cm^{-3}}$) and at a much slower velocity ($< 140\,\mathrm{km\,s^{-1}}$) in nearby dense molecular clouds ($n_\mathrm{H} \sim 150\,\mathrm{cm^{-3}}$) where it gives rise to optical and UV emission. The X-ray continuum is a sum of recombination radiation from various ions plus thermal bremsstrahlung, aka free–free emission, the latter being given for an ion with charge Ze by

$$\frac{j_E}{n_e n_+} = \frac{32}{3} \left(\frac{\pi}{6}\right)^{\frac{1}{2}} \frac{e^6 Z^2}{\hbar m_e^2 c^3} \left(\frac{m_e}{kT}\right)^{\frac{1}{2}} g\, e^{-\frac{h\nu}{kT}} = 1.65 \times 10^{-23} Z^2 g T_6^{-\frac{1}{2}} e^{-\frac{E}{11.6 T_6}} \quad (3.71)$$

$\mathrm{erg\,cm^3\,s^{-1}\,keV^{-1}}$, where the Gaunt factor g is a slowly varying function of order unity, E is in keV and T_6 is the temperature in units of $10^6\,\mathrm{K}$, equivalent to $0.086\,\mathrm{keV}$. The continuum of N49 is fitted by one of a plasma with temperatures in the region of $kT \simeq 0.6\,\mathrm{keV}$, modulated at low energies (below about $1\,\mathrm{keV}$) by interstellar absorption from a column of $2 \times 10^{21}\,\mathrm{H\,atoms\,cm^{-2}}$, and the lines come from a combination of recombination-cascade and collisional excitation of highly charged ions. A multi-phase model, consistent with the Sedov solution and

allowing for non-equilibrium ionization,[9] gives elemental abundances in good agreement with those found from optical SNR spectra and H II regions in the LMC.

The intra-cluster gas in clusters of galaxies is generally hotter and in collisional ionization equilibrium, and the continuum is dominated by bremsstrahlung, making the interpretation of at least the hydrogen-like and helium-like K-shell emission lines relatively straightforward, but they are comparatively weak and an accurate determination of the temperature(s) is critical.

3.5 Abundances: main results
3.5.1 Solar and local Galactic abundances

- Photospheric absorption lines (Fraunhofer lines) provide element:hydrogen number ratios M/H for commoner elements with suitable features in the optical or IR from neutral atoms, singly charged ions or molecules such as CH, CN, CO, OH, MgH; there have been great improvements in knowledge of oscillator strengths in recent years and abundances thus found for selected elements are given in Table 3.4. He, Ne and Ar are common elements not determinable in this way, and most information on them comes from hot stars or nearby H II regions like Orion. There is but limited information on rare elements such as the actinides (U, Th) and rare earth elements, and on isotope ratios, which are restricted to those that can be determined from molecules, e.g. C, O and Mg. Photospheric analysis shows that the number ratio (C + N + O)/H (the commonest elements after He, not counting Ne) is close to 10^{-3} and that of easily ionized metals (Na, Mg, Al, Si, Ca, Fe) contributing essentially one free electron per atom is 10^{-4}. In terms of mass fractions, $Z/X \simeq 0.020$ and $Z \simeq 0.015$ if one assumes a helium mass fraction $Y = 0.27$. Among fragile light elements, D has been completely destroyed in the photosphere and Li has been reduced by two orders of magnitude, but Be and B are not significantly depleted.

- Emission lines from the solar chromosphere, prominences and corona, especially in the far UV, provide somewhat less accurate indications of abundances (including those of He, Ne and Ar) in the outer solar atmosphere. There is some evidence for element segregation in these regions, including a relative enhancement of elements with a low first ionization potential ('FIP effect'), an effect also found in high-energy particles from solar flares (sometimes called solar cosmic rays) and in the solar wind; a similar-looking effect is also found in source abundances in Galactic cosmic rays which are determined by correcting for propagation effects in the ISM, but this now seems more likely to be a

---

[9] 'Equilibrium' (i.e. local steady-state) ionization leads in this régime to solar-corona-like conditions where collisional ionization is balanced by recombination and the degree of ionization is fixed by the temperature alone, the electron density cancelling out. However, here departures from equilibrium occur because the time taken to establish ionization equilibrium is not negligible with respect to the timescale of expansion.

Table 3.4. *Solar abundances relative to* $\log N_H = 12.00$; *meteoritic abundances relative to* $\log N_{Si} = 7.51$

Element		Photospheric	Meteoritic	Element		Photospheric	Meteoritic
1	**H**	12.00		21	**Sc**	3.05	3.04
2	**He**	(10.93)		22	**Ti**	4.90	4.89
3	**Li**	1.05	3.25	23	**V**	4.00	3.97
4	**Be**	1.38	1.38	24	**Cr**	5.64	5.63
5	**B**	2.7	2.75	25	**Mn**	5.39	5.47
6	**C**	8.39		26	**Fe**	7.45	7.45
7	**N**	7.78		27	**Co**	4.92	4.86
8	**O**	8.66		28	**Ni**	6.23	6.19
9	**F**	4.6:	4.43	29	**Cu**	4.21	4.23
10	**Ne**	(7.84)		30	**Zn**	4.60	4.61
11	**Na**	6.17	6.27	37	**Rb**	2.6	2.33
12	**Mg**	7.53	7.53	38	**Sr**	2.92	2.88
13	**Al**	6.37	6.43	39	**Y**	2.21	2.17
14	**Si**	7.51	7.51	40	**Zr**	2.59	2.57
15	**P**	5.36	5.40	56	**Ba**	2.17	2.16
16	**S**	7.14	7.16	57	**La**	1.13	1.15
17	**Cl**	5.5:	5.23	58	**Ce**	1.58	1.58
18	**Ar**	(6.18)		60	**Nd**	1.45	1.43
19	**K**	5.08	5.06	63	**Eu**	0.52	0.49
20	**Ca**	6.31	6.29	90	**Th**		0.06

Data are from a review by Asplund, Grevesse and Sauval (2005). When two decimal places are given, the estimated error of photospheric abundances is of the order of ± 0.1; the meteoritic ones are usually somewhat more accurate. Values in brackets are based on solar wind and energetic particles normalized to oxygen; they are reasonably consistent with results from Galactic nebulae. The recent photospheric figures, largely based on 3D hydrodynamical simulations with non-LTE effects taken into account, correspond to a somewhat lower heavy-element content than was usually assumed earlier (e.g. Anders & Grevesse 1989): specifically, $(X, Y, Z, Z/X) \simeq (0.739, 0.249, 0.012, 0.0165)$, but the downward revision is hard to reconcile with helioseismology and has been disputed (e.g. Delahaye & Pinsonneault 2006). Solar System abundances, allowing for diffusion, are given and discussed by Lodders (2003); they are typically about 10 per cent higher.

preference for refractories locked in dust grains (Meyer, Drury & Ellison 1998; see Section 9.2). The solar wind is a vital source of information on ^{3}He (see Chapter 4).

- The Earth's crust, mantle and core are strongly influenced by 'differentiation' processes which could have resulted from gravitational separation ('smelting') in an early molten phase of the planet, or from the sequence in which different chemical species condensed from the primitive solar nebula and were subsequently accreted. Seismology indicates that there is a liquid core (with a solid inner core) with radius 3500 km consisting mainly of iron (with some Ni and FeS) surrounded by a plastic (Fe, Mg silicate) mantle of thickness 2900 km.

The solid crust is only 30 to 40 km thick under continents, where it is mainly granite (Al-rich silicates), and still thinner (10 km) under the oceans where it is mainly basaltic (Mg-rich silicates), and slow convection in the mantle drives plate tectonics. The oceans and atmosphere are thought to have been formed after the surface solidified. Terrestrial elements are therefore segregated according to geochemical affinities (Goldschmidt 1954): 'Atmophile' (e.g. N_2, O_2, inert gases, favouring the atmosphere); 'lithophile' (O-rich minerals, Na, K, Ca, rare earths, actinides, favouring silicate rocks); 'chalcophile' (S, Cu, Zn, Sn, Pt, Ag, Cd, Hg, favouring sulphur-rich minerals in ore deposits and the interior); and 'siderophile' (Fe, Ni, Ga, Ge, Ru, Rh, Os, Ir, Pt, favouring metallic iron–nickel phases that have largely sunk down into the core). Moon rocks, returned to Earth by the Apollo astronauts in 1969–72, are also highly differentiated.

Terrestrial isotope ratios are mainly unaffected by these processes and therefore provide valid information about standard abundances of individual nuclear species except in special cases where they have been modified by fractionation (e.g. D/H), differential escape from the atmosphere or radioactive decay, e.g. ^{40}Ar is enhanced in the atmosphere relative to ^{36}Ar by ^{40}K decay and there is extra ^{136}Xe thought to result from fission of ^{244}Pu.

- Meteorites play an essential role in the story. Meteorites come in three main types, stones, stony irons and irons, the latter consisting of metallic iron alloyed with Ni in various crystalline forms. The stones are divided into 'achondrites', which are a residue from melting, and 'chondrites', which have never been molten. Chondrites contain rounded glassy drop-like inclusions 0.5 mm to 1 cm in diameter called 'chondrules' together with specks of metallic iron and FeS in a surrounding 'matrix' that mainly consists of iron magnesium silicates (olivine and pyroxene). Chondrites differ in such properties as degree of oxidation, metamorphism (by which the chondrules gradually diffuse) and equilibration, i.e. the approach to chemical equilibrium between adjoining mineral phases; but their atomic composition (not counting volatile elements such as H, C, N, O, S ...) is fairly uniform and in agreement with the best determinations from the solar Fraunhofer lines. Most meteorites result from the break-up of small parent bodies (asteroids) that were not subjected to the kind of differentiation that affects major planets like the Earth (and Moon). The least metamorphosed and most highly altered by water are a subtype of the carbonaceous chondrite class called CI1, e.g. Orgueil (France) 1864, containing water in clay minerals and organic compounds, which implies that they have not been subjected to high temperatures.

CI1 meteorites provide a particularly good match to solar, and are used to fill in the gaps left by unknown or inaccurate photospheric abundances; as the latter have improved over the years, the agreement with CI1 (except in the special

situation of Li) has become even better, so that it is almost an article of faith that these objects have an atomic composition representing that of the Solar System. The solar iron abundance has played an interesting historical role in this comparison: in the early 1960s, the photospheric estimate of Fe (relative to Si which is the meteoritic standard) was an order of magnitude low compared to meteoritic, which gave rise to much speculation, but this was later found to be a result of bad oscillator strengths. In recent years, the position has been nearly reversed, in that some photospheric determinations based on Fe I are slightly higher than meteoritic, but the disagreement (which is in any case under 0.2 dex) is almost certainly equally spurious, particularly in view of the fact that solar Fe II gives agreement with the meteorites. Table 3.4 gives photospheric and meteoritic (CI1) logarithmic abundances for selected elements. The complete table, together with terrestrial and occasionally meteoritic isotope ratios, forms the basis for the standard local abundance distribution of nuclides illustrated in Fig. 1.4. That distribution is typical (as far as one can tell) of most nearby stars and the local ISM, apart from variations by factors up to 2 or 3 in Fe/H or Z/X, which on average is 0.1 ± 0.1 dex below solar, and moderate (but interesting) variations in O/Fe and other element ratios that will be discussed in Chapter 8.

3.5.2 Isotopic anomalies in meteorites

Meteorites show a number of isotopic variations or 'anomalies' which are only partially understood and give some tantalizing clues as to events in the formation of the Solar System that may have affected the 'Standard' abundance distribution itself. All meteorites are affected by radioactivity. Long-lived activities enable minerals to be age-dated (see Chapter 10) and short-lived ones lead to fission tracks from ^{244}Pu and to decay products that may significantly enhance the abundance of an intrinsically rare species, e.g. ^{22}Na $\rightarrow ^{22}$Ne, ^{26}Al $\rightarrow ^{26}$Mg, ^{129}I $\rightarrow ^{129}$Xe. Meteoritic isotope ratios are also affected by exposure to cosmic rays.

The carbonaceous chondrite Allende (type CV3) landed in Mexico in February 1969 just at an opportune time when laboratories had geared up with ultra-refined mass-spectrometer and related techniques for the purpose of studying lunar samples brought back by the Apollo astronauts. Approximately 2 tons of Allende fell, providing a supply of an unusually large quantity of material. It is highly unequilibrated, containing chondrules and a variety of grains of various minerals that appear to have quite distinct chemical histories. Much attention has been devoted to coarse-grained refractory inclusions, rich in calcium and aluminium (calcium-aluminium-rich inclusions or CAIs), with sizes of the order of several mm, which display a uniform overabundance (relative to Si) of a wide range of refractory elements with quite different chemical properties. This suggests condensation in a

high temperature environment (presumably at the very first stage of the formation of solid bodies in the Solar System, something also suggested by age-dating) without subsequent equilibration with the residual gas, or with the solids that condensed from it later. This is in contrast to the bulk of Solar-System material which is supposed to have undergone some form of condensation sequence under conditions approaching thermal equilibrium. Isotopic anomalies in these inclusions can result either from their having had a separate nucleosynthetic history, e.g. by incorporating dust grains formed in the ejecta from supernovae and other stars in advanced stages of evolution and surviving unchanged in the early Solar System (D. Clayton 1982; Hoppe & Zinner 2000), or merely because their peculiar composition leads to an enhanced sensitivity to events that may have affected the Solar System as a whole. The latter might have included (i) inheritance from the general interstellar medium, in the case of short-lived radioactivities after a free-decay interval of a few half-lives or less; (ii) injection of recently and locally synthesized nuclides from a nearby AGB star or supernova that might also have acted as a trigger for the formation of the Solar System itself; or (iii) production by energetic particles from the early Sun.

Substantial abundance anomalies occur among the heavy oxygen isotopes ^{17}O and ^{18}O, which are underabundant by up to about 4 per cent relative to ^{16}O in oxide grains of certain of the CAIs, compared with the bulk composition in which the isotope ratios are closer to a terrestrial standard. The intriguing feature of these anomalous ratios is that, in common with some other meteorites, but in contrast to terrestrial and lunar samples, the relative deviations of the two heavy isotopes are equal; most normal fractionation processes would cause ^{18}O to have twice the anomaly of ^{17}O, as indeed is observed in terrestrial samples and more differentiated meteorites, where the anomalies are also usually much smaller. While there has been speculation that there might be a substantial admixture of pure ^{16}O from a supernova, there are fractionation mechanisms that may be able to account for the effect, e.g. photo-dissociation of molecules affected by self-shielding (R. Clayton 2002). In this case, it is possible that the terrestrial standard is enriched in the heavy O-isotopes while the inclusions have more nearly the true solar ratio.

Another isotopic anomaly, discovered in Allende inclusions, concerns magnesium, for which an intrinsically low abundance in these samples makes its isotope ratios sensitive to small effects. Certain of the inclusions show a correlation between ^{26}Mg and ^{27}Al, indicating an origin of excess ^{26}Mg from radioactive decay of ^{26}Al (mean life 1 Myr), the existence of which had previously been postulated as a heat source for meteorite parent bodies (Fig. 3.32). Other short-lived activites that seem to have been alive in the early Solar System are ^{10}Be (mean life 2.2 Myr) from a correlation of ^{10}B with ^9Be, and ^{41}Ca (mean life 0.15 Myr) from a correlation of
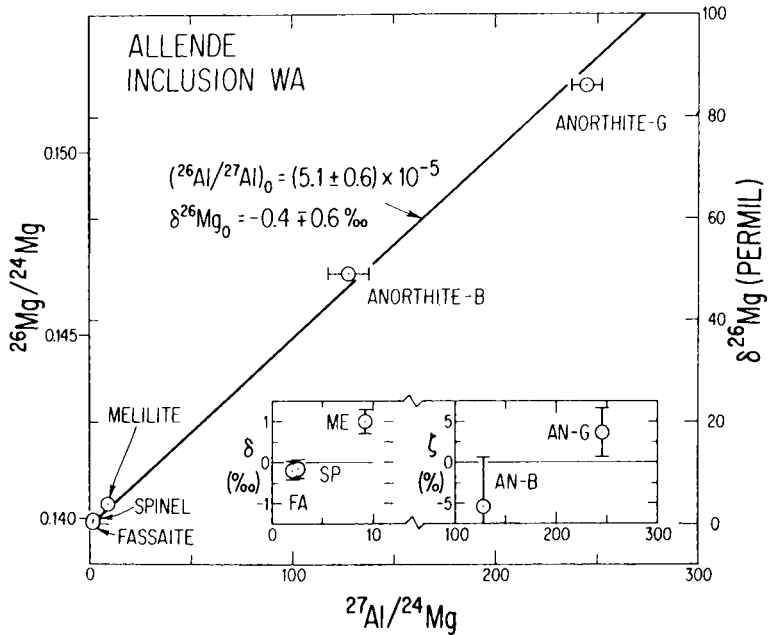
Fig. 3.32. Diagram of ^{26}Al–^{26}Mg evolution for a Ca–Al inclusion from Allende containing minerals with a wide range of Al/Mg. Data taken by an ion microprobe. After Lee, Papanastassiou and Wasserburg (1977). Courtesy G. J. Wasserburg.

^{41}K with ^{40}Ca. Some implications of long- and short-lived radioactivities for the chronology of the Solar System will be discussed in Chapter 10.

A few inclusions are exceptional in that they show isotopic anomalies for virtually every element studied, notably in the heavier isotopes of O, Mg, Si, Ca, Ti etc.; these have been called FUN (fractionation and unknown nuclear) anomalies by Wasserburg and his colleagues and they may be due to unmodified stellar ejecta that were incorporated into the solar nebula in a solid form in which they survived.

Meteorites contain traces of inert gases, either from radioactive decay or 'trapped', which can be released by stepped heating, and their isotope ratios can vary by orders of magnitude because of the low abundance of any 'normal' component. The trapped components are classified as 'solar' (resembling the solar wind), 'planetary' (resembling the Earth's atmosphere and related to solar by mass fractionation and radioactive decay) or 'exotic', e.g. Neon-E. Neon-E is 30 to 100 per cent ^{22}Ne, whereas solar and planetary neon have ^{20}Ne and ^{22}Ne in proportions of about 10:1, and ^{21}Ne occurs in highly variable amounts from spallation by cosmic rays. Ne-E has been found to have at least two components that are released at different temperatures according to the refractoriness of their mineral carriers: almost pure ^{22}Ne which may result from decay of ^{22}Na (mean life
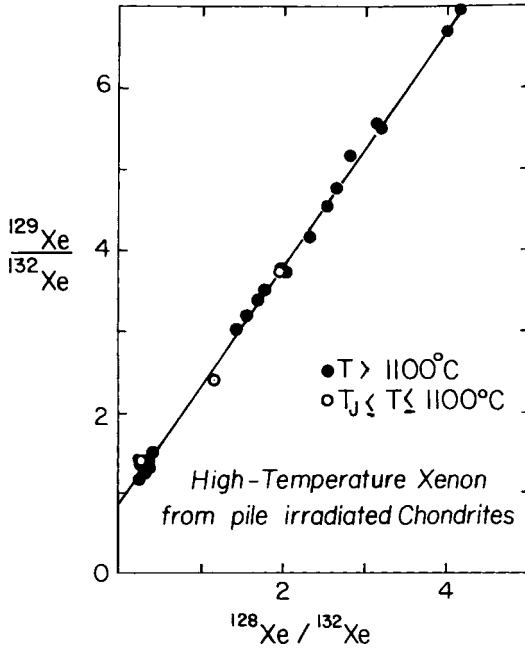
Fig. 3.33. $^{129}Xe/^{132}Xe$ for several different meteorites irradiated with neutrons from a reactor to produce ^{128}Xe from ^{127}I present in the meteorites. The samples were heated to various temperatures and the Xe isotopic compositions measured. The correlation between ^{129}Xe and iodine demonstrates the presence in the primordial Solar System of ^{129}I (mean life 23 Myr) with an abundance $10^{-4} \times$ that of the stable isotope ^{127}I. Data from Hohenberg, Podosek and Reynolds (1967), adapted from Wasserburg and Papanastassiou (1982).
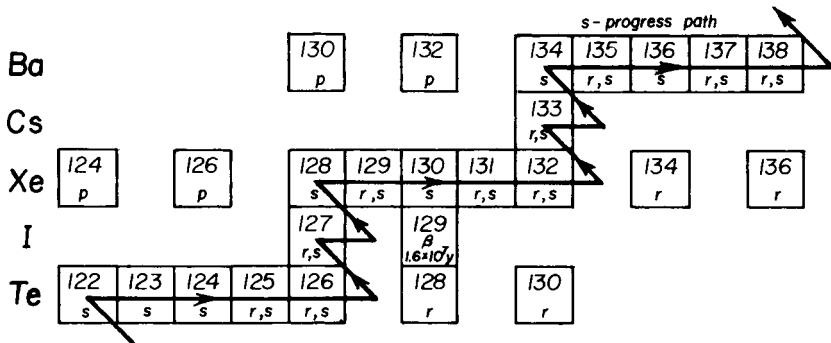
Fig. 3.34. s-process path in the Xe region. Adapted from Anders (1988).

3.9 yr), perhaps created in a nova outburst, and a more impure component that could arise from helium-burning on ^{14}N, e.g. in an AGB or Wolf–Rayet star (see Chapter 5).

Xenon shows several interesting isotopic variations (see Figs. 3.33, 3.34) including excess abundance of ^{129}Xe, due to radioactive decay of ^{129}I, in meteorites of

all kinds (see Chapter 10), and so-called Xe-HL with excess abundances by factors of 2 or so of both the heavy (r-process) and light (p-process) isotopes relative to the middle (mainly s-process) isotopes in grains contained in the matrix of carbonaceous chondrites.[10] The r- and p-process nuclei may have been created in the same event or could be present in different grain components, although no separation has been achieved. Another anomalous xenon type, known as Xe-S, shows complementary anomalies, i.e. mainly just the s-process isotopes, and its discovery and isotopic composition (Srinivasan & Anders 1978) was a striking confirmation of the reality of the s-process and its application to the classification of the xenon isotopes (Clayton & Ward 1978).

While isotopic anomalies in meteoritic inert gases have been known since the early 1960s, their carrier grains were only discovered, by the University of Chicago group, in 1987 (Lewis *et al*. 1987). They are tiny (micron or submicron size) presolar grains embedded in the fine-grained matrix of primitive meteorites and are believed to have acquired their inert gases and other impurities by ion implantation in stellar ejecta. Several are carbon-bearing: nano-diamonds (carriers of Xe-HL), graphite, silicon carbide SiC and titanium carbide TiC, formed in a carbon-rich environment (i.e. C/O > 0 as in carbon stars and in certain interior zones of pre-supernovae). Silicon carbide, which is the second most common type of carrier after nano-diamonds, comes in several varieties distinguished by their isotopic make-up, particularly with respect to C and N (see Fig. 3.35); most of them are 'main-stream', with ^{15}N/^{14}N reduced and ^{13}C/^{12}C slightly enhanced, and these are likely to be carriers of Xe-S and related Kr isotopes, along with a subset of graphite grains, but there are also SiC 'X-grains' (supernova grains?) and 'nova-grains' that have ^{15}N enhanced, and 'A' and 'B' grains with ^{12}C/^{13}C near its equilibrium value for the CNO cycle. All have high proportions of (extinct) ^{26}Al, especially the X- and nova-grains. Most types seem to come together in the behaviour of the silicon isotopes (Fig. 3.36), which show a tendency for the more neutron-rich species to be enhanced by varying amounts. The trend of ^{29}Si against ^{30}Si is linear with a slope of 1.3 and a slight offset from solar, and with X-grains relatively deficient, perhaps because of extra ^{28}Si. There are also non-carbonaceous grains, e.g. corundum Al_2O_3 and spinel $MgAl_2O_4$ (another Ne-E carrier) formed in an oxygen-rich environment (C/O < 1, as is also the case for the CAIs). All are chemically highly resistant and they are extracted using fierce acids and oxidizing agents to remove the carriers of normal-type trapped gases. The peculiar isotope ratios of both the grains and the trapped gases confirm their extra-solar origin, and isotopic anomalies have been found among the grains also for other elements, e.g. D, N and Ba in diamonds, C in graphite and sometimes enormous variations among Ca, Ti, Sr,

---

[10] The isotope ratios differ from the corresponding r- and p-process ratios in the Solar System, but this could be due to fractionation effects. Krypton also shows 'HL'-type anomalies, but the details are different.
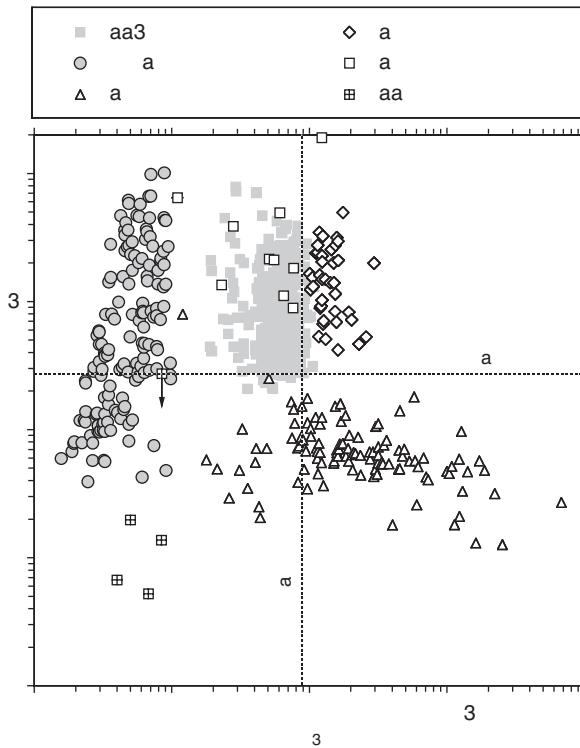
Fig. 3.35. Isotopic variations of carbon and nitrogen in various silicon carbide grains, after Amari *et al.* (2001). Courtesy Sachiko Amari.

Ba, Nd and Sm – as well as those in C, N, Al and Si already described – in silicon carbide. Diamonds may come from supernovae and SiC and TiC grains probably from AGB carbon stars, while the broad ^{12}C/^{13}C distribution in graphite suggests a variety of sources.

Some implications of long- and short-lived radioactivities for the chronology of the Solar System will be discussed in Chapter 10.

3.5.3 Brief overview of abundances outside the Solar System

Introduction

Until about 1950, the conventional wisdom was that all stars have the same chemical composition with the sequence of spectral types caused essentially by differences in temperature and gravity, with two main exceptions:

- Carbon stars with spectral types R, N (or C) and S. R and N stars are cool giants with temperatures roughly corresponding to normal spectral types K and
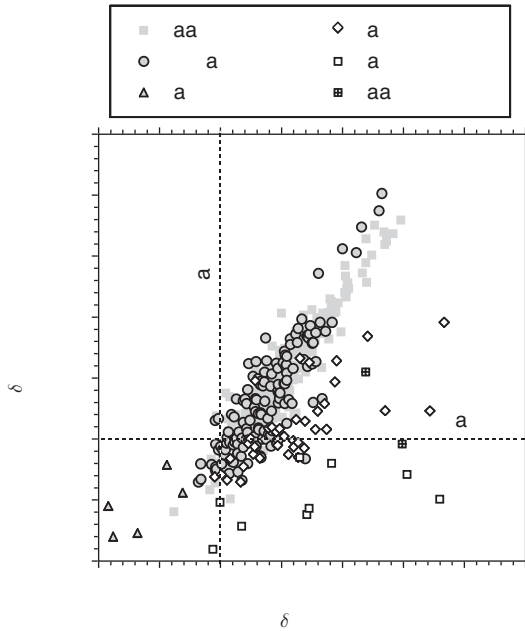
Fig. 3.36. Isotopic variations of silicon in various silicon carbide grains, after Amari *et al.* (2001). The axes are deviations from solar in parts per mil. Courtesy Sachiko Amari.

M respectively, but which show bands of CH, C_2 and CN instead of TiO, while S stars show ZrO bands instead of, or in addition to, TiO. In a classic paper, Russell (1934) explained these spectral differences (which also correspond to the nature of condensates such as those mentioned in the previous section) on the basis of the high degree of stability of the CO molecule, which locks up essentially all of either carbon or oxygen according to which has the lower abundance. In M stars, which have C/O < 1 like the Sun and other normal stars, some oxygen is left over and available to form TiO, VO etc., whereas in carbon stars the situation is reversed (as we now believe, owing to nucleosynthesis) and so other carbon molecules are formed. In S stars, oxygen is but slightly more abundant than carbon, favouring ZrO against the less stable TiO, but as we now know Zr is also overabundant as a result of the s-process (see Fig. 1.8).

- Wolf–Rayet (WR) stars, which are hot stars of high luminosity like O stars, but have peculiar spectra with broad emission bands of He^+, N^{++} (WN), C^{++} and C^{+++} (WC) or O^{++++} (WO) and with hydrogen weak or absent. These are now believed to be massive stars (initially $\geq 40\,M_\odot$) undergoing extensive mass loss in the course of which their surface temperature steadily rises and outer layers are successively peeled off revealing the results of more advanced nuclear burning stages.
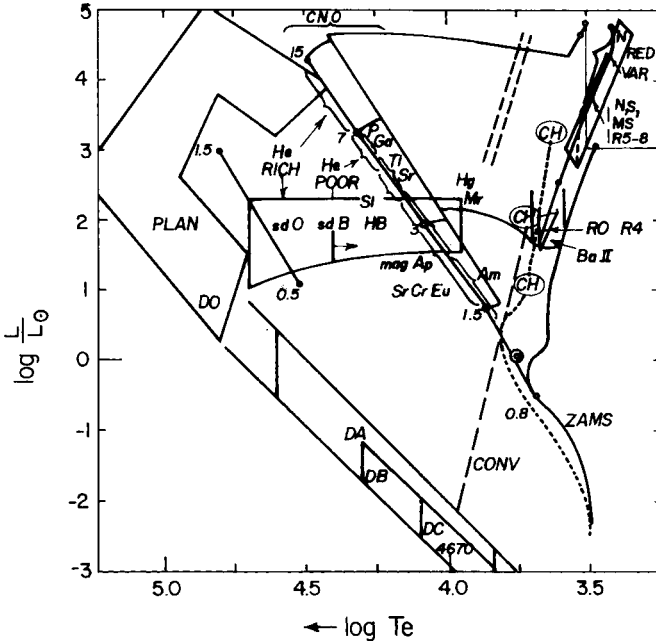
Fig. 3.37. Rough locations of chemically evolved and peculiar stars in the HR diagram. Full lines show the ZAMS with stellar masses indicated and evolutionary tracks for 0.8, 3 and 15 $M_\odot$, the helium main sequence (0.5 to 1.5 $M_\odot$), PN nucleus, horizontal-branch and white-dwarf regions. The dotted line shows a schematic main sequence and evolutionary track for Population II, while various dashed lines show roughly the Cepheid instability strip, the transition to surface convection zones and the helium-shell flashing locus for Population I. After Pagel (1977). Copyright by the IAU. Reproduced with kind permission from Kluwer Academic Publishers.

Progress in understanding stellar evolution and nucleosynthesis, and the discovery by Merrill (1952) of the unstable element technetium in the S star R Andromedae, demonstrating the occurrence of stellar nucleosynthesis within a few half-lives of Tc (i.e. < about 1 Myr; see Fig. 1.8), has led to acceptance of the idea that abundance variations among stars are perfectly natural as a consequence of three main effects (see Fig. 3.37):

(i) Internal nuclear reactions followed by loss of the envelope or mixing to surface layers in advanced evolutionary stages, e.g. WR and carbon stars. The Ba II and CH stars have anomalies related to those of carbon stars but too low luminosities to be expected to have undergone the third dredge-up in thermally pulsing AGB evolution. They are believed to belong to binary systems in which the companion underwent such evolution and shed part of its envelope on to the star that we see. The white dwarfs are classified according to spectral features as DO (He$^+$), DB (He), DA (H) and DC (continuum sometimes with C_2 bands); their surface composition is affected by gravitational settling and possibly accretion.

(ii) Population effects. Stars are born with a composition reflecting that of the ISM at the time and place of formation, which in turn has been enriched in nucleosynthesis products to varying degrees by previous stellar activity. The first stars to have been born in the Galaxy have abundances of heavy elements not produced in the Big Bang that are far below solar, as was first found to be the case in a study by J. W. Chamberlain and L. H. Aller in 1951 of two classical 'subdwarf' stars HD 140283 (actually a subgiant) and HD 19445 which belong to the sparse 'halo' population (see below) and have [Fe/H] values of -2.4 and -2.0 respectively.

(iii) Certain stars with $T_{\text{eff}} \geq 8000\,\text{K}$ or so, called Chemically Peculiar (CP, also known from their spectral types as Bp, Ap, Am), including the magnetic spectrum variables, display extraordinary over- and underabundances of different elements, often concentrated in spots that come into and go out of view as the star rotates. Most of these effects are attributed to a combination of gravitational settling and radiative levitation (which favours rare, exotic elements: P, Ga, Hg etc.) modified by the magnetic field, and they are not now considered to have any direct relationship with nucleosynthesis. Another type of peculiarity, also unrelated to nucleosynthesis, is displayed by certain stars with spectral types around A which display an enormous deficiency in iron, calcium and other refractory elements, while C, N, O, S and Zn are normal for Population I. This peculiarity, which recalls the pattern of depletion of elements from the gas phase on to dust grains in the ISM (see Fig. 3.42 below), is characteristic of the so-called λ Boötis stars and is also found in some post-AGB stars with dusty envelopes and in variable stars of the RV Tauri class which are cooler but also have dusty envelopes; it presumably arises from the selective accretion (or retention) of gas, but not dust, at the photospheric level (Lambert 2004).

Metallicities and stellar populations

Following on from his success in resolving the nucleus of the Andromeda galaxy M31 using red-sensitive photographic plates under blackout conditions on Mount Wilson in 1944, Walter Baade introduced in 1948 the influential idea of two stellar populations, Pop I and Pop II, distinguished by age, kinematics and chemical composition. Population I was identified with the gas-rich disk of the Galaxy (see Fig. 3.38) containing young stars and with the light dominated by blue stars on or above the upper main sequence; the associated stellar orbits are nearly circular and close to the Milky Way plane, leading to low velocity dispersion and low velocities relative to the Sun which forms part of the system. Population II was identified with the spheroidal system or halo, sparse in the solar neighbourhood but more concentrated to the centre of the Galaxy; this population is traced by globular clusters and high-velocity stars with more elongated and inclined orbits. Here all the stars are old, the more massive stars have left the main sequence and the light is dominated by red giants. The distinction that he then made between classical Cepheids (Pop I) and RR Lyrae variables (Pop II) played an important role in expanding the adopted extragalactic distance scale.
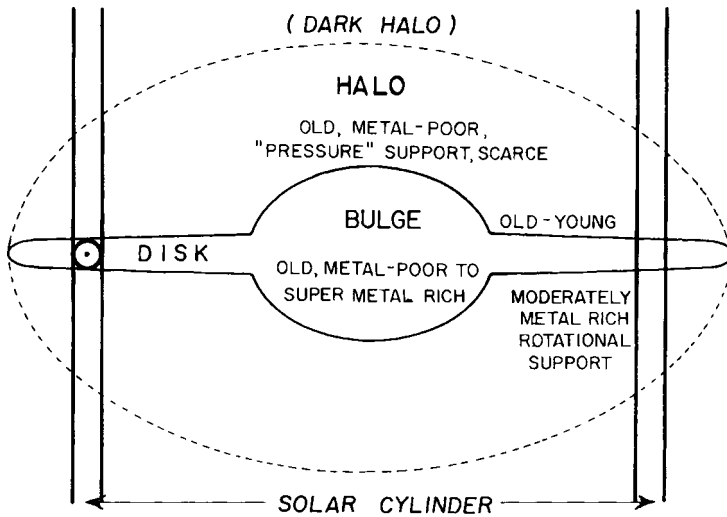
Fig. 3.38. Schematic cross-section through the Galaxy.

Pop I was considered to be metal-rich, like the Sun and the Hyades open cluster, and Pop II metal-poor by factors of up to 100 or more like certain globular clusters and subdwarfs, resulting in especially luminous red giants that Baade had resolved in M31. However, as is illustrated in Fig. 3.38, and noted by Baade (1963) himself, the situation is by no means so simple. Stars in the bulge of our Galaxy and of M31 are mostly metal-rich, although old, and so there are large-scale spatial gradients in metallicity as well as age effects.

Locally, however, there are significant correlations between kinematics and metallicity: high-velocity stars (relative to us) tend to have [Fe/H] < 0 and there is a loose correlation with age measured from isochrones based on theoretical stellar evolutionary tracks. Eggen, Lynden-Bell and Sandage (ELS 1962), in a classic discussion, presented UV excesses and orbital characteristics (eccentricity, specific angular momentum and velocity at right angles to the plane, from which the maximum height above the plane can be estimated) for stars from two catalogues, one of ordinary nearby stars and one of high-velocity stars selected by proper motion, i.e. angular motion across the sky (see Fig. 3.39). Taking UV excess (equivalent to [Fe/H]) as an indicator of age, they put forward the theory that the Galaxy formed by collapse on a free-fall timescale (then estimated at a few $\times 10^8$ yr) from a single proto-galactic cloud. The first stars were formed in early stages of the collapse, with large orbital energies, i.e. large eccentricities and maximum heights, and have retained these properties (which are adiabatic invariants) forming what we now see as the halo, whereas the remaining gas clouds dissipated their energy by collisions and radiation and settled into a disk with nearly circular orbits from which
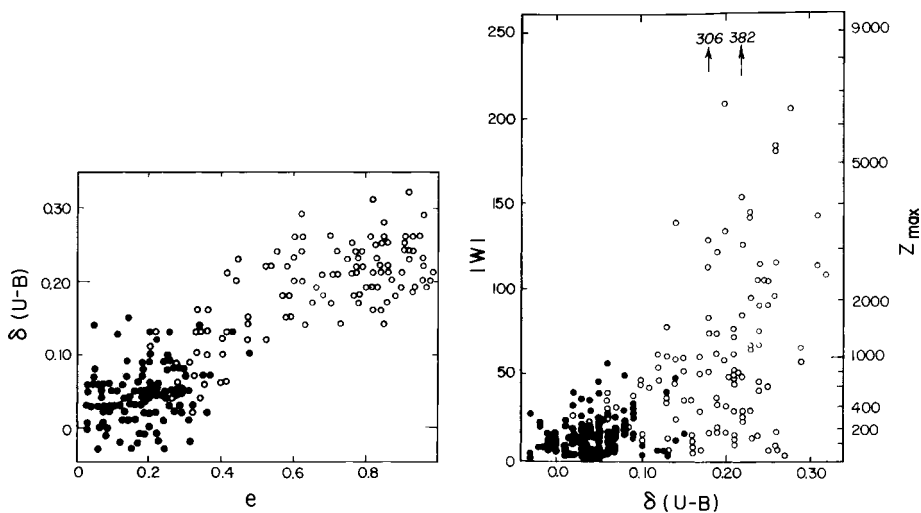
Fig. 3.39. Correlations between UV excess and stellar orbital eccentricity and velocity at right angles to the plane of the Milky Way. Adapted from Eggen, Lynden-Bell and Sandage (1962).

Pop I stars subsequently formed, inheriting their orbital characteristics from the disk gas.

This picture has given rise to several debates, e.g. how short should the collapse time actually be in relation to age differences among globular clusters, the lack of a radial abundance gradient (to be expected from a dissipative process; see Appendix 5) in the outer halo and the severe difference in angular momentum between the halo (which is virtually non-rotating on average) and the disk (which rotates at about $200 \, \mathrm{km \, s^{-1}}$). Kinematic biases in the catalogues led ELS to overlook a significant population component known alternatively as 'Intermediate Population II' or the 'thick disk', consisting of stars with modest eccentricities but substantial velocities at right angles to the plane and $[\mathrm{Fe/H}] \leq -0.5$ or so with a range overlapping halo metallicities, so that it populates the empty top left corner in the left panel of Fig. 3.39. An alternative picture of halo formation has been put forward by Searle and Zinn (1978) who argue that it results from the capture of fragments such as dwarf galaxies over lengthy periods of time – an event that has probably been witnessed with the discovery of the Sagittarius dwarf system (Ibata, Gilmore & Irwin 1994). The formation of the thick disk could also have been a consequence of such a merger event.

As will be discussed further in Chapter 8, there is probably some truth in both pictures. The inner halo and bulge have properties consistent with a dissipative collapse, while the outer halo is likely to have had a more chaotic origin. The disk has two components: a 'thick' disk consisting of old stars and a gas-rich 'thin'
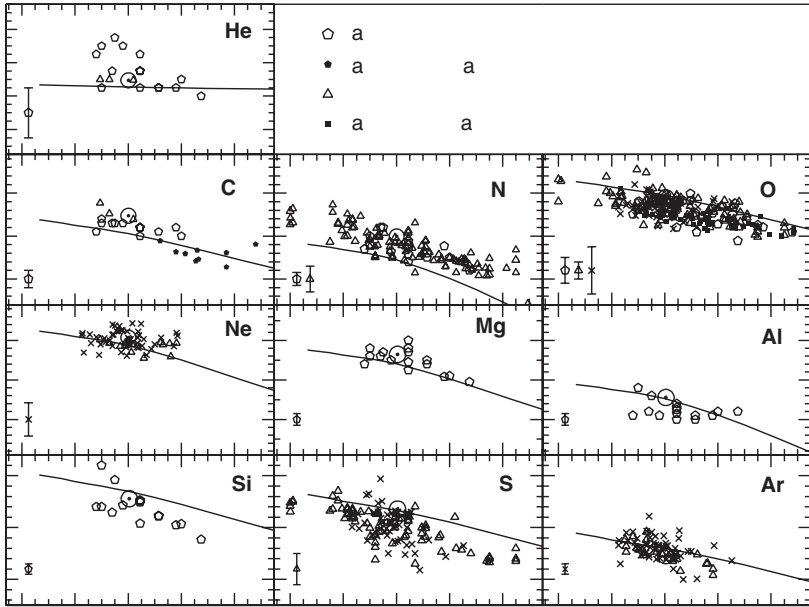
Fig. 3.40. Abundances in Galactic stars, H II regions and planetary nebulae, as a function of Galactocentric distance, with the Sun shown for comparison. After Hou, Prantzos and Boissier (2000). The curves show a model calculation by the authors; nitrogen is underproduced in the model because only massive stars were considered.

disk which may have accumulated over a long period, longer in the outer parts than in the inner parts. The gas fraction (in a column perpendicular to the plane) increases, and abundances in stars and H II regions decrease, with distance from the centre of the Galaxy, the metallicity decreasing at a rate of between about 0.05 and 0.1 dex kpc^{-1} (Figs. 3.40, 3.41).

The cold interstellar medium

The interstellar medium has a complex structure involving hot X-ray gas, warm ionized and neutral gas, dusty molecular clouds, H II regions and diffuse H I clouds; the latter emit 21-cm radio waves from a hyperfine structure transition and produce interstellar absorption lines in the optical and UV. Advances in UV spectroscopy in recent years have provided substantial information on the chemical composition of diffuse clouds in our Galaxy and the Magellanic Clouds and ground-based work has led to corresponding results for intervening absorption-line systems in front of quasars with high redshifts.
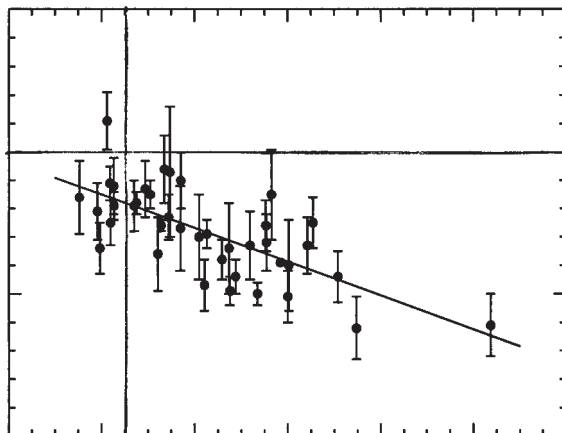
Fig. 3.41. Iron abundances in intermediate-age open Galactic clusters as a function of Galactocentric distance, with the Sun shown by the axes. The line corresponds to a gradient of -0.06 dex kpc^{-1}. Adapted from Friel *et al.* (2002).

Figure 3.42 shows that most elements are substantially depleted from the H I gas, due to their being locked on dust grains, with the notable exceptions of sulphur and zinc. The degree of depletion increases fairly smoothly with condensation temperature, consistent with the idea that these elements are ejected from stars in the form of dust in the first place. The degree of depletion is lower in high-velocity clouds (where the line ratio Ca II/Na I is greater) and much lower in H II regions and supernova remnants, owing to the destruction of grains by various processes, although Fe and Si are still substantially depleted in the Orion nebula.

The warm halo gas has been extensively studied with the International Ultraviolet Explorer (IUE) satellite launched in 1978 and the Far Ultraviolet Explorer satellite (FUSE) launched in 1999. It shows high-ionization states such as C IV and N V which are also seen in high-redshift intervening systems on the line of sight to QSOs, where they may also come from galactic halos. Intervening systems with large H I column densities in the range 10^{20} to 10^{21} cm^{-2} (damped Lyman-α systems) more closely resemble the local diffuse clouds; they are usually metal-deficient as judged from undepleted S and Zn, typically [M/H] ~ -1 to -2, and they show milder depletion effects for other elements. Molecular hydrogen, common in local diffuse clouds, is absent in intervening systems except in a few cases that seem to be associated with the QSO itself and also have high metallicities. Abundances at high redshift are discussed further in Chapter 12.

Dense molecular clouds are too dusty to be studied by optical means, but radio and mm wave observations reveal numerous molecules such as CO, CH$_2$O, HCN, NH$_3$ etc. which give valuable information on isotope ratios across the Galaxy and
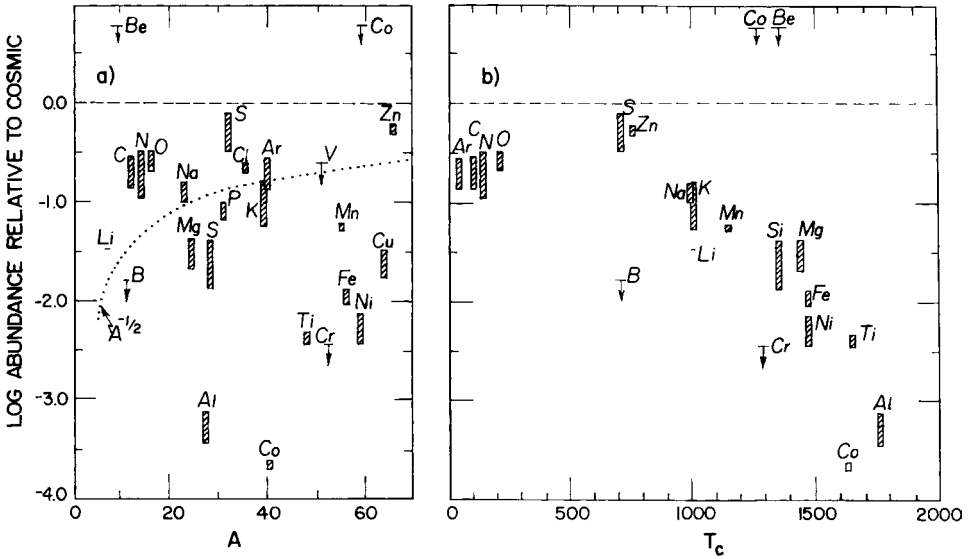
Fig. 3.42. Depletion below solar abundances of elements in the H I gas towards ζ Ophiuchi plotted against atomic mass number in (a) and condensation temperature in (b), based in part on the curve of growth shown in Fig. 3.11. Vertical boxes indicate error bars. The dotted curve in the left panel represents an $A^{-1/2}$ dependence expected for non-equilibrium accretion of gas on to grains in the ISM. The condensation temperature gives a somewhat better, though not perfect, fit, suggesting condensation under near-equilibrium conditions at a variety of temperatures either in stellar ejecta or in some nebular environment. Note the extreme depletion of Ca ('Calcium in the plane stays mainly in the grain'). After Spitzer and Jenkins (1975). Copyright by Annual Reviews, Inc.

in other galaxies (see Fig. 3.43). The increase in relative abundance of ^{13}C and ^{18}O towards the Galactic centre indicates a more advanced degree of what is sometimes known as 'secondary processing', where the production rate of these species is enhanced by an increased abundance of their 'primary' progenitors ^{12}C and ^{16}O; but time delays in the evolution of lower-mass stars can also be involved and the nitrogen isotope ratio does not fit this pattern very well anyway.[11] ^{18}O/^{17}O has a constant value of 3.2 across the Galaxy, consistent with both of these isotopes being secondary, but the Solar System ratio is apparently somewhat higher at 5.5.

Abundances in planetary nebulae

Planetary nebulae (PN) display basic abundance patterns characteristic of the age and location of their parent stellar populations, on which are superimposed the effects of evolution through giant, AGB and post-AGB stages of their own central

---

[11] The 'solar' ^{14}N/^{15}N ratio in Fig. 3.43, based on the terrestrial atmosphere, may be underestimated owing to differential escape.
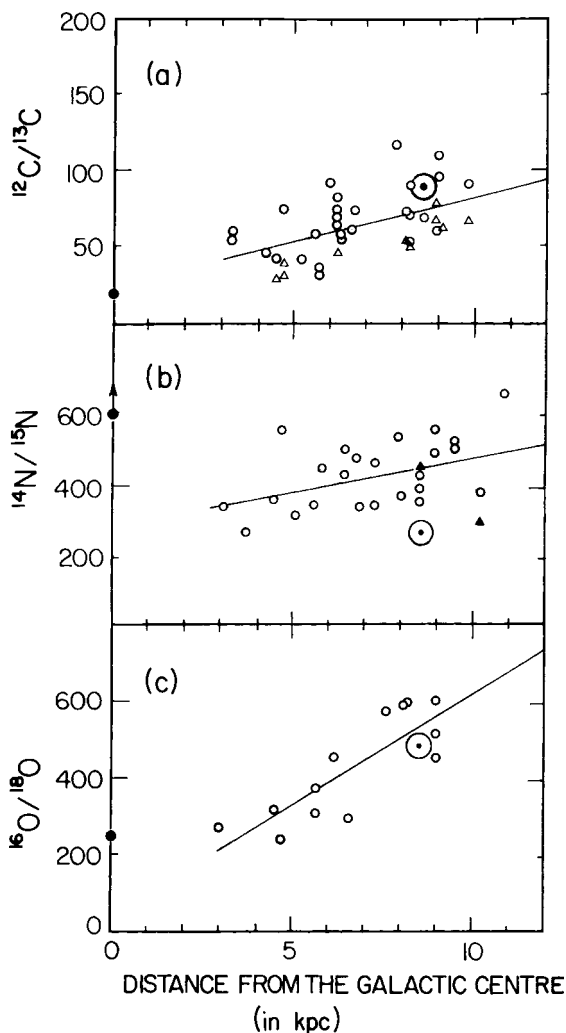
Fig. 3.43. Variation of CNO isotopic ratios with Galactocentric distance, deduced from mm wave measurements of molecules in molecular clouds. (a) $^{12}C/^{13}C$ from CO (triangles) and formaldehyde CH_2O (circles). (b)$^{14}N/^{15}N$ from HCN (circles) and NH_3 (triangles). (c)$^{16}O/^{18}O$ from formaldehyde. Solar–System values are indicated by the $\odot$ sign and Galactic centre values (or a lower limit in the case of $^{14}N/^{15}N$) by a filled circle. Adapted from Wilson and Rood (1994).

stars, initially of intermediate mass between about 1 and 8 $M_\odot$, affecting their He, C, N and s-process abundances. A few show signs of still more advanced nuclear processing.

Peimbert (1978) has divided Galactic PN into four classes:

• Type I, He- and N-rich, with bipolar filamentary structure. These are thin-disk objects, with young, relatively massive central stars.

- Type II, moderately C- and N-rich, belonging to an intermediate-age disk population like the Sun. This is the commonest class, and it shows Galactic abundance gradients compatible with those derived from stars and H II regions, although the N/O ratio is 2 or 3 times higher.
- Type III, high-velocity (and hence old) objects, moderately N-rich with solar-like composition in O and Ne, perhaps identifiable with the thick disk.
- Type IV, halo objects with heavy elements an order of magnitude or so below solar, while helium is normal; one of these is K 648 in the globular cluster M15. These are relatively rare, apparently because mass ejection is less efficient at low metallicities and masses.

Abundances in external galaxies

Apart from spectroscopy of individual supergiant and giant stars in Local Group galaxies such as the Magellanic Clouds, most information on abundances in galaxies comes from emission lines from H II regions and supernova remnants in gas-rich systems and from features like Mg_2 in the integrated spectra of old stellar populations. Another source of information in nearby dwarf spheroidals is the location of the red giant branch of old stars in the HR diagram, which becomes brighter and bluer with decreasing metallicity, increasingly supplemented by high-resolution spectroscopy with 8- to 10-m telescopes.

Broadly speaking, the abundances in nearby galaxies show two main features:

- There is a general tendency for average abundances to increase with increasing luminosity of the parent galaxy (see Fig. 3.44), ranging from slightly above solar ('super metal-rich') in the dominant component of the nuclear regions of the biggest spirals and ellipticals to a factor of about 100 below solar in dwarf spheroidals and blue compact gas-rich dwarfs, roughly corresponding to the relation

$$\langle Z \rangle \propto L_{\rm B}^{0.3} \propto M_{\rm S}^{0.25}, \tag{3.72}$$

where $\langle Z \rangle$ is the luminosity-weighted mean 'metallicity' and $M_{\rm S}$ the total mass of stars (living or dead) and gas in the galaxy. This may reflect the ability of the gravitational potential well to retain processed material expelled from supernovae, and/or bursts of star formation and concomitant 'metal' enrichment accompanying mergers of small systems to form larger ones (see Chapter 11).
- Most spirals and many ellipticals display a large-scale radial abundance gradient analogous to what seems to be the case in the Milky Way (see Figs. 3.45, 3.46). Such gradients may result from a combination of many factors, including differing timescales of evolution, differing exposure to inflowing material and slow inward radial flows of gas due to energy dissipation, viscosity or other effects. The gradients tend to be lower in barred spirals where the non-axisymmetric potential can give rise to rapid radial flows and mixing.
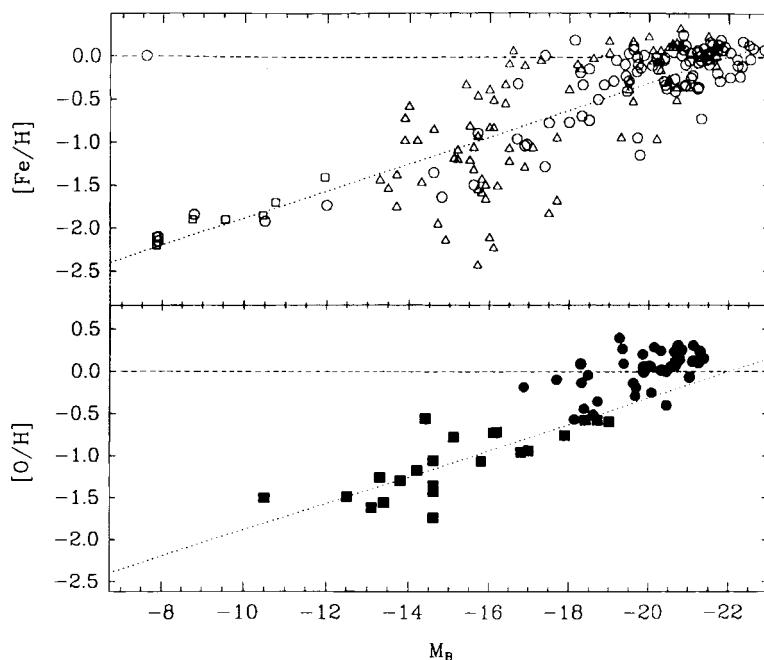
Fig. 3.44. Metallicities in gas-poor galaxies (open symbols) and oxygen abundances at a representative radius in gas-rich disk galaxies (filled symbols), as a function of galaxy luminosity in blue light. The dotted lines in each panel represent identical trends for '[Fe/H]' and [O/H] and the ordinate 0.0 represents solar composition. Adapted from Zaritsky, Kennicutt and Huchra (1994).

Notes to Chapter 3

More information about the topics discussed in this chapter can be found in the following textbooks:

G. B. Rybicki and A. P. Lightman, *Radiative Processes in Astrophysics*, Wiley-Interscience 1979.

H. G. Kuhn, *Atomic Spectra*, Longman 1971.

C. W. Allen, *Astrophysical Quantities (AQ)*, Athlone Press, London 1981, is an invaluable, concise and instructive source of atomic and astronomical data and formulae.

D. Mihalas, *Stellar Atmospheres*, W. H. Freeman & Co., San Francisco, 1970, 1978. The first edition of this classic text deals with radiative and convective equilibrium and line formation in normal stellar atmospheres, while the second treats non-LTE effects in more detail.

D. F. Gray, *The Observation and Analysis of Stellar Photospheres*, Cambridge University Press 2005, gives many useful practical details in this field, including a description of Fourier analysis of line profiles.
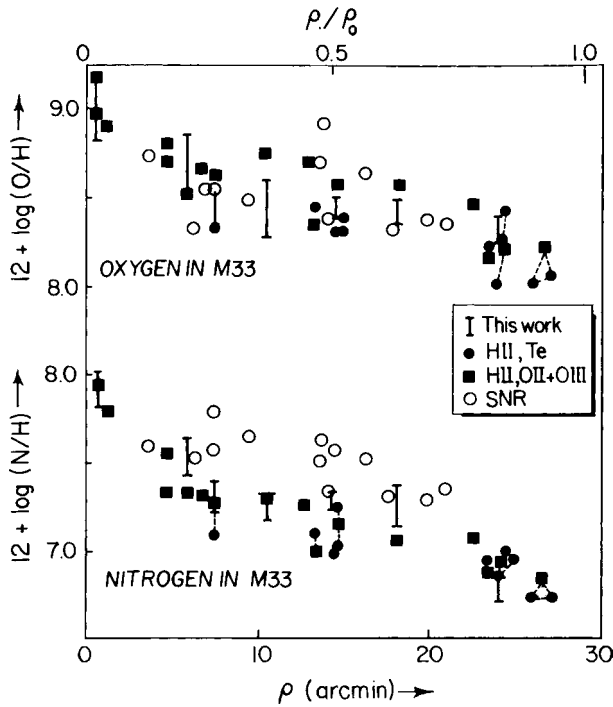
Fig. 3.45. Abundances of oxygen and nitrogen in the Scd spiral M33, measured in H II regions and supernova remnants, as a function of galactocentric distance; 1 arcmin ≡ 200 pc and ρ_0 is the de Vaucouleurs radius corresponding to a visual surface brightness of 25^m arcsec^{-2}. After Vílchez *et al.* (1988).

D. E. Osterbrock and G. J. Ferland, *Astrophysics of Gaseous Nebulae and Active Galactic Nuclei*, University Science Books, Mill Valley, Cal., 2006, is another classic text, indispensable for studies of emission nebulae.

M. A. Dopita and R. S. Sutherland, *Astrophysics of the Diffuse Universe*, Springer-Verlag 2003, give an excellent and lucid account of absorption and emission lines, gas dynamics and other interstellar topics.

C. R. Cowley, *An Introduction to Cosmochemistry*, Cambridge University Press 1995, covers similar ground to some of this book, but with different emphasis, giving more details about Solar System chemistry, atomic and molecular spectra and chemically peculiar stars.

J. Binney and S. Tremaine, *Galactic Dynamics*, Princeton University Press 1987, 2008, is another classic text, recommended for background reading on Galactic aspects of abundances.

Some important references for atomic and molecular spectra are:
R. D. Cowan, *The Theory of Atomic Structure and Spectra*, University of California Press, Berkeley, 1981.
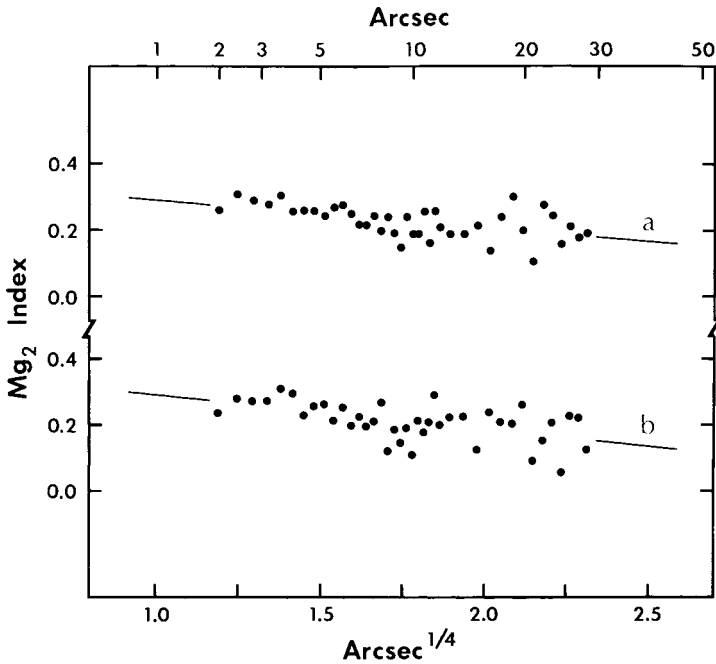
Fig. 3.46. Radial trend of Mg_2 index in the elliptical galaxy NGC 4881, after Thomsen and Baum (1987). 1 arcsec $\equiv$ 500 pc, the surface brightness in the adjoining continuum decreases from 17th to 26th magnitude per square arc-sec over the range of the diagram in accordance with de Vaucouleurs' law $I \propto e^{-(r/a)^{1/4}}$ and 'a' and 'b' refer to observations taken on separate dates. Courtesy Bjarne Thomsen.

G. R. Harrison, *MIT Wavelength Tables*, Wiley, New York, 1939.

C. E. Moore, *A Multiplet Table of Astrophysical Interest*, Revised Edition *(RMT)*, *NSRDS-NBS* **40**, Nat. Bur. Stand., Washington, 1972.

C. E. Moore, *An Ultraviolet Multiplet Table*, NBS Circular no. 488, Nat. Bur. Stand., Washington, 1962.

Line identifications and other data can also be found on the website
http://www.pa.uky.edu/∼peter/atomic, and in

W. F. Meggers, C. H. Corliss and B. F. Scribner, *Tables of Spectral Line Intensities*, NBS Monograph **145**, Govt. Printing Office, Washington, 1975.

G. Herzberg, *Molecular Spectra and Molecular Structure I. Spectra of Diatomic Molecules*, Van Nostrand, Princeton, 1950.

G. Herzberg, *Molecular Spectra and Molecular Structure II. Infra-red and Raman Spectra of Polyatomic Molecules*, Van Nostrand, Princeton, 1945.

G. Herzberg, *Molecular Spectra and Molecular Structure III. Electronic Spectra and Electronic Structure of Polyatomic Molecules*, Van Nostrand, New York, 1966.

G. Herzberg, *The Spectra and Structures of Simple Free Radicals*, Cornell University Press, Ithaca, 1971.

W. Gordy and R. L. Cook, *Microwave Molecular Spectra*, Wiley, New York, 1984.

M. S. Cord, J. D. Peterson, M. S. Lojko and R. H. Haas, *Microwave Spectral Tables V. Spectral Line Listing*, Govt. Printing Office, Washington, 1968.

Up-to-date microwave spectral line listings can be found on the website
http://spec.jpl.nasa.gov/
Spectral line data are also given in Reports of IAU Commissions 14 and 29 in *Transactions of the International Astronomical Union*, published triennially.

The literature on transition probabilities (or oscillator strengths) is vast, rapidly growing and difficult to summarize. A small selection for atoms and molecules is given in Allen, *AQ* and larger selections in

W. L. Wiese and G. A. Martin, *Wavelengths and Transition Probabilities for Atoms and Atomic Ions*, NSRDS-NBS68, 1980, and

W. L. Wiese, J. R. Fuhr and T. M. Dieters, *Atomic Transition Probabilities for Carbon, Nitrogen and Oxygen: A Critical Data Compilation, J. Phys. Chem. Ref. Data*, Monograph 7, 1996.

Wavelengths and oscillator strengths for ultraviolet and other lines relevant to interstellar work have been given by

D. C. Morton *Ap. J. Suppl.*, **149**, 285, 2003.

A vast and very complete data set for atoms and ions, with very variable accuracy (but sufficient for statistical calculations of line blanketing for model atmospheres in which molecules are not too important), is given by

R. L. Kurucz and E. Peytremann, 'A Table of Semiempirical *gf* Values', *Smithsonian Astrophys. Obs. Special Rep.*, **362**, 1975, and Kurucz CD-Rom 23 (Cambridge, Mass.: Smithsonian Astrophysical Observatory, 1995).

A guide to the literature is provided in

W. C. Martin, 'Sources of Atomic Spectroscopy Data for Astrophysics', in P. L. Smith and W. L. Wiese (eds.), *Atomic and Molecular Data for Space Astronomy: Needs, Analysis and Availability*, Springer, Berlin, 1992.

A list of 'solar oscillator strengths' for selected lines (based on a solar model with assumed abundances) is given in

T. Meylan, I. Furenlid, M. S. Wiggs and R. L. Kurucz, *Ap. J. Suppl.*, **85**, 163, 1993.

This does not really replace the classic and indispensable revision of what was originally Rowland's table of spectral lines from the centre of the solar disk:

C. E. Moore, M. Minnaert and J. Houtgast, 'The Solar Spectrum 2935 Å to 8770 Å', *Nat. Bur. Stand. Monograph* **61**, Washington 1966.

The best theoretical data for oscillator strengths and other atomic properties are becoming available from the Stellar Opacity Project (Seaton 1987; Seaton

et al. 1994) and the IRON Project (Hummer *et al.* 1993). Some results are given in

M. J. Seaton, *The Opacity Project, Vol. I: Selected Research Papers, Atomic Data Tables for He to Si;* Vol II: *Atomic Data Tables for S to Fe, Photo-ionization Cross-sections Graphs*, Inst. Phys. Publ., Bristol, 1996. References to other papers, and papers on atomic data computed in course of the OP are given in the website **http://vizier.u-strasbg.fr/topbase/publi.html**.

A full account of the appearance of different elements in stellar spectra is given in

C. Jaschek and M. Jaschek, *The Behavior of Chemical Elements in Stars*, Cambridge University Press 1995.

The art of computing model stellar atmospheres has progressed rapidly with increases in computer power. A guide to atmospheres of cool stars is given by

B. Gustafsson, 'Chemical Analyses of Cool Stars', *Ann. Rev. Astr. Astrophys.*, **27**, 701, 1989.

LTE line-blanketed models and spectrum synthesis programs for stars hotter than $T_{\text{eff}} = 5500$ K are under continuing development by R. L. Kurucz at the Smithsonian Astrophysical Observatory, Cambridge, Mass., and available from their author in CD-Rom or on his website

http://kurucz.harvard.edu/.

A sample publication is

R. L. Kurucz, 'Model Atmospheres for G, F, A, B and O Stars', *Ap. J. Suppl.*, **40**, 1, 1979.

These and other models have been combined to produce a standard library of synthetic stellar flux spectra and colours as a function of effective temperature, gravity and metallicity by Lejeune, Cuisenier and Buser (1997, 1998) and Westera *et al.* (2002).

Non-LTE models for solar-type stars are described in, e.g.,

C. Allende Prieto, I. Hubeny and D. L. Lambert, 'Non-LTE Model Atmospheres for Late-Type Stars II: Restricted Non-LTE Calculations for a Solar-like Atmosphere', *Ap. J.*, **591**, 1192, 2003.

Models for the hottest stars, taking into account non-LTE and dynamical effects, are described in, e.g.,

R. F. Kudritsky and D. G. Hummer, 'Quantitative Spectroscopy of Hot Stars', *Ann. Rev. Astr. Astrophys.*, **28**, 303, 1990; W. Schmutz, C. Leitherer and R. B. Gruenwald, 'Theoretical Energy Distributions of Wolf-Rayet Stars', *Pub. Astr. Soc. Pacific*, **104**, 1164, 1992; A. W. A. Pauldrach, T. L. Hoffmann and M. Lennon, 'Radiation-driven winds of hot luminous stars. XIII: A description of NLTE line blocking and blanketing towards realistic models for expanding atmospheres', *A &*

A, **375**, 161, 2001; and T. Lanz and I. Hubeny, 'A Grid of Non-LTE Line-blanketed Model Atmospheres of O-type Stars', *Ap. J. Suppl.*, **146**, 417; **147**, 225, 2003.

Photo-ionization models of H II regions have been published by (*inter alia*)

G. Stasinska and C. Leitherer, 'H II Galaxies versus Photoionization Models for Evolving Starbursts', *Ap. J. Suppl.*, **107**, 661, 1996, and M. A. Dopita, L. J. Kewley, C. A. Heisler and R. S. Sutherland, *Ap. J.*, **542**, 224, 2000.

The 'Cloudy' program for photo-ionization modelling is described by G. J. Ferland, K. C. Korista, D. A. Verner *et al.*, *Pub. Astr. Soc. Pacific*, **110**, 761, 1998. The 'Mappings' program for modelling radiative shocks and some applications are described by L. Binette, M. A. Dopita and I. R. Tuohy, *Ap. J.*, **297**, 476, 1985; R. S. Sutherland and M. A. Dopita, *Ap. J. Suppl.*, **88**, 253, 1993 and Dopita and Sutherland, *Ap. J.*, **455**, 468, 1995. A more recent program and tables taking into account effects of instabilities and magnetic pressure are given by R. S. Sutherland, G. V. Bicknell and M. A. Dopita, *Ap. J.,* **591**, 238, 2003. Kewley and Dopita (2002) have given systematic procedures for H II region abundance determinations from photo-ionization modelling using nebular lines only, but there are some underlying assumptions.

Calculations of the X-ray emission of a hot plasma are given by J. C. Raymond and B. W. Smith, *Ap. J. Suppl.*, **35**, 419, 1977.

'Starburst 99' (Leitherer *et al.* 1999, 2001) gives synthetic spectra for actively star-forming galaxies assuming a selection of different ages, metallicities and initial mass functions.

Programs to construct synthetic models combining stellar evolutionary calculations with flux or spectrum libraries include PEGASE, accessible via

http://www2.iap.fr/users/fioc/PEGASE.html.

Multicolour photometric systems that have been used for various sorts of stellar and stellar-population classification are listed with their spectral reponse curves in the website

http://ulisse.pd.astro.it/ADPS/.

A catalogue of stellar abundances based on high-resolution spectroscopy is described (along with references to earlier catalogues) by

G. Cayrel de Strobel, C. Soubiran, and N. Ralite, 'Catalogue of [Fe/H] determinations for FGK stars: 2001 edition', *A & A*, **373**, 159, 2001.

Isotopic abundances in the Solar System and elsewhere, and their significance, are well described (without diagrams or equations) in

D. D. Clayton, *Handbook of Isotopes in the Cosmos: Hydrogen to Gallium*, Cambridge University Press, 2003.

Abundances in our own and other galaxies are discussed in:

B. E. J. Pagel and M. G. Edmunds, 'Abundances in Stellar Populations and the Interstellar Medium in Galaxies', *Ann. Rev. Astr. Astrophys.*, **19**, 77, 1981.

G. Gilmore, R. F. G. Wyse and K. Kuijken, 'Kinematics, Chemistry and Structure of the Galaxy', *Ann. Rev. Astr. Astrophys.*, **27**, 555, 1989.

J. C. Wheeler, C. Sneden and J. W. Truran, 'Abundance ratios as a function of metallicity', *Ann. Rev. Astr. Astrophys.*, **27**, 279, 1989.

G. A. Shields, 'Extragalactic H II Regions', *Ann. Rev. Astr. Astrophys.*, **28**, 525, 1990.

A. McWilliam, 'Abundance Ratios and Galactic Chemical Evolution', *Ann. Rev. Astr. Astrophys.*, **35**, 503, 1997.

R. B. C. Henry and Guy Worthey, 'The Distribution of Heavy Elements in Spiral and Elliptical Galaxies', *Publ. Astr. Soc. Pacific*, **111**, 919, 1999.

Problems

1. Check the integrations leading to Eqs. (3.41) and (3.54) for the damping branches of simple curves of growth. Obtain an expression for the ratio of one to the other, taking $\eta_0 \equiv N\alpha_0$.

2. The equivalent width of Lyman-β, λ 1025, in the spectrum of γ Cas is $1.14\,\text{Å}$ (Vidal-Madjar *et al.* 1977). Use the damping formula Eq. (3.42) to estimate the H I column density, given the parameters $f = 0.079$, $\gamma = A_{3p,1s} + A_{3p,2s} = 1.87 \times 10^8\,\text{s}^{-1}$.

3. The Na I D-lines have wavelengths and oscillator strengths $\lambda_1 = 5896\,\text{Å}$, $f_1 = 1/3$, and $\lambda_2 = 5889\,\text{Å}$, $f_2 = 2/3$. In a certain interstellar cloud, their equivalent widths are measured to be $230\,\text{mÅ}$ and $370\,\text{mÅ}$ respectively, with a maximum error of $\pm 30\,\text{mÅ}$ in each case. Assuming a single cloud with a Gaussian velocity dispersion, use the exponential curve of growth to find preferred values of Na I column density and b, and approximate error limits for each of these two parameters. (Doublet ratio method.)

4. Use the solar Fe I curve of growth in Fig. 3.12 to deduce the solar iron abundance, using $\theta_{\text{ion}} = 0.9$ and given that Fe I has an ionization potential of $7.87\,\text{eV}$ and that the partition function of Fe II is 42. Compare the result with the one in Table 3.4.

5. Use the differential curve of growth in Fig. 3.13 to estimate [Fe/H] for μ Cas.

6. From the analogue of Saha's equation for the dissociation of a diatomic molecule AB, one can define a dissociation 'constant' depending only on temperature

$$K_{\text{AB}} = \frac{p_{\text{A}} p_{\text{B}}}{p_{\text{AB}}}, \tag{3.73}$$

where the p's represent partial pressures. Show that, in a situation where the atomic abundances of carbon and oxygen are significantly depleted by CO formation, but other molecules are negligible and the hydrogen pressure is P_H, the partial pressures of oxygen and carbon are given by

$$2\frac{p_O}{P_H} = \left(\frac{O}{H} - \frac{C}{H}\right) - \frac{K_{CO}}{P_H} + \left[\left(\frac{K_{CO}}{P_H} + \frac{O}{H} + \frac{C}{H}\right)^2 - 4\frac{O}{H}\frac{C}{H}\right]^{1/2} \qquad (3.74)$$

and

$$2\frac{p_C}{P_H} = \left(\frac{C}{H} - \frac{O}{H}\right) - \frac{K_{CO}}{P_H} + \left[\left(\frac{K_{CO}}{P_H} + \frac{O}{H} + \frac{C}{H}\right)^2 - 4\frac{O}{H}\frac{C}{H}\right]^{1/2}. \qquad (3.75)$$

Deduce that the depletion of the free atoms becomes appreciable when K_{CO} gets down to values comparable to the (undepleted) partial pressure of the more abundant element.

7. Given that the transition probability for the nebular [O III] line λ 4959 is $7 \times 10^{-3}\,s^{-1}$, estimate the critical density if the electron temperature is 10^4 K and $\Omega_{12} = 2$. The upper and lower levels of the line have $J = 2$ and $J = 1$ respectively.

8. Flesh out the $\langle \bar{\lambda}^2 V \rangle$ in Eq. (3.67) in terms of fundamental physical constants and show that this leads to the numerical coefficient given.

4

Cosmological nucleosynthesis and abundances of light elements

> But the helium which we handle must have been put together at some time and some place. We do not argue with the critic who urges that the stars are not hot enough for this process; we tell him to go and find a *hotter place*.
>
> A. S. Eddington, *The Internal Constitution of the Stars*

4.1 Introduction

The 'Hot Big Bang' theory of the Universe was pioneered by George Gamow, R. A. Alpher and R. C. Herman in the late 1940s and early 50s. They supposed that during the first few minutes of the (then radiation-dominated) Universe, matter was originally present in the form of neutrons and that, after some free decay, protons captured neutrons and successive captures, followed by β-decays, built up all the elements (Alpher & Herman 1950).

C. Hayashi (1950) first put the theory on a sound physical basis by pointing out that, at the high densities and temperatures involved, there would be thermal equilibrium between protons and neutrons at first, followed by a freeze-out, and this did nothing to overcome the difficulty already known to be inherent in that theory that the absence of stable nuclei at mass numbers 5 and 8 would prevent significant nucleosynthesis beyond helium. In the meantime, progress in the theory of stellar evolution and nucleosynthesis (see Chapter 5) led to comparative neglect of Big Bang nucleosynthesis theory (BBNS)[1] until the discovery by A. A. Penzias and R. Wilson in 1964 of the microwave background radiation, existence of which Gamow and his colleagues had predicted. The 'standard Big Bang nucleosynthesis theory' (SBBN), developed subsequently by P. J. E. Peebles, R. V. Wagoner, W. A. Fowler,

---

[1] Apart from improved calculations of the primordial helium abundance by Alpher, Follin and Herman (1953) and in a prescient paper by Hoyle and Tayler (1964).

F. Hoyle, D. N. Schramm, G. Steigman and others, which assumes standard cosmology and particle physics and a uniform baryon density, has been very successful in several respects, e.g.:

- It accounts, at least approximately, for what can be deduced from astrophysical and cosmochemical measurements about the primordial abundances of ^{2}D, ^{3}He, ^{4}He and ^{7}Li, over 9 orders of magnitude in abundance.
- It led to a prediction that the number of different sorts of neutrino (equivalent in standard particle physics to the number of families of quarks and leptons) is less than 4 and probably no more than 3. This prediction was subsequently confirmed (subject to slight reservations about differences between effective numbers of neutrino species in the laboratory and in the early Universe) by measurements of the width or lifetime of the Z^0 boson at CERN in 1990.
- Until 1989, measurements of the neutron half-life had given somewhat discrepant results. SBBN predicted that the half-life should not exceed 10.4 minutes and the currently accepted value is 10.28 minutes, considerably less than had been assumed some years earlier.

At the same time, questions have been raised about SBBN. One feature once found unattractive by some scientists has been that it leads to a low density of baryonic matter, $\Omega_{b0} < 0.1$, where Ω_{b0} is the smoothed-out cosmological density of baryons at the present time in units of the closure density corresponding to the spatially flat Einstein–de Sitter world model, once favoured by many cosmologists on the basis of the inflationary scenario or for other reasons. Balloon and satellite measurements of the angular fluctuation spectrum of the microwave background from 2001 onwards confirm that the Universe is indeed spatially flat to a good approximation. The gap has been bridged by assuming the existence of substantial non-baryonic dark matter in the form of massive neutrinos, which make but a minor contribution, exotic particles ('cold dark matter') predicted by supersymmetry or other theories of particle physics, and 'dark energy', which seems to contribute the lion's share and accounts for evidence from distant supernovae that the expansion of the Universe is accelerating. Before the emergence of these kinds of evidence, there were many attempts to modify BBNS theory to allow higher baryonic densities, e.g. by invoking baryonic density fluctuations due to earlier cosmological phase transitions or subsequent modification of BBNS products by high-energy processes. Suggestions have been made from time to time that there could be detectable primordial abundances of elements such as ^{9}Be, not expected from SBBN, that might show up in the spectra of stars with extremely low metallicity. However, detailed investigations have not enhanced the attractions of these alternatives to SBBN and that theory can be considered to be in a pretty healthy state, its conclusions being broadly supported by the results of the above-mentioned

observations of the microwave background; at the same time, the questions raised have been a valuable spur to related astrophysical investigations of nucleosynthesis, stellar abundances, cosmic rays, γ-ray background etc.

4.2 Background cosmology

The basic assertion of the 'Hot Big Bang' theory is that, as one goes back to early times, one encounters almost unlimited high temperatures and densities. The basic evidence for this is threefold:

- The Hubble expansion law

$$cz \simeq V = H_0 D; \quad H_0 = 100h \ \text{km s}^{-1}\text{Mpc}^{-1} = (10^{10}\text{yr})^{-1}h \qquad (4.1)$$

where the dimensionless number h, now thought to be close to 0.7, expresses our uncertainty in the value of the Hubble constant H_0. Expansion gives rise to a redshift z such that

$$1 + z \equiv \frac{\lambda}{\lambda_{\text{lab}}} = \frac{R_0}{R_z} \qquad (4.2)$$

where R_0 is the scale factor of the Universe now and R_z the scale factor at the time when the radiation was emitted.

- The microwave background radiation has very precisely the spectrum of a black body with a temperature

$$T_{\gamma 0} = 2.73 \pm 0.01 \ \text{K} \qquad (4.3)$$

leading with adiabatic expansion to temperatures at earlier times

$$T_\gamma(z) = T_{\gamma 0} R_0 / R = T_{\gamma 0} (1 + z). \qquad (4.4)$$

The combination of high temperatures and densities at early times leads to the existence of a phase close to thermal equilibrium, when the significant particle reaction rates dominated over the expansion rate. This enables precise calculations to be made.

- Abundances of light elements. In particular, the very existence of substantial deuterium is an argument for BBNS because nuclear reactions in stars destroy it and no plausible high-energy effects are known that could create D without over-producing other light elements (Epstein, Lattimer & Schramm 1976). This argument was already used by Gamow at a time when only the terrestrial abundance was known. Another consideration is that the mass fraction Y of ^4He is more than 0.2 in virtually all objects investigated, even when abundances of all elements from carbon upwards are very low. Finally, the existence of primordial ^7Li was a prediction of the theory that was subsequently confirmed.

SBBN assumes

- Normal physical laws (including standard particle physics).
- A small degree of matter–antimatter asymmetry, with a baryon number B (ratio of net number of baryons $N_B - N_{\bar{B}}$ in a co-moving volume to the entropy S) in the range 10^{-11} to 10^{-8}.
- Absence of electron or neutrino degeneracy, corresponding to lepton numbers L_e, L_μ, L_τ that are zero or at least not large compared to B, where

$$L_e \equiv (N_{e^-} - N_{e^+} + N_{\nu_e} - N_{\bar{\nu}_e})/S, \qquad (4.5)$$

$$L_{\mu,\tau} \equiv (N_{\nu_{\mu,\tau}} - N_{\bar{\nu}_{\mu,\tau}})/S \qquad (4.6)$$

(after μ, τ decay), together with zero charge number. S is related to the number of photons by a factor related to g_* in Table 4.1, which is nearly constant over substantial periods, so that in practice one can use number-density ratios n/n_γ as an approximation to the baryon and lepton numbers.

- Gravitation described by General Relativity.
- A large measure of thermal equilibrium in the early Universe, which implies, roughly speaking, that particles and antiparticles with $mc^2 < kT_\gamma$ are present in comparable numbers to photons, whereas when kT_γ falls below mc^2, they annihilate and exist only in trace quantities.
- The 'Cosmological Principle' which states that the Universe is always homogeneous and isotropic and leads to the Robertson–Walker metric

$$ds^2 = c^2 dt^2 - R^2(t)\left[\frac{dr^2}{1 - kr^2} + r^2(d\theta^2 + \sin^2\theta \, d\phi^2)\right]. \qquad (4.7)$$

Here r, θ, ϕ are dimensionless co-moving coordinates attached to fundamental observers and $R(t)$ a scale factor with a dimension of length depending only on cosmic time t. k is the curvature constant, which with suitable choice of units takes one of the three values +1 (closed world model with positive curvature), 0 (flat, open model) or -1 (open model with negative curvature). Some consequences of Eq. (4.7) are the relation between redshift and scale factor Eq. (4.2) and the variation of temperature

$$RT_i = \text{const.} \qquad (4.8)$$

for adiabatic expansion of a relativistic gas i with $\gamma = 4/3$.

The expansion of the Universe is governed by the field equations of General Relativity for isotropic expansion or contraction:

$$8\pi G\rho R^2 = 3kc^2 + 3\dot{R}^2 - \Lambda R^2, \qquad (4.9)$$

Table 4.1. *Brief thermal history of the Universe*

	Time	kT_γ	T_γ	g_*	
Un-certain physics	10^{-42} s 10^{-35} s 10^{-9} s 10^{-4} s	10^{19} GeV 10^{15} GeV 100 GeV 150 MeV		~ 100 20	Planck era; quantum grav. GUTs, Infl., Primord. fluct. Electroweak trans. Q-H trans.; meson decay
Physics fairly well known	1 s 100 s	1 MeV 0.1 MeV	10^{10} K 10^9 K	43/4 3.36	Weak interaction decoupl.; $e^\pm$ annihilation; $T_\nu < T_\gamma$ BBNS (D, ^{3}He, ^{4}He, ^{7}Li)
Un-certain details	4×10^5 yr 10^8 yr 10^{10} yr	0.2 eV 4×10^{-3} eV 2×10^{-4} eV	3000 K 50 K 3 K		Matter domination (Re)comb.; MWB last scat. Re-ionization; Structure formation Present

where ρc^2 is the total energy density. Since the 'cosmological constant' Λ, although non-zero, is not very greatly dominant now, it is negligible at early times when the total density ρ in Eq. (4.9) was much greater; so we can take $\Lambda = 0$ in that equation and obtain the Friedman equation

$$H^2 \equiv \left(\frac{\dot{R}}{R}\right)^2 = \frac{8\pi G\rho}{3} - \frac{kc^2}{R^2}. \tag{4.10}$$

Thus $k = 0$ if

$$\rho = \rho_{\text{crit}} \equiv 3H^2/8\pi G, \tag{4.11}$$

the critical density, which has the present-day value

$$\rho_{\text{crit},0} = 1.88h^2 \times 10^{-29} \text{ gm cm}^{-3}, \text{ or } 2.77 \times 10^{11} h^2 M_\odot \text{ Mpc}^{-3}, \tag{4.12}$$

and one can define a dimensionless density parameter Ω by[2]

$$\Omega \equiv \rho/\rho_{\text{crit}}. \tag{4.13}$$

From the Friedman equation, because ρ varies as R^{-4} (radiation-dominated) or at least as R^{-3} (matter-dominated), $\Omega = 1$ at early times, to a very good approximation. (If it is minutely below 1, it becomes very much less than 1 at later times, and conversely; only if it is exactly 1 does it remain so.) With $\Omega = 1$, Eq. (4.10) becomes

$$V^{-1}\frac{dV}{dt} \equiv 3R^{-1}\dot{R} = (24\pi G\rho)^{1/2} \tag{4.14}$$

---

[2] In a cosmology with significant cosmological constant, one can similarly define $\Omega_\Lambda \equiv \Lambda/3H^2$.

for the physical volume occupied by a given set of particles (fixed co-moving volume).

Another equation from General Relativity (expressing the First Law of Thermodynamics) is the 'pressure equation'

$$\frac{d}{dt}(\rho V) + \frac{P}{c^2}\frac{dV}{dt} = 0. \tag{4.15}$$

At early times, dominated by radiation and relativistic particles, $3P = \rho c^2$, so that

$$\rho \propto R^{-4}, \text{ or } R \propto \rho^{-1/4}. \tag{4.16}$$

Substituting (4.16) in (4.14) with $\rho(0) \rightarrow \infty$ gives the density as a function of time, i.e. the expansion history:

$$\rho = \frac{3}{32\pi G} t^{-2}. \tag{4.17}$$

4.3 Thermal history of the Universe

Given the total density from Eq. (4.17), the temperature follows from the equation of state which depends in turn on what particles are present. For any one species i, with temperature T_i, we have from the Fermi–Dirac or Bose–Einstein distribution, Eq. (2.41),

$$c^2\rho_i = 4\pi g_i\, kT_i \left(\frac{kT_i}{hc}\right)^3 \int_{x_i}^{\infty} \frac{x^2(x^2 - x_i^2)^{1/2}\, dx}{e^{x-y_i} \pm 1}, \tag{4.18}$$

where $x \equiv \tilde{E}/kT_i$, $x_i \equiv m_ic^2/kT_i$, $y_i \equiv \mu_i/kT_i$ and the + and − signs refer to fermions and bosons respectively. In the fully relativistic ($x_i \rightarrow 0$) and non-degenerate ($y_i \rightarrow 0$) limits, the integration gives

$$c^2\rho_i = \frac{\pi^2}{30} g_i\, kT_i \left(\frac{kT_i}{\hbar c}\right)^3 \quad \text{(bosons)} \tag{4.19}$$

$$= \frac{7}{8}\left[\frac{\pi^2}{30} g_i\, kT_i \left(\frac{kT_i}{\hbar c}\right)^3\right] \quad \text{(fermions)}. \tag{4.20}$$

At each stage, particles coupling to photons ($T_i = T_\gamma$) with $m_ic^2 < kT_\gamma$ are relativistic and present in comparable numbers to photons. When kT_γ drops to m_ic^2, they annihilate with their antiparticles and/or decay, or if the coupling is so weak that $T_i \ll T_\gamma$, they contribute little mass–energy and are 'suppressed'. The temperature is then fixed as a function of density, and hence time, by the relation

$$\frac{\pi^2}{30} g_* \frac{(kT_\gamma)^4}{(\hbar c)^3} \equiv \frac{1}{2} g_* a T_\gamma^4 = \rho c^2, \tag{4.21}$$

where g_* is the effective number of degrees of freedom given by

$$g_* = \sum_{bos, x_i \ll 1} g_i \left(\frac{T_i}{T_\gamma}\right)^4 + \frac{7}{8} \sum_{ferm, x_i \ll 1} g_i \left(\frac{T_i}{T_\gamma}\right)^4 \tag{4.22}$$

and a is the normal Stefan radiation-density constant. The resulting thermal history of the Universe is sketched in Fig. 4.1 and Table 4.1.

During most of the first 0.1 second after the Big Bang (ABB), the relativistic particles are photons, electrons, positrons and N_ν species of neutrinos and antineutrinos; N_ν is expected to be 3, from ν_e, ν_μ and ν_τ. There is a sprinkling of non-relativistic protons and neutrons which make a completely negligible contribution to the energy density. The temperature is then given by
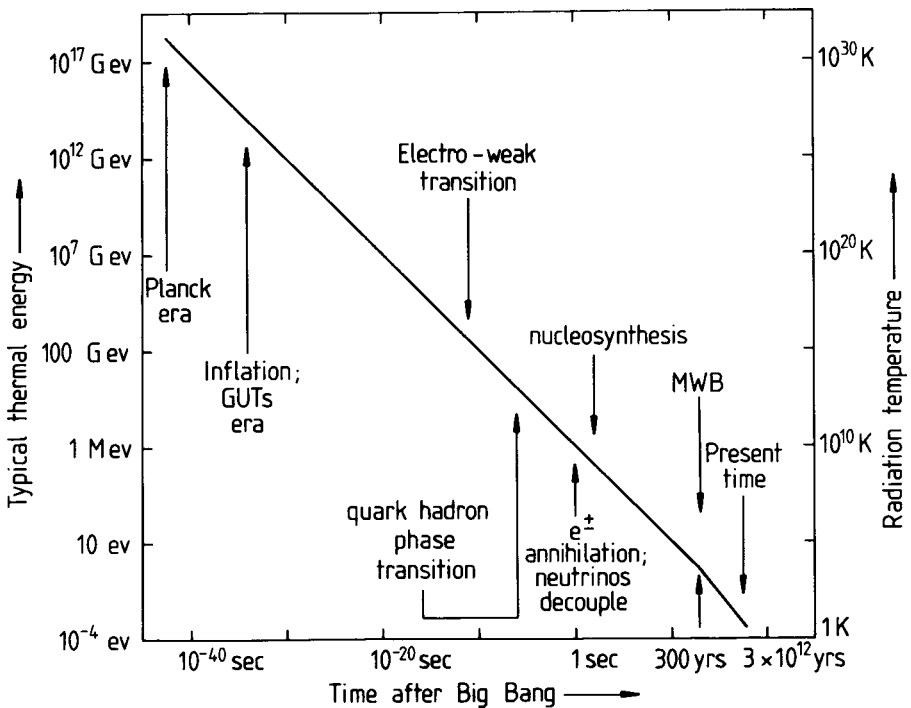
Fig. 4.1. Schematic thermal history of the Universe showing some of the major episodes envisaged in the standard model. GUTs is short for grand unification theories and MWB is short for (the last scattering of) the microwave background radiation. The Universe is dominated by radiation and relativistic particles up to a time a little before that of MWB and by matter (including non-baryonic matter) thereafter, with dark energy eventually taking over.

$$\rho c^2 = c^2 \sum \rho_i = \frac{1}{2} g_* a T_\gamma^4 \tag{4.23}$$

$$= a T_\gamma^4 \left[1 + \frac{7}{4} + \frac{7}{8} N_\nu \left(\frac{T_\nu}{T_\gamma} \right)^4 \right], \tag{4.24}$$

where the 1 in Eq. (4.24) comes from the photons, the 7/4 from electrons and positrons and the $(7/8)N_\nu$ from the neutrinos ($g_i = 1$ for each neutrino species because of their helicity). Before weak-interaction decoupling, $T_\nu = T_\gamma$, and so from Eqs. (4.17) and (4.24),

$$T_\gamma = T = 0.96 \times 10^{10} \, t^{-1/2} \, \text{K}, \tag{4.25}$$

or

$$kT = 0.8 \, t^{-1/2} \, \text{MeV}. \tag{4.26}$$

After 1 s or so, the neutrinos decouple from the cosmic plasma and expand isentropically for ever afterwards remaining as 'microwave neutrinos' with

$$RT_\nu = \text{const.} \tag{4.27}$$

(as long as $kT_\nu \gg c^2 m_\nu$). Photons, electrons and positrons do the same for the time being with $T_\gamma = T_\nu$ until $e^\pm$ annihilation several seconds ABB, which transfers entropy to the photon gas. Since the photon entropy density $s_\gamma \propto T_\gamma^3$ and s_γ is multiplied by 11/4 at $e^\pm$ annihilation according to Eq. (4.24), one has subsequently

$$T_\gamma^3 = \frac{11}{4} T_\nu^3 \tag{4.28}$$

(which implies $T_\nu = 0.7 \, T_\gamma$ as long as $kT/c^2 \gg$ neutrino mass). After $e^\pm$ annihilation (and in particular during nucleosynthesis), photons and nucleons are both conserved, so the ratio of their number densities

$$\eta \equiv n_b/n_\gamma = \text{const.} \sim 10^{-10} \text{ to } 10^{-9}. \tag{4.29}$$

The number η, together with the known background temperature $T_{\gamma 0}$, measures the cosmological baryon density today:

$$\Omega_{b0} h^2 = 3.65 \times 10^{-3} \, (T_{\gamma 0}/2.73 \, \text{K})^3 \, \eta_{10} \tag{4.30}$$

where η_{10} is η in units of 10^{-10}.

Since density and temperature are fixed functions of time during BBNS, *the outcome of the relevant nuclear reactions is a function of the single cosmological parameter η.*

4.4 Neutron:proton ratio

Before ν_e decoupling at around $1\,\text{MeV}$, neutrons and protons are kept in mutual thermal equilibrium through charged-current weak interactions:

$$n + e^+ \quad \longleftrightarrow \quad p + \bar{\nu}_e \tag{4.31}$$

$$p + e^- \quad \longleftrightarrow \quad n + \nu_e \tag{4.32}$$

$$n \quad \longleftrightarrow \quad p + e^- + \bar{\nu}_e. \tag{4.33}$$

Equilibrium in the two-body reactions implies a relation between the chemical potentials:

$$y_p - y_n = y_{e^+} - y_{\bar{\nu}_e} = y_{\nu_e} - y_{e^-}. \tag{4.34}$$

Since the chemical potentials of particles and antiparticles that are in equilibrium with photons are equal and opposite, it can be shown from consideration of the integral in Eq. (4.18) in the relativistic limit ($x_i \to 0$) that for any such pair, to order of magnitude,

$$y_i \sim (n_i - n_{\bar{\imath}})/n_\gamma \text{ if } |y_i| \leq 1. \tag{4.35}$$

Because of charge neutrality, $y_{e^-} \sim \eta \sim B$ and is consequently negligible. That the same thing holds for y_{ν_e} (and for $y_{\nu_{\mu,\tau}}$) is a postulate, but a very plausible one because otherwise we would have neutrino or antineutrino degeneracy with $|L_\nu| \gg B$. The upshot is that the chemical potentials of neutrons and protons are equal and so from Eq. (2.43) one has a simple Boltzmann-type equilibrium ratio

$$(n/p)_{\text{eq}} = e^{-(m_n - m_p)c^2/kT} = e^{-1.29\,\text{MeV}/kT}. \tag{4.36}$$

Now the reaction rate per neutron is $n_{\nu_e} c \langle \sigma \rangle$ where the weak-interaction cross-section $\langle \sigma \rangle$ is an increasing function of the energy, roughly proportional to T in this régime (the exact dependence is given, e.g., by Sarkar 1996), and to the reciprocal neutron half-life for free decay, $\tau_{1/2}^{-1}$, which measures the intrinsic strength of the interaction (a combination of Fermi and Gamow–Teller weak-interaction coupling constants). Since $n_{\nu_e} \propto T^3$, the reaction rate varies about as $T^4/\tau_{1/2}$ and declines steeply with decreasing temperature. The expansion rate, on the other hand, varies as

$$\rho^{1/2} \propto \left(\frac{11}{4} + \frac{7}{8} N_\nu \right)^{1/2} T^2 \tag{4.37}$$

and thus declines much more slowly. Thus, as T goes down, there comes a point at $kT_d \simeq 0.8\,\text{MeV}$ where the weak-interaction rate falls rather suddenly below the expansion rate and the ratio n/p is frozen (apart from free decay and some residual weak interactions) at a value

$$e^{-1.29\,\text{MeV}/kT_d} \simeq 0.2, \tag{4.38}$$

which later fixes the primordial helium mass fraction Y_P because virtually all sur-
viving neutrons are soaked up to make ^{4}He. Hence (after free decay for about
200 s)

$$Y_P = \frac{2n}{n+p} \simeq 0.25. \tag{4.39}$$

The precise value of the decoupling temperature T_d depends on the two physical
constants N_ν and $\tau_{1/2}$:

$$T_d{}^2 \propto \tau_{1/2} \left(\frac{11}{4} + \frac{7}{8} N_\nu \right)^{1/2}, \tag{4.40}$$

implying that larger values of either of these constants lead to higher T_d, higher
n/p and hence more primordial helium, for given η.

4.5 Nuclear reactions

During the first few seconds ABB, nuclear abundances are in statistical equilibrium
(i.e. thermal equilibrium subject to the appropriate n/p ratio), but the correspond-
ing abundance of any nucleus above neutrons and protons is very low because of
the low value of η or the high entropy per baryon. When kT falls to 0.3 MeV, the
equilibrium mass fraction of ^{4}He reaches about 0.15 (for $n/p \simeq 0.2$), but by this
time equilibrium no longer applies: nuclear reactions have become too slow, partly
from Coulomb barriers and partly because of low (still near-equilibrium) abun-
dances of the lighter nuclei D, ^{3}H and ^{3}He. Only when the d/p ratio (depending
on the balance between $p - n$ captures and photo-disintegration) has built up to a
value of order 10^{-5}, at $kT \simeq 0.1$ MeV, do nuclear reactions effectively build up to
^{4}He, which then soaks up virtually all the neutrons remaining from freeze-out and
subsequent decay (see Fig. 4.2). After the formation of ^{4}He, traces of the lighter
elements survive because nuclear reactions are frozen out by low density and tem-
perature before their destruction is complete, and still smaller traces of ^{7}Li and
^{7}Be (which later decays by K-capture to ^{7}Li) are formed and survive. The outcome
of primordial nucleosynthesis is calculated by numerically following a series of
nuclear reactions including in particular the following (and their reverse):

$$
\begin{align}
p + n &\longrightarrow d + \gamma \tag{4.41} \\
d + p &\longrightarrow {}^3\text{He} + \gamma \tag{4.42} \\
d + d &\longrightarrow {}^3\text{He} + n, \ \ {}^3\text{H} + p \tag{4.43} \\
{}^3\text{He} + d &\longrightarrow {}^4\text{He} + p \tag{4.44} \\
{}^3\text{H} + d &\longrightarrow {}^4\text{He} + n \tag{4.45}
\end{align}
$$
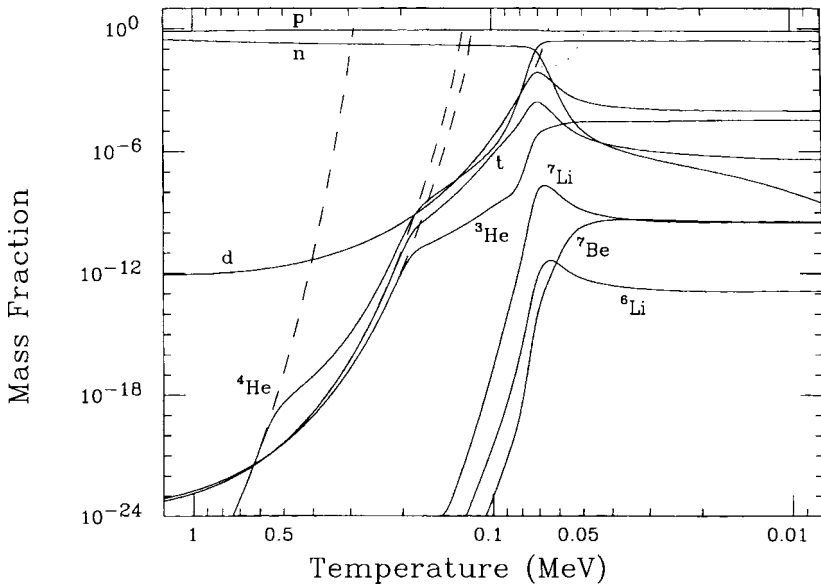
Fig. 4.2. Evolution of light-element abundances with temperature, for $\eta_{10} = 3.16$. The dashed curves give the nuclear statistical equilibrium abundances for ^{4}He, ^{3}He, ^{3}H(t) and ^{2}D(d) respectively; the dotted curve for ^{2}D allows for the diminishing number of free neutrons. After Smith, Kawano and Malaney (1993). Courtesy Michael Smith.

$$^3\mathrm{H} + \alpha \longrightarrow {}^7\mathrm{Li} + \gamma \tag{4.46}$$

$$^3\mathrm{He} + \alpha \longrightarrow {}^7\mathrm{Be} + \gamma \tag{4.47}$$

$$^7\mathrm{Be} + n \longrightarrow {}^7\mathrm{Li} + p \tag{4.48}$$

$$^7\mathrm{Li} + p \longrightarrow 2\,{}^4\mathrm{He} \tag{4.49}$$
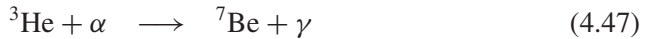
which are followed by ^{3}H decay to ^{3}He ($\tau_{1/2} = 12.2\,\mathrm{yr}$) and ^{7}Be decay to ^{7}Li (by K-capture, after recombination).

The final outcome of these reactions, as a function of η or equivalently $\Omega_{b0}h^2$, is shown in Fig. 4.3. The primordial helium mass fraction Y_P, shown on a large scale, is not very sensitive to η, since this parameter only affects the time for neutron decay before nucleosynthesis sets in, and it can be fitted by the relation

$$Y_\mathrm{P} = 0.226 + 0.025 \log \eta_{10} + 0.0075(g_* - 10.75) + 0.014(\tau_{1/2}(n) - 10.3\,\mathrm{min}). \tag{4.50}$$

The deuterium abundance, on the other hand, is a steeply decreasing function because it is destroyed by two-body reactions with p, n, D and ^{3}He. ^{3}He declines more gently because this nucleus is more robust. ^{7}Li has a bimodal behaviour because at low baryon densities it is synthesized from ^{3}H by reaction (Eq. 4.46) and both nuclei are destroyed by two-body reactions, whereas at higher densities it
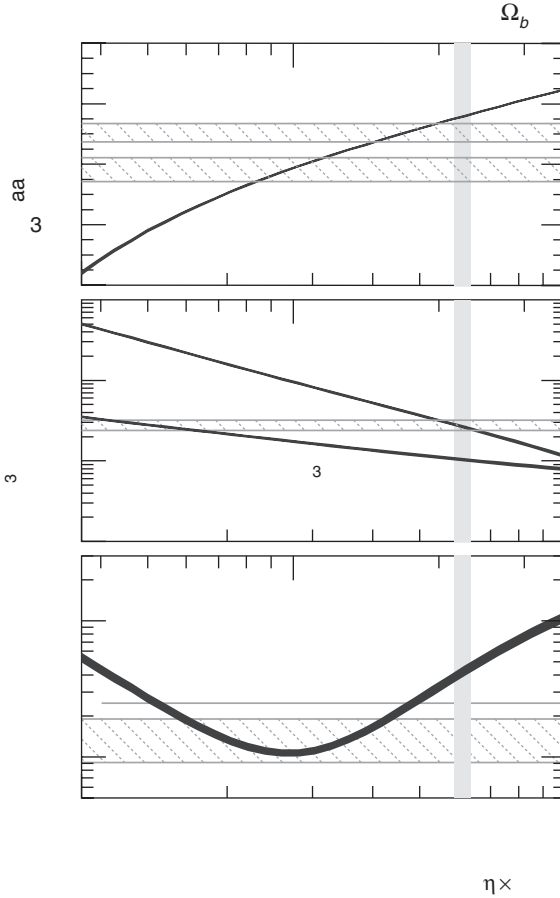
Fig. 4.3. Primordial abundances from SBBN as functions of η or, equivalently, $\Omega_{b0}h^2$. Curves show theoretical predictions, with their $\pm 1\sigma$ uncertainty limits represented by the thickness of the curves, while the horizontal error boxes indicate various limits derived from observation. (Observational estimates of ^{4}He have since been revised upwards.) The vertical bar indicates the range of η deduced from WMAP observations of the angular fluctuation power spectrum of the MWB (Spergel *et al.* 2003). After Coc *et al.* (2004).

results from reaction (Eq. 4.47) on ^{3}He to make ^{7}Be and the comparative robustness of both these nuclei causes an increase with η. The comparison with observations, and deductions therefrom, are discussed in the following sections.

4.6 Deuterium and ^{3}He

Essentially all deuterium in the Universe is believed to come from BBNS, because thermonuclear reactions in stars only cause net destruction of D and it is vastly

more abundant than other light nuclei like ^{6}Li or ^{9}Be that are believed to result from spallation processes (Epstein, Lattimer & Schramm 1976). However, deuterium in both terrestrial and meteoritic water is enhanced by factors of 6 or more owing to fractionation. The first evidence for 'cosmic' deuterium arrived in the early 1970s from studies of the solar wind, planetary atmospheres and the interstellar medium.

The composition of the solar wind is studied by ion counters on space probes, by analysis of samples collected on metal foils placed on the Moon and from the outer layers of gas-rich meteorites. These give an average ^{3}He/^{4}He ratio of 3.8×10^{-4}, equivalent to ^{3}He/H $\simeq 3.6 \times 10^{-5}$, since for the Sun's atmosphere He/H $\simeq 0.09$. D. C. Black (1971) and Geiss and Reeves (1972) noted that helium gas released by heating carbonaceous chondrites had a lower ^{3}He/^{4}He ratio of about 1.5×10^{-4}, which they identified as the proto-solar ^{3}He abundance present in the wind from the primitive Sun, attributing the excess in the present-day solar wind to proto-solar deuterium that had been burned to ^{3}He during the Sun's evolution. The proto-solar deuterium abundance D/H is thus about 2.0×10^{-5}, which is in fair agreement with observations of deuterated molecules (HD and CH_3D) in the atmospheres of the major planets (Geiss & Gloeckler 2003).

Searches for the D I hyperfine structure line transition at 91.6-cm wavelength from the Galaxy have mostly been unsuccessful, apart from a tentative detection in the Galactic anti-centre region (Chengalur *et al.* 1997), but in the early 1970s interstellar deuterium was detected by Penzias, Wilson and others in the form of DCN and DCH$^+$ from microwave transitions in molecular clouds, and by L. Spitzer and others who found UV transitions of HD and D I (Lyman series) caused by diffuse clouds on the line of sight to hot stars observed with the Copernicus satellite (Rogerson & York 1973). Whereas quantitative interpretation of the molecular lines is greatly complicated by various fractionation effects (which can either increase or reduce the D/H ratio according to circumstances), the atomic lines, with deuterium having a reasonably large isotopic blue shift of $82\,\mathrm{km\,s^{-1}}$ relative to ^{1}H, give quite accurate column densities from which an average interstellar D/H ratio of about 1.5×10^{-5} has been inferred, marginally below (but not really inconsistent with) the proto-solar value (see Fig. 4.4). Nearby cool stars like Capella have Lyman-α in emission from their chromospheres with interstellar absorption components superposed that have been observed and analyzed using the Hubble Space Telescope and FUSE and lead to a D/H ratio of $(1.5 \pm 0.1) \times 10^{-5}$ (Linsky 2003) in the 'local bubble' surrounding the Sun. But beyond $100\,\mathrm{pc}$ or so there is evidence for variations in D/H along different sight-lines (e.g. 0.7×10^{-5} towards δ Orionis and 2.2×10^{-5} towards γ^2 Velorum; Sonneborn *et al.* 2000), and the value is uniformly low at long distances with large column densities, presumably because the line of sight passes through dense molecular clouds with substantial amounts of deuterium locked into molecules and dust grains (Wood
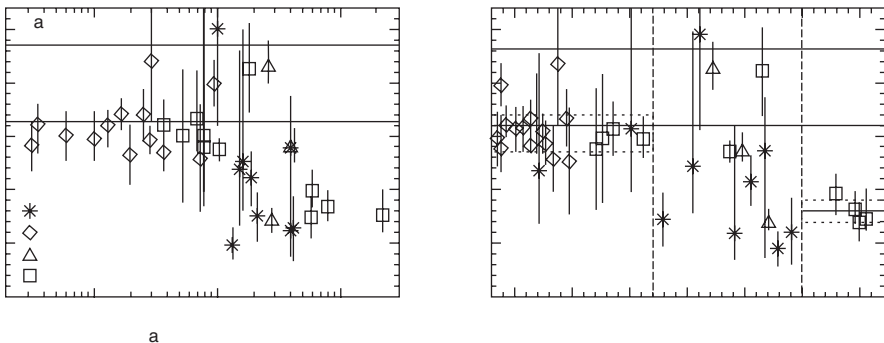
Fig. 4.4. D/H ratios measured along the lines of sight to stars in the Galaxy. The horizontal parallel lines indicate upper and lower limits to the ratio in the proto-solar cloud after Geiss and Gloeckler (2003). Adapted from Wood *et al*. (2004).

et al. 2004); one then infers that the highest values, of order 2.2×10^{-5} and thus similar to the proto-solar value, are a lower limit to the true D/H ratio in the local ISM (Linsky *et al*. 2006).

Because of the destruction of D when interstellar gas is recycled through stars, its present-day abundance is a firm lower limit to the primordial one. Adopting the local bubble value as representative of the Galaxy places an upper limit on the baryonic density parameter,

$$\eta_{10} < 8.5, \quad \text{or} \quad \Omega_{b0}h^2 < 0.032 \quad \text{and} \quad \Omega_{b0} < 0.13 \tag{4.51}$$

assuming $h \geq 0.5$. Qualitatively, the destructive effect of recycling through stars, or 'astration', is supported by the fact that emission lines from deuterated molecules are relatively weaker in the Sagittarius B2 clouds near the Galactic centre, where stellar evolution and nucleosynthesis are believed to have gone further than in the solar neighbourhood. Thus there could be a positive gradient in D/H with Galactocentric distance corresponding to the negative gradient in metallicity and $^{13}C/^{12}C$, but the precise factor by which D/H has been reduced in this way is model-dependent and correspondingly uncertain. The modest abundance of ^{3}He in the Solar System has been used to place limits on that factor (Yang *et al*. 1984), on grounds that ^{3}He is the main product of deuterium burning, but uncertainties about the Galactic chemical evolution of ^{3}He itself – involving both production and destruction in stars – make it difficult to reach robust conclusions in this way.

With the advent of 8- to 10-metre class telescopes in the 1990s, it became possible to approach the primordial deuterium problem more directly, by measuring the isotopic component in absorption lines of hydrogen due to intervening gas along
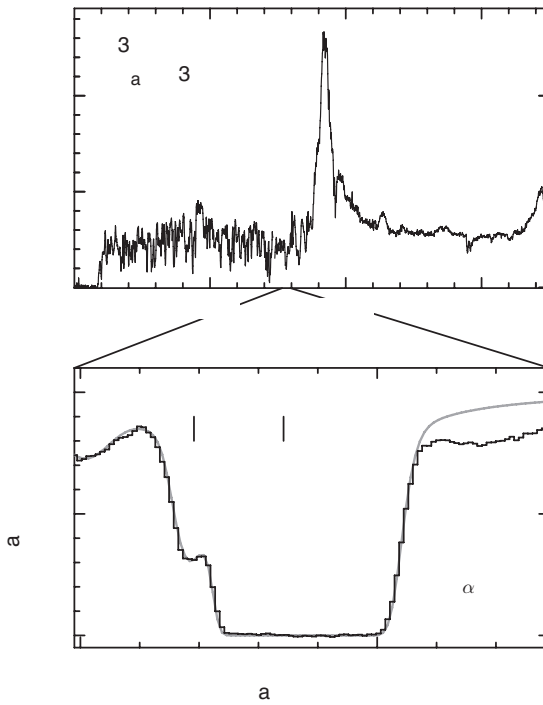
Fig. 4.5. Determination of the D/H ratio in an intervening (Lyman-limit) absorption-line system in front of the quasar 1937-1009. The upper panel shows Lyman-α and a few other emission lines from the quasar, while shortward of Lyman-α there is a multitude of Lyman-α absorption lines (the 'Lyman-α forest') from density fluctuations in the intergalactic medium, with one cloud having sufficient column density to produce strong absorption at the Lyman limit, redshifted to 4200 Å. The factor 100 drop in the continuum at that point (measured on spectra with higher signal:noise) gives the hydrogen column density. The lower panel shows a high-resolution spectrum of the Lyman-α line from the same system in which the deuterium component clearly appears and enables the deuterium column density to be determined, giving D/H = $(3.3 \pm 0.3) \times 10^{-5}$. This is one of a mere handful of known systems deemed to be 'clean', i.e. free from contamination by hydrogen moving at around 82 km s^{-1} towards us relative to the main component. Reprinted from Tytler, O'Meara, Suzuki and Lubin (2000). With permission from Elsevier.

the line of sight to quasars at high redshift. These are classified in order of increasing column density as: the Lyman-α forest, representing local density maxima in the intergalactic medium; Lyman-limit systems with a measurable break at the redshifted Lyman limit, representing some sort of circum-galactic or intergalactic clouds (see Fig. 4.5); and damped Lyman-α (DLA) systems with measurable damping wings of the Ly-α line which may represent the progenitors of spiral or dwarf disk galaxies. These systems generally have low metallicity, typically 1/100
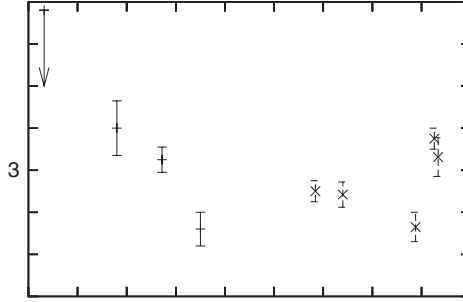
Fig. 4.6. Comparison of D/H measurements at high redshift from Lyman-limit and damped Lyman-α systems. The measurements come from O'Meara *et al.* (2001; 3 Lyman-limit systems and one marginal DLA), Crighton *et al.* (2004; the highest column density Lyman-limit system), Kirkman *et al.* (2003; another marginal DLA), Pettini & Bowen (2001), Levshakov *et al.* (2002) and O'Meara *et al.* (2006) (three classical DLAs). There is no convincing evidence for systematic trends with either column density or metallicity up to about 1/30 solar.

of solar, so that the degree of destruction of deuterium by astration can be assumed to be negligible and their D/H ratio is primordial. There are problems, however, with contamination from hydrogen clouds moving towards us at around $82\,\mathrm{km\,s^{-1}}$ relative to the main components, which led to some overestimates of D/H in the early days. Only a handful of systems thought to be 'clean' – mostly discovered by David Tytler and co-workers – are known, and these include both Lyman-limit and DLA systems; the latter give a potentially more accurate H I column density than the Lyman break, and a larger choice of lines up the Lyman series, but it is clear from Fig. 4.6 that substantial discrepancies still exist. The upshot is that primordial D/H is probably somewhere between 2 and 4×10^{-5}, implying

$$4.5 \leq \eta_{10} \leq 7, \ \ \mathrm{or} \ \ 0.015 \leq \Omega_{b0}h^2 \leq 0.025. \tag{4.52}$$

The upper end of the range in η is in excellent agreement with what has been deduced from WMAP measurements of the angular fluctuation spectrum of the cosmic microwave background (see Fig. 4.3 and Section 4.9).

^{3}He has been detected in Galactic H II regions and a few planetary nebulae using the hyperfine transition of ^{3}He$^+$ at 3.46 cm. The observations are difficult, requiring large single-dish radio telescopes and careful background removal, as well as realistic H II region models, because the collisionally excited and de-excited ^{3}He$^+$ transition, governed by a Boltzmann equilibrium (and therefore linearly dependent on particle density), is compared to the bremsstrahlung continuum proportional to n_e^2. In PN, the ^{3}He/H ratio can occasionally be quite high, in one case reaching
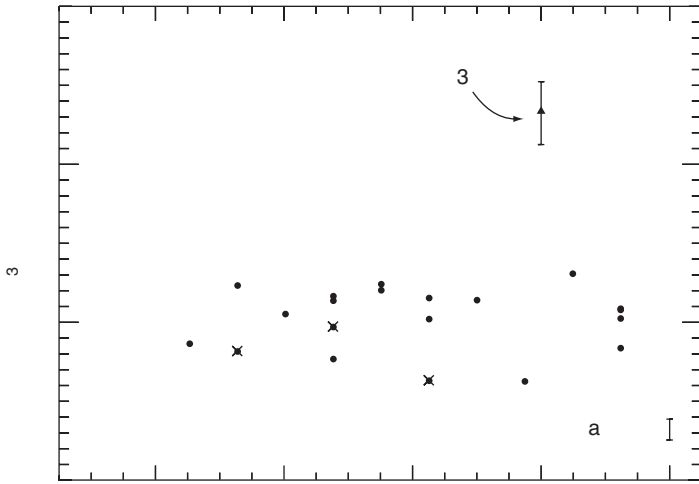
Fig. 4.7. ^{3}He/H in 'simple' Galactic H II regions, i.e. those thought to be reasonably well represented by homogeneous spherical models (Balser *et al*. 1999), and one planetary nebula, as a function of their oxygen abundance. ^{3}He/H is plotted on a logarithmic scale relative to the proto-solar value of 1.5×10^{-5}. After Bania, Rood and Balser (2002). Reprinted by permission from Macmillan Publishers Ltd. Courtesy Tom Bania.

as much as 3×10^{-4}, whereas in H II regions it is more than an order of magnitude lower (see Fig. 4.7) and not significantly different from the proto-solar value over a large range in Galactocentric distance and metallicity. The PN data partially support earlier theoretical predictions that there is net production of ^{3}He in low-mass stars, but the overall effect of Galactic chemical evolution appears to be almost neutral, with production being largely cancelled out by destruction from non-classical mixing processes that could arise from meridional currents driven by rotation (Sweigart & Mengel 1979) or from Rayleigh–Taylor instabilities revealed by sophisticated numerical modelling in 3 dimensions (Dearborn, Lattanzio & Eggleton 2007).

Further information about the abundance of ^{3}He in the local ISM comes from the Ulysses spacecraft, by its sampling of 'pick-up ions' which enter the Solar System as neutral atoms and are then ionized and swept outwards by the solar wind (Gloeckler & Geiss 1996). Table 4.2 gives a summary of current estimates of D and ^{3}He in the Solar System and the local ISM.

Comparison with the estimates of primordial deuterium in the light of Fig. 4.3 suggests that there has been some net increase in ^{3}He/H while (D + ^{3}He)/H has hardly changed since the Big Bang.

Table 4.2. *Interstellar and proto-solar deuterium
and ^{3}He*

	ISM	Pre-solar
10^5 (D + ^{3}He)/H	3.6 ± 0.3	3.6 ± 0.35
10^5 D/H	1.5 ± 0.2	2.0 ± 0.35
10^5 ^{3}He/H	2.1 ± 0.2	1.5 ± 0.06

Data from Geiss and Gloeckler (2003).

4.7 Helium

Helium is the second most abundant element in the visible Universe and accordingly there is a mass of data from optical and radio emission lines in nebulae, optical emission lines from the solar chromosphere and prominences and absorption lines in spectra of hot stars. Further estimates are derived more indirectly by applying theories of stellar structure, evolution and pulsation. However, because of the relative insensitivity of Y_P to cosmological parameters, combined with the need to allow for additional helium from stellar nucleosynthesis in most objects, the requirements for accuracy are very severe: better than 5 per cent to place cosmological limits on N_ν and better still to place interesting constraints on η or Ω_{b0}. One can, however, assert with confidence that there is a universal 'floor' to the helium abundance in observed objects corresponding to $0.23 \le Y_P \le 0.25$.

The historical development has been quite interesting. In the early 1950s, data were available only for a few representative B-type stars and planetary nebulae, consistent with $y \equiv$ He/H $\simeq 0.1$ or $Y \simeq 0.3$, and in fair agreement with early BBNS predictions by Hayashi (1950) and by Alpher, Follin and Herman (1953); at that time it was widely taken for granted that this abundance was universal, in common with others. With the arrival of evidence for nucleosynthesis in stars, and the development of the related theory, it became fashionable to suppose that the oldest, lowest-metallicity objects would also have a low helium abundance, although B^{2}FH in 1957 wisely left open the possibility that there might be 'some helium in the initial matter of the Galaxy' and several authors noted at various times that a purely stellar origin for the large present-day helium abundance implied a very high luminosity for galaxies in the past. In 1963, C. R. O'Dell, M. Peimbert and T. D. Kinman at the Lick Observatory found a normal helium abundance in a planetary nebula belonging to the globular cluster M15 (in which the stars have [Fe/H] $\simeq -2$). This discovery stimulated F. Hoyle and R. J. Tayler to point out in a prescient paper in 1964 (just before discovery of the microwave background was announced) the crucial importance to cosmology of the presence or absence of a

universal helium 'floor', and to give a fresh calculation of Y_P from BBNS in which they pointed out the influence of N_ν; the ν_μ had then been recently discovered. (This consideration was used later by Shvartsman (1969), Steigman, Schramm and Gunn (1974) and others to place limits on the number of families of quarks and leptons waiting to be discovered.) After the microwave background observation, opinion gradually came round in favour of a helium floor, based on several arguments: R. F. Christy's studies of the pulsation of RR Lyrae stars, energized by He^+ in the envelope; J. Faulkner and I. Iben's modelling of stellar evolution in globular clusters (see Fig. 4.8) and the relative lifetimes on the red giant branch (hydrogen shell burning) and on the horizontal branch (helium core burning); and the masses, luminosities and effective temperatures of low-metallicity subdwarfs, which lie somewhat below the Population I lower main sequence in the HR diagram, but have larger luminosities for the same mass (see Chapter 5). Some contrary indications also came up, in particular the so-called subdwarf B-stars which lie at the extreme
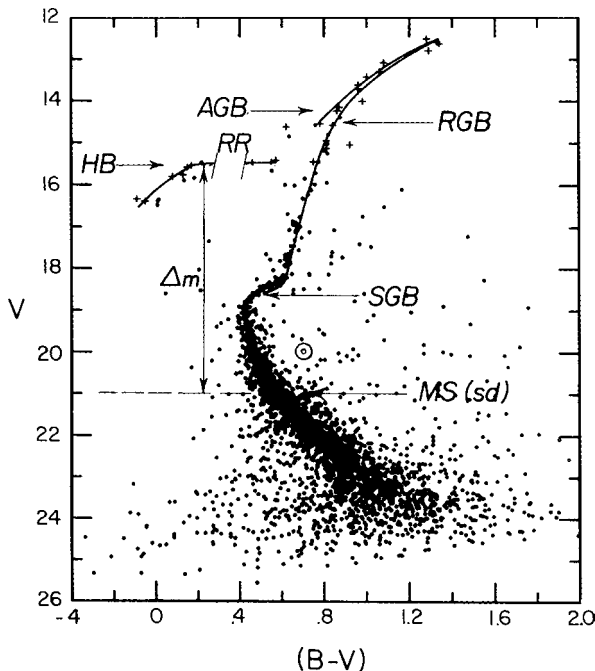
Fig. 4.8. Colour–magnitude (HR) diagram of the globular cluster Messier 68 with [Fe/H] $\simeq -2$. In order of successive evolutionary stages, MS (sd) indicates the main sequence occupied by cool subdwarfs, with the position of the Sun shown for comparison, SGB indicates the subgiant branch, RGB the red giant branch, HB the horizontal branch including a gap in the region occupied by RR Lyrae pulsating variables and AGB the asymptotic giant branch. Adapted from McClure *et al.* (1987).

blue end of the horizontal branch: their atmospheres are helium-deficient, but it was shown fairly soon afterwards that they also have other anomalies similar to those of CP stars (see Chapter 3), leading to the conclusion that the helium deficiency is just a superficial effect due to gravitational settling. (The same phenomenon seems to have occurred, to a minor extent, even in the Sun.) The argument was finally settled, to every reasonable person's satisfaction, in 1972, when L. Searle and W. L. W. Sargent discovered that two blue compact galaxies previously discovered by Fritz Zwicky, II Zw 40 and I Zw 18, were dominated by giant H II regions with low abundances of oxygen and other heavy elements (I Zw 18 still holds the record for low abundances in extragalactic H II regions with [O/H] $\simeq -1.5$), but nearly normal helium. This discovery set the stage for the modern era, marked by systematic attempts to estimate Y_P by measuring or estimating helium abundances in a variety of objects with differing metallicities and extrapolating to zero metallicity.

Table 4.3 shows some estimates of helium abundance in various objects. The value for the interior of the proto-Sun is based on theoretical models of its evolution (see Chapter 5) constrained by its known mass, age, chemical composition (apart from Y) and present-day luminosity and radius. Helium, through its effect on the mean molecular weight, influences the structure of a star and speeds up its evolution. Uncertainties include the opacity κ, the precise equation of state and the treatment of convection; the deficit of solar neutrinos relative to prediction has now been shown to be due to neutrino physics rather than weaknesses in the solar models. Solar seismology (based on observations of minute oscillations with periods of the order of 5 minutes) has led to greatly improved understanding of the Sun's internal structure in recent years, but it also indicates an appreciably lower helium abundance ($Y = 0.24$) in the convective envelope, which is attributed to gravitational settling. Estimates of helium abundance in the chromosphere have been made on the basis of hydrogen and helium emission lines from prominences, but these are quite imprecise, owing to the difficulty in modelling radiative transfer effects and the populations of atomic levels. Finally, because there has been net production of helium during the evolution of the Galaxy, and the Sun is a relatively young object, its helium abundance is expected to exceed the primordial value by some hundredths.

The B stars, with $10^4 \, \text{K} \leq T_{\text{eff}} \leq 3 \times 10^4 \, \text{K}$, show He I lines in absorption, but again these are young objects and the inferred helium abundances are not yet very precise.

The most metal-deficient stars comprise field stars in the solar neighbourhood (where in some cases distances and luminosities can be found from parallaxes) and stars in globular clusters where the morphology of the HR diagram can be studied (Fig. 4.8). Such stars are of particular interest because their content of heavy elements (synthesized in still earlier generations of stars) is so low that they can

Table 4.3. *Estimates of primordial helium mass fraction*

Objects	Y_P	Method	Ref.	Problems
Sun	$< .28 \pm .02$	Interior	1	κ; Eq. of st.
" "	$< .28 \pm .05$	Prom. He I	2	Level pops.
B stars	$< .30 \pm .04$	Abs. lines	3	Precision
μ Cas	$.23 \pm .05$	Bin. orbit	4	Precision
Globular	$.23:$	RR, Δm	5	Physical
clusters	$.244 \pm .006:$	N(HB)/N(RG)	6	basis of
	$.23 \pm .02 :$	M15 HB	7	stellar
	$\leq .24 \pm .02$	47 Tuc HB	8	evolution
Gal.	$.22 \pm .02$	Plan. neb.	9	Self + gal. enr.
neb.	$.22:$	H II reg.	10	He^0; gal. enr.
	$.233 \pm .005$	Irr. + BCG	11	He^0; data
Extra-	$< .243 \pm .010$	BCG	12	II Zw 40
galactic	$.228 \pm .005$	Irr. + BCG	13	I Zw 18
H II	$.234 \pm .002$	Irr. + BCG	14	
regions	$.244 \pm .002$	BCG	15	
	$.250 \pm .004$	BCG	16	
	$.249 \pm .003$	BCG + Irr.	17	
	$.247 \pm .003$	Irr. + BCG	18	

References: 1. Turck-Chièze & Lopez (1993). 2. Heasley & Milkey (1978). 3. Kilian (1992). 4. Haywood, Hegyi & Gudehus (1992); Drummond, Christou & Fugate (1995). 5. Caputo, Martínez Roger & Páez (1987); Sandquist (2000). 6. Buzzoni *et al*. (1983); Cassisi *et al*. (2003). 7. Dorman, Lee & VandenBerg (1991). 8. Dorman, VandenBerg & Laskarides (1989). 9. Peimbert (1983). 10. Mezger & Wink (1983). 11. Lequeux *et al*. (1979). 12. Kunth & Sargent (1983). 13. Pagel *et al*. (1992). 14. Olive, Steigman & Skillman (1997). 15. Izotov & Thuan (1998). 16. Fukugita & Kawazaki (2006). 17. Izotov, Thuan & Stasinska (2007). 18. Peimbert, Luridiana & Peimbert (2007).

be considered to have been born with essentially the primordial helium abundance. That abundance influences certain of their structural properties: the location of the lower main sequence in absolute magnitude, the blue edge of the instability strip occupied by RR Lyrae variables, the luminosity along the 'zero-age' horizontal branch ZAHB (which can be estimated from Δm, the magnitude difference from a fiducial point along the main sequence), the relative numbers (i.e. lifetimes) along the HB and the RGB and (in some cases) the detailed distribution in the diagram of stars evolving away from the ZAHB. Helium also affects the mass–luminosity relation, which has been used in studies of the visual-interferometric binary μ Cassiopeiae. Some estimates of Y_P derived from these various properties are shown in
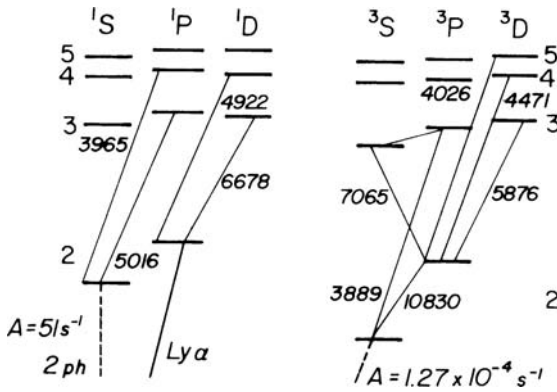
Fig. 4.9. Term scheme for He I, showing some of the transitions of interest.

Table 4.3, but the errors are hard to quantify because many features of stellar evolution are sensitive to uncertainties in the input physics and the helium abundance is generally only one of many factors influencing stellar structure at different stages of evolution (see Chapter 5).

The most accurate helium abundances come from measurements of recombination lines of hydrogen and helium in the emission spectra of planetary nebulae and H II regions (see Fig. 3.22), using theoretical effective recombination coefficients calculated from quantum mechanics. The He I term scheme and several optical transitions of interest are shown in Fig. 4.9; in Galactic H II regions it is also possible to measure radio recombination lines, which is especially useful when the optical spectrum is obscured by dust. Silvia and Manuel Peimbert in 1974 outlined a programme whereby measurements in Galactic and extragalactic H II regions having different Z's (represented mainly by oxygen) could be used to plot a regression represented by

$$Y = Y_P + Z\frac{\Delta Y}{\Delta Z} = Y_P + (O/H)\frac{\Delta Y}{\Delta(O/H)}. \tag{4.53}$$

Extrapolation to $Z = (O/H) = 0$, would give the primordial helium abundance Y_P, while the slope of the regression, $\Delta Y/\Delta Z$ (not necessarily a constant), would place a significant constraint on stellar nucleosynthesis by giving the rate at which helium is freshly synthesized and ejected into the ISM compared to the corresponding rate for carbon and heavier elements. The application of this idea to objects in our own Galaxy suffers from the fact that the abundances represented by Z are so high that rather a large extrapolation is needed; in addition, planetary nebulae need a small correction for helium dredged up to the surface during prior stellar evolution, while Galactic H II regions mostly have ionizing stars that are not hot enough to guarantee

the absence of undetectable neutral helium, He^0, especially with the limited angular resolution of radio telescopes.

Consequently the best objects in which to apply this idea are extragalactic H II regions in dwarf irregular galaxies like the Magellanic Clouds and in blue compact (or H II) galaxies where the abundances of oxygen and other heavy elements are low and the ionizing stars often very hot, so that the regions of ionized hydrogen and helium coincide within 1 per cent or so. Two lines of Table 4.3 summarize the outcome of two of the more accurate early investigations in this field, which led to slightly contradictory results: Lequeux *et al*. (1979) found a linear regression with a slope $\Delta Y/\Delta Z = 3$, whereas Kunth and Sargent (1983) found no evidence for a slope, but their results may have been somewhat biased by the high weight given to II Zw 40, for which the yellow helium line λ 5876 is redshifted to coincide with, and be somewhat absorbed by, interstellar sodium λ 5889 in the Milky Way.

In recent years, intensive efforts have been made to improve the determination of the pre-Galactic helium abundance (generally assumed to be the same as Y_P) and $\Delta Y/\Delta Z$ from observations of extragalactic H II regions. Advantages of this method are:

- The theory of recombination for hydrogen and helium seems to be well understood, at least to 1 or 2 per cent, and the line intensities are not very sensitive to temperature or density; in particular, there is no exponential factor.
- Low abundances (extending down to [O/H] $\simeq$ -1.5 in the case of I Zw 18) ensure that little extrapolation to $Z = 0$ is needed.
- One can assure oneself that neutral helium is negligible by assessing that the effective temperatures of the ionizing stars are high enough (say, above 40 000 K). One way to do this is to compare the degrees of ionization of oxygen (O II/O III) and sulphur (S II/S III), which have widely differing ionization potentials, with predictions from numerical photo-ionization models.

There are also difficulties:

- Experimental problems: signal:noise, detector linearity (Hα/λ 6678 is typically about 100), calibration, reddening.
- Underlying absorption lines in the stellar continuum.
- Line absorption in the intervening interstellar gas, or Earth's atmosphere.
- Fluorescence and collisional excitation, arising primarily from the metastability of the 2^3S level (see Fig. 4.9), in which consequently a high population accumulates which can cause additional emission from lines such as λ 4471, λ 5876 by either collisional excitation or radiative transfer effects following absorption of higher lines in the $2^3S - n^3P$ series. The singlet line λ 6678 can also be enhanced by collisional excitation from 2^3S. The collisional effects can be calculated from the known electron temperature and density, and are quite small at

typical electron densities of the order of 100 cm^{-3} except in the case of λ 7065. The latter line, once collisional effects are allowed for, can also be used to gauge the influence of radiative transfer effects, which are normally found to be small for extragalactic H II regions. Collisional excitation can also slightly affect the hydrogen lines, especially Hα, when the electron temperature is high, i.e. at the lowest metallicities (Davidson & Kinman 1985).

- While the triplet levels exist only from $n = 2$ upwards, the singlets have an analogue to the hydrogen Lyman-α line and consequently, like hydrogen, have Cases A and B (or intermediate). The assumption of Case B, which is usually made, could be slightly inaccurate if Ly-α were to either partially escape or be absorbed by small amounts of dust in the nebula. However, the above-mentioned lines are not very sensitive to Case A or B, while λ 5016, which is very sensitive because of the strong transition from its upper state 3^1P to the ground state 1^1S, is found to be in agreement with Case B whenever it is measured.

- Temperature gradients and local temperature fluctuations usually parameterized by t^2 (Peimbert 1967) lead to a systematic bias when the electron temperature determined conventionally from [O III] λ 4363/λ 5007 is substituted into the expressions for effective recombination coefficients of hydrogen and helium.

- $\Delta Y/\Delta Z$ or $\Delta Y/\Delta$(O/H) may vary, either systematically as a function of Z or randomly, e.g. if some H II regions are self-polluted with helium and other elements (e.g. N) ejected in winds from massive embedded stars. There is some evidence that this actually happens in a very few cases, such as the nucleus of NGC 5253, where the continuum shows a strong, broad feature at the He$^+$ wavelength λ 4686, due to Wolf–Rayet stars.

Figure 4.10 shows part of a high-resolution high signal:noise spectrum typical of more recent attempts to determine helium abundance in low-Z H II regions, and Fig. 4.11 shows some resulting regressions against oxygen and nitrogen. The preferred oxygen regression using modern emissivities gives the result (Izotov, Thuan & Stasinska 2007)

$$Y = 0.2509 + 52(\text{O/H}) \tag{4.54}$$
$$\pm 0.0012 \pm 9;$$

The two error terms refer to Y_{p} and the regression slope respectively. In contrast to some earlier work, based on less homogeneous data sets and apparently affected by underlying absorption lines, notably in I Zw 18, this result, together with a similar one by Peimbert, Luridiana and Peimbert (2007), gives a primordial helium abundance in excellent agreement with the one predicted theoretically on the basis of the microwave background fluctuations and the lower estimates of deuterium abundance (see Fig. 4.3), a comparatively small value of about 2 for $\Delta Y/\Delta Z$ and no
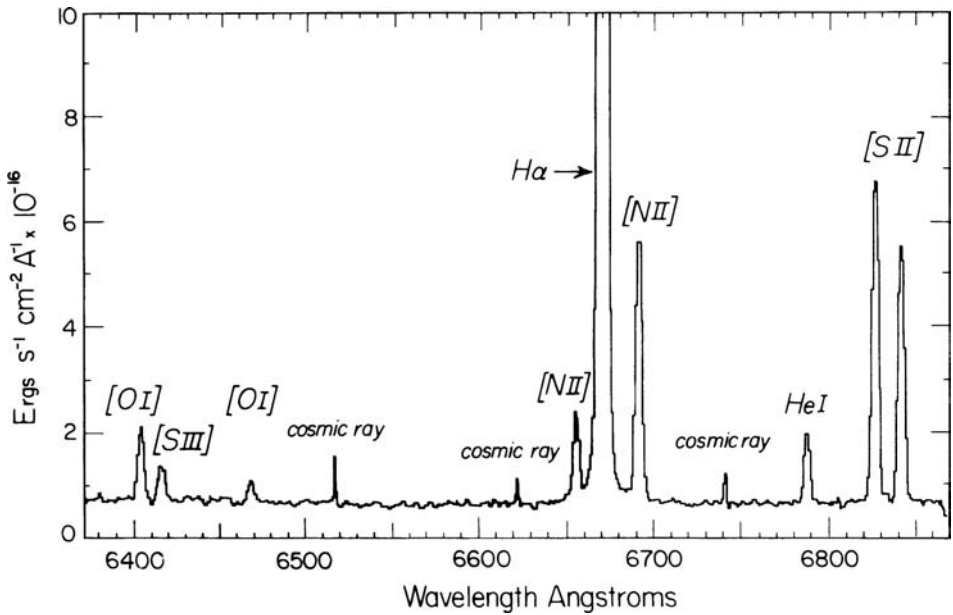
Fig. 4.10. Portion of the red spectrum of the H II galaxy Tololo 0633-415 with a redshift of 0.016, showing diagnostic features for helium (Hα and λ 6678), electron density ([S II]) and ionization ([S III]). The features marked 'cosmic ray' are due to impacts of charged particles on the CCD detector. After Pagel *et al.* (1992).

evidence for any individual deviations from the regressions against either oxygen or nitrogen in their sample. The more recent results involve various refinements such as improved He I emissivities including collisional effects (Benjamin, Skillman & Smits 1999, 2002; Porter *et al.* 2005), allowance for collisional excitation of hydrogen and attention to effects of temperature fluctuations and gradients (Peimbert, Peimbert & Luridiana 2002); but the main factor leading to increased estimates of Y_P has been the inclusion of a larger correction for underlying stellar absorption lines, the full extent of which was first noted by Fukugita and Kawazaki (2006).

4.8 Lithium 7

The lithium resonance doublet line λ 6707 is fairly easy to observe in cool stars of spectral types F and later, and it has also been detected in diffuse interstellar clouds. There is thus an abundance of data, although in the ISM the estimation of an abundance is complicated by ionization and depletion on to dust grains. The youngest stars (e.g. T Tauri stars that are still in the gravitational contraction phase before reaching the main sequence) have a Li/H ratio that is about the same as the Solar System ratio derived from meteorites, Li/H = 2×10^{-9}, which is thus taken as the Population I standard.
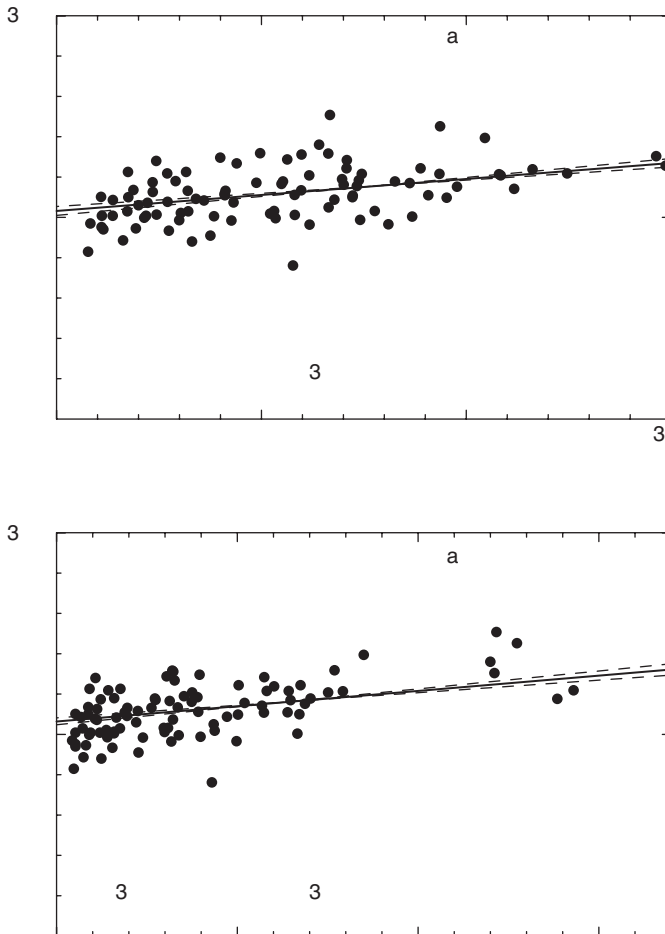
Fig. 4.11. Regressions of helium against oxygen and nitrogen in extragalactic
H II regions, after Izotov, Thuan and Stasinska (2007).

As stars become older, lithium at their surface becomes gradually depleted by
mixing with deeper layers at temperatures above 2.5×10^6 K where it is destroyed
by the (p, α) reaction, Eq. (4.49). This destruction takes place more rapidly in
cooler stars with deeper outer convection zones, so that there is a trend for lithium
abundance to decrease with both stellar age and diminishing surface temperature;
in cooler stars some depletion takes place already in the pre-main-sequence stage.
Thus, in the young Pleiades cluster ($\sim 10^8$ yr), lithium has its standard abun-
dance down to $T_{\text{eff}} = 5500$ K (type G5), whereas in the older Hyades cluster
($\sim 6 \times 10^8$ yr) it is noticeably depleted below $T_{\text{eff}} = 6300$ K (F7) and also in

a narrow range of effective temperatures around 6600 K. ^{6}Li is still more fragile than ^{7}Li and is accordingly virtually absent in most stars, although it is detected in interstellar clouds when the spectral resolution and sensitivity are high enough. When stars evolve up the giant branch, their surface ^{7}Li is diluted by the dredge-up of Li-free material from below, but fresh lithium is created in some AGB stars, including 'super lithium-rich' carbon stars such as WZ Cassiopeiae and a number of luminous long-period variables in the Magellanic Clouds, so that astration of the ISM leads to both destruction and creation of ^{7}Li. However, the destruction mechanisms are not completely understood, notably in the case of the Sun where the depletion (by a factor of 150) has gone much further than predicted by standard models including convection (the Sun's surface convection zone extends down to a temperature of only 1×10^6 K) and atomic diffusion, and there is presumably some special mechanism not taken into account in those models, e.g. additional mixing due to processes associated with rotation such as meridional circulation, shear turbulence or gravity waves.

Against this background, it occasioned some surprise when Spite and Spite (1982) discovered lithium in Population II stars, with a quite uniform abundance of the order of 0.1 of the standard Population I value, although their metallicities are down by factors of 100 or more. Figure 4.12 shows an ensemble of data which exhibits a lithium 'plateau' (for stars with $T_{\text{eff}} > 5500$ K or so) extending down to [Fe/H] ≤ -4. Apart from a few exceptions not shown in the diagram, the Population II stars have a much smaller range in lithium abundance than do Population I stars, suggesting that depletion effects are mild or absent (in agreement with standard stellar models) and that here one is indeed seeing the primordial abundance or a close approximation thereto (represented by a rectangular error box in Fig. 4.3). The upper envelope for Population I stars presumably represents a net increase due to AGB stars and/or other Galactic sources. The range of abundances on the plateau (where at least a part of the spread is due to errors in the determinations) has a reasonable though not brilliant overlap with the range of baryonic densities deduced from deuterium, but is a factor of 2 or 3 lower than expected from the baryon density favoured by the microwave background data. The true primordial lithium abundance is most unlikely to be lower than the lower bound of the plateau at $12 + \log(\text{Li/H}) = 2.0$, because these stars are evidently formed from material that had undergone only minute amounts of processing from stellar nucleosynthesis. It will be higher if depletion is a significant factor, which it is likely to be as a result of atomic diffusion under gravity and other forces, turbulent transport and/or meridional circulation, even though the surface convection zone is too shallow to cause direct mixing with temperatures where lithium is burned.

Constraints on the degree of surface depletion of ^{7}Li along the plateau are provided by (i) the relative smoothness of the plateau revealed by more recent
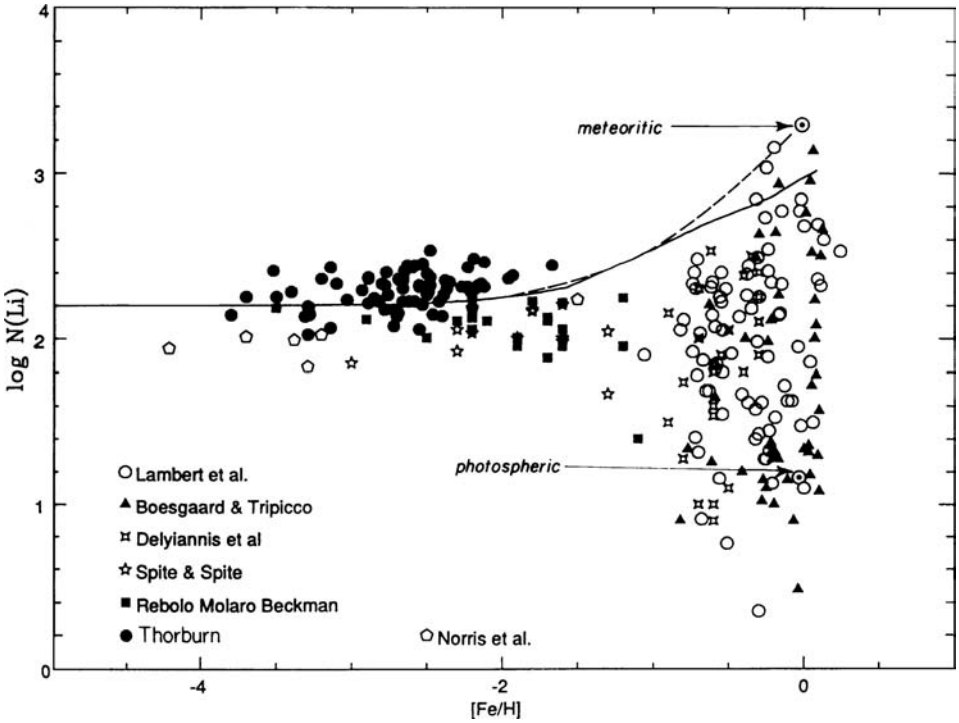
Fig. 4.12. Stellar lithium abundances (log of the number per 10^{12} H atoms) among main-sequence stars as a function of metallicity. The full-drawn curve shows the prediction of a numerical Galactic chemical evolution model, while the broken-line curve gives the sum of a primordial component and an additional component proportional to iron and normalized to meteoritic abundance. Adapted from Matteucci, D'Antona and Timmes (1995).

measurements; and (ii) the detection of a small amount (about 5 per cent) of ^{6}Li in several stars near the turn-off from the main sequence (Fig. 4.13). ^{6}Li is not produced in observable amounts by BBNS, and its main source in the Galaxy (e.g. in meteorites where ^{7}Li/^{6}Li = 12) is believed to be spallation of CNO nuclei and $\alpha - \alpha$ fusion reactions at high energies either from cosmic rays in the interstellar medium or from effects of particle acceleration in supernova remnants, stellar flares or elsewhere. Such processes might be expected to produce ^{6}Li along with beryllium (which is known to be present) in the young Galaxy, resulting in an abundance increasing roughly in proportion to metallicity. Strangely, the behaviour of ^{6}Li at low metallicities is more suggestive of a plateau, around $1\frac{1}{2}$ orders of magnitude below that of ^{7}Li (see Chapter 9); possible sources could be $\alpha - \alpha$ fusion in pre- or intergalactic cosmic rays, accelerated, e.g., by Population III stars postulated to explain the re-ionization of the Universe at high redshifts (Montmerle 1977), or non-thermal processes some time after BBNS (Jedamzik 2004). ^{6}Li is
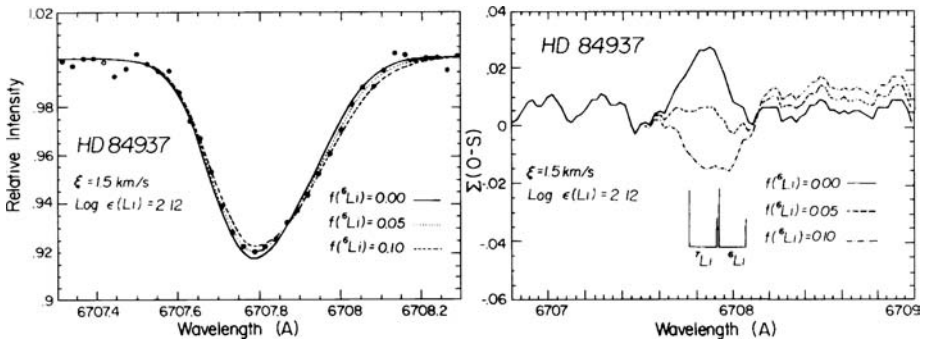
Fig. 4.13. Evidence for the presence of 5 ± 2 per cent ^{6}Li in the warm halo subdwarf HD 84937 with [Fe/H] = -2.4, T_{eff} = 6090 K. The left panel shows synthesized profiles for 0, 5 and 10 per cent ^{6}Li with the observational points on an absolute wavelength scale in the rest frame of the stellar photosphere. The right panel shows the central wavelengths of the doublets of each isotope and a deviation plot for the three hypotheses on ^{6}Li/^{7}Li. Adapted from Smith, Lambert and Nissen (1993).

a more fragile nucleus than ^{7}Li, so that in standard stellar models it is predicted (and it is also found) to be completely absent in the cooler subdwarfs on the ^{7}Li plateau, but it could survive at effective temperatures above 6000 K (close to the turn-off from the main sequence in Population II), and slightly lower temperatures along the subgiant branch. The finding of evidence (see Fig. 4.13) for about 5 per cent ^{6}Li in such stars (an observational tour de force) is evidence that the standard models are indeed approximately correct; here evidently ^{6}Li has been depleted by only a modest factor and it then follows that ^{7}Li is not depleted by much, although the exact factor corresponding to 'not much' is quite model-dependent.

The discrepancy of about a factor of 3 between the reported ^{7}Li abundance on the Spite plateau, extrapolated to zero metallicity, and the prediction from cosmological parameters deduced from the microwave background currently constitutes the most serious area of disagreement among primordial abundance estimates, leading to a number of studies of the prospects that the gap might be bridged by surface depletion combined with the possibility of a slight underestimate due to stellar atmosphere effects (e.g. the T_{eff} scale). In particular, while some models lead to a stratified structure with distinct exclusion zones depending on the temperature needed for destruction and there is a fine line between complete and little destruction, meridional circulation leads to less drastic differences where, for example, ^{6}Li might be depleted by a factor of 3 when ^{7}Li is depleted by 0.2 dex (Pinsonneault *et al.* 1999). Models with atomic diffusion combined with a modest amount of turbulent mixing may predict almost equal depletion factors for both isotopes, and a smooth ^{7}Li plateau against effective temperature and metallicity, combined

with depletion by a factor of 2 or so (Richard, Michaud & Richer 2005). Korn *et al.* (2006) have found striking support for this kind of model from trends in Fe and Li abundances along the turn-off, subgiant and giant branches of the globular cluster NGC 6397. Both elements are mildly depleted at the turn-off (where $A_{Li} = 2.35$), in accordance with expectations from diffusion; then with evolution up the subgiant and giant branches and the advent of turbulent mixing, the iron recovers its 'natural' abundance while lithium steeply declines. Thus the discrepancy with cosmological prediction may have a purely astrophysical explanation.

4.9 Conclusions

SBBN theory has been remarkably successful and does not seem to be in need of any modification except just possibly in the case of ^{7}Li. The limits that it sets on baryonic density are most robust in the case of deuterium $(2 < 10^5 D/H < 4)$ implying

$$4.5 \leq \eta_{10} \leq 7, \quad \text{or} \quad 0.015 \leq \Omega_{b0}h^2 \leq 0.025, \quad \text{or} \quad 0.03 \leq \Omega_{b0} \leq 0.05. \quad (4.55)$$

This agrees very well with the result from WMAP

$$\Omega_{b0}h^2 = 0.0223 \pm 0.0009 \quad (4.56)$$

(Spergel *et al.* 2007), but greatly exceeds the smoothed-out cosmological density of luminous matter deduced from galaxy redshift surveys, which give a luminosity density in blue light

$$l_B \simeq 2 \times 10^8 h L_{B\odot} \text{ Mpc}^{-3}, \quad (4.57)$$

where $L_{B\odot}$ is the blue-light luminosity of the Sun, which can be combined with an expression for the critical density in solar units

$$\rho_{crit,0} = 2.8 \times 10^{11} h^2 M_\odot \text{ Mpc}^{-3} \quad (4.58)$$

to relate Ω_{lum} to a typical mass:light ratio (in solar units)

$$\langle M_{lum}/L_B \rangle = 1500 h \Omega_{lum}. \quad (4.59)$$

A typical mass:light ratio of 5 solar units for stars and detected gas in galaxies thus contributes only $\Omega_{lum} = 0.003h^{-1}$ to the smoothed-out mass density, corresponding to $\eta_{10} \leq 1$.

The existence of dark matter (either baryonic or non-baryonic) is inferred from its gravitational effects on galactic rotation curves, the velocity dispersions and hydrostatic equilibrium of hot (X-ray) gas in clusters and groups of galaxies, gravitational lensing and departures from the smooth Hubble flow described by Eq. (4.1). This dark matter resides at least partly in the halos of galaxies such as our

own, and there may be other dark matter that is more smoothly distributed, e.g. as tenuous intergalactic gas, and thus less easy to detect unambiguously. That this is a likely candidate is strongly suggested by the statistics of the Lyman-α forest at redshifts between about 2 and 4, since these imply an association with enough ionized gas to supply an Ω_b of the order implied by primordial deuterium or by WMAP. Galactic halos contribute $\Omega_{halos} \simeq 0.014h^{-1}$ but need not be mainly baryonic; counts of micro-lensing objects on lines of sight towards the Magellanic Clouds reveal some dark objects with masses somewhere between about 0.1 and 1 times that of the Sun ('MACHOs') which would be baryonic, but apparently not abundant enough to account for the mass of the Galactic dark halo. Some baryonic dark matter could also be in cold molecular gas or in black holes. The question of the nature (and chemical composition) of baryonic dark matter, raised by considerations of BBNS, is an on-going concern which will be discussed further in Chapter 12.

Similarly, dynamical evidence from clusters of galaxies, supported by the WMAP data, that Ω_m (representing all matter) is about 0.24, combined with the BBNS arguments, gives a strong indication for the existence of non-baryonic dark matter (NDM). NDM is also invoked in theories of structure and galaxy formation from the gravitational effects of very small density perturbations in the early Universe; a popular candidate for this is 'cold dark matter', i.e. some kind of particles which decoupled from radiation very early on and have been cooling non-relativistically ever since. These could be weakly interacting massive particles ('WIMPS') or very tiny particles known as axions. Massive neutrinos ('hot dark matter') add a minor contribution. BBNS considerations are a strong spur, though not the only one, to active laboratory searches for these exotic particles.

Notes to Chapter 4

Excellent descriptions of BBNS theory are given in the classic text:

S. Weinberg, *Gravitation and Cosmology*, Wiley 1972, in

E. W. Kolb and M. S. Turner, *The Early Universe*, Addison-Wesley Press 1990, and in the comprehensive introduction to modern cosmology

John A. Peacock, *Cosmological Physics*, Cambridge University Press 1999.

S. Sarkar, in *Rep. Prog. Phys.*, **59**, 1493, 1996, gives a detailed discussion of Big Bang nucleosynthesis and physics beyond the Standard Model.

H. Reeves, in F. Sánchez, M. Collados and R. Rebolo (eds.), *Observational and Physical Cosmology*, Cambridge University Press 1990, p. 73, includes a description of the physics of the quark–hadron phase transition.

The nuclear reaction rates and their uncertainties (at the time) are described in detail by

M. S. Smith, L. H. Kawano and R. A. Malaney, *Astrophys. J. Suppl.*, **85**, 219, 1993, and more recently by

P. Descouvemont, A. Adahchour, C. Angulo, A. Coc and E. Vangioni-Flam, *At. Data and Nuclear Data Tables*, **88**, 203, 2004.

Observational data and their interpretation have been reviewed many times, notably by

A. Boesgaard and G. Steigman, *Ann. Rev. Astr. Astrophys.*, **23**, 319, 1985;

C. J. Copi, D. N. Schramm and M. S. Turner, *Science*, **267**, 192, 1995;

P. Crane (ed.), *The Light Element Abundances*, Springer-Verlag 1995;

A. Coc, E. Vangioni-Flam, P. Descouvement, A. Adahchour and C. Angulo, *Astrophys. J.*, **600**, 544, 2004;

G. Steigman, *Int. J. Mod. Phys. E*, **15**, 1, 2006; and

B. D. Fields and S. Sarkar, *Rev. Part. Phys.*, **33**, 1, 2006.

More detailed discussions of dark matter can be found in:

V. Trimble, *Ann. Rev. Astr. Astrophys.*, **25**, 425, 1987; in

D. Lynden-Bell and G. Gilmore (eds.), *Baryonic Dark Matter*, Kluwer, Dordrecht, 1990, and in Sarkar (1996).

The formation of galaxies and large-scale structure according to the Cold Dark Matter theory is described by

G. R. Blumenthal, S. M. Faber, J. L. Primack and M. J. Rees, *Nature*, **311**, 517, 1984.

Problems

1. Derive Eq. (4.9) by considering a unit mass at the surface of an expanding sphere of uniform density and radius $R(t)$ using Newton's laws supplemented by a repulsive force per unit mass $\Lambda R/3$ and taking kc^2 as an integration constant which can be identified with $-2 \times$ the total energy per unit mass in the case when $\Lambda = 0$.

2. Estimate the present-day temperature of a population of WIMPS that decoupled from radiation at a temperature corresponding to their rest-mass of, say, 100 GeV and subsequently cooled like an adiabatic monatomic gas. ($1\,\text{GeV} \equiv 1.16 \times 10^{13}\,\text{K}$.)

3. Assuming $\eta = 3 \times 10^{-10}$, $T_{\gamma 0} = 2.73\,\text{K}$, use Saha's equation to find the redshift where hydrogen is 1 per cent ionized, corresponding to the epoch of last scattering. (The photon density is $20.3\,T^3\,\text{cm}^{-3}$, the quantum concentration for electrons is $2.42 \times 10^{15}\,T^{3/2}\,\text{cm}^{-3}$ and the ionization potential is 13.6 eV.) Assess the validity of assuming Saha's equation given that the recombination coefficient is of the order of $10^{-12}\,\text{cm}^3\,\text{s}^{-1}$.

4. Find the redshift of the epoch of mass–density equality between radiation and matter, assuming (a) $\Omega_m = 1$ (i.e. $\rho_0 = 1.88h^2 \times 10^{-29}$ gm cm^{-3}); (b) $\Omega_m = 0.1$. Compare with the redshift deduced in the previous example for the last scattering of the microwave background. The energy density of radiation is $7.56 \times 10^{-15} T^4$ erg cm^{-3}, which should be increased by a factor of up to 1.68 to allow for 3 species of effectively massless neutrinos at a temperature of a few tenths of 1 eV ($g_* = 3.36$ in Eq. 4.22).

5. Assuming a baryon:photon ratio $\eta = 3.16 \times 10^{-10}$ and a neutron:proton ratio $n/p = 0.15$, use Saha's equation (2.48) to calculate the D/H ratio in thermal equilibrium at temperatures of 10^9 and 2×10^9 K respectively, using the following information:

Neutron mass excess	8.071 44 MeV	neutron spin 1/2
H atom mass excess	7.288 99 MeV	proton spin 1/2
D atom mass excess	13.135 91 MeV	deuteron spin 1

$kT = 0.0862 \, T_9$ MeV, where T_9 is the temperature in units of 10^9 K; photon number density is $2.4\pi^{-2}(kT/\hbar c)^3 = 2.0 \times 10^{28} \, T_9^3$ cm^{-3}. The quantum concentration for protons is $(2\pi m_p kT/h^2)^{3/2} = 5.94 \times 10^{33} \, T_9^{3/2}$ cm^{-3}.

Compare your answers with the graph in Fig. 4.2.

6. Given a value of η such that $Y_P = 0.24$ for 3 kinds of light neutrinos, find the corresponding value of Y_P for 4 kinds.

7. If the He/H ratio by number of atoms (e.g. as found from emission-line ratios) is y, show that

$$Y = \frac{4y(1-Z)}{1+4y}. \tag{4.60}$$

8. From Eq. (4.9), show that the contribution of the cosmological constant (aka 'dark energy') to the total energy density, in units of the critical density, is $\Omega_\Lambda = \Lambda/3H^2$. Deduce the value of Λ (in s^{-2}) if $\Omega_\Lambda = h = 0.7$ today.

5

Outline of stellar structure and evolution

Fred Hoyle: Basically speaking a star is a pretty simple structure.
R. O. Redman: Fred, *you*'d look pretty simple at a distance of 10 parsecs!
Overheard at Cambridge Observatory Club *c*. 1954.

5.1 Introduction

A star is a ball of gas held in static or quasi-static equilibrium by the balance between gravity and a pressure gradient. The pressure can in general be supplied by one or more of a hot perfect ionized gas, radiation and a degenerate electron (or neutron) gas, depending on circumstances. For main-sequence stars like the Sun, nuclear reactions maintain stability over long periods and the pressure is predominantly that of a classical gas at water-like densities. For much larger masses (above about $100\,M_\odot$), radiation pressure leads to instabilities, while for much smaller masses (below about $0.08\,M_\odot$) the central temperature never becomes high enough to ignite hydrogen and the star slowly contracts releasing gravitational energy until halted by degeneracy pressure at densities $\sim 10^3\,\mathrm{gm\,cm^{-3}}$; such stars are called 'brown dwarfs'. Below about $10^{-3}\,M_\odot$ (the mass of Jupiter), ordinary solid-state forces take over from electron degeneracy pressure in supporting the body against gravity at water-like densities, giving a planet rather than a star. The formation of stars is a complicated process, many aspects of which are still poorly understood although it is observed to happen in dense, dusty molecular clouds. A basic concept is the Jeans instability in a uniform medium: gravitational collapse occurs on length scales $\lambda \geq \lambda_J$ (the 'Jeans length') such that the propagation time for pressure waves λ/c_s exceeds the free-fall time $(G\rho)^{-1/2}$, where c_s is the sound speed and ρ the density. Alternatively one may apply the Virial Theorem (Eq. 5.14 below with $\gamma = 5/3$) to a spherical gas cloud on the verge of collapse. This leads to a critical 'Jeans mass'

$$M_J \sim \left(\frac{\pi kT}{G\mu m_H}\right)^{3/2} \rho^{-1/2} \sim 1000\,M_\odot \left(\frac{T}{10\,\mathrm{K}}\right)^{3/2} \left(\frac{\rho}{10^{-24}\,\mathrm{gm\,cm^{-3}}}\right)^{-1/2},$$

(5.1)

where μ is the mean molecular weight and m_H the mass of a hydrogen atom. Fred Hoyle noted in 1953 that the inverse dependence on density leads to the possibility of successive fragmentation in a collapsing cloud, as long as it can cool fast enough to remain isothermal by radiating away the gravitational energy released or consuming it in dissociation and ionization. Eventually a minimum fragment mass is formed that is optically thick and no longer able to cool within its collapse timescale (Hoyle 1953; Lynden-Bell 1973; Low & Lynden-Bell 1976; Rees 1976); this minimum stellar mass is estimated to be somewhere in the neighbourhood of 0.01 $M_\odot$.

However, collapse is resisted by magnetic fields, rotation and turbulence. For sufficiently high density or mass, the magnetic resistance may be overcome by gravity, or it may be circumvented more slowly by the process of ambipolar diffusion in which neutral molecules slip through the ions that are coupled to the magnetic field. Millimetre wavelength observations of molecular clouds show that most stars are formed in transient clusters in dense cloud cores with masses ranging from about 1000 to 1 $M_\odot$, e.g. the Trapezium cluster in Orion. This has a density of about 5×10^4 stars pc^{-3} or 4×10^{-18} gm cm^{-3}. Such clusters generally have a short lifetime because most of the mass of the cloud core is still in the form of gas which is blown away rapidly (compared to the crossing-time) by radiation and winds from massive stars shortly after their formation. The resulting mass loss causes disruption of the cluster and dispersal of its constituent stars into a stellar association; if the efficiency of star formation is high, however, with less gas remaining to be lost, then a bound cluster can form. Such clusters, known as galactic or open clusters, are common in the Milky Way. Globular clusters, which formed in our own Galaxy predominantly in the remote past, but may still be forming in other systems such as the Magellanic Clouds, have larger masses of the order of 10^5 or 10^6 $M_\odot$.

Before a gas cloud can reach densities remotely approaching stellar values, later settling into the more or less spherical configuration that is assumed to exist for most of its life, it has to lose angular momentum. In the early stages there is a disk-like configuration and the material of the disk loses angular momentum, transferring it outwards by dissipative processes. It is gradually accreted on to the central star, while presumably somewhere along the line and in at least some cases, planets are formed at locations within the disk. It appears that magnetic fields play an essential role in the process, linking the rotating star to the disk and to material expelled from the star in the form of winds and bipolar molecular outflows or jets, collimated along the rotation axis by the magnetic field. As the star grows in mass, it eventually reaches a point where residual circumstellar material is either exhausted or blown away, the proto-star emerges from its dusty cocoon and settles down into a state of quasi-static gravitational contraction; such stars are seen as variables with emission lines in their spectra known as T Tauri stars and related

classes. The jets often impinge on nearby clouds of material and shock-excite them producing emission-line spectra of so-called Herbig–Haro objects.

Terrestrial planets form by accretion of solid materials in the accreting disk, while 'gas giants' like Jupiter and the extra-solar planets discovered in the late 1990s and early 2000s may start in a similar process, thereafter capturing ambient gaseous material, or they may result from gravitational instabilities in the disk. Planets are thus distinguished from stars by their mode of formation as well as by their mass.

5.2 Timescales and basic equations of stellar structure

5.2.1 Timescales

Three timescales are of importance in stellar evolution:

- Dynamical timescale

$$\tau_{\text{dyn}} \simeq (G\overline{\rho})^{-1/2} \simeq 1\,\text{hour for the Sun}, \tag{5.2}$$

where $\overline{\rho}$ is the mean density. This is associated with gravitational collapse or radial pulsation.

- Thermal or Kelvin–Helmholtz timescale

$$\tau_{\text{th}} \simeq \frac{GM^2}{RL} \simeq 10^7\,\text{yr for the Sun}, \tag{5.3}$$

where R is the radius and L the luminosity. This is the timescale for quasi-static gravitational contraction and for changes in the interior to propagate outwards to the surface.

- Nuclear timescale

$$\tau_{\text{nuc}} \simeq \frac{0.007q\,X M c^2}{L} \simeq 10^{10}\,\text{yr for the Sun}, \tag{5.4}$$

where q is the fraction of the mass (about 10 per cent) occupied by the helium core when the star leaves the main sequence.

Usually

$$\tau_{\text{dyn}} \ll \tau_{\text{th}} \ll \tau_{\text{nuc}} \tag{5.5}$$

and the star is effectively in hydrostatic equilibrium. Under somewhat less general conditions, the star is also in thermal equilibrium, i.e. the rate of nuclear energy generation in central regions is equal to the luminosity at the surface. When a departure from thermal equilibrium occurs, equilibrium is restored by expansion or contraction on the thermal timescale.

5.2.2 Hydrostatic equilibrium

The equation of hydrostatic equilibrium is

$$\frac{dP}{dr} = -\frac{Gm(r)\rho(r)}{r^2}. \tag{5.6}$$

Using the self-evident relation (in spherical symmetry)

$$\frac{dm}{dr} = 4\pi r^2 \rho(r), \tag{5.7}$$

this can be written as

$$\frac{dP}{dm} = -\frac{Gm}{4\pi r^4}. \tag{5.8}$$

It is often convenient to treat all the internal variables as functions of the included mass $m(r)$, rather than of r itself.

From Eq. (5.8), one can get an estimate of the internal pressure of the Sun (mass $M_\odot = 2 \times 10^{33}$ gm; radius $R_\odot = 7 \times 10^{10}$ cm):

$$P_c \simeq P_c - Ps = -\int \frac{dP}{dm}dm > \frac{GM^2}{8\pi R^4} = 4 \times 10^{14} \text{ cgs or } 4 \times 10^8 \text{ atm.} \tag{5.9}$$

5.2.3 Virial Theorem

Writing Eq. (5.8) in the form

$$4\pi r^3 dP = -\frac{Gm\,dm}{r} \tag{5.10}$$

and integrating over the star using V to denote the included volume,

$$3\int_c^s V\,dP = -\int \frac{Gm\,dm}{r} = \Omega, \tag{5.11}$$

the total gravitational potential energy. Integrating by parts,

$$3[PV]_c^s - 3\int_0^{V_s} P\,dV = \Omega. \tag{5.12}$$

The first term on the left of Eq. (5.12) vanishes in the absence of external pressure, which leads to the Virial Theorem

$$3\int_0^M \left(\frac{P}{\rho}\right)dm + \Omega = 0, \tag{5.13}$$

which is the same as

$$3(\gamma - 1)U + \Omega = 0, \tag{5.14}$$

where U is the total internal energy and γ the ratio of specific heats (assumed uniform). For a perfect gas, neglecting radiation pressure,

$$P = nkT = \frac{\rho}{\mu m_H} kT, \tag{5.15}$$

and, for a fully ionized gas, $\gamma = 5/3$. Since (with density increasing inwards)

$$-\Omega > \frac{0.6\,GM^2}{R}, \tag{5.16}$$

Eq. (5.13) leads to

$$k\overline{T} \equiv \frac{\int kT\,dm}{M} > \frac{m_H}{5}\frac{\mu M}{R}, \tag{5.17}$$

which makes

$$\overline{T} > 5 \times 10^6\,\mu\text{K for the Sun.} \tag{5.18}$$

For a fully ionized gas,

$$\frac{1}{\mu} = 2X + \frac{3}{4}Y + \frac{1}{2}Z = \frac{1}{2} + \frac{3}{2}X + \frac{1}{4}Y < 2, \tag{5.19}$$

so the mean temperature inside the Sun is more than 2.5×10^6 K.

In the absence of nuclear energy sources, a star contracts on a thermal timescale and radiates energy at the expense of gravitational potential energy. Since, by the Virial Theorem, the total energy

$$E = U + \Omega = -U(3\gamma - 4), \tag{5.20}$$

U, and hence the temperature, rises as the star contracts, as is also obvious from Eq. (5.17), as long as $\gamma > 4/3$. An ideal gaseous star has a negative specific heat and can't cool unless energy is supplied! With $\gamma = 5/3$, once the interior is fully ionized, half of the gravitational energy released by contraction goes into internal energy and the other half is lost from the surface. Once nuclear reactions have started, they act as a thermostat; contraction leads to an increase in energy generation which causes expansion and cooling, and vice versa, thereby ensuring stability.

5.2.4 Energy transport

There are three ways in which energy can be transported outwards in a star: radiative transfer, convection and conduction. The mean free path for radiation, $\lambda \equiv 1/\kappa\rho \simeq 1\,\text{cm}$, greatly exceeds that for conduction ($\lambda \ll 1\,\text{cm}$) except in degenerate material, so that radiative transfer dominates in those regions where the corresponding temperature gradient is stable to convection. The equation of

radiative transfer can be treated in the plane-parallel diffusion approximation that was applied to stellar atmospheres in Chapter 3. From Eqs. (3.14) to (3.17), the radiative luminosity $l(r)$ at radius r, mass coordinate $m(r)$, is given by

$$\frac{l(r)}{4\pi r^2} = 4\pi H = -\frac{4}{3}\frac{1}{\kappa\rho}\frac{d}{dr}(\sigma T^4), \tag{5.21}$$

or, using the energy density constant $a \equiv 4\sigma/c$,

$$l(r) = -\frac{4}{3}\pi ac\frac{r^2}{\kappa\rho}\frac{dT^4}{dr} \tag{5.22}$$

or

$$\frac{dT}{dm} = -\frac{3\kappa l}{64\pi^2 acr^4 T^3}. \tag{5.23}$$

Convection occurs if $|dT/dr|$ from Eq. (5.23) is so steep that a rising/falling piece of gas expanding/contracting adiabatically under the ambient pressure continues to move owing to buoyancy forces, i.e. if (for constant chemical composition)

$$\nabla \equiv \frac{d\log T}{d\log P} > \frac{\gamma - 1}{\gamma}. \tag{5.24}$$

At sufficiently high densities (e.g. cores of upper main-sequence stars), the $>$ sign virtually becomes an equality (adiabatic stratification), but at lower densities (e.g. envelopes of the Sun and cooler stars) an exact calculation is very difficult and in most models a crude approximation based on mixing-length theory is used. In a situation where the chemical composition changes with depth, Eq. (5.24) (known as the Schwarzschild criterion) needs to be replaced by more complicated considerations.

5.2.5 Opacity sources

The effective opacity is given by taking the wavelength-dependent opacity of the material at the relevant temperature and density and forming the (harmonic) Rosseland mean:

$$\frac{1}{\kappa} = \int \frac{1}{\kappa_\nu}\frac{dB_\nu}{dT}d\nu \bigg/ \int \frac{dB_\nu}{dT}d\nu. \tag{5.25}$$

This is a harmonic mean because it is really the mean free path that is relevant. At high temperatures ($> 10^5$ K), the main sources of opacity and approximate formulae for them (the first two originally due to H. Kramers) are:
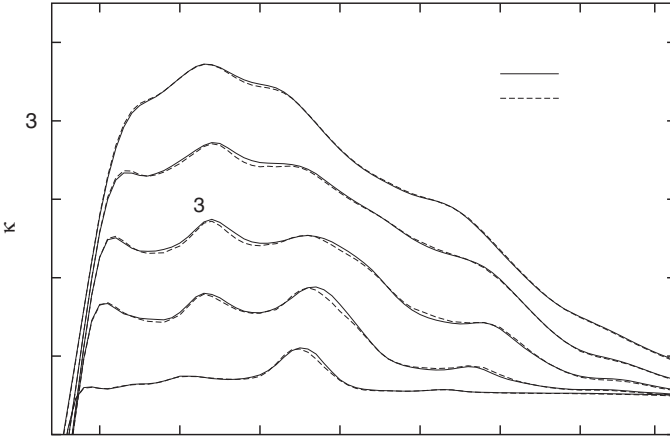
Fig. 5.1. Opacity of stellar material with $X = 0.7$, $Z = 0.02$ (roughly solar composition) as a function of temperature and the parameter $\log R$, where $R \equiv \rho/T_6^3$ is approximately constant throughout a main-sequence star, corresponding to a polytrope with $n = 3$ (see Appendix 4); e.g. at $1\,M_\odot$ $\log R$ varies from -1.5 at the centre to 0.0 in the envelope, while at $10\,M_\odot$ the corresponding range is from -3.5 to -4.0. (Density in units of $\mathrm{gm\,cm^{-3}}$, T_6 in units of $10^6\,\mathrm{K}$, opacity in units of $\mathrm{cm^2\,gm^{-1}}$.) 'OP' and 'OPAL' refer to two independent opacity calculation projects. After Badnell, Bautista, Butler *et al.* (2005).

- Bound–free transitions, due to photo-ionization of H-like ions of oxygen etc.:

$$\kappa_{\mathrm{BF}} \simeq k_1 \rho Z (1 + X) T^{-3.5}; \tag{5.26}$$

- Free–free transitions (inverse bremsstrahlung):

$$\kappa_{\mathrm{FF}} \simeq k_2 \rho (1 + X) T^{-3.5}; \quad \text{and} \tag{5.27}$$

- Thomson scattering from free electrons:

$$\kappa_{\mathrm{es}} = 0.2(1 + X) \ \mathrm{cm^2\,gm^{-1}}. \tag{5.28}$$

The $(1 + X)$ in all these expressions comes from the number of free electrons per atomic mass unit, usually expressed by the molecular weight per electron

$$\frac{1}{Y_e} \equiv \mu_e \simeq \frac{2}{1 + X}. \tag{5.29}$$

At the lower temperatures of stellar envelopes and atmospheres, neutral hydrogen, H^- and bound–bound transitions from absorption lines make a significant contribution and the above formulae do not apply (see Fig. 5.1). In the Sun, the opacity is of the order of $1\,\mathrm{cm^2\,gm^{-1}}$ in the photosphere and the deep interior, but

rises to a peak of the order of $10^4 \, \text{cm}^2 \, \text{gm}^{-1}$ at a temperature of about $30\,000 \, \text{K}$ in the outer envelope.

5.2.6 Energy generation

The final equation governing stellar structure is that for nuclear energy generation:

$$\frac{dl}{dm} = \epsilon - \epsilon_\nu - \left\{ \frac{\partial u}{\partial t} + P \frac{\partial}{\partial t} \left(\frac{1}{\rho} \right) \right\} \tag{5.30}$$

$$\simeq \epsilon - \epsilon_\nu - \frac{3}{2} \rho^{2/3} \frac{\partial}{\partial t} (P \rho^{-5/3}). \tag{5.31}$$

Here ϵ represents nuclear energy generation (corrected for neutrino losses arising in the nuclear reactions themselves), while ϵ_ν represents neutrino losses from plasma processes (chiefly $e^{\pm}$ pair production and annihilation) that take place anyway at sufficiently high densities and temperatures as a result of direct $e - \nu$ coupling via the weak interaction. Both neutrino sources act as a local energy sink because the neutrinos instantly escape from the star.[1] The last term, which is usually negligible except in gravitational contraction phases, represents changes in thermal energy and $P\,dV$ work. The second version of the equation applies to a perfect monatomic gas with no radiation pressure.

5.3 Homology transformation

The differential equations (5.7), (5.8), (5.21) and (5.30), together with the equation of state and suitable boundary conditions at the stellar centre ($l = r = m = 0$) and surface ($P_s \simeq T_s \simeq 0$), fix the structure of a star of given mass and homogeneous chemical composition in radiative equilibrium with negligible radiation pressure.[2] Over limited regions of parameter space, in which κ and ϵ can be represented by simple power laws, the structure of such stars is homologous, i.e. the dimensionless numbers $r(m)/R$, $l(m)/L$, $P(m)/P_c$ etc. become fixed functions of the dimensionless mass coordinate m/M. This in turn implies that the derivatives in the above equations can be replaced (apart from constants that remain the same at corresponding points in different stars) by P_c/M, T_c^4/M etc., and the equations used to estimate how global quantities such as luminosity and radius scale with the mass, mean molecular weight etc.

To begin with, we assume that the opacity scales as

$$\kappa = \kappa_0 \, \rho^r \, T^{-t}. \tag{5.32}$$

---

[1] Except in the dense collapsing core of a massive supernova.
[2] For an estimate of radiation pressure, see the description of Eddington's Standard Model in Appendix 4.

From radiative equilibrium, Eq. (5.23), and hydrostatic equilibrium with the ideal-gas equation of state Eq. (5.15),

$$T_c^{t+4} \propto \kappa_0 M^{r+1} L / R^{3r+4} \propto (\mu M / R)^{t+4}, \tag{5.33}$$

so that

$$L \propto \kappa_0^{-1} \mu^{t+4} M^{t-r+3} R^{3r-t} \tag{5.34}$$

$$\propto \kappa_0^{-1} \mu^4 M^3 \text{ (e.s.)} \quad \text{or} \quad \kappa_0^{-1} \mu^{15/2} M^{11/2} R^{-1/2} \text{ (Kramers).} \tag{5.35}$$

Thus, without having yet made any appeal to the law of energy generation, one has a mass–luminosity–radius relation. This is independent of the radius for electron-scattering (e.s.) opacity (which dominates for stellar masses greater than about $3 \, M_\odot$) and only slowly dependent on it for Kramers-type opacity. The system of equations is closed by the law of energy generation, which fixes the radius and hence the effective temperature. For hydrogen burning we assume (see Section 2.5)

$$L \propto \epsilon_0 M \rho \, T_c^\nu, \tag{5.36}$$

where $\nu \simeq 4$ for the proton–proton chain (dominating in low-mass stars $\leq 1.1 \, M_\odot$) and $\simeq 17$ for the CNO cycle (dominating in higher-mass stars and in later stages of evolution). Replacing T_c by $\mu M / R$, we have

$$L \propto \epsilon_0 \mu^\nu M^{\nu+2} / R^{\nu+3}. \tag{5.37}$$

L or M can then be eliminated from Eqs. (5.35) and (5.37), giving R, and hence $T_{\rm eff}$, as functions of M or L respectively. The general equations become rather messy at this point, so only two selected sets of numerical results will be given, both assuming energy generation by the CNO cycle with $\nu = 17$, Case (a) for Kramers opacity and Case (b) for electron scattering (Table 5.1).

The homology relations give a rough guide to the dependence of luminosity, effective temperature and main-sequence lifetime $\tau_{\rm ms}$ on the star's mass and chemical composition. The luminosity increases as a high power of the mass and mean molecular weight, which latter depends on the helium (or hydrogen) content according to

$$\mu = \frac{4}{3 + 5X - Z} \simeq \frac{4}{3 + 5X} \tag{5.38}$$

since $Z \leq 0.02$ (see Eq. 5.19). X typically varies from about 0.7 in Population I stars like the Sun to about 0.75 ($= 1 - Y_{\rm P}$) in Population II stars (e.g. metal-weak globular clusters), resulting in a change in μ from 0.62 to 0.59, i.e. a reduction of 5 per cent, which in itself leads to a reduction of about 30 per cent in the luminosity

Table 5.1. *Homology relations for main-sequence stars*

	Case (a) $r = 1, t = 3.5, \nu = 17$	Case (b) $r = t = 0, \nu = 17$	
$R(M) \propto$	$(\epsilon_0 \kappa_0)^{2/39} \mu^{19/39} M^{9/13}$	$(\epsilon_0 \kappa_0)^{1/20} \mu^{13/20} M^{4/5}$	
$L(M) \propto$	$\epsilon_0^{-1/39} \kappa_0^{-40/39} \mu^{283/39} M^{67/13}$	$\kappa_0^{-1} \mu^4 M^3$	$(\forall \nu)$
$M(L) \propto$	$\epsilon_0^{1/201} \kappa_0^{40/201} \mu^{-283/201} L^{13/67}$	$\kappa_0^{1/3} \mu^{-4/3} L^{1/3}$	$(\forall \nu)$
$\tau_{\mathrm{ms}}(M) \propto XM/L \propto$	$\epsilon_0^{0.026} \kappa_0^{1.026} \mu^{-7.26} X M^{-4.15}$	$\kappa_0 \mu^{-4} X M^{-2}$	$(\forall \nu)$
$\tau_{\mathrm{ms}}(L) \propto XM/L \propto$	$\epsilon_0^{0.005} \kappa_0^{0.20} \mu^{-1.41} X L^{-0.81}$	$\kappa_0^{1/3} \mu^{-4/3} X L^{-2/3} (\forall \nu)$	
$L \propto R^2 T_{\mathrm{eff}}^4 \propto$	$\epsilon_0^{0.15} \kappa_0^{0.52} \mu^{-1.33} T_{\mathrm{eff}}^{5.5}$	$\epsilon_0^{0.21} \kappa_0^{1.36} \mu^{-1.79} T_{\mathrm{eff}}^{8.6}$	

at a given mass. This, however, is more than compensated by the reduction in opacity, which is proportional to Z as long as bound–free processes dominate, i.e. as long as Z does not become too small. Thus the lifetime at a given mass is lower for Population II stars, but the lifetime at a given main-sequence luminosity is much less sensitive to chemical composition.

The last line of the table gives main-sequence relations in the HR diagram. The effect of decreasing metallicity is to lower the luminosity at a given T_{eff}, since $\kappa_0 \propto Z$ (if not too small) in Case (a) and ϵ_0 is so in Case (b). On the other hand, this is partly compensated by the aforementioned reduction in μ from the helium abundance, leading to a near-balance among Population I stars with metallicities differing by factors of a few. At very low metallicity ($< 0.1\,Z_\odot$ or so), κ_0 becomes constant from free–free processes and electron scattering, and μ likewise settles down to its minimum value, leading to a subdwarf main sequence that lies below the Population I main sequence (see Fig. 4.8), although stars at a given mass are actually more luminous than their Population I counterparts. Numerical results for main-sequence stars with different masses are given in Chapter 7.

5.4 Degeneracy, white dwarfs and neutron stars

5.4.1 Introduction

Examination of the Fermi–Dirac distribution function Eq. (2.41) shows that the condition for applicability of the ideal-gas distribution to electron velocities is

$$(m_e c^2 - \mu)/kT \gg 0, \tag{5.39}$$

whereas under the opposite condition,

$$(m_e c^2 - \mu)/kT \ll 0, \tag{5.40}$$

all possible momentum states are filled and electron energies are fixed by the Pauli Exclusion Principle rather than by the temperature; this is the state known as (complete) electron degeneracy. From Eq. (2.44) for the chemical potential, one can therefore define a degeneracy parameter

$$\psi \equiv \ln \frac{n_e}{2n_Q} = \ln \frac{1}{2} n_e \left(\frac{2\pi\hbar^2}{m_e kT} \right)^{3/2} = \ln \left(1.2 \times 10^{-4} \rho T_8^{-3/2} / \mu_e \right), \tag{5.41}$$

where T_8 is the temperature in units of 10^8 K. As a star consumes its hydrogen fuel in central regions, the core contracts, roughly following the homology law (see Eq. 5.17)

$$T \propto M^{2/3} \rho^{1/3}, \tag{5.42}$$

so that ψ tends to increase, roughly as $\frac{1}{2} \ln \rho$ or $\ln (T^{3/2}/M)$. Thus, at what stage degeneracy is actually reached depends mainly on the star's mass: high-mass stars may not reach it until the pre-supernova stage, whereas stars with mass of the order of 0.1 $M_\odot$ or less do so even before hydrogen-burning can set in. Stars with masses in the range 1 to 8 $M_\odot$ or so develop degenerate cores after leaving the main sequence; subsequent mass-loss episodes, especially along the AGB and in the planetary nebula stage, eventually leave this degenerate core exposed and it cools down and becomes a white dwarf.

5.4.2 Equations of state for degenerate matter

When thermal energy is negligible, cells in phase space are uniformly occupied up to the Fermi momentum p_F, given by

$$n_e = \int_0^{p_F} 8\pi p^2 dp / h^3, \quad \text{or} \quad p_F = h \left(3n_e/8\pi \right)^{1/3}. \tag{5.43}$$

For a non-relativistic electron gas ($p_F \ll m_e c$), the pressure is given by

$$P \simeq P_e = \frac{1}{3} n_e <pv> = \frac{1}{3} \frac{n_e}{m_e} <p^2> \tag{5.44}$$

$$= \frac{1}{5} \frac{n_e}{m_e} p_F^2 = \frac{1}{20} \frac{h^2}{m_e} \left(\frac{3}{\pi} \right)^{2/3} n_e^{5/3}. \tag{5.45}$$

Because at this stage the material has usually been processed into helium and heavier elements, electrons outnumber nuclei and make the dominant contribution to the pressure, the more so when their energy from degeneracy greatly exceeds kT; it is

the small electron mass that ensures that electrons become degenerate long before nucleons. The electron density is given by

$$n_e = \frac{\rho}{\mu_e m_H} = \frac{1}{2}(1 + X)\rho/m_H \rightarrow \frac{1}{2}\rho/m_H \quad (5.46)$$

(see Eq. 5.29), when $X \rightarrow 0$.

There is a critical density ρ_{crit} above which the electrons become relativistic, i.e.

$$p_F^2/2m_e = m_e c^2, \text{ or } p_F = m_e c \sqrt{2}, \quad (5.47)$$

whence

$$\rho_{crit} = \frac{8\pi}{3}\mu_e m_H (m_e c \sqrt{2}/h)^3 = \frac{6 \times 10^6}{1 + X} \text{ gm cm}^{-3}. \quad (5.48)$$

For fully relativistic degeneracy ($\rho \gg \rho_{crit}$), the pressure is given by

$$P = P_e = \frac{1}{3}n_e c <p> = \frac{hc}{8}(3/\pi)^{1/3} n_e^{4/3}. \quad (5.49)$$

In each case, the pressure is mainly fixed by the density and quite insensitive to temperature. A consequence of this is that, when a new nuclear reaction (e.g. helium-burning) sets in in degenerate material, the additional heat cannot be taken up (as it would be in an ideal gas) by expansion and there is a thermal runaway (Mestel 1952). The temperature rises very strongly until it becomes high enough for the degeneracy to be removed, and the star adjusts to a new structure with lower central density.

5.4.3 Structure of white dwarfs

Once again, using the idea of a homology transformation, we can approximate the hydrostatic equation (5.8) replacing dP/dm with P_c/M, leading to

$$P_c \simeq GM^{2/3}\overline{\rho}^{4/3}. \quad (5.50)$$

Expressing P_c in terms of $\overline{\rho}$ using the non-relativistic expression Eq. (5.45), together with Eq. (5.46),

$$M(\overline{\rho}) \simeq \left(\frac{2\hbar^2}{Gm_e}\right)^{3/2} (m_H \mu_e)^{-5/2}\overline{\rho}^{1/2} \quad (5.51)$$

$$\simeq 0.1\left(\frac{m_e c^2}{Gm_H\mu_e}\right)^{3/2} \rho_{crit}^{-1}\overline{\rho}^{1/2}. \quad (5.52)$$

This leads to a mass–density or mass–radius relation

$$R \propto M^{-1/3}\mu_e^{-5/3} \simeq \text{a few} \times 1000 \text{ km}. \quad (5.53)$$

White dwarfs are formed hot and gradually cool at nearly constant radius. With increasing mass, the star becomes squashed down until it is highly relativistic and very small.

In the fully relativistic case, Eqs. (5.50), (5.49) and (5.46) lead to a unique mass:

$$M_{Ch} \simeq \left(\frac{\hbar c}{G}\right)^{3/2} \left(\frac{\rho_c}{\rho}\right)^2 (\mu_e m_H)^{-2} \simeq \frac{2}{\mu_e^2} \left(\frac{\rho_c}{\rho}\right)^2 M_\odot. \tag{5.54}$$

This is the Chandrasekhar–Landau limiting mass for white dwarfs, whose actual value (derivable from the theory of polytropic stars; see Appendix 4) is

$$M_{Ch} = 5.8\, M_\odot / \mu_e^2 = 1.45\, M_\odot \tag{5.55}$$

for a He or CO white dwarf. A white dwarf cannot have a mass greater than this: larger masses either collapse into a neutron star or black hole, or become incinerated, which is the favoured mechanism for Type Ia supernovae.

An interesting feature of Eq. (5.54) is that it can be re-written

$$M_{Ch} \simeq \left(\frac{e^2}{\alpha G m_H^2}\right)^{3/2} m_H/\mu_e^2 = (\alpha_G \alpha)^{-3/2} m_H/\mu_e^2, \tag{5.56}$$

where α is the well-known fine-structure constant $1/137$ and α_G is the corresponding 'gravitational fine-structure constant' $G m_H^2/e^2 = 8.0 \times 10^{-37}$, where e is the electronic charge. The number of nucleons in the Chandrasekhar limiting mass is thus essentially the 3/2 power of the famous large cosmological numbers of order 2×10^{38} which fascinated Eddington and Dirac. Arguments can also be made that the number of nucleons in an ordinary main-sequence star, which avoids degeneracy by not being too small and also avoids disruption by radiation pressure by not being too large, must also be of this order, which is set by a few basic dimensionless physical constants (Carr & Rees 1979).

5.4.4 Neutron stars

The chemical potential of highly degenerate electrons is essentially equal to the Fermi energy $c p_F$, since virtually all levels below this are filled. At densities that are so high that the Fermi energy exceeds the mass–energy difference between protons and neutrons (i.e. $\rho > \sim 10^7 \mu_e$ gm cm^{-3} for a difference in binding energy of 1 MeV), the reaction

$$p + e^- \rightarrow n + \nu_e \tag{5.57}$$

goes forward to the right, i.e. electrons are crushed on to protons to make neutron-rich nuclei by inverse β-decays, e.g. in the collapsing core of a massive supernova. Equilibrium (which may be rapidly brought about at high densities by

pycnonuclear reactions) then favours increasingly neutron-rich nuclei, e.g. $^{118}_{36}\text{Kr}_{82}$ at a density of 4×10^{11} gm cm^{-3}. At this point, however, the binding energy for additional neutrons vanishes, so that at still higher densities there is a release of free neutrons (the effect known as neutron drip; see Fig. 6.9), which dominate when the density exceeds about 10^{13} gm cm^{-3}. The neutrons themselves become degenerate at densities exceeding 10^{15} gm cm^{-3} (a few times nuclear density), corresponding to a radius of about 10 km. Neutron stars have a maximum mass corresponding to the Chandrasekhar mass for white dwarfs and of the same order of magnitude, since Eq. (5.54) is independent of the mass of the degenerate particles and the replacement of $\mu_e = 2$ for white dwarfs by $\mu_n = 1$ for neutron stars is approximately compensated by General-Relativistic effects. However, the equation of state, and consequently the exact limiting mass, are uncertain because of uncertainties in the properties of such extreme nuclei and the possible formation of meson condensates, quark matter or other exotic phases. The limiting mass is believed to lie somewhere in the range of 2 to 3 $M_\odot$. Neutron stars are observed in the form of radio pulsars and of components of binary stellar X-ray sources, and are thought to be the typical remnants of at least a subset of massive supernovae energized by core collapse (Type II and related classes).

5.5 Hayashi effect

In cool stars ($T_{\text{eff}} \leq 6000$ K), neutral hydrogen becomes positively ionized below the photosphere, reducing the adiabatic gradient (from low γ) and increasing the radiative gradient through the growth of opacity (mainly from H$^-$ formed from the extra free electrons). Thus the surface convection zone becomes deep and the outer boundary condition grows more significant: the approximations of Section 5.3 ($P_s \simeq T_s \simeq 0$) are no longer adequate. At some effective temperature T_{H} the star is fully convective down to the centre and for $T_{\text{eff}} < T_{\text{H}}$ stars cannot have a stable structure. This effect is important both in pre-main-sequence contraction stages (see Fig. 5.2) and in post-main-sequence evolution, since it limits the region of the HR diagram that a star can traverse, independently of its nuclear history.

The Hayashi track (Hayashi 1961, 1966) is the locus of fully convective stars in the HR diagram, dependent on the mass, luminosity and chemical composition. However, it is mainly the surface properties – luminosity and radius or luminosity and effective temperature – that govern the entire stellar structure by fixing the adiabatic constant. A sketch derivation of its properties is the following.

Throughout the star, there is a single adiabat:

$$P = K\rho^{5/3} \propto K^{-3/2} T^{5/2}. \tag{5.58}$$
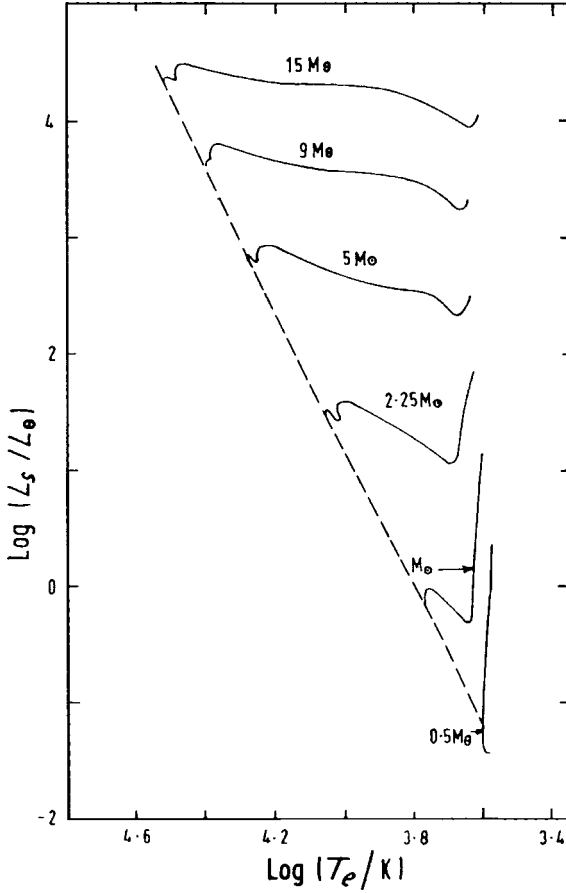
Fig. 5.2. Pre-main-sequence contraction of stars with different masses. Adapted from Iben (1965).

In the interior, we can apply the global version of the hydrostatic equation (5.8)

$$P_{\text{int}} \propto M^2/R^4, \tag{5.59}$$

which relates the adiabatic constant to the mass and radius:

$$K \propto \frac{M^2}{R^4} \left(\frac{M}{R^3}\right)^{-5/3} \propto M^{1/3} R, \tag{5.60}$$

whence throughout the star (and in particular at the surface where $T = T_{\text{eff}}$)

$$P \propto M^{-1/2} R^{-3/2} T^{5/2}. \tag{5.61}$$

At the surface, there is another (local) hydrostatic condition:

$$dP = -g\rho dz \quad \text{and} \quad d\tau = -\kappa\rho dz, \tag{5.62}$$

whence

$$\frac{dP}{d\tau} = \frac{g}{\kappa},\tag{5.63}$$

or

$$P_{\rm ph} \simeq \frac{g}{\kappa} \propto \frac{M}{R^2} P_{\rm ph}^{-a} T_{\rm eff}^{-b},\tag{5.64}$$

say, where $a \simeq 1$ and $b \simeq 3$ (mainly from H$^-$ supplied by electrons from H$^+$) and we have taken $\tau \sim 1$. Equating (5.61) with $T = T_{\rm eff}$ to (5.64) and replacing R by $L^{1/2}/T_{\rm eff}^2$, one finally obtains

$$T_{\rm eff} \propto M^{\frac{a+3}{11a+2b+3}} L^{\frac{3a-1}{22a+4b+6}} \quad\text{or}\quad M^{0.2} L^{0.05},\tag{5.65}$$

which leads to an almost vertical line in the HR diagram with $T_{\rm eff} \sim 4000\,$K for solar metallicity (Fig. 5.2).

A proto-star resulting from condensation of a fragmented gas cloud thus first reaches quasi-hydrostatic equilibrium somewhere on the Hayashi track, along which it then contracts gravitationally at nearly constant effective temperature on the thermal timescale, Eq. (5.3). Meanwhile its internal temperature increases in accordance with the Virial Theorem and minor nuclear reactions like deuterium burning are ignited, but have little effect (apart from destruction of D and of ^{6}Li and ^{7}Li in cooler stars) because the relevant abundances are so low. Eventually, the interior ceases to be convective and the star then contracts radiatively, with its luminosity slightly rising again in accordance with the homology relation (5.35), until hydrogen-burning is ignited at the centre; this halts further contraction and the star is now on the zero-age main sequence (ZAMS).

5.6 Hydrogen-burning

5.6.1 pp chains and solar neutrinos

The first major set of nuclear reactions in stellar evolution involves hydrogen-burning through the *pp* chains and the CN cycle or CNO bi-cycle, which liberate 6.68 MeV of energy per proton minus neutrino losses (2 neutrinos are emitted for each ^{4}He nucleus synthesized). The first two reactions of the *pp* chains are

$$^1{\rm H} + {}^1{\rm H} \rightarrow {}^2{\rm D} + e^+ + \nu + 0.16\,{\rm MeV},\tag{5.66}$$
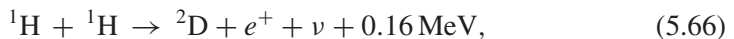
with a further 1.02 MeV released by annihilation of the positron; and

$$^2{\rm D} + {}^1{\rm H} \rightarrow {}^3{\rm He} + \gamma\ (5.49\,{\rm MeV}).\tag{5.67}$$

Reaction (5.66) involves the weak interaction through the β^+-decay and is accordingly exceedingly slow. The condition for an allowed decay is that the two

leptons (e^+ and ν) are emitted with zero orbital angular momentum ℓ and with spins that are either parallel (Gamow–Teller transition) or anti-parallel (Fermi transition). Since the nucleons in the ^{2}D nucleus have $\ell = 0$, and ℓ is unchanged by the allowed β-decay, the same applies to the protons, which thus have to scatter in an s-wave and have opposite spins by virtue of the Pauli Exclusion Principle. However, the deuteron spin is 1, so the proton that decays into a neutron has to flip its spin and the balancing spin is carried off by the two leptons. Their spins then have to be parallel, making this a pure Gamow–Teller transition, and the cross-section thus depends on the GT axial vector coupling constant C_A (deduced from laboratory measurements of related free decays of neutrons, ^{3}H and ^{6}He) as well as on spin and spatial matrix elements and phase-space and barrier-penetration factors. The cross-section at $E_p(\text{lab}) = 1\,\text{MeV}$ is only $10^{-47}\,\text{cm}^2$, far too small to be measured directly. The calculated value of $S(E_0')$ in the interior of the Sun is about $5 \times 10^{-22}\,\text{keV barn}$, so that from Eq. (2.60) with $\tau = 13.7$ the rate coefficient is

$$\langle \sigma v \rangle \simeq 7.6 \times 10^{-44}\,\text{cm}^3\,\text{s}^{-1}. \tag{5.68}$$

At a density of $150\,\text{gm cm}^{-3}$ and $X \simeq 0.5$, typical of the centre of the Sun, i.e. $n_p = 6 \times 10^{25}\,\text{cm}^{-3}$, this leads to a hydrogen-burning lifetime

$$\tau_{pp} = (n_p \langle \sigma v \rangle)^{-1} \simeq 10^{10}\,\text{yr}. \tag{5.69}$$

The remaining reactions are much faster, e.g. the time for (5.67) is only 1.6 s, leading to a steady-state D/H ratio of the order of 10^{-17}.

After reaction (5.67), there are two alternatives: 86 per cent of the time (in the case of the Sun), there is the final link of the $pp - 1$ chain

$$^3\text{He} + {}^3\text{He} \rightarrow {}^4\text{He} + 2{}^1\text{H} + 12.86\,\text{MeV}, \tag{5.70}$$
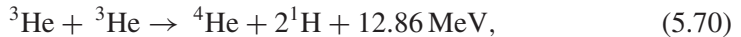
which gives a steady-state ^{3}He/H ratio $\sim 10^{-5}$ at the centre, although a larger ^{3}He abundance is built up some way out. The remainder of the time one has the $pp - 2$ and $pp - 3$ chains summarized in Table 5.2, with associated neutrino losses.

In recent years, the energetic neutrinos from $pp - 3$, and the less energetic neutrinos from other reactions in the chains (see Fig. 5.3), have been detected in direct experiments using either inverse β-decays in chlorine or gallium or Cherenkov radiation in water, but with somewhat lower fluxes than predicted (Table 5.3). The reason for the discrepancy (aka the 'solar neutrino problem') has long been suspected to lie neither in the solar model nor in nuclear reaction rates, but in neutrino physics: neutrinos, having a small but non-zero rest-mass, undergo flavour oscillations between ν_e and ν_μ, say, as a result of the mass eigenstates being different from the flavour eigenstates.

Table 5.2. *Reactions of the pp chains*

| $p(p, e^+ \nu)d$ |
| $d(p, \gamma)^3\mathrm{He}$ |

$^3\mathrm{He}(^3\mathrm{He},2p)^4\mathrm{He}$		$^3\mathrm{He}(\alpha, \gamma)^7\mathrm{Be}$	
	$^7\mathrm{Be}(e^-, \nu)^7\mathrm{Li}$		$^7\mathrm{Be}(p, \gamma)^8\mathrm{B}$
	$^7\mathrm{Li}(p, \alpha)^4\mathrm{He}$		$^8\mathrm{B}(e^+, \nu)^8\mathrm{Be}^*$
			$^8\mathrm{Be}^*(\alpha)^4\mathrm{He}$
$pp-1$ (86%)	$pp-2$ (14%)		$pp-3$ (0.02%)
$Q_{\mathrm{eff}} = 26.20\,\mathrm{MeV}$	$Q_{\mathrm{eff}} = 25.66\,\mathrm{MeV}$		$Q_{\mathrm{eff}} = 19.17\,\mathrm{MeV}$
(2.0% loss)	(4.0% loss)		(28.3% loss)

Data from Rolfs and Rodney (1988).
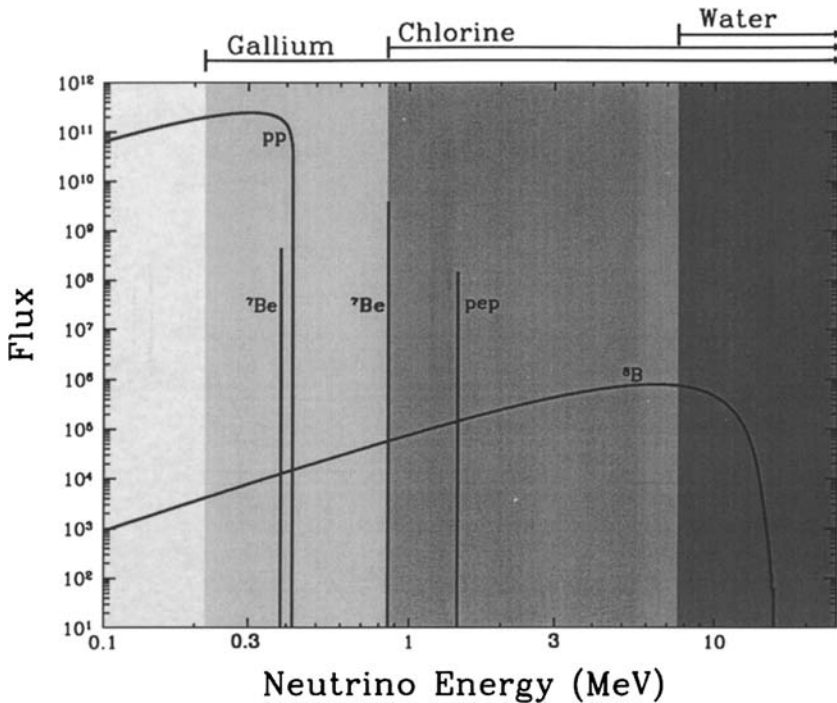
Fig. 5.3. Energy spectrum of solar neutrinos predicted from a standard solar model (e.g. Bahcall *et al*. 1982), omitting the undetectably small flux due to the CNO cycle. Fluxes are in units of $\mathrm{cm}^{-2}\,\mathrm{s}^{-1}\,\mathrm{MeV}^{-1}$ for continuum sources and $\mathrm{cm}^{-2}\,\mathrm{s}^{-1}$ for line sources. Detectors appropriate in various energy ranges are shown above the graph. Courtesy J. N. Bahcall.

Table 5.3. *Solar neutrino fluxes expected and detected in different experiments*

Detector	Source	Exp. flux[a]	Obs. flux
^{37}Cl	^{7}Be	1.15	
	^{8}B	6.20	
	Total	7.6 ± 1.2 :	2.56 ± 0.23
Kamiokande	^{8}B	5.05 ± 0.9	2.8 ± 0.4
Gallex,	pp	70	
SAGE II	^{7}Be	34.5	
	^{8}B	13.1	
	Total	128 ± 8	75 ± 8

[a] For the radiochemical detectors (chlorine and gallium), fluxes are expressed in snu, where 1 snu ('solar neutrino unit') $\equiv 10^{-36}$ events per target atom per second. For the Kamiokande water detector the unit is 10^6 neutrinos cm^{-2} s^{-1}.
After Bahcall, Pinsonneault and Basu (2001).

Table 5.4. *Solar neutrino fluxes from heavy water experiments*

Reaction	Nature	Expected flux[a]	Observed flux
$\nu_e + d \rightarrow p + p + e^-$	Charged current	5 ± 1	1.76 ± 0.14
$\nu_x + d \rightarrow p + n + \nu_x$	Neutral current	5 ± 1	5.09 ± 1.0
$\nu_x + e^- \rightarrow \nu_x + e^-$	Electron scattering	5 ± 1	2.32 ± 0.11^{b}

[a] In units of 10^6 cm^{-2} s^{-1}, assuming no oscillations.
[b] More precise result from Super-Kamiokande.
After Ahmad *et al.* (2002).

The 'smoking gun' that finally established this explanation as the correct one was provided by the SNO[3] experiment utilizing heavy water as the detector. Table 5.4 shows the reactions involved and the fluxes found from the signatures (angular distribution and energy spectrum of Cherenkov photons) of the various reactions. The neutral current reaction, detected from 6.25 MeV γ-rays resulting from subsequent neutron captures on deuterium, is equally sensitive to neutrinos of all three flavours and indeed gives the expected flux, whereas the charged-current reaction gives a similar discrepancy to that found in the chlorine experiment. The electron scattering reaction (detected in both heavy and light water experiments) is excited by neutrinos of all three flavours, but for $\nu_{\mu,\tau}$ the cross-section is only 0.15 of that for ν_e, so again there is an apparent deficit, but the deduced flux is 30 per cent greater.

[3] Sudbury Neutrino Observatory, Ontario.

$$
\begin{array}{rcl}
^{12}\mathrm{C} + {}^{1}\mathrm{H} &\to& {}^{13}\mathrm{N} + \gamma \\
^{13}\mathrm{N} &\to& {}^{13}\mathrm{C} + e^{+} + \nu \\
^{13}\mathrm{C} + {}^{1}\mathrm{H} &\to& {}^{14}\mathrm{N} + \gamma \\
^{14}\mathrm{N} + {}^{1}\mathrm{H} &\to& {}^{15}\mathrm{O} + \gamma \\
^{15}\mathrm{O} &\to& {}^{15}\mathrm{N} + e^{+} + \nu \\
^{15}\mathrm{N} + {}^{1}\mathrm{H} &\to& {}^{12}\mathrm{C} + {}^{4}\mathrm{He}
\end{array}
$$

CN cycle

ON cycle

$$
\begin{array}{rcl}
&\to& {}^{16}\mathrm{O} + \gamma \\
^{16}\mathrm{O} + {}^{1}\mathrm{H} &\to& {}^{17}\mathrm{F} + \gamma \\
^{17}\mathrm{F} &\to& {}^{17}\mathrm{O} + e^{+} + \nu \\
^{17}\mathrm{O} + {}^{1}\mathrm{H} &\to& {}^{14}\mathrm{N} + {}^{4}\mathrm{He}
\end{array}
$$
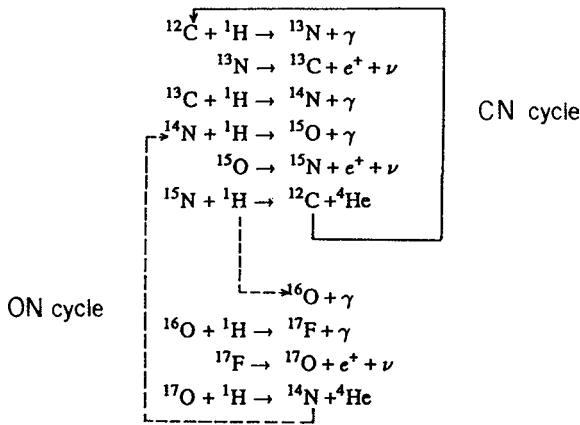
Fig. 5.4. The CNO bi-cycle. Adapted from Kippenhahn and Weigert (1990).

5.6.2 The CNO cycles

At somewhat higher temperatures than inside the Sun, hydrogen burning takes place more rapidly by a catalytic cycle involving the CNO elements (provided, of course, that at least one of these is present, i.e. we are not dealing with a star of the first generation). The reactions involved are shown in Fig. 5.4. The main part of the cycle involves C and N, while the ON cycle usually contributes little energy, but becomes significant at high temperatures when it can lead to destruction of oxygen and enhancement of the ratio $^{17}\mathrm{O}/^{16}\mathrm{O}$ compared to the Solar-System value of 4×10^{-4}. Owing to the significant Coulomb barriers, the CN cycle is highly temperature-sensitive (see Section 2.5), its rate being fixed by the slowest reaction $^{14}\mathrm{N}\,(p, \gamma)^{15}\mathrm{O}$ (Coulomb barrier plus electromagnetic interaction). Figure 5.5 shows the temperature dependences of the pp chain and CNO cycle.

At temperatures of several $\times\,10^{7}$ K, the CNO cycle breaks out into third and fourth branches leading to destruction of $^{18}\mathrm{O}$ relative to its Solar-System abundance ($^{18}\mathrm{O}/^{17}\mathrm{O} = 5.5$) and to higher H-burning cycles, the neon–sodium and magnesium–aluminium cycles (see Fig. 5.6). There are uncertainties in relevant nuclear reaction rates, but spectroscopic observations of enhanced features of sodium and aluminium in red giants in some globular clusters (though not in Population II field stars) provide evidence that these latter cycles can actually operate in later stages of hydrogen-shell-burning. At still higher temperatures ($> 10^{8}$ K), e.g. in novae, nuclear reactions become so fast that there is not enough time for β-decays such as that of $^{13}\mathrm{N}$ (which take times in the range 100 to 1000 s) and one then has a so-called fast CNO process leading into hot Ne–Na and Mg–Al cycles, possibly followed by a break-out to heavy proton-rich nuclei in what is known as the rp-process.
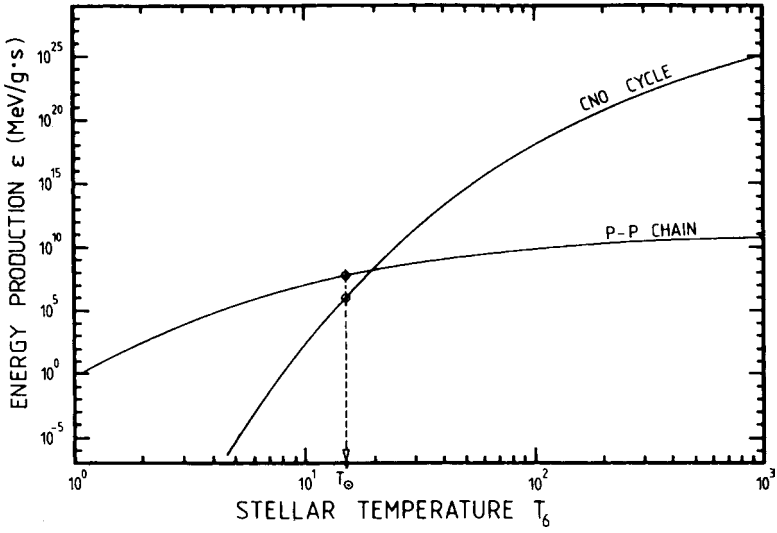
Fig. 5.5. Dependence on temperature of energy production rates by the *pp* chain and CNO cycle (for solar abundances). After Iben (1965) and Rolfs and Rodney (1988). Copyright by the University of Chicago. Courtesy Claus Rolfs.
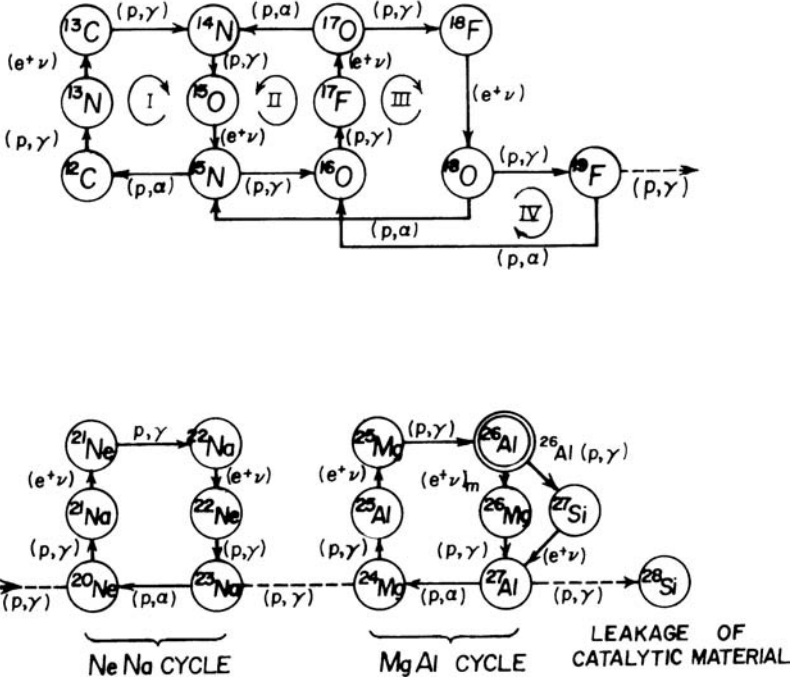
Fig. 5.6. CNO tri- and quadri-cycles and Ne–Na and Mg–Al cycles. Adapted from Rolfs and Rodney (1988).

Because of the differing rates of the component reactions, the CNO cycle modi-fies the initial composition of the material, which typically has O > C > N, making more ^{14}N (and more ^{13}C relative to ^{12}C) at the expense of carbon and (at the higher temperatures) oxygen. Thus in H-burning zones the CN mixture is rapidly modified, and the CNO mixture somewhat more slowly modified, to reach steady-state ratios,[4] e.g. at $T = 3 \times 10^7$ K the steady-state percentages of CNO isotopes, compared to Solar-System values, are as follows:

	^{12}C	^{13}C	^{14}N	^{15}N	^{16}O	^{17}O
CNO 'eq.' 3×10^7 K	1.6	0.39	97	3×10^{-3}	1.3	4.3×10^{-4}
Solar System	28	0.30	8.3	3×10^{-2}	64	8.3×10^{-3}

and virtually all the initial C and N (and at higher temperatures O) in the burning zone ends up as ^{14}N. Subsequent dredge-up episodes to the surface lead to minor or major corresponding changes in the surface composition of red giants. In some cases, e.g. WN stars, it appears that the exposed layers have reached complete CNO 'equilibrium'. The sum of C, N and O abundances remains unchanged, however.

Owing to its steep temperature dependence, the CNO cycle energy source in upper main-sequence stars is highly concentrated in a small central core which is convective because a finite surface area is required to carry radiation through a fixed temperature gradient (see Eq. 5.22). Consequently, in stars bigger than about 1.1 $M_\odot$, the chemical profile $X(m)$ resembles a step function, and when all the hydrogen in the core is used up one has an isothermal helium core surrounded by a hydrogen-burning shell. Less massive stars have a radiative core and a con-vective envelope (e.g. the outer 30 per cent of the solar radius), while stars with $\leq 0.3\, M_\odot$ are fully convective (apart from a thin radiative skin at the photosphere) in accordance with the Hayashi effect.

5.7 Evolution from the main sequence: the Schönberg–Chandrasekhar limit

As hydrogen becomes used up in the core of a star, a discontinuity in molec-ular weight develops, which causes the star to move upwards from the ZAMS in the HR diagram (points marked '2' in Fig. 5.7). When central hydrogen is almost exhausted, the entire star undergoes contraction, which heats the interior to the point where hydrogen is ignited in a shell (points marked '3' in the figure) and the star begins to expand again. One thus has a growing isothermal core support-ing the surrounding envelope, and it was shown by Schönberg and Chandrasekhar (1942) that there is an upper limit to the mass fraction q of the star occupied by the core for which such a configuration can be in equilibrium. A sketch of the argument

[4] Commonly referred to as equilibrium ratios.
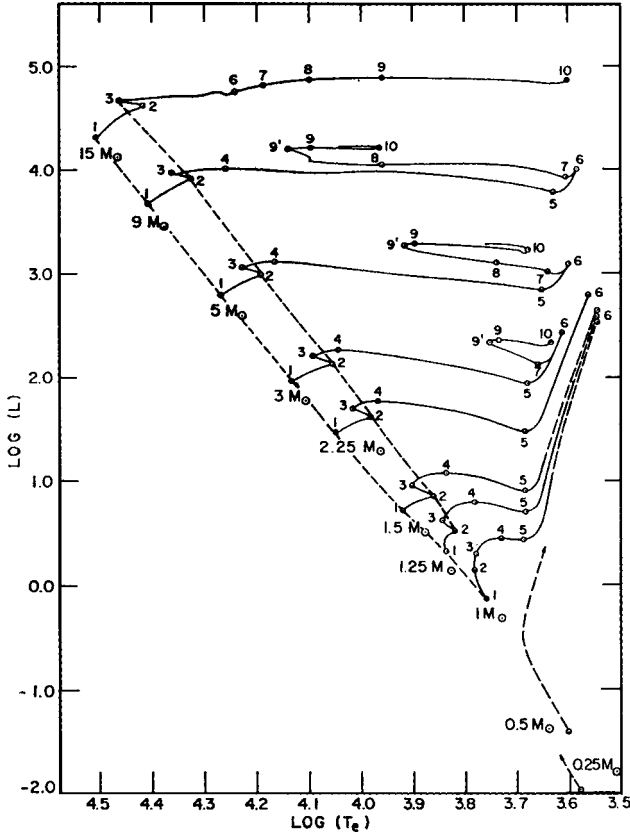
Fig. 5.7. Evolutionary tracks for $Z = 0.02$ (near solar metallicity) stars with different masses in the HR diagram. (Luminosities are in solar units.) Points labelled '1' define the ZAMS and points labelled '2' the terminal main sequence (TAMS), the point where central hydrogen is exhausted. The Schönberg–Chandrasekhar limit may be reached either before or after this (for $M \geq 1.4\,M_\odot$). Points marked '3' show the onset of shell hydrogen-burning. Few stars are found in the 'Hertzsprung gap' between point '4' and point '5', where the surface convection zone has grown deep enough to bring nuclear processed material to the surface in the first dredge-up. Adapted from Iben (1967).

is the following: apply the Virial Theorem, Eq. (5.14), to the isothermal core with radius R_c, but now with an external pressure P_0.

$$2U + \Omega = 4\pi R_c^3 P_0, \quad \text{or} \tag{5.71}$$

$$P_0 = \frac{2U + \Omega}{4\pi R_c^3} = \frac{C_V M_c T}{2\pi R_c^3} - \frac{\beta G M_c^2}{4\pi R_c^4} \tag{5.72}$$

$$= \frac{C_1 M_c T_0}{\mu_c R_c^3} - C_2 \frac{M_c^2}{R_c^4}, \tag{5.73}$$

where C_V is the specific heat, β is a number of order unity, T_0 is the temperature of the H-burning shell and C_1, C_2 are constants. Differentiation of Eq. (5.73) shows that $P_0(R_c)$ has a maximum given by

$$R_{\mathrm{max}} = C_3 \frac{M_c \, \mu_c}{T_0}; \quad P_{0,\mathrm{max}} = \frac{C_4 \, T_0^4}{\mu_c^4 \, M_c^2}. \tag{5.74}$$

Applying the homology version of the hydrostatic equation (5.8) to the envelope, one obtains another condition for the pressure at the edge of the core:

$$P_{\mathrm{ext}} \propto \frac{M^2}{R^4} = \frac{C_5 \, T_0^4}{\mu_{\mathrm{env}}^4 \, M^2}, \tag{5.75}$$

the last relation following from $T \propto \mu M/R$, Eq. (5.17). The fitting condition at the core boundary

$$P_{\mathrm{ext}} < P_{0,\mathrm{max}} \tag{5.76}$$

then implies (inserting the numerical factor from more detailed calculations)

$$q_0 \equiv \frac{M_c}{M} \leq q_{\mathrm{SC}} \simeq 0.37 \left(\frac{\mu_{\mathrm{env}}}{\mu_c} \right)^2 \simeq 0.09. \tag{5.77}$$

When this limit is reached, the isothermal core is no longer capable of supporting the envelope, the core contracts and the envelope expands by virtue of a sort of 'mirror' or 'see-saw' effect for which it is difficult to give a neat explanation. The star accordingly moves quickly (i.e. on the thermal timescale of the core) across the 'Hertzsprung gap' in the HR diagram to the neighbourhood of the Hayashi track (Fig. 5.7), where the surface convection zone becomes deep, and begins its ascent of the red-giant branch (RGB) where its evolutionary lifetime is of the order of 0.1 of that on the main sequence. However, in stars with total mass below about 1.4 $M_\odot$, contraction of the core is limited at this stage by the onset of degeneracy.

5.8 Helium-burning

During RGB evolution, the H-exhausted core continues to contract in radius (while expanding in the mass coordinate as the H-burning shell eats its wayoutwards in mass) and heat up, although this process is slowed down by degeneracy in the case of low-mass stars. Eventually (at points marked '6' in Fig. 5.7), helium-burning, which is the start of nucleosynthesis proper, sets in at temperatures of the order of 10^8 K and densities $\sim 10^4 \, \mathrm{gm\,cm^{-3}}$ through the triple α reaction (Öpik 1951; Salpeter 1952; Hoyle 1954)

$$2\alpha \rightleftharpoons {}^8\mathrm{Be} - 0.09 \, \mathrm{MeV}; \tag{5.78}$$
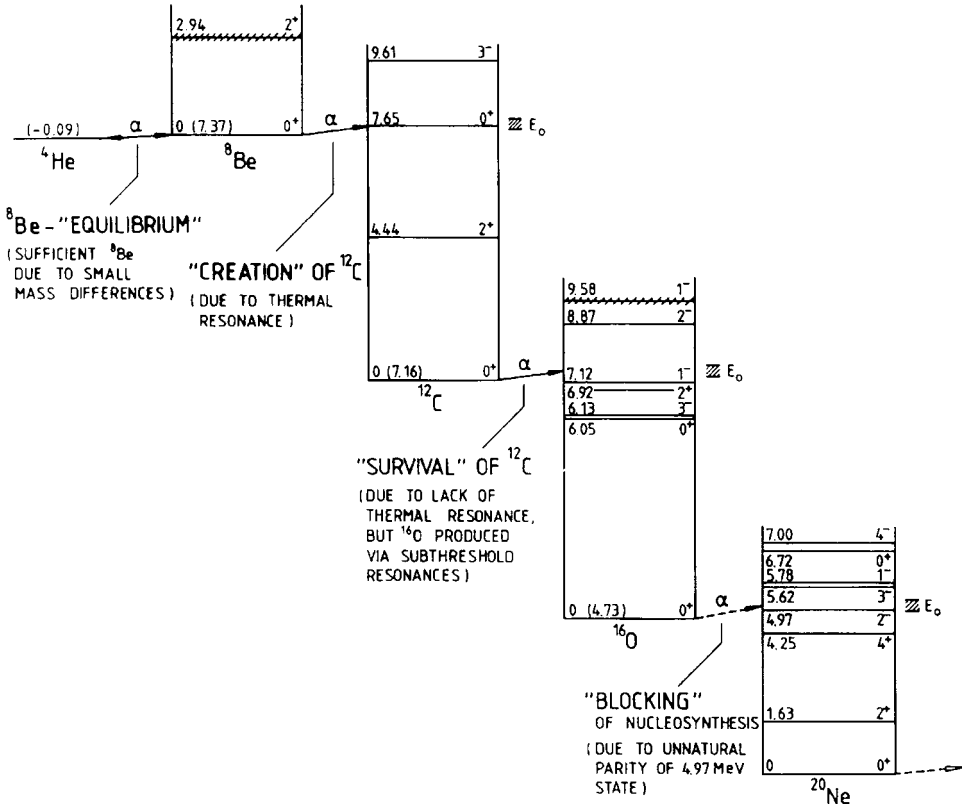
Fig. 5.8. Nuclear energy levels involved in the 3α reaction. After Rolfs and Rodney (1988). Copyright by the University of Chicago. Courtesy Claus Rolfs.

$$^8\text{Be} + \alpha \rightleftharpoons {}^{12}\text{C}^{**}(7.65\,\text{MeV})\,(\gamma\gamma)\,{}^{12}\text{C}\,(\text{ground state}). \qquad (5.79)$$
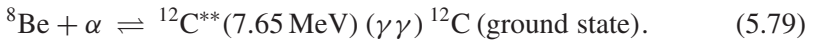
Figure 5.8 shows the nuclear energy levels involved, which display a number of remarkable coincidences that have played an essential role in the creation of the elements needed for life. A Saha-type equilibrium exists (apart from screening factors very near to 1) between 2α and ^8Be (which decays in a time of the order of 10^{-16} s), and also between ^8Be and the excited 7.65 MeV 0^+ state of ^{12}C, whose existence was brilliantly predicted by Hoyle (1954) on the grounds that carbon would not otherwise exist in anything like its cosmic abundance. The 7.65 MeV state of ^{12}C mostly decays back into $3\alpha(\Gamma_\alpha \simeq 8.3\,\text{eV})$, but has a small probability (corresponding to $\Gamma_\gamma = 3.6 \times 10^{-3}\,\text{eV}$) of electromagnetic decay (supplemented by a still smaller probability of decay by $e^\pm$ pair emission) eventually leading to the ground state. Some carbon is then transformed to oxygen by the $^{12}\text{C}(\alpha, \gamma)^{16}\text{O}$ reaction, but further α-particle captures are inhibited (fortunately for us) by the unfavourable parity of the 2^-, 4.97 MeV state of ^{20}Ne.

In massive and intermediate-mass stars, $M > 2.3\,M_\odot$, the interior is still not degenerate when helium-burning sets in; the new energy source causes the core to expand and the envelope to contract, and the star undergoes some loops in the HR diagram (Fig. 5.7). In less-massive stars, the core is degenerate and a thermal runaway ensues, known as the (core) helium flash. This is followed by a readjustment of the structure, with helium-burning in a non-degenerate convective core, and metal-rich stars end up lower down the giant branch near $\log(L/L_\odot) \simeq 2$. Old, metal-poor stars spread out along a horizontal branch (see Figs. 4.8, 5.15); the spread is largely caused by stochastic variations in mass loss during previous RGB evolution, whereas the luminosity (still largely provided by H-burning in the shell) is essentially fixed by the mass of the core when the helium flash set in (about $0.5\,M_\odot$). Some other important reactions involving He-burning are the following:

- ^{12}C$(\alpha, \gamma)^{16}$O converts a substantial fraction of the carbon from 3α into oxygen; the rate is still somewhat uncertain because it is affected by the tails of sub-threshold resonances (Fig. 5.8; see also Fig. 2.12), and this uncertainty is significant for calculations of more advanced stages of nucleosynthesis.
- More advanced He-burning reactions ^{16}O$(\alpha, \gamma)^{20}$Ne$(\alpha, \gamma)^{24}$Mg may take place at temperatures $\sim 10^9$ K under some conditions, e.g. shell-burning in advanced stages and explosive nucleosynthesis.
- Helium-burning on CNO material previously converted into ^{14}N by H-burning leads to the series of reactions

$$^{14}\text{N}(\alpha, \gamma)^{18}\text{F}(\beta^+\nu)^{18}\text{O}(\alpha, \gamma)^{22}\text{Ne}, \tag{5.80}$$
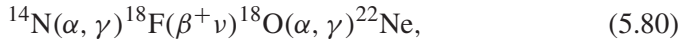
which lead to a neutron excess proportional to the intial $Z_{\text{CNO}} \simeq Z$. This is important in explosive nucleosynthesis (where the overall n/p ratio is unaltered because there is no time for β-decays) and as a source of free neutrons for the neutron capture processes in massive stars from ^{22}Ne$(\alpha, \text{n})^{25}$Mg. Another important neutron source, which operates also in low-mass stars, is ^{13}C$(\alpha, \text{n})^{16}$O.

5.9 Further burning stages: evolution of massive stars

In stars below a certain initial mass M_{up}, core-burning is halted by formation of a degenerate CO core which later becomes a white dwarf. The value of M_{up} is rather uncertain, depending on the treatment of convection and semi-convection during core helium-burning and on mass loss in the AGB phase, but is thought to be around $8\,M_\odot$. Stars with initial mass about $10\,M_\odot$ or more ignite carbon in the core non-degenerately. Owing to neutrino (and antineutrino) emission at the high temperatures involved, due to $e^\pm$ annihilation and other processes, subsequent evolution is greatly accelerated, the nuclear timescale becomes shorter than the

overall thermal timescale and nuclear evolution occurs before the envelope (blue or red supergiant) has time to adjust. The main reactions are

- Carbon-burning ($T \simeq 10^9$ K, $t \simeq 1000$ yr)

$$^{12}\text{C} + {}^{12}\text{C} \rightarrow {}^{24}\text{Mg}^* \rightarrow {}^{20}\text{Ne} + \alpha + 4.6\,\text{MeV} \tag{5.81}$$

$$\rightarrow {}^{23}\text{Na} + p + 2.2\,\text{MeV} \tag{5.82}$$

$$\rightarrow {}^{23}\text{Mg} + n - 2.6\,\text{MeV}, \tag{5.83}$$
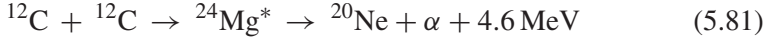
followed by partial burning of sodium through $^{23}\text{Na}(p, \alpha)^{20}\text{Ne}$.
- Neon-burning ($T \simeq 1.5 \times 10^9$ K, $t \simeq 1$ yr)

$$^{20}\text{Ne}(\gamma, \alpha)^{16}\text{O}; \ {}^{20}\text{Ne}(\alpha, \gamma)^{24}\text{Mg}; \ {}^{24}\text{Mg}(\alpha, \gamma)^{28}\text{Si}. \tag{5.84}$$
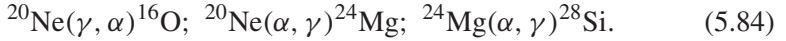
- Oxygen-burning ($T \simeq 2 \times 10^9$ K, $t \simeq \frac{1}{2}$ yr)

$$\text{O} + \text{O} \rightarrow \text{Si, S etc.,} \tag{5.85}$$

including some neutron-rich nuclei resulting from weak interactions, in partially degenerate conditions. Core O-burning is accompanied by shell C-burning (where the ^{22}Ne neutron source is active for the s-process) etc., leading to a
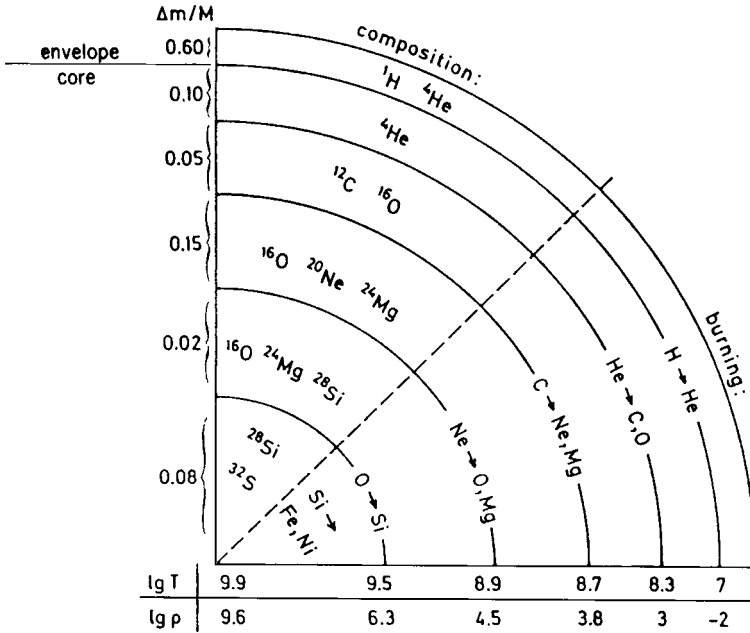
Fig. 5.9. Schematic illustration (not to scale) of the 'onion-skin' structure in the interior of a highly evolved massive star ($25\ M_\odot$). Numbers along the vertical axis show some typical values of the mass fraction, while those along the horizontal axis indicate temperatures and densities (gm cm^{-3}). Adapted from Kippenhahn and Weigert (1990).

concentric onion-like structure with increasingly heavy nuclei towards the interior (Fig. 5.9). However, convective zones caused by some of the shell sources will tend to complicate this picture by blurring composition boundaries and the extent of this effect is obscured by uncertainties in nuclear reaction rates and in the influence of convective overshooting and semi-convection, which latter is a slow mixing process that can arise in regions with a gradient in molecular weight.

- Silicon-burning ($T \geq 3 \times 10^9$ K, $t \simeq 1$ day) can be described as 'photo-disintegration-rearrangement', with

$$^{28}\mathrm{Si}(\gamma, \alpha)^{24}\mathrm{Mg} \tag{5.86}$$

followed by

$$^{28}\mathrm{Si} + \alpha + p + n \rightarrow \text{ iron peak elements.} \tag{5.87}$$

Equation (5.87) summarizes many fast reactions which take place while ^{28}Si slowly 'melts'. The fast reactions in many cases are balanced by reverse reactions, so that there is an approximation to nuclear statistical equilibrium ('quasi-equilibrium'), favouring the more stable nuclei; the outcome is then a function of just three parameters: the temperature, the density and the neutron excess, resulting from previous nuclear reactions and inverse β-decays. At this stage, an inner mass of the order of M_{Ch} is degenerate and dominated by neutron-rich nuclei (mainly ^{56}Fe, ^{54}Fe and ^{52}Cr), owing to the high density (see Section 5.4.4), while further out there are 'onion skins' consisting successively of silicon, oxygen, helium and hydrogen with minor constituents (Fig. 5.10).

The next stage is dynamical collapse of the core, on a dynamical timescale of milliseconds, caused by electron capture followed by photo-disintegration (and/or $e^{\pm}$ pair creation for $M \geq 100\,M_\odot$) from the increase in temperature in a thermal runaway following gravitational contraction when the silicon fuel is exhausted. According to the standard picture, the collapse leads to disintegration of the (mainly iron) nuclei first into α-particles and then into protons and neutrons, whereafter electrons are crushed onto protons to make neutrons and the neutrons themselves become degenerate making a neutron star. This leads to copious neutrino emission (in all six varieties) and to a bounce at nuclear density which causes a shock to propagate outwards. The shock is weakened by the absorption of energy in photo-disintegration and neutrino emission, but reinforced by absorption of energetic neutrinos (as first proposed by Colgate and White 1966), and this is presumed to lead to expulsion of the outer layers in an explosion identified with supernovae of Type II and related types Ib etc. The inner layers are modified by explosive synthesis due to sudden heating caused by the shock and subsequent freeze-out from the expansion (Fig. 5.10). The gravitational energy released is of the order of 10^{53} erg, 99 per cent of which is carried away by the neutrinos, as was strikingly verified in
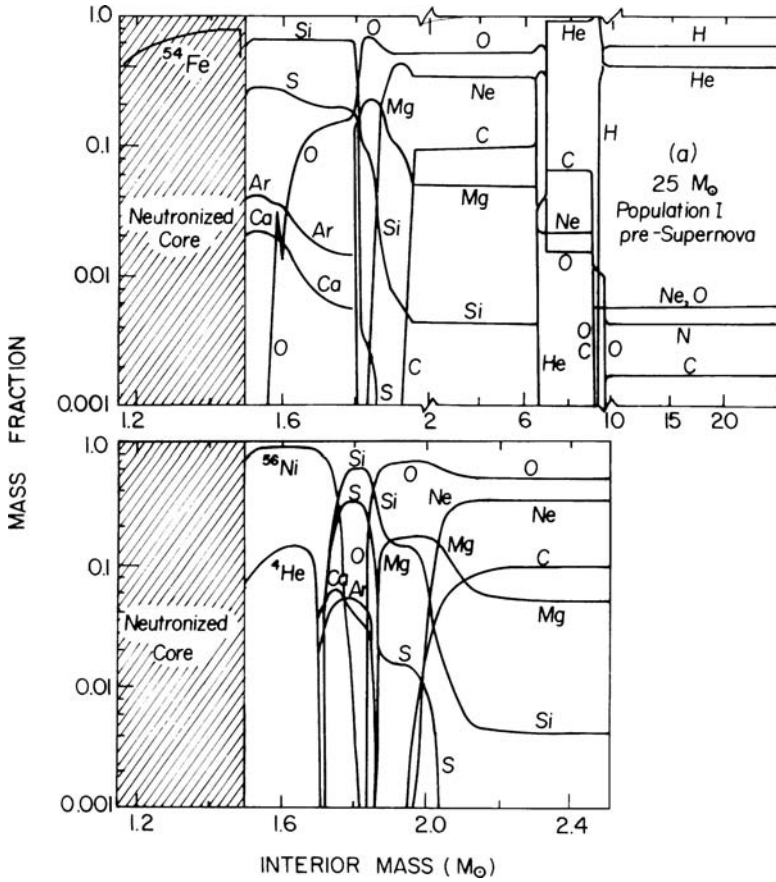
Fig. 5.10. Upper panel: chemical profile of a 25 $M_\odot$ star immediately before core collapse. (Note change in horizontal scale at 2 $M_\odot$.) Lower panel: the same, after modification by explosive nucleosynthesis in a supernova outburst. The amount of ^{56}Ni (which later decays to ^{56}Fe) ejected depends on the mass cut, somewhere in the ^{28}Si→^{56}Ni zone, and is uncertain by a factor of 2 or so. Adapted from Woosley and Weaver (1982).

the case of SN 1987A in the Large Magellanic Cloud (Hirata *et al.* 1988). About 1 per cent, i.e. 10^{51} erg, goes into the shock and only 1 per cent again of that appears as visible radiation, largely powered by radioactive decay in the stages following maximum light; around 10^{50} erg, or 10 per cent of the shock energy, are needed to eject the envelope against gravity. Figure 5.11 shows the relative amounts of elements previously synthesized in hydrostatic stellar evolution that are ejected in a typical model of the explosion.

The shock takes the form of an expanding high-entropy bubble, dominated by radiation, so that the maximum temperature reached in each layer is essentially
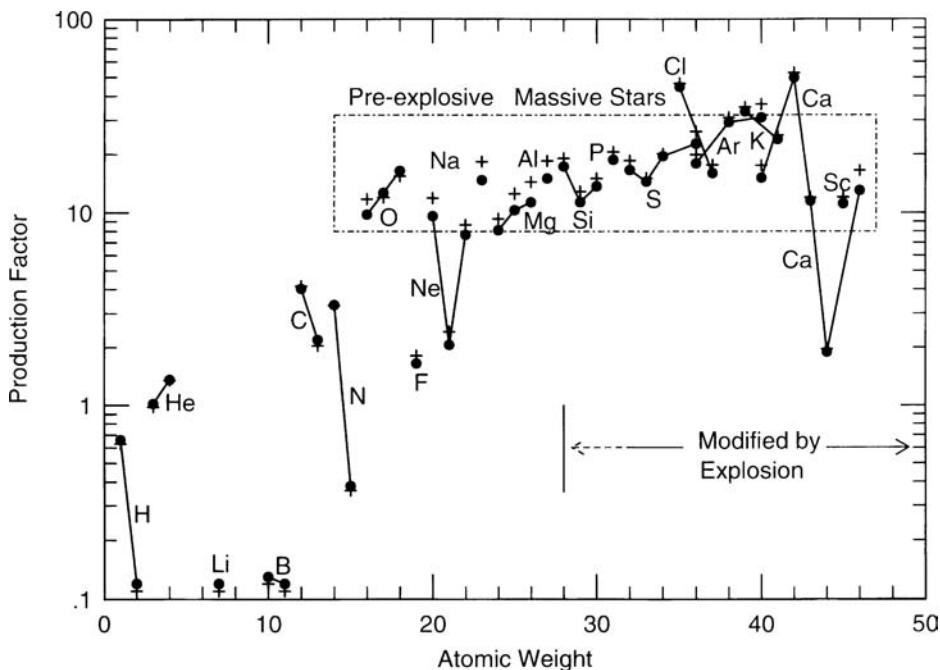
Fig. 5.11. Amounts, in units of relative Solar-System abundances, of nuclear species resulting from hydrostatic evolution of an average pre-supernova. Filled circles represent an initial mass function with slope -2.3 and plus signs one with slope -1.5. The dashed box encloses 28 species co-produced within a factor of 2 of solar values, assuming a $^{12}C(\alpha, \gamma)^{16}O$ rate $1.7 \times$ that given by Caughlan and Fowler (1988). Reprinted from Weaver and Woosley (1993). Reproduced with kind permission of Elsevier Science. Courtesy Tom Weaver.

fixed by the shock energy E_0 (usually input into calculations as a parameter $\simeq 10^{51}$ erg) and the radius:

$$\frac{4}{3}\pi r^3 a T^4 = E_0, \tag{5.88}$$

giving $kT_{max} \geq 0.5$ MeV (adequate for complete explosive silicon-burning) at a radius of 3700 km (corresponding to an included mass of 1.7 $M_\odot$ in the silicon layer of a 20 $M_\odot$ star). The composition of the silicon and the inner part of the oxygen layer is then modified by explosive synthesis during the expansion timescale of the order of seconds, which differs from previous 'hydrostatic' nucleosynthesis by higher temperatures and entropies and by allowing no time for β-decay. The nuclear statistical quasi-equilibrium is thus subject to the overall neutron:proton ratio previously established, which corresponds to a neutron excess

$$\eta \equiv \sum_i (N_i - Z_i)Y_i = 1 - 2Y_e = 1 - 2/\mu_e \sim 10^{-3}. \tag{5.89}$$
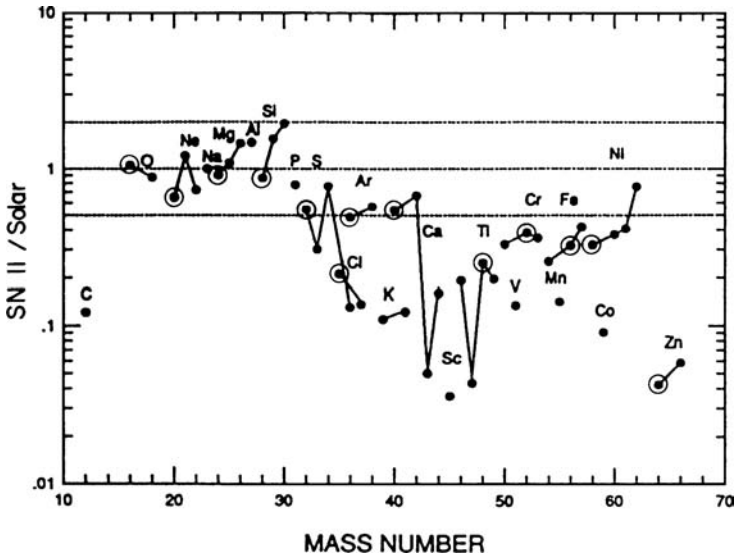
Fig. 5.12. Calculated abundances after decay of ^{56}Ni and other radioactive nuclei, relative to solar, in material ejected from a typical Type II supernova explosion, averaged over initial masses 10 to 50 $M_\odot$. Dominant isotopes of each element are circled. Adapted from Tsujimoto (1993).

(Here N and Z are neutron and proton numbers in each nucleus present with a numerical abundance $Y_i \equiv X_i/A_i$ per amu.) The value of the neutron excess depends somewhat on the initial chemical composition (more initial CNO leading to more ^{22}Ne after helium-burning), but this dependence is damped down by various nuclear reactions that have taken place in previous hydrostatic burning stages. With the small neutron excess of order 10^{-3} and the high entropy, the result of explosive synthesis favours α-particle nuclei (mainly ^{56}Ni; see Fig. 5.10) and α-particles themselves, resulting in a so-called α-rich freeze-out in the innermost ejected layers. (An α-rich freeze-out occurs generally at low densities where the 3α reaction is not fast enough to keep the helium abundance in equilibrium during the expansion and cooling in explosive events.) Resulting abundances calculated after explosion, freeze-out and radioactive decay are shown in Fig. 5.12, assuming the mass cut above which material is ejected to be such as to yield 0.07 $M_\odot$ of ^{56}Ni in accordance with observations of Supernova 1987A, i.e. at 1.6 $M_\odot$ for a 20 $M_\odot$ star. These massive stars are believed to supply most elements up to and including the iron group in stars of Population II and nuclides shown in the box in Fig. 5.11 in Population I, either in the explosions or in preceding mass-loss episodes from stellar winds. However, there is a deficit by a factor of the order of 2 or 3 in the relative abundance of iron-group elements compared to the Sun, which is believed to be made up by supernovae of Type Ia.

Broadly speaking, O, Ne and Mg originate mainly from hydrostatic burning shells and the amount synthesized and ejected rises sharply with progenitor mass
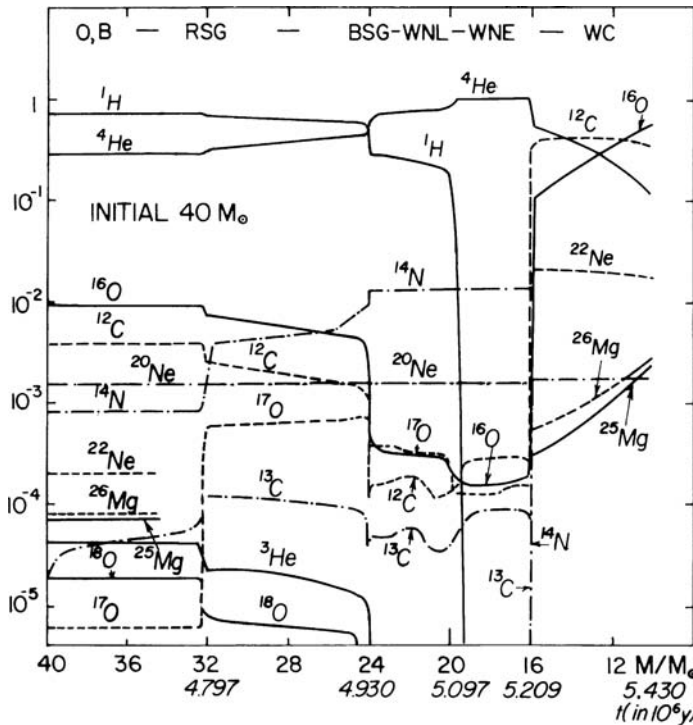
Fig. 5.13. Time evolution of the chemical profile of a $40\,M_\odot$ star that becomes a Wolf–Rayet star as a result of the outer layers peeling off in stellar winds. The spectrum evolves from type O to type B to a red supergiant (RSG) and then back to a blue supergiant (BSG) and towards increasing effective temperatures ending up well to the left of the main sequence. The chemically modified spectrum evolves from nitrogen-rich late, i.e. relatively cool (WNL), to nitrogen-rich early (WNE) to carbon-rich (WC); in some cases still hotter stars are observed that are oxygen-rich (WO). After Maeder and Meynet (1987).

(or strictly speaking the mass of the helium core), at least up to $30\,M_\odot$ or so above which heavy mass loss sets in, whereas S, Ar, Ca and Fe are mostly due to explosive burning and the dependence of their ejected mass on the initial stellar mass is not very clear.

However, there are uncertainties in the range of initial stellar masses where this standard picture applies: more massive stars may leave behind a black hole instead of a neutron star, with or without a supernova explosion, depending on the equation of state of nuclear matter and how much initially outgoing material falls back. Long-duration γ-ray bursts are associated with some supernovae of Type Ic (lacking both hydrogen and helium in their spectra) that are another order of magnitude more powerful than Type II's and are accordingly known as hypernovae; these could make a significant contribution to nucleosynthesis, particularly in early phases of galaxy evolution. A further complication is that mass loss in the pre-supernova stages can have drastic effects on the evolution of stars of $40\,M_\odot$ or
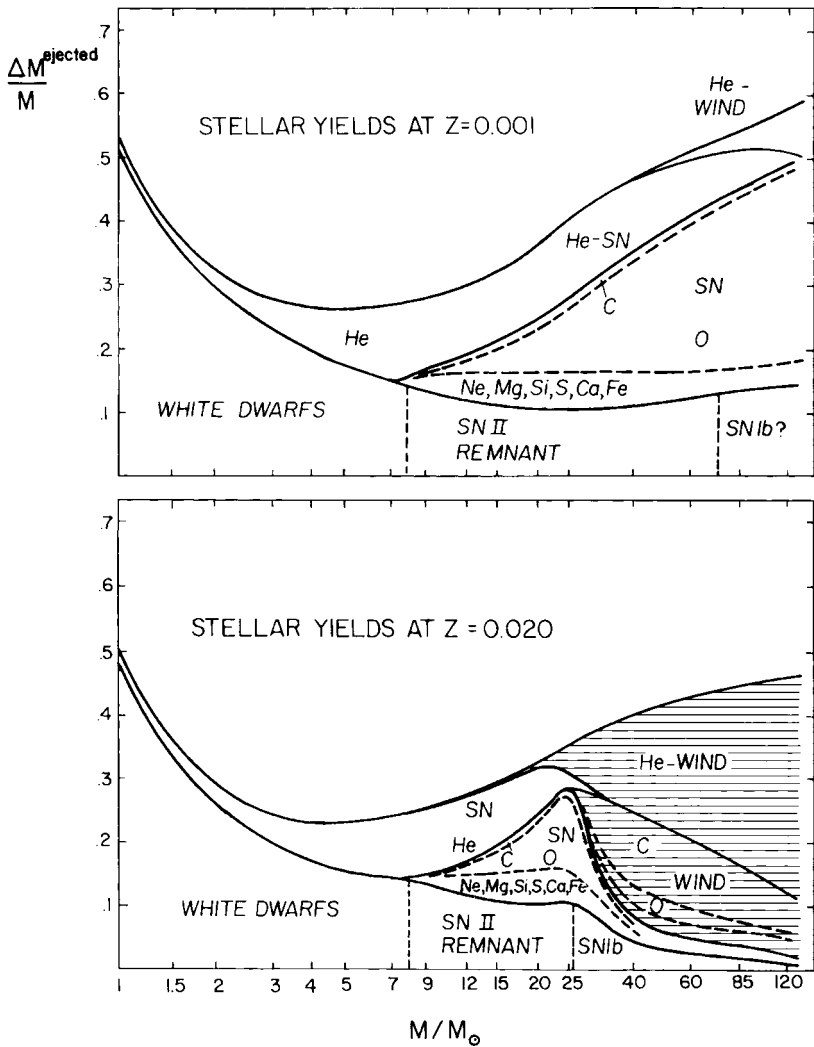
Fig. 5.14. Element production in winds and supernova ejecta from stars affected by strong mass loss, as a function of initial mass. Upper panel: stars with about 1/20 solar heavy-element abundance. Lower panel: stars with approximately solar composition, for which the effects of mass loss are believed to be more drastic. Horizontal shadings indicate outer layers that are expelled in winds prior to SN explosion. After Maeder (1992).

more, especially at higher metallicities (Maeder 1992, 1993). Figure 5.13 shows the chemical profile calculated for a solar-metallicity star of initial mass $40\,M_\odot$ (He core mass $M_\alpha = 19\,M_\odot$) in which the peeling away of the outer layers by stellar winds gradually exposes increasingly nuclear-processed material that appears at the surface of Wolf–Rayet stars and reduces the total mass to $12\,M_\odot$ before the supernova explosion. Figure 5.14 shows schematically, as a function of initial

stellar mass and for two initial chemical compositions, the amounts of different sorts of material ejected in winds and subsequent supernova explosions calculated under the assumption that strong mass loss normally occurs. The most massive stars (above 50 $M_\odot$, say) may lose their expected supernova ejecta in a black hole, but still contribute lighter elements like C, N, O and Ne (especially ^{22}Ne) in winds during their prior evolution.

5.10 Evolution of intermediate- and low-mass stars
5.10.1 Introduction

Figure 5.15 gives an overview of stellar evolution in the HR diagram. Both intermediate- and low-mass stars end their lives as white dwarfs after having expelled a substantial amount of mass in winds and planetary nebulae, the basic reason being the formation of a degenerate CO core that is not massive enough
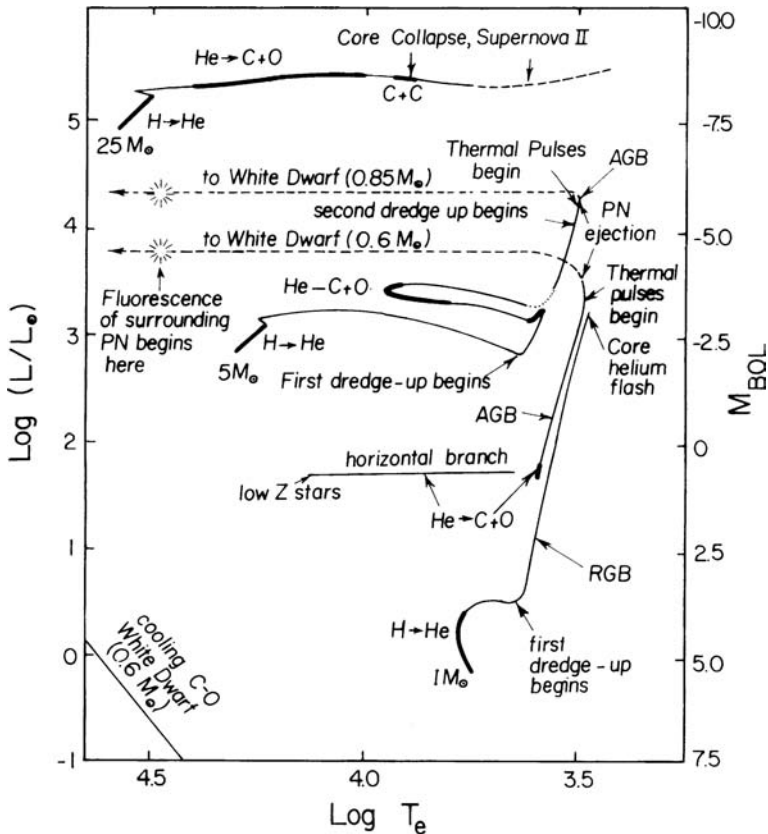
Fig. 5.15. Evolutionary tracks of stars with mass 1, 5 and 25 $M_\odot$ in the HR diagram. Adapted from Iben (1985, 1991).
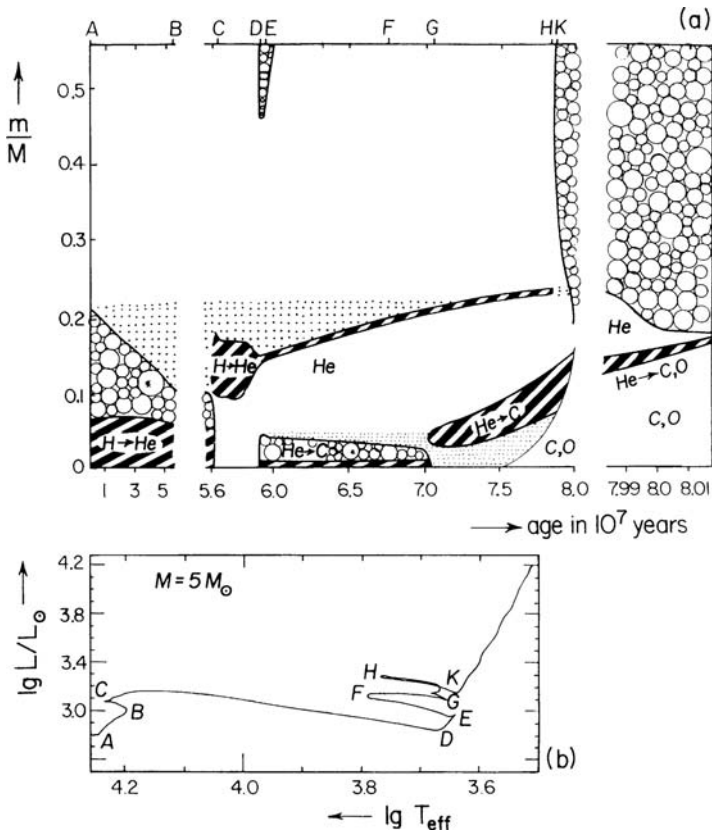
Fig. 5.16. Evolution of a $5\,M_\odot$ star of extreme Population I, shown in chemical profile and in the HR diagram. 'Cloudy' areas indicate convective regions; heavily hatched areas indicate significant nuclear energy generation ($> 10^3$ erg gm^{-1} s^{-1}); and dotted areas are regions of variable chemical composition. After Kippenhahn and Weigert (1990). Copyright by Springer-Verlag.

to ignite carbon. They differ in that intermediate-mass stars (2.5 to 8 $M_\odot$ or so) start with convective cores and ignite helium non-degenerately, whereas lower-mass stars start with small or non-existent convective cores, become degenerate during hydrogen shell-burning and eventually ignite helium with a 'flash'.

5.10.2 Evolution of intermediate-mass stars

Figure 5.16 shows a model for the evolution of an intermediate-mass star. At A it is on the ZAMS burning hydrogen in a convective core which gradually retreats, leaving behind a radiative region enriched in helium. At B the central hydrogen is reaching exhaustion and overall gravitational contraction sets in, leading to ignition of hydrogen in a thick shell at C. The star then rapidly moves across the Hertzsprung gap to D, where an outer convection zone develops, the burning shell

becomes thin and the first dredge-up phase sets in: Li, Be and B in the atmosphere are destroyed by dilution and some ^{13}C and ^{14}N may be dredged up, depending on the depth of convective penetration plus overshoot. At E, core helium-burning sets in, halting the contraction of the core and concomitant expansion of the envelope, and the outer convection zone retreats again. During core helium-burning, from E to G, the star carries out a loop in the HR diagram, due to another phase of core gravitational contraction and envelope expansion as the helium fuel runs out, and at G it starts another loop when the helium shell source is ignited and eventually causes the hydrogen shell source to be quenched at H by cooling due to expansion. The whole helium core then contracts, leading to expansion of the envelope back to the Hayashi track at K, where the second dredge-up occurs (above a certain mass limit) and causes an increase in helium abundance and conversion of C and O into ^{14}N in the atmosphere. (These loops take the star several times through the Cepheid instability strip.)

At K, the hydrogen shell source is re-ignited by heat from the helium shell source and the star now evolves up the asymptotic giant branch (AGB) where extensive mass loss takes place culminating in PN ejection and the cooling of the degenerate CO core to form a white dwarf (see Fig. 5.15). Mixing processes during later stages of AGB evolution, to be described in more detail below, lead to the production and expulsion in winds and PN of ^{7}Li, C, N and s-process isotopes and maybe others.

5.10.3 Evolution of low-mass stars to the helium flash

Low-mass stars ($\leq \sim 2.3 M_\odot$) have small or vanishing convective cores while on the main sequence and hydrogen-burning by the *pp* chain leads to some enrichment in helium out to a fair fraction (20 to 50 per cent or so) of the total mass, well beyond the central core which eventually becomes exhausted of hydrogen and degenerate. They do not experience the Schönberg–Chandrasekhar limit and Hertzsprung gap, and their main-sequence configurations are in any case fairly close to the Hayashi track (see Fig. 5.7). The first dredge-up occurs at the base of the red-giant branch, point '5' in Fig. 5.7, and results in dilution of the helium from previous nuclear core burning in regions just above the deepest layer reached by the outer convection zone, as well as in some changes in surface abundances: that of ^{14}N is approximately doubled at the expense of ^{12}C which is reduced by about 30 per cent, the $^{12}C/^{13}C$ ratio is reduced to between 20 and 30, Li, Be and B are virtually wiped out by dilution, but ^{16}O is essentially unaffected. In many cases, larger amounts of ^{13}C (relative to ^{12}C) are found than predicted by classical theory, and sometimes other anomalies like a (perhaps temporary) reappearance of ^{7}Li. These observations suggest the existence of 'extra mixing', i.e. mixing processes other than from straightforward convection. A prominent candidate for these is

the existence of meridional circulation currents caused by rotation, which become effective after the H-burning shell has passed the deepest point of penetration previously reached by the surface convection zone, thereby removing the 'μ-barrier', the gradient in molecular weight that had previously inhibited such effects (Sweigart & Mengel 1979). Such extra mixing (sometimes referred to as 'cool-bottom processing' at temperatures of the order of 2.5×10^7 K) can lead to either creation or destruction of ^{7}Be, transport of which into the atmosphere is the source of fresh ^{7}Li (Sackmann & Boothroyd 1999), and the destruction of ^{3}He (Charbonnel & Do Nascimento 1998). Even without rotation, sophisticated numerical modelling in 3 dimensions reveals a mixing process driven by Rayleigh–Taylor instability that can produce these effects (Eggleton, Dearborn & Lattanzio 2006).

This phase is followed by a long period on the red-giant branch (RGB) where the degenerate helium core gradually grows by the slow combustion of hydrogen in its surrounding shell. The rate of growth of the core is governed by the luminosity, which itself is a strong function of the core mass M_c and nearly independent of the mass of the increasingly distended, tenuous envelope around it, basically because the core is highly concentrated, gravity at its surface is very large making a large pressure drop from $|dP/dm| \propto m/r^4$ (with core radius $R_c \sim 10^4$ km) and a much smaller one further out with typical radii orders of magnitude more and only a slightly greater included mass. Thus the pressure drops to a small fraction of its inner value in a small range of mass through the burning shell; the envelope is nearly weightless and has little influence on the shell.

Under these conditions, the dependence of physical parameters of the shell, and hence of the total luminosity, on the mass M_c of the core can be estimated by a homology argument due to Refsdal and Weigert (1970), described in the textbook by Kippenhahn and Weigert (1990). Assume negligible radiation pressure and negligible energy production from gravitational contraction, electron-scattering opacity, $\kappa = \kappa_0/\mu = \text{const.}$ (the proportionality to $1/\mu$ is a rough approximation), CNO burning, $\epsilon = \epsilon_0 \rho T^\nu/\mu$, ideal gas conditions $P \propto \rho T/\mu$ and a constant included mass M_c through the shell, in which we also assume there to exist homology relations (with $x \equiv R_c/r$ where R_c is the radius of the core):

$$\rho(x) = M_c^{\rho_1} R_c^{\rho_2} \mu^{\rho_3} f_\rho(x); \tag{5.90}$$

$$T(x) = M_c^{t_1} R_c^{t_2} \mu^{t_3} f_t(x); \tag{5.91}$$

$$l(x) = M_c^{l_1} R_c^{l_2} \mu^{l_3} f_l(x), \tag{5.92}$$

where the f's are universal functions. The exponents of M_c, R_c and μ in these equations can be found from the basic equations of stellar structure. The hydrostatic equilibrium equation (5.6) can be written

$$dP = G\rho M_c \, d(1/r) = G\rho M_c R_c^{-1} dx \tag{5.93}$$

which integrates up to

$$\rho(x)T(x) \propto \mu P(x) \simeq \frac{GM_c\mu}{R_c} \int_0^x \rho dx' = GM_c^{\rho_1+1} R_c^{\rho_2-1} \mu^{\rho_3+1} \int_0^x f_\rho(x')dx'.$$
(5.94)

This implies

$$T \propto \mu M_c/R_c, \quad \text{or} \quad t_1 = t_3 = 1 = -t_2.$$
(5.95)

The radiative transfer equation, Eq. (5.22), can be written

$$d(T^4) \propto \kappa\rho l R_c^{-1} dx$$
(5.96)

and integrates to

$$M_c^4 R_c^{-4} \mu^4 \propto T^4(x) \simeq \kappa_0 M_c^{\rho_1+l_1} R_c^{\rho_2+l_2-1} \mu^{\rho_3+l_3-1} \int_0^x f_\rho(x') f_l(x')dx', \quad (5.97)$$

which implies

$$\rho_1 + l_1 = 4; \quad \rho_2 + l_2 = -3; \quad \rho_3 + l_3 = 5.$$
(5.98)

Finally, the energy generation equation

$$dl \propto \epsilon\rho d(r^3) \propto \epsilon\rho R_c^3 x^{-4} dx$$
(5.99)

integrates to

$$M_c^{l_1} R_c^{l_2} \mu^{l_3} \propto l(x) \simeq \epsilon_0 M_c^{2\rho_1+\nu} R_c^{2\rho_2+3-\nu} \mu^{2\rho_3+\nu-1} \int_0^x x'^{-4} f_\rho(x') f_t^{\ \nu}(x')dx',$$
(5.100)

which implies

$$l_1 = 2\rho_1 + \nu; \quad l_2 = 2\rho_2 + 3 - \nu; \quad l_3 = 2\rho_3 + \nu - 1.$$
(5.101)

The simultaneous equations (5.98) and (5.101) give the values of the exponents:

$$\rho_1 = (4-\nu)/3 \simeq -3; \quad \rho_2 = -\rho_3 = (\nu-6)/3 \simeq 7/3;$$
(5.102)

$$l_1 = (8+\nu)/3 \simeq 7; \quad l_2 = -(3+\nu)/3 \simeq -16/3; \quad l_3 = (9+\nu)/3 \simeq 22/3,$$
(5.103)

assuming $\nu \simeq 13$. We thus have

$$L \equiv l(0) \propto \mu^{22/3} M_c^7 R_c^{-16/3},$$
(5.104)

or, using as a very crude approximation the mass–radius relation for cold white dwarfs, Eq. (5.53),

$$L \propto \mu^{16} M_c^{8.8},$$
(5.105)

a very steep relation. The core mass then grows according to

$$\dot{M}_c = \frac{L}{X_H E_H} \propto M_c^{8.8}, \tag{5.106}$$

where E_H is the energy gain per unit mass of hydrogen, except during a brief phase when the shell source penetrates into the slightly more hydrogen-rich region left behind by the retreating outer convection zone and the luminosity is temporarily reduced by the μ factor, leading to a 'red giant bump' in the HR diagram with a peak in the luminosity function. In the meantime, the temperature (which is more or less uniform throughout the highly conducting core) grows according to

$$T(x \geq 1) \propto \mu M_c/R_c \sim \mu M_c^{4/3}, \tag{5.107}$$

reaching the value of about 10^8 K, where core helium-burning sets in (somewhat off-centre as a result of neutrino losses), when M_c reaches a value close to $0.5\,M_\odot$ and a corresponding luminosity $\sim 2000\,L_\odot$; these values are quite insensitive to the total stellar mass, but dependent on chemical composition through the effects of helium on molecular weight and of heavy elements on opacity and energy generation. Because the degenerate material cannot take up the resulting extra heat energy by expansion, there is a thermal runaway known as the (core) helium flash, the core heats up suddenly to temperatures $\sim 2.5 \times 10^8$ K at which degeneracy is removed and then expands, leading to contraction of the envelope and a new structure on the zero-age horizontal branch (ZAHB). Here the luminosity is again mainly fixed by the core mass (leading to a virtually constant HB lifetime of about 10^8 yr), but the core is no longer degenerate, its radius is larger and the luminosity (still coming mainly from the hydrogen shell) correspondingly lower (around $50\,L_\odot$). The core flash is not believed to lead to significant mixing that might affect the composition of the atmosphere. The location on the ZAHB depends on the chemical composition and the total mass (after any mass loss that may have occurred along the RGB). Metal-rich stars form a clump close to the RGB, whereas metal-poor stars, e.g. in globular clusters, have higher effective temperatures and a spread, the spread probably being largely due to stochastic variations in the mass loss, and the very bluest ZAHB stars have but a very thin envelope overlying the helium core, which has the 'helium main sequence' structure of a homogeneous helium star. While the average effective temperature along the ZAHB of globular clusters tends to increase with diminishing metallicity, there is not a one-to-one correlation, a fact often referred to as the 'second-parameter problem'. For a fixed core mass, the location on the ZAHB depends on the total mass, less-massive stars being hotter and bluer. Thus a major factor must be some combination of the initial mass (and hence the age) with variable amounts of mass loss during the preceding passage up the RGB.
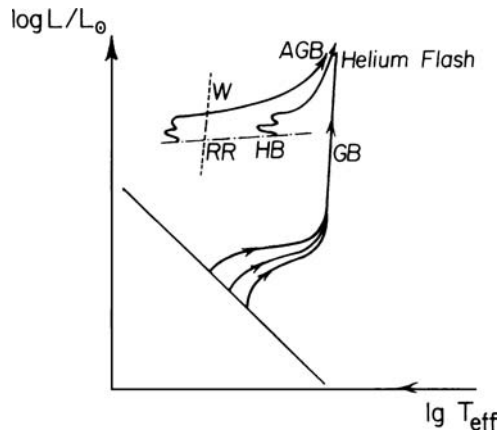
Fig. 5.17. Sketch of the evolution of low-mass stars in the HR diagram. For three slightly different initial masses, with a given chemical composition, the evolutionary tracks from the main sequence merge in the RGB, along which variable amounts of mass (between 0 and $\sim 0.2\,M_\odot$) are lost through stellar winds. After the helium flash, they appear on the ZAHB, evolve (after some loops) towards the upper right and merge in the asymptotic giant branch (AGB). The broken line indicates locations of pulsating variables, RR Lyrae (RR) and W Virginis (W) stars. After Kippenhahn and Weigert (1990). Copyright by Springer-Verlag.

5.10.4 AGB evolution and the third dredge-up

ZAHB stars have a helium-burning convective core surrounded by unburned helium surrounded by a hydrogen-burning shell surrounded by a hydrogen-rich envelope. The helium core gradually increases in mass from hydrogen shell-burning, leading to increasing luminosity, and the star evolves towards the asymptotic giant branch (AGB; see Fig. 5.17). In the meantime, helium-burning at the centre leads to the formation of a growing CO inner core, which becomes degenerate and increases in mass and temperature up to a point where helium-burning is ignited in a shell around the CO core. This causes expansion and cooling of the helium layer and the hydrogen shell source is temporarily switched off during early AGB (E-AGB) evolution, at which point in the more-massive intermediate-mass stars the surface convection zone penetrates deeply into the helium layer in the so-called second dredge-up phase (see Fig. 5.18). This causes substantial changes in the composition of the envelope and atmosphere: helium is enhanced and both carbon and oxygen are partly replaced by ^{14}N. (There is no second dredge-up for low-mass stars.)

As the surface convection zone deepens, bringing down fresh hydrogen, it approaches closer and closer to the helium-burning shell coming up towards it (speaking in terms of the mass coordinate) from below, and this eventually supplies enough heat to re-ignite the hydrogen shell source. The E-AGB phase then
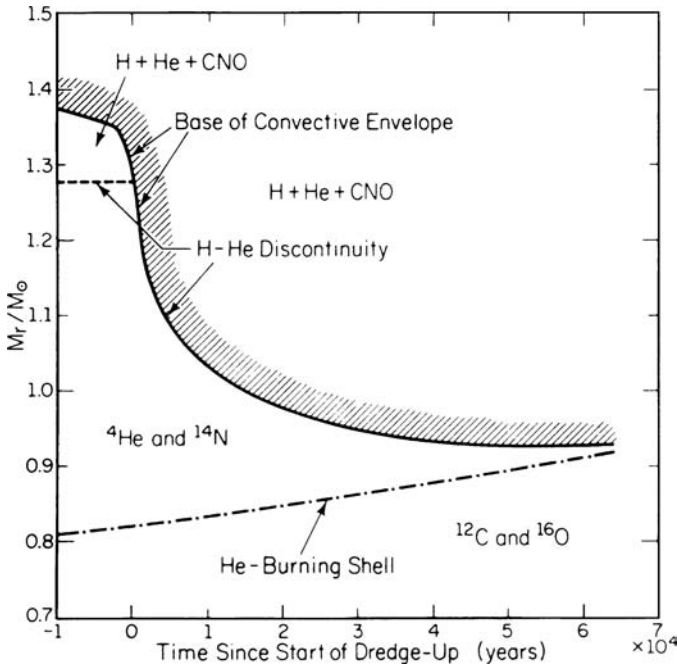
Fig. 5.18. Interior composition of a model 7 $M_\odot$ star during the second dredge-up phase. After Iben (1991).

gives way to a situation where there are two shell-burning sources separated by a small interval in the mass coordinate; this is subject to an instability giving rise to thermal pulses (also called 'helium shell flashes' although in this case degeneracy is not directly involved) and is known as the TP-AGB stage (see Figs. 5.15, 5.19). The instability is a consequence of the high temperature sensitivity of the rate of helium-burning combined with the thinness of the shell in which it occurs: the Thin Shell Instability. Consider a thin shell of thickness D surrounding a sphere of much larger radius r. If the shell expands as a result of local heating, its change in density is magnified compared to that which results in the sphere as a whole:

$$-\frac{d\rho}{\rho} = \frac{dD}{D} = \frac{r}{D}\frac{dr}{r}. \tag{5.108}$$

But from the hydrostatic equation (5.8), for a fixed included mass m, there is a reduction in pressure,

$$-\frac{dP}{P} = 4\frac{dr}{r} = 4\frac{D}{r}\left(-\frac{d\rho}{\rho}\right) < -\frac{d\rho}{\rho} \quad \text{if} \quad \frac{D}{r} < \frac{1}{4}. \tag{5.109}$$

For a perfect gas with $P \propto \rho T$, the temperature must therefore go up, which leads to instability, provided that the temperature sensitivity of the reaction rate is
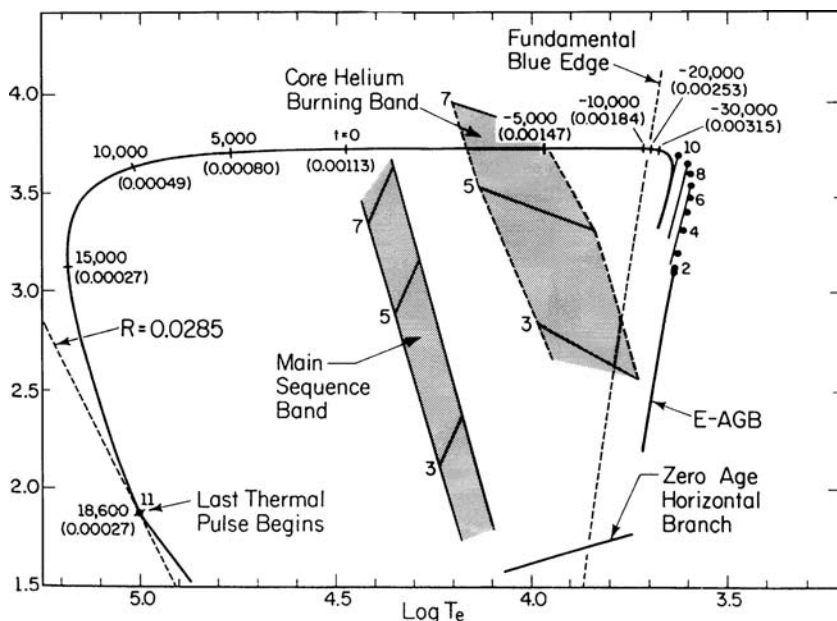
Fig. 5.19. Evolutionary track in the HR diagram of an AGB model of total mass $0.6\,M_\odot$, initial composition $(Y, Z) = (0.25, 0.001 \simeq Z_\odot/20)$. Heavy dots marked 2 to 11 indicate the start of a series of thermal pulses (see Fig. 5.20), which lead to excursions along the steep diagonal lines. Numbers along the horizontal and descending track indicate times in years relative to the moment when an ionized planetary nebula appears and (in parentheses) the mass of the envelope in units of $M_\odot$. $R = 0.0285$ indicates a line of constant radius (R in solar units) corresponding to the white-dwarf sequence. Shaded areas represent earlier evolutionary stages for stars with initial masses 3, 5 and $7\,M_\odot$ and the steep broken line marks the high-temperature boundary of the instability strip in which stars pulsate in their fundamental mode. The y-axis gives $\log L/L_\odot$. Adapted from Iben and Renzini (1983).

high enough to cover the losses. The result of this instability is a series of thermal pulses in which the helium-burning shell greatly increases in luminosity. This causes expansion of the inter-shell region and cooling of the hydrogen-burning shell which is temporarily switched off, and the intense He-burning creates a convective layer ascending through the inter-shell region which is thereby enriched in ^{12}C and ^{22}Ne; in massive stars, this latter generates neutrons through (α, n) reactions and contributes to s-process nucleosynthesis, products of which are also mixed out into practically the whole of the helium layer. Eventually the helium-burning shell is sufficiently expanded and cooled to die down, the inter-shell region contracts and warms up again and the hydrogen-burning shell resumes, contributing the bulk of the star's luminosity, until the next pulse comes along (Fig. 5.20). Resulting changes in surface properties are shown for a low-mass star in Fig. 5.19.
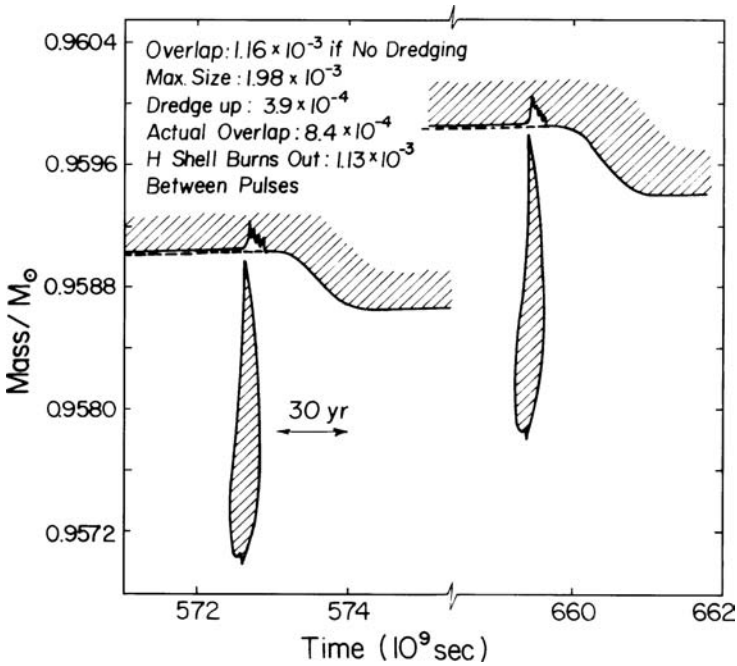
Fig. 5.20. Convective regions during the 15th and 16th pulses in a model of mass 7 $M_\odot$ and solar composition. Shading indicates where convection occurs, and the dashed lines indicate the location of the H–He discontinuity before dredge-up begins. After Iben and Renzini (1983). Copyright by Annual Reviews, Inc.

After the pulse has died down, the outer convection zone penetrates the former inter-shell region (see Fig. 5.20) and brings up carbon and products of the s-process to the surface (this is the third dredge-up process). Furthermore, protons and/or ^{13}C (an alternative neutron source that operates at lower temperatures and therefore in less-massive stars than does the ^{22}Ne source) are probably ingested into the helium layer at some stage (see Chapter 6). Among various mechanisms that might account for this is semi-convective mixing of protons during a third dredge-up episode into the ^{12}C-rich region left behind by the preceding pulse, followed by their conversion to ^{13}C when hydrogen shell-burning is re-ignited. The ^{13}C is then consumed by ^{13}C$(\alpha, n)^{16}$O, mostly during the inter-pulse period. For the process to work, the proton abundance should be comparable to, or less than, the ^{12}C abundance, since an excess of protons would lead to the production of ^{14}N which is a neutron 'poison' that competes with ^{56}Fe as a neutron absorber. Finally, for sufficiently massive stars (details depend on the assumed mixing length, composition, opacities etc.), the base of the outer convection zone becomes hot enough in the intervals between pulses to convert the fresh ^{12}C into ^{14}N (and ^{13}C) by a process known as 'hot-bottom burning'; this is a so-called primary source of nitrogen
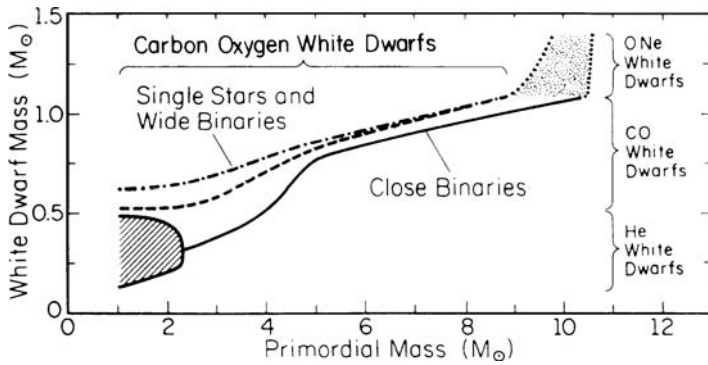
Fig. 5.21. Initial mass – final mass relation for intermediate-mass stars. After Iben (1991).

nucleosynthesis, in which the amount produced is relatively insensitive to the initial chemical composition of the star, whereas the amount produced in the first and second dredge-ups is limited by the initial C and O abundances and these are known as secondary sources. Another consequence of the third dredge-up is the appearance of fresh lithium at the surface of some luminous AGB stars (WZ Cas carbon stars and some giants with masses of around 4 to 6 $M_\odot$ in the Magellanic Clouds). This results from the ^{3}He + ^{4}He $\rightarrow ^7$Be reaction (Cameron & Fowler 1971) at the base of a 'hot-bottom' convective envelope at temperatures of the order of 5×10^7 K, followed by mixing up to the surface where it decays by K-electron capture to ^{7}Li (Sackmann & Boothroyd 1992).

A further effect during evolution up the AGB is mass loss through stellar winds, at an increasing rate as the star increases in luminosity and radius and becomes unstable to pulsations which drive a 'super-wind' in the case of intermediate-mass stars. For stars with an initial mass below some limit, which may be of order 6 $M_\odot$, the wind 'evaporates' the hydrogen-rich envelope before the CO core has reached the Chandrasekhar limiting mass (see Section 5.4.3), the increase in luminosity ceases and the star contracts at constant luminosity, eventually becoming a white dwarf (Figs. 5.15, 5.19). A computed relation between initial stellar mass and the final white-dwarf mass is shown in Fig. 5.21.

The ejected material forms a cool molecular and dusty envelope which initially veils the star from optical observations as it goes through the stages of Mira variable followed by OH-infrared star or infrared carbon star; later the star becomes hot enough to ionize part or all of the expanding gas–dust envelope forming a planetary nebula.

The star continues to burn hydrogen in a thin shell until the bluest point on its evolutionary track, at which point H-burning is switched off and both the H-rich envelope and the He-rich layer contract rapidly. At this point, in most cases, it is

expected that nuclear burning dies out and the remnant cools as a white dwarf. In some cases, however, there can be a final helium flash (Iben, Tutukov & Yungelson 1996) leading to the 'born-again AGB' scenario in which the star is transported back to the AGB and back again to the white dwarf sequence in tens or hundreds of years, exemplified by peculiar variable stars with s-process and/or carbon enhancement such as FG Sge (Gonzalez *et al.* 1998, but see also Jeffrey & Schoenberner 2006) and the R CrB-like Sakurai's object V4335 Sgr (Asplund *et al.* 1999). The hydrogen-deficient carbon stars could be another result.

A group of planetary nebulae known as M. Peimbert's Type I is especially rich in nitrogen (N/O $\simeq$ 1.2), with more or less normal oxygen and modest enhancements of helium and carbon, and probably represents the combined effects of the first and third dredge-ups with hot-bottom burning, whereas in classical carbon stars and other types of planetary nebulae there seems to be more or less normal nitrogen and oxygen with an enhancement of ^{12}C (C/O $\simeq$ 1.3; Kingsburgh & Barlow 1994). Carbon stars tend to be more common in regions of lower metallicity (e.g. the Magellanic Clouds compared to the solar neighbourhood and the Galactic bulge), reflecting the fact that less carbon needs to be dredged up in order to make C/O > 1 when the oxygen abundance is lower in the first place.

Stars that are of too low mass to ignite carbon non-degenerately but of high enough mass to produce a degenerate CO core above the Chandrasekhar limit have been predicted to undergo a 'carbon flash' and explode in a supernova outburst referred to as a Type I$\frac{1}{2}$ supernova (sharing some characteristics of both Types I and II); there is little evidence that this ever happens, except perhaps in very low metallicity stars that lose mass inefficiently, but they could be a subset of Type II. A star at the upper end of the intermediate-mass range may ignite carbon non-degenerately but form a degenerate O,Ne,Mg core, which could either collapse and explode as a Type II supernova or end up as a white dwarf with that composition.

5.11 Interacting binary stars

Among the equipotential surfaces in a system of coordinates rotating with the line joining the two components of a binary star system treated as two point masses, there is a critical equipotential consisting of two so-called Roche lobes which touch each other, as shown in Fig. 5.22. At the contact point, the gravitational attractions of the two stars cancel each other out; thus if one star in the course of expansion from evolution or accretion, or as a result of orbital shrinkage, comes to fill its Roche lobe, the overflowing material is lost to that star and may end up on the other one, normally by way of an accretion disk in which orbital angular momentum is dissipated. In other cases, it may form a common envelope or leave the system altogether. The resulting mass transfer effects may lead to more than one exchange
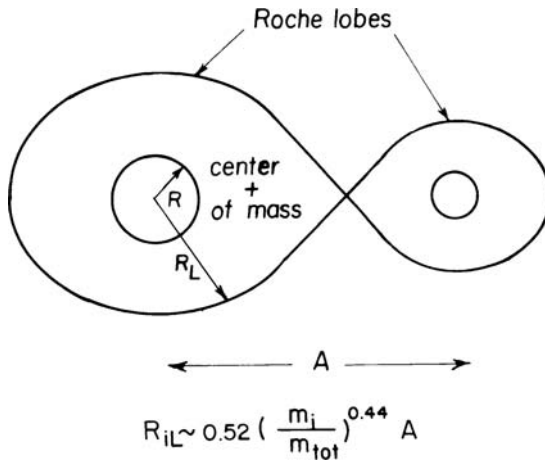
Fig. 5.22. Roche-lobe geometry. Adapted from Iben (1991).

between the initially more massive and the initially less massive component. There can be rich consequences, including the production of cataclysmic variables, novae, Type Ia supernovae and binary X-ray sources from accretion on to a compact star (white dwarf, neutron star or black hole); the appearance of abundance peculiarities of extraneous origin in, e.g., Ba II stars and some varieties of carbon star, notably CH stars, owing to accretion of material from an AGB star on to a normal star; and enhancement of the mass-loss rates from evolving binary components compared to otherwise similar but isolated stars. Since a supergiant or AGB star can reach a radius of the order of 4 astronomical units (800 $R_\odot$), it is evident that effects of this kind can arise in binary stars with (initial) orbital periods of up to several years.

Mass transfer in a red-giant or main-sequence – white dwarf binary system can cause explosive burning processes giving rise to novae. If the accretion rate of hydrogen-rich material does not exceed $6 \times 10^{-8}\ M_\odot\ \mathrm{yr}^{-1}$, unburned hydrogen layers pile up on the surface of the white dwarf. After an envelope of 10^{-5} to $10^{-4}\ M_\odot$ has formed (depending on the mass of the white dwarf), pycnonuclear ignition under degenerate conditions triggers a thermonuclear runaway until the degeneracy is lifted and thermonuclear burning sets in, reaching peak temperatures of maybe $2-3 \times 10^8$ K at densities of the order of 10^3 to $10^4\ \mathrm{gm\,cm}^{-3}$ and going on for $10-1000$ s before the partially burned hydrogen is ejected. During this time there is a sudden rise in luminosity, more or less reversing the previous evolution from AGB tip to white dwarf, followed by fading over weeks or months and a fresh outburst after a suitably long period. The typical energy release in such an outburst is between 10^{46} and 10^{47} erg. The main energy source of the thermal runaway is the fast CNO cycle (Section 5.6.2) in which ^{12}C, ^{14}N and ^{16}O are converted by proton captures in the first second into ^{14}O, ^{15}O and ^{17}F respectively, followed

by ^{17}F(p, γ)^{18}Ne(β^+, ν)^{18}F(p, α)^{15}O; ^{14}O and ^{15}O subsequently β^+-decay after 1 or 2 minutes to ^{14}N and ^{15}N respectively, produced in comparable amounts. If ^{20}Ne and ^{24}Mg are initially abundant, as in an O,Ne,Mg white dwarf giving rise to a neon nova, the fast Ne–Na cycle begins to operate after 10 s or so (owing to slowness of the triggering ^{20}Ne (p, γ) reaction) and may reach up to P and S isotopes (van Wormer *et al.* 1994). The ejected envelope has a small mass, about $10^{-5} M_\odot$, so that the importance of this process in Galactic chemical evolution is confined to rare species like ^{15}N. X-ray burst sources are also thought to result from a thermonuclear runaway, this time from accretion on to a neutron star, which leads to nuclear reactions with still higher temperatures and shorter timescales.

Supernovae of Type I are distinguished by having no hydrogen lines in their spectra, and it was already suggested by Hoyle and Fowler (1960) that they result from explosive carbon-burning in a CO white dwarf. More recently they have been divided into subclasses Ia, Ib and Ic, with different light curves, spectra and progenitor masses (which can be estimated from the stellar populations with which they are associated). Type Ia supernovae occur in galaxies of all types and are not confined to regions of very recent star formation; their spectra at maximum light display absorption lines of Si, Ca, Fe and Ni and their light curves (which are so nearly homogeneous as to allow their use as standard candles) are energized after maximum by the electron capture and positron decay ^{56}Ni(EC, half-life 6.1d)^{56}Co(EC, β^+, ν, half-life 77d)^{56}Fe, just as in the case of Type II's, but involving a larger mass ($\sim 0.6 M_\odot$) of radioactive material. Type Ib have helium features in their spectra and are associated with young stellar populations; they are believed to result from core collapse in stars that have undergone severe mass loss (see Fig. 5.13), possibly as a result of binary interaction, and become helium or WR stars, so that their internal properties relate them more closely to Type II. The same probably applies to Type Ic, which, however, have much weaker helium lines and more rapidly declining light curves, and may result from an initially massive star that has been stripped down to its CO inner core by binary mass transfer; some Type Ic's are 'hypernovae' associated with long-duration γ-ray bursts.

SN Ia (aka thermonuclear supernovae) are believed to result from accretion of material from a companion on to a white dwarf until it reaches the Chandrasekhar limiting mass, at which point it collapses and explodes, although 'sub-Chandrasekhar' scenarios have also been put forward (Woosley & Weaver 1994). Some possible fates of an accreting CO white dwarf, depending on the accretion rate and the initial mass, are shown in Fig. 5.23. The accreted material may come from a normal companion star ('single-degenerate' model; Whelan & Iben 1973), or, in the 'double-degenerate' model of Iben and Tutukov (1984a, 1987), there may be two white dwarfs that merge after orbital shrinkage by the formation of a common envelope followed by radiation of gravitational waves. Possible
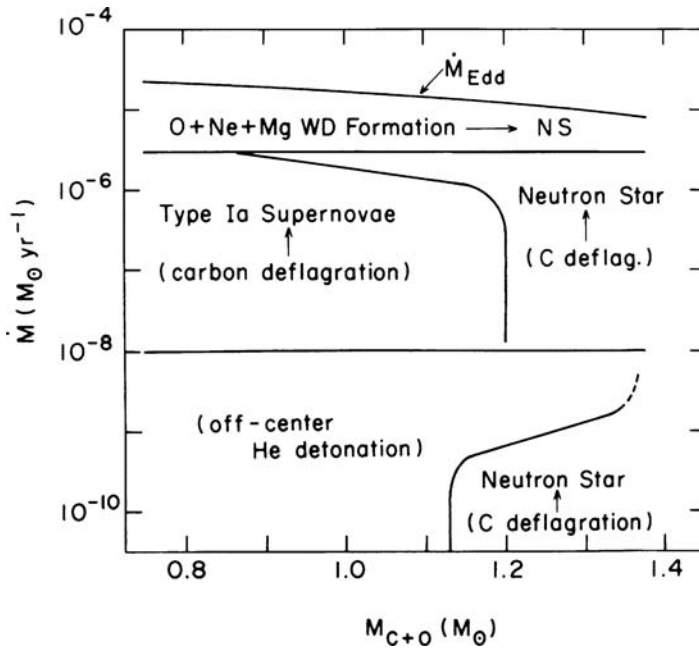
Fig. 5.23. Possible outcomes of accretion on to a CO white dwarf, according to its mass and accretion rate. $\dot{M}_{Edd}$ is the critical (Eddington) rate above which radiation pressure drives material out. After Nomoto and Kondo (1991). Courtesy Ken-ichi Nomoto.

precursors, of the single-degenerate type, are the super-soft binary X-ray sources. Arrival of the accreted material may have a variety of consequences, including the formation of a neutron star; the ignition of helium shell flashes already at masses well below M_{Ch}; resulting detonations of helium and carbon; and deflagration of carbon in which the burning front spreads out at a subsonic speed, which latter seems to give the best fit to observations, although a late detonation (spreading supersonically) may also be involved. The problem with the straightforward detonation scenarios is that they lead to incineration of virtually all the C and O to ^{56}Ni, whereas observations reveal the presence of substantial amounts of lighter elements like Si and Ca. It turns out that, for a reasonably large rate of accretion, hydrogen and helium shell flashes are relatively weak, so that the main effect of accretion is a steady growth in the mass and temperature of the CO core similar to that in an AGB star. When the mass comes close to M_{Ch}, carbon is explosively ignited at the centre and a deflagration wave propagates outwards at a subsonic speed and causes explosive burning (see Fig. 5.24) and disruption of the entire star with an energy of the order of 10^{51} erg. The inner 0.7 $M_\odot$ or so is incinerated to nuclear statistical equilibrium, but the diminution of peak temperature and density with time and distance from the centre of the star allows reasonable quantities of elements from oxygen
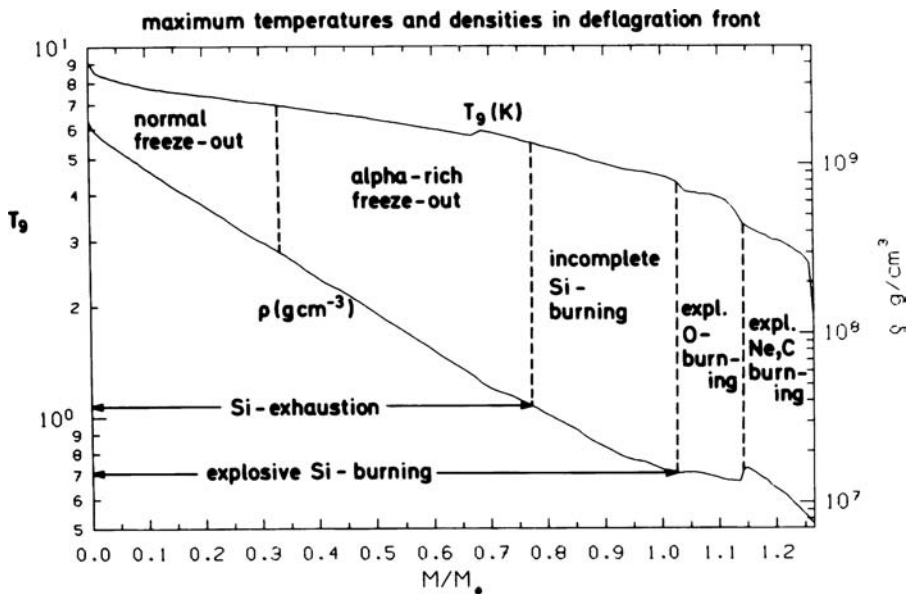
Fig. 5.24. Maximum temperatures and densities calculated for an outward propagating deflagration front in a model (model W7) of an SN Ia explosion from accretion on to a CO white dwarf with initial mass $1\,M_\odot$ at a rate of $4 \times 10^{-8}\,M_\odot\,\mathrm{yr}^{-1}$. Zones of different burning conditions are indicated. After Thielemann, Nomoto and Yokoi (1986). Courtesy Ken-ichi Nomoto.
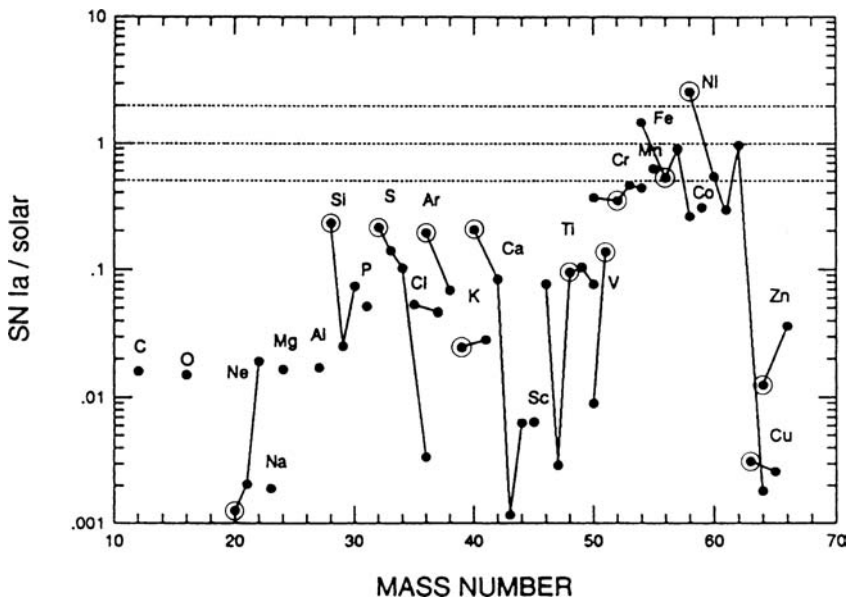
Fig. 5.25. Nucleosynthetic outcome (after radioactive decay) of model W7 for Type Ia supernovae (Nomoto, Thielemann & Yokoi 1984, and Thielemann, Nomoto & Yokoi 1986), compared to Solar-System abundances. Dominant isotopes of multi-isotope elements are circled. Adapted from Tsujimoto (1993).
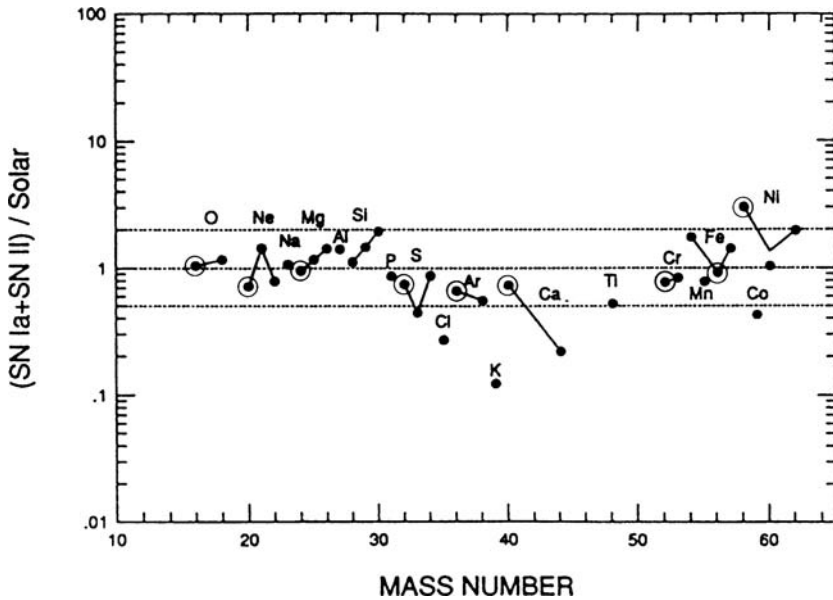
Fig. 5.26. Nucleosynthesis products from SN Ia (Fig. 5.25) and SN II (Fig. 5.12) combined in a ratio of 1:10, compared to Solar-System abundances. (A slightly higher ratio of 1:7 gives optimal fit to elemental, as opposed to individual nuclidic abundances.) Dominant isotopes of multi-isotope elements are circled. Adapted from Tsujimoto (1993).

upwards to survive. The outcome of one of the more successful models is shown in Fig. 5.25, where it can be seen to more or less compensate for the deficiency of iron-group elements expected from Type II supernovae (Fig. 5.12). Figure 5.26 shows the outcome when the two types of supernovae are combined in suitable proportions; the overall fit is fair, but some obvious discrepancies remain.

Notes to Chapter 5

An excellent account of stellar structure and evolution is given in the classic text:

R. Kippenhahn and A. Weigert, *Stellar Structure and Evolution*, Springer-Verlag 1990.

A more recent also very useful text giving applications to observational material for clusters and galaxies and a list of useful websites is

M. Salaris and S. Cassisi, *Evolution of Stars and Stellar Populations*, John Wiley, Chichester, 2005.

These are usefully supplemented (especially for the evolution of close binaries) by the following review article:

I. Iben, Jr, 'Single and Binary Star Evolution', *Ap. J. Suppl.*, **76**, 55 (1991).

Basic physical principles are given, and the consequences of nuclear reactions worked out, in much more detail in the older, but still very useful classic text:

D. D. Clayton, *Principles of Stellar Evolution and Nucleosynthesis*, McGraw-Hill 1968 and University of Chicago Press 1984.

A more up-to-date treatment of many aspects of stellar evolution and nuclear astrophysics is available in the book by

David Arnett, *Supernovae and Nucleosynthesis*, Princeton University Press 1996.

An encyclopaedic account of the physical basis of stellar structure theory is given in the textbook by Cox and Giuli, *Principles of Stellar Structure* (Weiss *et al.* 2004).

Detailed information about specific nuclear reactions at different stages of stellar evolution and the measurement of nuclear reaction cross-sections is given (together with a good overview of the whole of astrophysics) in

C. E. Rolfs and W. S. Rodney, *Cauldrons in the Cosmos*, University of Chicago Press 1988.

Excellent readable elementary introductions to the subject are given by

R. J. Tayler, *The Stars: Their Structure and Evolution*, Cambridge University Press 1994, and

Dina Prialnik, *An Introduction to the Theory of Stellar Structure and Evolution*, Cambridge University Press 2000, while

A. C. Phillips, *The Physics of Stars*, Wiley 1999, gives a readable introduction with a firm grip on the physical foundations.

The question of why stars become red giants after core hydrogen exhaustion has been discussed and argued about in many papers. Notable among these are the numerical experiments of Iben (1993) and an analytical discussion by Faulkner (2005).

An overview of the reaction sequences in all stages from helium- to silicon-burning is given by Arnett (1996). Evolution and explosion of massive stars are reviewed by Nomoto and Hashimoto (1988), and by Woosley, Heger and Weaver (2002). Evolution of intermediate-mass stars is discussed by Iben and Renzini (1983, 1984) as well as in the article by Iben (1991) quoted above.

Tables of stellar opacities computed at Lawrence Livermore National Laboratory for temperatures up to 10^8 K are given by Rogers and Iglesias (1992; see also **http://www-phys.llnl.gov/Research/OPAL/index.html**) and up to 10^7 K by Seaton *et al.* (1994; see also **http://vizier.u-strasbg.fr/topbase/publi.html**).

Abundance anomalies displayed by red giants in globular clusters, and the difficulties that they raise for canonical stellar evolution theory, are discussed, e.g., by Kraft (1994).

Much information on the theoretical and observational aspects of AGB evolution can be found in H. R. Johnson and B. Zuckerman (eds.), *Evolution of Peculiar Red Giant Stars*, Cambridge University Press 1989.

Problems

1. (a) A homogeneous sphere of cold (i.e. pressure-free) gas with density ρ collapses homologously starting from rest. Show that it collapses to a point after a time $(3\pi/32G\rho)^{1/2}$.

(b) Before radiating energy as a result of quasi-static contraction, a proto-star has to generate enough gravitational energy to dissociate molecular hydrogen (4.5 eV) and ionize hydrogen (13.6 eV) and helium (24.6 + 54.4 eV). Show that this leads to a radius

$$\frac{R}{R_\odot} \simeq 50 \frac{M}{M_\odot}. \tag{5.110}$$

2. Compare the Fermi energy, the electrostatic energy due to nearby ions and the thermal energy per electron,
    (a) in a carbon white dwarf, $T = 10^8$ K, $\rho \simeq 10^5$ gm cm^{-3};
    (b) in a hydrogen 'brown dwarf', $T = 5 \times 10^6$ K, $\rho \simeq 10^3$ gm cm^{-3}.

What does this mean for the relative importance of gravity and electrostatic forces in the two cases? Make a rough estimate of the mass of the largest body that can be held up against gravity by electrostatic forces.

3. Verify using Saha's equation (2.48) that the most populated form of the oxygen in the centre of the Sun is fully stripped of electrons (O^{8+}) and estimate the proportion of oxygen having one bound electron (O^{7+}), using the following information:

$T_6 = 15$, $X = 0.5$, $\rho = 100$ gm cm^{-3}, O^{7+} ionization potential = 0.87 keV, $kT \equiv 0.0862\, T_6$ keV, $(m_e kT/2\pi\hbar^2)^{3/2} \equiv 2.4 \times 10^{27}\, T_6^{3/2}$ cm^{-3}, $n_e \equiv \rho/(\mu_e m_H)$.

Given that the absorption cross-section of O^{7+} at the photo-ionization threshold is 10^{-19} cm^2 and that the oxygen abundance is 10^{-2} by mass, find the bound–free opacity (cm^2 gm^{-1}) due to oxygen at that frequency, and compare it to the electron scattering opacity.

Show also that hydrogen has to be fully ionized under these conditions.

4. Derive the formula (5.25) for the Rosseland mean opacity by comparing the transfer equation for K, Eq. (3.15), for monochromatic and integrated radiation.

5. Show that, if the monochromatic opacity varies as $\nu^{-3} T^{-1/2}$ over relevant frequency ranges, the Rosseland mean varies as $T^{-3.5}$, as in Eq. (5.26).

6. Show that the Eddington limiting luminosity, at which the gradient of radiation pressure balances gravity near the surface, is given by

$$L_{\text{Edd}} = 4\pi cGM/\kappa \qquad (5.111)$$

and estimate its value in units of the solar luminosity $L_{\odot} = 4 \times 10^{33}$ erg s^{-1} when κ is given by electron scattering.

7. From Eq. (5.8), derive the inequality

$$P_{\text{c}} < \left(\frac{\pi}{6}\right)^{1/3} GM^{2/3}\rho_{\text{c}}^{4/3} \qquad (5.112)$$

for the central pressure of a star of mass M. Supposing that a fraction β of the pressure comes from an ideal gas and the remainder $(1 - \beta)P_{\text{c}}$ from radiation pressure, find an upper limit to the value of $(1 - \beta)/\beta^4$ and estimate numerical values for stars of masses 1, 20 and 40 $M_{\odot}$. (The radiation density constant $a = 7.56 \times 10^{-15}$ erg cm^{-3} deg^{-4}; $G = 6.67 \times 10^{-8}$ dyn cm^2 gm^{-2}.)

8. Using the parameters for the centre of the Sun given in Problem 3, estimate the degeneracy parameter from Eq. (5.41).

9. Supposing that at the surface of a star $(m = M,\ l = L)$, the opacity is given by a formula of the form

$$\kappa = \kappa_0 P^p T^{-t}, \qquad (5.113)$$

use the hydrostatic equation (5.6) and the radiative transfer equation (5.22) to show that the pressure is related to the temperature by

$$P^{p+1} - P_s{}^{p+1} = \frac{16\pi ac}{3\kappa_0} \frac{GM}{L} \frac{p+1}{4+t} (T^{4+t} - T_{\text{eff}}{}^{4+t}), \qquad (5.114)$$

where P_s is the pressure at the photosphere where the temperature is T_{eff}. Thus, as long as $t \geq -2$ or so, which holds while hydrogen is mainly positively ionized and neutral hydrogen the main opacity source, the pressure–temperature relation below the surface is quite insensitive to the values at the surface itself, justifying the 'zero boundary condition' $P_s \simeq T_s \simeq 0$. A different situation arises when hydrogen is mainly neutral and opacity comes from H$^-$.

10. Supposing that the atmospheric opacity of a 'fully' convective star is proportional to the abundance of easily ionized metals (which at low temperatures replace hydrogen as the source of free electrons to make H$^-$), correct Eq. (5.65) for the Hayashi track by finding an appropriate power of Z to multiply by.

11. Use the Saha-type equilibrium that exists between α-particles, ^{8}Be and the 7.654 MeV excited state of ^{12}C to estimate the production rate per unit volume of

ground-state ^{12}C nuclei in helium with a density of 10^5 gm cm^{-3} and a temperature of 10^8 K (neglecting screening factors). The mass excesses are

^{4}He 2.425 MeV
^{8}Be x
^{12}C 0.000

and the spins are zero in all cases. The contribution of the width of the ^{12}C** excited state from γ-ray emission is $\Gamma_\gamma = 0.003\,67$ eV $\ll \Gamma_\alpha$. The frequency associated with 1 eV is 2.42×10^{14} s^{-1}.

12. Use the formula Eq. (2.44) for chemical potential to show that the equilibrium number abundance of a nucleus i with mass number $A_i = Z_i + N_i$, partition function u_i and binding energy B_i with respect to free protons and neutrons is given by

$$Y_i = \left(\frac{\rho}{m_H}\right)^{A_i-1} \frac{u_i}{2^{A_i}} A_i^{3/2} \left(\frac{2\pi\hbar^2}{m_H kT}\right)^{3(A_i-1)/2} e^{B_i/kT} Y_p^{Z_i} Y_n^{N_i}. \tag{5.115}$$

13. When the core of a massive star exceeds the Chandrasekhar limit, it collapses and energy is absorbed by photo-disintegration of ^{4}He through the reaction

$$^4\text{He} + \gamma\ (28.3\ \text{MeV}) \rightarrow 2p + 2n. \tag{5.116}$$
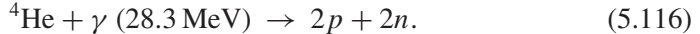
Assuming thermal equilibrium at a density of 10^8 gm cm^{-3}, find the temperature at which half the helium has been dissociated.

14. Using Eqs. (5.105) and (5.106), show that the time spent by a low-mass star evolving up the RGB in a given magnitude interval (and hence the relative number of stars in that interval) is predicted to vary approximately as $L^{-0.9}$. (In practice, the variation in globular clusters is more like $L^{-0.5}$.)

15. Estimate the amount of energy generated when a carbon white dwarf with the mass of the Sun is incinerated to ^{56}Ni (mass excess -53.9 MeV) and compare it with the energy needed to disrupt the star if its radius is 5000 km and its density assumed uniform. (1 MeV $\equiv 1.6 \times 10^{-6}$ erg; $G = 6.67 \times 10^{-8}$ dyn cm^2 gm^{-2}.)

6

Neutron capture processes

Dust as we are, the immortal spirit grows
Like harmony in music; there is a dark
Inscrutable workmanship that reconciles
Discordant elements.
W. Wordsworth, *The Prelude*

6.1 Introduction

As was mentioned in Chapter 1, elements above the iron group are not effectively produced by reactions between charged particles. Instead – apart from the rare 'p-process' nuclides – they result from a succession of neutron captures on a seed nucleus – predominantly ^{56}Fe. Broadly speaking, these neutron capture processes are of two distinct types: the slow or s-process, where neutrons are added on a long timescale compared to that of most β-decays, and nuclides are built ascending the β-stability valley up to ^{209}Bi (see Figs. 1.5, 6.1); and the rapid or r-process, in which very neutron-rich unstable nuclei are built up under extreme conditions, followed by a series of β^--decays (accompanied by fission of the heaviest nuclei) which continue after freeze-out leading to nuclides on the neutron-rich side of the stability valley (see Figs. 1.5, 6.9). The s-process occurs in cool giant stars, notably during mixing episodes in the course of AGB evolution, whereas the r-process may occur during SN II outbursts, or just possibly in other high-energy events related to neutron stars.

6.2 The s-process

6.2.1 The physical environment

A significant clue to the order of magnitude of neutron fluxes, temperatures and densities relevant to the s-process comes from the outcome of branchings, such as
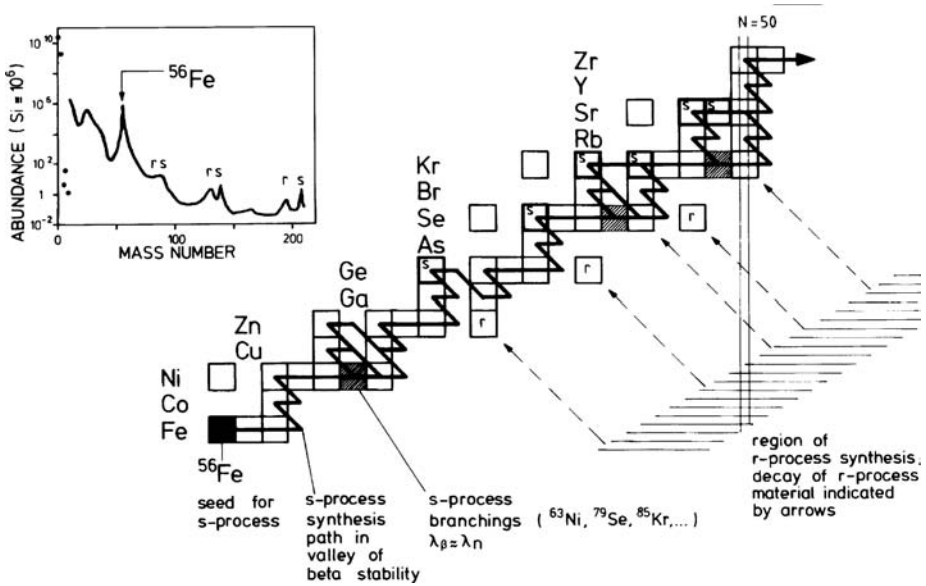
Fig. 6.1. Part of the s-process path, showing some s-only nuclei (marked 's') and some branchings between n-capture and β^--decay (shaded boxes), which give an idea of relevant neutron densities and temperatures. After Käppeler, Beer and Wisshak (1989). Copyright by IOP Publishing Ltd. Courtesy Franz Käppeler.

those shown in Fig. 6.1. The shortest lifetimes (e.g. 42 s for ^{104}Rh, 54 hours for ^{115}Cd) lead to β-decay preceding n-capture in all cases, whereas the longest (e.g. 7 Myr for ^{107}Pd) make the nucleus effectively stable. Branchings occur when

$$(t_{1/2})^{-1} \sim \sigma\phi, \tag{6.1}$$

where $t_{1/2}$ is the β-decay half-life (possibly less than under laboratory conditions if the nucleus has low-lying excited states), σ is the neutron capture cross-section and ϕ the neutron flux $n_n\langle v \rangle$. B^{2}FH noticed that ^{151}Sm (90 yr) decays along the s-process path, whereas ^{99}Tc (2×10^5 yr) does not, leading to timescales of the order of hundreds or thousands of years. However, the argument is complicated by the temperature dependence of both neutron-capture and some β-decay rates and consideration of these factors enables permitted regions of the (n_n, kT) plane to be identified. A crude argument, based on a typical temperature of 10^8 K (characteristic of helium-burning), giving $\langle v \rangle \simeq 10^8$ cm s^{-1}, a typical cross-section of 100 mb (see Fig. 6.2) and a lifetime of 300 yr gives

$$n_n \sim 10^7 \text{ cm}^{-3}. \tag{6.2}$$

More detailed considerations (Käppeler, Beer & Wisshak 1989) lead to a temperature range of up to 4×10^8 K and neutron densities up to about 10^8 cm^{-3}.
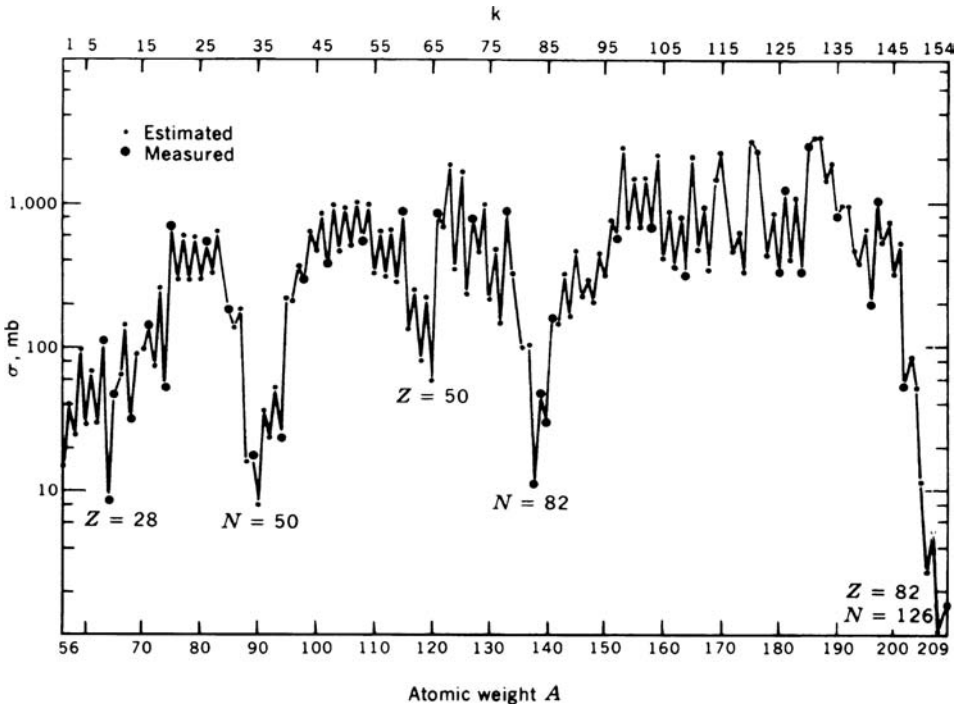
Fig. 6.2. Neutron-capture cross-sections at energies near 25 keV. Very large dips occur at the magic numbers. After Clayton (1984). Copyright by the University of Chicago. Courtesy Don Clayton.

Electron-density effects on β-decay lifetimes also enable the total density to be placed in the range 2500 to 13 000 gm cm^{-3}; all these parameters are characteristic of helium shell-burning zones as expected.

6.2.2 Analytical theory of the s-process

The classical analysis of the s-process assumes a simple chain starting from ^{56}Fe as the seed. The independent variable is the neutron 'irradiation', 'exposure' or 'fluence'

$$\tau \equiv \int \phi \, dt = \int n_n \langle v \rangle dt \tag{6.3}$$

and the abundances N_i are governed by the differential equation

$$\frac{dN_i}{d\tau} = \sigma_{i-1} N_{i-1} - \sigma_i N_i ; \quad 56 \leq i \leq k \leq 209 \tag{6.4}$$

with the initial conditions

$$N_{56}(0) = 1; \quad N_{i \neq 56}(0) = 0. \tag{6.5}$$

Thus, in a steady state, $dN_i/dt = 0$, one has $\sigma N = $ const., which actually holds over considerable ranges of mass number (thus being usable as a local approximation), but not globally (except if $\tau \to \infty$); in particular, it breaks down near the magic numbers (see Fig. 6.3).

The general solution of Eq. (6.4) is

$$N_k(\tau) = \sum_{i=56}^{k} C_{ki} e^{-\sigma_i \tau}, \qquad (6.6)$$

where

$$C_{56\,56} = 1; \ C_{57\,56} = -C_{57\,57} = \frac{\sigma_{56}}{\sigma_{57} - \sigma_{56}};$$

$$C_{ki} = \prod_{j=56}^{k} \left(\frac{\sigma_j}{\sigma_j - \sigma_i} \right); \ j \neq i. \qquad (6.7)$$

This solution is of little practical use, because small inaccuracies in $\sigma_j - \sigma_i$ lead to large errors in large terms with alternating signs, swamping the true differences. Clayton *et al.* (1961) derived an approximation, based on the Poisson-like distribution obtained when all the cross-sections are equal:
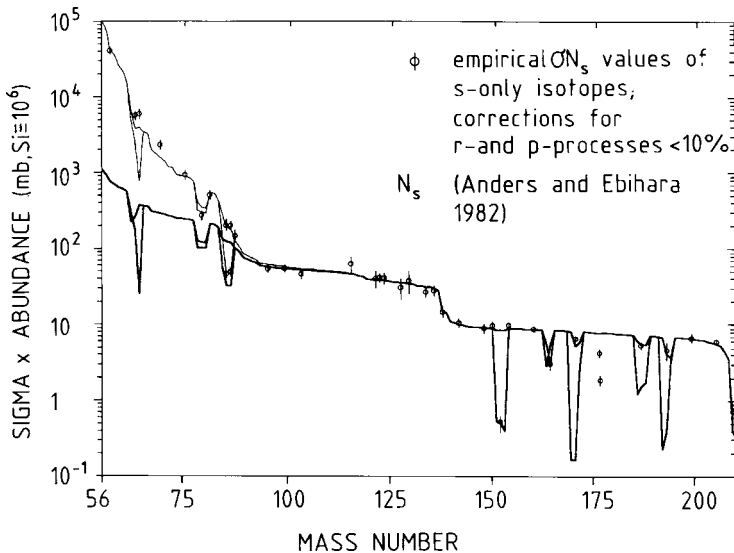
Fig. 6.3. Product σN of abundance and neutron capture cross-section for s-only nuclides in the Solar System. The main and weak s-process components are shown by the heavy and light curves respectively. Units are mb per 10^6 Si atoms. After Käppeler, Beer and Wisshak (1989). Copyright by IOP Publishing Ltd. Courtesy Franz Käppeler.

$$\sigma_k N_k(\tau) = \frac{\lambda_k^{m_k} \tau^{m_k-1}}{\Gamma(m_k)} e^{-\lambda_k \tau}; \quad \lambda_k \equiv \frac{\langle \sigma^{-1} \rangle_k}{\langle \sigma^{-2} \rangle_k};$$

$$m_k \equiv \frac{\langle \sigma^{-1} \rangle_k^2}{\langle \sigma^{-2} \rangle_k} \quad (k - 55). \tag{6.8}$$

This formula for a single exposure was found not to give a good fit to the Solar System σN curve for s-only isotopes. Seeger, Fowler and Clayton (1965) found, however, that a much better fit is obtained by assuming an exponential distribution of exposures given by the probability distribution

$$p(\tau) \, d\tau = e^{-\tau/\tau_0} \, d\tau/\tau_0. \tag{6.9}$$

The resulting abundances are given by

$$\tilde{N}(\tau_0) = \int_0^\infty N(\tau) \, p(\tau) \, d\tau, \tag{6.10}$$

which is a Laplace transform of the solution for a single exposure (Clayton & Ward 1974).

The Laplace transformation makes the solution of the differential equation (6.4) very easy. Operating on that equation as in Eq. (6.10), one obtains

$$\int_0^\infty \frac{dN_{56}}{d\tau} e^{-\tau/\tau_0} \frac{d\tau}{\tau_0} = -\sigma_{56} \tilde{N}_{56}(\tau_0). \tag{6.11}$$

Integrating the lhs of Eq. (6.11) by parts,

$$\tilde{N}_{56}(\tau_0) - 1 = -\tau_0 \sigma_{56} \tilde{N}_{56}(\tau_0). \tag{6.12}$$

Similarly,

$$\frac{1}{\tau_0} \tilde{N}_{57}(\tau_0) = -\sigma_{57} \tilde{N}_{57}(\tau_0) + \sigma_{56} \tilde{N}_{56}(\tau_0) \tag{6.13}$$

etc. This results in a series of *algebraic* equations, easily solved from the top down. Dropping the 'tildes',

$$\sigma_{56} N_{56} = \frac{1}{\tau_0} \left(1 + \frac{1}{\tau_0 \sigma_{56}} \right)^{-1}; \tag{6.14}$$

$$\sigma_{57} N_{57} = \frac{1}{\tau_0} \left(1 + \frac{1}{\tau_0 \sigma_{56}} \right)^{-1} \left(1 + \frac{1}{\tau_0 \sigma_{57}} \right)^{-1}; \tag{6.15}$$

$$\sigma_k N_k = \frac{1}{\tau_0} \prod_{i=56}^{k} \left(1 + \frac{1}{\tau_0 \sigma_i} \right)^{-1}. \tag{6.16}$$

Thus, as long as $\tau_0 \sigma_i$ is large, σN declines slowly with increasing atomic mass number k, but when σ becomes very small at the magic neutron numbers, there is a sudden drop (Fig. 6.3). (Such behaviour is characteristic of any distribution

Table 6.1. *Parameters of the two s-process components*

| | Fraction of Fe seeds, % | | Exposure τ or τ_0 | | n_c |
	Single	Exponential	Single	Exponential	Exponential
Main	—	0.057 ± 0.004	—	0.30 ± 0.01	10.7 ± 0.7
Weak	0.32	0.26	0.23	0.06 ± 0.01	1.4 ± 0.4

Adapted from Gallino (1989) and Käppeler *et al.* (1990).

of neutron exposures that declines gradually with τ; the exponential formula is mathematically convenient and has a physical interpretation that will be described below.) Equation (6.10) with $\tau_0 \simeq 0.3\,\text{mb}^{-1}$ (for cross-sections at $kT = 30\,\text{keV}$) gives an excellent fit to Solar-System abundances above $A = 80$ (Kr) to 90 (Zr), apart from the dips caused by branchings, and this exponential distribution of exposures is known as the main component of the s-process; the quality of the fit obtained from such simple considerations is arguably the most elegant result in the whole of nucleosynthesis theory, although the real situation is considerably more complicated. For lower mass numbers, an additional component, known as the weak component, is required, corresponding to either a single exposure with $\tau = (4\,\text{mb})^{-1}$ or an exponential distribution with $\tau_0 = (16\,\text{mb})^{-1}$; of these, the single exposure (probably arising in helium- and carbon-burning zones of a massive star) seems to be more successful in fitting certain details (Raiteri *et al.* 1993; Rauscher *et al.* 2002). There has also been a suggestion of a need for a third, 'strong' component to account completely for lead and neighbouring elements, but these can result from the main process at low metallicities where a fixed amount of ^{13}C operating on a reduced density of Fe nuclei results in larger values of the parameter n_c, defined below (Clayton 1988; Busso, Gallino & Wasserburg 1999).

Table 6.1 shows some other best-fit parameters to Solar-System s-process abundances. The seed nucleus is basically ^{56}Fe; light nuclei have low cross-sections (but can act as neutron 'poisons', e.g. ^{14}N for the ^{13}C(α, n) neutron source), whereas heavier nuclei are not abundant enough to have a major influence. Certain nuclidic ratios, e.g. ^{37}Cl/^{36}Ar and ^{41}K/^{40}Ca, indicate that under 1 per cent of Solar-System material has been s-processed.

Another parameter is the mean number n_c of neutrons captured by an iron seed, given by

$$n_c = \frac{\sum_{57}^{209}(A-56)\,N(A)}{N(56)} = \frac{1}{\tau_0}\sum_{57}^{209}\frac{A-56}{\sigma_A}\prod_{i=56}^{A}\left(1+\frac{1}{\tau_0\,\sigma_i}\right)^{-1}. \quad (6.17)$$

The mean exposure $\tau_0 = (3\,\text{mb})^{-1}$ implies $n_c \simeq 10$, which is quite a strong constraint on the physical environment, including in particular the abundance of the neutron source relative to iron. Thus the $^{22}\text{Ne}(\alpha, \text{n})^{25}\text{Mg}$ source, which arises naturally in helium-burning at temperatures of 3 to 4×10^8 K, is unlikely to contribute the bulk of the main component: the temperature and fluxes are too high and n_c is too low (because about 3/4 of the neutrons generated are captured by Ne and its neighbours acting as neutron 'poisons'). Furthermore, the Mg isotope ratios are observed to be unchanged in carbon stars, whereas one could expect an enhancement of the heavy isotopes ^{25}Mg, ^{26}Mg by a factor of the same order as that of the heavier s-process elements, i.e. an order of magnitude. The ^{22}Ne source could provide the weak component, however, and it is thought to make a minor contribution to the main one (see Fig. 6.5). The $^{13}\text{C}(\alpha, \text{n})$ source, which works at lower temperatures (10^8 K) and can fit the constraints under certain conditions, requires a non-classical mixing process (see Section 5.10.4) leading to a need for some arbitrary assumptions in the computational treatment.

6.2.3 An interpretation of the exponential exposure distribution

Originally, the exponential distribution of exposures was thought to be an accident of Galactic reprocessing, but it was shown by Ulrich (1973) that it may arise naturally as a result of successive thermal pulses in a single AGB star (Fig. 6.4; see Fig. 5.19). During an inter-pulse period, the helium core increases in mass as a consequence of hydrogen shell-burning by an amount ΔM_α; almost all of this is mixed into the inter-shell convective region of mass M_{isc} generated by the next pulse, giving rise to an exposure $\Delta\tau$ to slow neutrons (the source of the neutrons is discussed below). Thus, a fraction $\Delta M_\alpha / M_{\text{isc}} \equiv 1 - r$ receives an exposure $\Delta\tau$ for the first time, while the remaining fraction r overlaps with the previous pulse and has undergone an exposure of $2\Delta\tau$ (or more). A fraction r^2 overlaps two previous pulses, etc. Consequently, when a steady state is reached after a sufficient number of pulses, the probability of an exposure $n\Delta\tau$ is

$$(1 - r)\, r^{n-1} = \frac{1 - r}{r}\, r^{\tau/\Delta\tau} \propto e^{-\tau/\tau_0}, \qquad (6.18)$$

where

$$\tau_0 = \Delta\tau / \ln(1/r). \qquad (6.19)$$

Figure 6.4 also illustrates a mechanism whereby ^{13}C may be introduced into the inter-shell convection zone of a low- or intermediate-mass star. When that zone reaches its maximum extension, it covers almost the whole inter-shell region apart from a thin interval marked A. The mass of this region decreases from about
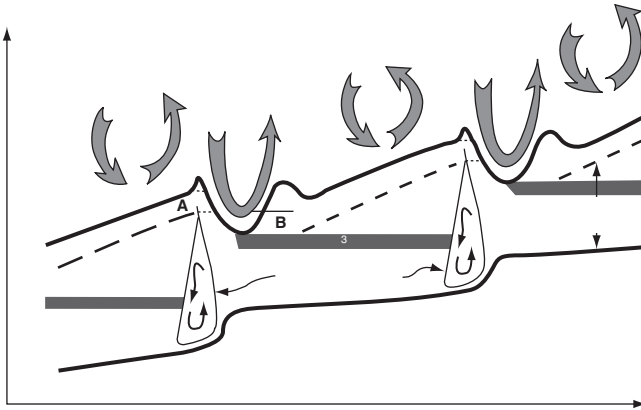
Fig. 6.4. Schematic view of ingestion during and after a thermal pulse in an AGB star. Pulses appear on an expanded scale owing to their short duration ($\sim$ 300 yr) compared to the inter-pulse period ($\sim 10^4$ to 10^5 yr). After Busso, Gallino and Wasserburg (1999). Reprinted with kind permission of Annual Reviews, Inc. Courtesy Maurizio Busso.

2×10^{-3} $M_\odot$ in the first cycles to about 10^{-4} $M_\odot$ in the final ones, as the mass of the helium core increases from about 0.5 $M_\odot$ to about 0.7 $M_\odot$. Immediately after the pulse, the outer layers of the star expand and cool, so that the H-burning shell is temporarily extinguished and the envelope convection may extend downward, dredging up H- and He-burning products to the surface. The material thus dredged up, labelled B, has two parts with different compositions: layer A contains only H-burning ashes, whereas the inner part has He-burning products like carbon and s-process nuclei. Some mechanism, e.g. a semi-convective region, driven by partial carbon recombination and consequent increases in opacity in the expanding material, or rotational shear or some other mechanism, may cause a small amount of protons from the border of the envelope convection zone at its maximum downward extension to enter the carbon-rich zone and generate ^{13}C and a little ^{14}N in a tiny pocket (represented by the black bands in Fig. 6.4) when the H-burning shell re-ignites. It was thought originally that the ^{13}C then survived unchanged until ingested by the next thermal pulse, during which it would generate neutrons from the ^{13}C$(\alpha,$ n$)^{16}$O reaction, supplemented by a small contribution from ^{22}Ne$(\alpha,$ n$)^{25}$Mg, as shown in Fig. 6.5. The amount of ^{13}C involved is a matter of guesswork; values in the range 10^{-6} to 10^{-5} $M_\odot$ are considered in some current models (Wasserburg *et al*. 1994).

Figure 6.5 shows a computation of the development of physical conditions during a pulse, according to the old picture. The ^{13}C source is activated at a relatively low temperature at the moment when the inter-shell convection zone reaches up to the level of the pocket. Later, after exhaustion of ^{13}C, the temperature rises
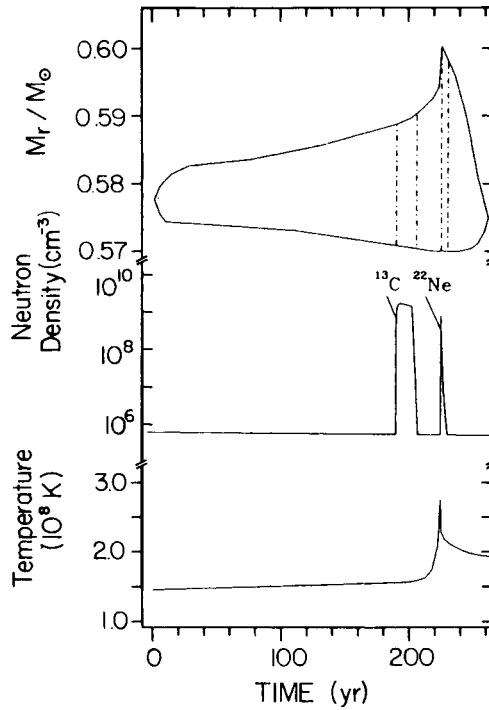
Fig. 6.5. Development of the convective region, neutron density from ^{13}C and ^{22}Ne sources and maximum temperature as functions of time during a thermal pulse in a low-mass star with $Z \simeq Z_\odot/3$, which seems to give the best fit to Solar-System abundances from the main s-process. However, more recent models imply that ^{13}C is all used up in the radiative phases. After Käppeler *et al.* (1990). Courtesy Maurizio Busso and Claudia Raiteri.

and the ^{22}Ne source is briefly activated, contributing significantly to a few isotopes that depend on temperature-sensitive branchings. In general, the results from this stellar evolutionary model agree well with the classical analytical treatment of Section 6.2.2, when the latter is corrected for branchings (with a neutron density of $(3.4 \pm 1.1) \times 10^8$ cm^{-3} and a temperature $kT = 29 \pm 5$ keV). The model leads to a mean neutron exposure $\tau_0 = 0.3$ mb^{-1} (for 30 keV), resulting from $\Delta\tau(30\,\text{keV})$ $= 0.17$ mb^{-1} per pulse and an overlap ratio $r = 0.6$ (see Eq. 6.19), in excellent agreement with the classical analysis of the main component. However, it now becomes clear that at least two very different timescales are involved, the short time of each neutron exposure $\Delta\tau$ (in this case 12 yr) and the long time between pulses (2×10^5 yr). Most nuclei have total lifetimes $\tau = 1/(\lambda_n + \lambda_\beta)$ that are either so long or so short that the pulsed nature of the exposure makes no difference, but an exception among the main s-process branch points is ^{85}Kr (shown by a shaded box in Fig. 6.1) with $\tau = 4$ yr at a temperature of 29 keV, so that there should be a noticeable effect on the abundance of its descendants ^{86}Kr and ^{87}Rb; in the detailed

stellar model, however, this goes away because the temperature is only 1.5×10^8 K (13 keV) at the relevant times (Käppeler *et al.* 1990). However, it became clear in the late 1990s that these models do not give a good fit to all details of the σN curve, and in more recent stellar evolution models, which follow the temperature evolution after the decay of a pulse in considerable detail using revised opacity tables and recipes for convection, as well as revised nuclear reaction rates and allowance for mass loss, the ^{13}C is already consumed in the inter-pulse period. This leads to a relatively low neutron density of the order of 10^7 cm^{-3}, which helps to solve any problem with the ^{85}Kr branching (Lambert *et al.* 1995); thus the ^{13}C neutron pulse shown in Fig. 6.5, that was the basis of the argument for an exponential exposure distribution, goes away, although the ^{22}Ne pulse is still present (Straniero *et al.* 1995; Gallino *et al.* 1998).

In the newer picture, reaction products from the ^{13}C pocket in the inter-shell zone (ISZ) during the radiative phase, rather than ^{13}C itself, having undergone a large single exposure $\sim$0.4 mb^{-1}, are ingested into the next convective pulse, by which they are spread throughout the ISZ and subjected to a small irradiation at high temperature and neutron density before being mixed out into the envelope by the surface convection zone. The resulting probability distribution of neutron exposures, $\rho(\tau)$, is much flatter than the exponential, and more closely represents a combination of a few single exposures (Gallino *et al.* 1998), although the broad pattern of ledges and precipices in the σN curve shown in Fig. 6.3 remains. With some freedom in choice of the detailed distribution of ^{13}C in the ISZ, and the mass and metallicity of the progenitor stars, the new models give a good fit to the abundances of s-only nuclides above ^{88}Sr in the Solar System and in AGB stars at various metallicities.

6.2.4 Surface abundances in red giants

Table 6.2 gives an overview of some of the stages of stellar evolution where carbon and/or s-process anomalies occur (see Fig. 3.37). The C/O ratio increases down the series. In addition to the types listed there, there are infrared carbon stars such as IRC +10216,[1] proto-planetary nebulae and a whole zoo of peculiar carbon stars, including J stars (strong ^{13}C as in the case of HD 52432 shown in Fig. 1.7) and hydrogen-deficient carbon stars which can be cool, e.g. R Cor Bor, RY Sag and HD 137613 shown in Fig. 1.7, or hot (when they look like extreme helium stars); such stars may have lost their envelopes by binary mass transfer, or they may be 'born-again' AGB stars.

---

[1] IRC stands for the CalTech infrared (2 µm) catalogue.

Table 6.2. *Spectral types of red giants*
with carbon and/or s-process anomalies

	$\leftarrow T_{\text{eff}}$		
	$L \rightarrow$		
RGB		AGB	
G, K, M	M	Mira	OH-IR
	MS	"	"
Ba II	S	"	$C \leq O$
Ba II	SC	"	$C \simeq O$
CH, Ba II	CS	"	$C > O$
(Early) R	N	"	C-stars

Planetary nebulae are often even more rich in carbon than cool carbon stars, and those classified by M. Peimbert as Type I are rich in nitrogen, indicating effects of hot-bottom burning in intermediate-mass progenitor stars. The s-process elements are not normally detectable in PN or their central stars, but a remarkable case is that of FG Sagittae, the central star of a fossil planetary nebula, which has cooled in the course of the twentieth century from around 25 000 K to around 5000 K at constant bolometric luminosity. This star suddenly showed an enhancement of s-process elements in its atmosphere between 1965 and 1972 (see Jeffrey & Schoenberner 2006, and references therein).

Observations of carbon stars in the Magellanic Clouds indicate luminosities between $10^{3.5}$ and $10^{4.3}$ $L_\odot$, in agreement with theoretical estimates of where the TP-AGB phase of evolution sets in for stars with initial mass 1 to 5 $M_\odot$ (see Fig. 5.19). The warmer and less luminous Ba II and CH stars, with about 100 $L_\odot$ (see Fig. 3.37), therefore presumably have never reached this stage of evolution, but rather have acquired processed material by binary mass transfer from an initially more massive companion which is now a white dwarf. These stars, being warmer, have spectra that are much easier to analyze than are those of AGB stars, and a Ba II star played an important role in early investigations of s-process nucleosynthesis (see Fig. 1.8). The same phenomenon of mass transfer may also be responsible for carbon and s-process enhancements in more luminous stars, e.g. some S stars which have similar composition to Ba II stars; a plausible criterion for this is the absence of technetium (present in some S stars such as R And shown in Fig. 1.8, but absent in others), which does not decay very much between pulses but would have done so over the much longer periods that have elapsed since the termination of the mass transfer episode. CH stars, with strong G-bands of CH and s-process enhancement, occur at various luminosities (see Fig. 3.37) and in different population groups, and are also believed to result predominantly from mass transfer. Certain CH stars of Population II, with low metallicity, display an unusually high

ratio of heavy s-process elements (e.g. Ba, Pb) to lighter ones (e.g. Sr), indicating high values of τ_0 and n_c; this is an expected result from a fixed amount of ^{13}C injection combined with a low abundance of iron seeds.

Figure 6.6 shows some observational correlations between s-process and carbon enhancements and between lighter and heavier (main) s-process products. There is a steady progression from M to MS to S to N stars, giving a fair correlation between s-elements and ^{12}C as one might expect from the thermal pulsing model, but this is not shared by J and R stars which have enhanced ^{13}C. The relation between lighter and heavier (main) s-process products is consistent in most cases with a mean exposure $\tau_0 \simeq 0.3 \, \mathrm{mb}^{-1}$ (for $kT = 30 \, \mathrm{keV}$), about the same as in the Solar System, which suggests that these low- to intermediate-mass carbon stars are typical of the progenitors of the Solar-System distribution. Jura (1989) has estimated the rate at which carbon and s-processed material are ejected into the ISM near the Sun by winds from these stars. From the Cal Tech 2 μm infrared survey, there are about 40 carbon stars per kpc^2 with a typical scale height of 200 pc, corresponding to an initial mass of order $1.5 \, M_\odot$, and the typical mass loss rate is around
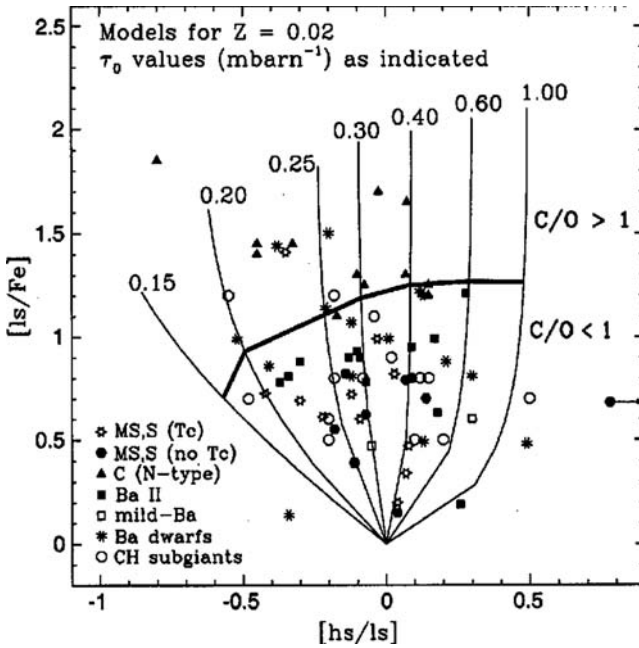
Fig. 6.6. Correlation of heavy (Ba, Nd etc.) and light (Y, Zr) s-process enhancements in AGB stars, with theoretical curves based on the old exponential-exposure model. $\tau_0 = 0.3$ corresponds approximately to the main s-process distribution in the Solar System. After Busso, Gallino and Wasserburg (1999). Reprinted with kind permission of Annual Reviews, Inc. Courtesy Maurizio Busso.

$2 \times 10^{-7} \, M_\odot \, \text{yr}^{-1}$, but dominated by a few stars with a much higher mass loss rate of over $10^{-5} \, M_\odot \, \text{yr}^{-1}$. The total mass loss rate from carbon stars, estimated from the IRAS $60 \, \mu$m survey, is within a factor of 2 or so $2 \times 10^{-4} \, M_\odot \, \text{kpc}^{-2} \, \text{yr}^{-1}$, leading over 10^{10} yr to an output of $2 \, M_\odot \, \text{pc}^{-2}$. Enriched by an order of magnitude and mixed with the total surface density of about $50 \, M_\odot \, \text{pc}^{-2}$, this would be enough to supply an average s-process abundance of 0.4 solar, which is a reasonable average for Pop I stars.

Thus the ^{13}C neutron source (with a little assistance from ^{22}Ne) in thermally pulsing low- and intermediate-mass stars is well established as the chief source of the main component of s-process nuclides in the Solar System. It is not quite clear, however, whether the τ_0 parameter is something unique, or just the average over a more-or-less broad distribution of values; nor is it clear why a similar s-process pattern is seen in stars that are metal-deficient by factors of up to 100 (see Pagel & Tautvaišienė 1997).

6.3 The r-process

6.3.1 Introduction

A separate neutron capture process is needed for neutron-rich nuclides by-passed by the s-process and for species above ^{209}Bi. A possible path for this 'rapid' or r-process is shown in Fig. 6.9.

The abundance curve for r-process products in the Solar System is obtained from 27 r-only nuclides, combined with numbers obtained by subtracting predicted abundances of an s-process contribution in the other cases (Fig. 6.7); the latter are correspondingly less accurate, particularly when the s-process contribution dominates, as is shown by the error bars in the figure. The result is a fairly smooth curve, with broad peaks corresponding to the progenitor magic numbers $N = 82$, 126, and a third peak centred on $A = 165$. Figure 6.8 shows the r-process curve in its relation to the corresponding curves for the s- and p-processes. It is presumably just a coincidence that in the local Galaxy the s- and r-process curves have about the same general level.

For purposes of comparison with stellar abundances, it is useful to have the relative contributions of s- and r-processes to the various elements (as opposed to nuclides) in the Solar System, because in most cases only element abundances without isotopic ratios are available from stellar spectroscopy. At the same time, elements formed in one process may often be expected to vary by similar factors in the course of stellar and Galactic evolution, but to be found in differing ratios to elements formed in another process. Relative contributions are listed for some key elements in Table 6.3.
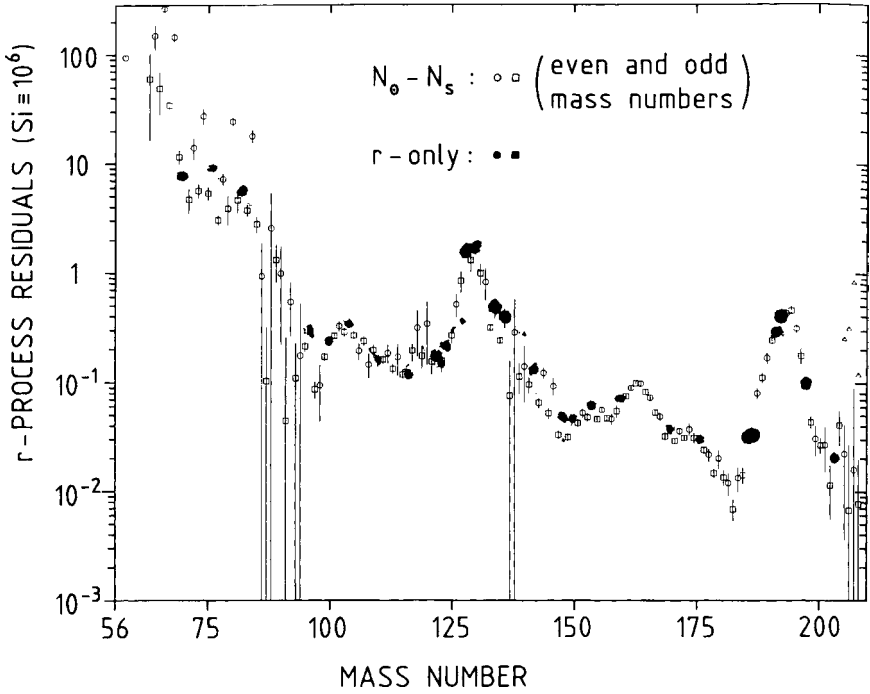
Fig. 6.7. r-process abundances in the Solar System. Filled circles represent r-only nuclides, while open circles with error bars show the result of subtraction of a calculated s-process contribution. After Käppeler, Beer and Wisshak (1989). Copyright by IOP Publishing Ltd. Courtesy Franz Käppeler.

6.3.2 Physical environment of the r-process

A possible path for the r-process is shown in Fig. 6.9. The iron seed nuclei need to capture many neutrons leading to unstable nuclei with very short β-decay half-lives, demanding a high neutron density:

$$t\,(n, \gamma) \ll t_\beta \simeq 10^{-3} \text{ to } 1\,\text{s} \;\Rightarrow\; n_n > 10^{19}\,\text{cm}^{-3}. \tag{6.20}$$

Such neutron densities are presumably associated with very high temperatures, leading to reverse (γ, n) reactions. At each Z, neutrons are added up to a so-called waiting point (which defines the r-process path); in the 'waiting-point approximation', (n, γ) and (γ, n) reactions balance, so that for given Z, there is a Saha-type equilibrium

$$\frac{n(A + 1, Z)}{n(A, Z)} \simeq 10^{-34}\, n_n\, T_9^{-3/2} e^{Q/kT}, \tag{6.21}$$

where Q is the neutron separation energy. Increasing n_n thus drives the abundance peak where $N(A + 1, Z) = N(A, Z)$ towards lower values of Q, i.e. closer
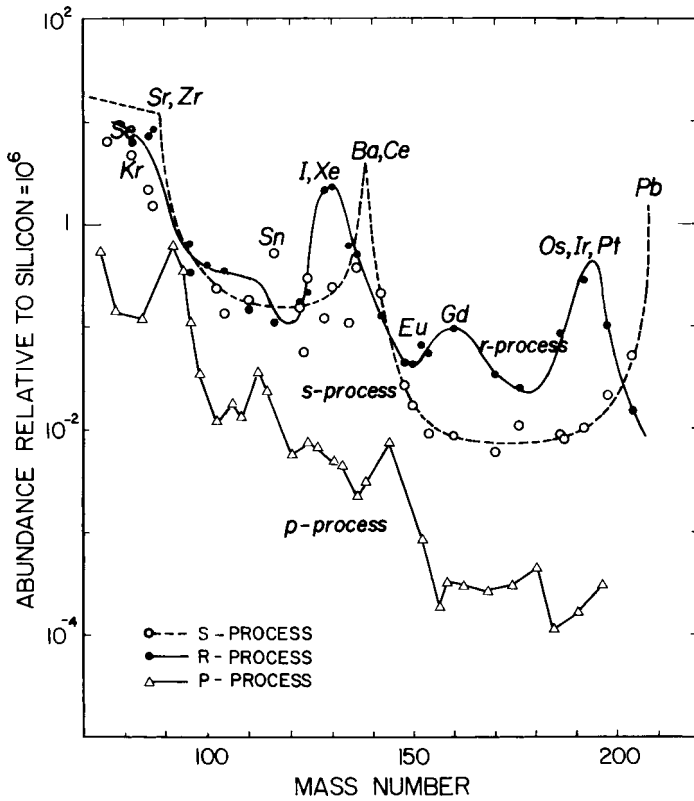
Fig. 6.8. Abundance curves for s-process (broken line), r- and p-process products (solid lines) in the Solar System. Adapted from Cameron (1982).

to the neutron drip line where $Q = 0$; the path shown in Fig. 6.9 was computed taking $Q = 2\,\text{MeV}$ for the abundance peak, corresponding to $T = 10^9\,\text{K}$; $n_n = 10^{24}\,\text{cm}^{-3}$. However, the estimation of $Q(A + 1, Z)$ – or in other words the determination of where in the (N, Z) plane one has $Q = 2\,\text{MeV}$ – depends on understanding the interaction between nucleons sufficiently well that one can estimate nuclear masses in unknown territory; the tentative neutron drip line shown in Fig. 6.9 is not the one used in computing the r-process path shown there. The abundance peak will actually be a few units wide in A or N because of odd–even effects in the neutron separation energy; these effects also have the result that neutron capture always terminates at an even value of N.

From time to time, a β-decay occurs, increasing Z by 1 unit; this leads to an increase in Q (corresponding to the increased distance above the neutron drip line) and consequently to further neutron captures until Q is again reduced to the appropriate value and a further β-decay occurs. At the magic numbers, this leads to a vertical zig-zag track, paralleling the rise in the neutron drip line. Along this track,

Table 6.3. *Relative r and s contributions to some
elements in the Solar System*

Element	log N	s-weak	s-main	r
37 Rb	2.40	.14	.39	.47 ± .10
38 Sr	2.93	.09	.77	.14 ± .07
39 Y	2.22	.04	.85	.11 ± .06 :
40 Zr	2.61	.02	.78	.20 ± .03
56 Ba	2.21	.01	.88	.11 ± .02
57 La	1.20	.01	.75	.25 ± .08
58 Ce	1.61	.01	.77	.23 ± .01
59 Pr	0.71	.01	.45	.54 ± .09
60 Nd	1.47	.00	.46	.53 ± .03
62 Sm	0.97	.00	.30	.70 ± .03
63 Eu	0.54	.00	.03	.97 ± .06
66 Dy	1.15	.00	.12	.88 ± .15

Numbers in the first 4 rows (apart from the error
estimates) are taken from Raiteri, Gallino and Busso
(1992). The others are based on data for individual
isotopes given by Käppeler, Beer and Wisshak (1989).
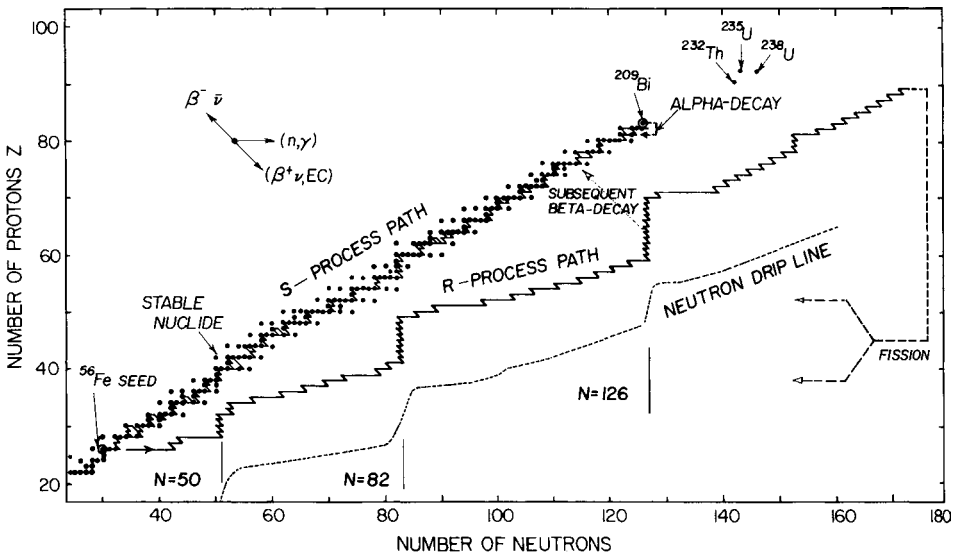
Fig. 6.9. Neutron capture paths in the N, Z plane. The r-process path was cal-
culated for a temperature of 10^9 K and a neutron density of 10^{24} cm^{-3} (Seeger,
Fowler & Clayton 1965). The dotted curve shows a possible location of the neu-
tron drip line after Uno, Tachibana and Yamada (1992). Adapted from Rolfs and
Rodney (1988).

each neutron capture is followed by a β-decay until the nucleus comes so close to the β-stability valley that its β-decay half-life becomes long enough for the chain of neutron captures to resume. In the 'steady-flow approximation', the chain of β-decays is assumed to reach a steady state, so that the abundance of a given element (fixed Z) is proportional to its β-decay lifetime at the waiting point,[2] and this is preserved in a freeze-out. After freeze-out, each nucleus decays at leisure to the nearest stable isobar. The final abundances for given T, n_n therefore depend essentially only on nuclear masses and β-decay rates (which themselves depend on nuclear masses, *inter alia*); the abundance peaks are due to the relatively long β-decay lifetimes of the magic-numbered progenitors (especially those nearest to the β-stability valley) and neutron capture cross-sections do not come in.

The r-process path is terminated by (neutron-induced or β-delayed) fission near $A_{max} = 270$, feeding matter back into the process at around $A_{max}/2$, followed by recycling as long as the neutron supply lasts, assuming sufficient seed nuclei to start the process off. The number of heavy nuclei is thus doubled at each cycle, which could take place in a period of a few seconds. β-delayed fission also occurs after freeze-out, when the β-decay leaves nuclei with $A \geq 256$ or so with an excessive positive charge (see Eq. 2.90).

In modern computations, the waiting-point approximation is replaced by detailed dynamical calculations in which neutron capture cross-sections are significant, particularly during the freeze-out. Alternatively, improved fits to abundances can be obtained by approximating the dynamical process with some combination of waiting-point calculations with different sets of parameters. However, all the parameters depend on estimates for nuclei that are far from stability; relevant measurements are currently in progress using radioactive beams (e.g. Kratz 2001) and are helping to refine theoretical nuclear models.

The site of the r-process is also not clear, but it seems that the conditions needed to reproduce Solar-System r-process abundances may hold in the hot bubble caused by neutrino winds in the immediate surroundings of a nascent neutron star in the early stages of a supernova explosion (see Fig. 6.10). Circumstantial evidence from Galactic chemical evolution supports an origin in low-mass Type II supernovae, maybe around $10\,M_\odot$ (Mathews, Bazan & Cowan 1992; Pagel & Tautvaišienė 1995). Another possibility is the neutrino-driven wind from a neutron star formed by the accretion-induced collapse of a white dwarf in a binary system (Woosley & Baron 1992) leading to a 'silent supernova' (Nomoto 1986). In stars with extreme metal-deficiency, the heavy elements sometimes display an abundance pattern characteristic of the r-process with little or no contribution from the s-process, and the

---

[2] More precisely, the inverse of the average decay constant of the various isotopes, weighted by their abundance according to the Saha equation expressed roughly by Eq. (6.21).
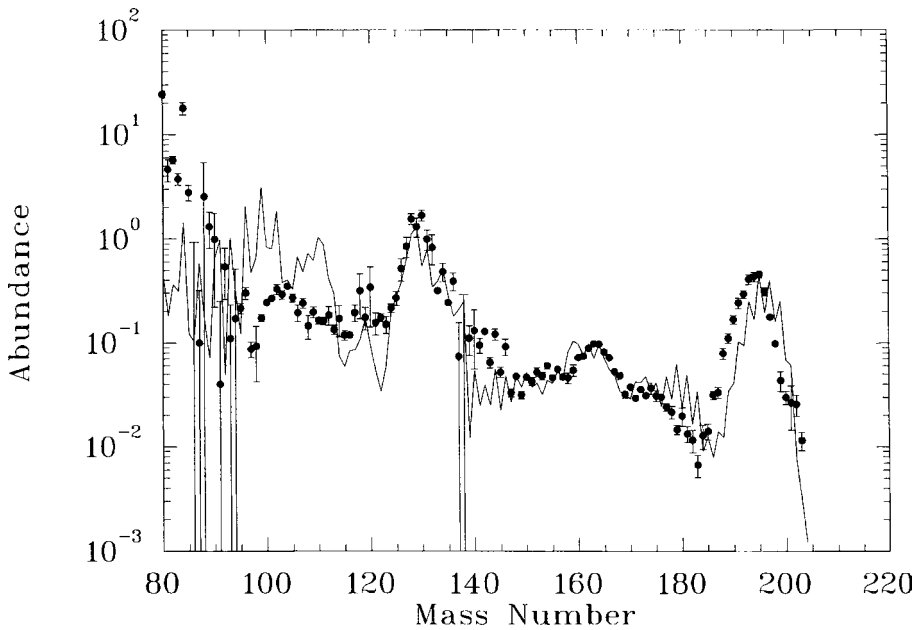
Fig. 6.10. Results of a dynamical calculation of the r-process in the hot neutrino bubble inside a 20 $M_\odot$ supernova (continuous curve) compared to the observed Solar-System abundance distribution (filled circles). After Woosley *et al.* (1994). Courtesy Brad Meyer.

pattern is remarkably close to that found for r-process elements in the Solar System, even in cases where r-process elements are highly overabundant relative to iron; in other cases there are s-process contributions and other differences which suggest that at least two distinct r-processes are involved (see Section 10.3.6).

Notes to Chapter 6

D. D. Clayton, *Principles of Stellar Evolution and Nucleosynthesis*, McGraw-Hill 1968, University of Chicago Press 1984, gives a very instructive account of both s- and r-processes. Some more recent developments are described in C. E. Rolfs and W. S. Rodney, *Cauldrons in the Cosmos*, University of Chicago Press 1988.

An excellent review of the s-process is given in the article by

F. Käppeler, H. Beer and K. Wisshak, *Rep. Prog. Phys.*, **52**, 945 (1989), while the evolution of stars through the AGB stage, with consequences for the s-process, is comprehensively reviewed by

M. Busso, R. Gallino and J. G. Wasserburg, *Ann. Rev. Astr. Astrophys.*, **37**, 239 (1999).

Modern dynamical calculations of the r-process are described by Cowan, Thielemann and Truran (1991ab), Takahashi, Witti and Janka (1994) and Woosley *et al.* (1994). Chen *et al.* (1995), Langanke and Wiescher (2001), Thielemann *et al.* (2001) and Kratz (2001) discuss the nuclear physics issues. Goriely and Arnould (2001) discuss the estimation of yields and their uncertainties.

The origin of the p-nuclei is discussed by Lambert (1992) and by Rayet *et al.* (1995).

Problems

1. Solve the differential equation (6.4) for the case when all neutron capture cross-sections are equal and show that it leads to the Poisson distribution for a single exposure τ. Use this to derive an equivalent to Eq. (6.16) for this case when there is an exponential distribution of exposures as in Eq. (6.9).

2. Given that seed nuclei are exposed to a flux of neutrons at $T = 1.5 \times 10^8$ K, $n_n = 10^9 \, \text{cm}^{-3}$ for 20 years during a pulse, and $\tau_0 = 0.3 \, \text{mb}^{-1}$, estimate the overlap fraction r between successive inter-shell convective zones.

3. Show that, for β-decay with highly relativistic electrons, the decay rate is proportional to $Q_\beta{}^5$ (the Sargent rule).

7

Galactic chemical evolution: basic concepts and issues

It ain't necessarily so.
It ain't necessarily so.
De t'ings dat yo' li'ble
To read in de Bible.
It ain't necessarily so.
George and Ira Gershwin, *Porgy and Bess*

7.1 Introduction

Different aspects of the evolution of galaxies include **dynamical**, involving diffuse material ('gas', which will be understood to include dust), stars and dark matter; **thermal** (mainly affecting the gas); **photometric + spectrophotometric** (involving stars and gas); and so-called **galactic chemical evolution** (GCE) which is not really about chemistry (an important topic in its own right) but concerns the origin and distribution of nuclear species (loosely referred to as elements) in stars and gas. True insights into the origin and evolution of galaxies need studies of all these different aspects and their inter-relations, but there are several results of GCE that can be at least partially understood using only the very broadest ideas about other poorly understood aspects (e.g. the physics of galaxy and star formation) and this makes GCE a topic that is worth studying in its own right. At the same time, there are still many uncertainties, both in the underlying theory of stellar evolution, nucleosynthesis and mass loss and in the galactic context in which these basic element-forming processes take place. These limit the extent to which safe deductions can be made and motivate one to use the simplest possible models. The present chapter describes some basic principles, while the following one will discuss some specific models and related observational results.

7.2 The overall picture

The general picture has been shown (very schematically!) in Fig. 1.1. The Big Bang leads to significant initial abundances of H, D, ^{3}He, ^{4}He and ^{7}Li in the primordial intergalactic medium (Chapter 4). The IGM is assumed to condense into galaxies consisting initially of gas (probably enclosed in dark-matter halos) which then cools, collapses and makes stars. The star formation may take place either on a short timescale (as appears to have happened in the formation of spheroidal systems like elliptical galaxies and the bulges and halos of spirals) or on a long timescale (in the formation of disk components in spiral and irregular galaxies in which substantial quantities of gas are still present). This picture may, however, be seriously oversimplified, as there is evidence that sudden violent star formation is often triggered by interactions and mergers, and such effects may be involved in the formation of many or even all spheroidal systems (see Chapter 11). In any case, galaxy formation is followed and/or accompanied by star formation leading to synthesis of heavier elements and modification of primordial abundances: D is destroyed by stellar activity, ^{4}He is mildly topped up and ^{3}He and ^{7}Li are both created and destroyed by stars.

When stars are formed, there are broadly three things that can happen to the interstellar medium as a result of their evolution (see Chapter 5). Small stars with less than about 1 solar mass have such long lifetimes that essentially nothing happens (except perhaps minor effects of flares and dwarf novae): they simply serve to lock up part of the gas and remove it from circulation, but they remain visible today as archaeological tracers of the composition of the ISM at the time and place where they were formed. Middle-sized stars (say 1 to 9 $M_\odot$) undergo various dredge-up processes in which first some ^{12}C is changed into ^{13}C and ^{14}N and later (in the third dredge-up) ^{3}He, ^{4}He, ^{7}Li, ^{12}C, ^{14}N and s-process elements are synthesized to varying degrees. The products can be seen in carbon stars and some planetary nebulae, and they are expelled in the form of stellar winds and PN, leaving behind a degenerate core (usually a white dwarf) which serves to lock up additional material in the course of time. Close binaries in this mass range can undergo still more dramatic effects as a result of mass transfer; in particular SN Ia, which contribute substantially to the nucleosynthesis of iron, are believed to result from a white dwarf which accretes enough mass from a companion (possibly even merging with a companion white dwarf) to exceed the Chandrasekhar limiting mass, ignite the degenerate CO core and disintegrate completely. Above about 9 $M_\odot$ we have the third category of stars, the big ones, which complete their evolution in well under 10^8 years and ignite carbon non-degenerately, whereafter (owing largely to neutrino losses) they rapidly evolve to core collapse. In the standard picture, the core becomes a neutron star and the rest is expelled in a supernova explosion (Type II

and some others) in which earlier nucleosynthesis products are ejected after partial modification through explosive nucleosynthesis in the inner layers. There are, however, considerable uncertainties in the range of initial stellar masses in which this picture holds, and the more massive stars could collapse into black holes with or without a previous SN outburst. Before completing their evolution, massive stars also undergo mixing and mass loss episodes of many different kinds, manifested by Wolf–Rayet stars, luminous blue variables like η Carinae and the circumstellar shells (presumably resulting from winds in the red supergiant phase) of certain WR stars and supernovae like the radio source Cassiopeia A and SN 1987A in the Large Magellanic Cloud. These all show evidence of CNO processing.

The net result of all these processes is to produce a 'standard' or 'local Galactic' abundance distribution in our vicinity with typical mass fractions $X \simeq 0.7$ for hydrogen, $Y \simeq 0.28$ for helium and $Z \simeq 0.01$ to 0.02 for heavier elements consisting chiefly of O, C, N, Ne, Mg, Si and Fe (see Fig. 1.4).

7.3 Ingredients of GCE models

To put together a model for the chemical evolution of galaxies, one needs the following ingredients:

  (i) Initial conditions.
 (ii) A picture of the end-products of stellar evolution, i.e. which stars eject how much of their mass in the form of various heavy elements after how much time?
(iii) The initial mass function (IMF) which gives the relative birthrates of stars with different initial masses.
(iv) A model of the total star formation rate as a function of time, gas mass, gas density and/or many other parameters including stochastic variables.
 (v) Assumptions about all other relevant processes in galactic evolution besides the birth and death of stars, such as mixing between different phases of the interstellar medium, large-scale flows within the galaxy and exchange of material with the intergalactic medium.

7.3.1 Initial conditions

Mostly one assumes that we begin with pure gas with primordial abundances from the Big Bang. But there are also models with a 'prompt initial enrichment' or 'initial nucleosynthesis spike'. The latter could represent either a hypothetical pre-galactic or proto-galactic process involving preferentially high-mass objects (Truran & Cameron 1971) or prior enrichment of the system by products from some neighbouring more evolved system, e.g. of the disk of the Galaxy by the bulge or the halo.

Table 7.1. *Representative stellar data*

	On zero-age main sequence (ZAMS):					τ_{ms} Myr or	τ_{tot} Myr or
$M_{init.}$ $(M_\odot)$	log $L/L_\odot$	T_{eff} (10^3 K)	Sp	M_V	(B−V)	Gyr[a]	Gyr[b]
120	6.2	53(59)				3.0(2.9)	3.9(3.2)
60	5.7	48(52)				3.5(3.9)	4.0(4.3)
40	5.4	44(48)	O5	−5.6	−0.32	4.4(5.1)	5.0(5.5)
20	4.6	35(39)	O8	−5.0	−0.31	8.2(9.4)	9.0(10.2)
12	4.0	28(32)	B0.5	−4.0	−0.28	16(18)	18(20)
7	3.3	21(25)	B2	−1.5	−0.22	43(45)	48(50)
5	2.8	17(21)	B4	−0.8	−0.19	94(88)	107(100)
3	1.9(2.1)	12.2(16.1)	B7	−0.2	−0.12	350(290)	440(340)
2	1.2(1.4)	9.1(12.2)	A2	1.4	0.05	1.16(0.86)	1.36(1.03)
1.5	0.68(0.92)	7.1(9.6)	F3	3.0	0.40	2.7(1.84)	(2.0)
1.0	−0.16(0.15)	5.64(6.71)	G5	5.2	0.65	10.0(7.3)	
0.9	−0.39(−0.07)	5.30(6.31)	K0	5.9	0.89	15.5(10.7)	
0.8	−0.61(−0.31)	4.86(5.86)	K2	6.4	0.94	25(15)	

[a] Time to end of core H-burning.
[b] Time to end of C- or He-burning.
Sources: Schaller *et al.* (1992); Meynet *et al.* (1994); Tinsley (1980); Allen (1973).

7.3.2 *End-products of stellar evolution*

In principle these should be predictable from theory, but in practice there are many grey areas such as the effects of rotation, convective mixing, mass loss, the mechanism of stellar explosions, nuclear reaction rates such as $^{12}C(\alpha, \gamma)^{16}O$, the evolution of close binaries and the corresponding mass limits between which various things happen for differing initial chemical compositions. Figure 5.14 shows a version of what may happen in single stars with different initial masses and two metallicities, $Z \simeq Z_\odot$ and $Z \simeq Z_\odot/20$.

Other representative data for stars with different initial masses are given in Table 7.1. Numbers in brackets refer to $Z = 0.001$, $Y = 0.24$, others to $Z = 0.02$, $Y = 0.28$, i.e. near solar. The luminosities of the most massive stars are quite insensitive to Z.

The contributions of different stars to nucleosynthesis depend on their initial mass and chemical composition, their mass loss history in the course of evolution and effects of close binaries (especially SN Ia). When mass loss is small, as is believed to be the case for low metallicities, the distribution of 'primary' elements (those synthesized directly from hydrogen and helium) in ejecta from massive stars is mainly the result of hydrostatic evolution with some modifications to deeper layers resulting from explosive nucleosynthesis in the final SN outburst, classically

associated with SN II (see Chapter 5). The resulting production of He, C and O is then quite insensitive to initial chemical composition as such, although it will be affected by the tendency of mass loss to increase with metallicity, especially for the biggest stars. There is also the possibility that stars above some initial mass limit – which could itself depend on metallicity – may collapse into black holes instead of leaving a neutron star remnant. Production of other elements, often referred to as 'secondary', such as ^{14}N and ^{22}Ne, will depend on the initial abundance of their progenitors (mainly CNO), while that of many odd-numbered elements, such as Na and Al, may depend on the neutron excess and hence again on the initial chemical composition.

Some sample results of calculations of stellar yields, i.e. the mass of a nuclear species freshly synthesized and ejected from a star of given initial mass and chemical composition, are given in Tables 7.2, 7.3 and 7.4. The last column of Table 7.2 gives an IMF-integrated yield which can be compared with the Solar-System abundances.

According to detailed modelling of nuclear evolution in massive stars by Weaver and Woosley (1993), Solar-System relative abundances of nearly all isotopes with $16 \leq A \leq 46$ are reproduced within a factor of 2 or better after purely hydrostatic evolution, when certain adjustments are made to the assumed $^{12}C(\alpha, \gamma)^{16}O$ rate (see Fig. 5.11). The subsequent explosion affects only rare species in this mass range (which will also depend on progenitor metallicity), as well as affecting those with $A \geq 44$. However, even for the lighter elements substantial uncertainties and discrepancies remain. Serious uncertainties arise from the treatment of convection (Langer & Henkel 1995; Langer 2004). Furthermore, for stars of higher metallicity, e.g. $Z = 0.02$ (approx. solar) and high mass ($M_{init} > 35 M_{\odot}$ or so), significant mass loss changes the outcome considerably and the uncertainties are correspondingly greater. Nucleosynthesis of helium and carbon leads to the ejection of substantial amounts of these elements in winds before the onset of core collapse, while at the same time the final masses (and hence those of the He and CO cores) are drastically reduced, leading to corresponding reductions in the amounts of heavy elements that are finally ejected. Further complications arise if stars above a certain upper mass limit collapse into black holes rather than leaving a neutron-star remnant, because such stars will still contribute the elements ejected in winds without contributing those in the SN ejecta. This can cause drastic changes in certain element:element ratios, e.g. dY/dZ or C/O (Maeder 1992, 1993). Tables 7.3 and 7.4 give Maeder's calculations of nucleosynthesis from massive stars undergoing respectively modest and strong mass loss.

Intermediate-mass stars with $M_{init} > 3$ to a mass M_{up} somewhere between 5 and 8 $M_{\odot}$, depending on chemical composition and evolutionary details, undergo three dredge-up episodes in the course of evolution, the first one during the first

Table 7.2. *Theoretical yields of selected species from massive stars*

Species	20 $M_\odot$			25 $M_\odot$			Yield
Ref.	1	2	3	1	2	3	3
^{12}C		(0.29)	(0.13)		(0.53)	(0.22)	(4.1E–4)
2.4E-3	0.22	0.32	0.21	0.41	0.61	0.14	6.8E–4
^{14}N		(3.7E−3)	(0.013)		(4.6E−3)	(9.2E−3)	(2.8E–5)
7.8E-4	0.064	0.062	0.072	0.081	0.072	0.084	2.4E–4
^{16}O		(1.4)	(2.2)		(2.3)	(3.8)	(8.0E–3)
6.4E-3	2.2	1.4	1.0	3.3	2.4	2.2	6.1E–3
^{20}Ne		(0.54)	(0.63)		(0.53)	(1.2)	(1.4E–3)
1.2E-3	0.07	0.54	0.29	0.54	0.72	0.65	1.7E–3
^{22}Ne		(0.0020)	(0.0012)		(0.0028)	(0.0015)	(3.4E–6)
8.5E-5	0.020	0.030	0.009	0.028	0.051	0.017	2.8E–5
^{23}Na		(3.2E−3)	(1.8E−3)		(3.6E−3)	(8.1E−3)	(8.2E–6)
3.8E-5	2.2E−3	0.013	0.012	0.013	0.024	0.014	5.4E–5
^{24}Mg		(0.16)	(0.24)		(0.15)	(0.18)	(6.7E–4)
5.5E-4	0.067	0.13	0.069	0.12	0.13	0.21	4.1E–4
^{27}Al		(4.4E−3)	(7.0E−3)		(3.7E−3)	(5.0E−3)	(2.5E–5)
6.6E-5	0.012	0.019	8.6E−3	0.026	0.031	0.023	6.5E–5
^{28}Si		(0.10)	(0.13)		(0.24)	(0.12)	(7.1E–4)
7.3E-4	0.44	0.16	0.094	0.35	0.24	0.12	4.6E–4
^{32}S		(0.044)	(0.056)		(0.11)	(0.055)	(2.9E–4)
3.9E-4	0.20	0.066	0.048	0.15	0.12	0.044	2.0E–4
^{36}Ar		(0.009)	(0.010)		(0.021)	(0.009)	(4.2E–5)
8.8E-5	0.05	0.011	0.007	0.023	0.021	0.007	3.0E–5
^{39}K		(1.9E−5)	(1.4E−5)		(3.8E−5)	(1.5E−5)	(1.4E–7)
4.1E-6	1.0E−4	1.4E−4	1.4E−4	5.8E−4	3.7E−4	6.8E−5	3.4E–7
^{40}Ca		(0.008)	(0.009)		(0.019)	(0.008)	(3.3E–5)
7.0E-5	0.027	0.009	0.0050	0.017	0.016	0.0057	2.4E–5
^{48}Ti		(1.8E−4)	(1.4E−4)		(2.0E−4)	(1.2E−4)	(5.0E–7)
2.5E-6	2.3E−4	1.8E−4	7.4E−5	2.0E−4	2.0E−4	1.7E−4	5.7E–7

1. Rauscher *et al.* (2002); $Z = 0.02$, including wind mass loss.
2. Chieffi and Limongi (2004); $Z = 0.02$. Numbers in brackets are for $Z = 0.001$. No wind mass loss assumed.
3. Nomoto *et al.* (2006), including wind mass loss, $Z = 0.02$, with numbers in brackets for $Z = 0.001$.
Species are given with their proto-solar abundance by mass fraction, after Lodders (2003). The last column gives the yield calculated by Nomoto *et al.* for core-collapse supernovae within a Salpeter IMF between mass limits of 0.07 and 50 $M_\odot$.

Table 7.3. *Primary element production from massive stars with modest mass loss*

M_{init}	M_{fin}[a]	M_α[b]	M_{CO}[c]	He	C	O	Z
120	81	81	59	9.8	0.88	35	42
85	62	62	38	8.1	0.72	23	27
60	47	28	25	6.0	0.70	14	17
40	38	17	14	4.2	0.55	6.8	10
25	25	9	7	3.5	0.40	2.4	4.4
20	19	7	5	2.1	0.30	1.3	2.9
15	15	5	3	1.6	0.20	0.46	1.5
12	12	4	2	1.4	0.10	0.15	0.8
9	9	3	2	1.0	0.06	0.004	0.3
5	5	1	1	0.45			
3	3			0.09			

[a] Final mass at end of carbon-burning (or helium-burning for lower masses).
[b] Mass of He core at end of carbon- or helium-burning.
[c] Mass of CO core at end of carbon- or helium-burning.
Source: Maeder (1992) for the case $Z = 0.001$, $Y = 0.24$.

Table 7.4. *Primary element production from stars with drastic mass loss*

M_{init}	M_{fin}	He a	He b	C a	C b	O a	O b	Z a	Z b
120	2.4	42.7	−0.1	8.0	0.3	0.0	0.2	10.1	0.7
85	3.5	16.7	−0.4	13.5	0.4	4.0	0.6	19.3	1.6
60	3.0	13.5	−0.3	7.2	0.3	1.4	0.4	9.8	1.2
40	3.6	6.1	−0.4	4.9	0.4	2.1	0.6	8.0	1.6
25	11.3	1.5	0.6	0.30	0.32	2.6		4.5	
20	14.0	1.6	1.5	0.22		1.3		2.7	
15	13.6	1.4	1.3	0.14		0.4		1.3	
12	11.5	1.2		0.07		0.1		0.7	
9	8.6	0.9		0.03		0.0		0.2	
5	4.9	0.40							
3	3.0	0.07							

[a] Sum of amounts freshly produced and expelled in wind and in final ejecta (SN or PN).
[b] Amount freshly produced and expelled in final ejecta (SN or PN).
Source: Maeder (1992) for the case $Z = 0.02$, $Y = 0.28$, high mass-loss rates.

ascent of the red-giant branch (RGB) and the second and third on the asymptotic giant branch (AGB) (see Section 5.10). Less massive stars experience only the first and third dredge-ups. In the first dredge-up, the outer convection zone reaches into regions where ^{12}C was partly converted into ^{13}C and ^{14}N during the main-sequence and post main-sequence phases. Correspondingly ^{14}N and ^{13}C are

enhanced at the surface at the expense of ^{12}C while ^{16}O is substantially unchanged and a little ^{4}He is produced. In the second episode, following ignition of the He-burning shell, the convective envelope penetrates into the helium core, dredging up helium and nitrogen (see Fig. 5.18). Once again the surface abundances of ^{14}N and ^{4}He are enhanced, while C and O are correspondingly reduced. The third phase consists of several individual mixing episodes: following each helium shell flash the base of the convective envelope may penetrate through the H–He discontinuity bringing up helium, carbon and s-process elements. If the temperature at the base of the convective zone is high enough, some or all of this carbon is changed into primary ^{14}N by so-called 'hot-bottom burning', which takes place above some mass limit which depends on chemical composition and the assumed model of convection. While all this is happening, the star continuously loses mass through a stellar wind, which gradually increases in intensity as the star expands, cools and becomes vibrationally unstable; eventually the remaining amount of mass above that of the final remnant is expelled in the form of a planetary nebula and the remnant becomes a white dwarf. The wind and the planetary nebula are the means by which nucleosynthesis in these stars affects galactic chemical evolution.

The prediction of yields from intermediate-mass stars (IMS) resulting from the outcome of these processes was pioneered by Renzini and Voli (1981). Their work is now superseded by more recent calculations using updated physics and more realistic (and larger) estimates of mass loss rates, which lead to drastic reduction in the number of thermal pulses experienced by a typical AGB star. Tables 7.5 and 7.6 give two sets of estimates from synthetic models based on the detailed Geneva and Padova evolutionary calculations respectively and using parameters (in particular for mass loss and convection) that seem to give the best fit to observations, notably of luminosity functions of carbon stars in the Magellanic Clouds and abundances in planetary nebulae. Quantities are in units of $M_\odot$ (except for Z's and overall yields) and numbers in brackets in Table 7.6 indicate primary components of ^{13}C and ^{14}N, the rest being secondary. The lowest sections give the overall contribution of IMS to the yield from a stellar population, to be compared with the solar abundances of the corresponding species, which can be taken as a sort of target, since the solar abundances are typical of the local Galaxy.

Certain trends are clear in both sets of yields. Hot-bottom burning sets in at about $4\,M_\odot$ leading to primary nitrogen production; at lower masses nitrogen is secondary and roughly proportional to Z, and below about 1 to 1.5 $M_\odot$, only the first dredge-up occurs, i.e. no fresh carbon. There are also notable differences between the two sets of calculations, e.g. Marigo produces more ^{12}C and less ^{14}N than van den Hoek and Groenevegen, i.e. less mixing, and a lower value of M_{up}, the largest initial stellar mass to end up with a degenerate CO core. Thus the former set could make IMS the major contribution to Galactic ^{12}C at the expense of underproducing

Table 7.5. *He, C and N production from intermediate-mass stars: Version 1*

M_{init}	Z	M_{rem}	$^4\mathrm{He}\times100$ 3	$^{12}\mathrm{C}\times1000$ 2.4	$^{13}\mathrm{C}\times10^4$ 0.27	$^{14}\mathrm{N}\times1000$ 0.8	$^{16}\mathrm{O}\times10^4$ 64
	0.004	1.20	3.3	0.33	1.3	9	−3.2
	0.008	1.20	4.1	−0.05	1.6	11	−10
8	0.02	1.15	3.9	−0.92	1.8	11	−16
	0.001	1.15	5.6	1.7	2.1	18	9.6
	0.004	0.98	2.5	0.3	0.88	6.4	2.6
	0.008	0.97	2.6	0.0	0.97	6.4	0.7
5	0.02	0.92	3.1	−0.7	1.4	7.3	−2.9
	0.001	1.03	4.8	2.5	4.7	14	13
	0.004	0.91	2.0	0.8	2.7	4.5	2.8
	0.008	0.90	2.6	0.7	3.0	4.4	0.6
4	0.02	0.79	3.1	4.6	0.70	1.8	−2.2
	0.001	0.89	3.6	14	−0.13	0.07	12
	0.004	0.66	3.2	7.4	0.13	0.44	5.1
	0.008	0.64	3.4	6.8	0.24	0.78	3.0
3	0.02	0.62	3.3	5.1	0.67	1.7	−0.01
	0.001	0.71	4.4	13	−0.22	0.07	12
	0.004	0.62	2.7	4.9	0.11	0.34	3.6
	0.008	0.61	2.5	4.4	0.22	0.58	2.5
2	0.02	0.60	2.0	2.4	0.60	1.3	0.78
	0.001	0.64	3.5	9.5	−0.19	0.037	8.4
	0.004	0.60	1.9	2.2	0.10	0.20	2.1
	0.008	0.59	1.9	2.5	0.18	0.36	2.2
1.5	0.02	0.59	1.6	0.80	0.51	0.99	3.7
	0.001	0.59	1.8	1.7	−0.14	0.028	1.5
	0.004	0.58	1.5	0.68	0.074	0.12	0.64
	0.008	0.58	1.3	−0.17	0.14	0.24	0.54
1	0.02	0.58	1.9	−0.12	0.48	0.77	9.8
	0.001	0.58	1.3	−0.021	−0.13	0.025	−0.02
	0.004	0.58	1.2	−0.09	0.065	0.10	−0.01
	0.008	0.58	1.2	−0.15	0.12	0.20	0.28
0.9	0.02	0.57	1.0	−0.42	0.31	0.48	−0.39
	0.001		1.4	1.5	0.15	1.4	2.0
Over-	0.004		1.5	1.6	0.36	1.4	1.5
all	0.008		1.6	1.5	0.45	1.6	0.5
yield	0.02		1.7	1.0	0.52	1.8	1.0

After van den Hoek & Groenevegen (1997), with their standard parameters, except that for $Z = 0.001$ the mass loss parameter η in the Reimers (1975) formula is 1 instead of 4. The lowest block represents the overall yields contributed by intermediate-mass stars in a population governed by a Salpeter mass function between 0.1 and 120 $M_\odot$, calculated from the above stellar yields by Marigo (2001), to be compared with solar abundances (by mass) given in the second line.

Table 7.6. *He, C and N production from intermediate-mass stars: Version 2*

M_{init}	Z	M_{rem}	$^4\mathrm{He}\times100$	$^{12}\mathrm{C}\times1000$	$^{13}\mathrm{C}\times10^4$	$^{14}\mathrm{N}\times1000$	$^{16}\mathrm{O}\times10^4$
	0.004	1.04	17	1(4)	6.9(6.5)	47(43)	1(31)
	0.008	1.03	32	−3(2)	3.2(2.7)	22(14)	−27(13)
5	0.019	1.00	29	4(11)	37(23)	13(3)	−40(14)
	0.004	1.00	20	2(4)	7(7)	44(42)	23(35)
	0.008	0.98	14	8(10)	34(29)	14(11)	5(20)
4	0.019	0.90	13	16(20)	2(2)	5(0)	−12(18)
	0.004	0.97	22	78	0.58	0.62	62
	0.008	0.89	16	47	0.54	1.46	29
3	0.019	0.79	14	36	1.38	3.36	5.8
	0.004	0.75	18.5	71	0.11	0.23	58
	0.008	0.68	9.0	29	0.32	0.67	19.6
2	0.019	0.63	6.0	16	0.88	1.53	5.3
	0.004	0.64	8.1	30	0.095	0.083	25
	0.008	0.61	3.3	8.4	0.25	0.18	6.4
1.5	0.019	0.58	1.7	2.4	0.58	0.56	1.5
	0.004	0.61	0.59	−0.020	0.046	0.018	0.0011
	0.008	0.61	3.3	8.4	0.25	0.32	6.4
1.0	0.019	0.54	0.70	−0.078	0.21	0.069	0.00
	0.004	0.59	0.048	0.0031	−0.096	0.0080	0.00
	0.008	0.58	0.49	−0.021	−0.058	0.018	−0.002
0.9	0.019	0.54	0.51	−0.045	0.13	0.038	0.00
Over-	0.004		3.1	9	1.0	1.0	7.5
all	0.008		1.8	4.0	0.40	0.40	2.5
yield	0.019		1.4	2.5	0.32	0.40	0.1

After Marigo (2001) with standard parameters. Numbers in brackets denote the primary contribution from masses 4 and 5 $M_\odot$. (Primary contributions are necessarily positive, whereas secondary ones can be either positive or negative.) Overall yields defined as in Table 7.5.

nitrogen, while in the latter it is the other way round and there is room for a major contribution to carbon from massive stars. However, these results are very sensitive to such details as the treatment of convection and estimates of dredge-up efficiency (the ratio of the mass in the region marked B in Fig. 6.4 to the mass ΔM_α added to the core by H-burning during the previous inter-pulse period). They should thus be treated as semi-quantitative only. One can say that IMS contribute a large part of the enrichment in ^{4}He, they may contribute significantly to ^{12}C, they are significant sources of ^{14}N and they dominate the production of ^{13}C and the main s-process elements.

Further important contributions to GCE come from Type Ia supernovae and possibly other interacting binary systems. In the canonical SN Ia model, a CO white

Table 7.7. *Element production from SN Ia*

Species	Mass/$M_\odot$	$[X_i/X_{56}]^a$
^{24}Mg	0.09	-1.1
^{28}Si	0.16	-0.3
^{32}S	0.08	-0.4
^{36}Ar	0.02	-0.3
^{40}Ca	0.04	0.1
^{54}Fe	0.14	0.6
^{56}Fe	0.61	0.0
^{58}Ni	0.06	0.4
Cr–Ni	0.86	

[a] Logarithmic element: ^{56}Fe ratio relative to solar.
Source: Nomoto *et al*. (1984), model W7; see
also Thielemann *et al*. (1986).

dwarf accretes matter at a rate between 4×10^{-8} and $10^{-6} \, M_\odot \, \text{yr}^{-1}$ from a binary companion, processes the accreted matter to C and O via hydrogen and helium shell flashes, approaches the Chandrasekhar limiting mass and ignites degenerate carbon at its centre. A subsonic nuclear burning front (a deflagration) propagates outwards, incinerating an innermost $0.6 \, M_\odot$ of the star to iron-peak isotopes, principally radioactive ^{56}Ni, and burning an outer portion to elements of intermediate mass from O to Ca (see Fig. 5.24), corresponding to features observed in the light curve and spectrum development. The entire star is disrupted in the process. Indirect evidence (the behaviour of the O/Fe ratio as a function of metallicity in normal stars) suggests that about 2/3 of the iron in the Solar System comes from this process (which involves a significant time delay of the order of a Gyr), the remainder coming from massive stars associated with SN II. Table 7.7 gives estimated yields from a $1 \, M_\odot$ CO white dwarf accreting hydrogen-rich material from a red-giant companion.

The table suggests that SN Ia may contribute noticeably to Si, S, Ar and Ca, as well as iron. In addition, there might possibly be contributions to the s-, r- and especially the p- (or γ-) process (Howard, Meyer & Woosley 1991). Other types of SN, e.g. Ib, could also be binaries and make a distinctive contribution, but their nature is not well known at present. Roughly speaking, a mean SN Ia rate of 1 per century over 10 Gyr produces $5 \times 10^7 \, M_\odot$ of iron, equivalent to an overall abundance $Z(\text{Fe}) \simeq 10^{-3} \simeq Z_\odot(\text{Fe})$, while a similar SN II rate (with a typical oxygen production of $2 \, M_\odot$) produces the equivalent of an overall abundance $Z(\text{O}) \simeq 3 \times 10^{-3} \simeq 0.5 \, Z_\odot(\text{O})$. Thus reasonable time-averaged SN rates of 1 per century for Type Ia and 2 per century for Type II give the right orders of magnitude.

7.3.3 Initial mass function (IMF)

The IMF $\phi(m) \propto dN/dm$ or $\xi(m) \propto dN/d\log m \propto m\phi(m)$ describes the relative birthrates of stars with different initial mass $m M_\odot$ in a given interval dm or $d\log m$, at a given time and in a given region such as the solar cylinder, i.e. a cylinder perpendicular to the Galactic plane through the Sun and presumably representing the population of the Galactic disk at the Sun's distance from the centre. It can be studied for either clusters or field stars, each method having its own advantages and problems. For the solar neighbourhood the IMF is obtained in a series of steps, first applied by Salpeter (1955), beginning with the luminosity function dN/dM_V for the local volume, the mass–luminosity relation $dM_V/d\log m$ and the appropriate scale heights $h(M_V)$ (all referring to average main-sequence stars) to give the present-day mass function (PDMF) for the solar cylinder:

$$\text{PDMF}(\log m) = \frac{dN}{dM_V} \times 2h(M_V) \times \frac{dM_V}{d\log m}. \tag{7.1}$$

The relation between the PDMF and the IMF then depends on the lifetimes of the stars. For long-lived stars ($m \leq 0.9$),

$$\text{IMF} = \text{PDMF}/(T\langle\psi(t)\rangle), \tag{7.2}$$

where T is the age of the Galactic disk and $\langle\psi(t)\rangle$ is the mean rate of star formation (SFR) over that time.[1] For short-lived stars, i.e. those that have only been able to live for such a short time that there has been no change in $\psi(t)$, say $m > 2$,

$$\text{IMF} = \text{PDMF}/\{\tau_{\text{ms}}(m)\psi(T)\}. \tag{7.3}$$

For intermediate masses,

$$\text{IMF} = \text{PDMF}\bigg/ \int_{T-\tau_{\text{ms}}(m)}^{T} \psi(t)dt. \tag{7.4}$$

Determination of the local IMF thus involves several non-trivial steps, including corrections for evolved stars and unresolved binary or multiple systems, knowledge of scale heights and the mass–luminosity relation and the procedure whereby the three different pieces are fitted together, which itself requires assumptions about the age of the Galaxy and the past history of the SFR, as well as an assumption that the IMF itself either has not changed (the more usual assumption, built in to the above equations) or has changed in some specified manner. Furthermore, the rarity of very massive stars can introduce a statistical bias if the sample is not sufficiently large.

---

[1] It is implicitly assumed here that the IMF has been constant over time, i.e. that the creation rate of stars of any given mass can be separated into a function of time only and a function of mass only.
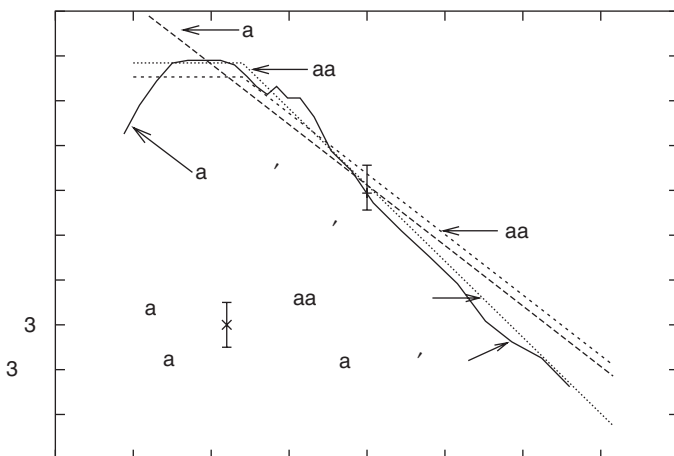
Fig. 7.1. Local IMFs after Scalo (1986) with $b' = 1$, Salpeter (1955) extended down to $0.1\,M_\odot$ and versions with a flat slope below $0.5\,M_\odot$, consistent with suggestions by Kroupa (2002). The IMFs are normalized to a total mass of $1\,M_\odot$, between adopted lower limits (zero in the case of the flattened functions) and $120\,M_\odot$.

A number of arguments (mainly based on the observed distribution of stellar ages, together with the assumption that there are no large discontinuities in the IMF since there are none in Galactic clusters) suggest that the present SFR in the disk of the Galaxy is not very different from its average value in the past; specifically

$$0.5 \leq b(T) \equiv \frac{\psi(T)}{\langle \psi(t) \rangle} \leq 1.5, \tag{7.5}$$

and this enables the three pieces to be patched together. Some resulting IMFs are shown in Fig. 7.1, together with the effect of the parameter $b' \equiv 12\,b(T)/T\,(\mathrm{Gyr})$. The normalization here is to a total mass of $1\,M_\odot$, so that the level above $m = 2$ or so is inversely proportional to b' as shown by the vertical error bar at $m \simeq 3$. Additional typical errors are shown by the error bar in the lower left of the figure.

For GCE purposes, a convenient normalization is such that

$$\int_{m_L}^{m_U} m\phi(m)dm = 1 \tag{7.6}$$

where m_L and m_U are lower and upper limits of integration. Salpeter's law, originally derived between lower and upper limits of $0.4\,M_\odot$ and $10\,M_\odot$, but now mostly quoted between limits of 0.1 and $120\,M_\odot$, is a simple power law

$$m\phi(m) \propto m^{-x} \tag{7.7}$$

Table 7.8. *Parameters of selected IMFs*

	x	α_0	α_1	$F_M(> 1)$	$F_M(> 10)$	α
Salpeter(0.1)	1.35		0.17	0.39	0.13	0.70
Kroupa–Salpeter	1.35	0.58	0.23	0.53	0.17	0.60
Kroupa–Scalo	1.7	0.83	0.26	0.36	0.06	0.75

with $x = 1.35$. Specifically, with our normalization (hereafter Salpeter(0.1) IMF),

$$m\phi_{\text{Sal}(0.1)}(m) = 0.17m^{-1.35}. \tag{7.8}$$

The Salpeter function (above $1\,M_\odot$ or so) has been confirmed in studies of star formation in spiral galaxies (Kennicutt 1983) and of young star clusters in the Galaxy and the Magellanic Clouds, though with individual variations (Scalo 1998). For field stars in the solar neighbourhood, on the other hand, a better fit seems to be provided by steeper functions such as that by Scalo (1986). In any case, the function flattens or even declines below $0.5\,M_\odot$, and the irregularities in the Scalo function near $1\,M_\odot$ arise largely from variations in the slope of the mass–luminosity relation (Kroupa, Tout & Gilmore 1990), so for simplicity one may as well just use a flat function below $m = 0.5$ and a power law above it (see Kroupa 2002), i.e.

$$m\phi(m) = \begin{cases} \alpha_0, & 0 < m \le 0.5 \\ \alpha_1 m^{-x} = 2^{-x}\alpha_0\, m^{-x}, & 0.5 \le m \le 120 \end{cases}$$

The IMF has a number of important integral properties including the following (see Table 7.8):

(i) The mass fraction $F_M(> m)$ of a generation of stars that is born with stellar masses above some limit:

$$F_M(> m) = \int_m^{m_U} m'\phi(m')dm'. \tag{7.9}$$

In particular, one is interested in the mass fraction $\zeta \equiv F_M(> m_\tau)$ of stars with a lifetime $\tau(m)$ less than the age of the system. E.g. if $m_\tau = 1$, a characteristic value for the Galaxy, then ζ is in the region of 0.35 to 0.5; acknowledged uncertainties imply a corresponding uncertainty in ζ of at least ± 0.1.

(ii) The return fraction R or the lock-up fraction $\alpha \equiv (1 - R)$. R is the mass fraction of a generation of stars that is returned to the interstellar medium, and it increases with time as progressively smaller stars complete their evolution, while α correspondingly decreases, but by a proportionately smaller amount as long as $R < 0.5$. α is the fraction that remains locked up in long-lived stars and compact stellar remnants and is given by

$$\alpha = 1 - F_M(> m_\tau) + \int_{m_\tau}^{m_U} m_{\text{rem}}(m)\,\phi(m)dm, \tag{7.10}$$

where m_{rem} can be approximated by

$$m_{\text{rem}} = \begin{cases} 0.11m + 0.45; & m \leq 9.5 \\ 1.5; & m > 9.5 \end{cases}$$

(Iben & Tutukov 1984b). For $m_\tau = 1$, $\alpha \simeq 0.6$ to 0.8, again with an uncertainty of the order of ± 0.1, which is comparable to the amount by which it decreases after the first few hundred million years.

(iii) The yield p of primary elements produced by massive stars, e.g. oxygen, which is defined as the mass of element freshly produced and ejected by a generation of stars in units of the mass that remains locked in long-lived stars and compact remnants. (This will be referred to as the *true yield*, as opposed to an *effective yield* deduced from observed abundances with the aid of GCE models.) The mass produced relative to the initial mass of the generation is $q \equiv \alpha p$. The true yield is given by

$$p_i = \alpha^{-1} \int_{m_\tau}^{m_U} m \, q_i(m) \, \phi(m) \, dm \tag{7.11}$$

where $q_i(m)$ is the fraction of the initial mass of a star ejected in the form of freshly synthesized element i and can be deduced (or summed over elements to find p_Z) from the kind of data given as $m \, q_i(m)$ in Tables 7.2 to 7.6. The oxygen yield for the Scalo IMF, using the modest mass-loss results in Table 7.3 and $m_\tau = 1$, is 0.006, or about solar, but this is uncertain by about a factor of 2 because of the uncertainty in b' and by further factors related to mass loss and the upper mass limit for SN II.

Is the IMF universal? No systematic dependence on identifiable parameters has been detected, but there are local variations, e.g. in the solar neighbourhood versus giant extragalactic H II regions. These may be biased samples from some more universal function, e.g. if stars are born in clusters of differing size subject to a cluster mass distribution function (CMDF). In such a case, the slope of the resulting IMF depends on that of the CMDF, becoming steeper the more relatively small clusters there are; thus it may be that only stars born in rich clusters display the relatively shallow Salpeter slope (Kroupa & Weidner 2003; Goodwin & Pagel 2005).

7.3.4 Star formation rates (SFR)

It is convenient, though not necessarily realistic, to describe the SFR by some simple laws, e.g. as a given function of time or of the mass of gas present, possibly involving other parameters like the total surface density or galactic rotation constants, all of which presumably play a role. Parameterizations found in the literature include

(i) Simple exponential decay:

$$\psi = \psi_0 \, e^{-\nu t}. \tag{7.12}$$

Typical timescales $1/\nu$ range from as little as 10^8 years (roughly the dynamical timescale) for a starburst galaxy to maybe 2×10^9 years in an early-type spiral to

indefinitely large and even formally negative times ($b(T) \geq 1$ in Eq. 7.5) in late-type spirals and irregulars (Kennicutt, Tamblyn & Congdon 1994; Kennicutt 1998a).

(ii) Schmidt laws (Schmidt 1959) :

$$\Sigma_{SFR} = \nu \Sigma_g^n, \tag{7.13}$$

where Σ_g is the surface density of gas and n a power-law index in the range 1 to 2.[2] In a closed model of constant total mass, Eq. (7.13) with $n = 1$ leads to Eq. (7.12). Kennicutt (1998ab), in extensive studies comparing Hα, far infrared and Brackett-γ emission (indicating the formation rate of massive stars and extrapolating with the Salpeter(0.1) law) with the distribution of H I and CO (indicating the surface density of gas) in disk and starburst galaxies finds a good fit with an index of 1.4, above a certain surface density threshold of a few solar masses per square parsec, varying from one galaxy to another. Specifically, he finds

$$\Sigma_{SFR} = (0.25 \pm 0.07) \, \Sigma_g^{1.4 \pm 0.15} \quad M_\odot \, pc^{-2} \, Gyr^{-1}, \tag{7.14}$$

where Σ_g is in units of $M_\odot \, pc^{-2}$, up to $\Sigma_g \simeq 5 \times 10^4$.

(iii) A more elaborate formulation, which depends in addition on the total mass surface density, was suggested by Talbot and Arnett (1975) and by Dopita and Ryder (1994) and can be written as

$$\Sigma_{SFR} = \nu \Sigma_{total}^{n_1} \Sigma_g^{n_2}, \tag{7.15}$$

with $n_1 \sim 1/3$ and $n_2 \sim 5/3$. This kind of SFR is related to the feedback between energy injected into the ISM by supernovae and stellar winds in relation to the local gravitational potential well. Larson (1976) considered other modifications to the Schmidt law (expressed in terms of volume density rather than surface density) accounting schematically for possible effects of velocity dispersion and tidal forces.

(iv) As an alternative to the above Schmidt law, Kennicutt (1998ab) found an almost equally good fit to a linear dependence on gas density and angular speed of rotation (as might be expected if the SFR is influenced by shocks from encounters with a spiral arm of low pattern speed – Oort 1974; Wyse & Silk 1989; Portinari & Chiosi 1999):

$$\Sigma_{SFR} = 0.017 \, \Omega \, \Sigma_g \quad M_\odot \, pc^{-2} \, Gyr^{-1}, \tag{7.16}$$

where $\Omega \equiv 2\pi/T_{orb}$ is the angular velocity in radians per Gyr. This corresponds to a star formation rate of the order of 10 per cent of the available gas per orbit. With a local surface density of gas of $10 \, M_\odot \, pc^{-2}$, Eqs. (7.14) and (7.16) both imply a star formation rate of about $6 \, M_\odot \, pc^{-2} \, Gyr^{-1}$ in the solar cylinder. Andrievsky *et al.* (2004) have explored consequences of a spiral pattern speed close to the Galactic rotation rate in the solar vicinity.

---

[2] Sometimes expressed in terms of volume density – equivalent to surface density in a uniform or exponentially stratified medium of fixed thickness or scale height.

Such simple laws, basically empirical although supportable by hand-waving physical arguments, are not always applicable, at least in detail. In disk galaxies, star formation is quite sporadic, in gas-rich dwarf galaxies star formation may be dominated by a small number of bursts separated by extremely long intervals of time, and in large starburst and luminous IRAS galaxies one has a very violent burst of star formation triggered by an interaction or merger. Other effects that have been considered include stochastic self-propagating star formation, self-regulated star formation and the presence of (surface) density thresholds. In our own Galaxy, the highest SFR occurs in the 4 kpc ring, roughly half-way between here and the Galactic centre, where total surface density, gas density, gas pressure, temperature, chemical composition, gravitational potential, Galactic rotation effects, spiral shocks, magnetic fields and the frequency of collisions between clouds all may play a role. There is also strong star formation activity around the centre itself, but little in the region between, the main factor probably being a shortage of gas.

From the point of view of GCE, one is interested primarily in effects averaged over long periods of time of the order of Gyr; but in dwarf galaxies which may have experienced only a few star formation bursts over a Hubble time the sporadic character may have appreciable effects, especially when one bears in mind that much of the abundance data for such objects comes from H II regions which are intrinsically the result of a current burst, and there is indeed evidence for a cosmic dispersion in certain element abundance ratios such as N/O in such objects (see Chapter 11).

No attempt will be made here to enter into a more detailed discussion of the physics of the SFR, but a few comments will be made on the basis of some very simple parameterizations. Considering for example the exponential time-dependence of Eq. (7.12), the restriction on $b(T)$ in Eq. (7.5) implies that $\nu^{-1} > 0.9\,T \simeq 10\,\mathrm{Gyr}$. A related argument can be made about the past evolution of the luminosity of the disk – closely related to both the SFR and the IMF – from considerations of nuclear fuel consumption. All energy radiated corresponds to the synthesis of helium and/or heavy elements from hydrogen at a rate

$$L \simeq -0.007\, Mc^2\, dX/dt \tag{7.17}$$

which translates into an overall present-day abundance in the whole system (including stellar interiors and white dwarfs)

$$\langle Z + \Delta Y \rangle \simeq 0.005\, \frac{L_1}{M}\, \frac{e^{\nu T} - 1}{\nu} \tag{7.18}$$

where L_1 is the present-day bolometric luminosity and the mass is assumed to have remained unchanged. Since about 10 per cent of luminous matter in the solar

neighbourhood is in the form of white dwarfs (Fleming, Liebert & Green 1986) and in the rest of the material $Z \simeq 0.01$ and $dY/dZ \simeq 2.5$ (Izotov & Thuan 1998; Pagel & Portinari 1998), one can estimate that

$$\langle Z + \Delta Y \rangle \simeq 0.15. \tag{7.19}$$

Since $L_1/M \simeq 1$ (in cgs units), it follows from a comparison of equations (7.18) and (7.19) that, for exponential decay in bolometric luminosity, $\nu^{-1} \sim 7$ Gyr. Thus a single strong initial burst seems to be ruled out as a dominant contributor in the solar neighbourhood.

The simplest possible parameterization of the SFR is to assume that it is just proportional to the surface density of gas (a special case of Schmidt's law, with an exponent of 1). This at least has the merit of simplicity and of taking into account the necessity of having gas as the raw material from which stars are formed, and will be used widely here as it has been elsewhere, while always bearing in mind that the coefficient may vary with ambient conditions (as, e.g., in Kennicutt's alternative law Eq. 7.16) or stochastically. A number of the results of GCE theory are insensitive to the SFR, while others are affected by many other difficulties anyway.

7.3.5 The Galactic context

Figure 3.38 shows a schematic cross-sectional view of the Galaxy, indicating the main stellar population groups (disk, bulge, halo and solar cylinder) that will figure in subsequent discussions and Table 7.9 gives some relevant statistics.

The final ingredient of GCE models is a set of assumptions about the conditions in which stellar births and deaths take place. In particular, it makes a considerable difference whether we are allowed to consider an isolated, well-mixed system or whether inflows and/or outflows of gas and inhomogeneities are important. For example, in 'chemo-dynamical' models (Burkert & Hensler 1989; Burkert, Truran & Hensler 1992), massive stars energize and enrich the hot component of the ISM, some of which may escape in the form of a metal-enhanced wind, whereas fresh stars are formed from cold material where the enrichment lags behind that of the hot component. It may also be necessary to contemplate changes in the yields (with or without variations in IMF) as a function of chemical composition or other variables. Changes in the slope or upper or lower mass limits of the IMF have all been proposed for particular situations, such as violent star formation bursts, but the evidence is not very clear; at the same time, Maeder (1992, 1993) has predicted substantial changes in the yields, even with a constant IMF.

Table 7.9. *Some properties of the Galaxy and the solar cylinder*

	Galaxy	Solar cylinder
Age	10 to 15 Gyr	
Mass now in stars[a]	$7 \times 10^{10}\,M_\odot$	$45\,M_\odot\,\mathrm{pc}^{-2}$
Mass now in gas[b]	$\sim 7 \times 10^9\,M_\odot$	$7\ \mathrm{to}\ 14\,M_\odot\,\mathrm{pc}^{-2}$
Gas fraction	~ 0.1	0.14 to 0.25
Surface brightness		$23 m_V,\, m_{bol}\ \mathrm{arcsec}^{-2}$
$(M/L_V)/(M/L_V)_\odot$ [a]	5	3
	Processes tending to deplete the gas:	
Average past SFR	$(5\ \mathrm{to}\ 7)\alpha^{-1}\,M_\odot\,\mathrm{yr}^{-1}$	$(3\ \mathrm{to}\ 4.5)\alpha^{-1}\,M_\odot\,\mathrm{pc}^{-2}\,\mathrm{Gyr}^{-1}$
Gas consumption time	~ 1 Gyr	1.5 to 5 Gyr
	Processes tending to restore the gas:	
Mass ej. from AGB+PN[c]		$0.8\,M_\odot\,\mathrm{pc}^{-2}\,\mathrm{Gyr}^{-1}$
Mass ej. from O stars[d]		$\sim 0.05\,M_\odot\,\mathrm{pc}^{-2}\,\mathrm{Gyr}^{-1}$
Mass ej. from SN[d]	$\sim 0.15\,M_\odot\,\mathrm{yr}^{-1}$	$\sim 0.05\,M_\odot\,\mathrm{pc}^{-2}\,\mathrm{Gyr}^{-1}$
(Total mass ejection from stars		$\sim 1\,M_\odot\,\mathrm{pc}^{-2}\,\mathrm{Gyr}^{-1}$)
Net inflow from IGM[e]	$\leq 2\,M_\odot\,\mathrm{yr}^{-1}$	$\leq 1\,M_\odot\,\mathrm{pc}^{-2}\,\mathrm{Gyr}^{-1}$

Sources: [a] Binney & Tremaine (1987); [b] Kulkarni & Heiles (1987); [c] Jura (1989); [d] Pottasch (1984); [e] Lacey & Fall (1985).

7.4 The GCE equations

7.4.1 Basic equations

In the standard case there are four variables to be calculated: the total system mass M (not counting non-baryonic dark matter), the mass of 'gas' g, the mass existing in the form of stars (including compact remnants) s and the abundance Z of the element(s) of interest, assuming certain initial conditions and laws governing the SFR and flows of material into and out of the system.

For the system mass, we have

$$M = g + s \tag{7.20}$$

and

$$dM/dt = F - E \tag{7.21}$$

where F is the rate of accretion of material from outside the system and E the rate of ejection, e.g. in a galactic wind.

The mass of gas is governed by

$$dg/dt = F - E + e - \psi \tag{7.22}$$

where ψ is the star formation rate (by mass) and e the ejection rate of matter from stars, and the mass of stars by

$$ds/dt = \psi - e, \tag{7.23}$$

where

$$e(t) = \int_{m_{\tau=t}}^{m_U} (m - m_{\text{rem}}) \, \psi \, (t - \tau(m)) \, \phi(m) \, dm. \tag{7.24}$$

The abundance of a stable (i.e. non-radioactive) element in the gas (and in newly formed stars if the ISM is homogeneous) is governed by

$$\frac{d}{dt}(gZ) = e_Z - Z\psi + Z_F F - Z_E E, \tag{7.25}$$

where the first term on the rhs represents the total amount of the element ejected from stars, the second one the loss to the ISM by star formation, the third one the addition from any of the element that may exist in inflowing material and the fourth one the loss by a galactic wind (if any). Generally two possibilities are considered for a wind: if it is *homogeneous* then $Z_E = Z$, while if it is *metal-enhanced*, $Z_E > Z$ for the elements affected. In the latter case it may sometimes be necessary to distinguish between the abundances in different phases of the ISM, the hot one being metal-enhanced and contributing to the wind and the cool one fixing the abundances in stars (Burkert & Hensler 1989; Pagel 1994).

When the stellar yields are only a function of mass and chemical composition, the term e_Z is given by

$$e_Z(t) = \int_{m_{\tau=t}}^{m_U} [(m - m_{\text{rem}})Z(t - \tau(m)) + m q_Z(m)] \, \psi \, (t - \tau(m)) \, \phi(m) dm \tag{7.26}$$

where the first term in square brackets represents recycling without change in abundance (this does not apply to fragile elements like D, Li, Be, B which are wholly or partly destroyed by recycling in stars or 'astration') and the second represents fresh production by nuclear processes in stellar evolution followed by ejection. The return fraction R, or rather $\alpha = 1 - R$, and the true yield p_Z are given by equations (7.10) and (7.11) respectively. However, the situation becomes more complicated when the role of binarity is taken into account, notably with respect to SN Ia. Supposing that a fraction A of stars or binary pairs born between mass limits m_1 ($\sim 3\,M_\odot$) and m_2 ($\sim 15\,M_\odot$) end up as SN Ia, starting as binaries with mass ratio $\mu/(1-\mu)$, the part of the integral in Eq. (7.26) between m_1 and m_2 is multiplied by $(1-A)$ (assuming $m_\tau < m_1$) and one adds the SN Ia contribution (assuming the 'single degenerate' model with the secondary a red giant of initial mass m_{sec})

$$e_Z(t)_{\text{SN Ia}} = A \int_{m_1}^{m_2} \phi(m_{\text{bin}}) dm_{\text{bin}}$$

$$\int_{\mu_{\min}(t)}^{0.5} mq_Z(t - \tau(m_{\text{sec}}))\psi(t - \tau(m_{\text{sec})})f(\mu)d\mu, \qquad (7.27)$$

where $f(\mu)$ is the distribution function of mass ratios and A is chosen somewhere between 0.05 and 0.09 (Matteucci & Greggio 1986; Matteucci 2001).

Full numerical solution of the above equations involves many detailed assumptions and it is not always easy to visualize the effects of these assumptions on the outcome. Therefore it is useful to consider the much simpler approach of the next section.

7.4.2 The instantaneous recycling approximation

In the instantaneous recycling approximation, first explicitly used by Schmidt (1963), one assumes that all processes involving stellar evolution, nucleosynthesis and recycling take place instantaneously on the timescale of galactic evolution, so that quantities such as α and p do not depend explicitly on time, although they may of course be affected by changes in chemical composition or other parameters that themselves vary with time. This enables a variety of results to be derived analytically in a straightforward manner. The approximation is often quite good for products of massive-star evolution, like oxygen, if the SFR does not vary violently on a short timescale, if the return fraction is not too dependent on long-lived, low-mass stars and the residual gas fraction not too small. It is poor in any case for elements like iron, nitrogen, s-process and possibly carbon, which come partly or wholly from lower-mass stars with significant evolutionary timescales of the order of a Gyr. These can actually be handled to an extent by a 'delayed production' approximation (Section 7.4.3).

The corresponding equations in instantaneous recycling are:

$$S(t) = \int_0^t \psi(t')dt', \qquad (7.28)$$

where $S(t)$ is the mass of all stars that have been born up to time t;

$$s(t) = \alpha S(t), \qquad (7.29)$$

where $s(t)$ is the mass still in the form of stars (or compact remnants);

$$M(t) = s(t) + g(t) = M_0 - M_{\text{ej}} + M_{\text{accr}} \qquad (7.30)$$

and

$$dg/dt = F - E - ds/dt \qquad (7.31)$$

or (eliminating time)

$$\frac{dg}{ds} = \frac{F - E}{\alpha\psi} - 1. \tag{7.32}$$

Assuming a homogeneous ISM, the abundance in the gas (and in newly formed stars) of a stable robust element is governed by

$$\frac{d}{dS}(gZ) = q + RZ - Z - Z_E\frac{E}{\psi} + Z_F\frac{F}{\psi} \tag{7.33}$$

where the suffix $_Z$ has been dropped and the terms on the rhs represent respectively new production, recycling, lock-up in stars, loss in galactic wind and gain from accretion. (For a fragile element, the RZ term is absent or reduced.) For a homogeneous wind with $Z_E = Z$, combining $RZ - Z \equiv -\alpha Z$ and dividing by α, we have

$$\frac{d}{ds}(gZ) = p - Z\left(1 + \frac{E}{\alpha\psi}\right) + Z_F\frac{F}{\alpha\psi} \tag{7.34}$$

or, using Eq. (7.32),

$$g\frac{dZ}{ds} = p + (Z_F - Z)\frac{F}{\alpha\psi}. \tag{7.35}$$

Equations (7.34) and (7.35) can also be written in a form making no explicit mention of ψ or α as follows:

$$\frac{d}{ds}(gZ) = p - Z(1 + \frac{dM_{\text{ej}}}{ds}) + Z_F\frac{dM_{\text{accr}}}{ds} \tag{7.36}$$

or

$$g\frac{dZ}{ds} = p + (Z_F - Z)\frac{dM_{\text{accr}}}{ds}. \tag{7.37}$$

7.4.3 The delayed production approximation

Instantaneous recycling cannot be used to describe the formation of elements, such as iron, to which there is a significant contribution from stars that take a non-negligible time to complete their evolution. This case can still be handled within the framework of analytical models by a 'delayed production approximation' (Pagel 1989a), which works by the simple device of assuming that the delayed element or component thereof starts to be released at a single time Δ after the onset of star

formation and is then instantaneously recycled. Equation (7.34), with the time variable re-introduced, is then modified as follows:

$$\frac{d}{dt}(gZ) = 0; \quad t < \Delta \tag{7.38}$$

$$= p\left(\frac{ds}{dt}\right)_{t-\Delta} - Z(\alpha\psi + E); \quad t \geq \Delta \tag{7.39}$$

(assuming $Z_F = 0$) and in general p is simply replaced by $p\,\psi(t - \Delta)/\psi(t)$. The models now have two additional parameters: the division between instantaneous and time-delayed contributions to the yield, and the dimensionless product $\omega\Delta$, where $\omega \equiv \alpha\psi/g$ (see Eq. 8.15 in the next chapter).

7.4.4 Radial flows in the Galactic disk

In general, radial flows (usually inward in the main body) can occur in the disks of spirals as a result of angular momentum transfer through viscosity (Lin & Pringle 1987; Sommer-Larsen & Yoshii 1990), gravitational interaction with density waves or a mismatch of angular momentum between material in the plane and any material being accreted from outside the disk (Mayor & Vigroux 1981; Pitts & Tayler 1989). In this case, Eqs. (7.31) to (7.37) are replaced by partial differential equations. For example, in place of (7.31) we have

$$\frac{Dg}{Dt} \equiv \frac{\partial g}{\partial t} + \frac{1}{R}\frac{\partial}{\partial R}(RVg) = -\alpha\psi + F \tag{7.40}$$

and in place of (7.37)

$$g\frac{DZ}{Dt} \equiv g\left(\frac{\partial Z}{\partial t} + V\frac{\partial Z}{\partial R}\right) = p\alpha\psi - (Z - Z_F)F, \tag{7.41}$$

where R is galactocentric radius and V radial velocity (counted positive outwards) (Tinsley 1980). If $V \simeq -1\,\mathrm{km\,s^{-1}}$ ($\simeq 1\,\mathrm{kpc}$ per Gyr) in the solar neighbourhood, then both $\partial Z/\partial t$ and $V\partial Z/\partial R$ are comparable, of the order of $0.1\,Z_\odot\,\mathrm{Gyr^{-1}}$, so that an inward flow of this order is compatible with, and can enhance, a negative gradient (which is observed) and a more rapid one could be associated with a small or zero gradient. However, much depends on the details (Lacey & Fall 1985; Götz & Köppen 1992; Edmunds & Greenhow 1995; Portinari & Chiosi 2000); in particular, a linear Schmidt law with R-independent coefficient and $F = 0$ (or $F \propto g$) can be seen from Eq. (7.41) not to allow any gradient to build up – flow or no flow – unless there is a cut-off in star formation at some outer boundary (Lacey & Fall; Clarke 1989; Edmunds & Greenhow).

7.5 Mixing processes in the interstellar medium

How well mixed is the ISM? Metals are ejected from supernovae in the form of hot gas seen in X-rays, which spreads out typically over a radius of 50 pc in a period of order 10^5 years before being slowed down to interstellar velocities. With a density of 1 H-atom cm^{-3}, the mass in this sphere would be of order $10^4 \, M_\odot$ and a single SN expelling $2 \, M_\odot$ of oxygen would contribute a mass fraction $\delta Z_O \sim 2 \times 10^{-4}$ or $Z_\odot/30$. Thus it has taken of order 30 such events to build up the present abundance in any given location and a Poissonian $\sqrt{N}$ fluctuation would correspond to a random variation of ± 20 per cent or so. However, such variations in the gas are smoothed out by various processes, notably azimuthal homogenization by shear-induced turbulence from differential rotation, followed by molecular diffusion, on timescales of under 1 Gyr, although radial gradients can persist for much longer (Edmunds 1975; Roy & Kunth 1995; Elmegreen & Scalo 2004 and references therein) unless there is a central bar capable of inducing substantial radial motions. Another possible driver of radial motions is provided by transient spiral arms which would churn both the stars and the gas leading to substantial scatter in the stellar age–metallicity relation similar to what is seen in Fig. 8.41 (Sellwood & Binney 2002); this would tend to suppress the abundance gradient, which would then have to be regenerated somehow.

Notes to Chapter 7

A fine account of the structure and content of galaxies is given in Mihalas and Binney (1981) and excellent introductions to many questions in GCE are to be found in Truran and Cameron (1971) and Tinsley (1980). A good modern account of the kinematics and abundance distribution of the Galaxy is given by Gilmore, Wyse and Kuijken (1989).

Early GCE papers (Talbot & Arnett 1971, 1973a) used a slightly different definition of the yields q and p from that given here, which included the amounts of ejected elements already present in processed zones of the star before nucleosynthesis, so that the resulting GCE equations are slightly different; the difference is only significant in the case of helium, however. The definition here is identical to that introduced by Searle and Sargent (1972) and used by Renzini and Voli (1981), Maeder (1992) and other authors, although many of these use the symbol y for the yield whereas I have preferred p because it looks less like a variable. Note that there can be negative yields in some cases. For a very thorough discussion of the IMF, see Scalo (1986), and tables of return fractions and oxygen yields for a number of different IMFs with various values of $m_{\tau=t}$ have been published by Köppen and Arimoto (1991). However, with the most 'top-heavy' IMFs, with large

yields and return fractions (e.g. Kennicutt, Tamblyn & Congdon 1994), the instantaneous recycling and delayed production approximations can sometimes become quite poor because progressive gas consumption and enrichment are diluted or even reversed by mass ejection from older stars.

For critical discussions of supposed evidence for variations in the IMF, see Scalo (1986, 1998) and McGaugh (1991); star counts in the Large Magellanic Cloud between about 1 and 100 $M_\odot$ seem to be consistent with either the Salpeter law (Melnick 1987; Richtler, de Boer & Sagar 1991) or the steeper Scalo law (Parker & Garmany 1993), but observations of Galactic and extragalactic H II regions using the Hubble Space Telescope indicate close agreement with the Salpeter law (above $4\,M_\odot$ at any rate) over a broad range in metallicities; the observed upper mass limit is mainly governed by the age of the stars (Waller, Parker & Malamuth 1996). Information on the relative numbers of older and younger stars in the solar neighbourhood comes from the study of chromospheric ages based on the strength of the Ca^+ K_2 emission line component (Soderblom, Duncan & Johnson 1991), while in external galaxies models of past star formation rates (assuming a fixed IMF) are constrained by colours (e.g. Larson & Tinsley 1978) and spectra (e.g. Bica 1988) of the integrated light.

The question of upper mass limits to stars which explode as SN II and leave neutron-star remnants is discussed by Maeder (1992, 1993) and by Brown, Bruenn and Wheeler (1992); it is highly controversial. (Note that Köppen and Arimoto (1991) when referring to the Scalo IMF use the version with $b'(T) = 1$, as I have done, whereas Maeder (1993) uses the version with $b'(T) = 0.48$, corresponding to yields that are 3 times higher!)

Interesting variants on the simplest star formation laws include stochastic self-propagating star formation (Gerola & Seiden 1978; Dopita 1985), self-regulating star formation (Arimoto 1989; Hensler & Burkert 1990), stochastic star-formation bursts (Matteucci & Tosi 1985), separate laws for the halo and disk, the latter including terms that account for cloud collisions and induced star formation from interactions between massive stars and clouds (Ferrini *et al*. 1992, 1994), and the existence of a threshold surface gas density for star formation (Kennicutt 1989; Chamcham, Pitts & Tayler 1993).

The estimates of mass densities and mass:light ratios are meant to include only gas, living stars and stellar remnants, not counting dark matter which may be detected by purely gravitational means, and this distinction is not so clear in the older literature. Furthermore, there is controversy about the amount of such dark matter in the solar neighbourhood; see Bahcall, Flynn and Gould (1992). This has a direct bearing on considerations of the past luminosity, since Larson (1986) suggested that there might be a very large population of undetected white dwarfs resulting from an early IMF strongly weighted towards massive stars and

accounting for the 'missing mass'. Following the work of Bienaimé, Robin and Crézé (1987), Kuijken and Gilmore (1989) and Flynn and Fuchs (1994), it seems that there is no real evidence for considerable amounts of such dark matter in the solar neighbourhood, however, and so I do not count it.

Problems

1. Use the IMFs in Table 7.8 to calculate the relative numbers of stars more massive than $0.1 \, M_\odot$ born with less and more mass than $1 \, M_\odot$.

2. Assuming the star formation rate for the Galaxy given in Table 7.9 and that all stars between 10 and $100 \, M_\odot$ explode as Type II supernovae, estimate the corresponding supernova rates for the IMFs in Table 7.8. How much difference does it make if the upper mass limit for SN is $50 \, M_\odot$? (The observed rate for SN II in galaxies like our own is of the order of 2 to 3 per century.)

3. Approximating the oxygen masses in Table 7.3 by power laws

$$m \, q_O(m) \quad = \quad 2.4(m/25)^3; \quad 10 \le m \le 25 \tag{7.42}$$
$$= \quad 2.4(m/25)^2; \quad 25 \le m \le 100, \tag{7.43}$$

show that, if all stars between 10 and $100 \, M_\odot$ become supernovae, then an average supernova ejects $2.0 \, M_\odot$ of oxygen assuming the Kroupa–Scalo IMF or $2.7 \, M_\odot$ for the Salpeter functions. Now use the results of the previous problem to estimate the oxygen yield from a generation of stars and compare with the solar oxygen mass fraction $Z_\odot^O = 0.006$. (Note that the star formation rate cancels out in this calculation.)

8

Some specific GCE models and related observational data

Quot homines tot sententiae: suo quoque mos.

Terence, *Phormio*

8.1 The 'Simple' (1-zone) model

The 'Simple' model of Galactic chemical evolution, which goes back to early papers by van den Bergh (1962) and Schmidt (1963), is still widely used despite its failure, pointed out in those papers, to account for the metallicity distribution function of long-lived stars in the solar neighbourhood (the 'G-dwarf problem', which will be discussed below). Its popularity is due to its simplicity, and to the fact that it may have at least a limited applicability in other contexts, such as the Galactic halo, dwarf galaxies and elliptical galaxies and bulges. Furthermore, its simplicity makes it a useful standard of comparison for more sophisticated models.

The assumptions of the Simple model (with a capital 'S') are:

(i) The system is isolated with a constant total mass, i.e. no inflows or outflows, so

$$g(t) + s(t) = M = \text{const.} \tag{8.1}$$

(ii) The system is well mixed at all times, i.e.

$$Z = Z(t) \tag{8.2}$$

is the abundance of any element(s) in the gas and in newly born stars.

(iii) The system starts as pure gas with primordial abundances, i.e.

$$g(0) = M; \quad Z(0) = S(0) = 0. \tag{8.3}$$

(iv) The IMF and nucleosynthetic yields of stars with given initial mass are unchanging as far as 'primary' elements (such as oxygen) are concerned.

251

8.2 The Simple model with instantaneous recycling

In the Simple model with instantaneous recycling (to be referred to as the instantaneous Simple model), we have from Eq. (8.1)

$$dg = -ds \qquad (8.4)$$

and hence from Eq. (7.37) (applying to stable, robust elements)

$$g\frac{dZ}{ds} = -g\frac{dZ}{dg} = p, \qquad (8.5)$$

whence

$$Z = p\ln\frac{M}{g} = p\ln\frac{s+g}{g} = p\ln\frac{1}{\mu}, \qquad (8.6)$$

say, where μ is the 'gas fraction'. Equation (8.6), first derived explicitly by Searle and Sargent (1972) although it was implicit in earlier work, is the fundamental equation of the instantaneous Simple model. Since the yield is assumed constant, and is not very well determined anyway, it is often convenient to use $z \equiv Z/p$ in place of Z. If there is a finite initial abundance, e.g. in the case of helium, Z in Eq. (8.6) is replaced by $Z - Z_0$. Equation (8.6) is, of course, subject to the restriction that, by definition, $Z < 1$, which implies that, should Z approach 1, the yield as defined in Chapter 7 must obviously become small (or negative). Since both p and Z (or $Y - Y_P$) are at most only a few per cent, this does not lead to any difficulty in practice.

Equation (8.6) refers to abundances in the gas and young stars. For the average abundance of a stellar population (with $Z_0 = 0$) we have instead

$$\langle z \rangle = \frac{1}{s}\int_0^s z(s')ds' = 1 + \frac{\mu\ln\mu}{1-\mu} \qquad (8.7)$$

$$\rightarrow 1, \quad \text{for } \mu < 0.1, \text{ say}, \qquad (8.8)$$

i.e. the average abundance (in stellar surface layers) approaches the yield from below when the gas fraction becomes small. This result holds also in models with inflow of unprocessed material, but it should be noted that this is a **mass-weighted** average. Observations of integrated spectra from stellar populations will rather give a **luminosity-weighted** average which will be different, usually less, because luminosities of red giants are higher at low metallicities.

8.3 Some consequences of the instantaneous Simple model

8.3.1 Estimation of yields

For a stellar population,

$$\langle Z \rangle \leq p ; \tag{8.9}$$

$$\langle Z \rangle \rightarrow p \ \text{ as } \ \mu \rightarrow 0. \tag{8.10}$$

For example, in the solar neighbourhood, $-0.2 \leq \langle [\text{O/H}] \rangle \leq 0.0$, implying a yield slightly below solar abundance. This **effective yield** is in fairly good accordance with the **true yield** of $Z_{\odot}(\text{O})$ derived in Problem 3 of Chapter 7 assuming small mass-loss rates (Table 7.3) and the Kroupa–Scalo IMF. With large mass-loss rates, one would need an IMF with a higher proportion of massive stars, to reach a similar true yield for oxygen. These ambiguities indicate that true yields are still subject to large uncertainties.

8.3.2 Abundance ratios of 'primary' elements

For any two primary elements,

$$\frac{Z_i}{Z_j} = \frac{p_i}{p_j} = \text{const.} \tag{8.11}$$

An example is dY/dZ or $(Y - Y_{\text{P}})/(\text{O/H})$, which comes out as a by-product of the determination of primordial helium abundance Y_{P} by extrapolation of the relation between He/H and O/H in low-abundance extragalactic H II regions to O/H = 0 (Lequeux *et al.* 1979; Pagel *et al.* 1992; Izotov & Thuan 1998; see Fig. 4.11). Figures 8.1 and 8.2 show results for Ne/O, S/O and Ar/O derived from observations of Galactic and extragalactic H II regions, which are more or less consistent with constant (and solar) yield ratios (except perhaps in the case of argon where uncertainties are quite large), while Figs. 8.3 and 8.4 show data for C/O indicating that this ratio increases with metallicity. Possible reasons are (i) effects of increasing mass loss from big stars, as predicted by Maeder (1992); or (ii) an increasing contribution from intermediate-mass stars at higher metallicities, e.g. if those systems have had more time to evolve.

Another important deviation from constancy in the abundance ratio of elements supposed to be primary is displayed by the ratios Fe/O and [Fe/α-elements] in stars, which increase systematically with [Fe/H] (Figs. 8.5, 8.6). This is usually attributed to the existence of a substantial contribution to the production of iron found in the younger, more metal-rich stars (like the Sun) by SN Ia, which take times of the order of a Gyr to complete their evolution and therefore cannot be treated
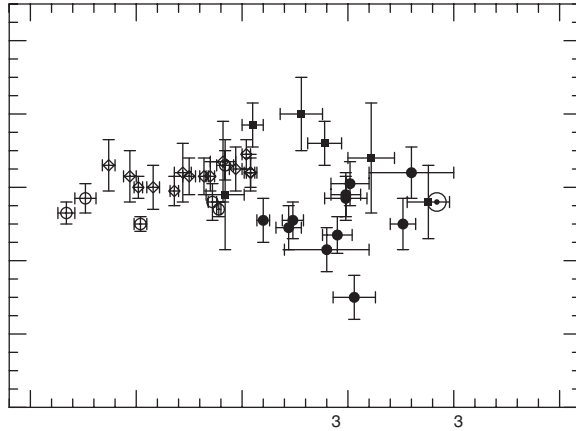
Fig. 8.1. Ne/O ratio vs. O/H from (mainly optical) observations of H II regions in spiral and irregular galaxies and the Sun. Filled and open symbols represent results from different authors. After Garnett (2004).

in the instantaneous recycling approximation. As there is much more information available about stellar iron abundances than about their oxygen or α-element abundances, this introduces some complication in the interpretation of the data.

A schematic indication of how the O/Fe and α/Fe effects might arise from different production timescales is given in Fig. 8.7. If star formation has taken place rapidly relative to the solar neighbourhood (denoted by S.N. in the figure), as may apply to the Galactic bulge, the O/Fe ratio remains high up to large metallicities. Conversely, if it has been relatively slow, or has happened in bursts separated by long intervals, as may apply in the Magellanic Clouds (SMC, LMC), the O/Fe ratio becomes solar (or less) at subsolar metallicities (see Gilmore & Wyse 1991; Pagel & Tautvaišienė 1998), and low-lying points at moderate metal deficiencies in Fig. 8.5 could represent debris from dwarf satellite galaxies incorporated in the Galactic halo (Nissen & Schuster 1997). The evolution of dwarf galaxies will be discussed further in Chapter 11.

Other element:iron ratios, measured in stars of the Galactic disk in the solar neighbourhood, are shown in Fig. 8.8. With the exception of C and N, all of the observed lighter elements up to Ti show a tendency to have higher abundances relative to iron as one goes to low metallicities. Corresponding ratios among ultra-metal-poor stars in the halo are shown in Figs. 8.9 and 8.10. Disregarding a handful of unusual stars, the even-numbered α-elements define a remarkably flat, smooth plateau fitting Eq. (8.11), whereas for sodium a rise towards lower metallicities in the disk is replaced by a downward trend to still lower metallicities in the halo. The sodium trend is qualitatively in accordance with the dependence of theoretical yields on neutron excess (see Table 7.2); aluminium, for unknown reasons, behaves
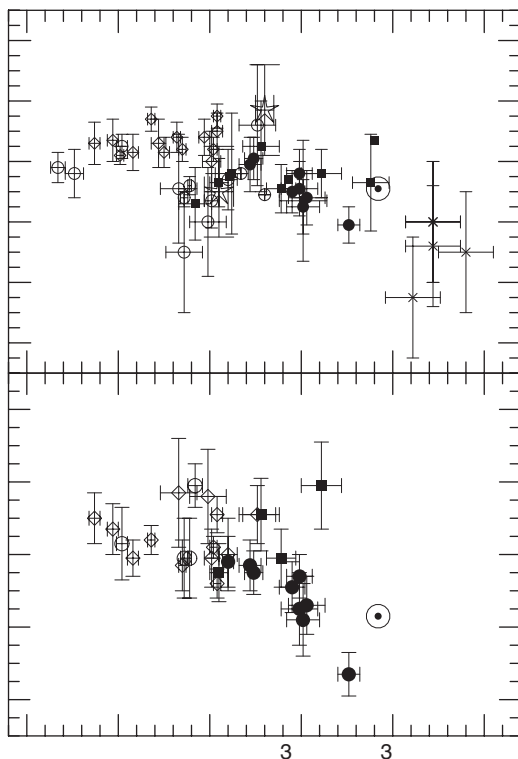
Fig. 8.2. S/O and Ar/O ratios vs. O/H in Galactic and extragalactic H II regions, compared to the Sun. After Garnett (2004).

somewhat differently, in that the Al/Fe ratio seems to descend to a plateau which happens to be more-or-less equal to solar, instead of going on down.

8.3.3 'Primary' and 'secondary' elements

For a secondary element such as nitrogen resulting from CNO burning of previously existing C (and maybe O) and ejected in winds from massive or intermediate-mass stars, the yield is (roughly) proportional to the abundance of the primary progenitor, so that, since in Eq. (8.5) $dZ_{sec}/d\ln\mu \propto Z_{prim} \propto \ln\mu$, we have

$$\frac{Z_{sec}}{Z_{prim}} \propto Z_{prim}. \tag{8.12}$$

Figure 8.11 shows that there is indeed a tendency for N/O to increase with O/H, but not in the simple linear fashion implied by Eq. (8.12). The overall trend is actually remarkably like that of carbon, and there has to be a primary component
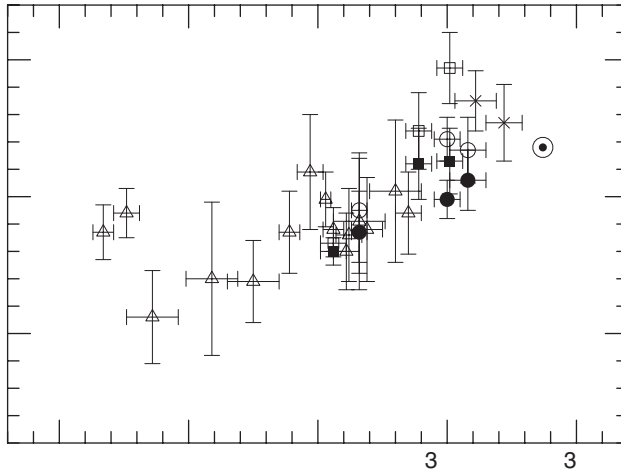
Fig. 8.3. C/O ratio vs. O/H in Galactic and extragalactic H II regions, based on International Ultraviolet Explorer (IUE) and Hubble Space Telescope (HST) observations. After Garnett (2004).
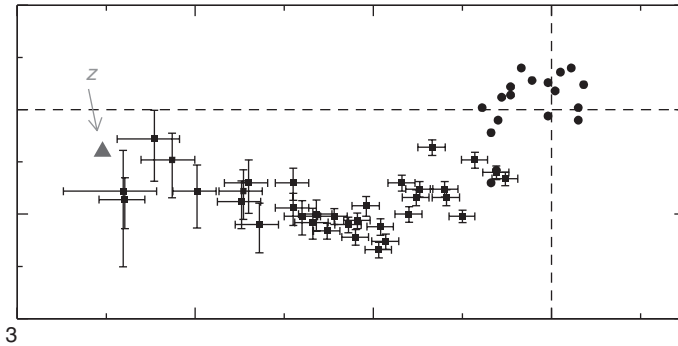
Fig. 8.4. [C/O] vs. [O/H] in stars, after Akerman *et al.* (2004) and references therein, with an additional point representing a damped Lyman-α system at a high redshift. The broad trend is in fair agreement with the H II region results shown in Fig. 8.3; there is a hint of a possible upturn at the lowest metallicities. Courtesy Max Pettini.

that dominates at low metallicities unless the effects of secondary production are offset by some complication, such as preferential loss of supernova ejecta from these dwarf galaxies. There is substantial scatter, some of which is probably real. In NGC 5253, variations are seen across a single H II region, the highest values occurring near the central ionizing cluster which contains Wolf–Rayet stars (Pagel, Terlevich & Melnick 1986); the effect may be due to local pollution by winds
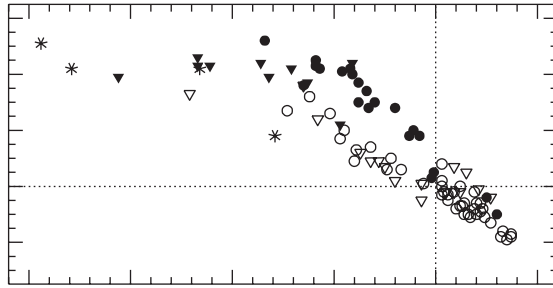
Fig. 8.5. Variation of [O/Fe] with [Fe/H] in stars, after Bensby, Feltzing and Lundström (2004a). Filled and open symbols represent stars of the thick and thin disks respectively, while asterisks represent stars of the halo.
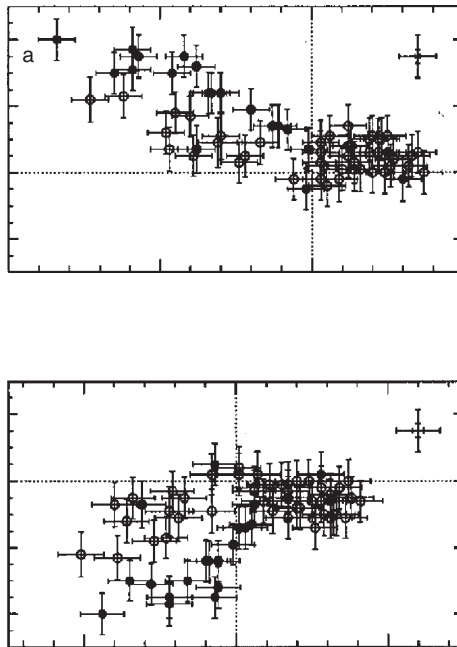
Fig. 8.6. Variation of [Mg/Fe] with [Fe/H] in stars, after Bensby, Feltzing and Lundström (2003). The lower panel shows the converse plot of [Fe/Mg] vs. [Mg/H], which is more straightforwardly related to the progress of Galactic chemical evolution. Filled and open symbols represent stars of the thick and thin disks respectively.
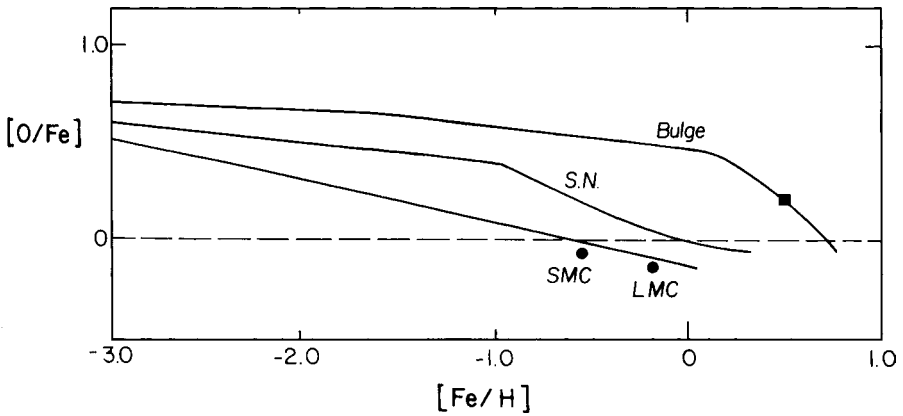
Fig. 8.7. Predicted [O/Fe] vs. [Fe/H] relations, after Matteucci (1991).

from these (or from their red supergiant or luminous blue variable progenitors). Other possible sources of scatter are differences in the ages of prominent stellar populations, either in a continuous or in a bursting star-formation mode, leading to differences in the contribution of intermediate-mass stars.

To summarize the observed behaviour of element:element ratios, one group (oxygen and α-elements) varies approximately in lockstep and potentially can be described by the instantaneous Simple model. There is no proof that the actual yields are constant, but their ratios may place constraints on the upper IMF slope and its variability. A second group (C, N, Fe) increases by factors between 2 and about 10 from the lowest metallicity systems observed to solar metallicity, relative to the first group. This is usually attributed to time-delay effects (plus effects of secondary production in the case of nitrogen), but their yields relative to those of the first group could also vary, e.g. as a consequence of stellar winds becoming more significant at higher metallicities. Metals up to Ti show intermediate behaviour, which is probably due to varying contributions from massive and Type Ia supernovae, while heavier metals tend to track iron more or less, except at extremely low metallicities where neutron-capture elements show special effects; r-process elements like Eu track oxygen more closely than iron.

8.3.4 Relation with gas fraction

According to Eq. (8.6), the 'primary' abundances should increase as the logarithm of the gas fraction, the proportionality coefficient giving another estimate of the yield. For example, from the data in Table 7.9, assuming solar oxygen abundance in the local ISM, the effective yield is between 0.5 and 0.7 $Z_\odot$. Other gas-rich systems in which one may try to test this relationship (which obviously does not apply,
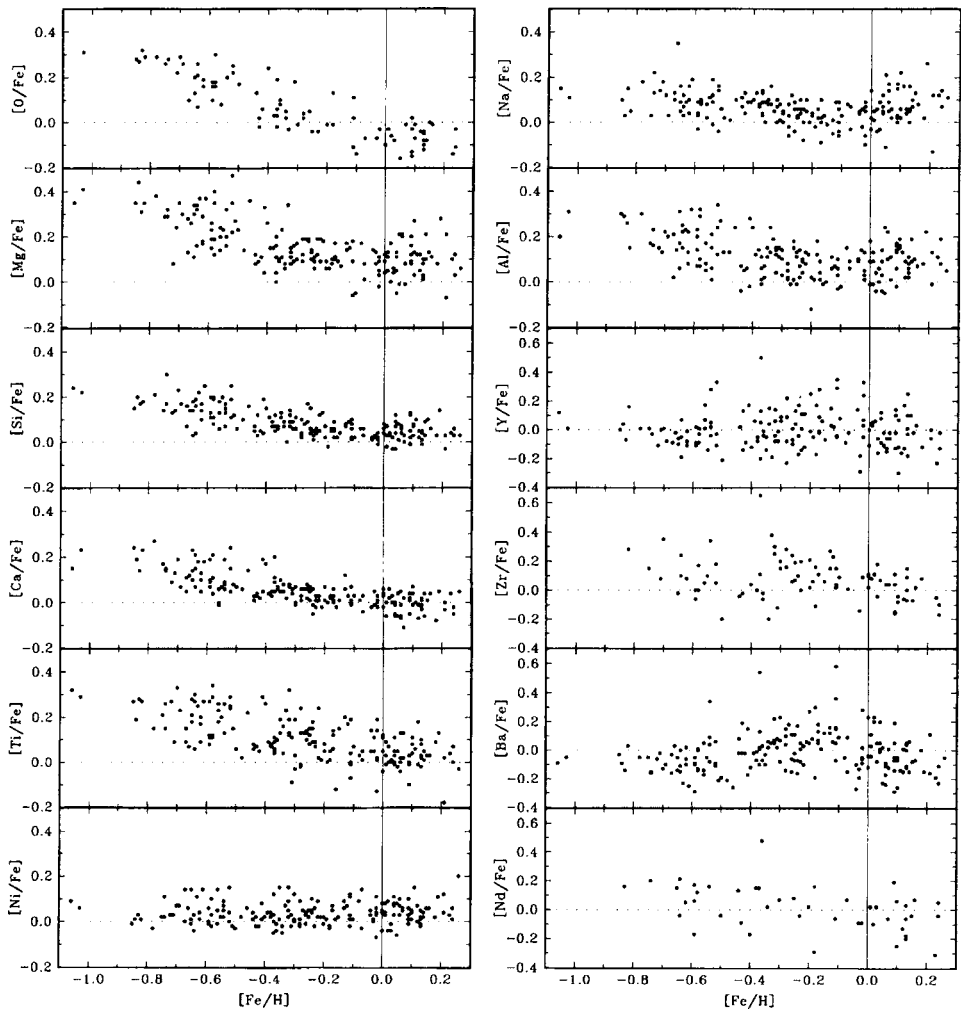
Fig. 8.8. Element:iron ratios measured in Galactic disk stars, after Edvardsson *et al.* (1993). Courtesy Johannes Andersen.

or at least no longer applies, to gas-poor systems) are the dwarf irregular and spiral galaxies with O-abundance determinations from H II regions within them, but there are some difficulties in estimating both the mass of gas (which may include undetected H_2 molecules as well as the observed H I) and the total stellar mass, which cannot be accurately deduced from gravitational effects like rotation curves because of the influence of dark matter. Thus one has to rely on 'photometric' determinations assuming a mass:light ratio based on some kind of stellar population synthesis. Furthermore, the H I gas is often much more extended than the stellar population, particularly in blue compact galaxies (BCGs), so that it is not
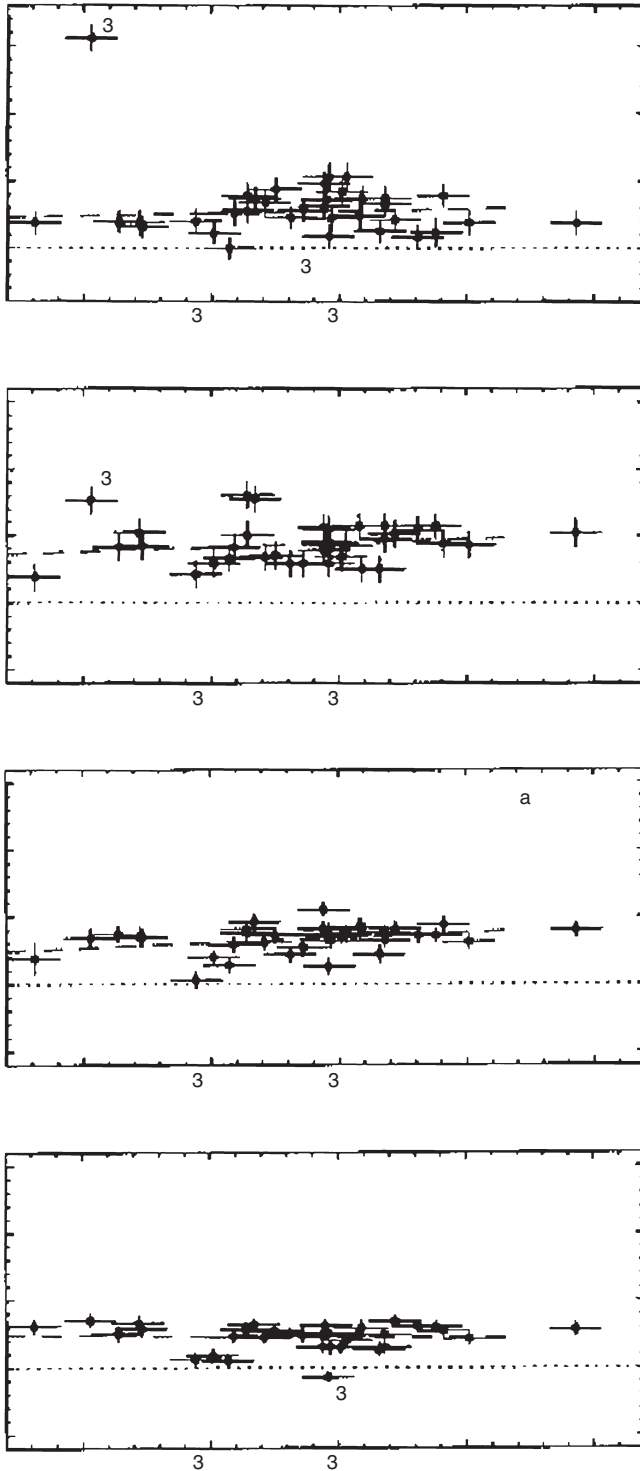
Fig. 8.9. Even-numbered element:iron ratios measured in ultra-metal-deficient Galactic halo stars, after Cayrel *et al.* (2004).
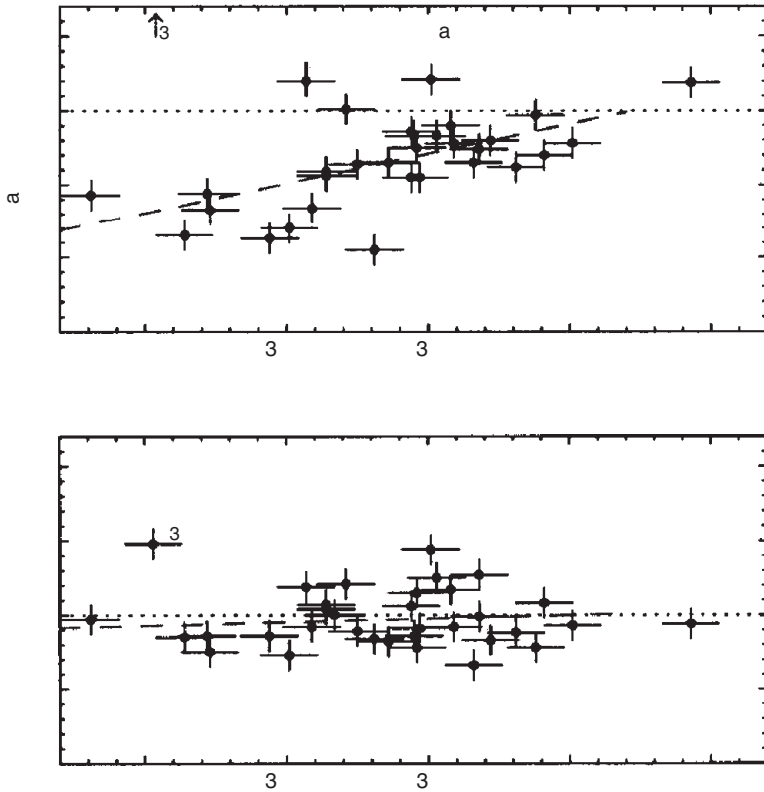
Fig. 8.10. Odd-numbered element:iron ratios measured in ultra-metal-deficient Galactic halo stars, after Cayrel *et al.* (2004).

clear how much of it shares the reasonably homogeneous chemical composition displayed in any one system by the H II regions themselves. Thus the comparison is best (but still not very well) carried out in irregulars and spirals rather than BCGs.

With these caveats, Fig. 8.12 shows an attempt at such a comparison, with some estimates of uncertainties. A rough relationship of the predicted form is indeed apparent for the spirals, whereas in the less massive irregulars, the effective yield (defined as $Z_O/(-\ln \mu)$) is low, going down to about 4 times less than the estimates for the solar neighbourhood. This is usually attributed to a preferential loss of hot metal-enriched stellar ejecta in galactic winds escaping from the shallow potential wells of these systems, although it has also been suggested that the true yield may increase with metallicity, e.g. if the low-metallicity IMF has a larger proportion of low-mass stars (Peimbert & Serrano 1982).
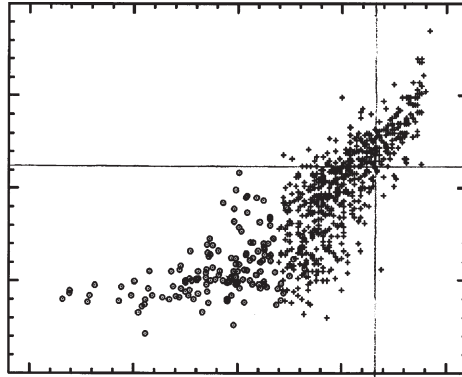
Fig. 8.11. N/O ratio vs. O/H in H II regions of irregular (circles) and spiral galaxies (plus signs), adapted from Pilyugin, Thuan and Vílchez (2003). Solar values are indicated by the axes.
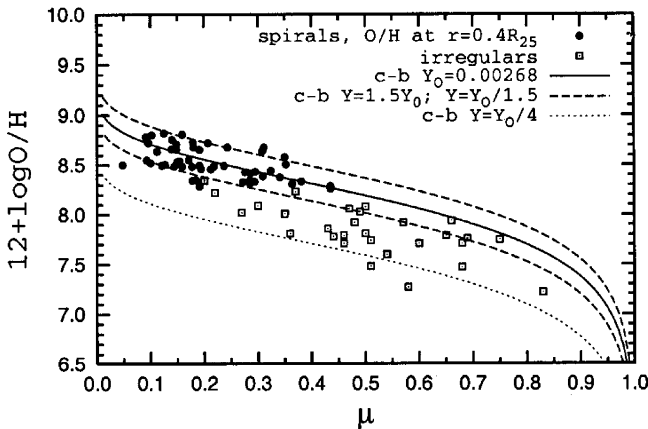
Fig. 8.12. Relation between oxygen abundance of H II regions in irregular (open squares) and spiral galaxies (filled circles, taking abundances at 0.4 of the de Vaucouleurs isophotal radius R_{25}) plotted against the gas fraction, after Pilyugin, Vílchez and Contini (2004). The heavy curve shows expectation from the Simple model with an oxygen yield of 0.0027 (or about 0.5 $Z_\odot$) and the broken curves show the same with the yield 1.5 × higher or lower, whereas the dotted curve shows a yield 4 × lower. The effective yield, defined as $Z_O/(-\ln\mu)$, increases systematically with luminosity, and the gas fraction decreases.

A relationship also exists between abundances and luminosity of the host galaxy, whether gas-rich or otherwise (Fig. 3.44), and especially with the rotational velocity in disk galaxies (Fig. 8.13). Similarly, studies of elliptical galaxies in general suggest that the primary factor fixing the mean metallicity of their stellar
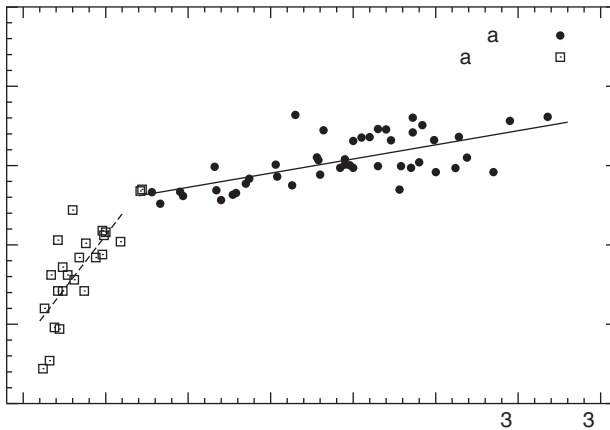
Fig. 8.13. H II region oxygen abundance against rotational velocity for irregular and spiral galaxies (at a radius of $0.4R_{25}$), after Pilyugin, Vílchez and Contini (2004).

populations is the velocity dispersion, which in turn may be closely related to the escape velocity, related, in turn, to total mass (see Chapter 11).

8.3.5 Radial abundance gradients in spiral disks

The Simple model can account to some extent for the existence of radial abundance gradients in the ISM of spiral galaxies (see Figs. 3.40, 3.41, 3.43 and 3.45), if it is assumed (a) that evolution takes place in isolated concentric zones analogous to the solar cylinder, and (b) that the gas fraction decreases inwards towards the Galactic centre (Searle & Sargent 1972), implying faster timescales for conversion of gas into stars in the inner regions. A much smaller gradient would apply to the stellar population according to Eqs. (8.7), (8.8). The stellar surface density falls off exponentially with Galactocentric distance with a scale length $\alpha_*^{-1} \simeq 4$ kpc, while the distribution of H I + H_2 shown in Fig. 8.14 can be quite well approximated between 4 and 17 kpc (assuming the KBH rotation curve) as an exponential with a scale length $\alpha_g^{-1} \simeq 12$ kpc. Equation (8.6) then leads to an abundance distribution law in the ISM

$$z(R) = -\ln \mu(R_\odot) - (\alpha_* - \alpha_g)(R - R_\odot) + \ln\left(\frac{1 + g(R)/s(R)}{1 + g(R_\odot)/s(R_\odot)}\right) \qquad (8.13)$$

$$\simeq 1.8 - 0.17(R - R_\odot) + 0.0013\, R^2. \qquad (8.14)$$

The oxygen abundance then decreases more or less linearly from about $2\,Z_\odot$ near the centre to $Z_\odot$ in the solar neighbourhood, reaching about $0.3\,Z_\odot$ at 20 kpc.
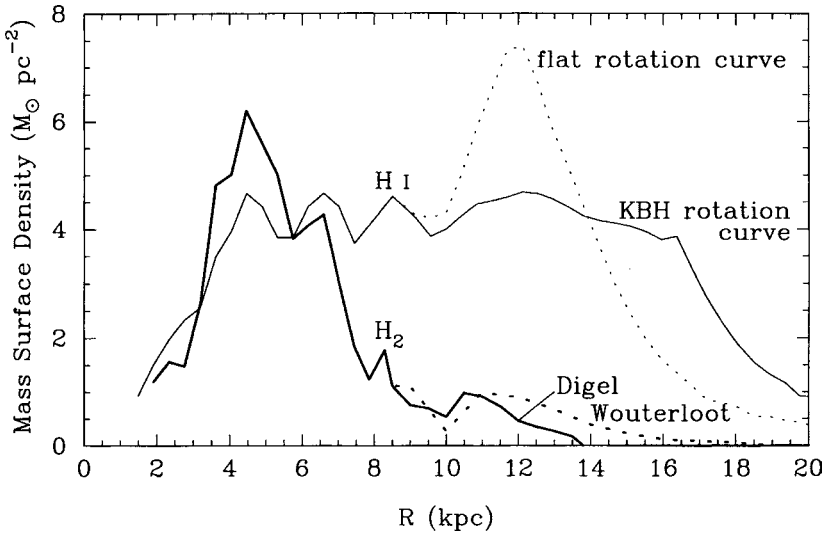
Fig. 8.14. Surface densities of atomic and molecular hydrogen in the Galaxy as a function of Galactocentric distance; the Sun is at 8.5 kpc. Beyond that distance, the deduced surface density depends on the assumed law of Galactic rotation; KBH refers to Kulkarni, Blitz and Heiles (1982). Assuming their rotation curve, the total gas surface density falls by about a factor of 2 between 4.5 and 13 kpc, corresponding to an exponential fall-off with a scale length α_g^{-1} of about 12 kpc. After Dame (1993). Courtesy T. M. Dame.

This corresponds to logarithmic gradients of $-0.03 \, \text{dex kpc}^{-1}$ between 5 and 10 kpc and a slightly steeper one of $-0.04 \, \text{dex kpc}^{-1}$ between 10 and 15 kpc. The observed gradient is somewhere between about -0.07 and $-0.04 \, \text{dex kpc}^{-1}$ (Shaver *et al.* 1983; Deharveng *et al.* 2000) and fairly uniform in logarithmic terms (see Fig. 3.40), although there could be a flattening outside the solar circle. Given all the uncertainties, the simple gas-fraction effect is probably at least a significant contributor to the gradient and it may be the main cause in the outer parts of the Galaxy. Other influences on the gradient, which may become dominant in the more inner regions, are dissipative processes such as inward radial flows of gas driven by viscosity or by a mismatch of angular momentum of inflowing material. A generic relation between dissipation and abundance gradients in the stellar population is discussed in Appendix 5, but its effect on the abundance gradient in the gas depends on details of the velocity field. Other factors influencing abundance gradients include differential effects of inflow of unprocessed material at different radii (apart from any dynamical effects) and radial mixing caused by perturbations of axial symmetry, e.g. by a central bar.

8.3.6 Age–metallicity relation in different stellar populations

The instantaneous Simple model predicts a monotonic increase in the abundance of any robust element with time, which can be quantified if a star formation law is assumed. If, for example, the SFR is assumed proportional to the mass of gas as

$$ds/dt = \omega g \tag{8.15}$$

with ω constant, the abundance of a primary element increases linearly with time according to

$$z = \omega t. \tag{8.16}$$

More generally, ω may be treated as variable, thus not appealing to any particular star formation law, in which case we still have

$$z(t) = \int_0^t \omega(t')dt' \equiv u, \tag{8.17}$$

say, where u is some single-valued non-decreasing function of time. An increase with time is found in a qualitative sense in the low metallicities observed in most stars of the Galactic halo population and in high-redshift absorption-line systems on the line of sight to quasars, including the damped Lyman-α systems which are believed to represent an early form of disk galaxies. However, the scatter at a given redshift is large, which is not surprising given that star formation probably began at different times in different places, and overall ambient density turns out to be more significant in cosmic chemical evolution than is time as such (Cen & Ostriker 1999). Coming back to our own Galaxy, Fig. 8.15 shows the relationship between metallicity and Galactic rotation velocity for high proper motion stars, which probably give a fair sample of the halo population while undersampling the disk in a kinematically biased way. The disk stars, with numerically small relative velocities V in the direction of Galactic rotation, overlap in age and metallicity with the halo stars, which have an average $\langle V \rangle \simeq -220 \, \text{km} \, \text{s}^{-1}$, but there is a sparsely populated diagonal region in the diagram which enables most individual stars to be assigned to one class or the other. The two populations have very different abundance (as well as dynamical) properties, as will be described below, which reflect their distinct evolutionary histories. The halo stars are old, with ages somewhere between 10 and 14 Gyr (this range is a combination of systematic uncertainties with probably some real variation), while the ages of disk stars range from zero to values typical of halo stars.

It is therefore among the disk stars of the solar neighbourhood that one looks for quantitative evidence for an age–metallicity relation; some relevant data are shown in Figs. 8.16, 8.17 and 8.41.
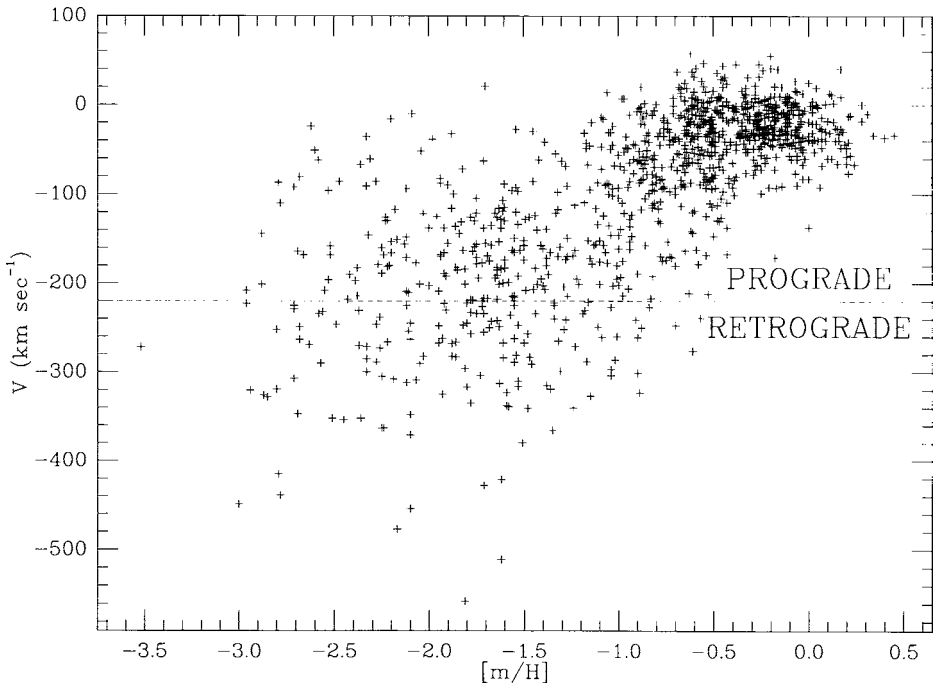
Fig. 8.15. Plot of velocity V along the direction of Galactic rotation, relative to the local standard of rest, against metallicity [m/H] (essentially [Fe/H]) for high proper motion stars, after Carney *et al.* (1996). A relatively sparsely populated gap runs from upper left at $(-1.6, 0)$ towards lower right at $(-0.5, -200)$. Courtesy John Laird.

An overall relation of the form of Eq. (8.16) gives as good a fit as any to the average of the data in the solar neighbourhood, but there has been much argument as to how much scatter there is over and above determinational uncertainties (especially in the ages), and as to the influence of selection effects, and doubts have even been expressed as to the very existence of an age–metallicity relationship; the issue is complicated by the fact that most stars with [Fe/H] < -0.5 belong to the thick disk referred to in more detail below. Some of the scatter comes from the presence in the sample of stars originating at different Galactocentric distances with different evolutionary timescales (Edvardsson *et al.* 1993); see Fig. 8.17. A contribution from the latter effect is suggested by a tendency noted by Edvardsson *et al.* for [O/Fe] and [α/Fe] to be larger (for given [Fe/H]) at smaller mean Galactocentric distances (see the 'bulge' point in Fig. 8.7), implying faster enrichment rates there if most of the iron comes from SN Ia progenitors with significant lifetimes.

Figure 8.8 shows a marked increase in the scatter of [α/Fe] as one goes down through [Fe/H] $= -0.4$, at which point there is also a marked change in kinematic properties, notably the dispersion of velocities W perpendicular to the Galactic
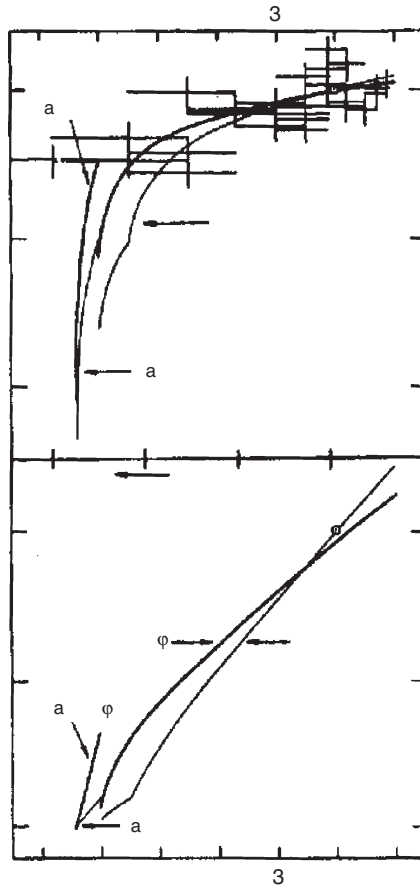
Fig. 8.16. Upper panel: stellar values of [O/H] plotted against age for disk stars, after Nissen, Edvardsson and Gustafsson (1985). Curves show theoretical values of [O/H] and [Fe/H] from an analytical model. The lower panel shows the same curves plotted on a linear scale, where $\log \phi \equiv$ [O/H] and $\log f \equiv$ [Fe/H]. After Pagel (1989a).

plane (Fig. 8.18). The stars on the left of this divide are usually referred to as belonging to the 'thick disk', or 'Intermediate Population II', and have ages ranging from about 8 Gyr up to that of the halo stars. There are doubts as to whether the sudden increase in velocity dispersion can be explained by conventional dynamical heating mechanisms from gravitational action by molecular clouds or spiral structure. It could be related to cooling processes in the early formation of first the halo, then the thick disk and then (after enhancement of cooling efficiency by growing metallicity) the thin disk (Burkert, Truran & Hensler 1992), but another possibility is that the disk was dynamically heated at the appropriate stage by capture of one or more satellite galaxies which themselves may or may not have been part of the
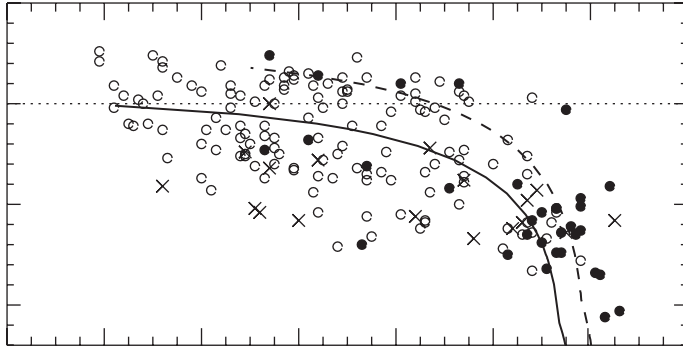
a

Fig. 8.17. Age–metallicity relation for disk stars using data from Edvardsson *et al*. (1993). Open circles, filled circles and crosses represent respectively stars with mean Galactocentric distances 7 to 9 kpc (like the Sun), stars from the inner Galaxy (under 7 kpc) and from the outer Galaxy (over 9 kpc). Model curves assume linear star-formation laws with $\omega = 0.3\,\mathrm{Gyr}^{-1}$ and an age of 15 Gyr (full-drawn curve) outward of 7 kpc and $\omega = 0.45\ \mathrm{Gyr}^{-1}$ and an age of 16.5 Gyr (broken-line curve) inward of 7 kpc. Stars older than 10 Gyr mostly belong to the thick disk. After Pagel and Tautvaišienė (1995).

primeval halo (Freeman 1990). Residual gas in the disk would then have cooled and collapsed leading to the thin disk. There may be a discontinuity in chemical history between the thick and thin disks, comparable to the differences between the disk and the halo; hardly any thin-disk stars are found with [Fe/H] < -0.5 (Fig. 8.17).

8.3.7 Stellar abundance distribution functions and the 'G-dwarf problem'

Unlike the age–abundance relation, the distribution function of stellar abundances of primary elements is independent of past rates of star formation as long as instantaneous recycling holds, and this makes it a potentially powerful clue to the evolutionary histories of stellar populations.

This can be seen by rewriting Eq. (8.6) as

$$\frac{g}{M} = 1 - \frac{s}{M} = e^{-z} \tag{8.18}$$

or

$$\frac{s(z)}{M} = 1 - e^{-z}, \tag{8.19}$$
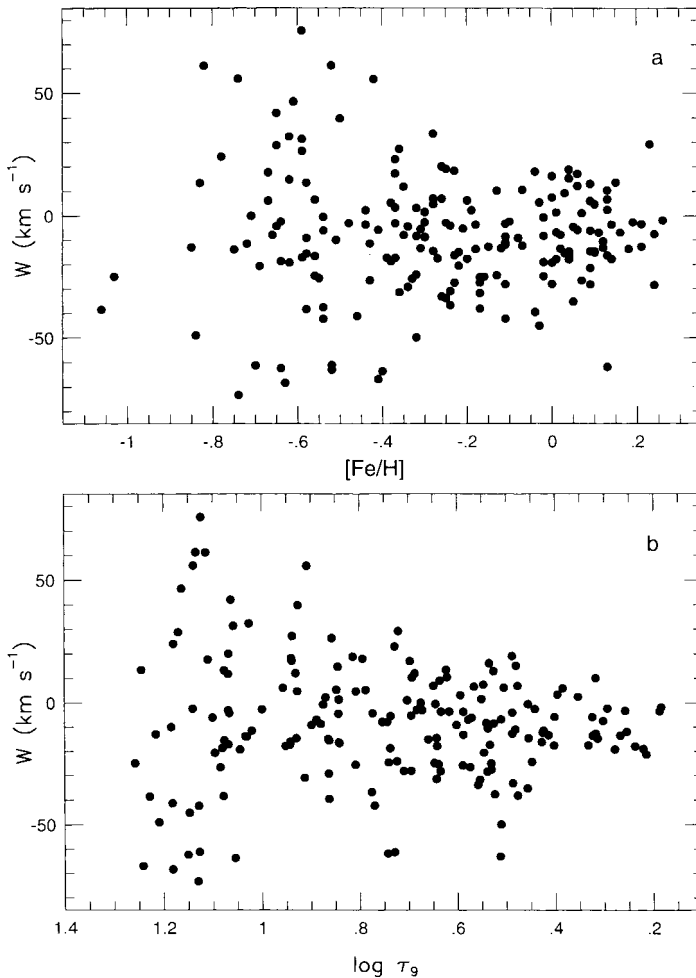
Fig. 8.18. W-velocities vs. age and metallicity for the nearby F and early G star sample, after Edvardsson *et al*. (1993). Courtesy Bengt Edvardsson.

whence

$$\frac{ds}{d\log z} \propto z e^{-z}; \quad z \leq \ln\left(\frac{1}{\mu}\right). \tag{8.20}$$

This equation (with a characteristic peak value at $z = 1$ or $Z = p$) is expected to apply primarily to oxygen and α-elements in stars that have lived long enough since the origin of the Galaxy to be still observable today, but may also apply approximately to iron in cases where O, α/Fe $\simeq$ const.

Figure 8.19 shows an estimate of the distribution function of oxygen abundances among field stars of the Galactic halo and Fig. 8.20 shows the iron abundance
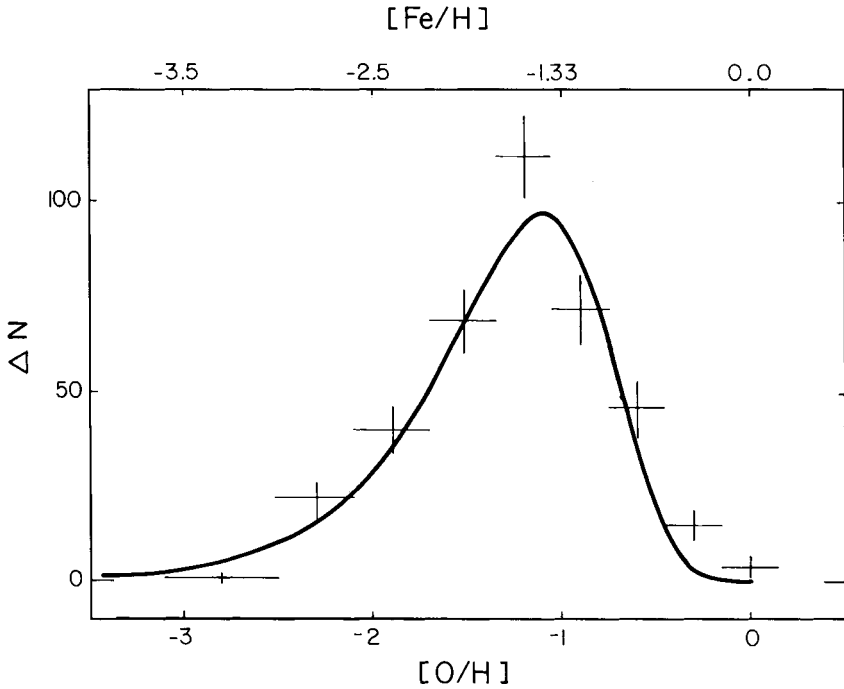
Fig. 8.19. Distribution function of oxygen abundances among halo field stars taking [Fe/H] from Fig. 8.15 and assuming an Fe–O relation similar to those in Fig. 8.5, after Pagel (1992b). With kind permission from Kluwer Academic Publishers.
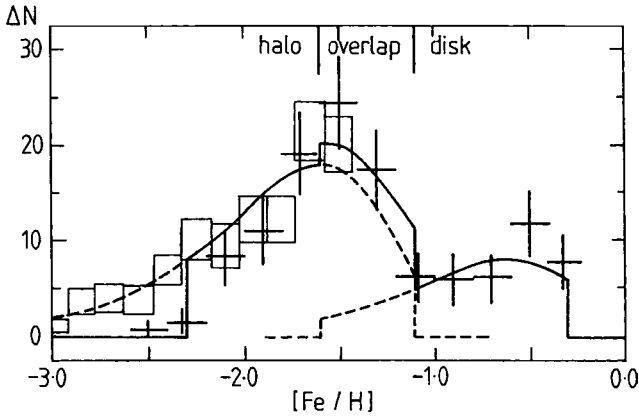
Fig. 8.20. Metallicity distribution function of globular clusters (crosses indicating error bars and bin widths) and halo field stars (boxes), after Pagel (1991). Copyright by Springer-Verlag.

distribution function for globular clusters with a portion of the one for halo field stars superposed.

The distribution function for field stars in the halo is reasonably well fitted by the Simple model equation (8.20) with a small remaining gas fraction, but with a very low effective yield $p \simeq 10^{-1.1} Z_{\odot}$ for oxygen (see earlier comments on dwarf galaxies). This was first noted (actually for globular clusters) by Hartwick (1976), who pointed out that it could be readily explained by continuous loss of gas from the halo in the form of a homogeneous wind with a mass loss rate from the system proportional to the rate of star formation. In this case,

$$\frac{E}{\alpha \psi} = \text{const.} = \eta, \tag{8.21}$$

say. Then we have from Eq. (7.35), with $F = 0$,

$$g\frac{dz}{ds} = 1, \text{ i.e. } \frac{dz}{ds} = \frac{1}{g} \tag{8.22}$$

and then from Eq. (7.32)

$$g\frac{dz}{dg} = -\frac{1}{(1+\eta)}, \tag{8.23}$$

whence

$$\frac{g}{M_0} = e^{-(1+\eta)z}, \tag{8.24}$$

where M_0 is the initial mass of the system, so from Eq. (8.22)

$$\frac{ds}{d\log z} \propto z\frac{ds}{dz} \propto z\,e^{-(1+\eta)z}, \tag{8.25}$$

similar to the Simple model but with an effective yield $p/(1 + \eta)$. (Note that a *terminal* wind, in which all the gas is expelled at a particular time when the metallicity is still low but the effective yield is undiminished, would lead to a completely different distribution function rising monotonically up to a cut-off (Yoshii & Arimoto 1987).) If there were a metal-enhanced wind rather than a homogeneous one, the relative amount of mass required to be lost would be smaller.

The distribution function for globular clusters is somewhat more complicated, as there appear to be two (probably overlapping) distributions corresponding to the halo and the thick disk, respectively. These have been tentatively fitted in Fig. 8.20 with a Simple model truncated at [Fe/H] = −1.1 for the halo and a model for the thick disk clusters with an initial abundance [Fe/H] = −1.6 (the mean metallicity of the halo) and truncated at [Fe/H] = −0.35. The disk-like character of the more metal-rich clusters is supported by their spatial distribution (Zinn 1985). Furthermore, there is a marginally significant shortage of globular clusters in the lowest

metallicity bins which, if real, could reflect some difference in the chemical evolution of cluster and field stars. However, disregarding the disk clusters, the overall distributions of cluster and field star abundances are quite similar.

What happened to the gas expelled from the halo? A traditional answer based on monolithic models of a Galaxy collapsing through successive stages of halo, thick disk and thin disk would be that the expelled gas formed the raw material of the disk. This hypothesis faces some severe difficulties. For one thing, the remaining mass in the halo should then be about 10 per cent of the mass of the disk, whereas it is probably a factor of 5 or so less than this (Carney, Latham & Laird 1990). Another difficulty is the specific angular momentum, as is apparent qualitatively from Fig. 8.15 and is illustrated quantitatively in Fig. 8.21.

The bulge metallicity distribution also shows a rough compatibility with a Simple model (Fig. 8.22), although the exact metallicities here (based on multicolour photometry) depend on those of globular clusters used for calibration which are not quite certain. Nevertheless, broadly similar distributions have been derived from direct spectroscopy (Fulbright, McWilliam & Rich 2006). An initial enrichment corresponding to [Fe/H] = −1.6 (as could be expected from inflow of halo gas) is not excluded by the data.

The data discussed so far have not been in violent conflict with the ideas underlying the Simple model. However, as was pointed out long ago by van den Bergh
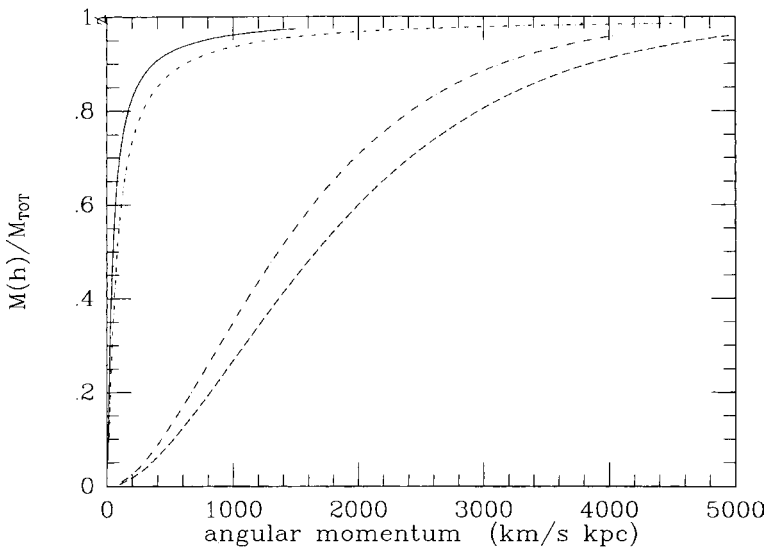
Fig. 8.21. Cumulative distribution function of specific angular momentum in the thin disk (broken line), thick disk (dots and long dashes), halo (dots and short dashes) and bulge (solid line), after Wyse and Gilmore (1992). Courtesy Rosemary Wyse.
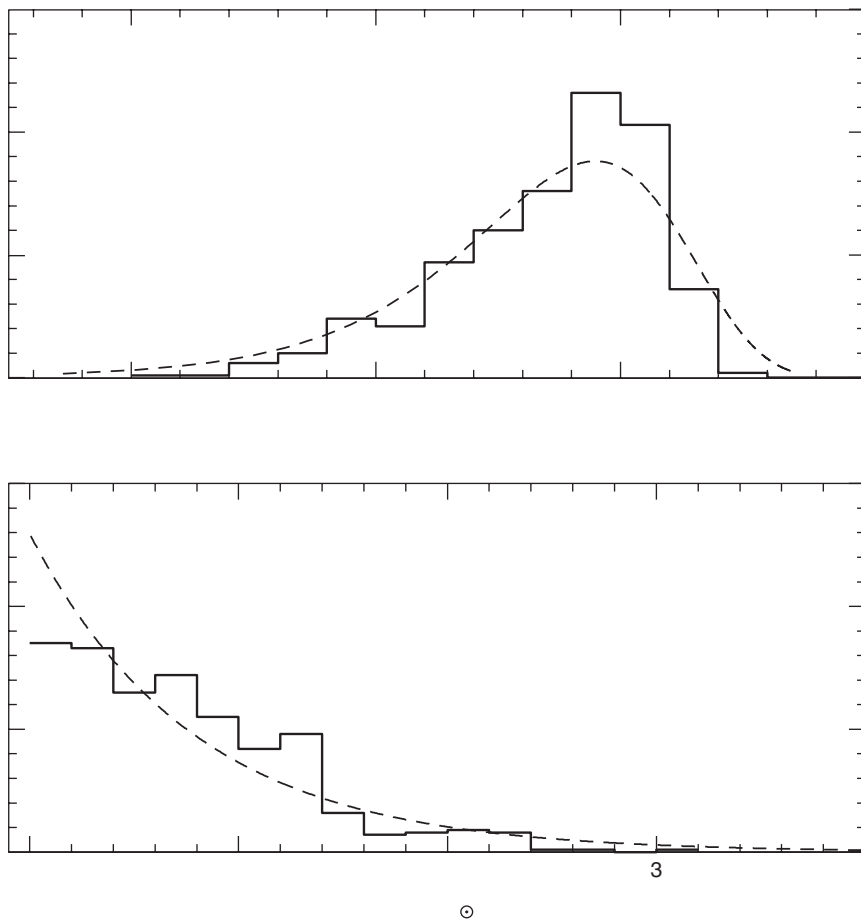
Fig. 8.22. Metallicity distribution function for giants in the Galactic bulge, after Zoccali *et al.* (2003), fitted with a Simple model having a yield of $Z_\odot$.

(1962) and Schmidt (1963), the abundance distribution function for long-lived stars (G dwarfs) in the solar neighbourhood is in sharp contradiction to these ideas because there are relatively too few low-metallicity stars compared to Eq. (8.20). This 'G-dwarf problem' is illustrated in Fig. 8.23, which shows two estimates of the oxygen abundance distribution function in the solar cylinder, based on ultra-violet excess statistics for nearby stars, together with an iron–oxygen relation and allowance for the dependence of the scale height of the spatial distribution of stars as a function of metallicity. These corrections lead to the substantial uncertainties indicated by the error boxes in the figure, and the data have subsequently been improved, but the contradiction with the prediction of the Simple model is evident, the more so after its relative success with the halo and the bulge.
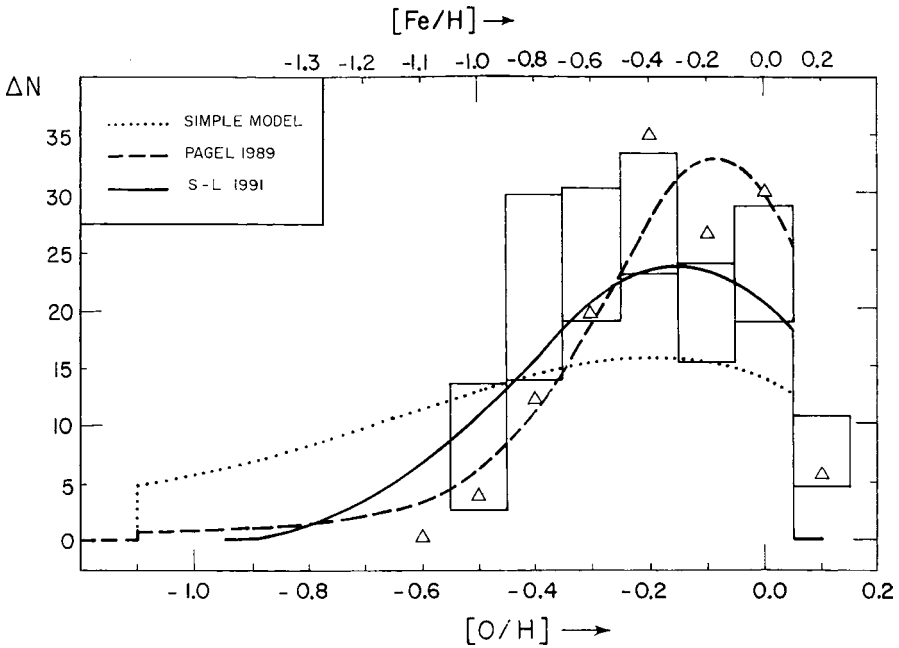
Fig. 8.23. Distribution function of oxygen abundances of 132 G dwarfs in the solar cylinder, binned in intervals of 0.1 in [O/H]. Triangles show the data points after Pagel (1989ab), based on a re-analysis of those discussed by Pagel and Patchett (1975), and boxes show lower and upper limits based on a new discussion of the dependence of the scale height on age and metallicity by Sommer-Larsen (1991a). The dotted curve shows predictions of an instantaneous Simple model with an initial enrichment [O/H] = −1.1 from the halo. The other model curves are discussed below. After Pagel (1992a). Copyright by Springer-Verlag.

Errors in the use of the instantaneous recycling approximation need to be considered, depending on the assumed history of star formation and mass ejection. After long times, e.g. 15 Gyr, low-mass stars eject relatively metal-poor material and modify the distribution in a similar way to what happens in some of the inflow models discussed below. However, it is still rather doubtful whether any Simple model can explain the abundance distribution function as well as satisfying other constraints.

The 'G-dwarf problem' has inspired numerous attempts to devise more sophisticated GCE models, some of which may be more realistic than the Simple one.

8.4 Suggested answers to the G-dwarf problem

A great variety of solutions to the G-dwarf problem have been proposed, including the following:

(i) The problem is a pseudo-problem arising either (a) from poor selection of stars, because the G dwarfs are not long-lived enough; (b) from a combination of factors including (i) corrections to the photometric metallicity scale which bring the peak in the local volume-limited sample up to solar metallicity rather than 0.1 to 0.2 dex below, (ii) the adoption of a relatively high normalization for the thick disk, and (iii) the assumption of a chemical evolution model that leads to relatively small values of [O/Fe] or [Mg/Fe] at low metallicities (Haywood 2001); or (c) because the older stars have migrated away from the solar neighbourhood into the inner Galaxy. The first point is believed to be an additional source of corrections to the adopted distribution law, but not to be so strong as to remove the 'problem' (Bazan & Mathews 1990); there is, after all, no obvious shortage of low-metallicity G dwarfs in the halo. Their masses are probably somewhat smaller than those of more metal-rich G dwarfs, but given the small slope of the IMF in this region, that can have only a minor influence.

The third point, which has been raised by Grenon (1989, 1990), is somewhat more interesting. Grenon's conclusions are based on a survey of parallax and proper motion stars which is kinematically biased against the 'silent majority' of ordinary stars of the (thin) disk, and the problem is to balance the number of stars that have moved out of the solar cylinder due to kinematic heating and related effects against the number that have moved in for the same reason. However, only insignificant radial abundance gradients are found for old G and K giant populations in the disk (Neese & Yoss 1988; Lewis & Freeman 1989); thus no major effect is expected, although the problem does deserve to be looked at more closely.

(ii) The solution originally proposed by Schmidt (1963) was that yields were higher in the past, due to an IMF with more high-mass stars. (A similar result would follow from Maeder's oxygen yields for strong mass loss, even for fixed IMF, if all stars up to 120 $M_\odot$ undergo SN explosions, see Carigi (1994); if, however, only those below 25 or 30 $M_\odot$ did so, the result would be the opposite.) The problem is that the drop in numbers below [Fe/H]= -1 is very sudden, so the required behaviour of the yield looks rather contrived.

(iii) Talbot and Arnett (1973b, 1975) suggested the hypothesis of 'metal-enhanced star formation' in which there would be large fluctuations in the metallicity of the ISM and stars would be preferentially formed in high-metallicity regions. This idea also requires contrived-looking parameters and is now only of historical interest; chemo-dynamical models (Burkert & Hensler 1989) suggest precisely the opposite effect, i.e. that the hot ISM is more enriched (from supernova ejecta) than the cold molecular clouds from which stars form.

(iv) If for some reason there is a finite initial abundance Z_0 of the order of [O/H]= -0.6 or [Fe/H] $\simeq -1$, due to an initial production spike or 'prompt initial enrichment' (Truran & Cameron 1971), an excellent fit to the distribution function is immediately obtained at the expense of excluding the few stars that actually do lie in the low-metallicity tail. Such initial enrichment could come from prior star formation activity in the halo (Ostriker & Thuan 1975) or preferably the bulge. Köppen and Arimoto (1990) have put forward a model in which the bulge evolves with a large true yield (1.7 $Z_\odot$) and

ends star formation by expelling 1/10 of its mass as gas with an abundance 2.5 $Z_\odot$ in a terminal wind which is captured by the proto-disk. Assuming the latter to have a mass equal to that of the bulge, this results in an initial disk abundance of 0.25 $Z_\odot$ after mixing. This picture is obviously consistent with the metallicity distribution functions of both the bulge (if we consider only α-elements like Mg with [Mg/Fe] $>$ 0 in the bulge) and the disk, apart from its low-metallicity tail. The possible relevance of this picture regarding both the high yields in the bulge and its large mass:light ratio (similar to elliptical galaxies and attributed to a high proportion of white dwarfs resulting from the relatively flat IMF that causes the high yield) is contingent on the reality of high α-metallicities among bulge stars; from observation, the iron and oxygen yields, in contrast to those of magnesium and titanium, appear to be no greater than locally (Sadler, Rich & Terndrup 1996; McWilliam & Rich 2004).

(v) Starting with the work of Larson (1972) in connection with dynamical models of galaxy formation, it has been a popular idea to account for the G-dwarf metallicity distribution on the basis of inflow models, i.e. formation of the Galactic disk by gradual accretion of unprocessed or partially processed material which only starts to form stars after it has fallen into the disk, as was first proposed by Oort (1966) as an explanation of the high-velocity H I clouds. These models have many attractive features and will be described in some more detail in the next section.

(vi) Merger models, which have gained popularity in recent years as a result of cosmological simulations of large-scale structure formation, can also provide a solution (Nagashima & Okamoto 2006); these are discussed further in Section 11.3.4.

8.5 Inflow models

Inflow models are attractive because they can shed light on dynamical processes during galaxy formation. The inflowing gas may be regarded as primordial or as having a modest amount of enrichment, e.g. if it comes from the gaseous halo as exemplified by the high-velocity H I clouds, from outer parts of the galactic disk or from the accretion of small satellite galaxies. The disk itself may be regarded as being formed entirely from such inflowing gas or as having a small (compared to its ultimate mass) initial mass and/or metallicity.

8.5.1 Extreme inflow model (Larson 1972)

In this case, which may be regarded as the opposite extreme to the Simple model, it is supposed that, through feedback processes, accretion occurs at just such a rate as to compensate the loss of gas in star formation, i.e.

$$g = \text{const.} \tag{8.26}$$

Then from Eq. (7.35) with $Z_F = 0$, $F = \alpha \psi$,

$$\frac{dZ}{ds} + \frac{Z}{g} = \frac{p}{g}$$

(8.27)

whence

$$Z = Z_0 e^{-s/g} + p (1 - e^{-s/g})$$

(8.28)

$$\rightarrow p, \quad \text{as } s/g \rightarrow \infty.$$

(8.29)

Thus the mass of stars and that of the whole system steadily increase while z soon approaches 1 and the stellar metallicity distribution is very narrow (see Fig. 8.24). The accretion rate is constant in time if the star formation rate is any fixed function of the mass of gas. Other models in which the accretion rate is constant, but less than in the extreme model, have been quite often considered in the older literature (e.g. Twarog 1980), but are less popular now because they are not well motivated from a dynamical point of view, there is an upper limit to the present inflow rate into the whole Galaxy of about $1 \, M_\odot \, \text{yr}^{-1}$ from X-ray data (Cox & Smith 1976) and they do not provide a very good fit to the observed metallicity distribution function.
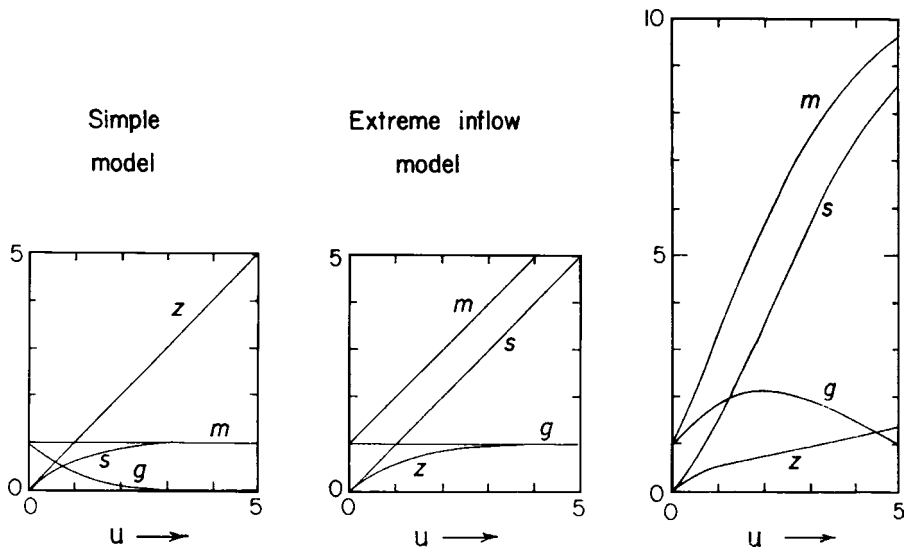
Fig. 8.24. Schematic behaviour of gas mass, total mass and metallicity in the Simple model (left), the extreme inflow model of Larson (1972) (middle) and a model with time-decaying inflow (right). The abscissa is $u \equiv \int_0^t \omega(t')dt'$ where ω is the (constant or otherwise) transition probability per unit time for gas to change into stars. The initial mass has been taken as unity in each case.

8.5.2 Analytical models with declining inflow rates

Larson (1974a, 1976) constructed dynamical models of the formation of the Galactic disk in which the disk develops outward from the central parts by inflow of gas at a rate which declines in the course of time as gas runs out, the mass of the system (and that of stars) approaches an asymptotic limit and the mass of gas reaches a maximum before declining at later stages more or less as in the Simple model. He noted that this picture can give a good representation of the G-dwarf metallicity distribution, and Lynden-Bell (1975) developed analytical versions of these and other models, among which his 'Best Accretion Model' is especially elegant. This model postulates a non-linear relation between gas mass and star mass which is the simplest quadratic relation having the desirable properties of leading to a maximum in the gas mass and a smooth decay at late times when star formation approaches completion:

$$g(s) = (1 - s/M)(1 + s - s/M) \tag{8.30}$$

where all quantities are in units of the initial mass and $M (\geq 1)$ is the final mass of the system. The case $M = 1$ reduces to the Simple model whereas, for larger values of M, $g(s)$ has a parabolic dependence with a maximum when $M \geq 2$. Equation (7.34) with $Z_F = E = 0$ can now be written

$$\frac{d}{ds}(Zg) = p - Z = p - \frac{Zg}{g} \tag{8.31}$$

with the solution (taking $Z_0 = 0$)

$$z(s) = \frac{1}{g(s)} e^{-\int_0^s \frac{ds'}{g(s')}} \int_0^s e^{\int_0^{s'} \frac{ds''}{g(s'')}} ds' \tag{8.32}$$

$$= \left(\frac{M}{1 + s - s/M}\right)^2 \left[\ln \frac{1}{1 - s/M} - \frac{s}{M}\left(1 - \frac{1}{M}\right)\right] \tag{8.33}$$

and

$$\frac{ds}{d \ln z} = \frac{z[1 + s(1 - 1/M)]}{(1 - s/M)^{-1} - 2z(1 - 1/M)}. \tag{8.34}$$

This generates a series of abundance distribution functions with M as a parameter (Fig. 8.25). As M increases, the distribution becomes more like a Gaussian (i.e. a parabola on this logarithmic plot) on the low-metallicity side of the peak (although there is still always a low-metallicity tail), and the peak itself shifts to lower metallicities in units of the yield.

Other analytical inflow models less sophisticatedly refer to a specific star formation law, usually linear

$$\alpha \psi \equiv \frac{ds}{dt} = \omega g(t); \quad \omega = \text{const.} \tag{8.35}$$
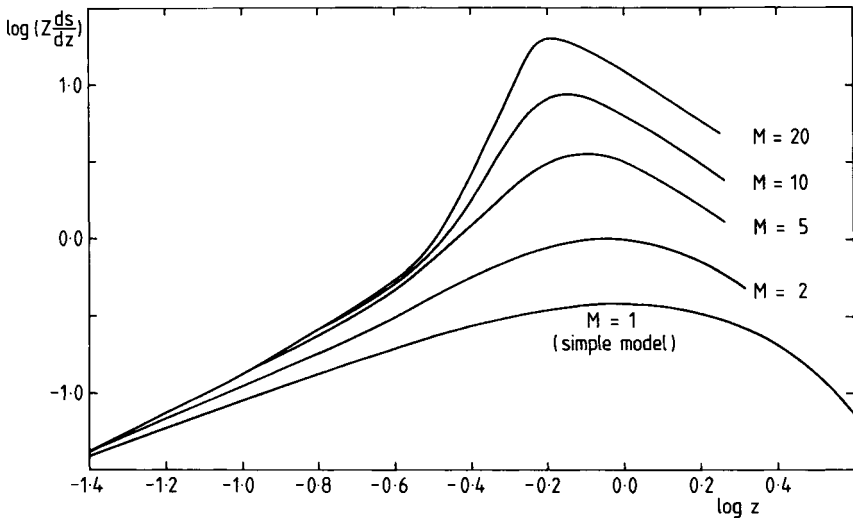
Fig. 8.25. Theoretical abundance distribution functions according to Lynden-Bell's 'Best Accretion Model' for different values of M, after Pagel (1989b).

This, however, can be generalized (except for cases where actual time is significant, as in the age–metallicity relation or cosmochronology) by letting ω vary arbitrarily with time and defining a time-like variable u by Eq. (8.17). Clayton (1985ab, 1987, 1988) has developed a very convenient series of models in which the inflow rate is parameterized by

$$F(t) = \frac{k}{t + t_0}\, g(t), \ \text{or}\ F(u) = \frac{k}{u + u_0}\, g(u), \tag{8.36}$$

where k is a small integer and t_0 or u_0 arbitrary. With Eq. (8.35), the mass of gas (in units of the initial mass) is then

$$g(t) = \left(1 + \frac{t}{t_0}\right)^k e^{-\omega t}, \ \text{or}\ g(u) = \left(1 + \frac{u}{u_0}\right)^k e^{-u} \tag{8.37}$$

giving the desirable maximum and (with $Z_F = Z_0 = 0$) one has

$$z(u) = \frac{u_0}{k+1}\left[1 + \frac{u}{u_0} - \left(1 + \frac{u}{u_0}\right)^{-k}\right] \tag{8.38}$$

and

$$\frac{ds}{d \ln z} = \frac{z(k+1)(1 + u/u_0)^k\, e^{-u}}{1 + k(1 + u/u_0)^{-(k+1)}} \tag{8.39}$$

with k and u_0 as parameters. The dashed curve in Fig. 8.23 shows a model of this kind with $k = 4$, after Pagel (1989a).

A still simpler inflow model, based on a dynamical model due to Sommer-Larsen (1991b), assumes inflow according to the law

$$F(u) = A\omega e^{-u}; \quad A = \text{const.} \tag{8.40}$$

Then from Eq. (7.31)

$$g(u) = (g_0 + Au) e^{-u} \tag{8.41}$$

where g_0 is the initial mass of the system assumed to be pure gas, while

$$M(u) = g_0 + A(1 - e^{-u}), \tag{8.42}$$

$$s(u) = g_0(1 - e^{-u}) + A[1 - (1 + u)e^{-u}] \tag{8.43}$$

and from Eq. (7.35), taking u as the independent variable instead of s,

$$z(u) = \frac{z_F}{1 + g_0/(Au)} + \frac{z_0}{1 + Au/g_0} + \frac{u(1 + \frac{1}{2}Au/g_0)}{1 + Au/g_0} \tag{8.44}$$

$$\to z_F + u/2 \quad \text{as } Au/g_0 \to \infty. \tag{8.45}$$

The full-drawn curve in Fig. 8.23 shows a model of this kind with $g_0 = Z_0 = 0$ and $Z_F = 0.1 \, Z_\odot$ for oxygen.

When $g_0 = Z_0 = Z_F = 0$, there are some very simple relations:

$$M(u) = A (1 - e^{-u}) \tag{8.46}$$

$$g(u) = Au \, e^{-u} \tag{8.47}$$

$$s(u) = A[1 - (1 + u)e^{-u}] \tag{8.48}$$

$$\mu(u) = u/(e^u - 1) \tag{8.49}$$

$$z(u) = u/2 \tag{8.50}$$

$$<z> = 1 - \frac{\frac{1}{2}u^2}{e^u - (1 + u)} \tag{8.51}$$

$$\frac{ds}{d\ln z} = 4Az^2 e^{-2z}; \quad z \le u/2. \tag{8.52}$$

The last relation is essentially the square of the corresponding one for the Simple model, Eq. (8.20); this does not go far enough to fit the G-dwarf metallicity distribution, but the above relations are useful in giving a quick estimate of the kind of departures from Simple model predictions that may be caused by inflow.

8.6 Models for the Galactic halo and disk

8.6.1 Did the Galaxy form by collapse?

Many models that have been put forward to describe the chemical evolution of the Galaxy (e.g. Hartwick 1976; Tinsley & Larson 1978, 1979; Chiosi 1980; Matteucci & François 1989; Pagel 1989a) have been largely inspired by the classic paper of Eggen, Lynden-Bell and Sandage (1962) who used correlations between the ultraviolet excess (i.e. metal-deficiency) of stars and their orbital eccentricity and motions perpendicular to the Galactic plane (see Fig. 3.39) to infer that the Galaxy had collapsed on a 'rapid' timescale from a proto-Galactic cloud, eventually forming the disk by a slower dissipative process. Since then, complications have appeared in this simple picture, notably an age spread among globular clusters, indications of a possible duality in the halo (Hartwick 1987; Norris 1994) and the suggestion that the latter is composed of merged satellite galaxies or 'fragments', as opposed to being a well-preserved relic of the initial collapse (Searle & Zinn 1978). The original ELS picture has been stoutly defended (with some modifications) by Sandage (1990), who sums up his point of view as 'SZ = ELS + noise!' Eventually some synthesis of the two viewpoints is likely to emerge, but one significant modification of the original ELS picture is occasioned by the identification of the thick disk (Gilmore & Reid 1983; previously identified, but with a different nomenclature, by Yoshii 1982) – broadly overlapping what had previously been known as 'Intermediate Population II' (Strömgren 1987 and references therein) – which consists of metal-deficient stars with only moderate eccentricities (see Fig. 8.15) and was missed by ELS owing to observational selection effects. Subsequent studies based on more extensive data for high-velocity stars (Sandage & Fouts 1987; Carney, Latham & Laird 1990; Ryan & Norris 1991; Nissen & Schuster 1991) and on kinematically unbiased objective-prism surveys (Norris, Bessell & Pickles 1985; Morrison, Flynn & Freeman 1990; Beers & Sommer-Larsen 1995) have revealed an ever-increasing degree of overlap in metallicity between thick-disk and halo stars. Some salient features of the thick disk have been shown above in Figs. 8.5, 8.6, 8.8 and 8.17. At the same time, the angular momentum distribution of halo stars (Fig. 8.21) suggests that the halo is quite disconnected from the evolution of at least the local part of the disk, so that the sort of connections studied by ELS should rather be sought among stars of the thick disk; within 1 kpc of the Galactic plane, these account for a significant proportion (about 30 per cent) of the stars with $[Fe/H] \leq -1.5$ as well as essentially all stars with $-1.0 \leq [Fe/H] \leq -0.5$ (Beers & Sommer-Larsen 1995).

Numerical modelling of the chemical evolution of the Milky Way and/or similar disk galaxies, taking into account dynamical effects, was pioneered by Larson (1976) and Tinsley and Larson (1978). Because of many uncertainties in the details

of stellar nucleosynthesis (some of which still persist), they simply parameterized the overall yield as a single constant, but explored in some detail the consequences of Larson's dynamically self-consistent collapse models. Features of those models have been at the basis of most subsequent efforts at modelling galactic chemical evolution, including rapid star formation and loss of angular momentum by the bulge and formation of the disk from the inside outwards by a slow dissipative collapse with continuing inflow of metal-poor gas. Tinsley (1979) first investigated the influence of progenitor lifetimes on the evolution of primary element ratios like O/Fe, a subject that was integrated into theories of the evolution of binary progenitors of SN Ia by Greggio and Renzini (1983) and Matteucci and Greggio (1986).

8.6.2 *Developments in analytical modelling*

Pagel (1989a) put forward an analytical model that was intended to give a minimal but reasonably comprehensive description of the relevant data for the solar neighbourhood: abundance distribution functions for the halo and disk; the relation between abundances of oxygen and magnesium, taken to be instantaneously produced, and elements involving a time delay, mainly iron and barium; and the age–metallicity relation for disk stars as it appeared at the time. Barium was taken to be produced at early times just by the r-process (Truran 1981; Lambert 1989), which accounts for about one tenth of its abundance in the Solar System (see Table 6.3), and its s-process contribution was taken to be 'primary' with a dimensionless time delay $\omega\Delta = 0.06$, to be compared with 0.5 for the delayed component of iron. Halo evolution was modelled following Hartwick (1976), assuming $1 + \eta = 10$ in Eqs. (8.21) to (8.25) (so as to fit an abundance distribution function like that in Fig. 8.19) and the linear star-formation law Eq. (8.15). With the delayed production approximation this leads to enrichment of the ISM according to

$$Z(t) = p\, e^{(1+\eta)\omega\Delta}\, \omega\,(t - \Delta); \quad t > \Delta \tag{8.53}$$

where p is the true yield. Halo evolution was assumed to end at $u \equiv \omega t = 0.5$, i.e. just before the onset of delayed iron, and to lead to deposition of gas with a mean $[O/H] = \log(p/10\, Z_\odot) = -1.1$ which formed the proto-disk. Disk evolution was then followed according to Clayton's formalism with Eq. (8.38) modified to allow for an initial abundance and delayed production as follows:

$$Z(t) = (1 + t/t_0)^{-k}\, [Z_0 + \frac{\omega t_0}{k+1}\, p\, e^{\omega\Delta}\{(1 + \frac{t-\Delta}{t_0})^{k+1} - 1\}]; \quad t > \Delta. \tag{8.54}$$

k was chosen to be 4 and ωt_0 to be 2 (corresponding to a final to inital mass ratio of 10.5), so as to give the disk abundance distribution function shown by the broken-line curve in Fig. 8.23.

Since then, there have been several developments suggesting that the above assumptions need to be modified. The r-process itself may involve a small time delay (Mathews & Cowan 1990) and the short time delay for the s-process gives too high abundances relative to iron at moderately low metallicities (Pagel 1991). The G-dwarf abundance distribution function, based on the old data of Pagel and Patchett (1975), was somewhat too narrow because of insufficient allowance for the larger scale height of low-metallicity stars resulting from poor statistics, and so more recently I have used the distribution shown by the boxes in Fig. 8.23. There are now better data on the relation between oxygen, α-elements and iron (Ryan, Norris & Bessell 1991; Bessell, Sutherland & Ruan 1991; Nissen & Edvardsson 1992; Edvardsson *et al.* 1993); see Figs. 8.5, 8.6, 8.8, 8.9. Finally, there no longer seem to be any strong grounds for believing that gas expelled from the halo provided the initial configuration of the disk. It seems rather that the thick disk began with zero metallicity and that the disk and halo have evolved independently.

Pagel and Tautvaišienė (1995) developed a simple analytical disk model which can reproduce the abundance distribution functions found by Sommer-Larson (1991a) for the solar neighbourhood and by Beers and Sommer-Larsen (1995) for the metal-weak thick disk and also the new data on certain element-to-element ratios. The thick-disk data indicate that we should now begin the game with a Simple model that goes on for a time t_1 such that $u_1 \equiv \omega t_1 = 0.14$ (assuming a true yield $p = 0.7 Z_\odot$ for oxygen), whereafter we switch on inflow into what will become the thin disk according to Clayton's formalism with $k = 3$, $u_0 = 1.3$ corresponding to an ultimate mass multiplication factor of 7. This reproduces the data in Fig. 8.26 fairly well and leads to an age–metallicity relation given by the solid curve in Fig. 8.17.

Table 8.1 shows some of the parameters in the model that determine the element:element ratios. Each element is assumed to have an instantaneous component, due to production by massive stars, giving a yield p_1, and a delayed component (treated by the delayed-production approximation) due to the contribution of SN Ia (for Si, Ca, Ti and Fe) or of low-mass SN II (for the r-process element Eu), giving a yield p_2 with a time-delay Δ. These are all independent of the mean Galactocentric distance R_m of the stars, but it is assumed that ω increases from $0.3\,\mathrm{Gyr}^{-1}$ in the solar neighbourhood to $0.45\,\mathrm{Gyr}^{-1}$ in the inner Galaxy, so that the dimensionless time-delay $\omega\Delta$ (as well as the metallicity at a given time; see Fig. 8.17) is larger in the latter case. The yields assumed ad hoc in Table 8.1 imply relative SN II and SN Ia rates in fair agreement with those derived by Tsujimoto *et al.* (1995) from detailed nucleosynthesis calculations and with observation, i.e. one SN Ia for about 7 SN II.

Table 8.2 gives an indication of the time-dependence of various quantities of interest, according to the model. The quantities given are the dimensionless time

Table 8.1. *Yields and time delays assumed in the analytical model for the Galactic disk*

El.	$p_1/Z_\odot$	$p_2/Z_\odot$	$\omega\Delta$ $R_m \geq 7\,\mathrm{kpc}$	$\omega\Delta$ $R_m < 7\,\mathrm{kpc}$
O	0.70	0.00		
Mg	0.88	0.00		
Si	0.70	0.12	0.4	0.6
Ca	0.56	0.18	0.4	0.6
Ti	0.70	0.12	0.4	0.6
Fe	0.28	0.42	0.4	0.6
Eu	0.08	0.66	0.008	
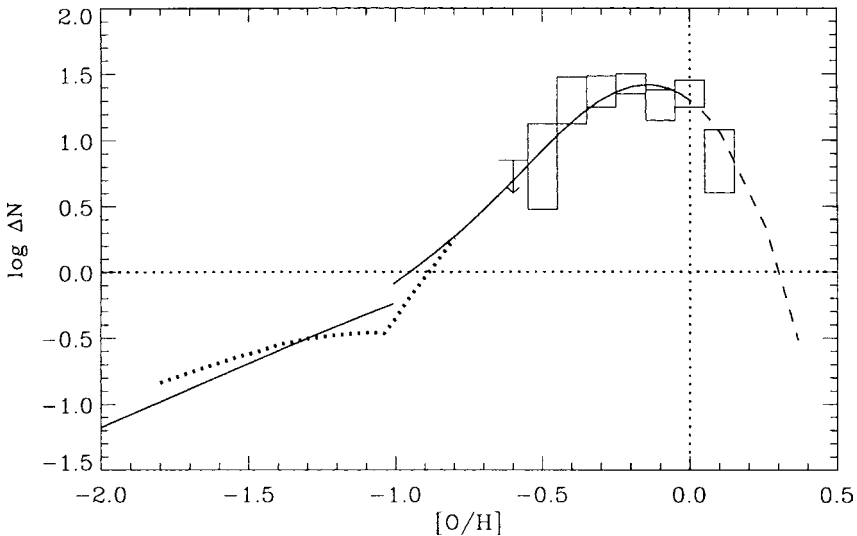
Fig. 8.26. Oxygen abundance distribution function for disk stars. Data deduced from observation are shown by the boxes (same as in Fig. 8.23, after Sommer-Larsen 1991a) and by the dotted line and curve at lower left (after Beers & Sommer-Larsen 1995). The solid curve shows the distribution given by the model of Pagel and Tautvaišienė (1995).

parameter u, the gas mass g, the total mass M, the gas fraction $\mu \equiv g/M$, the abundance z_1 of a promptly produced element in units of its yield, the corresponding abundance distribution function and abundances of representative elements. Delayed Eu comes in already at $u = 0.008$ (corresponding to a time delay of, very roughly, 25 Myr, which fits a $\sim 10\,M_\odot$ star) and at $u = 0.14$ the abundance distribution function changes owing to the onset of inflow. At $u = 0.4$ ($t \simeq 1.3\,\mathrm{Gyr}$), SN Ia

Table 8.2. *Model of chemical evolution of the disk in the solar neighbourhood*

u	g	M	μ	z_1	$z_1\, ds/dz_1$	[O/H]	[Ca/H]	[Fe/H]	[Eu/H]
0.001	1.00	1.00	1.00	0.001	0.001	−3.15	−3.25	−3.55	−4.10
0.008	0.99	1.00	0.99	0.008	0.008	−2.25	−2.35	−2.65	−3.19
0.14	0.87	1.00	0.87	0.14	0.12	−1.01	−1.11	−1.41	−1.00
0.14					0.172				
0.40	1.10	1.49	0.74	0.29	0.66	−0.69	−0.79	−1.09	−0.67
1.60	1.65	3.78	0.44	0.70	4.1	−0.31	−0.31	−0.37	−0.28
3.20	1.24	5.79	0.22	1.12	5.5	−0.11	−0.08	−0.10	−0.08
4.10	0.87	6.38	0.14	1.35	4.7	−0.02	0.01	0.00	0.00
4.50	0.75	6.55	0.11	1.45	4.2	0.00	0.05	0.05	0.03

start to contribute a major portion of Fe and minor portions of Si–Ti. $u = 1.60$ is the phase of maximum star-formation rate (2.3 times the present rate), $u = 3.20$ is the time of formation of the Solar System and $u = 4.50$ at the present time. $u = 4.10$ at the time of formation of stars now undergoing SN Ia outbursts. Figure 8.27 shows the fits of the model to oxygen and α-element to iron ratios derived from observation and Fig. 8.28 shows the corresponding fits for the r-process elements Eu and Th, the latter involving a small correction for radioactive decay. The overall fits in the two figures are quite good, bearing in mind that some of the most metal-deficient halo stars have composition anomalies such as are displayed by the remarkable iron-poor r-process-rich CS 22892−052 ([Fe/H] = −3.1; [m/Fe] $\simeq$ 1.5 for all r-process elements; Sneden *et al*. 1996) and such stars in general may display outputs from individual supernovae acting as star formation 'triggers' (Tsujimoto, Shigeyama & Yoshii 1999). Thus there is no reason to expect a smooth trend depending on stellar lifetimes and the left side of the curves in Fig. 8.28 should be flat with a large scatter (see Fig. 8.29). An alternative view is that the highly metal-deficient stars showing large excesses of r-process (and sometimes s-process as well as CNO) elements relative to iron are contaminated by binary companions – possibly neutron stars resulting from accretion-induced collapse of white dwarfs which generated some of the r-process elements in the first place (Qian & Wasserburg 2003).

The behaviour of elements like Ba, which have an s-process contribution at least in the case of the more metal-rich stars, may require two components: one with a short time delay as assumed by Pagel (1989a) and another one with a time delay slightly exceeding that for SN Ia (Edvardsson *et al*. 1993; Pagel & Tautvaišienė 1997); see Fig. 8.30.

Some further developments in analytical modelling are described in Section 8.6.4.
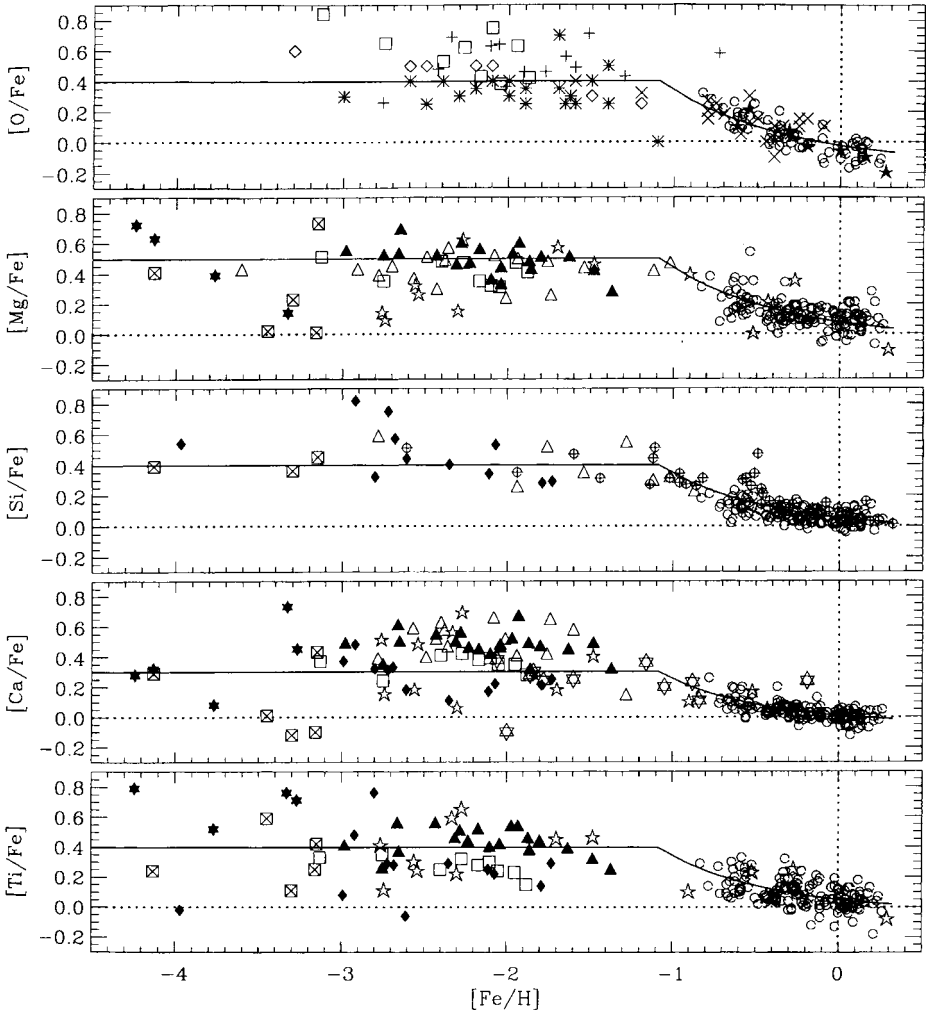
Fig. 8.27. Fits of the model to element-to-iron ratios measured by Edvardsson *et al.* (1993) for disk stars and by various authors for Population II stars which include a significant component from the metal-weak thick disk. The model curve is for $\omega\Delta = 0.4$. After Pagel and Tautvaišienė (1995).

8.6.3 Developments in numerical modelling

Numerical models offer the possibility to take into account all the details of stellar nucleosynthesis and time delays in a self-consistent manner, while still relying on various assumptions about star formation, inflow etc. that have little more physical justification than the crude approximations needed for analytical modelling, but can be chosen to fit the observational data.
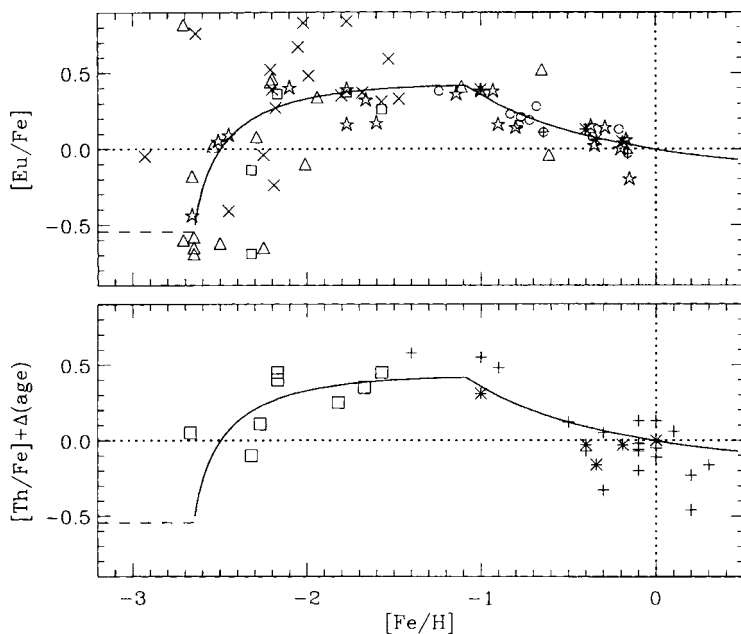
Fig. 8.28. Europium and thorium to iron ratios plotted against metallicity [Fe/H]. Curves represent the model predictions as in Table 8.2 and the symbols represent observational results by different authors. After Pagel and Tautvaišienė (1995).

Basic assumptions made in the models by Matteucci and her colleagues (e.g. Matteucci & Greggio 1986) involve a star formation law similar to the modified Schmidt law, Eq. (7.15):

$$\psi = \nu M \left(\frac{g}{M} \right)^k \tag{8.55}$$

with typically $\nu = (1.3\,\text{Gyr})^{-1}$, $k = 2$ and the total mass surface density $M = 0$ initially and $M(T) = 1$ in the solar cylinder at the present time; and an inflow rate

$$F = M(T) \frac{e^{-t/\tau_{\text{inf}}}}{\tau_{\text{inf}}(1 - e^{-T/\tau_{\text{inf}}})} \tag{8.56}$$

(Chiosi 1980).[1] Evolution is assumed to take place in isolated concentric zones of the Galactic plane, with inflow parameters depending on Galactocentric distance in such a way as to reproduce the radial distribution of gas surface density and abundance gradients (Matteucci & François 1989). The inflow timescale τ_{inf} was taken to be 4 Gyr in the solar neighbourhood; such a long timescale compared to that for

---

[1] Clayton (1988) has given analytical solutions for inflow models of this type.
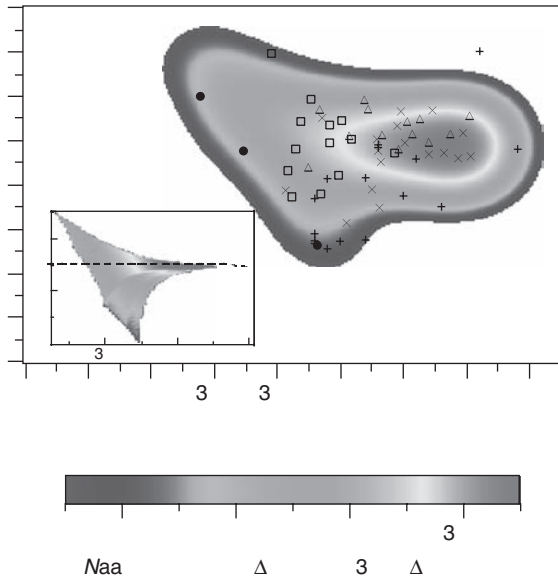
Fig. 8.29. Europium to iron ratios plotted against metallicity [Fe/H] according to the model of supernova-induced star formation, after Tsujimoto, Shigeyama and Yoshii (1999). Grey scales represent predicted stellar surface densities in the ([Fe/H],[Eu/Fe]) plane convolved with a Gaussian with $\sigma = 0.2$ dex for Eu/Fe and 0.15 dex for Fe/H, and symbols show observational data from various authors. The inset shows the unconvolved predictions.

star formation provides acceptable solutions to the 'G-dwarf problem', correspond-ing to large values of k in Eq. (8.36). Figure 8.31 shows the rates of star formation and supernova rates resulting from one such model. Following increasing attention to the distinctive properties of the thick disk (cf. Figs. 8.5, 8.6 and 8.17), Chiap-pini, Matteucci and Gratton (1997) developed 'two-inflow' models incorporating fast infall times for the inner halo plus thick disk (leading to a quasi-Simple model situation), much longer infall times for the thin disk and a surface-density threshold of $7 \, M_\odot \, \mathrm{pc}^{-2}$ for star formation, which has the effect of cutting it off from time to time. Figure 8.32 shows the resulting fluctuating star formation history in one of their models, assuming $k = 1.5$, and Fig. 8.33 the resulting relations between iron, oxygen, magnesium and calcium. Figure 8.34 shows similar plots for sulphur and carbon after Portinari, Chiosi and Bressan (1998), based on a fresh compilation of metallicity-dependent yields using the supernova predictions of Woosley and Weaver (1995) in combination with Padua stellar evolutionary models for mas-sive stars and yields by Marigo for intermediate- and low-mass stars. While the data for carbon shown in Fig. 8.34 are probably not very accurate, the theoretical
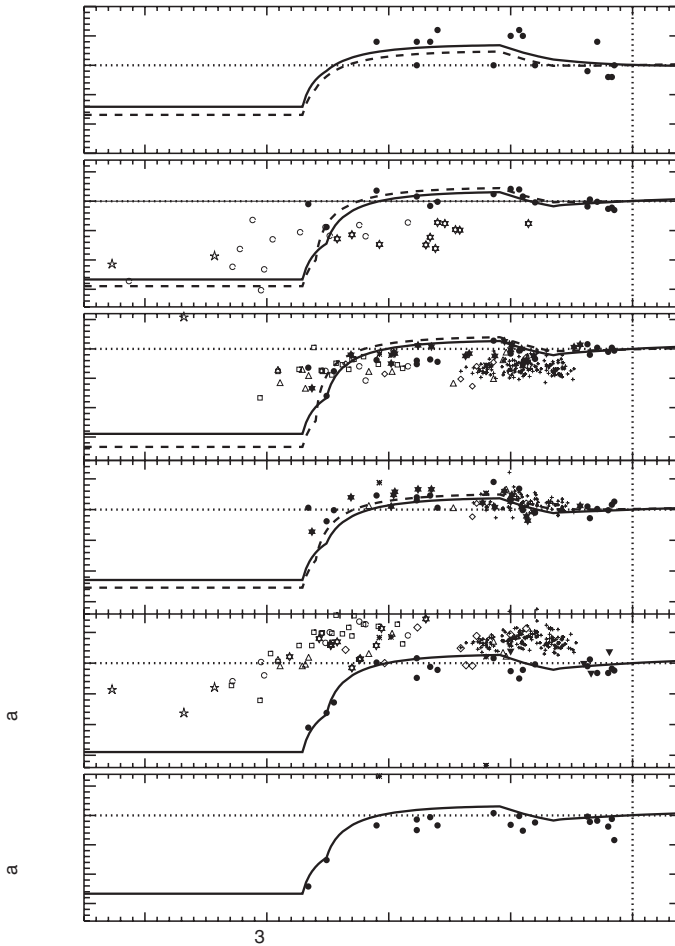
Fig. 8.30. Main s-process element to iron ratios plotted against metallicity [Fe/H] according to the analytical model by Pagel and Tautvaišienė (1995), compared to observational data. The s-process begins to contribute, superimposed on a pure r-process contribution, already at [Fe/H] = −2.5 ($\omega\Delta = 0.01$; $\Delta \sim 0.3$ Gyr), followed by a more delayed s-process that sets in at [Fe/H] = −0.65 ($\omega\Delta = 0.8$; $\Delta \sim 2$ Gyr, compared to ~ 1 Gyr for iron). The large scatter displayed by strontium is probably real. After Pagel and Tautvaišienė (1997).

curves give quite a good match to the more recent data shown in Fig. 8.4, when the behaviour of [O/Fe] is allowed for.

The Galactic chemical evolution of heavy neutron-capture elements was studied by Travaglio *et al.* (1999, 2001) on the assumption that a small pocket of ^{13}C is mixed into the inter-shell zone after the decay of each thermal pulse and generates neutrons supplemented by a small contribution from ^{22}Ne during the next pulse; see
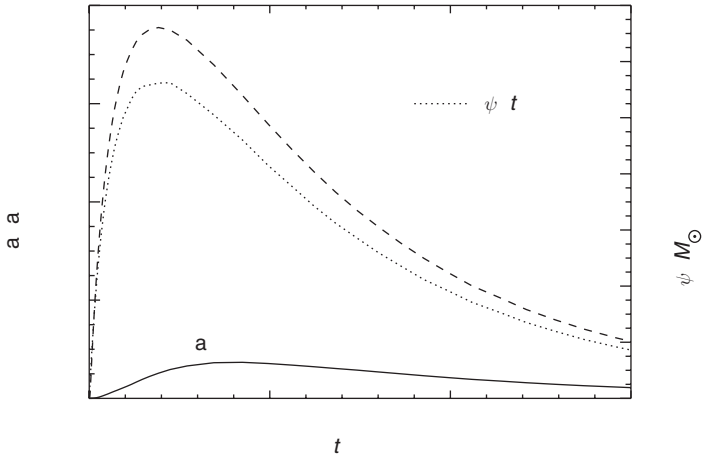
Fig. 8.31. Calculated star formation rates (dotted curve, right-hand scale) and SN Ia and SN II rates as a function of time. The parameter *A* in Eq. (7.27) has been chosen to fit observational estimates. The time difference between the peaks of the two SN rates roughly corresponds to the parameter Δ used in the analytical models. After Thomas, Greggio and Bender (1998).
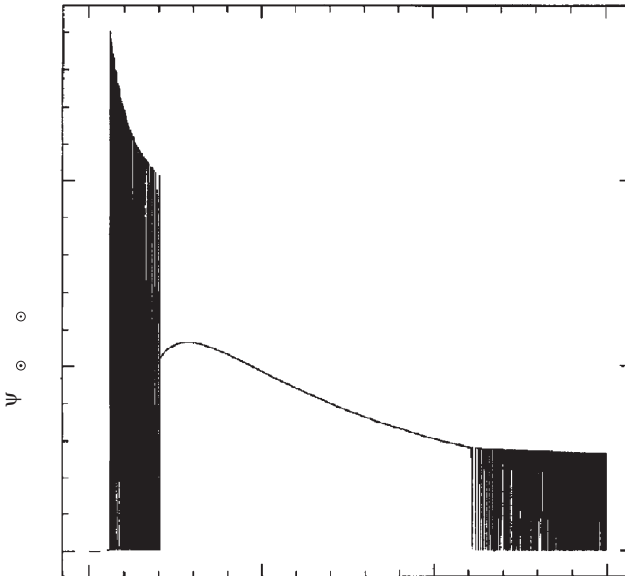
Fig. 8.32. Calculated star formation rates as a function of time, after Chiappini, Matteucci and Gratton (1997).
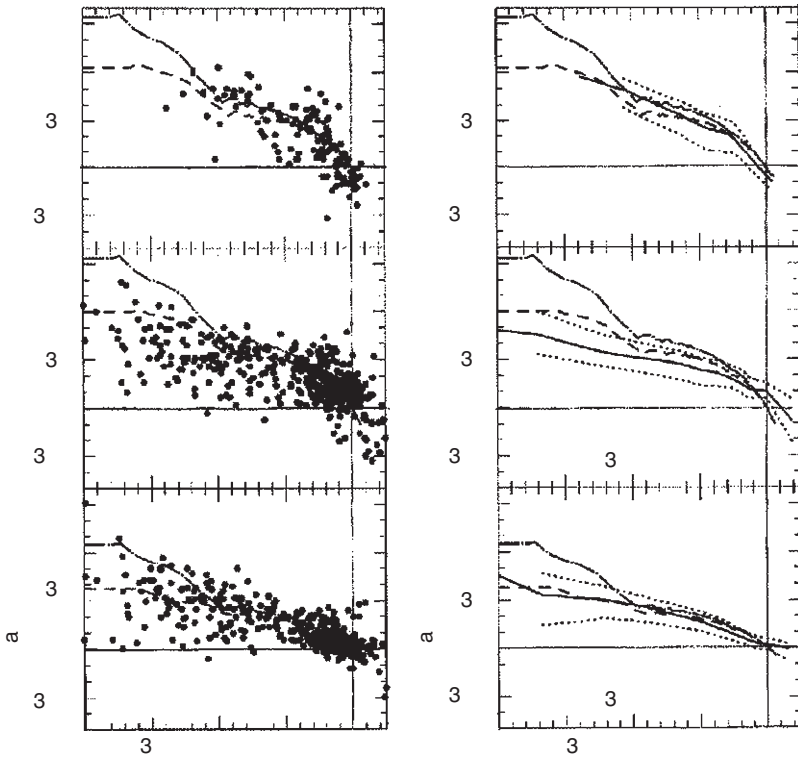
Fig. 8.33. [O,Mg,Ca/Fe] vs. [Fe/H], after Chiappini *et al.* (1999). Yields are from Woosley and Weaver (1995) (dashed lines) and Thielemann, Nomoto and Hashimoto (1996) (dot-dash lines) together with SN Ia synthesis according to model W7 (Nomoto, Thielemann & Yokoi 1984) using the IMF of Scalo (1986). The same model predictions are shown in the right-hand panels, together with the typical trend of the data (solid lines) and a measure of their dispersion (dotted lines). r is the number of points in each estimation window and s is the fraction of data used in locating the summary line.

Fig. 8.35. According to their calculations, the efficiency of the s-process increases sharply as the metallicity decreases to about 0.1 solar, but thereafter decreases rapidly at still lower metallicities because of shortage of iron seeds and a relatively high amount of neutron 'poisons' such as C, N and O. Thus below [Fe/H] $= -1$ or so, heavy nuclei like Ba are predominantly due to the r-process and are assumed to track europium.

A careful study of assumptions underlying chemical models for the solar neighbourhood and their comparison with observation was carried out by Thomas, Greggio and Bender (1998). They considered nucleosynthetic yields calculated
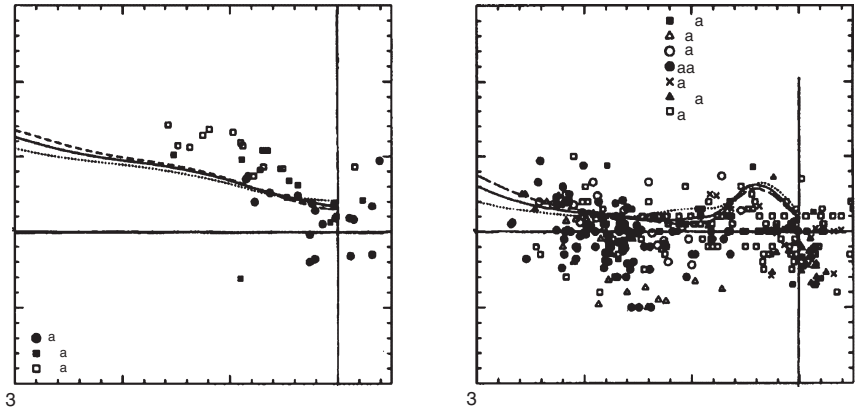
Fig. 8.34. [S/Fe] and [C/Fe] vs. [Fe/H], adapted from Portinari, Chiosi and Bressan (1998). Model curves are coded according to the exponent k in the modified Schmidt star formation law, Eq. (8.55). Dotted curve: $k = 1$; solid curve: $k = 1.5$; dashed curve: $k = 2$.
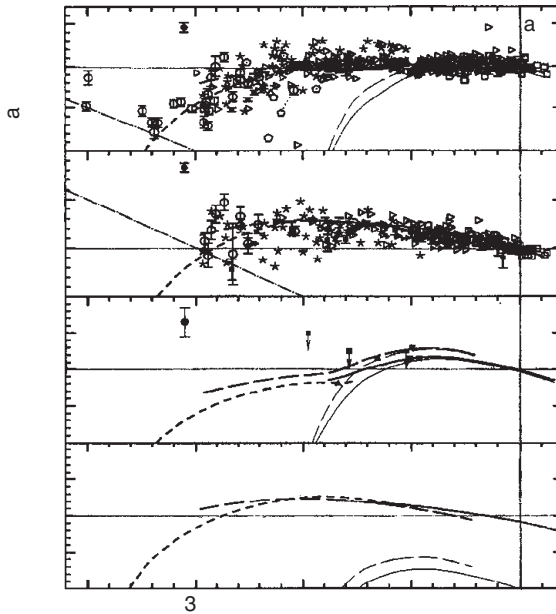
Fig. 8.35. Evolution of Eu and heavy s-process elements with [Fe/H], adapted from Travaglio *et al.* (2001). Heavy solid, long-dashed and short-dashed curves represent the thin disk, the thick disk and the halo respectively, while the lightly drawn curves represent the s-process contribution in the thin and thick disks. The downward sloping long-dashed lines in the two upper panels represent observational detection limits.

Table 8.3. *Some parameters of the mixing model* [a]

τ_{mix}	0	0.01 Gyr	0.1 Gyr	1 Gyr
$g_C(T)$		0.13	0.13	0.135
$g_H(T)$		7×10^{-5}	7×10^{-4}	8×10^{-3}
$g(T)$	0.13	0.13	0.13	0.136
$Z_C(T_\odot)$		0.019	0.019	0.021
$Z_H(T_\odot)$		0.057	0.057	0.057
$Z(T_\odot)$	0.019			

[a] After Thomas, Greggio & Bender (1998).

by Woosley and Weaver (1995) up to $40\,M_\odot$ and by Thielemann, Nomoto and Hashimoto (1996) up to 40 or $70\,M_\odot$ combined with the Salpeter(0.1) IMF. A notable advance over most previous work (other than the 'chemo-dynamical' model outlined below) was to take into account finite mixing times, thus relaxing the 'instantaneous mixing approximation' used in most models of this kind, by means of a simple formalism. The ISM is considered as having two components:

$$g = g_H + g_C, \tag{8.57}$$

where g_H is the surface density of a hot, metal-enriched component with metallicity Z_H fed by ejecta from massive stars and g_C is that of a cool component with metallicity Z_C into which hot gas gradually mixes on a fixed timescale τ_{mix} (treated as a free parameter) and from which fresh stars are formed. Then using the notation of Chapter 7 and Eq. (8.56), and assuming $Z_F = 0$, the other evolutionary equations run as follows:

$$\frac{dg_H}{dt} = e - \frac{g_H}{\tau_{mix}}; \tag{8.58}$$

$$\frac{dg_C}{dt} = F - \psi + \frac{g_H}{\tau_{mix}}; \tag{8.59}$$

$$\psi = \nu M \left(\frac{g_C}{M}\right)^k; \tag{8.60}$$

$$g_H \frac{dZ_H}{dt} = e_Z - Z_H\, e; \tag{8.61}$$

$$g_C \frac{dZ_C}{dt} = (Z_H - Z_C)\frac{g_H}{\tau_{mix}} - Z_C F. \tag{8.62}$$

Table 8.3 gives their results for the present-day fractional surface densities and their metallicities at the time of formation of the Sun using different assumed mixing times and Fig. 8.36 shows the effect of finite mixing times on the relation
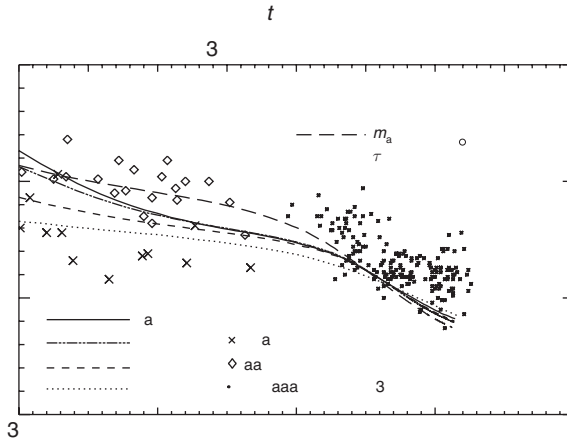
Fig. 8.36. Abundance ratio [Mg/Fe] as a function of [Fe/H] and time (for the case $\tau_{\text{mix}} = 0.1 \, \text{Gyr}$), for three different assumptions about τ_{mix}. Yields are taken from Thielemann, Nomoto and Hashimoto (1996) up to $40 \, M_{\odot}$; the long-dashed line shows an extension to an upper mass limit of $70 \, M_{\odot}$ (with $\tau_{\text{mix}} = 0.1 \, \text{Gyr}$); SN Ia yields are from Model W7 (Nomoto, Thielemann & Yokoi 1984). After Thomas, Greggio and Bender (1998).

between Mg/Fe and Fe/H. As expected, the initial slope due to slightly less massive supernovae exploding slightly later is flattened out, so that crude analytical models neglecting such effects actually give a somewhat better representation of the data; see Fig. 8.27.

A more detailed consideration of mixing (as well as other) processes is provided in 'chemo-dynamical' models which combine the dynamical approach pioneered by Larson with a treatment of stellar nucleosynthesis and lifetimes, the structure of the interstellar medium and dynamical interactions between stars and gas. Figure 8.37 shows the various components considered in the model of the Milky Way by Samland, Hensler and Theis (1997). The stars are divided into three mass ranges and the ISM is considered, following in outline the picture developed by McKee and Ostriker (1977), as having two phases in pressure equilibrium, a tenuous hot medium ($T > 10^4 \, \text{K}$) fed by massive stars and a cooler cloudy medium ($T < 10^4 \, \text{K}$ down to $80 \, \text{K}$) from which stars form, the two phases interacting by evaporation, condensation and mutual drag. Stars form from the cloudy medium according to a quadratic Schmidt law in the volume density (motivated by the idea of self-regulation with the cooling rate going as ρ^2) modulated by a diminishing function of temperature to account for its effect on molecular abundance. Dynamics is treated using moments over the equations of stellar and gas dynamics, taking
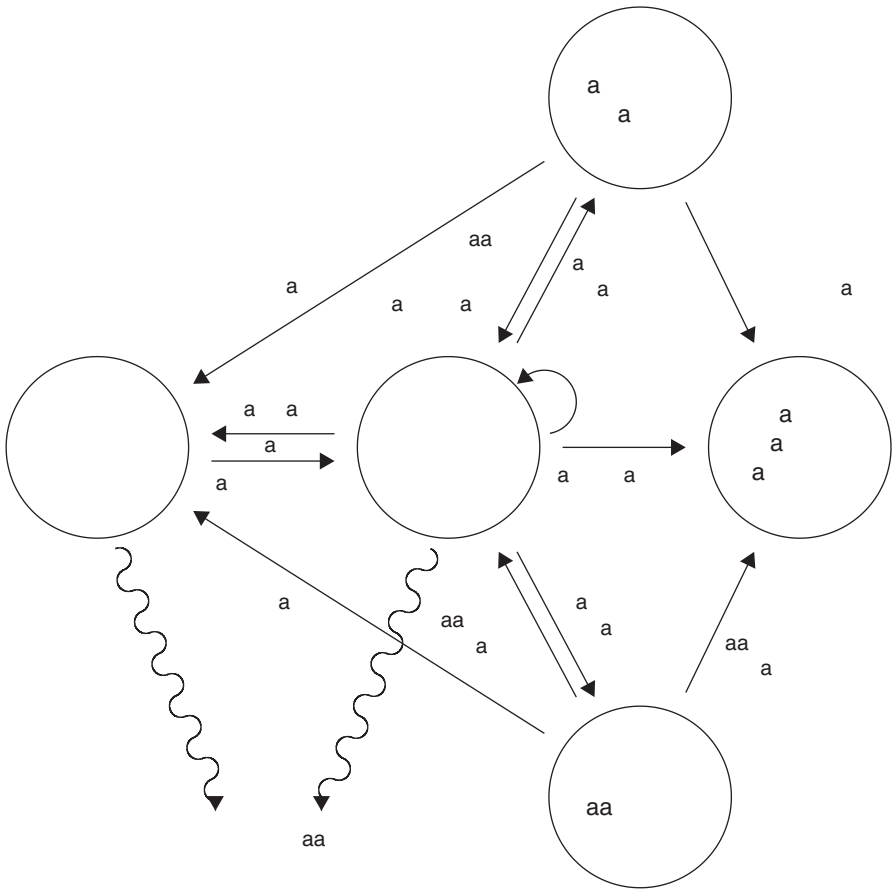
Fig. 8.37. The different gaseous and stellar components connected via mass, momentum and energy exchange, with their principal interactions, in the chemo-dynamical model of the Galaxy, after Samland, Hensler and Theis (1997). Courtesy Gerhard Hensler.

into account destruction of clouds by mutual collisions and calculating the changing gravitational potential self-consistently. As in the models by Larson, the model begins with an intergalactic cloud collapsing as a result of energy dissipation from cloud collisions and radiation. Star formation occurs at first predominantly in the halo, later transferring to the bulge and disk when the halo gas is exhausted from star formation and loss of gas to them. Intense star formation in the bulge leads to an overpressure of hot gas which escapes into the halo and outer disk before it can contribute to the star-forming clouds; this leads to a positive radial metallicity gradient in the early stages that is reversed only later (see Fig. 8.38). At age 6 Gyr (9 Gyr before present), when the abundance distribution was nearly uniform in the bulge and disk, major flows died away and chemical evolution came to be governed
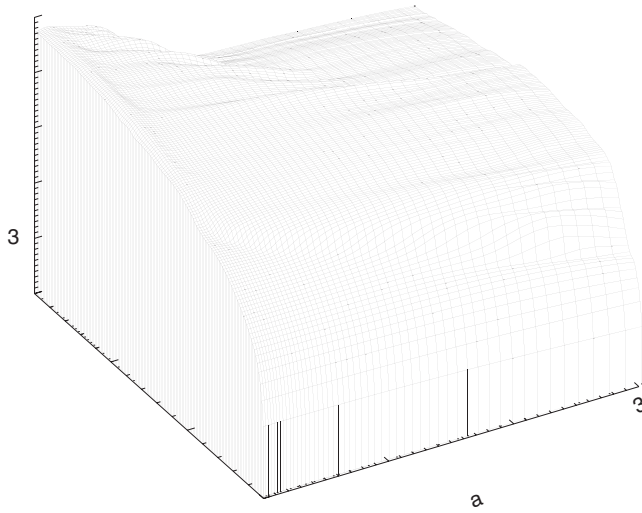
Fig. 8.38. Evolution of oxygen abundance as a function of time and Galactocentric radius, after Samland, Hensler and Theis (1997). Courtesy Gerhard Hensler.

by more local processes; this time may be considered that of the formation of the disk. (There is no distinction between thick and thin disk in this model.) Present-day abundance gradients, abundance distribution functions in the halo, bulge and disk and Fe,O relations are quite well reproduced.

Stellar evolution has consequences in the development of luminosity and colours of stellar populations, as well as chemical enrichment. Boissier and Prantzos (1999) have produced a more-or-less classical model of the evolution of the Milky Way, making a detailed study of this aspect, known as 'chemo-photometric evolution', using an IMF similar to the Kroupa–Scalo function in Chapter 7; this detail is significant because the Salpeter(0.1) function often used has a smaller contribution from stars of around solar mass which dominate the light at late times. The chemical evolution results are combined with metallicity-dependent stellar isochrones, synthetic stellar spectra by Lejeune *et al.* (1997) and a detailed treatment of extinction by dust. Some of their results are shown in Fig. 8.39.

8.6.4 *The thin and thick disks: analytical models revisited*

Neither analytical nor numerical models have paid much attention to the separate role of the thick disk, as opposed to treating it as some sort of transition from the halo to the thin disk. After discovery of the thick disk, Gilmore and Wyse (1986) suggested that (a) the thick disk was initially enriched by gas from
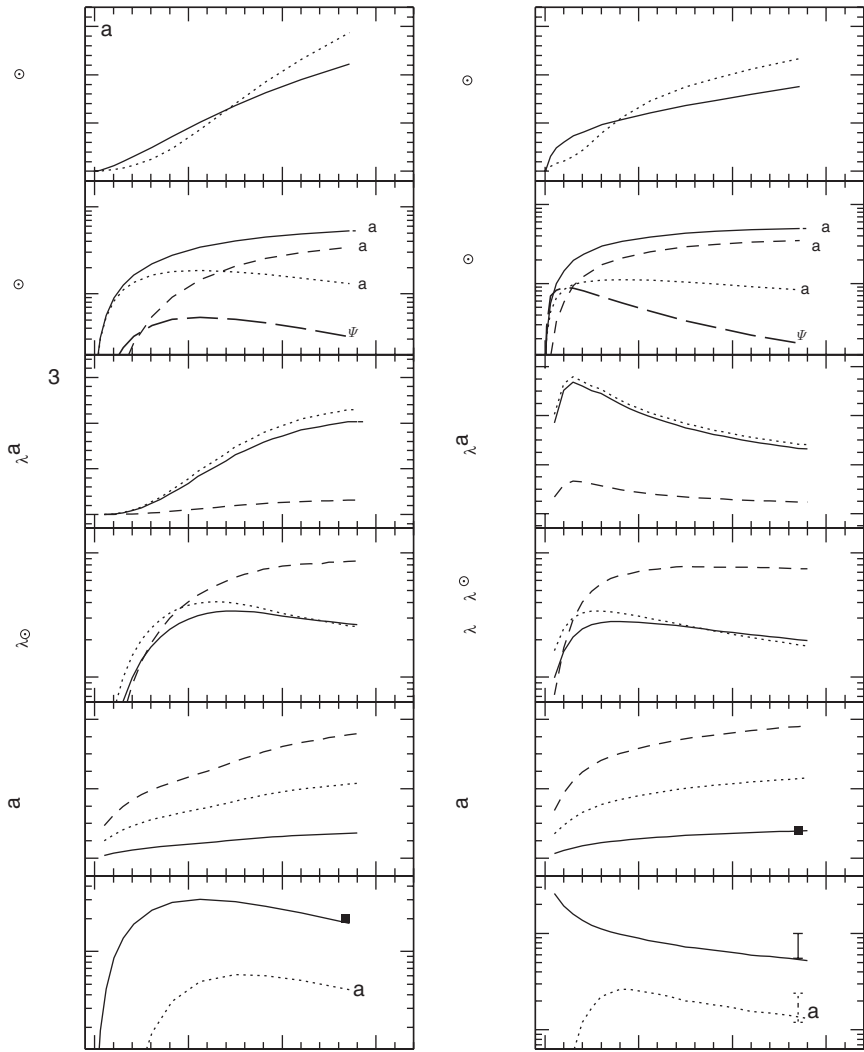
Fig. 8.39. Chemo-spectrophotometric evolution of the solar neighbourhood (left) and the whole Milky Way (right) as a function of time. Panels aA show the oxygen and iron abundances, bB the mass of stars and gas and the star formation rate, cC the extinction in B, V and K bands along a line of sight normal to the plane, dD the luminosity in solar units (taking extinction into account), eE the colour indices and fF the supernova rates. Note that panels aA are in linear units (see Fig. 8.16), while the others are all logarithmic. After Boissier and Prantzos (1999).

the halo – an idea that encounters a difficulty with the angular momentum distributions shown in Fig. 8.21; and (b) that the thin disk was similarly enriched by gas shed from the thick one. The second idea was explored by Pagel (2001) using the metallicity distribution functions for the two disks obtained from an *in situ* sample of thick-disk stars by Wyse and Gilmore (1995), combined with the respective relations between [Fe/H] and [Mg/H] found by Fuhrmann (1998) to produce a magnesium MDF to which it is reasonable to apply instantaneous recycling, shown in Fig. 8.40. It appears that the thick disk can be explained by the simple inflow model of Eqs. (8.46) to (8.52) (not very different from the Simple model) with a yield 0.15 dex below solar, a final gas fraction of 0.1 and a timescale short enough to exclude major contributions from SN Ia, at least until solar Mg/H is reached (cf. Fig. 8.6). For the thin disk, there are more choices. A pure prompt initial enrichment model gives a barely acceptable fit, while a pure inflow model using Clayton's formalism with $k = 4$ produces too much of a low-metallicity tail. A combined PIE-inflow model fits very well, possibly representing terminal thick-disk gas (as suggested by Gilmore and Wyse), diluted by inflow of unprocessed material before onset of the Clayton episode – thus a 'three-inflow' model.
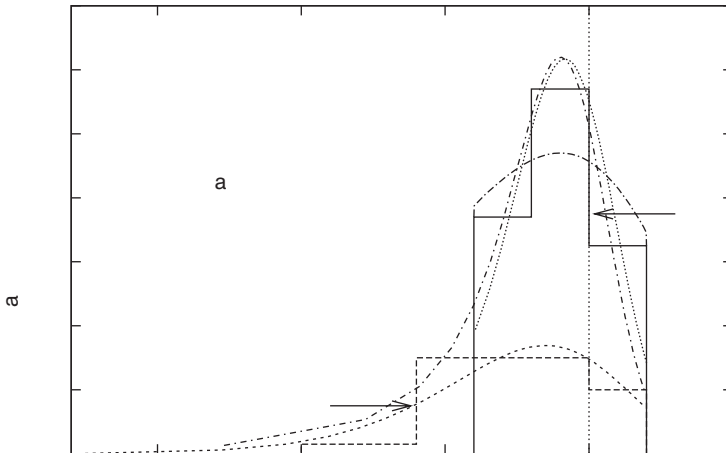
Fig. 8.40. Magnesium abundance distribution functions for the thick and thin disks. Histograms: Fe/H distributions from Wyse and Gilmore (1995) converted to Mg/H from the relations found by Fuhrmann (1998). Curves: dashed, simple inflow model (Eqs. 8.46 to 8.52) for the thick disk; dotted, prompt initial enrichment model plus inflow for the thin disk; short-dash-dotted, inflow model without PIE; long-dash-dotted, PIE without inflow. After Pagel in E. Vangioni-Flam *et al.* (2001). Copyright by World Scientific.
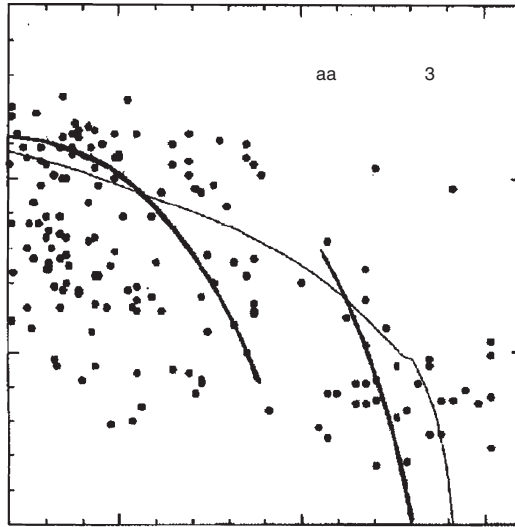
Fig. 8.41. Thin curves: age–metallicity relation predicted by the 'two-inflow' model of Chiappini, Matteucci and Gratton (1997). Thick curves: sketch of suggested separate AMRs for the thick and thin disks. Data points are from Edvardsson *et al*. (1993). Adapted from Chiappini *et al*. (1997) by Pagel (2004).

Figure 8.41 sketches an age–metallicity scenario compatible with the above picture. As in the 'two-inflow' model of Chiappini, Matteucci and Gratton (1997), there are two timescales of inflow: a fast one for the thick disk which gives high Mg/Fe ratios and involves only small effects of inflow on the MDF; and a slow one for the thin disk giving higher Fe/Mg ratios and a narrowed MDF. The new feature is the high degree of overlap, which accounts for some of the scatter in the overall age–metallicity relation, and the PIE of the thin disk, which accounts for the very small degree of overall enrichment during its lifetime. Ironically, considering the disk as a whole, the overlap phase could be regarded as 'Prompt Initial Impoverishment'!

Notes to Chapter 8

A good account of the chemical evolution of the Galaxy, giving details of the phases of stellar evolution and model calculations, is provided in the monograph by Matteucci (2001).

Properties of the **1-zone model** were systematically studied by Talbot and Arnett (1971), who contrasted the instantaneous recycling approximation with an 'initial burst' approximation which is the opposite extreme. In the latter case, most of the

gas is quickly used up in forming the first generation of stars and later the little gas that remains is heavily diluted by their ejecta so that metallicity actually decreases. This model does not seem to apply to the Galactic disk, where there is no evidence for an excess of old stars (Soderblom *et al.* 1991) and the presence of some old, metal-rich stars is more naturally explained by infiltration from the thick disk and the inner part of the Galaxy where enrichment was quicker (and possibly more efficient; see Grenon 1999). However, repeated star-formation bursts may influence the evolution of dwarf galaxies (see Chapter 11).

The predictions of **ratios of primary elements** formed by massive stars are not specific to the Simple model; that model just provides a convenient framework in which to discuss them. The case for other element ratios may be more complicated; there is an illuminating discussion by Wheeler, Sneden and Truran (1989) who comprehensively review the older literature, and there is a more recent review by McWilliam (1997). Regarding the data in Figs. 8.1 and 8.2, all stellar nucleosynthesis models lead one to expect a nearly constant O/Ne ratio, but the O/S ratio could conceivably vary because sulphur is more affected by explosive (as opposed to hydrostatic) nucleosynthesis with a yield per star that is estimated not to increase greatly with the star's initial mass (Table 7.2 and references therein). Figure 8.2 provides little evidence for any variation in practice.

The α/**Fe effect** was found in extreme subdwarfs by Aller and Greenstein (1960) and in disk stars by Wallerstein (1962). The O/Fe effect was noted in Arcturus by Gasson and Pagel (1966) (see Fig. 3.15) and in a sample of several giants by Conti *et al.* (1967). The [O/Fe] data have been subject to many discrepancies and controversies in recent years; in particular the change in slope near [Fe/H] $= -1$ (see Fig. 8.5) has been interpreted as a transition from the halo to the disk, but it is not clear that factors other than the simple time delay are involved. Recent investigations (Gratton *et al.* 2000; Bensby, Feltzing & Lundström 2004ab) indicate that the high O/Fe ratio characteristic of stars with [Fe/H] < -1 actually continues towards higher metallicities in the thick disk, leading to a bifurcation where the curve defined mainly by thin-disk stars in Fig. 8.27 starts to go down and thus to the increased scatter as one goes to lower metallicities in Fig. 8.8. The same effect was found for magnesium by Fuhrmann (1998). The most reliable oxygen abundance data are probably those derived from the forbidden line λ 6300, which unfortunately becomes too weak to measure in the most metal-deficient stars, particularly in dwarfs, and so one then has to rely on the stronger permitted lines, which are highly sensitive to temperature and non-LTE effects, or on OH bands which also involve some uncertainties. Part of the scatter in Fig. 8.27 is due to these problems, and it is still not clear at the time of writing whether O/Fe is flat for [Fe/H] < -1 as assumed in the analytical model, or whether it actually continues to increase towards lower metallicities as claimed by Garcia-López *et al.*

(2001) and Boesgaard (2001). A more recent analysis using very high resolution and high signal:noise spectra, using only the forbidden line and allowing for granulation (non-LTE is not an issue for this line) exhibits a similar pattern to that shown in Fig. 8.5 with a flat trend down to [Fe/H] = −1.9 or so, followed by a modest rise to [O/Fe] ≃ 0.5 at [Fe/H] ≃ −2.4 (Nissen *et al*. 2002). However, Mg, Si, Ca and Ti show the very flat behaviour shown in Fig. 8.9 (Cayrel *et al*. 2004; Cohen *et al*. 2004), and an equally flat behaviour for O/Fe in the range −3.2 ≤ [Fe/H] ≤ −0.7 has been derived by Meléndez *et al*. (2006) from the permitted lines using the new scale of effective temperatures applied to the primordial lithium problem by Meléndez and Ramírez (2004) with non-LTE corrections.

The suggestion that **Type I** (or as one would rather say now, **Ia**) **supernovae** with a significant evolution time contribute substantially to the iron found in the Solar System and in disk stars goes back to Chevalier (1976) and was treated in some detail by Tinsley (1979). Modern discussions are by Greggio and Renzini (1983), Matteucci and Greggio (1986) and Matteucci and Tornambé (1987). An alternative explanation, that the O/Fe and α/Fe yield ratios are a decreasing function of metallicity, has been suggested by Edmunds *et al*. (1991); but the order-of-magnitude suitability of SN Ia ages, frequency and composition, and indications of a high Mg/Fe ratio in Galactic bulge stars (McWilliam & Rich 1994, 2004), make the time-delay explanation look more promising.

s-process elements have often been naively regarded as 'secondary', but it is obvious from the behaviour of Ba/Fe in Fig. 8.8 that this is not so. A plot of Ba/O against O/H might suggest some dependence on chemical composition in that sense, but a more important factor is probably a time delay similar to, but somewhat exceeding, the one that applies to iron (Edvardsson *et al*. 1993; Pagel & Tautvaišienė 1997). This corresponds quite nicely with the model by Käppeler *et al*. (1990) illustrated in Fig. 6.5, but an additional s-process source may be needed (over and above the r-process) to account for heavy-metal abundances in the more metal-rich halo stars. The whole 'primary/secondary' concept is much too simplistic to be applied in this case; see Clayton (1988), Mathews, Bazan and Cowan (1992) and Travaglio *et al*. (2001).

Evidence for a **spread in ages** of 2 or more Gyr in the halo comes from colour–magnitude diagrams of globular clusters of equal metallicity (Chaboyer, Demarque & Sarajedini 1996) and from photometric determinations of surface temperatures and gravities of field stars (Nissen & Schuster 1991). (An age–metallicity relation, if any, for halo stars cannot be established beyond doubt because of uncertainties about abundance-dependent systematic errors in the age determination.) The clump of stars in the upper right corner of Fig. 8.15 represents mostly the 'thick disk' (Gilmore & Reid 1983; Gilmore & Wyse 1985) or 'Intermediate Population II' (Strömgren 1987) whose properties stand out quite clearly in Fig. 8.18. The scale

height of the thick-disk population is of the order of 1 kpc, compared to 300 pc for the old thin disk, so that thick-disk stars are relatively under-represented (compared to their column density) in a sample taken from the local volume. The selection effects on their relative frequency in Fig. 8.15 are difficult to judge, because larger volumes have been sampled for the rarer low-metallicity stars.

The main causes of **scatter in the age–metallicity relation** have not been completely clarified. Wielen, Fuchs and Dettbarn (1996) suggested that it can all be accounted for by a combination of a constant abundance gradient of $-0.09 \, \text{dex} \, \text{kpc}^{-1}$ combined with stellar orbital diffusion in the course of time, while Sellwood and Binney (2002) invoke transient spiral arms as a driver of radial mixing. Another factor that may be important is a spasmodic variation in the inflow rate, which can cause a temporary decrease in metallicity (Edvardsson *et al.* 1993). A third factor could be a measure of self-enrichment in star-forming regions (Pilyugin & Edmunds 1996), for which there is some evidence in the Orion Association for the elements oxygen and silicon (Cunha & Lambert 1992, 1994), but no variation has been found for iron (a result consistent with the SN Ia hypothesis) and the age–metallicity relation scatter for iron is at least as great as for oxygen and α-elements. The very existence of an age–metallicity relation in the Galactic disk has been questioned (Feltzing, Holmberg & Hurley 2001; Nordström *et al.* 2004), but the picture may be clarified by distinguishing the various Galactic orbits (as in Edvardsson *et al.* 1993) and the contribution of thin and thick disks; a statistical age–metallicity relation does appear to be present in the thick disk (Bensby, Feltzing & Lundström 2004b).

Figure 8.19 differs from the more composite-looking **halo abundance distribution function** given by Laird *et al.* (1988) for essentially the same data set because their z mainly represents iron. The iron–oxygen conversion that was used tends to 'iron out' the bulge that appears on the high-metallicity side of their diagram, and this will also affect Fig. 8.20 if [Fe/H] is replaced by [O/H]. In view of the possible compositeness of the halo, the fit to Hartwick's modified Simple model should not necessarily be taken literally. On the other hand, no better model of comparable simplicity has emerged, and one may perhaps think of the distribution as a mixture of modified Simple (or other) models (see Norris 1994). Malinie, Hartmann and Mathews (1991) have put forward a chemical evolution model with a density gradient in a collapsing halo which can reproduce the metallicity distribution function with a yield near solar abundance and no continuous wind, but this model predicts strong abundance gradients and the question of whether these could have been smoothed out by subsequent violent relaxation or other processes is a difficult one.

Many discussions of the **'G-dwarf problem'** have been based on an influential paper by Pagel and Patchett (1975) which with hindsight could have been much

better. In particular, I now regret having used mainly cumulative distribution functions in that paper, as opposed to the differential distribution shown in Fig. 8.23. The cumulative distribution (in which one plots $Z(s)$ against s) does have the advantage of being independent of binning, but the errors are harder to quantify and the influences of yield and cut-off are less apparent. Also, the data used were of rather poor quality and the corrections for differing scale heights were insufficient owing to poor statistics. The whole analysis has been done again *ab initio* by (among others) Gilmore, Wyse and Jones (1995), Rocha-Pinto and Maciel (1996, 1998), Favata, Micela and Sciortino (1997), Flynn and Morell (1997), Jørgensen (2000), Haywood (2001, 2002) and Kotoneva *et al*. (2002), the latter investigation referring to K dwarfs. M dwarfs also present a narrow ADF (Mould 1978). The results of these investigations are all fairly similar, except that Haywood argues for a peak at solar metallicity rather than 0.1 to 0.2 dex below, as found in most of the other studies, and finds that the distribution can be fitted to the Simple model. Other ways of presenting the (differential) distribution function have been presented by Pagel (1989b), and Clayton (1987) has derived relationships between gas fraction and abundance for his and Lynden-Bell's inflow models. Casuso and Beckman (2004) review the evidence for inflow of (relatively) unprocessed material into the Galaxy, and argue for an inflow rate that is constant or even increasing with time, rather than decreasing as in most other models.

Ideas on **prompt initial enrichment** have undergone some evolution in step with ideas on the nature of the halo. Dynamical evidence for a massive halo prompted Truran and Cameron (1971) to postulate a pre-Galactic population of massive stars which enriched the proto-disk and collapsed into black holes or 'collapsars', while Ostriker and Thuan (1975) envisaged a large population of normal stars in the halo which enriched the proto-disk with supernova ejecta. Later the idea was accepted that the massive dynamical halo (as opposed to the sparse stellar halo) consists of dark matter, e.g. brown dwarfs or 'MACHOs', for which there is now some evidence from micro-lensing effects (Alcock *et al*. 2000; Aubourg *et al*. 1993; Tisserand *et al*. 2007), and probably still more non-baryonic matter, which has not been involved at all in the chemical evolution of the Galaxy. However, 'prompt initial enrichment' has returned as a consequence of a possible high yield in the bulge or as a result of the evolution of the thick disk. A different sort of PIE could apply (at a much lower metallicity level) to the intergalactic medium at high redshift resulting from a pre-Galactic population of massive stars ('Population III') postulated to account for re-ionization of the Universe.

For a description of additional numerical Galactic chemical evolution models, as well as aspects of nucleosynthesis (e.g. from novae) not discussed in this book, see the monograph by Matteucci (2001).

Problems

1. Assuming instantaneous recycling, write an equation to replace Eq. (7.33) for the case of deuterium, which has no stellar production and is destroyed in recycled gas.

Show that, in the Simple model (no inflow and no Galactic wind), the evolution of deuterium abundance in the interstellar medium is given by

$$X_D/X_{D0} = \mu^{(\alpha^{-1}-1)} = e^{-z(\alpha^{-1}-1)}, \qquad (8.63)$$

where μ is the gas fraction, $\alpha \equiv 1 - R$ is the lock-up fraction and z the abundance of a primary element in units of its yield. Supposing $\mu = 0.2$, contrast the effects of assuming $\alpha = 0.8$ or 0.5.

2. Consider the model of Hartwick (1976) in which gas is lost to the system in a homogeneous wind at a rate η times the net star formation rate with $\eta = $ const. Assuming instantaneous recycling, derive the following relations:

$$m = 1 - \eta s; \quad g = 1 - (1 + \eta)s; \quad s(\infty) = 1/(1 + \eta), \qquad (8.64)$$

where m is the mass of the system in units of its initial mass and s and g the masses of stars and gas in the same units;

$$z(t) = u \equiv \int_0^t \omega(t')dt' = \frac{1}{1 + \eta} \ln \frac{1}{1 - (1 + \eta)s} \qquad (8.65)$$

where $\omega(t)$ is the transition probability for gas to change into stars;

$$\frac{ds}{d \ln z} = z\, e^{-(1+\eta)z}, \qquad (8.66)$$

so that the abundance distribution function has a peak at $(1 + \eta)^{-1}$ times the yield, and that the average abundance in the stars approaches $(1 + \eta)^{-1}$ times the yield asymptotically from below.

Considering the gas fraction $\mu \equiv g/(g + s)$, show that

$$z = \frac{1}{1 + \eta} \ln \left[\frac{1}{\mu} + \eta \left(\frac{1}{\mu} - 1 \right) \right]. \qquad (8.67)$$

Now consider the destruction of deuterium in this model and show that the second expression in Eq. (8.63) still applies, although the first one does not.

3. Neglecting the variation in the denominator of Eq. (8.39), show that the abundance distribution function in Clayton's inflow model peaks in the neighbourhood of $z = 1$.

4. Using the relation

$$\frac{N_{Ia}}{N_{II}} = \frac{p_2}{p_1} \frac{m_{II}}{m_{Ia}} \frac{\dot{s}(u_{now} - \omega\Delta)}{\dot{s}(u_{now})}, \tag{8.68}$$

with the yields p_1 and p_2 for iron given in Table 8.1 and assuming that a SN II ejects $m_{II} = 0.09\,M_\odot$ and a SN Ia ejects $m_{Ia} = 0.74\,M_\odot$ of iron, find the relative rates of SN Ia and SN II.

5. Show that, in Twarog's model with inflow of unprocessed material at $f \times$ the net star formation rate ($f = \text{const.} < 1$), in instantaneous recycling, the abundance grows as

$$Z = \frac{p}{f}(1 - g^{f/(1-f)}), \tag{8.69}$$

where g is the mass of gas in units of its initial mass.

6. Derive Eqs. (8.61) and (8.62).

7. Show that, in the simple inflow model described by Eqs. (8.46) to (8.52), the ratio of a secondary to a primary element is 4/3 times what it is in the Simple model at the same (primary) metallicity.

8. Show that in Hartwick's continuous outflow model, the relation between gas-phase abundance and gas fraction is

$$z = \frac{\ln(\frac{1+\eta}{\mu} - \eta)}{1 + \eta}. \tag{8.70}$$

9. Show that in Larson's extreme inflow model with initial abundance $Z_0 = 0$, the abundance distribution function is given by

$$\frac{ds}{dz} = \frac{g}{1 - z}; \quad z < 1. \tag{8.71}$$

9

Origin and evolution of light elements

> ... how turn ye again to the weak and beggarly elements,
> whereunto ye desire again to be in bondage?
>
> Galatians 4:9

9.1 Introduction

The light elements (D to B, apart from ^{4}He) have such fragile nuclei (see Table 9.1) that they tend to be destroyed, rather than created, in thermonuclear burning, although certain special processes can lead to stellar production of ^{3}He, ^{7}Li and ^{11}B.

B^{2}FH accordingly postulated for their creation an 'x'-process involving spallation by fast particles at high energy, but low temperature and density. They considered stellar flares and supernova shells as possible sites, while also envisaging the possibility of ^{7}Li creation in H-free helium zones in stars. Since then, it has been accepted that all D, some ^{3}He and some ^{7}Li come from the Big Bang (see Chapter 4), where rapid expansion and cooling allow traces of these elements to be preserved; and that a significant clue to the origin of Li, Be and B comes from their relative overabundance (by factors of 10^4 to 10^5) in Galactic cosmic rays (Fig. 9.1).

9.2 Sketch of cosmic-ray physics

Cosmic rays reaching the ground are secondary particles resulting from the impact of primary cosmic rays coming mainly from the Galaxy. The latter are mostly protons and α-particles with a sprinkling of heavier nuclei, coming in with a broad distribution of energies. The most energetic, with energies up to 10^{20} eV or so, are quite rare but are detected occasionally in the form of extensive air showers.

The origin and cause of acceleration of cosmic rays is somewhat uncertain, but the power-law energy spectrum suggests some kind of electromagnetic process

Table 9.1. *Destruction of light nuclei in stellar interiors*

^{2}D	destroyed by	$(p, \gamma)\,^3$He	for $T >$	0.5×10^6 K
^{6}Li	" "	$(p, \alpha)\,^3$He	for $T >$	2×10^6 K
^{7}Li	" "	$(p, \alpha)\,^4$He	for $T >$	2.5×10^6 K
^{9}Be	" "	$(p, \alpha)\,^6$Li; $(p,$ D$)\,^8$Be$\rightarrow 2\,^4$He	for $T >$	3.5×10^6 K
^{10}B	" "	$(p, \alpha)\,^7$Be $(EC)\,^7$Li	for $T >$	5.3×10^6 K
^{11}B	" "	$(p, \alpha)\,^8$Be$\rightarrow 2\,^4$He	for $T >$	5×10^6 K
^{3}He	" "	$(^3$He$, \alpha)\,^4$He $+ 2\,^1$H	for $T >$	$\sim 10^7$ K
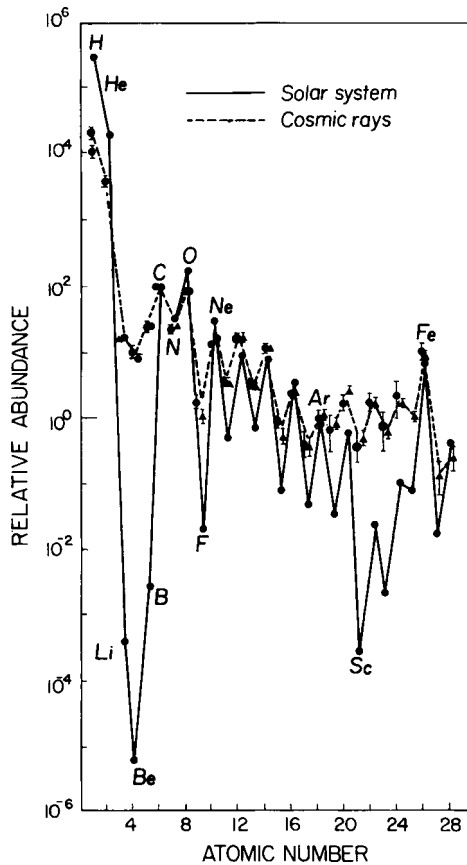
Fig. 9.1. Abundances in primary cosmic rays reaching the top of the Earth's atmosphere, compared to Solar-System abundances. (Both normalized to C = 100.) After Rolfs and Rodney (1988). Copyright by the University of Chicago. Courtesy Claus Rolfs.

analogous in some ways to laboratory accelerators. The most promising mechanisms, due originally to Fermi (1949, 1954), are based on repeated reflections from moving magnetized gas clouds. These could well take place in interstellar shock fronts due to supernova ejecta; the shell-like remnant of Tycho's supernova displays a close correspondence between synchrotron radiation from cosmic-ray electrons and hot X-ray plasma, and the moving clouds could well be the plasmas on either side of a supernova shock front which converge with a relative velocity $u_1 - u_2$ (see Fig. 3.28). If the particles are injected with sufficient energy to avoid strong deflection, they can be accelerated by passing back and forth through the shock many times (Bell 1978), until their Larmor radius becomes large enough for them to leak out (see Eq. 9.2 below). Energetic particles with energies up to a few GeV are also ejected by the Sun and presumably other stars during phases of high activity associated with flares, and the ejecta from supernovae have an initial kinetic energy of the order of an MeV per nucleon. One recent view (Meyer, Drury & Ellison 1998) is that interstellar gas and electrically charged dust particles in the ISM undergo acceleration when engulfed by the supernova shock and the dust particles are destroyed by sputtering, releasing ions of refractory elements that are then accelerated further. This picture is in good agreement with (and was largely inspired by) a comparison of cosmic-ray source abundances with those of the Solar System (see item (ii) below).

Another view, equally consistent with the source abundances and better suited to account for the abundance of light elements like beryllium in stars of the Galactic halo (see below), is that dust particles in the supernova ejecta are the source of ions that are preferentially accelerated within the hot, tenuous gas of superbubbles surrounding regions of star formation (Lingenfelter, Ramaty & Kozlovsky 1998).

The initial spectrum of cosmic rays is expected to be a power law in the momentum p of particles, e.g.

$$N(E)\, dE \propto p^{-2} dp \equiv \frac{E + E_0}{[E(E + 2E_0)]^{3/2}}\, dE, \tag{9.1}$$

where E is the kinetic energy per nucleon and E_0 the rest-mass energy 0.93 GeV. The initial spectrum thus has a negative energy dependence, steepening from $E^{-3/2}$ at low energies ($\ll 1$ GeV) to E^{-2} at high energies ($\gg 1$ GeV). The cosmic rays then diffuse through the Galaxy scattering off irregularities in the magnetic field. The Larmor radius is

$$R_{\text{Larmor}} = \frac{pc}{eB} = 10^{-7} E_{\text{GeV}} \text{ pc} \tag{9.2}$$

(for a Galactic magnetic field $B = 10^{-5}$ gauss) so that the cosmic rays are closely confined by the field up to energies of 10^{18} eV or so. During their propagation through the Galaxy, the cosmic rays suffer a number of effects (see Fig. 9.2):
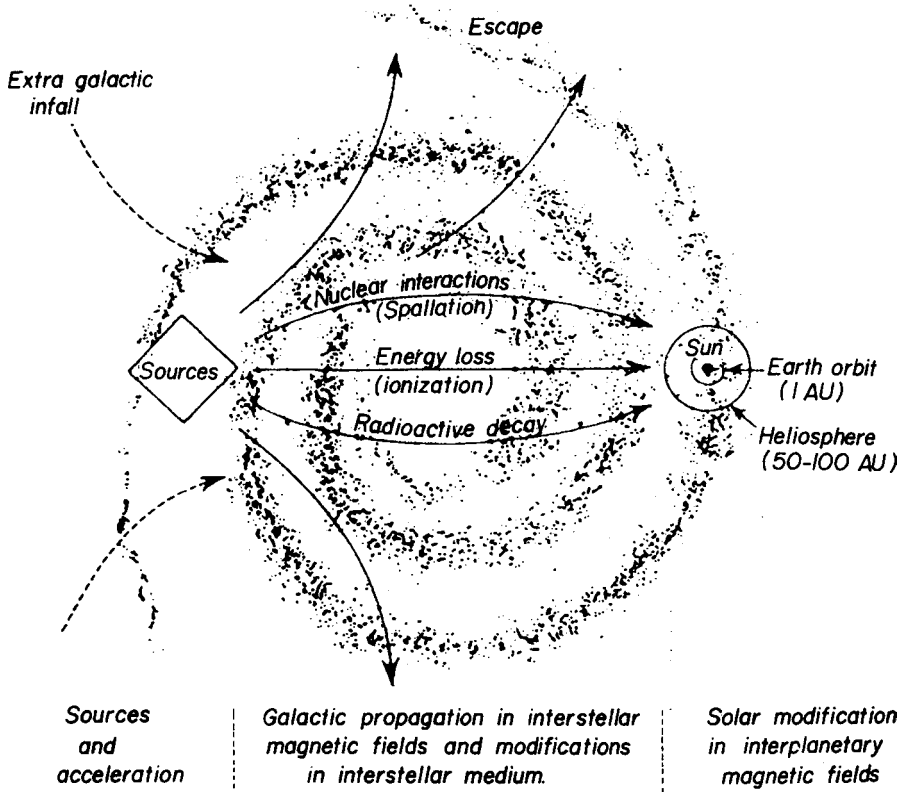
Fig. 9.2. Schematic view of the life history of a cosmic ray from acceleration in the source through propagation in the Galaxy to observation above the Earth's atmosphere. Adapted from Rolfs and Rodney (1988).

(i) Energy loss by ionization, especially at low energies; this tends to flatten the spectrum.

(ii) Fragmentation by high-energy nuclear (spallation) reactions with nuclei in the interstellar medium. This converts abundant nuclei into their lighter neighbours, accounting for the abundances in Fig. 9.1. The source abundances, derived by correcting for this propagation effect, are more like those of the Solar System,[1] but with significant modifications: an enhancement of refractory elements[2] and heavy volatiles relative to H and He by factors of up to about 30; and an excess of ^{22}Ne and perhaps ^{12}C probably due to previously existing ejecta from Wolf–Rayet stars.

(iii) Escape from the Galaxy. This is often represented by the 'leaky box' model, of which a simple form represents the escape probability as an exponential function of the mass column density (or 'grammage') passed through before escaping:

$$P(M)\,dM = e^{-M/\Lambda}\,dM/\Lambda, \qquad (9.3)$$

---

[1] Hubert Reeves once summed up the similarity of cosmic-ray source and Solar-System abundances in the form of a graffito seen at times in Paris: 'CRS = SS'!

[2] Sometimes identified earlier with the 'FIP' effect (see Section 3.5.1).

where from the amount of fragmentation observed one finds

$$\Lambda \simeq 8 \text{ gm cm}^{-2}. \tag{9.4}$$

From the abundances of the radioactive nuclei ^{10}Be (mean life 2.2 Myr) and ^{26}Al (mean life 1.0 Myr), one also has an idea of the timescale for escape, which seems to be of the order of 10^7 yr and perhaps an order of magnitude longer than the time to pass through Λ at an average density of one atom $(2 \times 10^{-24}$ gm$)$ cm^{-3} in the Galactic plane.

(iv) Finally, some reach the Solar System, where they suffer solar modulation: they are decelerated by the solar wind, especially at lower energies (< 0.5 GeV per nucleon) and during high levels of solar activity. The observed spectrum from satellites is demodulated on the basis of theoretical models down to about 100 MeV per nucleon and more or less guessed below that (Fig. 9.3). The interstellar proton flux is deduced to be given by

$$\phi_p(E)\,dE \simeq 12.5\,(E + E_0)^{-2.6} dE \text{ cm}^{-2}\,\text{s}^{-1} \tag{9.5}$$

(E in GeV), giving a flat spectrum for $E \ll E_0 \simeq 1$ GeV. Heavy nuclei have similar spectra in energy per nucleon.
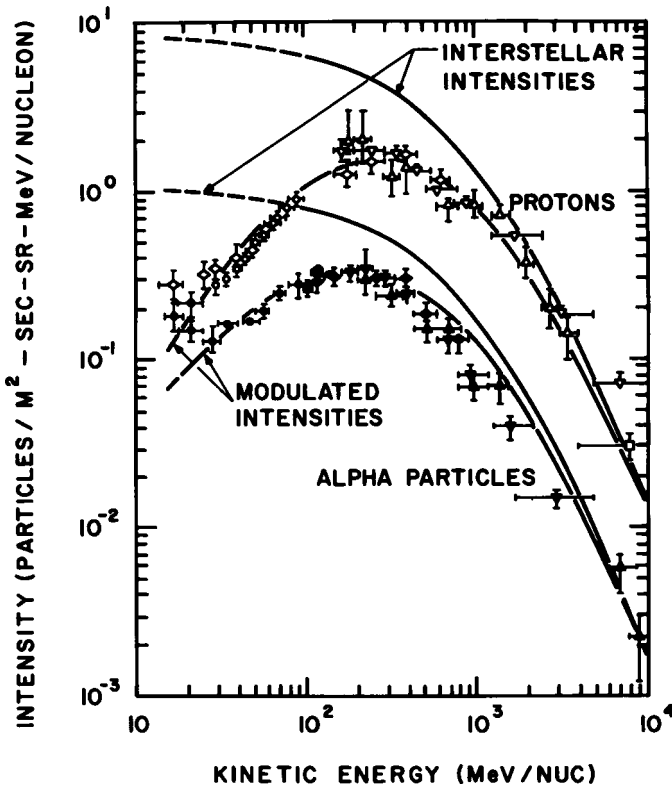
Fig. 9.3. Proton and α-particle spectra of primary cosmic rays and their demodulated versions. After Goldstein *et al.* (1970). Courtesy Reuven Ramaty.

9.3 Light element production

The light elements present in cosmic rays are partly thermalized, i.e. brought down to low velocities by ionization losses, and thus make a minor contribution to their abundance in the ISM (perhaps about 20 per cent). The main source is usually thought to come from reactions of cosmic-ray protons and α-particles with stationary nuclei of He, C, N and O in the ISM.

The reactions can be divided into $\alpha - \alpha$ fusion reactions

$$\alpha + \alpha \quad \rightarrow \quad {}^6\text{Li} + p + n - 36\,\text{MeV} \tag{9.6}$$

$$ {}^7\text{Li} + p - 44\,\text{MeV} \tag{9.7}$$

$$ {}^7\text{Be}\,(EC)\,{}^7\text{Li} + n - 44\,\text{MeV} \tag{9.8}$$

and spallation reactions

$$p, \alpha + \text{C, N, O} \rightarrow {}^{6,7}\text{Li},\ {}^9\text{Be},\ {}^{10,11}\text{B} \ - \ \text{about } 30\,\text{MeV}. \tag{9.9}$$

About 80 per cent of the cosmic-ray flux is at energies above 150 MeV per nucleon where the cross-sections are more or less constant (Fig. 9.4).

A simple calculation neglecting GCE refinements is based on the assumption of a constant production rate:

$$\frac{dN_\text{L}}{dt} = N_\text{CNO} \int \overline{\sigma}_\text{CNO}(E)\,\phi(E)\,dE \simeq N_\text{CNO}\langle\overline{\sigma}\rangle\phi \tag{9.10}$$

for each incident particle type, i.e. p, α. Assuming the rhs to be constant, the abundance by number of atoms relative to hydrogen is

$$\frac{\text{L}}{\text{H}} = \frac{\text{CNO}}{\text{H}}\langle\overline{\sigma}\rangle\phi_p\,T = 4 \times 10^{-12}\left(\frac{T}{10\,\text{Gyr}}\right)\langle\overline{\sigma}\rangle_\text{mb}, \tag{9.11}$$

where CNO/H is assumed to be solar, T is the age of the Galaxy and only protons are considered. This treatment thus neglects the effects of lock-up and destruction of light elements in stars and any variations with time in the cosmic-ray flux and in the abundances of CNO in the ISM. Results of this simple calculation are shown in Table 9.2, where it can be seen that, while meteoritic abundances of the three nuclear species ${}^6\text{Li}$, ${}^9\text{Be}$, ${}^{10}\text{B}$ are reproduced within a factor of 2 or so, ${}^7\text{Li}$ is underproduced by an order of magnitude (which is probably also the case for cosmological production; see Fig. 4.12). This suggests a major component from thermonuclear synthesis in stars, e.g. AGB stars – see Section 5.10 – and/or supernovae or novae.[3]

---

[3] Curiously, there are some nearby interstellar diffuse clouds displaying anomalously low isotope ratios for ${}^7\text{Li}/{}^6\text{Li}$, with a ratio apparently as small as 2 in one case (Lemoine *et al.* 1994; Knauth, Federman & Lambert 2003), compared to the Solar-System (and more usual interstellar) ratio of 12; the 'anomaly' here is that the low ratio in such clouds is consistent with cosmic-ray spallation whereas that in the Solar-System is not.
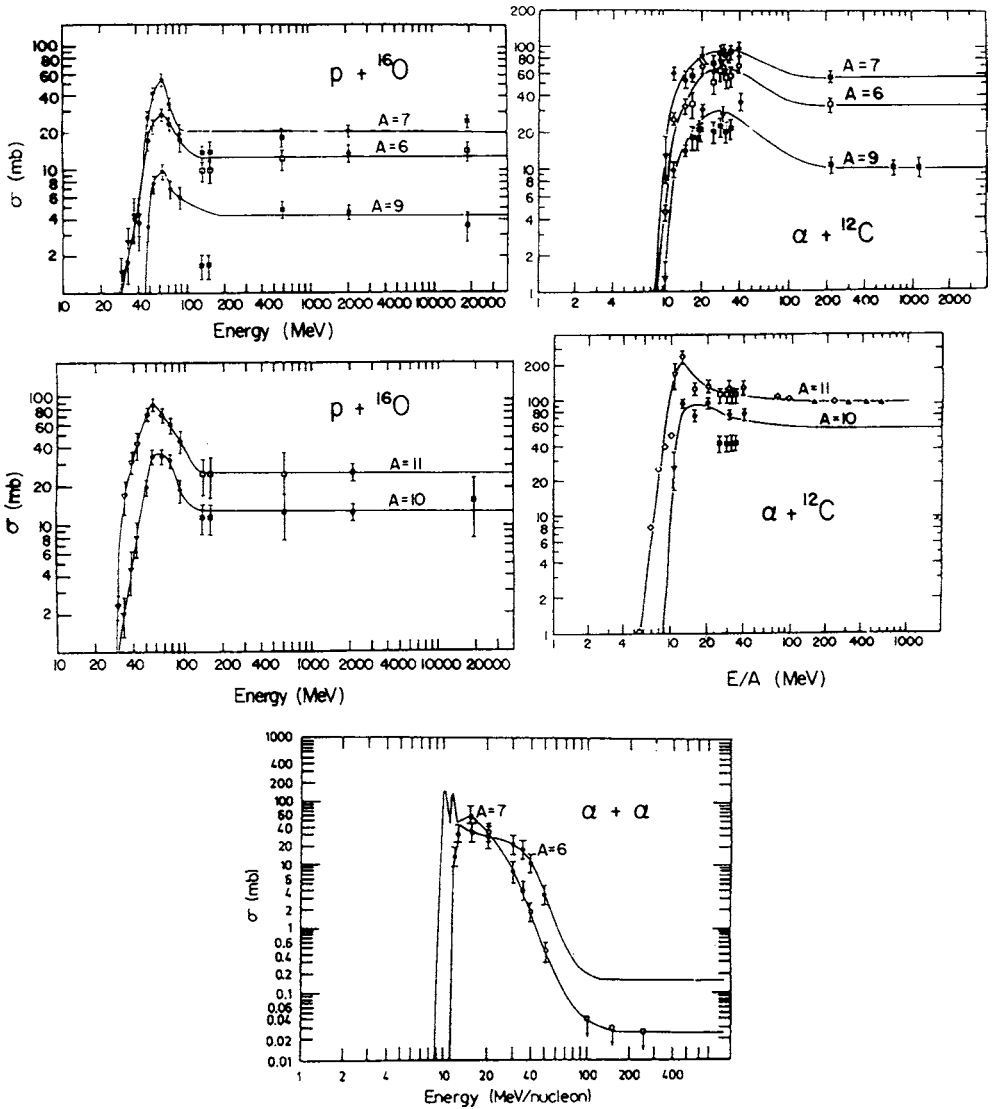
Fig. 9.4. Reaction cross-sections, as a function of energy per nucleon, for the production of light elements for some typical cases. Adapted from Read and Viola (1984). Courtesy Vic Viola.

Also, the ratio $^{11}B/^{10}B$ is underpredicted by a smaller factor ~ 1.5 which could also come from stellar production, notably from the neutrino process in core-collapse supernovae (Woosley & Weaver 1995; Timmes, Woosley & Weaver 1995), the efficiency of which is quite uncertain.[4]

---

[4] The suggestion that ^{11}B could be enhanced by a low-energy component of cosmic rays over and above the flat spectrum usually assumed (Meneguzzi & Reeves 1975) is excluded because it would lead to overproduction of light elements in general.

Table 9.2. *Results of simple calculations of light element abundances*

	$\overline{\sigma}_{\mathrm{CNO}}$ (mb)	$10^{11}\frac{\mathrm{L}}{\mathrm{H}}$	$10^{11}\frac{\mathrm{L}}{\mathrm{H}}$	$10^{11}\frac{\mathrm{L}}{\mathrm{H}}$	
	$E > 150\,\mathrm{MeV}$	Eq. (9.11)	WMV 85[a]	meteoritic	
$^6\mathrm{Li}$	13	5	7	17	✓
$^7\mathrm{Li}$	20	8	10	210	✗✗
$^9\mathrm{Be}$	4	1.6	1.5	2.6	✓
$^{10}\mathrm{B}$	16	6	7	15	✓
$^{11}\mathrm{B}$	34	14	18	62	✗
$^6\mathrm{Li}/^9\mathrm{Be}/^{10}\mathrm{B}$		3/1/4	5/1/5	7/1/6	✓

[a] Numerical calculation by Walker, Mathews and Viola (1985).

9.4 Galactic chemical evolution of light elements

9.4.1 Introduction

Special features of the light elements are

(i)   Initial abundance Z_0 and/or abundance in inflowing material Z_F from the Big Bang.
(ii) Creation in both stars and cosmic rays.
(iii) Destruction by astration.

Using the instantaneous recycling approximation (Section 7.4.2), Eq. (7.33) now has to be replaced by

$$\frac{d}{dS}(gZ) = q + \beta R Z - Z + \frac{N_{\mathrm{CNO}}\sigma\phi A m_{\mathrm{H}} + Z_F F - Z_E E}{\psi}, \qquad (9.12)$$

where $0 \leq \beta \leq 1$ allows for astration (for complete destruction, $\beta = 0$) and we have replaced $\langle\sigma\rangle$ by σ for brevity. A is the atomic mass number of the relevant light element, and $\alpha - \alpha$ fusion reactions have been neglected. We need also to bring in time, which we do using the variable u (Eq. 8.17), noting that

$$\frac{\psi}{\omega} \equiv \frac{dS}{du} = \frac{g}{\alpha} \equiv \frac{g}{1 - R}, \qquad (9.13)$$

whence

$$\frac{d}{du}(gZ) = g\left(p + \frac{A}{A_{\mathrm{CNO}}}\sigma Z_{\mathrm{CNO}}\frac{\phi}{\omega} - \frac{Z}{\alpha'}\right) + \frac{Z_F F - Z_E E}{\omega}, \qquad (9.14)$$

where p is the true yield from stellar production and

$$\alpha' \equiv \frac{\alpha}{1 - \beta(1 - \alpha)} \tag{9.15}$$

$$\rightarrow \alpha \quad \text{for complete destruction} \tag{9.16}$$

$$\rightarrow 1 \quad \text{for no destruction.} \tag{9.17}$$

We now consider two special cases:

(i) D, ^{7}Li: Z_0, $Z_F > 0$, cosmic-ray production neglected.
(ii) Cosmic-ray nuclei, $Z_0 = Z_F = 0$, stellar production neglected.

9.4.2 D, ^{7}Li in the Simple or homogeneous outflow model

The assumptions of these models are:

$$F = 0, \tag{9.18}$$

$$E = \eta \frac{ds}{dt} = \eta \, \omega \, g, \tag{9.19}$$

$$Z_E = Z, \tag{9.20}$$

$$\alpha' = \alpha \quad \text{(complete destruction)}, \tag{9.21}$$

$$\frac{dg}{du} = -(1 + \eta) \, g. \tag{9.22}$$

From Eq. (9.14),

$$g \frac{dZ}{du} - Z(1 + \eta)g = g\left(p - \frac{Z}{\alpha}\right) - Z\eta g. \tag{9.23}$$

g, η conveniently cancel out and the differential equation simplifies to

$$\frac{dZ}{du} + Z\left(\frac{1}{\alpha} - 1\right) = p, \tag{9.24}$$

with the solution

$$Z = Z_0 e^{-v} + \frac{p}{\alpha^{-1} - 1}(1 - e^{-v}), \tag{9.25}$$

where

$$v \equiv \left(\frac{1}{\alpha} - 1\right)u \simeq \frac{1}{2}u \quad \text{if } \alpha \simeq 0.67. \tag{9.26}$$

Results for the Simple model are shown in Fig. 9.5. Oxygen abundance simply increases in proportion to u, whereas that of ^{7}Li starts from a finite base and tends to a limiting value $p_{\text{Li}}/(\alpha^{-1} - 1)$ owing to its eventual destruction by astration. Deuterium ($p = 0$ in Eq. 9.25) suffers little destruction as long as the oxygen abundance (or metallicity) is less than about 0.1 of the true yield (assumed to be comparable to solar abundance), e.g. in high-redshift absorption-line clouds, but
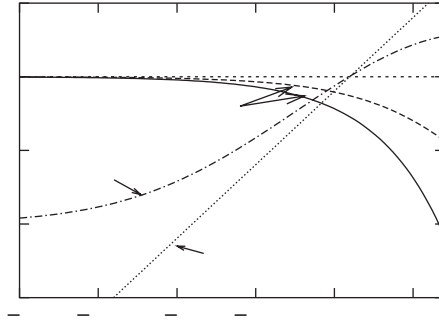
Fig. 9.5. Schematic of decline of D and growth of ^{7}Li and oxygen abundances in the Simple or homogeneous outflow model, assuming instantaneous recycling with $\alpha = 0.67$ and yields $p(O) = 0.8\, Z_\odot(O)$; $p(^7Li) = 0.7\, Z_\odot(^7Li)$; $Z_0(^7Li) = 0.1\, Z_\odot(^7Li)$. The long-dashed curve indicates deuterium depletion in the simple inflow model.

declines as e^{-v} or $\mu^{(1/\alpha - 1)}$ in the Simple model (Ostriker & Tinsley 1975) reaching a cut-down factor at solar metallicity of about 2 in the case shown in Fig. 9.5. This factor is very sensitive to α, however, which is an uncertain quantity owing to uncertainty in the initial mass function (see Section 7.3.3), but it is unlikely in any case that $\alpha < 0.5$. The small cut-down factor $\simeq 1.2$ found in the local ISM (Linsky *et al.* 2006) implies either a considerably larger α or the effect of inflow of unprocessed material – possibly both.

9.4.3 D, ^{7}Li in the simple inflow model

Using the simplest inflow model of Section 8.5.2, our assumptions are:

$$g_0 = E = 0; \tag{9.27}$$

$$F = A\omega e^{-u}; \tag{9.28}$$

$$g = Aue^{-u} \quad (\text{Eq. 8.47}). \tag{9.29}$$

Then Eq. (9.14) becomes

$$\frac{d}{du}(Zg) = pAue^{-u} - \frac{Zg}{\alpha} + Z_F Ae^{-u}, \tag{9.30}$$

with the solution

$$Z = Z_F \frac{1 - e^{-v}}{v} + \frac{p}{\alpha^{-1} - 1}\left(1 - \frac{1 - e^{-v}}{v}\right). \tag{9.31}$$

For example, at the time of formation of the Solar System, $\mu \simeq 0.2$, $u = 2.5$, $v = 1.25$, assuming $Z_F(\text{D})$ is the primordial value,

$$\frac{Z(\text{D})}{Z_F(\text{D})} \simeq 0.6, \tag{9.32}$$

i.e. the cut-down factor for deuterium is smaller than in the no-inflow models (with the same yield and the same oxygen abundance) and remains moderate even for quite large values of u (see Fig. 9.5). Thus the presence of a modest amount of deuterium at the Galactic centre is a natural consequence of infall of unprocessed material. With the yield $p_{\text{Li}} = 0.8 \, Z_\odot(^7\text{Li})$,

$$Z(^7\text{Li}) = 0.1 \, Z_\odot(^7\text{Li}) \frac{1 - e^{-v}}{v} + 1.8 \, Z_\odot(^7\text{Li}) \left(1 - \frac{1 - e^{-v}}{v}\right). \tag{9.33}$$

9.4.4 Pure cosmic-ray spallation products: ^{6}Li, Be, B

In this case, Eq. (9.14) becomes

$$\frac{d}{du}(gZ) + \frac{gZ}{\alpha'} = \frac{A}{A_{\text{CNO}}} \, g \, Z_{\text{CNO}} \, \sigma \, \frac{\phi}{\omega} + \frac{Z_F F - Z_E E}{\omega}. \tag{9.34}$$

In making models, it is usually assumed that ϕ is proportional to the supernova rate and therefore to the star formation rate ψ (e.g. Reeves & Meyer 1978), i.e.

$$\frac{\phi/\omega}{(\phi/\omega)_1} = g/g_1, \tag{9.35}$$

where the suffix $_1$ refers to the present epoch. Thus in the Simple model we have

$$E = F = 0, \quad g = e^{-u}, \tag{9.36}$$

$$Z_{\text{CNO}} = p_{\text{CNO}} u, \tag{9.37}$$

$$\frac{dZ}{du} + (\alpha'^{-1} - 1)Z = \frac{A}{A_{\text{CNO}}} \, \sigma \, p_{\text{CNO}} \, \frac{\phi_1}{\omega_1} u \, e^{-(u - u_1)}, \tag{9.38}$$

$$= k \left(\frac{\sigma \phi}{\omega}\right)_1 u \, e^{u_1 - u}, \tag{9.39}$$

$$Z = k \left(\frac{\sigma \phi}{\omega}\right)_1 e^{u_1} \frac{e^{-u}[e^{v'} - (1 + v')]}{(2 - 1/\alpha')^2}, \tag{9.40}$$

where

$$k \equiv \frac{A}{A_{\text{CNO}}} \, p_{\text{CNO}} \tag{9.41}$$

and

$$v' \equiv (2 - 1/\alpha')u \simeq u/2 \quad \text{if } \alpha' \simeq 2/3. \tag{9.42}$$

This leads to the limiting behaviours

$$Z \propto \frac{1}{2}u^2 \qquad \text{as } u \to 0 \text{ ('secondary dependence');} \qquad (9.43)$$

$$\propto \frac{e^{-(u-v')}}{(2 - 1/\alpha')^2} \quad \text{as } u \to \infty. \qquad (9.44)$$

The predictions of this model (normalized to meteoritic abundance for solar metallicity) are illustrated in Fig. 9.6 and compared with observational data for beryllium in stars, based on ground-based measurements of the near-UV Be II doublet λ 3130. Assuming that surface Be can suffer some destruction in some of the metal-rich disk stars, there is fair agreement down to about 0.1 of solar abundance, but the 'secondary' trend predicted at still lower metallicities is too steep.
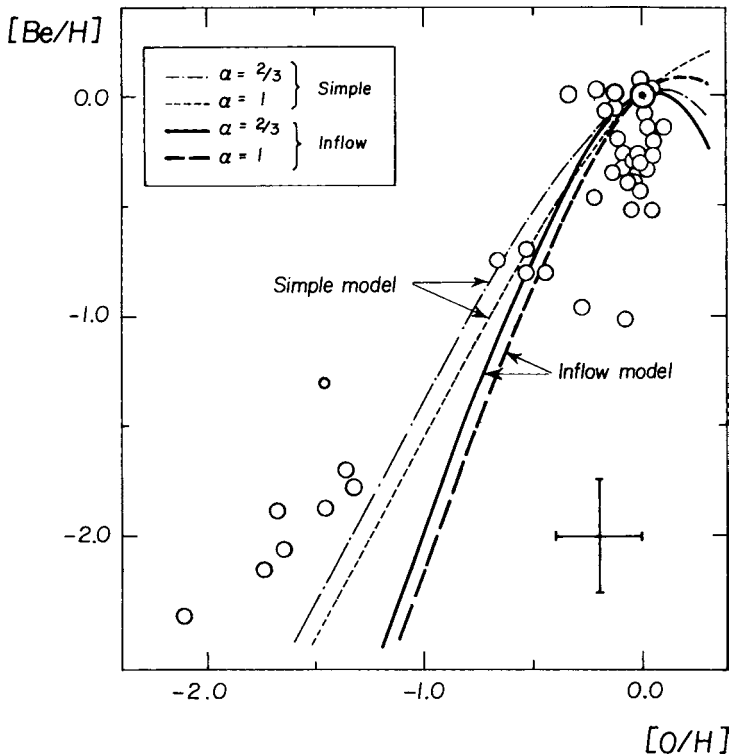
Fig. 9.6. Beryllium abundance as a function of oxygen abundance, according to models (curves) and observations (open circles) by Gilmore *et al.* (1992). (α in the key is actually the quantity called α' in the text.) After Pagel (1994). With kind permission from Kluwer Academic Publishers.

Considering now the simple inflow model, we again have Eqs. (9.27) to (9.29) together with

$$Z_{CNO} = \frac{1}{2} p_{CNO} u \quad \text{(Eq. 8.50)} \tag{9.45}$$

and Eq. (9.14) becomes (assuming $Z_F = 0$)

$$\frac{d}{du}(gZ) = \frac{A}{A_{CNO}} \frac{\sigma\phi}{\omega} gZ_{CNO} - g\frac{Z}{\alpha'} \tag{9.46}$$

$$= \frac{k}{2}\left(\frac{\sigma\phi}{\omega}\right)_1 \frac{e^{u_1}}{u_1} u^3 e^{-2u} - \frac{gZ}{\alpha'} \tag{9.47}$$

with the solution

$$Z = \frac{k}{2}\left(\frac{\sigma\phi}{\omega}\right)_1 \frac{e^{u_1}}{u_1} \frac{e^{-u}[6(e^{v'}-1) - 6v' - 3v'^2 - v'^3]}{u(2 - 1/\alpha')^4}, \tag{9.48}$$

where v' is defined by Eq. (9.42). The limiting behaviours in this case are

$$Z \propto \frac{u^3}{24} \qquad\qquad \text{for } u \to 0; \tag{9.49}$$

$$\propto \frac{6}{(2 - 1/\alpha')^4} \frac{e^{-(u-v')}}{u} \quad \text{for } u \to \infty. \tag{9.50}$$

This solution is also shown in Fig. 9.6, where it can be seen that its fit at low metallicities is still worse than for the (otherwise less satisfactory) Simple model. This is basically because of the assumption that the cosmic-ray flux is proportional to the total star formation rate. The latter is low at early times in this model because the mass of gas at such times is small and the assumption may well not apply, especially in this case. The discovery of beryllium (and boron from the UV B I line λ 2497 measured using the Hubble Space Telescope) in these metal-deficient stars was nevertheless a surprising one, which was made in part because of predictions (now no longer taken very seriously) that there might be cosmological production of these elements in an inhomogeneous Big Bang (see Chapter 4). As it is, the nearly constant ratio of Be and B to primary elements like iron and oxygen raises a problem to which no definitive solution has yet been found, although there have been various ideas which we discuss in the next two sections.

9.4.5 Halo models with homogeneous outflow

Ryan *et al.* (1992) noted that in models for the Galactic halo assuming homogeneous outflow (Hartwick 1976), the limiting behaviour of Eq. (9.44) sets in at a

low metallicity, thus counteracting the steep u^2 dependence of the Simple model. In this case, Eq. (9.36) is replaced by

$$E = \eta \, \omega g; \quad g = e^{-(1+\eta)u}, \tag{9.51}$$

where $\eta \simeq 9$ is the ratio of mass lost in a homogeneous wind to mass locked up in stars (see Section 8.3.7). Equation (9.39) then becomes (bearing in mind that $Z_{CNO} = p_{CNO} \, u$ as in the Simple model and using the initial value $(\sigma\phi/\omega)_0$ in place of the present-day value of that parameter used before)

$$\frac{dZ}{du} + Z(1/\alpha' - 1) = k \left(\frac{\sigma\phi}{\omega} \right)_0 u \, e^{-(1+\eta)u} \tag{9.52}$$

with the solution

$$Z = k \left(\frac{\sigma\phi}{\omega} \right)_0 \frac{e^{-(1/\alpha' - 1)u}}{(\eta + 2 - 1/\alpha')^2} [1 - e^{-w}(1 + w)], \tag{9.53}$$

where

$$w \equiv (\eta + 2 - 1/\alpha')u \simeq (1 + \eta)u. \tag{9.54}$$

Thus the limiting behaviour is

$$Z \propto u^2 \quad \text{for } u \to 0; \tag{9.55}$$

$$\propto (\eta + 2 - 1/\alpha')^{-2} \simeq (1 + \eta)^{-2} = \text{const. for } u \simeq 0.1, \tag{9.56}$$

whereafter ordinary disk evolution takes over. The trend is shown by the lower parts of the solid curves in Fig. 9.7. However, there is an obvious difficulty in that, to get an adequate yield, $(\sigma\phi/\omega)_0$ has to be much larger than $(\sigma\phi/\omega)_1$ applying at the present time. Specifically, if we compare Eq. (9.40) with Eq. (9.53) for $u = 0.02$ ([O/H] = -2) and $u_1 = 2$, we find that, to match the production of light elements from the Simple model, we need to have

$$\left(\frac{\sigma\phi}{\omega} \right)_0 = 8 \left(\frac{\sigma\phi}{\omega} \right)_1 \tag{9.57}$$

and the Simple model itself fails by about an order of magnitude (see Fig. 9.6). Thus a cosmic-ray boosting factor of nearly two orders of magnitude is needed. Apart from having to think of a mechanism for this, it was pointed out by Steigman and Walker (1992) that such a boost would result in unacceptably high primary production of lithium isotopes by $\alpha - \alpha$ fusion if the cosmic-ray spectrum is assumed to be unchanged. An interesting solution to both dilemmas was proposed by Prantzos *et al.* (1993), who suggested that, because of the greater extent of the Galaxy at right angles to the plane in early phases of collapse, the grammage parameter Λ could have been up to 2 orders of magnitude greater than at present (cosmic-ray confinement model), leading to both a higher flux and a flatter spectrum, which
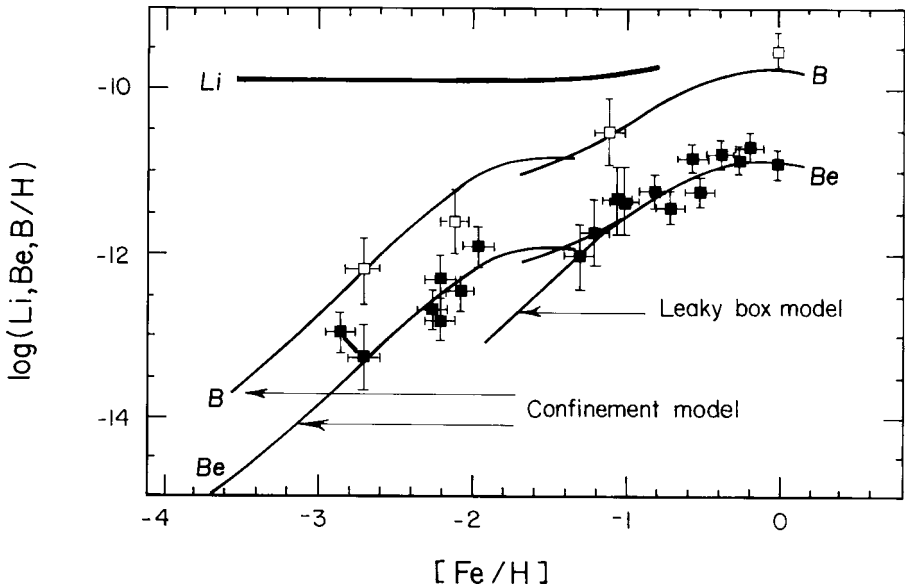
Fig. 9.7. Evolution of Be and B abundances according to the model based on confinement of cosmic rays in the early Galaxy (solid curves). Some observational data points are shown with error bars. Adapted from Prantzos, Cassé and Vangioni-Flam (1993).

latter serves to avoid the Li overproduction (cf. Fig. 9.4). However, this model still leads to secondary-like production at the lowest metallicities (which does not fit more recent data; see Fig. 9.8) and the amount by which Λ can ever be enhanced is well below 2 orders of magnitude because of nuclear fragmentation processes (Malaney & Butler 1993). The required boost factor can be reduced by invoking a 'chemo-dynamical' model of Galactic evolution (Burkert & Hensler 1989) in which there is a hot medium consisting of metal-rich stellar ejecta and a cool medium of lower metallicity from which stars form, but this still offers no escape from quadratic behaviour (Pagel 1994). Casuso and Beckman (1997), on the other hand, do have a model with similar ideas to those of Prantzos *et al.* in which quasi-primary behaviour is reproduced in consequence of certain assumptions about rates of inflow and outflow.

Nevertheless, as has been emphasized by Ramaty *et al.* (2000), the kind of boost to the cosmic-ray flux per supernova implied by Eq. (9.57) is untenable on energetic grounds. From present-day abundances, one can estimate the quantity Q/W, the number of Be atoms per erg of cosmic-ray energy. Given an iron yield of 0.2 $M_\odot$ per average supernova (of both types) today, and a Be/Fe ratio of 10^{-6}, one finds a yield of 4×10^{48} Be atoms per supernova. If the typical supernova explosion energy is 10^{51} erg and the cosmic-ray acceleration efficiency is 10 per cent, this
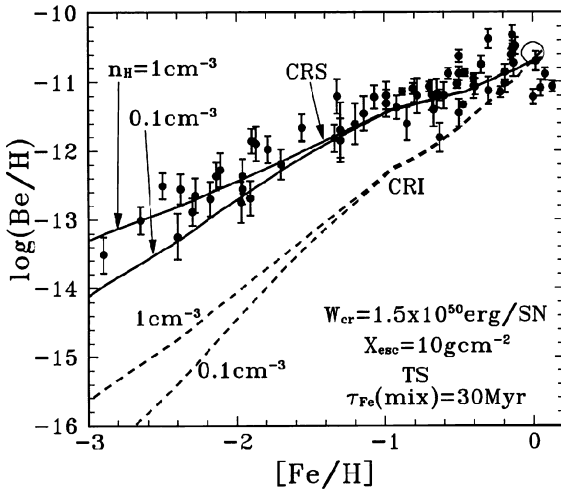
Fig. 9.8. Trend of beryllium abundance with metallicity compared to predictions from two models: (a) CRS denotes cosmic-ray acceleration in superbubbles rich in iron and oxygen as predicted from theoretical supernova yields (in this case those of Tsujimoto and Shigeyama 1998); and (b) CRI denoting cosmic rays accelerated from the general interstellar medium. The density dependence comes from its influence on the delay in the deposition of the synthesized Be. Virtually identical results were obtained using the yields from Woosley and Weaver (1995). After Ramaty *et al.* (2000).

makes $Q/W \simeq 0.04$ atoms per erg, which is also consistent with detailed model calculations (see Problem 3 below). Since the number of supernovae is fixed by the metallicity of the ISM, the only other factor that can be fixed to compensate the low CNO target abundances is the acceleration efficiency, which then has to be raised to 100 per cent or more.

9.4.6 Other possibilities

The above models are all rather unsatisfactory, because they involve somewhat arbitrary assumptions about the time-dependence of the cosmic-ray flux and spectrum and because they predict a secondary-like behaviour for Be and B abundances, whereas the overall trend indicated by the data is more like a primary one and there are the energetic difficulties pointed out above. In the case of ^{11}B, there is a possible primary mechanism for stellar production in supernovae by neutrino spallation processes (Woosley *et al.* 1990; Woosley & Weaver 1995), but the primary-like behaviour of beryllium in metal-poor stars, combined with a constant B/Be ratio of about 20 fully consistent with cosmic-ray spallation (García López *et al.* 1998) in the absence of any known similar process for Be, indicates that this does not solve the problem unless a primary process can be found for Be as well. Indeed,

the B/Be ratio (not appreciably different from solar) suggests that the supernova neutrino process may make just enough contribution to provide the excess of the meteoritic ^{11}B/^{10}B ratio over the value expected from cosmic rays.

Starting with the pioneering work of Duncan, Lambert and Lemke (1992), several authors have proposed, in more or less detail, that production of beryllium and boron at low metallicities is dominated either by the accelerated component of cosmic rays or by energetic particles in a hot bubble or superbubble surrounding a region of star formation, with the interior of the bubble consisting of hot ionized gas with a fixed, metal-rich composition from supernova ejecta not yet mixed into the general ISM. Carbon and oxygen nuclei could be accelerated to a few MeV on encountering the shock at the edge of the bubble, or by some other mechanism. Such a picture was partly inspired by reports of observations of the Orion Nebula with the Comptel telescope on the Compton γ-ray Observatory satellite, which were thought to reveal line transitions of ^{12}C and ^{16}O at energies of 4 to 6 MeV (Bloemen *et al*. 1994), but that claim was later withdrawn (Bloemen *et al*. 1999). Nevertheless, such γ-ray lines could be excited (below existing sensitivity thresholds) by the impact of ^{12}C and ^{16}O nuclei in supernova ejecta on protons and α-particles in the interstellar medium and, with certain assumptions, such particles could make a still larger contribution to light-element formation than do the Galactic cosmic rays, at least at low metallicity. In a model by Parizot and Drury (1999), light elements are formed from the impact of accelerated C,O nuclei on stationary atoms within a superbubble, *pari passu* with other products of supernova nucleosynthesis, building up to abundances of perhaps 0.1 solar. When the bubble eventually dissolves, it mixes in varying proportions with the surrounding very metal-poor ISM, leading to a range of abundances in which more-or-less solar ratios are preserved; relationships like those shown by the data in Figs. 9.6 to 9.8 thus represent mixing lines, rather than an evolution in time. (Possibly the same would apply to the flat α-element-to-iron ratios shown in Fig. 8.9.) Ramaty *et al*. (2000) perform detailed light-element abundance calculations based on a model (Higdon, Lingenfelter & Ramaty 1998) in which cosmic rays are accelerated to relativistic energies by repeated supernova shocks in superbubbles filled with tenuous gas having a similar composition to that of cosmic rays today, throughout Galactic history, thus avoiding large variations in Q/W and hence in the required cosmic-ray acceleration efficiency (see Fig. 9.8).

9.5 Cosmological cosmic rays and the ^{6}Li plateau

Production of ^{6}Li by $\alpha - \alpha$ fusion in the ISM is a primary process, so that its interstellar abundance at low metallicities would be expected to track primary elements

like O or Fe up to the point where reactions involving CNO nuclei take over. However, Montmerle (1977) pointed out that cosmological cosmic rays at high redshift, contributing to the suspected cosmic γ-ray background through π^0 decay, would also cause production of light elements, notably the two Li isotopes, because of the presence of a substantial helium abundance resulting from the Big Bang. Montmerle did not specify the origin of these cosmic rays; they could arise from either pre-Galactic stars ('Population III') postulated to account for the re-ionization of the Universe, or from 'structure formation shocks' resulting from galaxy–galaxy interactions such as mergers.

High-resolution spectroscopy of low-metallicity stars exhibiting the Spite (^{7}Li) plateau, using 8-m class telescopes, has led to several detections of ^{6}Li, generally at the level of about 5 per cent of ^{7}Li (Asplund *et al.* 2005), indicating that ^{6}Li also seems to exhibit a plateau at that level (see Fig. 9.9). Rollinde, Vangioni-Flam and Olive (2005) have used Montmerle's formalism in an updated cosmological model to investigate the production of ^{6}Li and ^{7}Li resulting from the formation of
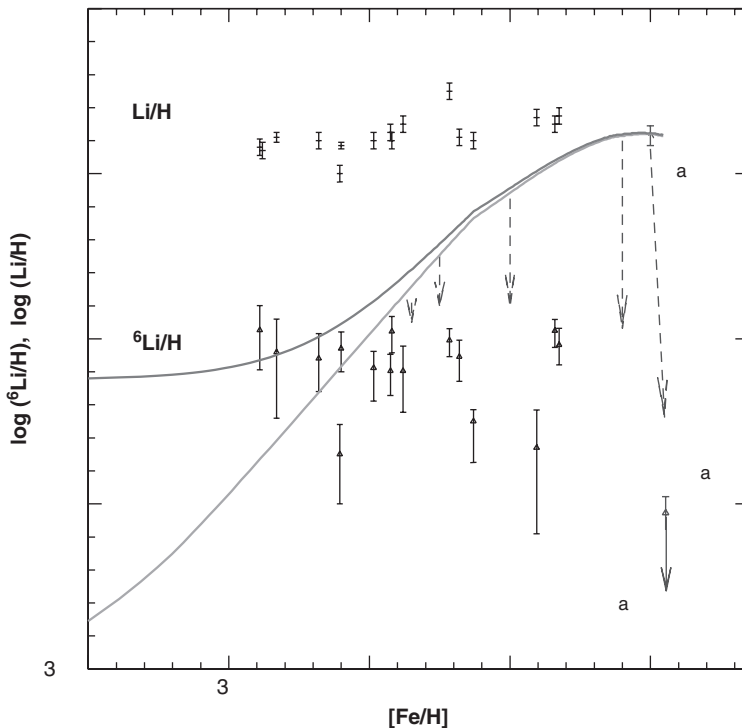
Fig. 9.9. Galactic chemical evolution of ^{6}Li, according to models with and without cosmological cosmic rays, the former providing a plateau at low metallicities. After Rollinde, Vangioni-Flam & Olive (2005).

a generation of massive stars in a burst at some high redshift between 10 and 100 or so, corresponding to possible periods of re-ionization of the Universe and well before the formation of the Galaxy, by which time the reactions have frozen out and a steady state is reached corresponding (for suitably chosen parameters) to the observed plateau. Since the cosmic-ray productions of ^{6}Li and ^{7}Li are comparable, this production does not seriously affect the ^{7}Li plateau resulting from the Big Bang unless there has been substantial differential depletion of ^{6}Li relative to ^{7}Li in the relevant stellar atmospheres (see Chapter 4). The energetic requirements for this picture are severe: upwards of about 16 erg per ^{6}Li nucleus or 100 eV per baryon in the Universe, depending on details of the cosmic-ray spectrum, if ^{6}Li/H $= 10^{-11}$ (Prantzos 2006). Reeves (2005) notes that this is comparable to the requirement for re-ionization of the Universe, possibly by a generation of massive Population III stars which did not release any metals. Another source could be radio-loud AGNs associated with black holes in clusters of galaxies, thought to be responsible for the excess entropy in the intra-cluster gas, compared to conventional gravitational scaling, which imposes similar energy requirements (Nath, Madau & Silk 2006).

Alternatively, ^{6}Li in low-metallicity stars could be the result of ^{4}He(^{3}He, p) reactions in stellar flares, analogous to effects found in some energetic solar flares (Tatischeff & Thibaud 2007). In this case there is expected to be real scatter in the ^{6}Li plateau, due to variations in (present or past) stellar rotation speed.

Notes to Chapter 9

The idea of cosmic-ray spallation as the major contributor to light-element production was first put forward in some detail by Reeves, Fowler and Hoyle (1970) and detailed physical models of cosmic-ray acceleration and propagation have been discussed by Meneguzzi, Audouze and Reeves (1971) and Meneguzzi and Reeves (1975). Calculations of both cosmic-ray and stellar-flare type production, using updated cross-sections, have been made by Walker, Mathews and Viola (1985), whose results for the cosmic-ray case are presented alongside my more simple-minded calculation in Table 9.2. The whole subject of cosmic rays in relation to the origin of light elements has been reviewed in its historical context by Vangioni-Flam, Cassé and Audouze (2000), and the physics of shock acceleration in plasmas is extensively discussed in Jones and Ellison (1991) and elsewhere.

Beryllium was first demonstrated to be present in low-metallicity stars by Gilmore, Edvardsson and Nissen (1991) and soon confirmed by others, e.g. Ryan *et al*. (1992) who gave the argument for a flattening in the Be/Fe ratio at [Fe/H] ~ -1. Extensive data are now available from their work and from that of Gilmore *et al*. (1992) and Boesgaard and King (1993). Boron was discovered in a few metal-deficient stars by Duncan, Lambert and Lemke (1992) using the Hubble Space

Telescope, but their abundance estimates have had to be corrected for line blend-ing and non-LTE effects (Edvardsson *et al*. 1994; Kiselman & Carlsson 1994; García López *et al*. 1998). King (2001) gives an extensive critical review of the Galactic evolution of light elements in relation to oxygen and iron, concluding that some combination of interstellar medium and superbubble formation seems to be required.

The discussion of the GCE of light elements formed by cosmic-ray spallation is based on Pagel (1994) and has a somewhat different outlook from many other treatments in the literature, e.g. Fields, Olive and Schramm (1995), which should be consulted to get another viewpoint. A numerical treatment of the Simple model by Vangioni-Flam *et al*. (1990) gave similar results to the ones derived more simply here, as did the discussion of inflow models by Prantzos (1994).

A number of authors have considered ways in which Be and B might be expected to show primary behaviour in the early Galaxy. Duncan, Lambert and Lemke (1992) suggested a possible dominance of the 'decelerated' component, while Feltzing and Gustafsson (1994) and Tayler (1995) considered other ways in which spallation might take place preferentially in a metal-enriched supernova environ-ment. The models by Parizot and Drury (1999) and by Ramaty *et al*. (2000) are refinements of these earlier more schematic ideas. Silk and Schramm (1992) con-sidered the contribution of a hypothetical early enhanced cosmic-ray flux to the γ-ray background. Vangioni-Flam *et al*. (1996) and Ramaty *et al*. (1997) developed models influenced by the suggestion of fast CNO nuclei in Orion, for which the experimental γ-ray evidence was subsequently withdrawn (Bloemen *et al*. 1999), but which could still be present.

The relation between ^{6}Li abundances and the (uncertain) cosmic γ-ray back-ground has been discussed by Fields and Prodanović (2005); as pointed out by Rollinde *et al*. (2005), there is no inconsistency with the plateau.

Overviews of the abundance and evolution of light elements are available in

P. Crane (ed.), *The Light Element Abundances*, Springer-Verlag 1995; and

L. da Silva, M. Spite and J.R. de Medeiros (eds.), IAU Symp. no. 198: *The Light Elements and their Evolution*, ASP publ. 2000.

Problems

1. Calculate the energy in MeV of a proton in supernova ejecta travelling at $10^4 \, \text{km s}^{-1}$.

2. Verify that the momentum and energy expressions in Eq. (9.1) are equivalent.

3. Calculate the total number density and (kinetic) energy density (in eV cm^{-3}) of cosmic-ray protons from Eq. (9.5) and deduce their average energy.

Assuming a cosmic-ray confinement time of 10^7 years and an interstellar hydrogen density of 1 atom cm^{-3}, with present-day CNO abundances, use Eq. (9.10) to deduce Q/W for beryllium.

4. Calculate the Solar-System Be/H ratio predicted by the Simple model (Eq. 9.40) using the cross-section from Table 9.2, the present-day cosmic-ray flux from Eq. (9.5) and assuming $u = u_1 = 2$, $\alpha' = 2/3$, $\omega^{-1} = 3\,\mathrm{Gyr}$.

5. Calculate the Solar-System Be/H ratio predicted by the simple inflow model, Eq. (9.48), with the same assumptions as in Problem 4, except that now $u = 3$.

6. Show that, in Larson's extreme inflow model (see Section 8.5.1), assuming infalling material to be pristine with primordial abundances, the deuterium abundance evolves according to

$$D/H = (D/H)_p \{ e^{-u/\alpha} + \alpha(1 - e^{-u/\alpha}) \}. \tag{9.58}$$

10

Radioactive cosmochronology

Time travels in divers paces with divers persons. I'll tell you who
Time ambles withal, who Time trots withal, who Time
 gallops withal and who he stands still withal.

W. Shakespeare, *As You Like It*

10.1 Introduction

Early in the twentieth century, Rutherford and his colleagues developed the use
of the fixed lifetimes of radioactive nuclei as a chronometer to measure ages of
terrestrial and meteoritic rocks, and in 1929 Rutherford extended their use to make
arguments about the age of the elements since their mean epoch of creation, related
to the age of the Galaxy and the Universe. In the 1950s and afterwards, Fowler and
Hoyle and others refined these arguments on the basis of improved understanding
of nucleosynthesis; complications raised by questions related to Galactic chemical
evolution will form a major topic of this chapter. In recent years, the discovery
of dead short-lived radioactivities (e.g. from the isotopic anomalies mentioned in
Chapter 3) has led to further inferences of timescales related to the formation of
the Solar System. Some of the relevant species are listed in Table 10.1.

10.2 Age-dating of rocks

The basic idea in radioactive age-dating of rocks (from the Earth, Moon and mete-
orites) is to find the ratio of daughter to parent in an isolated system. Thus the age
inferred is usually the 'solidification age' which is the time since the last occa-
sion when chemical fractionation was halted by solidification. (K–Ar dating gives
a 'gas-retention age' which can be slightly shorter.)

In general, the daughter nucleus will have an initial abundance at time zero,
which can be assumed to bear a constant ratio to another isotope of the same

Table 10.1. *Some radioactive species*

Parent	Daughter	Mean life λ^{-1}		
^{187}Re	^{187}Os	72	Gyr	
^{87}Rb	^{87}Sr	68	"	
^{232}Th	^{208}Pb	20.3	"	living
^{238}U	^{206}Pb	6.45	"	
^{40}K	^{40}Ar (^{40}Ca)	1.7	"	
^{235}U	^{207}Pb	1.02	"	
^{146}Sm	^{142}Nd	145	Myr	
^{244}Pu	^{232}Th	120	"	
^{129}I	^{129}Xe	23	"	
^{247}Cm	^{235}U	22.5	"	dead,
^{182}Hf	^{182}W	13	"	but live
^{107}Pd	^{107}Ag	9.4	"	in ISM
^{50}Mn	^{53}Cr	5.3	"	
^{60}Fe	^{60}Ni	2.2	"	
^{26}Al	^{26}Mg	1.03	"	
^{10}Be	^{10}B	2.18	Myr	in CAIs
^{36}Cl	^{36}Ar	0.43	"	in CAIs
^{41}Ca	^{41}K	0.14	"	in CAIs + pre-solar gr.
^{44}Ti	^{44}Ca	87	yr	in pre-solar grains

element (one that is not enhanced by the radioactive decay). This is because isotope ratios are usually not affected by chemical fractionation processes, whereas the initial ratio of parent to daughter can vary widely. By comparison of the three species, parent ^{A}P, daughter ^{A}D (assuming that we are dealing with β-decay) and isotope of daughter $^{A'}$D in different samples drawn from one or several meteorites, it is possible to generate an *isochrone* by plotting ^{A}D/$^{A'}$D against ^{A}P/$^{A'}$D (see Fig. 10.1), since after time t

$$\frac{^A P(t)}{^{A'}D} = \frac{^A P(0)}{^{A'}D} e^{-\lambda t}, \tag{10.1}$$

and

$$\frac{^A D(t)}{^{A'}D(t)} = \frac{^A D(0)}{^{A'}D} + \frac{^A P(0)}{^{A'}D} (1 - e^{-\lambda t}) \tag{10.2}$$

$$= \frac{^A D(0)}{^{A'}D} + \frac{^A P(t)}{^{A'}D} (e^{\lambda t} - 1). \tag{10.3}$$
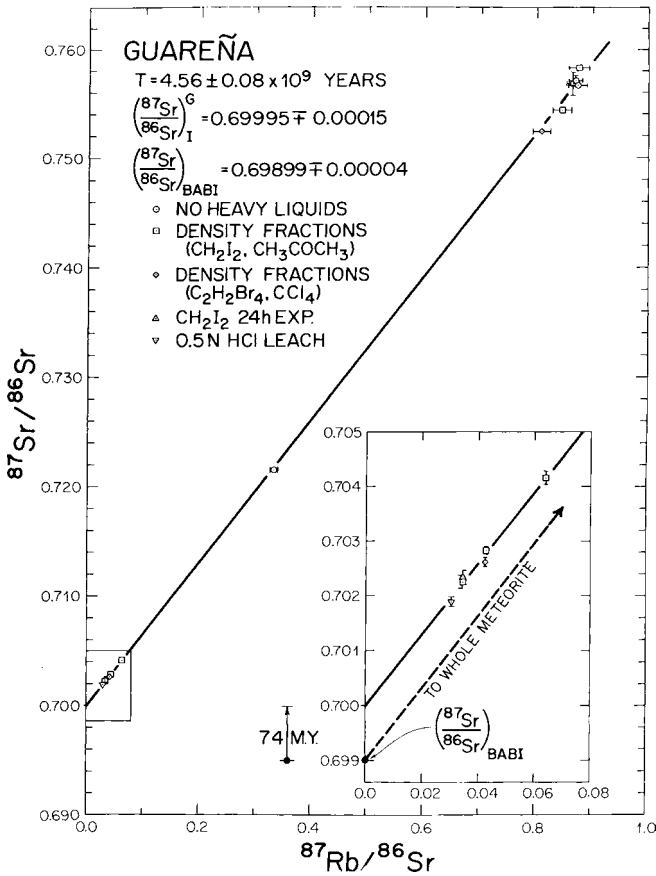
Fig. 10.1. Rb–Sr isochrone measured from separated components of the stony meteorite Guareña. The initial $^{87}Sr/^{86}Sr$ ratio is slightly higher than that inferred in basaltic achondrites (BABI) because of a period of metamorphism. After Wasserburg, Papanastassiou and Sanz (1969), with permission. Courtesy G. J. Wasserburg.

The first term in Eq. (10.3) is a constant, being the natural isotope ratio of, e.g., $^{87}Sr/^{86}Sr$, while the second has a slope ($e^{\lambda t} - 1$), representing the growth of the daughter nucleus ^{87}Sr due to decay of ^{87}Rb in the course of time. Thus the solidification age of meteorites is found to be 4.56 Gyr, which is identified as the age of the Solar System (and of the Sun). Subtle differences of the intercept relative to carbonaceous chondrites (Allende has the smallest initial $^{87}Sr/^{86}Sr$ ratio known) reveal brief melting episodes in certain meteorites prior to the last solidification.

A few meteorites have significantly younger ages; these are believed to come from the Moon and in some cases from Mars, rather than from asteroids.

10.3 Galactic cosmochronology

10.3.1 Some historical landmarks

Rutherford (1929) noted that the abundance ratio ^{235}U/^{238}U is 0.007 now and was 0.3 at the birth of the Solar System, and he pointed out that extrapolation still further back to the (mean) epoch of nucleosynthesis would give the production ratio; the assumption at that time was that elements had been synthesized in the Sun and that the planets were formed out of material extracted from the Sun by a passing star. Reasoning that the production ratio was likely to be a reasonably small number (< 10, say), he deduced that the mean nucleosynthesis epoch could not have been more than 4.3 Gyr before the formation of the Solar System.

A theory for the production ratio became available with the work of B^{2}FH and Cameron (1957), who established that the actinides (U, Th etc.) result from the r-process, probably in supernovae. A first estimate of production ratios results from the simple consideration that an actinide nucleus (Z, A) can be formed either directly via β-decay or indirectly by α-decay of a higher nucleus ($Z+2n$, $A+4n$), where n is limited by the occurrence of fission along the $A + 4n$ isobaric chain at a lower Z. Thus $^{238}_{92}$U can be formed either directly or by α-decay of $^{242}_{94}$Pu and $^{246}_{96}$Cm, but the chain becomes weaker at $^{250}_{98}$Cf, owing to partial fission of $^{250}_{96}$Cm, and stops altogether short of $^{254}_{100}$Fm owing to complete fission of $^{254}_{98}$Cf. Thus ^{238}U has effectively about 4 progenitors (including itself). Similar considerations result in about 6 progenitors for ^{235}U and ^{232}Th and 3 for ^{244}Pu[1] so that from this factor alone one might expect production ratios relative to ^{238}U of about 1.5 for ^{235}U and ^{232}Th, and 0.75 for ^{244}Pu. The theoretical production ratios have been steadily refined over the years by Hoyle, Fowler, Clayton, Schramm, Cameron, Thielemann, Truran, Cowan and others (see Chapter 6 and Table 10.2). The same authors have then proceeded to apply these ratios to the problem of estimating the age of the Galaxy from the abundance ratios of ^{235,238}U and ^{232}Th in the Solar System. Clayton (1964) suggested an additional 'aeonglass' in the form of the ratio ^{187}Re/^{187}Os. ^{187}Re has a very long lifetime (see Table 10.1), which has some advantages in reducing sensitivity to GCE details, but associated uncertainties (including enhancement of β-decay rates at stellar temperatures and the s-process contribution to ^{187}Os) have prevented any significant results from this so far (Yokoi, Takahashi & Arnould 1983). Butcher (1987) invented a completely new technique of judging stellar ages from the abundance of thorium, which has the advantage of being independent of either production ratios or Solar-System abundances, but involves some technical difficulties of its own. Schramm and Wasserburg (1970) and especially Tinsley (1977) and Clayton (1988) noted the sensitivity of Galactic age estimates

---

[1] An illustration of the relevant tracks in the (N, Z) plane is given by Thielemann, Metzinger and Klapdor (1983).
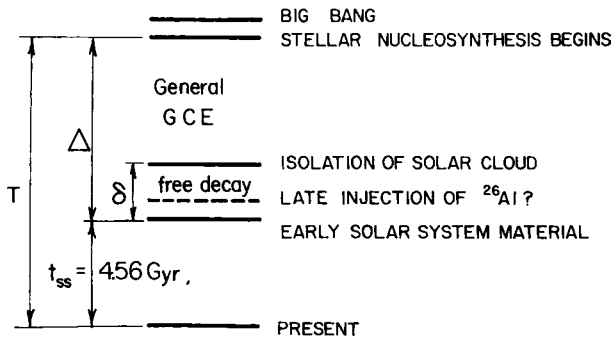
Fig. 10.2. Timescales related to Galactic cosmochronology.

based on radioactivity to the details of the GCE model adopted ('the aeonglasses leak'), but in principle (if perhaps not yet in practice) it may still be possible to obtain interesting constraints on both the GCE model and the age of the Galaxy and/or of individual stars by combining Solar-System and stellar data.

10.3.2 Galactic cosmochronology: theory

We assume that actinides are formed along with other elements in some sort of GCE history during a period of time Δ up to the formation of the Solar System (Fig. 10.2). Thus

$$T = \Delta + t_{SS} = \Delta + 4.56 \text{ Gyr} \tag{10.4}$$

is the age of the Galaxy since the beginning of nucleosynthesis. Possible complications are

(i) The Solar System could have been enriched by a late nucleosynthesis 'spike' due to a nearby supernova or AGB star. Supernova effects are not now usually considered significant, at least as a contributor to the r-process, because of the small abundance of ^{129}I (see Section 10.4.2), but there is a problem with ^{26}Al, and a late injection from an AGB star has been suggested by Wasserburg *et al.* (1994); this would not affect the actinides since they come from the r-process.

(ii) There is generally assumed to be a period δ of free decay while the parent cloud of the Solar System was isolated from the general ISM for some time before the system was formed and/or during solidification of meteorite parent bodies over periods dependent on individual mineralogies. Since the dead activities indicate $\delta \leq 10^7$ yr (see Section 10.4), the long-lived actinides will again be unaffected.

(iii) Actinides can undergo destruction by photo-fission in He zones (Malaney, Mathews & Dearborn 1989) which may lead to a modest degree of destruction by astration; we shall neglect this effect, however.

In the theoretical development, we assume instantaneous recycling with constant yields and generalize Eq. (7.34) to the case of a decaying element with $Z_F = 0$ using now time as the independent variable, bearing in mind that $E \equiv \eta \alpha \psi$ and neglecting free decay:

$$\frac{dN_i}{dt} \equiv \frac{d}{dt}\left(\frac{Z_i g}{A_i m_\mathrm{H}}\right) = p_i \frac{ds}{dt} - (1+\eta)\frac{ds}{dt}\frac{N_i}{g} - \lambda_i N_i, \qquad (10.5)$$

where N_i is the number of atoms in the ISM of a representative region, e.g. a cylinder at right angles to the Galactic plane through the Sun, and p_i is the yield expressed in number of atoms rather than mass. The solution of Eq. (10.5) is

$$N_i(t) = e^{-\lambda_i t - \nu(t)}\left[N_{i0} + p_i \int_0^t \alpha\,\underline{\psi(t')e^{\nu(t')}\,e^{\lambda_i t'}}\,dt'\right], \qquad (10.6)$$

where

$$\nu(t) \equiv \int_0^t [(1+\eta)\alpha\psi(t')/g(t')]\,dt'. \qquad (10.7)$$

The underlined factor in Eq. (10.6) is sometimes called the 'effective production function'.

To proceed further, we assume for simplicity (as has mostly been done in the literature) a linear model, i.e.

$$\alpha\psi \equiv \frac{ds}{dt} = \omega g \quad \text{with} \quad \omega = \text{const.}, \qquad (10.8)$$

and (without significant loss of generality) we take $\eta = 0$. Then $\nu = \omega t$ and Eq. (10.6) simplifies to

$$N_i(t) = e^{-(\omega+\lambda_i)t}\left[N_{i0} + p_i \int_0^t \alpha\psi(t')\,e^{(\omega+\lambda_i)t'}\,dt'\right]. \qquad (10.9)$$

For Solar-System actinides, given a set of production ratios p_i/p_j calculated from the theory of the r-process, one can use meteoritic abundance measurements to derive the 'observed' quantities

$$K_{ij}(\Delta) \equiv \frac{N_i(\Delta)/p_i}{N_j(\Delta)/p_j} \qquad (10.10)$$

at the time of formation of the Solar System.

10.3.3 Some data and models

Table 10.2 gives some of the data on K-ratios used by different authors, including some rather uncertain data for ^{244}Pu. There are significant differences among the

Table 10.2. *Some estimates of K-ratios in the Solar System*

	Meyer & Schramm 1986	Fowler 1987	Cowan *et al.* 1987, 91
p_{235}/p_{238}	$1.5^{+.4}_{-.3}$	$1.34 \pm .19$	1.16
N_{235}/N_{238} [a]	0.310	0.33	0.32
p_{232}/p_{238}	$1.6 \pm .2$	$1.71 \pm .07$	$1.65 \pm .05$
N_{232}/N_{238} [a]	$3.5 \pm .2$	2.30	2.32
p_{244}/p_{238}	0.12 to 1		
N_{244}/N_{238} [a]	$0.005 \pm .001$		
$K_{235,238}$	$0.21 \pm .05$	$0.246 \pm .035$	0.273
$K_{232,238}$	$2.2 \pm .3$	$1.35 \pm .10$	$1.40 \pm .05$
$K_{244,238}$	0.004 to 0.05		

[a] At formation of Solar System.

K-ratios adopted, and age estimates based on them are also dependent on the GCE model used, as will be illustrated with two such models.

The first one is that of Fowler (1987), which is a Simple closed model with an initial production spike (see Section 8.4, item (iv), in relation to the 'G-dwarf problem'). In this model the net star formation rate is

$$\alpha\psi = \omega g = A e^{-\omega t} \tag{10.11}$$

and the abundances are

$$N_i(\Delta) = e^{-\omega\Delta} \left[N_{i0} e^{-\lambda_i\Delta} + A \frac{p_i}{\lambda_i} (1 - e^{-\lambda_i\Delta}) \right] \tag{10.12}$$

for a radioactive element and

$$N_k(\Delta) = e^{-\omega\Delta} [N_{k0} + A p_k \Delta] \tag{10.13}$$

for a stable element. If a fraction S of the stable element in the Solar System comes from the initial spike and the stable element is produced *pari passu* with the radioactive one, then

$$\frac{N_{i0}}{A p_i} = \frac{N_{k0}}{A p_k} = \frac{S\Delta}{1 - S}, \tag{10.14}$$

so that, from Eq. (10.12),

$$\frac{e^{\omega\Delta}}{\Delta} \frac{N_i(\Delta)}{A p_i} = \frac{S}{1 - S} e^{-\lambda_i\Delta} + \frac{1 - e^{-\lambda_i\Delta}}{\lambda_i\Delta}. \tag{10.15}$$
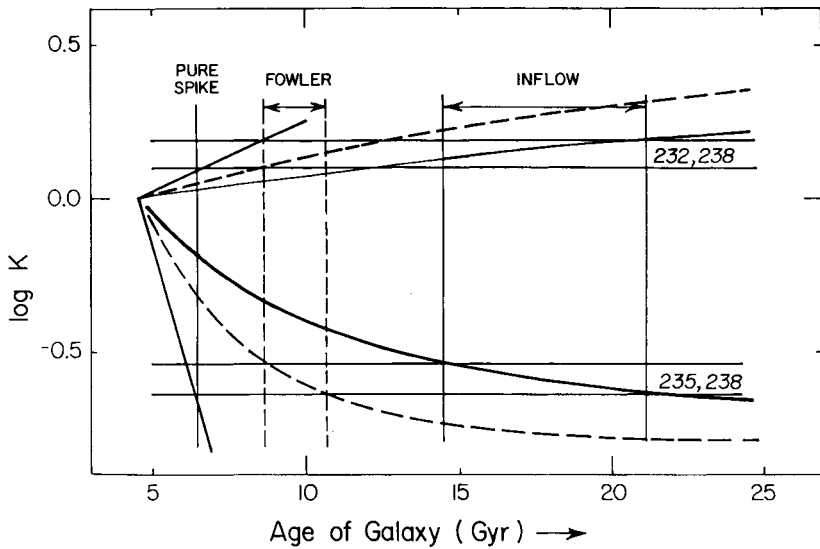
Fig. 10.3. 'Observed' K-ratios (estimated error limits shown by pairs of horizontal lines) and their theoretical variation with the age of the Galaxy according to three models: a pure initial spike (continuous straight lines); Fowler's (1987) model (broken-line curves); and the simple inflow model (continuous curves). After Pagel (1993).

Fowler uses $K_{235,238}$ and $K_{232,238}$ to solve for the two unknowns S and Δ (note that the K-ratios are independent of ω) finding

$$S = 0.17 \pm 0.02; \tag{10.16}$$

$$T = \Delta + 4.6 = 10.0 \pm 1.5\,\text{Gyr} \tag{10.17}$$

(see Fig. 10.3).

For these parameters, $K_{244,238} = 0.03$. It is to be noted that a pure initial spike ($S = 1$) would just fit the U–Th data in Fig. 10.3 with $T = 6.4\,\text{Gyr}$ (the rock-bottom limit to the age of the Universe), but at the expense of making $K_{244,238} = 4 \times 10^{-7}$, which is far too small unless one can appeal to some special factor (like a nearby supernova) that introduced Pu shortly before the formation of the Solar System. On the other hand, with S just slightly less than 1, this difficulty could be overcome, giving an age of still only 7 Gyr, say. However, there are other reasons for believing nucleosynthesis to have been a continuous process in our Galaxy.

Fowler's argument essentially applies to the thin disk, for which his age estimate of 10 Gyr is in impressive agreement with independent stellar age estimates (see Fig. 8.41). Pagel (2001) extended the argument to include the thick disk by supposing that the initial spike (taking S to be 0.4 in accordance with Fig. 8.40, rather than 0.2) resulted from thick-disk (or bulge) formation on a short timescale at an

Table 10.3. *K-ratios of actinide abundances at Solar-System formation*

	235,238	232,238	Eu,Th
'Observed' after Table 10.2	$0.25 \pm .04$	$1.38 \pm .10$	
From modified Fowler model, $T = 15$, Eq. (10.18)	0.24	1.45	1.23

After Pagel (2001).

interval $\epsilon = 3$ Gyr before the formation of the thin disk, which itself then evolved according to the Simple model for an interval $\Delta = 4.4$ Gyr before the formation of the Solar System, corresponding to a total age $T = 12$ Gyr for the Galaxy. In this case, Eq. (10.15) is modified to

$$\frac{e^{\omega\Delta}}{\Delta} \frac{N_i(\Delta)}{Ap_i} = \frac{S}{1-S} e^{-\lambda_i(\Delta+\epsilon)} + \frac{1 - e^{-\lambda_i\Delta}}{\lambda_i\Delta}, \qquad (10.18)$$

leading to the K-ratios given in Table 10.3, which are again in good agreement with the data.

As an alternative to these 'PIE' models, we now consider the simple inflow model of Section 8.5.2. In this model we assume

$$g_0 = z_0 = z_F = 0 \qquad (10.19)$$

and take the final mass of the system to be 1. We then have from Eq. (10.9) with $N_{i0} = 0$, $\alpha\psi = \omega g = \omega u e^{-u} = \omega^2\, t\, e^{-\omega t}$,

$$N_i(\Delta) = e^{-(\omega+\lambda_i)\Delta}\, p_i\, \omega^2 \int_0^\Delta t\, e^{\lambda_i t} dt \qquad (10.20)$$

$$= e^{-(\omega+\lambda_i)\Delta}\, p_i\, \omega^2 \frac{1}{\lambda_i^2} \left[\lambda_i \Delta e^{\lambda_i\Delta} - (e^{\lambda_i\Delta} - 1)\right], \qquad (10.21)$$

whence

$$\frac{e^{\omega\Delta}}{(\omega\Delta)^2} \frac{N_i(\Delta)}{p_i} = \frac{1}{\lambda_i\Delta} - \frac{1 - e^{-\lambda_i\Delta}}{(\lambda_i\Delta)^2}. \qquad (10.22)$$

This formula fits the same U, Th data for $13 \leq T \leq 20$ Gyr, and it can be seen from Fig. 10.3 that the upper limit could be infinity for slightly different models, basically because the beginning of nucleosynthesis is something that is now assumed to happen gradually. The inflow model gives $K_{244,238} = 0.04$, much the same as in Fowler's model. Thus *Solar-System actinide data do not provide any upper limit to the age of the Galaxy, nor do they strongly constrain GCE models.*
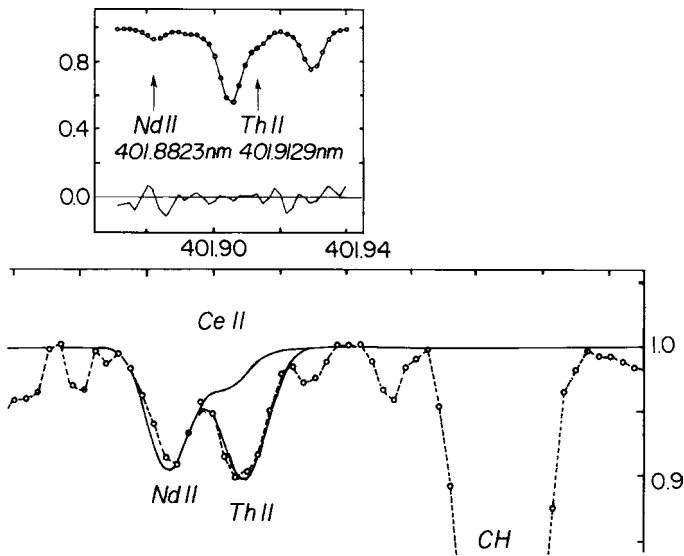
Fig. 10.4. Above: spectrum of the solar-type G-dwarf star HR 509 showing features of Th II and Nd II near λ 4019 Å, after Butcher (1987). Th II is blended with a strong feature due to Fe and Ni, as well as weaker features. The tracing around the zero level shows 10 × the difference between the observed spectrum (dots) and the fitted synthetic spectrum (continuous curve). Reproduced with permission from Macmillan Magazines Ltd. Below: spectrum of the same region in the very metal-poor giant star CS 22892−052 ([Fe/H] ≃ −3) with a large relative excess of r-process elements ([r/Fe] = 1.7), adapted from Sneden *et al.* (1996).

10.3.4 Stellar thorium chronology

Butcher (1987) invented a new original approach to Galactic cosmochronology based on spectroscopic observations of thorium in stars (see Fig. 10.4). The idea is to judge the ages of stars by the amount by which thorium has decayed compared to some expected standard: older stars may be expected to have relatively less thorium than younger ones, and this can act as an independent check on the age of the star deduced conventionally from its position in the HR diagram. This could be of importance in cosmology, since conventional age estimates of globular clusters and some field stars (12 to 20 Gyr) are in some cases too large to be reconciled with observational estimates of the Hubble constant, at least in Einstein–de Sitter cosmology.

The advantages of this method are

(i) Compared to the onset of nucleosynthesis in the Galaxy, which may be rather poorly defined, in this case one is dating a very well-defined event, namely the birth of the particular star. Consequently there is less sensitivity to GCE models, although there is still some, as discussed below.

(ii) No theoretical production ratios are needed. The Sun has a well-known age, so that its thorium abundance can be used as a standard.

There are also problems with the method:

 (i) The abundance determination is technically difficult in solar-type stars because of blending with other spectral lines (see Fig. 10.4).
(ii) There are difficulties in the choice of a stable element for comparison, so as to cancel out effects of differing metallicity. Butcher chose neodymium, because there is a Nd II line very nearby in the spectrum to the Th II line which has similar excitation potential making the ratio quite insensitive to stellar temperature and gravity. This choice is flawed, however, by differential GCE effects on the two elements, since about half of the Nd in metal-rich stars comes from the s-process (see Table 6.3) and Th exclusively from the r-process.

   Butcher argued that differential GCE effects between Th and Nd are negligible, because abundance measurements available at the time had not been able to detect any changes in s/r/Fe ratios at least in Galactic disk stars; more recent studies such as that by del Peloso, da Silva and Porto de Mello (2005) confirm his contention with regard to Nd relative to nearly pure r-process elements such as europium. From his failure to detect any change in Th/Nd correlated with the conventional ages of the stars, he deduced an age of 10 Gyr or less for the Galaxy, in agreement with Fowler. This led to a number of papers and counter-papers discussing the above points, and also to some new measurements which mostly reaffirmed Butcher's original results. Pagel (1989b) proposed that Th should be compared to another mainly r-process element, specifically Eu, and this has been done in a few investigations which support ages of 10 Gyr or less for the disk (del Peloso, da Silva & Porto de Mello 2005), but a larger one in the case of ultra-metal-poor (UMP) r-process enhanced stars such as CS 22892−052 (see Fig. 10.4) where the Th/Eu ratio is 0.1 to 0.2 dex lower than solar (while the Nd/Eu ratio is about half solar); at the same time, numerous stable r-process species in that star have abundance ratios in excellent agreement with those of the r-process contributions to the abundances of the corresponding elements in the Solar System (Sneden *et al*. 1996).

10.3.5 Galactic cosmochronology and stellar thorium abundances: theory

Two extreme models of the evolution of stellar thorium abundances can be considered:

 (i) The pure initial spike model for the r-process considered in Section 10.3.3. In this case, all the thorium was created at an initial instant and decayed at a constant rate up to the present, whether in stellar atmospheres or elsewhere. Hence no variation in Th
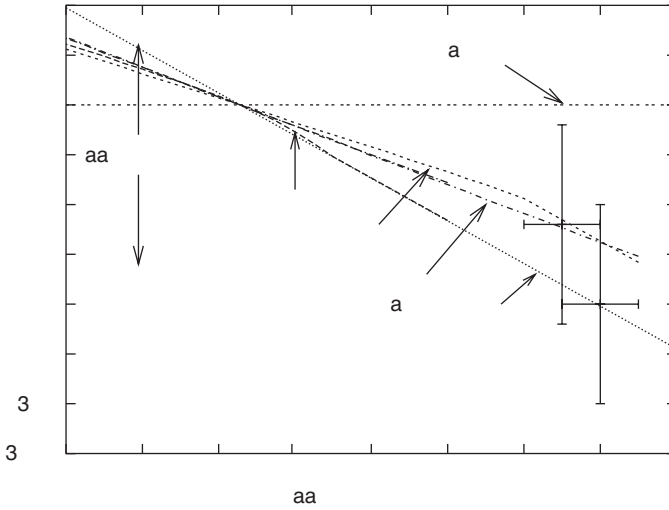
Fig. 10.5. Logarithmic differential Th/Eu ratios plotted against stellar age. The crosses represent the average of two UMP r-process-rich stars: CS 22892−052 and HD 115444 (Westin *et al.* 2000), and a third one: BD +17° 3248 (Cowan *et al.* 2002) which are a kind of 'Rosetta stone' for the r-process, assuming an age of 13 ± 1 Gyr. Curves show predictions from various models discussed in the text.

abundance with stellar age is to be expected ('pure initial spike' in Fig. 10.5) and the Solar-System K-ratios lead to an age of order 7 Gyr.

(ii) A model in which each star has a mix of r-process elements derived from a nearby supernova at the time of formation. In this case, the Th would be formed in a constant ratio to stable r-process nuclides and then undergo free decay with a half-life of 13 Gyr through the age of the star; this leads to the greatest effect that can ever be expected ('pure decay' in Fig. 10.5), but it is clearly unrealistic, at least for the Solar System, since it implies that all the K-ratios should $= 1$.

To be (a bit) more realistic, we consider again two of the models of Section 10.3.3. The abundance in a stellar atmosphere is the initial abundance given by Eq. (10.12) with Δ replaced by the formation time t of the star (with age $T - t$), modified by a factor $e^{-\lambda_i(T-t)}$ due to subsequent free decay. Thus in the modified Fowler model we have from Eq. (10.18)

$$\text{for Th} \quad e^{\omega t} \frac{N_i(t, T)}{A p_i} = e^{-\lambda_i T} \left[\frac{S\Delta}{1 - S} + \frac{e^{\lambda_i t} - e^{\lambda_i \epsilon}}{\lambda_i} \right]; \tag{10.23}$$

$$\text{for Eu} \quad e^{\omega t} \frac{N_k(t, T)}{A p_k} = \frac{S\Delta}{1 - S} + t - \epsilon, \tag{10.24}$$

where $\Delta = T - 4.6 - \epsilon$ Gyr.

In the simple inflow model we have from Eq. (10.21)

$$\text{for Th} \quad \frac{e^{\omega t}}{(\omega t)^2} \frac{N_i(t, T)}{p_i} = \frac{e^{-\lambda_i(T-t)}}{(\lambda_i t)^2} \left[\lambda_i t - (1 - e^{-\lambda_i t}) \right]; \tag{10.25}$$

$$\text{for Eu} \quad \frac{e^{\omega t}}{(\omega t)^2} \frac{N_k(t)}{p_k} = \frac{1}{2}. \tag{10.26}$$

For the halo stars, we can take $S = t = 0$ and their age is just T.

The resulting dependences of [Th/Eu] on stellar age are shown in Fig. 10.5, together with a selection of observational data from del Peloso *et al.* for disk stars; Westin *et al.* (2000) for two of the r-process enriched ultra-metal-poor (UMP) halo stars; and Cowan *et al.* (2002) for a third one. The range among disk stars is little more than can be expected from uncertainties in the determination, while the UMP stars show more or less the expected deficiency. For BD $+17°\,3248$, Cowan *et al.* used theoretical production ratios for Th relative to Eu, Ir and Pt, based on certain nuclear models, to deduce a Galactic-model-independent age of 13.8 ± 4 Gyr, which happens to fit our two production-ratio-independent model curves 'simple inflow' and 'modFowler $T = 15$' quite nicely, but the error bars are large so that what we have is more a test of consistency than an independent chronometer.

10.3.6 Deconstruction of the r-process; critique of Eu/Th chronology. Enter U/Th

The use of Eu–Th chronology arguments requires the assumption of a universal r-process abundance distribution – an assumption that initially seemed to be supported by the pattern in the super r-process-rich UMP stars CS $22892-052$ (Sneden *et al.* 1996) and BD $+17°\,3248$, the latter having very heavy elements like platinum and gold measured with aid of HST (Cowan *et al.* 2002), but has been challenged by subsequent developments. For one thing, the congruence with solar r-process abundances applies above the second peak ($A > 130$ or $Z > 54$) and through the third, but not below the second one, since the lighter r-process elements $_{32}$Ge and $_{47}$Ag fall somewhat below their solar relative abundance. This supports the suggestion by Wasserburg and colleagues (e.g. Wasserburg & Qian 2000) that there are at least two distinct r-process sources, operating at different time intervals, so as to account for discrepancies between short-lived radioactivities, e.g. ^{129}I (needing a long time interval for free decay) and ^{182}Hf (needing a short one); see next section.

It seems, however, that even the heavy section of the r-process is not completely robust over the long range in A between Eu (152) and Th (232). A better (in principle) chronometer, if it can be found, is uranium, for which the production ratio to thorium can be estimated more precisely (cf. Table 10.2). One r-process-rich UMP star, CS $31082-001$, has indeed been found in which there is a measurable line of

uranium, as well as several of thorium, and the logarithmic ratio Th/U is estimated to be 0.94 ± 0.11, giving for an estimated production ratio of 2.0 ± 0.1[2] an age of 14 ± 2.4 Gyr (Hill *et al.* 2002). The same star delivers a bombshell, however, to the widely used Eu/Th ratio, since [Th/Eu] = 0.2, a positive number! The actinides are about twice as abundant relative to Eu etc. as they are in r-process material in the Solar System and other r-process-rich UMP stars; this, of course, facilitated the measurement of uranium.

10.4 Short-lived radioactivities

10.4.1 Introduction

As was mentioned in Chapter 3, a number of decay products of dead, short-lived radioactive nuclei are found in meteorites; some of these are listed in Table 10.1. These could come from a variety of sources including:

(i) Inheritance from the interstellar medium (where they have some steady-state abundance from continuing nucleosynthesis), possibly after some interval(s) of free decay.

(ii) 'Cosmic chemical memory' (Clayton 1982), whereby decay products from short-lived activities formed in dust grains ejected from supernovae or AGB stars and these grains were later incorporated without substantial change in the meteorites. This explanation is clearly preferred for ultra-short-lived activities, e.g. ^{22}Na(β^+, ν)^{22}Ne, with a 2.6 yr half-life, which leads to Ne-E, and for a number of other isotopic anomalies found among fine grains in the matrix of carbonaceous chondrites. On the other hand, it can hardly apply to ^{129}I, because the ^{129}Xe is found associated with ^{127}I (actually ^{128}Xe produced from ^{127}I by neutron activation) in a variety of meteoritic sites comprising a substantial bulk of material in objects that have been thermally processed. Thus ^{129}I must have been alive in the early Solar System and similar arguments (plus the fission tracks) apply to ^{244}Pu. ^{107}Pd must also have been alive because it is found in the metal phase of iron meteorites, and so probably also was ^{26}Al, because its daughter ^{26}Mg is correlated with aluminium in bulky and thermally processed material. Such heating episodes would have destroyed any correlation with aluminium unless the ^{26}Mg was actually in the form of ^{26}Al at the time. However, there is also decayed ^{26}Al (often with much larger ratios of ^{26}Al/^{27}Al than the standard 5×10^{-5}) in fine oxide, graphite and SiC grains of extra-solar origin.

(iii) A late-time contribution to the Solar System from a nearby supernova (Cameron 1993) or an AGB star or planetary nebula.

(iv) Production in the Solar System itself by solar-flare or cosmic-ray activity, e.g. ^{14}C.

---

[2] This production ratio, after Goriely and Arnould (2001), is somewhat larger than the figures in Table 10.2, which would have led to a somewhat shorter age.

10.4.2 Short-lived activities and Galactic chemical evolution

For a sufficiently short-lived activity ($\lambda\Delta \gg 1$), Eqs. (10.15) and (10.22) both lead to

$$K_{ij} = \lambda_j/\lambda_i, \tag{10.27}$$

representing a steady state in the ISM where the decay is fast enough to balance creation and dominate other processes. Following Reeves (1991), we may define a related parameter

$$A_{ij} \equiv K_{ij}\,\lambda_i/\lambda_j = 1 \text{ in a steady state.} \tag{10.28}$$

For the abundance in the ISM of a stable or very long-lived element at the time of Solar-System formation, we can take

$$\lambda_k = 1/\Delta \tag{10.29}$$

in the Simple model, or

$$\lambda_k = 2/\Delta \tag{10.30}$$

in the simple inflow model. The A-parameters or equivalent data have been estimated for various short-lived activities by Reeves (1991) and by Wasserburg, Busso and Gallino (1996), whose results are shown graphically in Fig. 10.6, using ^{232}Th as a standard of comparison for r-process products and neighbouring stable nuclei for the others, and taking $1/\lambda_k = 10\,\text{Gyr}$ in each case.
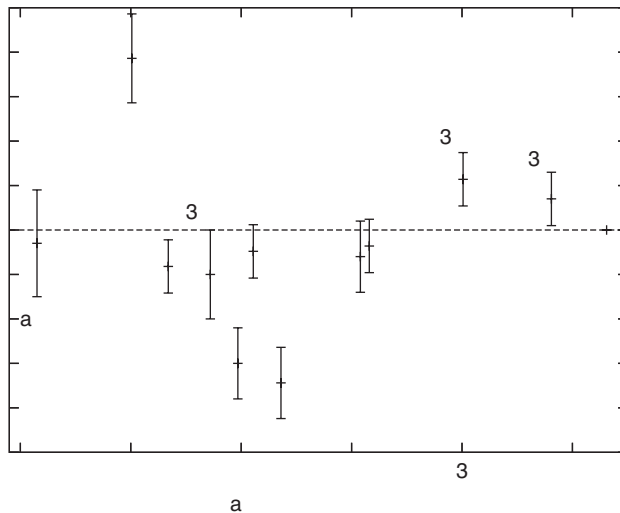
Fig. 10.6. Log–log plot of A_{ij} against mean life (Gyr). Data from Table 10.2 and Wasserburg, Busso and Gallino (1996), with estimated error bars.

For lifetimes exceeding 100 Myr, which may represent the mixing time for homogenization of the ISM (see Section 8.6.3), the abundances are much as expected for the steady state, but at shorter lifetimes there are deficits in ^{129}I and ^{107}Pd which were once attributed to an interval of free decay of order 10^8 yr between the end of nucleosynthesis affecting the Solar System and the solidification of rocky bodies (see Fig. 10.2). That view is no longer tenable in the light of the abundances of ^{182}Hf, ^{53}Mn and ^{60}Fe, which impose an upper limit of 10^7 yr on any such interval, or even less if ^{41}Ca is taken at face value, and not supposed to result from energetic particle bombardment in the early Solar System.

Since ^{129}I and ^{182}Hf both come from the r-process, it follows that the r-process cannot be unique. The hypothesis of Wasserburg and colleagues is that there are two kinds of r-process sources: supernova actinide producers (SNACs) which generate the heavy r-process nuclei with $A > 130$ in a quasi-continuous manner, i.e. at intervals below about 10^7 yr, and a more sporadic source with intervals typically about 10 times longer, to account for the lighter ones, giving scope for free decay.

The situation for ^{26}Al is different again, since the Solar-System abundance ratio ^{26}Al/^{27}Al $\simeq 5\times10^{-5}$ is actually higher than that inferred for the interstellar medium from γ-ray observations, so that in this case a late addition to the Solar System is indicated. Wasserburg *et al.* (1994, 1995) suggested that H-burning and s-process products from a nearby AGB star, contributing about 3×10^{-4} of the mass of the solar nebula, could account for the presence of ^{26}Al and possibly ^{41}Ca, ^{60}Fe and ^{53}Mn as well. The latter three have abundances compatible with equilibrium in the ISM without free decay. However, since the lifetimes of these species are much shorter than the typical Galactic mixing time, the 'ISM' in this context has to be close to the nucleosynthetic sources, e.g. in a stellar association, so that late injection and inheritance from the interstellar medium amount to more or less the same thing. A completely different hypothesis, which may be preferable, is that some or all of these species were created in situ, along with the pure spallation products ^{10}Be and ^{36}Cl, from irradiation of the proto-CAIs by solar cosmic rays resulting from impulsive flares on the primitive Sun (Gounelle *et al.* 2006).

Notes to Chapter 10

The theory of nucleo-cosmochronology (and developments up to that time) are described by Schramm (1974), and more recent developments by Cowan, Thielemann and Truran (1991ab).

D. D. Clayton, in W. D. Arnett and J. W. Truran (eds.), *Nucleosynthesis: Challenges and New Developments*, University of Chicago Press 1985, p. 65, gives a description and simple algorithms for GCE and nucleo-cosmochronological calculations on the basis of his standard inflow models. Our simple inflow model shares some

of the characteristics of Clayton's standard model with $k = 1$. See also Clayton (1985b).

Interpretations of Butcher's Th–Nd chronology have been discussed by Clayton (1988), Mathews and Schramm (1988) and Malaney and Fowler (1989b); these are outdated by the more recent use of Th/Eu ratios, and the treatment in this chapter is based on papers by Pagel (1989b, 1993, 2001).

For more detailed discussions of isotopic anomalies and short-lived radioactivities in the Solar System, see

G. J. Wasserburg and D. A. Papanastassiou, in C. A. Barnes, D. D. Clayton and D. N. Schramm (eds.), *Essays in Nuclear Astrophysics*, Cambridge University Press 1982, p. 77;

D. D. Clayton, *Quart. J. R. Astr. Soc.*, **23**, 174, 1982;

G. J. Wasserburg, *Earth Plan. Sci. Lett.*, **86**, 129, 1987;

F. A. Podosek and T. D. Swindle, in J. F. Kerridge and M. S. Matthews (eds.), *Meteorites and the Early Solar System*, University of Arizona Press, Tucson, 1988, p. 1093;

A. G. W. Cameron, in E. H. Levy, E. H. Lunine and M. Matthews (eds.), *Protostars and Planets III*, University of Arizona Press, Tucson, 1993, p. 47;

E. Anders and E. Zinner, *Meteoritics*, **28**, 490, 1993;

U. Ott, *Nature*, **364**, 25, 1993;

J. N. Goswami, K. K. Marhas and S. Sahijpal, *Ap. J.*, **549**, 1151, 2001; and

G. J. Wasserburg, M. Busso, R. Gallino and K. M. Nollett, *Nucl. Phys.*, **A777**, 5, 2006.

Problems

1. Supposing that Fig. 3.32 were to be interpreted as an isochrone (which it is not, in fact), what age would be deduced?

2. Show that, from the decay of ^{235}U and ^{238}U, one can derive a lead–lead isochrone given by

$$\frac{^{207}\text{Pb}(t)}{^{204}\text{Pb}} = \text{const.} + k \frac{e^{\lambda_{235}t} - 1}{e^{\lambda_{238}t} - 1} \frac{^{206}\text{Pb}(t)}{^{204}\text{Pb}}, \qquad (10.31)$$

where k is the present-day abundance ratio ^{235}U/^{238}U $= 0.0073$. (^{204}Pb has no radioactive progenitors.) Compare the slope of this isochrone with that of the Rb–Sr isochrone in Fig. 10.1.

3. Re-writing Eq. (10.6) in the form (neglecting N_{i0})

$$N_i(t) = e^{-\lambda_i(t - \langle \tau \rangle) - \nu(t)} \, p_i \int \alpha \psi e^{\nu} e^{\lambda_i(t' - \langle \tau \rangle)} dt' \qquad (10.32)$$

and expanding $e^{\lambda_i(t'-\langle\tau\rangle)}$ in the integral as a power series, verify that

$$N_i(t) = e^{-\lambda_i(t-\langle\tau\rangle)-\nu(t)} \, p_i \int \alpha\psi e^{\nu} \left[1 + \frac{1}{2}\lambda^2\langle(t-\langle\tau\rangle)^2\rangle + \cdots \right] dt', \quad (10.33)$$

where $\langle\tau\rangle$ is the mean time of formation of elements up to time t.

Hence show that, for sufficiently small λ's, independently of any model,

$$K_{ij}(t) = e^{-(\lambda_i-\lambda_j)(t-\langle\tau\rangle)}. \quad (10.34)$$

Apply this result to Solar-System ^{232}Th and ^{238}U to find the corresponding value of $\Delta - \langle\tau\rangle$ and make a rough estimate of the error. What does that make the age of the Galaxy, (a) if $\alpha\psi e^{\nu} = $ const.; (b) if all nucleosynthesis had taken place in a single event at the beginning?

4. If K_{ik} is the K-ratio for a radioactive element i relative to a stable element k, and $\lambda_i \Delta \gg 1$, show that, in Fowler's model,

$$K_{ik} = \frac{(1-S)}{\lambda_i \Delta} \quad (10.35)$$

whereas in the simple inflow model

$$K_{ik} = \frac{2}{\lambda_i \Delta} \quad (10.36)$$

(ignoring any period of free decay before incorporation into meteorites).

11

Chemical evolution in other sorts of galaxies

As we are used to call the appearance of the heavens, where it is surrounded with a bright zone, the Milky Way, it may not be amiss to point out some other very remarkable Nebulae which cannot well be less, but are probably much larger than our own system; and, being also extended, the inhabitants of the planets that attend the stars which compose them must likewise perceive the same phenomena. For which reason they may also be called milky-ways by way of distinction.

William Herschel, 'On the Construction of the Heavens',
Phil. Trans., LXXV (1785), 213.[1]

11.1 Dwarf galaxies

11.1.1 Introduction

Nearby dwarf galaxies are classified in four main types: (i) dwarf irregular (dIrr) galaxies are the most common type by number, and are usually unstructured gas-rich systems with varying levels of star formation occurring in a haphazard manner across the galaxy. (ii) Blue compact dwarf (BCD) or H II galaxies are gas-rich systems dominated by very active star formation and resembling giant H II regions found in large galaxies. They appear to be forming stars at a rate which they can only maintain for a short period. (iii) Dwarf spheroidal (dSph) galaxies usually have no gas in their centre down to very low limits. Their stellar distribution is similar to that of globular clusters, although less centrally concentrated, but a detailed study of their HR diagrams often reveals that several distinct bursts of star formation have occurred in the past. (iv) Dwarf elliptical (dE) galaxies look similar to ordinary elliptical galaxies and are generally more massive than dwarf spheroidals, but again sequences of bursts of star formation, some of them quite recent, are

---

[1] Reproduced in Hoskin (1963).

needed to explain the characteristics of their stellar populations. Abundances in these various classes of galaxies may provide clues as to whether there is any evolutionary relationship between them.

11.1.2 *Applications of the Simple model with extensions*

The Simple model achieves a modest degree of success in accounting for abundances measured in dwarf galaxies, particularly the gas-rich dwarf irregulars and BCDs where several element abundances are measured from observations of H II regions and vary little across the parent galaxy. The relation with gas fraction (Fig. 8.12) is somewhat problematic and controversial, but as far as it goes it suggests a rather low effective yield of about $0.25 \, Z_\odot$ (compared to about $0.7 \, Z_\odot$ for the solar neighbourhood). This could arise from a bottom-heavy IMF (Peimbert & Serrano 1982; Peimbert, Colin & Sarmiento 1994) or from galactic winds, which are discussed in Section 11.3.3 below. The wind models lead to certain scaling laws relating metallicity to galaxy mass or luminosity. Such scaling laws can also be derived on the assumption that the star formation bursts are driven by mergers in which the gas fraction successively decreases, followed eventually by expulsion of the remaining gas in a (homogeneous) terminal wind or by ram pressure in an intra-cluster medium (Tinsley & Larson 1979; Faber & Lin 1983). A tight relation between metallicity (as estimated from colours or line features, particularly Mg_2) and escape velocity or velocity dispersion (probably closely related) has been found in elliptical galaxies by Vigroux, Chièze and Lazareff (1981), Franx and Illingworth (1990) and Bender (1992); see Fig. 11.11. Removal of gas by one of the above processes could perhaps lead to the conversion of a gas-rich dwarf galaxy into a dwarf elliptical with roughly similar metallicity, in accordance with Fig. 11.1. However, there is an offset between stellar abundances in the two classes of galaxies which argues against such a straightforward evolutionary scheme, except in the case of a small class of dSph/dIrr transition galaxies (Fig. 11.2). Metal-enhanced winds involve much smaller overall mass loss rates (relative to star formation rates) than do homogeneous winds, and consequently are less likely to have dynamical effects on galaxy evolution, although the chemical effects could be quite similar in many respects.

Another effect that can be significant in dwarf galaxies is that of star formation bursts. In the instantaneous recycling approximation, changes in element-to-element ratios are attributed to primary/secondary effects. When this approximation is relaxed there can be significant consequences, either due to overall galactic timescales relative to production timescales for, say, nitrogen (Edmunds & Pagel 1978), or due to effects of star formation bursts localized in time and space. This
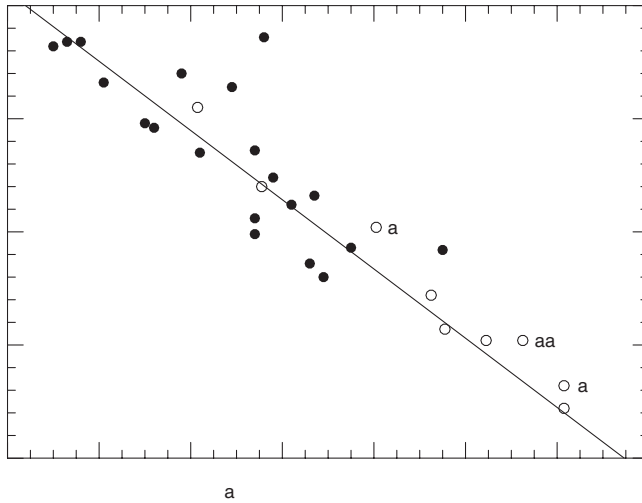
Fig. 11.1. Abundance against absolute magnitude for irregular, dwarf elliptical and dwarf spheroidal galaxies, after Skillman, Kennicutt and Hodge (1989). The vertical scale shows logarithmic oxygen abundances measured in H II regions of irregular galaxies (filled circles), while open circles show ⟨[Fe/H]⟩ + 8.9 for dwarf ellipticals and dwarf spheroidals using [Fe/H] deduced from colours of stars on the giant branch in the HR diagram. The dwarf ellipticals and spheroidals should probably have been plotted up to 0.4 dex higher to convert their mean [Fe/H] into their maximum [Fe/H] so as to be comparable to the young populations represented by H II regions (Richer & McCall 1995); the resulting offset can be attributed to fading after star formation ceased. Courtesy Evan Skillman.

would apply especially in dwarf galaxies that may have experienced only a few such bursts over a Hubble time and may have lost gas in wind-ejection episodes accompanying the bursts (Matteucci & Tosi 1985; Pantelaki & Clayton 1987; Gilmore & Wyse 1991).

11.1.3 The Magellanic Clouds and dwarf spheroidals

Because the Magellanic Clouds are relatively close, a great deal of detailed information is available from observations of luminous stars, H II regions, planetary nebulae and supernova remnants, and there have been several attempts at modelling their chemical evolution. Pagel and Tautvaišienė (1998) modelled α-element, iron and heavy-metal evolution in the Clouds assuming identical IMFs and yields to those in the solar neighbourhood (see Table 8.1) combined with inflow according to Clayton's formalism and homogeneous outflow, using the instantaneous recycling and delayed-production approximations with parameters listed in Table 11.1. Both continuous star formation and bursting models were considered, as illustrated in

Table 11.1. *Model parameters for the Magellanic Clouds*

	LMC	SMC	Local Gal.
$\langle\omega\rangle$ (Gyr^{-1})	0.18	0.12	0.3
Outflow parameter η	1.0	2.0	0
Final gas fraction	0.15	0.29	0.14
Final abundance in units of yield	0.78	0.43	1.4
Burst models $\quad\omega$ (0 to 2 Gyr)	0.15		
ω (2 to 11 Gyr)	0.08		
ω (11 to 14 Gyr)	0.5		
ω (0 to 1.33 Gyr)		0.1	
ω (1.33 to 10 Gyr)		0.01	
ω (10 to 14 Gyr)		0.35	

After Pagel and Tautvaišienė (1998).
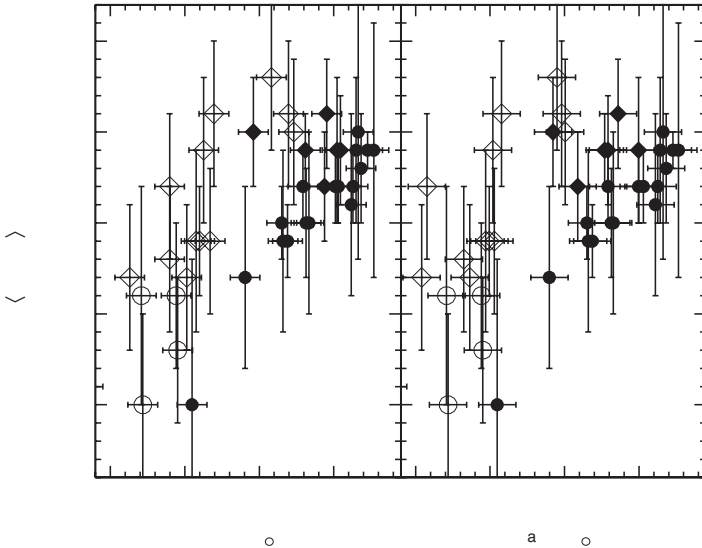
Fig. 11.2. Mean stellar iron abundances as a function of luminosity in dwarf spheroidals (filled circles), dwarf ellipticals (open circles), dSph/dIrr transition galaxies (filled diamonds) and dwarf irregulars (open diamonds). 'Baryonic luminosity' in the right panel includes the additional luminosity that irregulars would have if their gas were converted into stars. After Grebel, Gallagher and Harbeck (2003).

Fig. 11.3 for the LMC. Figure 11.4 shows the resulting age–metallicity relations; unlike the solar neighbourhood, there seems to be a reasonably well-defined relationship, despite the lack of clusters (from which ages were mainly determined at the time) at intermediate ages. The SMC, which does not suffer such a gap, shows
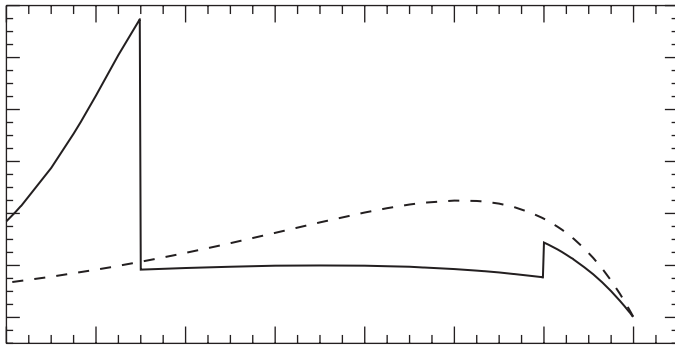
a

Fig. 11.3. SFR history of the LMC assumed in our models. The full curve shows the bursting model, while the broken curve shows a smooth model with $\omega = 0.18$, compared to $\omega \simeq 0.3$ for the solar neighbourhood. After Pagel and Tautvaišieṅe (1998).
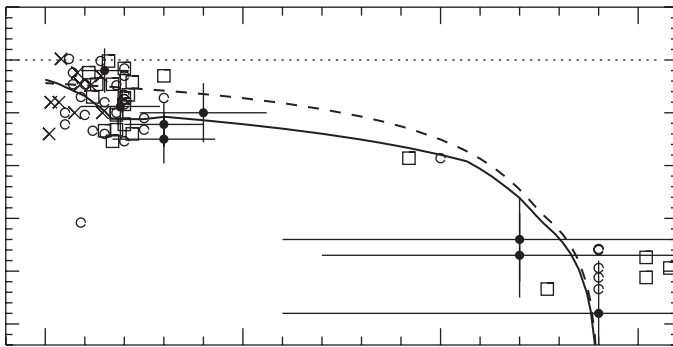
a

Fig. 11.4. Age–metallicity relation for the LMC, according to the SFR models shown in Fig. 11.3. After Pagel and Tautvaišieṅe (1998).

a quite similar pattern. These conclusions have been extended by observational determinations of star formation and metallicity histories based on comparison of synthetic HR diagrams with deep HST observations by Holtzman *et al.* (1999) in the LMC and by Harris and Zaritsky (2004) in the SMC.

Figure 11.5 shows the α-element to iron ratios in the LMC and in the anomalous halo stars of Nissen and Schuster (1997). The trend with metallicity is much reduced compared to the disk and the majority of halo stars in the Galaxy, which is attributed to the longer timescale for star formation in the Clouds; see Fig. 8.7. However, below [Fe/H] = −1.3, there are similar plateaux to those in the Milky Way,
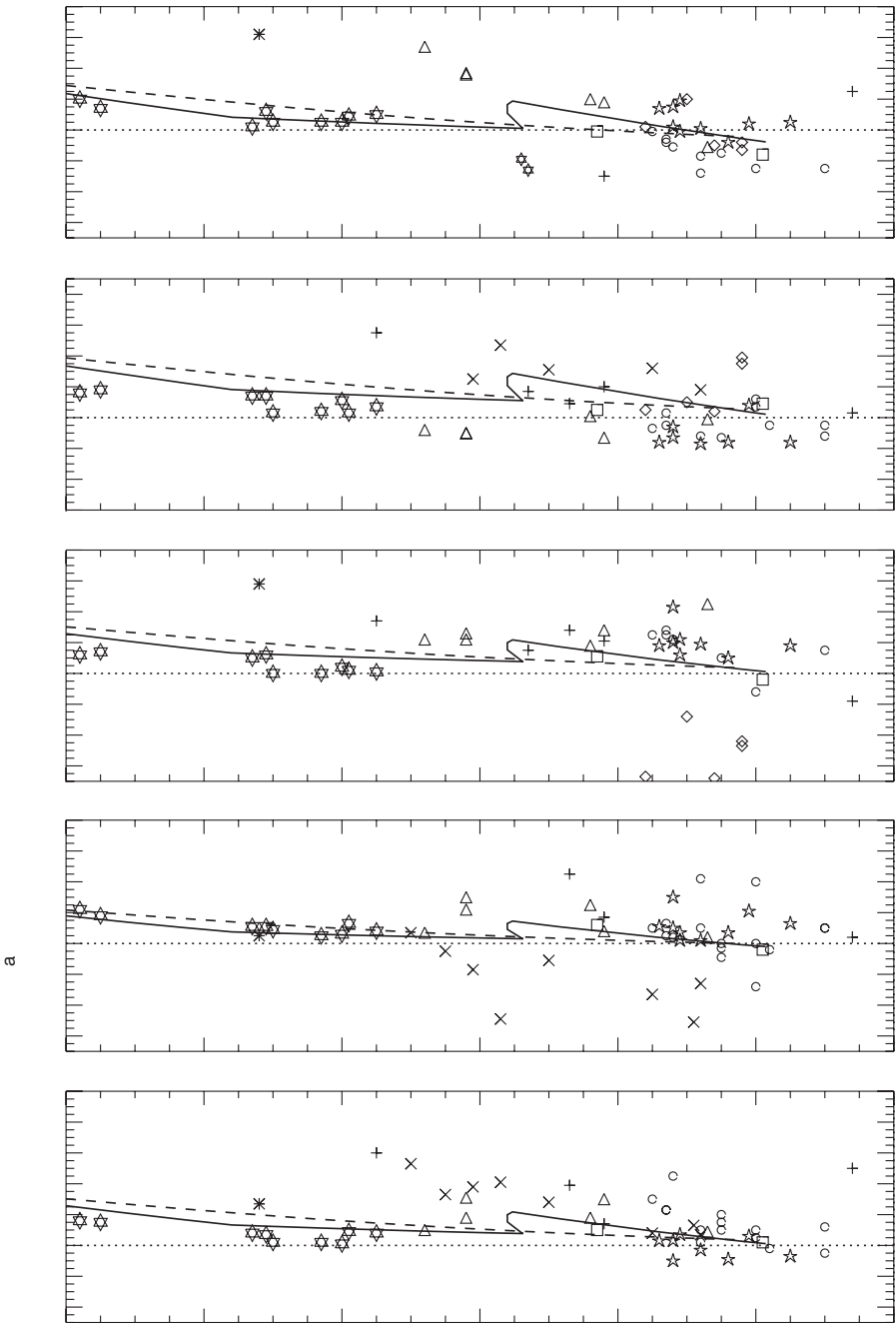
Fig. 11.5. Element-to-iron ratios for oxygen, α-particle elements and Ti in the LMC and in the anomalous Galactic halo stars of Nissen and Schuster (1997) shown by large six-pointed stars. The data points for oxygen in the LMC, based on observations of supergiants, were adjusted to be relative to Galactic supergiants rather than the Sun, but subsequent revisions in the solar oxygen abundance (Allende-Prieto, Lambert & Asplund 2001) have brought the two scales into agreement. After Pagel and Tautvaišiene (1998).

representing pure SN II products (Hill 2004). Similar patterns are found in dwarf spheroidal galaxies, e.g. Sculptor, where [O/Fe] and [Mg/Fe] $\simeq$ 0.4 for [Fe/H] ≤ -1.5, then going down to 0 (or below) at the maximum [Fe/H] of -1.0 (Shetrone 2004).

11.2 Helium, carbon and nitrogen

With contributions potentially from the full range of progenitor star masses above $1 \, M_\odot$ or so, the evolution of He, C and N involves more variables than those of iron and α-elements. The abundance of helium as a function of metallicity is quite smooth (see Fig. 4.11), in contrast to earlier suggestions that there might be local excesses due to winds from Wolf–Rayet stars (Pagel, Terlevich & Melnick 1986; Pagel *et al*. 1992), and the resulting value of $\Delta Y / \Delta Z \simeq 2$ or 3 is entirely consistent with the usually assumed stellar yields and IMFs.

Element-to-element ratios depend on the time and metallicity dependences of stellar yields as well as on details of galactic evolution. The C,O relation (Figs. 8.3, 8.4) is quite well explained by the metallicity-dependent yields of Maeder (1992) and Portinari *et al*. (1998) provided that effectively the full range of stellar masses above $10 \, M_\odot$ or so is assumed to undergo supernova explosions (Prantzos, Vangioni-Flam & Chauveau 1994; Gustafsson *et al*. 1999) and that carbon comes predominantly from massive stars, so that at low metallicities where stellar winds are weak the C/O ratio is relatively insensitive to any metal-enhanced wind. (This will also be the case for Fe/O when Fe comes predominantly from SN II.) Henry, Edmunds and Köppen (2000) have given analytical and numerical treatments for C, N and O. The situation for carbon is shown in Fig. 11.6, where the data have been fitted with numerical models that can be quite well approximated with a combination of primary and quasi-secondary yields for carbon. Thus, from Eq. (7.35), using the Simple model,

$$\frac{C}{O} = \frac{16}{12} \frac{Z_C}{Z_O} = 1.33 \left(p_{Cp} + \frac{1}{2} p_{Cs} Z \right) \bigg/ p_O, \qquad (11.1)$$

where $p_{Cp} \simeq 0.0007$, $p_{Cs} Z \simeq 0.9 \, Z_O$ and $p_O \simeq 0.005$ are respectively the primary carbon yield, the quasi-secondary carbon yield and the oxygen yield. These numbers agree quite well with the yields by Maeder (1992), integrated over a Salpeter(0.1) IMF, and because of the assumed predominance of high-mass stars as carbon producers, variations in the timescale of star formation have little effect on the C,O relation.

The case of nitrogen is somewhat similar, but there is a tendency to curve up above the purely secondary trend with oxygen (Figs. 8.11, 11.7), which, as argued by Henry, Edmunds & Köppen, can be explained on the basis that the nitrogen
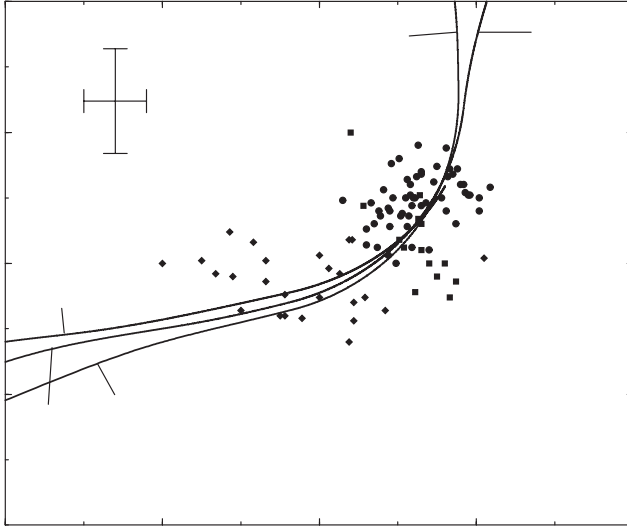
Fig. 11.6. C/O vs. O/H in stars and H II regions, from various sources. Curves A, B and C correspond to increasing star-formation efficiencies ($\nu_0 = 0.006$, 0.03 and 0.15 in the assumed SFR $\psi = \nu_0(1 + Z/0.001)M(g/M)^2 \, M_\odot \, \mathrm{Gyr}^{-1} \, \mathrm{pc}^{-2}$). After Henry, Edmunds and Köppen (2000).
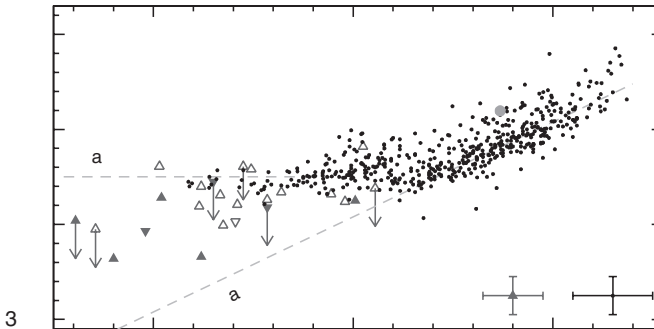
Fig. 11.7. N/O vs. O/H in extragalactic H II regions and damped Lyman-α absorption line systems shown by triangles, with schematic 'primary' and 'secondary' tracks. Open triangles show objects where sulphur was used as a proxy for oxygen. The Sun is shown by the large filled circle. After Pettini *et al*. (2002a), updated to Dec 2003. Courtesy Max Pettini.

yield tracks the abundance of carbon rather than oxygen. Then, by analogy with Eq. (11.1), we have

$$\frac{7}{8}\frac{N}{O} = \frac{Z_N}{Z_O} = \frac{p_{Np}}{p_O} + \frac{1}{2}\frac{p_{Ns}}{p_O}\frac{p_{Cp}}{p_O}Z_O + \frac{1}{6}\frac{p_{Ns}}{p_O}\frac{p_{Cs}}{p_O}\frac{p}{p_O}Z_O^2, \qquad (11.2)$$

where $p_{Np} \simeq 0.000\,15$ is the primary nitrogen yield, $p_{Ns}Z_C \simeq 0.285\,Z_C$ is the secondary nitrogen yield and $p \simeq 0.01$ is the total yield (see Fig. 11.8). These numbers are broadly consistent with the yields predicted by van den Hoek and Groenvegen (1997) and Marigo, Bressan and Chiosi (1996, 1998).

However, nitrogen production from low- and intermediate-mass stars involves a time delay, which may be relevant to the very considerable scatter in the data. Figure 11.9 shows numerical models by Henry, Edmunds and Köppen which give evolutionary tracks for different assumed star formation efficiencies and fixed time points. In the early stages, with primary nitrogen dominating, N/O acts like a clock (isochrones are nearly horizontal), while increasing the star formation efficiency mainly leads to more rapid enrichment in both elements. At later stages, nitrogen benefits from increasing yields and oxygen suffers decreasing ones because of mass loss (Maeder 1992), leading to the strong upswing of model C, while models A and B are quite well approximated by the analytical model in Fig. 11.8.
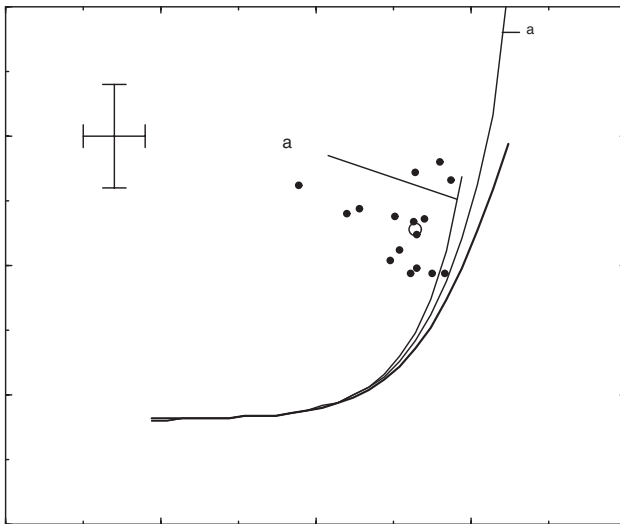
Fig. 11.8. N/O vs. O/H in stars and H II regions, from various sources, fitted with an analytical model. *a* is the coefficient in a Twarog-type inflow model with inflow rate $= a\alpha\psi$. After Henry, Edmunds and Köppen (2000).
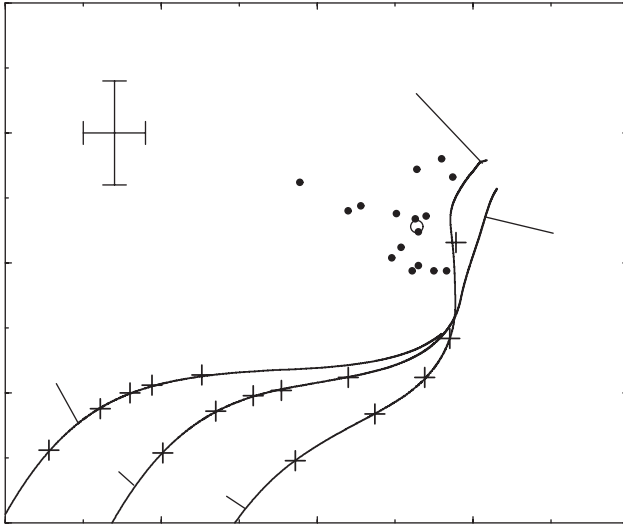
Fig. 11.9. N/O vs. O/H in stars and H II regions, from various sources. Curves A, B and C correspond to increasing star formation efficiencies ($\nu_0 = 0.006, 0.03$ and 0.15 in the assumed SFR $\psi = \nu_0(1 + Z/0.001)M(g/M)^2 M_\odot \, \mathrm{Gyr}^{-1} \, \mathrm{pc}^{-2}$). Plus signs denote ages of 0.25, 0.5, 0.75, 1.0 and 2.0 Gyr, going from bottom to top. After Henry, Edmunds and Köppen (2000).

These models do not account for the large scatter observed in Figs. 8.11, 11.8, 11.9. One candidate could be star formation in bursts separated by intervals of 0.5 Gyr or more (Garnett 1990; Larsen, Sommer-Larsen & Pagel 2001). The idea is that, immediately after a burst, oxygen is enhanced, while the nitrogen only comes out later, leading to a temporary downturn in N/O. The problem with this type of explanation is that it predicts scatter turning down from an upper envelope, whereas the observations rather suggest the reverse. Another possibility is self-enrichment of H II regions: the uniformity of composition over the Magellanic Clouds (Pagel *et al.* 1978) suggests that this is not very common, but there is some tentative evidence in its favour from studies of I Zw 18. Here the H I gas was found by Kunth *et al.* (1994) to have still lower oxygen abundance than the two major H II regions, but doubt was cast on this result on grounds of saturation of the O I line (Pettini & Lipman 1995) and subsequent data have not completely resolved the issue (Aloisi *et al.* 2003; Lecavelier des Etangs *et al.* 2004). A natural expectation would be that supernova ejecta would appear somewhat after the major ionization phase and rapidly escape from the H II region, whereas the slower ejecta in the form of stellar winds would appear sooner and hang around for a while. Pagel *et al.* (1992) attributed all the scatter in the (He,O) diagram (which for most

objects is only barely significant in relation to errors) to self-enrichment in He and N by winds from embedded massive stars that show their presence in the form of broad Wolf–Rayet features in the underlying stellar spectra. This is supported by the existence of inhomogeneous N and He abundances in the single giant H II region of NGC 5253 (see Walsh & Roy 1989), although there is no evidence for any such effect in other 'WR' galaxies. Thus, apart from NGC 5253, there is no evidence for any real scatter in the He,O relation, but the scatter in N/O remains and is in part due to temporary self-enrichment; galaxy-wide differences, such as are observed between e.g. the Magellanic Clouds and NGC 6822, are more likely due to galaxy-wide processes associated with time delays, as discussed by Edmunds and Pagel (1978) and Garnett (1990). Other possibilities are episodes of massive inflow of unprocessed gas (Köppen & Hensler 2005) and variable differential mass loss through galactic winds (e.g. Recchi *et al.* 2004), but there is no real evidence from abundance arguments that would enable us to choose between homogeneous and selective galactic winds.

Regardless of the details concerning self-enrichment and winds, the existence of isolated star formation bursts will also affect the iron–oxygen and iron–α relations, introducing scatter in Fe/O and possibly gaps in the iron abundance distribution function. When the interval between successive bursts exceeds the evolution time for SN Ia (maybe about 1 Gyr), iron will build up in the ISM resulting in an enhanced Fe/O ratio in the second burst so that one can end up with [Fe/O] > 0 (Gilmore & Wyse 1991); see Fig. 8.7.

The evolution of dwarf galaxies is discussed further in Section 11.3.3.

11.3 Chemical evolution of elliptical galaxies

11.3.1 Data sources

With the exception of nearby dwarf ellipticals and dwarf spheroidals for which some information can be obtained from magnitudes, colours and spectra of individual stars, all the information we have about abundances in E-galaxies comes from integrated colours and spectra of an entire stellar population which can be composite in both age and metallicity, while at the same time the number of independent parameters provided by observation is quite small (Faber 1973). Consequently, the interpretation of the data is not straightforward and some sort of modelling is needed. One technique is stellar population synthesis from a standard library of individual stellar types (e.g. Pickles 1985; Rose 1985) and another is evolutionary population synthesis on the basis of theoretical models of star formation and evolution. Such models in some cases assume a fixed metallicity (e.g. Guiderdoni & Rocca-Volmerange 1987; Bruzual & Charlot 1993) while in others they are

computed for a grid of metallicities (Buzzoni 1989) or for a self-consistent model including chemical evolution (e.g. Yoshii & Arimoto 1987). These models also need a standard stellar library in order to tie in with observable quantities.

A vital role in the interpretation of integrated stellar properties is played by globular clusters, in which both integrated and individual stellar features can be measured and related to the (usually unique) age and metallicity deduced from the latter. One feature that seems to be particularly useful in this regard is the Mg_2 index in the Lick system (see Section 3.2.4). A combination of single-burst evolutionary synthesis models and empirical data from globular clusters gives the approximate calibration (in magnitude units)

$$Mg_2 \simeq 0.1 \left[\frac{Z}{Z_\odot} t(Gyr) \right]^{0.41} \qquad (11.3)$$

(Bender, Burstein & Faber 1993), where $\log Z/Z_\odot$ is more or less equivalent to [Mg/H] (cf. Edmunds 1992).

A single feature like Mg_2 can only provide one parameter, e.g. some abundance equivalent if the entire stellar population is old. Other features such as hydrogen lines can be used to test whether this is so and whether different metals vary in constant ratios to one another or at least in some systematic mutual relation (see Fig. 3.19). Bica and Alloin (1986, 1987) developed a very interesting system for building up composite galaxy spectra from a cluster base containing integrated spectra of both Galactic globular clusters (old, with differing metallicities) and Magellanic Cloud clusters (having various ages). In this way, a whole model of chemical evolution can in principle be built up by fitting a small number of cluster spectra and imposing a few theoretical constraints, such as that metallicity should not decrease with time (Bica 1988). A great advantage of this method is that the IMF and stellar evolution details are already built in to the clusters themselves. However, the number of really independent parameters that can be deduced with the currently available spectral range is still only 2 or 3 (Schmidt *et al.* 1991) and all globular cluster applications suffer from a lack of known clusters having an accurately determined metallicity $\geq$ solar; at these compositions (relevant to the nuclei of giant galaxies) risky extrapolations have to be used.

11.3.2 *Systematics of elliptical galaxies and bulges*

Parameters of 'dynamically hot galaxies', i.e. various classes of ellipticals and the bulges of spirals, generally lie close to a 'Fundamental Plane' in the 3-dimensional space of central velocity dispersion, effective surface brightness and effective radius or equivalent parameter combinations (Fig. 11.10). This is explained by a combination of three factors: the Virial Theorem, some approximation to
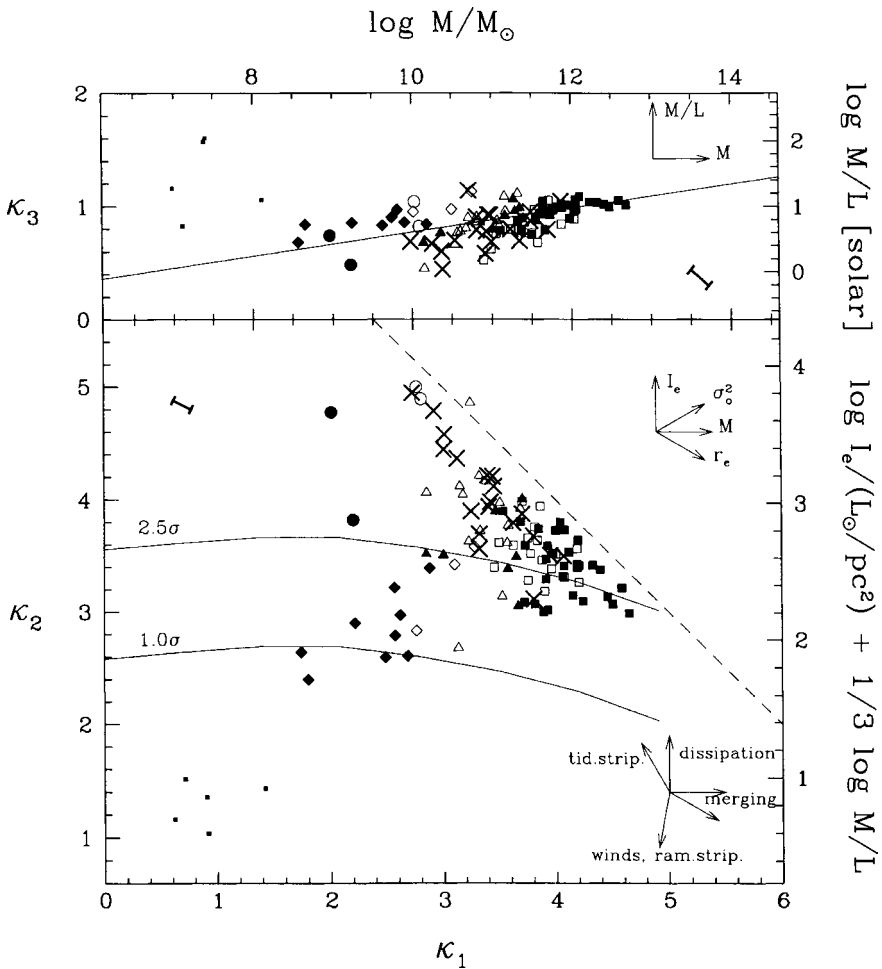
Fig. 11.10. Edge-on (above) and face-on (below) views of the Fundamental Plane in κ-space. κ_1 is essentially the total mass within the optical radius, κ_2 the effective surface brightness and κ_3 the mass:luminosity ratio, all in logarithmic units. Squares represent giant ellipticals, crosses spiral bulges, circles compact ellipticals, triangles intermediate-luminosity ellipticals, diamonds dwarf ellipticals and small dots dwarf spheroidals. Filled symbols represent galaxies with anisotropic velocity dispersion, open symbols nearly isotropic velocity systems supported by rotation. Arrows in the upper right-hand corners indicate the direction of variation of related parameters and those in the lower right corner indicate possible physical effects that could move galaxies around within the plane. The curves marked 2.5σ and 1.0σ represent hypothetical merger tracks from primordial density fluctuations with the corresponding amplitudes. Tick marks represent errors due to uncertainties in distance. After Bender, Burstein and Faber (1993). Courtesy Ralf Bender.

homologous structure (e.g. de Vaucouleurs' surface brightness law) and a fixed mass:luminosity ratio at a given mass. Within this plane, however, there are distinct locations and sequences that are presumably related to various effects in galaxy formation and evolution (Bender, Burstein & Faber 1992).

Most points in Fig. 11.10 lie near one or other of two distinct sequences in the Fundamental Plane. One of these is a dwarf sequence in which surface brightness increases with luminosity (perhaps because of loss of gas from shallow potential wells and consequent dynamical adjustment) and there is also a nearly perpendicular 'gas–star' sequence where the opposite occurs, perhaps because of differing degrees of dissipation (depending on the gas fraction) in mergers of different sizes. Given this complexity, it is hardly surprising that there should be a large scatter around the statistical relation between the metallicities and luminosities as expressed, e.g., by the colour–magnitude relation or the Mg_2–magnitude relation (Terlevich *et al.* 1981; see also Fig. 3.44). Despite this, however, galaxies from all parts of the Fundamental Plane lie on a remarkably tight relation between Mg_2 and central velocity dispersion (Fig. 11.11).

Colour and line-strength gradients are also observed across elliptical galaxies, as is to be expected from dissipative effects (see Appendix 5). However, the detailed
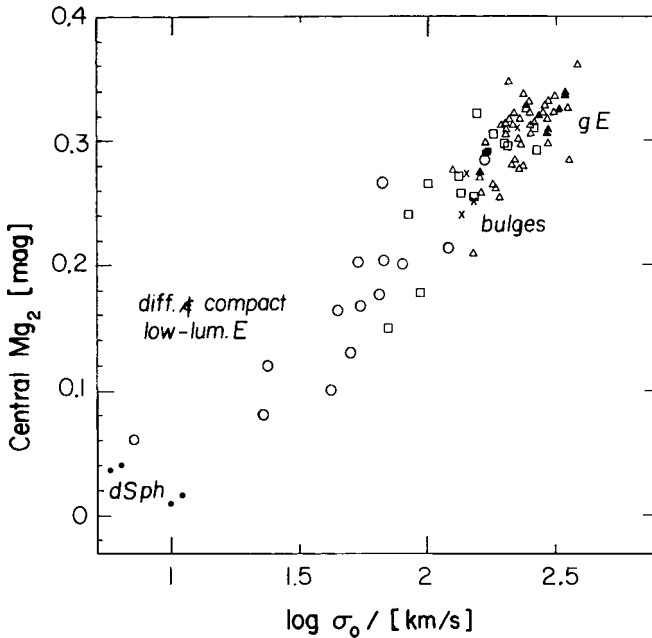
Fig. 11.11. Relation between central Mg_2 index and central velocity dispersion for dynamically hot galaxies. Coding as in Fig. 11.10. Adapted from Bender (1992).

character varies widely from one galaxy to another and these differences presumably give clues to differing evolutionary histories, e.g. from mergers at differing stages of star formation (Gorgas, Efstathiou & Aragón-Salamanca 1990). Franx and Illingworth (1990) found a universal relation between colour and local escape velocity in extra-nuclear as well as nuclear regions, but the interpretation of colours without line strength data is not too clear. A significant complication arises from the fact that not only metallic line strengths but also their ratios vary between elliptical galaxies, in the sense that the ratio $Mg_2/Fe \lambda 5270$ increases with central velocity dispersion (Gorgas *et al.* 1990; Worthey, Faber & Gonzales 1992), i.e. the outer parts of giant ellipticals have a larger Mg/Fe ratio than the central parts of smaller ellipticals with the same Fe line strength (Fig. 11.12). This differential α-rich effect
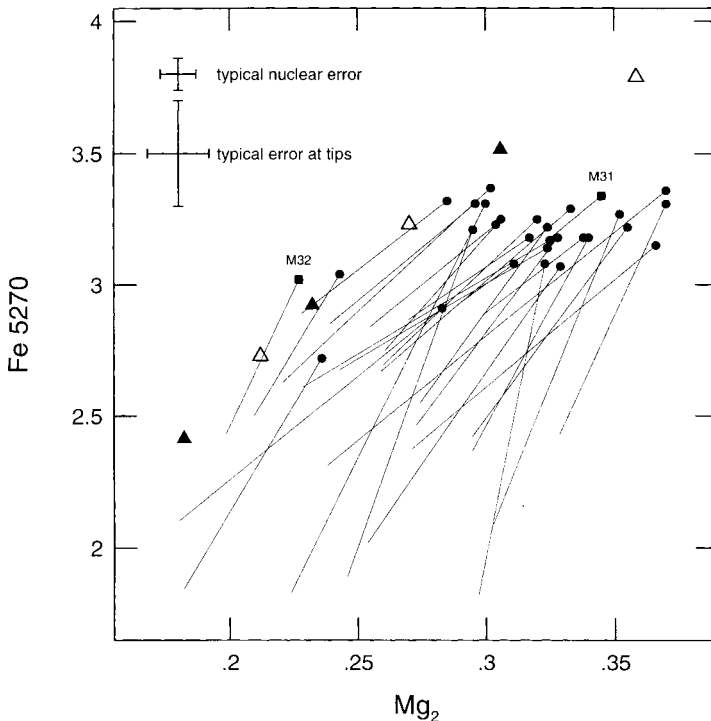
Fig. 11.12. Plot of an iron feature against Mg_2. Filled circles and squares represent the nuclear regions (central 5 arcsec) of elliptical galaxies, while the sloping lines show the mean trend with galactocentric distance in each one. Triangles show model predictions for ages of 9 (solid) and 18 Gyr (open), based on a single burst of star formation, which fit the features in globular clusters and assume [Mg/Fe] = 0. A young model with [Fe/H] = 0 fits the nucleus of M32 quite well, and the predicted trends with metallicity run roughly parallel to several of the observational lines, but the trend among nuclei is not fitted at all. After Worthey, Faber and Gonzalez (1992). Courtesy Guy Worthey.

presumably reflects faster rates of star formation as well as a higher degree of enrichment in the bigger objects; cf. Fig. 8.7 and Thomas *et al.* (2005). The models that have been put forward to account for the higher degree of enrichment in larger galaxies can be classified as either wind or merger models.

11.3.3 Wind models

Effects of a homogeneous continuous Galactic wind were discussed in Section 8.3.7 in connection with the evolution of the Galactic halo. Some kind of wind model for elliptical galaxies is favoured by the relation with velocity dispersion and by the presence of heavy elements in intra-cluster gas in clusters of galaxies, which was actually predicted (Larson & Dinerstein 1975) before it was discovered from X-ray observations. A number of models use the idea of a terminal wind caused by the gradual accumulation of hot gas from the interiors of supernova remnants which eventually overlap, making the whole ISM hot enough to reach escape velocity (Mathews & Baker 1971). The Salpeter(0.1) IMF, Eq. (7.8), gives an idea of the energy involved, assuming that all stars above $10\,M_\odot$ explode as supernovae releasing 10^{51} erg. The number of supernovae per solar mass of stars formed is $\int_{10}^{100} \phi(m)dm = 5 \times 10^{-3}$ giving about 2.5×10^{15} erg gm^{-1}. This corresponds to a velocity of 700 km s^{-1}, comparable to the escape velocity from a large galaxy like our own, if the losses due to cooling are not too great; it is the details of these losses, and in particular the ratio of cooling time to dynamical or star formation time, that fix whether, and if so when, the terminal wind occurs. The depth of the potential well which fixes the escape energy varies as M/R or roughly as $M^{1/2}$ (Fish 1964). (Probably only about a tenth of the supernova energy is available to drive the wind, but this is compensated by the return fraction of gas being of the same order.) The first such model to be worked out quantitatively is that of Larson (1974b), some of whose results are shown in Fig. 11.13. The condition for a wind is approached after some time (typically 2 Gyr), as the mass of gas and its volume density, which affects the SNR cooling rate, diminish, and the amount of gas then expelled relative to the mass remaining in stars varies inversely as the depth of the potential well, i.e. as $M^{-2/3}$ according to the scaling law assumed by Larson. This model, which uses the instantaneous recycling approximation and a simple bulk yield for some combination of heavy elements, was based on Larson's (1974a) earlier theory of the formation of elliptical galaxies, which predicted steep gradients in surface density and metallicity; these do not have time to develop when the gas fraction lost is 50 per cent or more, and the overall results are in good qualitative agreement with observational data.

A related analysis is the study of dwarf galaxies by Dekel and Silk (1986), who note the existence of two sequences of dwarf galaxies in the Fundamental Plane
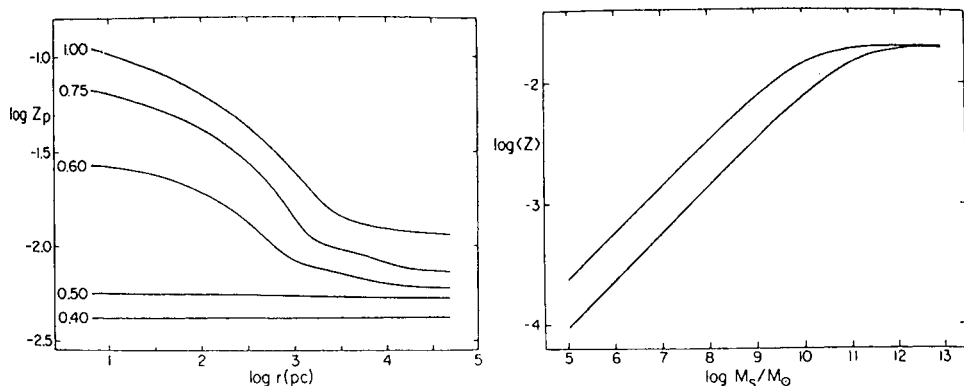
Fig. 11.13. Left panel: projected heavy-element abundance Z_p along lines of sight as a function of galactocentric distance, for differing values of the mass fraction in the form of stars at the onset of a terminal galactic wind. Right panel: (mass-weighted) mean abundance as a function of final total stellar mass, for two different assumptions as to the dependence of the amount of gas lost on the initial mass. The assumed bulk yield is 0.02 and the trend along the linear part of the curves is approximately $Z \propto M^{3/8}$. Adapted from Larson (1974b).

(Fig. 11.10) and base their model on the existence of dark-matter halos (cf. White & Rees 1978). Figure 11.10 shows a dwarf spheroidal–dwarf elliptical sequence ascending at about 45° from the lower left corner to meet a normal–compact elliptical sequence that goes more or less at right angles. Dekel and Silk's suggestion is that there is a critical gravitational potential, or virial velocity, below which a gaseous proto-galaxy forming stars can lose the bulk of its gas in the first burst of star formation, whereas for deeper potential wells the situation more closely resembles Larson's analysis. Dekel and Silk assume a number of scaling laws. A mass g_i of gas settles into the potential well of a dark spherical halo with a much larger mass $M \propto g_i$, radius R and virial velocity V satisfying a scaling law

$$M \propto R^{r_m} \propto g_i. \tag{11.4}$$

M, R and V are unaltered by the mass loss. The visible matter is assumed to satisfy the scaling laws

$$L \propto R^{r_l} \propto V^v \propto Z^z, \tag{11.5}$$

where L is the luminosity and the second proportionality is a generalization of the the Faber–Jackson (1976) relation. It follows from Eqs. (11.4), (11.5) and the Virial Theorem that

$$V^2 \propto M/R \propto R^{r_m-1} \propto L^{(r_m-1)/r_l} \tag{11.6}$$

so that

$$v = 2r_l/(r_m - 1), \tag{11.7}$$

which is one relation between the 4 unknowns v, r_l, r_m, z. Supposing now that a mass s of stars has formed, this fixes both the mass:luminosity ratio

$$M/L \propto M/s \tag{11.8}$$

and the stellar heavy-element abundance (Eq. 8.7 with $s/g \simeq 1 - \mu \ll 1$)

$$Z \propto 1 - \mu = s/g_i \propto s/M \propto L/M \propto R^{r_l - r_m} \propto L^{1 - r_m/r_l} = L^{1/z}. \tag{11.9}$$

This leads to a second relation between the 4 unknowns:

$$z = r_l/(r_l - r_m). \tag{11.10}$$

A third relation comes from the condition that the number of supernovae, proportional to s or L, should have been sufficient to supply the escape energy to the bulk of the gas mass g_i, itself assumed proportional to M, i.e.

$$L \propto MV^2, \tag{11.11}$$

which leads to

$$v = 2z. \tag{11.12}$$

The equations are closed by appealing to the observational result that $r_l = 4$ for these diffuse systems, whence

$$r_m = 5/2; \quad v = 16/3; \quad z = 8/3. \tag{11.13}$$

Thus $M/L \propto L^{-3/8}$ or $M^{-3/5}$, increasing towards low luminosities (cf. the position of dwarf spheroidals in the top panel of Fig. 11.10), and $Z \propto L^{3/8}$, $M^{3/5}$ or V^2. The latter relation compares reasonably well with the lower part of Fig. 11.11, calibrated with Eq. (11.3), and the first one compares very well with Fig. 11.1. The above assumptions are expected to apply only under certain conditions, fixed by supernova rates, their efficiency in transferring energy to the ISM, the cooling rates and the dynamical time; in Dekel and Silk's calculation, by far the most important parameter turns out to be the virial velocity, other parameters like the gas density more or less cancelling out. Thus their analysis applies below a certain critical velocity that is found by them to be very close to $100\,\mathrm{km\ s^{-1}}$ (line-of-sight velocity dispersion $60\,\mathrm{km\ s^{-1}}$). Above this velocity, a 'normal' galaxy is formed, which manages to convert most of its gas into stars.

Dekel and Silk argue that the alternative hypothesis of a self-gravitating cloud that becomes more diffuse as a result of losing most of its mass leads to a significantly flatter dependence of Z on L, $Z \propto L^{1/4}$, so that the observed relations are

evidence in support of the dominance of cold dark matter halos in these systems. However, this argument relies heavily on the $L \propto R^4$ law, and some dynamical adjustment could be a natural explanation for their diffuseness, the alternative being that they have failed to undergo dissipative episodes experienced by other galaxies.

A detailed semi-analytical study of the role of stellar feedback and the role of dark matter in the evolution of dwarf galaxies was made by Ferrara and Tolstoy (2000), who considered the effect of a sudden energy release by a supernova or a superbubble in an exponentially stratified medium. The velocity of the shock wave $\sim (P/\rho)^{1/2} \sim (E/z^3\rho)^{1/2}$, where E is the explosion energy. Along the z-axis this decreases up to 3 scale heights where it reaches a minimum and then increases again. If the minimum velocity exceeds escape velocity, then a modest amount of mass loss will take place in the form of a 'blowout' along the axis. Meanwhile, the shock will be propagating at a lower velocity in the central plane until overcome by a downward-propagating rarefaction wave from the blowout, at which point it enters the momentum-conserving or snowplough phase; if the momentum is high enough to accelerate the gas outside that point to escape velocity, then all of that gas will be lost in a 'blowaway'. Figures 11.14, 11.15 show the conditions derived by Ferrara and Tolstoy for the various possible outcomes in typical cases; according to their analysis, the effects of mass loss are relatively small in most cases, especially when the ratio ϕ of dark to luminous matter is large, but there is a lower limit to the oxygen abundance of a dwarf galaxy that can survive blowaway, similar to that of I Zw 18 ($12 + \log O/H \simeq 7.2$).
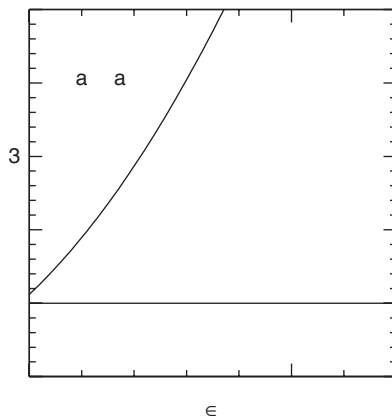
Fig. 11.14. Conditions for gas loss from a galaxy, as a function of axial ratio ϵ ($\epsilon = 1$ for a spherical galaxy) and ratio of minimum vertical velocity to escape velocity. After Ferrara and Tolstoy (2000).
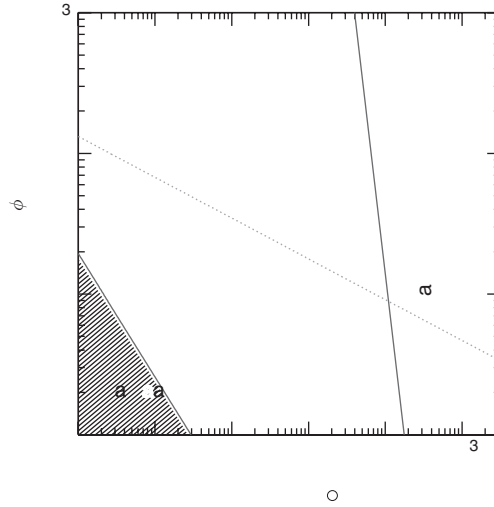
Fig. 11.15. Conditions for gas loss from a galaxy, as a function of gas mass M_g and the ratio ϕ of dark matter to baryons (stars + gas), assuming an energy input of 10^{38} erg s^{-1} and maximum dissipation from cloud–cloud collisions. PSS denotes the relation between ϕ and M_g deduced from observation by Persic, Salucci and Stel (1996). After Ferrara and Tolstoy (2000).

Two reservations need to be expressed about models for elliptical galaxies compared to colours or spectra in integrated light.

(i) The 'observed' metallicity from integrated light is not mass-weighted, as assumed in Eq. (8.7), but luminosity-weighted. This generally will lead to the mass-weighted metallicity being underestimated, because metal-weak giants are more luminous.

(ii) The (mass-weighted) average abundance according to Eq. (8.7) cannot exceed the true yield, either in a closed model or in one with inflowing unprocessed material. A mass-weighted average $Z > Z_\odot$ in giant elliptical galaxies, even if it applies to α-elements alone, requires a higher true yield than is believed to hold in the solar neighbourhood (see Section 8.3.1), if it is representative of the galaxy as a whole. If it is confined to the nucleus, on the other hand, then it can be accounted for by inflow of already processed material into the nuclear regions as envisaged in Larson's models (Fig. 11.13) and explained in Appendix 5; see also Edmunds & Greenhow (1995). Such dissipative effects may be revealed by metallicity gradients in certain ellipticals that show a marked steepening towards the centre, suggesting effects of a merger (Bender 1992).

Detailed numerical models for the photometric and chemical evolution of elliptical galaxies have been computed by Yoshii and Arimoto (1987), Matteucci and Tornambé (1987), Brocato *et al.* (1990) and Matteucci (1992, 1994). These are terminal wind models similar in their basic assumptions to that of Larson (1974b), but with differing assumptions as to IMFs and scaling laws that specify how the

rate of star formation and the depth of the potential well formed by an initial dissi-
pational collapse depend on the mass of the galaxy. The star formation efficiency
parameter ω was generally assumed to be lower in the more massive galaxies,
corresponding to longer free-fall times $\propto (M/R^3)^{-1/2}$ with $R \propto M^{1/2}$, but var-
ious models differ in that Yoshii and Arimoto assumed a rather flat IMF to get
the high yield, computing only one abundance parameter [Fe/H], neglecting SN Ia
and arriving at rather high mass:luminosity ratios because of a preponderance of
white dwarfs, whereas Matteucci and colleagues assumed a Salpeter IMF, include
SN Ia and predicted abundances of several elements. Both sets of models gave a
fair account of mass:light ratios (Yoshii and Arimoto marginally so) and colour–
luminosity relations, and Yoshii and Arimoto could also reproduce something
resembling the dwarf sequence in the Fundamental Plane from dynamical effects
of mass loss without any dark halos; Matteucci (1992) suggested that, while such
halos probably exist, they could be so diffuse as to have but little effect on chemical
evolution. A serious difficulty encountered by Matteucci and her colleagues (and
probably also by Yoshii and Arimoto, though to a lesser degree) is that the predicted
magnitude of Mg/Fe and its trend with luminosity are in flagrant disagreement with
the observational effects discussed above (Matteucci 1994). Matteucci suggested,
as had already been done by Worthey, Faber and Gonzalez (1992), that either star
formation efficiency increases or the IMF becomes flatter with increasing galaxy
mass, and considered certain other possibilities; among these it seems to me that
the real solution lies in violent star formation provoked by tidal effects or mergers
and not described by simple linear (or other power) laws in the gas mass. A fur-
ther problem with these terminal wind models is that they predict an abundance
distribution function similar to that of the Simple model, truncated at metallicities
that increase with the depth of the potential well. However, the application of syn-
thetic photometric models to observed galaxy spectra suggests the existence of a
'G-dwarf problem' (Bressan, Chiosi & Fagotto 1994; Worthey, Dorman & Jones
1996); this was already taken care of (at least as far as the bright central regions of
elliptical galaxies and bulges of spirals are concerned) in Larson's models, but the
more recent numerical models cited above do not include internal gas flows despite
being more refined in other ways.

Some of these problems are addressed in the 'inverse wind' scenario of Pipino
and Matteucci (2004), in which they allow for inflow and assume ad hoc that, the
higher the mass of the galaxy, the shorter the infall and especially the star for-
mation timescales. This makes the more massive objects older, in the sense that
star formation is stopped by a terminal wind at earlier times, permitting enhanced
metallicities and α/Fe ratios in the framework of the classical Salpeter(0.1) IMF.
Abundance gradients within elliptical galaxies are reproduced within their very
considerable uncertainties by an 'outside-in' scenario in which star formation

ceases earlier in the outer zones, where the gravitational potential is shallower, with a shorter infall timescale and an enhancement of Mg/Fe with radius. Passive evolution from shortly after the formation epoch at high redshifts accounts for the tightness of the Fundamental Plane and its modest dependence on redshift.

Alternative wind models assume a selective outflow of enriched material, either taking place at the time of star formation bursts in dwarf galaxies (Matteucci & Tosi 1985) or taking place continuously from the hot component of the ISM which is also assumed to be metal-enriched (Vader 1987; Ferreras, Scannapieco & Silk 2002). An analytical model by Lynden-Bell (1992) supposes that, of the return fraction $1 - \alpha$ from a generation of stars, a fraction $1 - f$ escapes, leading via Eq. (7.34) to

$$\frac{d}{ds}(gZ) = pf - Z[1 - f(1 - \alpha)]/\alpha. \tag{11.14}$$

Based on the scaling law $R \propto M^{1/2}$, i.e. $M/R \propto M^{1/2}$, Lynden-Bell suggests for f the *Ansatz*

$$f = ks^{1/2}/(V^2 + ks^{1/2}), \tag{11.15}$$

where V is a characteristic virial velocity, and assumes inflow of unprocessed material following a similar law as in Lynden-Bell (1975) (see Section 8.5.2, but in this case the initial mass is zero), which takes care of any 'G-dwarf problem'. The analytical solution is somewhat involved and will be passed over here, but Fig. 11.16 shows the results compared with some observational data. It is notable that the true yield required is rather high, about $5 Z_\odot$, because in early stages of the model most of the metals escape even from the (ultimately) largest galaxies to enrich the intergalactic medium. The true metallicity of those largest galaxies, and how representative the observed values are of the galaxy as a whole, are uncertain, however, and the results depend in any case on which element is used to define 'metallicity'. We return to the yield question in Section 11.3.5 below.

11.3.4 Merger models

Luminous star formation bursts, e.g. as observed by IRAS, are associated with mergers of gas-rich systems, and there are cogent arguments suggesting that at least a large subset of elliptical galaxies could have been formed in this way (Toomre 1977; Kormendy & Sanders 1992; Barnes 1995), perhaps following mergers of dark-matter halos (White & Rees 1978). The collision of large gas clouds leads to star formation, energy dissipation and possibly eventual expulsion of gas by a supernova-driven galactic wind, transforming gas-rich metal-poor systems with low phase-space density into gas-poor metal-rich systems of high surface brightness (see the 'merging' and 'dissipation' arrows in Fig. 11.10).
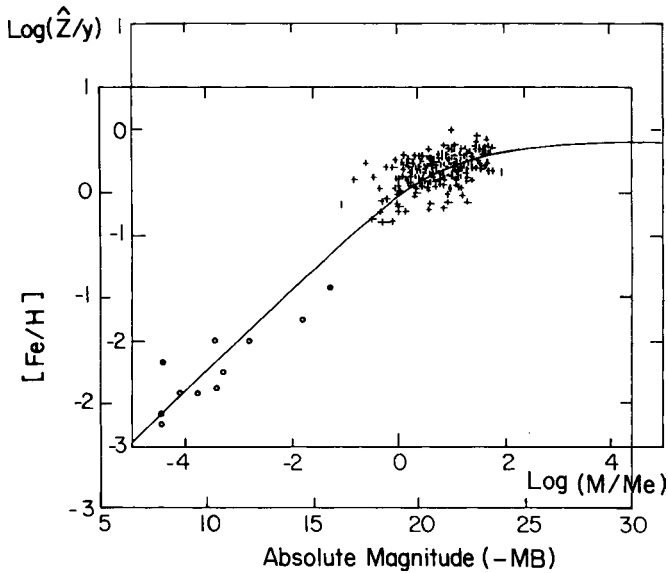
Fig. 11.16. Median metal abundance per unit true yield as a function of final mass with observations of dwarf spheroidal and elliptical galaxies superposed. The offsets of axes determine the characteristic mass M_e that constrains supernova debris and the true yield y (p in the text). MB is the corresponding blue absolute magnitude (neglecting any dark halos). The trend along the linear branch of the curve is for metallicity to increase approximately as $M^{1/2}$. After Lynden-Bell (1992).

Tinsley and Larson (1979) developed a simple chemical evolution model along these lines. They assume that ordinary matter is initially clumped into gas clouds of equal mass M_0, so that a galaxy is built up by a hierarchy of binary mergers leading to an increase in mass by a factor of 2 at each stage. A crucial assumption is that the efficiency of star formation, i.e. the fraction of gas that is converted into stars at each stage, is an increasing function of the total mass, varying as $(M/M_e)^p$, say. This leads to the recurrence relations for the nth merger

$$s_n - 2s_{n-1} = 2g_{n-1}(M_n/M_e)^p = 2^{np+1}g_{n-1}(M_0/M_e)^p, \qquad (11.16)$$

and

$$g_n = 2g_{n-1}[1 - 2^{np}(M_0/M_e)^p]. \qquad (11.17)$$

The initial values are $g_0 = M_0$, $s_0 = 0$, $\mu_0 = 1$. Using the Simple model equations (8.6), (8.7) and assuming numerical values $p = 1/3$, $M_0 = 1.2 \times 10^7 \, M_{\odot}$, $M_e = 3.2 \times 10^{12} \, M_{\odot}$, Tinsley and Larson obtain numerical values some of which are shown in Table 11.2. The abundance as a function of final mass is shown in Fig. 11.17.

Table 11.2. *Properties of a sequence of mergers with star formation*

n	$\log M_n/M_\odot$	$\log s_n/M_\odot$	$\log z_g$	$\log z_s$	$\log R$ (pc)	Min. $\log t_{dyn}$ (yr)	Max. $\log t_{cool}$ (yr)
0	7.08	$-\infty$	$-\infty$	$-\infty$	–	–	–
2	7.68	6.33	-1.35	-1.65	(3.2)	(8.2)	–
6	8.89	8.20	-0.63	-0.95	(3.6)	(8.2)	–
10	10.09	9.80	-0.14	-0.50	4.0	8.1	4.7
12	10.69	10.54	0.09	-0.31	4.2	8.2	5.7
16	11.898	11.888	0.58	-0.04	4.8	8.4	8.1
17	12.199	12.197	0.73	-0.01	4.9	8.5	9.1

Data from Tinsley and Larson (1979).
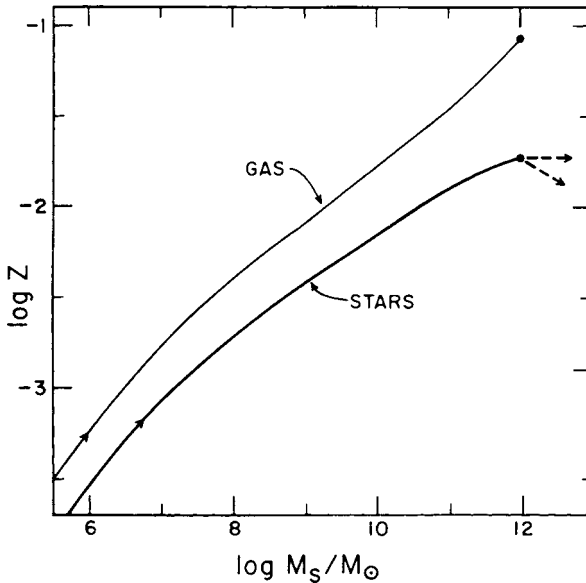
Fig. 11.17. Metallicities of stars and gas as a function of the total mass of stars in an elliptical galaxy growing by mergers, assuming a true yield of 0.02. The trend is for stellar Z to increase approximately as $M^{1/2}$ for small masses, flattening to $M^{1/4}$ for larger ones. Filled circles show the point beyond which there will be little star formation in mergers because the gas cannot cool sufficiently between collisions; arrows indicate possible outcomes of further mergers without star formation. After Tinsley and Larson (1979).

A simplified version of the argument has been given by Mould (1984).[2] With the above assumption about star formation efficiency, in a 'continuum' approximation,

[2] In what he refers to as 'The Simple Model with Bells and Whistles'.

$$\frac{ds}{dM} = (p+1) \left(\frac{M}{M_e}\right)^p, \tag{11.18}$$

so that

$$\frac{s}{M_e} = \left(\frac{M}{M_e}\right)^{p+1} \quad \text{or} \quad \frac{s}{M} = \left(\frac{M}{M_e}\right)^p = \left(\frac{s}{M_e}\right)^{p/(p+1)}. \tag{11.19}$$

The abundance in the gas is then given by the Simple model relation Eq. (8.6)

$$z = -\ln\left(1 - (s/M_e)^{p/(p+1)}\right) \rightarrow \left(\frac{s}{M_e}\right)^{p/(p+1)} \quad \text{as } s \to 0, \tag{11.20}$$

and the mean stellar abundance is

$$
\begin{aligned}
\langle z_s \rangle &= 1 - zg/s &&(11.21) \\
&= 1 + \frac{M-s}{s} \ln\left(1 - (s/M_e)^{p/(1+p)}\right) \\
&= 1 + \left((M_e/s)^{p/(p+1)} - 1\right) \ln\left(1 - (s/M_e)^{p/(p+1)}\right) &&(11.22) \\
&\rightarrow \left(\frac{s}{M_e}\right)^{p/(p+1)} \quad \text{as } s \to 0 &&(11.23) \\
&\rightarrow 1 \quad \text{as } s \to M_e. &&(11.24)
\end{aligned}
$$

Again, $p \simeq 1/3$ gives a fair fit to Fig. 11.17. The mass–metallicity relation is associated with the decrease in gas fraction concomitant with the increasing mass, and the G-dwarf problem is neatly solved; models of hierarchical structure formation make use of this and several other factors leading to rather similar effects to those of inflow discussed in Chapter 8 (Nagashima & Okamoto 2006).

Tinsley and Larson noted that collisions between galaxies tend to shock-heat the gas to approximately the virial temperature, which increases with total mass according to the Faber–Jackson relation, so that eventually the gas may become too hot to be able to cool enough to form stars before the next collision. Table 11.2 accordingly gives some estimates of cooling times and dynamical times, based on an empirical mass–radius relation, and it turns out that there is a critical mass, estimated to be in the region of $10^{12} M_\odot$, above which the cooling rate becomes too small to allow further star formation. Subsequent mergers with equal-sized objects leave the metallicity unaltered (horizontal arrow in Fig. 11.17), while mergers with smaller objects will lead to a reduction (downward-sloping arrow). This could perhaps be the process going on in the central-dominant (cD) galaxies in large clusters that are swallowing their neighbours. Once mergers have ceased at any stage, or possibly before, the galaxy can evolve to the point where its residual gas is driven out in a terminal wind, as discussed in the previous section, or it can become the central bulge of a spiral by accreting diffuse material that settles into a plane before itself forming stars.

In the years following the work by Tinsley and Larson, the idea of galaxy formation by hierarchical clustering of smaller units has gained ground as a result of numerical simulations of structure formation in the Universe, but the resulting effects on star formation and feedback are studied by 'semi-analytical' models involving many uncertainties and ad hoc assumptions (e.g. Kauffmann, White & Guiderdoni 1993; Somerville & Primack 1999). The increase in Mg/H and Mg/Fe with elliptical galaxy mass or velocity dispersion is one of the more significant constraints on such models (e.g. Nagashima *et al.* 2005b). Thomas, Greggio and Bender (1999) developed numerical models in which they considered two scenarios:

(i) *Fast clumpy collapse*. Massive objects are built up by mergers over short timescales ~ 1 Gyr. Star formation takes place at a constant rate during the merger. Gaseous dissipation causes enriched material to fall to the centre (see Appendix 5), so the result is not very different from the classical monolithic collapse model of Larson (1974b). The overall average abundances are as in the closed-box (Simple) model, but the high-metallicity tail of the distribution is concentrated towards the centre.

(ii) *Merging spirals*. The merging event takes place when the merging systems have already converted most of their gas into stars reaching solar-like abundances. At merging, the (enriched) residual gas flows down to the centre where it experiences a violent star formation episode with a short timescale.

The first of these two scenarios is suggested by the evidence from the Fundamental Plane that ellipticals formed rapidly a long time ago, while the second represents things that are actually seen to happen in the ultra-luminous infrared galaxies. In the first scenario, one has a similar situation to that in the Galactic disk and halo; with conventional yields and IMFs, they found that one can get [Mg/Fe] $\simeq 0.2$ if the star formation timescale is 1 Gyr or less; with a flatter IMF one can get larger ratios with longer timescales. All this naturally follows from the assumed dependence of the yields on progenitor mass and the assumed evolution of SN Ia after Greggio and Renzini (1983). The second scenario leads to somewhat lower [Mg/Fe] ratios. A significant difference between the two scenarios is that in the fast clumpy collapse case, with younger more metal-rich stars concentrated in the centre, the Mg/Fe ratio should increase outwards as with the metallicity dependence in our own Galaxy, whereas in the other case the outer stars have approximately solar ratios and the inner ones have Mg/Fe enhanced.

11.3.5 Metal supply to the intra-cluster medium

Rich clusters of galaxies, characterized optically as concentrations of hundreds (or even thousands) of galaxies within a region spanning several Mpc, are among

the brightest sources of X-rays in the sky. The hot intra-cluster medium filling the space between the galaxies has an average particle density of around 10^{-3} cm^{-3} and electron temperatures up to 10 keV or so, which enables abundance estimates to be made from their spectra (see Fig. 3.31), thus providing an additional constraint on the chemical evolution of elliptical galaxies from the supply of metals to the intra-cluster gas. This was discussed by Arnaud *et al.* (1992), who found a good correlation between the total mass g of gas in the cluster and the total luminosity L_V of E and S0 galaxies within the cluster (see Fig. 11.18) in the range

$$30 \ \leq \ \frac{g}{L_V} \ \leq \ 40 \tag{11.25}$$

which implies

$$6 \left(\frac{5}{M/L} \right) \ \leq \ \frac{g}{s} \ \leq 8 \ \left(\frac{5}{M/L} \right) \tag{11.26}$$
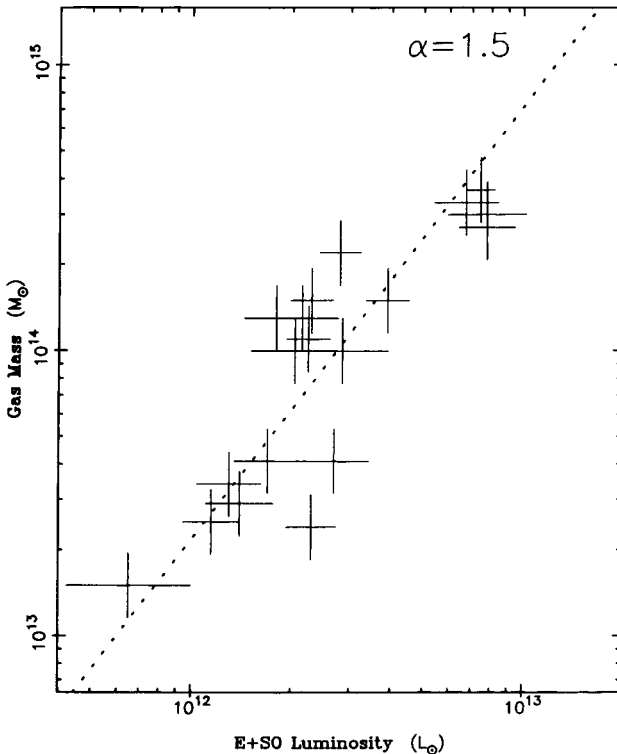
Fig. 11.18. Gas mass in clusters of galaxies plotted against the total luminosity of elliptical and lenticular (S0) galaxies in the cluster. The 1σ error in the slope α is ± 0.25. After Arnaud *et al.* (1992). Courtesy Monique Arnaud.

where M/L is the visual mass:luminosity ratio (in solar units) of the total stellar population of mass s. Such a large ratio of gaseous to stellar mass (given a return fraction probably no greater than 0.5) implies that at least 80 per cent of the intra-cluster gas is primordial. The total iron mass in the gas, $g\, Z_{Fe}$, is found to be proportional to L_V, i.e. to s. There is little evolution with redshift, out to $z = 1$ or more (e.g. Tozzi *et al*. 2003), consistent with the view that star formation in the constituent early-type galaxies effectively ceased a long time ago. However, the source of some or most of the intra-cluster metals could have been dwarf galaxies that disintegrated in a blowaway long ago, rather than the galaxies that we see now (e.g. Scannapieco & Broadhurst 2001).

The typical value [Fe/H] ~ -0.4 found in the intra-cluster gas, while not looking particularly remarkable in itself, becomes so when the large mass of gas is taken into account, since we now have

$$p_{Fe} \simeq \frac{(g+s)\, Z_{Fe}}{s} \geq 3\, Z_{Fe}^{\odot} \qquad (11.27)$$

for $(M/L) \leq 5$, requiring a high efficiency of iron production. One suggestion has been that the bulk of the iron comes from SN Ia which have exploded over the years and given rise to iron-rich winds (Ciotti *et al*. 1991); this would lead one to expect a high Fe/α ratio in the gas and a low one in the stars (Renzini *et al*. 1993). The latter effect is in good agreement with the Fe/Mg observations of the stellar populations. The situation in the gas is more complicated, and not necessarily explicable by conventional yields from supernovae of either type; e.g. Mg and Si seem to be enhanced relative to O and S, and Ni relative to Fe (Loewenstein 2004), but on average the α/Fe ratios are not very different from solar.

Pipino *et al*. (2002) have put forward a detailed model for the evolution of the intra-cluster gas in clusters having a range of total mass, using a Salpeter(0.1) IMF, which gives a good account of the iron abundance on the basis that the ejecta from Type Ia supernovae, which explode in an interstellar medium already heated by Type II's, are expelled with high efficiency. However, the oxygen (and presumably magnesium) abundances predicted by their favoured models are considerably lower than appears from the observations. Thus it seems from Eq. (11.27) that one indeed needs a yield in elliptical galaxies enhanced by a factor of 4 or so compared to the solar neighbourhood, as envisaged by Yoshii and Arimoto (1987), Lynden-Bell (1992) and others, at least for O and Mg; if this is associated with a flat IMF slope (possibly arising in a starburst triggered by a major merger), this could help to explain the Mg/Fe trends in the stars (see Thomas 1999; Nagashima *et al*. 2005a). Alternatively, there could be a significant contribution to the ICM enrichment from outflows from AGNs in the constituent galaxies (Moll *et al*. 2007).

Problems

1. With the assumptions of Section 11.3.2, and assuming a mass–luminosity relation $L \propto M^{1-\delta}$, show that the Fundamental Plane satisfies the relations

$$I \propto M^{-(1+\delta)}\sigma^4 \propto L^{-\frac{1+\delta}{1-\delta}}\sigma^4, \tag{11.28}$$

where σ is the velocity dispersion and I the surface brightness within some characteristic radius.

2. Assuming a continuous and homogeneous galactic wind with a mass flux $\eta\alpha\psi$ ($\eta = $ const.), combined with a selective (metal-enhanced) wind $\eta^* \times$ the mass of Type II supernova ejecta ($\eta^* = $ const. < 1), show that Eq. (8.6) for the Simple model is replaced by

$$\frac{Z}{\ln 1/g} = \frac{p(1-\eta^*)}{1+\eta+\eta^* R^*/\alpha} \simeq \frac{p(1-\eta^*)}{1+\eta}, \tag{11.29}$$

where R^* is the contribution of stars above $10\,M_\odot$ (winds and SN ejecta) to the return fraction. (An upper limit to R^* can be found from Eq. 7.8); g is the mass of gas remaining in units of the initial mass of the system.

3. Derive the metallicity distribution function implied by Eq. (11.20).

12

Cosmic chemical evolution and diffuse background radiation

...that a telescope with a power of penetrating into space, like my 40-feet one, has also, it may be called, a power of penetrating into time past. To explain this, we must consider that, from the known velocity of light, it may be proved, that when we look at Sirius, the rays which enter the eye cannot have been less than 6 years and $4\frac{1}{2}$ months coming from that star to the observer. Hence it follows, that when we see an object of the calculated distance at which one of these very remote nebulae may still be perceived, the rays of light which convey its image to the eye, must have been more than nineteen hundred and ten thousand, that is, almost two millions of years on their way; and that, consequently, so many years ago, this object must already have had an existence in the sidereal heavens, in order to send out those rays by which we now perceive it.

William Herschel, *Catalogue of 500 new Nebulae, nebulous stars, planetary Nebulae, and Clusters of Stars; with Remarks on the Construction of the Heavens*, *Phil. Trans. XCII* (1802), 477.[1]

12.1 Introduction

Observations of distant objects, notably high-redshift star-forming ('Lyman-break') galaxies and absorption line systems on the line of sight to quasars, give some information on chemical evolution at epochs not too far from when the first stars and most galaxies were presumably formed. Other information comes from two related effects:

- The overall abundance of helium and heavy elements in the Universe today. This reflects the total effect of fuel consumption and nucleosynthesis by all the stars that ever existed. Roughly speaking, one may consider this in two

---

[1] Reproduced in Hoskin (1963).

ways: (i) nucleosynthesis of 'Z' elements by massive stars in starbursts; these stars emit copious ultraviolet radiation which is subsequently redshifted and may also be reprocessed into the far infrared by dust. (ii) One may consider all the products of nuclear burning in stars including the non-cosmological helium ΔY and C, O etc. locked up in stellar interiors and remnants, mainly white dwarfs.

- Diffuse background radiation from the night sky (other than the cosmological microwave background). This is another global manifestation of past stellar activity which is directly related to the resulting abundances. It is quite difficult to measure, owing to the existence of strong foregrounds from Galactic starlight, zodiacal light and far infrared emission from dust clouds in the Galaxy, known as Galactic cirrus. In the optical, near infrared and sub-mm, lower limits are provided by galaxy counts at the faintest attainable magnitudes. An overview of current limits with a model based on various assumptions is shown in Fig. 12.1, where it appears that typical values of νI_ν or λI_λ (the energy in a relative frequency band of 1 in the natural logarithm) are of the order of 10 or 20 nanowatt m^{-2} sterad^{-1}. This is a few per cent of the peak of the cosmic microwave background, which is shown by the parabola-like curve at the right end of the diagram. Background radiation is attenuated by redshift, especially at the shorter wavelengths, so that most of it comes from relatively nearby objects ($z \simeq 1$) unless there has been extreme luminosity evolution, whereas the products of fuel consumption and nucleosynthesis remain whatever the redshift at which they were formed. There is, however, an exception to the former statement in the case of sub-mm radiation from dust, because in this case the black-body peak is actually shifted into the observable region (Franceschini *et al.* 1991; Blain & Longair 1993). Conversely, the onset of hydrogen absorption shortward of the Lyman limit ensures that there will be virtually no contribution to blue light from redshifts greater than 3.

12.2 Luminosity evolution and the diffuse background

The pioneering investigation in this field was that by Partridge and Peebles (1967; hereinafter PP), who computed a number of evolutionary synthesis models for a 'typical' galaxy, assumed similar to our own. These were based on the present-day luminosity density of the Universe (see Eq. 4.57) and the relation

$$I(\nu_0, t_0) = \frac{c}{4\pi} l(\nu_0, t_0) \int_0^{t_0} \frac{L(\nu(t), t)}{L(\nu_0, t_0)} dt, \qquad (12.1)$$

where $l(\nu_0, t_0)$ is the luminosity density per unit frequency interval, at frequency ν_0 at the present time t_0, and the ratio under the integral sign represents
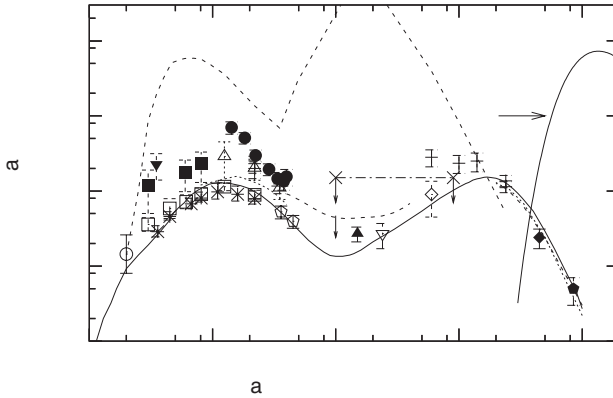
Fig. 12.1. Spectrum of background radiation from the night sky above the Earth's atmosphere, based on faint galaxy counts and direct measurements of a diffuse background or of its angular fluctuation power spectrum. The galaxy counts are by Armand *et al.* (1994) (open circle at 0.2 μm), Madau and Pozzetti (2000) (open squares), Totani *et al.* (2001) (stars), Fazio *et al.* (2004) (open pentagons at 3.6 and 4.5 μm), Metcalfe *et al.* (2003) (black triangle at 15 μm), Papovich *et al.* (2004) (inverted open triangle at 24 μm), Serjeant *et al.* (2004) (black diamond at 450 μm) and Smail *et al.* (2002) (black pentagon at 850 μm). Diffuse emission determinations are by Bernstein, Freedman and Madore (2005) (black squares between 0.3 and 0.8 μm), Mattila, Leinert and Schnur (1991) (black inverted triangle at 0.35 μm), Gorjian, Wright and Chary (2000) and Wright (2001) (open triangles between 1.25 and 3.5 μm), Matsumoto *et al.* (2005) (black circles between 1.4 and 4 μm), Miville-Deschênes *et al.* (2001) (open diamond at 60 μm), Finkbeiner *et al.* (2000), Fixsen *et al.* (1998), Lagache *et al.* (2005) and Hauser and Dwek (2001) (crosses at 60 to 150 μm, dotted and short-dashed curves between 200 and 1000 μm). The horizontal dash-dot line between 10 and 100 μm (Hauser & Dwek 2001), the short-dashed curve between 4 and 40 μm (Renault *et al.* 2001) and the dotted curve between 0.8 and 4 μm (Aharonian *et al.* 2006) show upper limits derived from absorption of high-energy γ-rays from blazars (or the lack of it), arising from photon–photon pair production. The solid curve is from the model by Pei, Fall and Hauser (1999), and the broken-line curve shows typical brightness of the disturbing zodiacal light foreground after Bernstein, Freedman and Madore (2002) shortward of 1 μm and Kelsall *et al.* (1998) at longer wavelengths. The spectrum of the cosmic microwave background is shown at the right side of the diagram.

a combination of luminosity evolution and redshift. Replacing $L_{B\odot}$ in Eq. (4.57) with $\nu L_{\nu\odot}(4400\,\text{Å}) = 2 \times 10^{33}\ \text{erg s}^{-1} \simeq L_\odot/2$, we have

$$\nu_0 \, l(\nu_0, t_0) \simeq 1.4 \times 10^{-32} \, h \ \ \text{erg s}^{-1}\ \text{cm}^{-3}. \qquad (12.2)$$

To get a very rough idea of the resulting background intensity, one can simply assume the factor under the integral sign in Eq. (12.1) to have been constant (i.e. 1) for $5h^{-1}$ Gyr (since larger ages would redshift the faint UV region into the blue

photometric band and therefore contribute little). In this way one derives $\nu I_\nu \simeq$ 5 nwt m^{-2} sterad^{-1}, which is comparable to the lower limit derived from galaxy counts in the B band (Fig. 12.1).

Partridge and Peebles computed several models making different assumptions about the star formation history of a typical galaxy. Their Model 1 assumes a constant star formation rate, corresponding to a nearly constant luminosity, and leads to a spectrum that closely resembles that of the more recent model by Pei, Fall and Hauser shown in Fig. 12.1 at wavelengths below 10 μm, thus nicely fitting the lower limits derived subsequently from galaxy counts in the visible and near infrared. They, however, preferred other models with more drastic evolution because they felt a need to explain all of the helium in the Universe as a result of stellar fuel consumption;[2] in addition, they assumed a cosmic density of stellar matter that is about an order of magnitude greater than modern estimates (see Table 12.1 at the end of the chapter). Some of these models led them to predict that newly formed galaxies would be highly luminous and possibly detectable in the wavelength region between 5 and 15 μm.

Since then there have been substantial advances in numerical modelling of galaxy evolution, including developments in stellar evolution theory, distinguishing between different sorts of galaxies and the inclusion of chemical evolution effects and radiation from AGNs and dust. These were developed partly in the hope of deducing basic cosmological parameters from counts and redshift surveys of galaxies, and in this respect they still make a significant contribution, notably the large-scale redshift surveys – the Anglo-Australian Two-degree Field Survey (2DF) and the Sloan Digital Sky Survey (SDSS) – when combined with studies of the cosmic microwave background and the redshift magnitude relation for SN Ia. In the meantime, more emphasis has been placed on the history of star and galaxy formation as a subject of study in its own right. The background spectrum has been computed by, among others, Yoshii and Takahara (1988) and Franceschini *et al.* (1991) with similar outcomes to that from PP Model 1, and by Oliver, Rowan-Robinson and Saunders (1992; hereinafter ORS) and Pei, Fall and Hauser (1999) who make explicit allowance for far-infrared emission from dust.

The IRAS satellite mission, launched in 1983, provided a more complete survey of disk and active galaxies containing dust than had been possible from optical observations. Follow-up measurements of redshifts and other properties led to significant results for cosmology and the discovery of many luminous star-forming and active galaxies enshrouded by dust. A typical spiral galaxy like our own

---

[2] Although Peebles had himself recently completed a calculation of primordial element synthesis including helium (Peebles 1966).

radiates something like 25 per cent of its energy at wavelengths between 10 and several hundred μm, coming from cool 'cirrus' clouds.

The IRAS galaxies provided some of the earliest evidence from redshift surveys, and from source counts as a function of observed flux, that the spiral galaxy population has undergone evolution (ORS; see Fig. 12.2). This result is analogous to similar evidence from source counts of radio galaxies and quasars, as well as quasar redshifts, and a correlation that has been observed between radio and infrared luminosity suggests that the evolution could be similar in both cases. Typical simple models for such evolution include luminosity evolution according to

$$\frac{L(t)}{L(t_0)} = e^{QH_0(t_0-t)}; \quad z \le z_{\text{max}}, \tag{12.3}$$

where Q is some dimensionless number, or

$$\frac{L(t)}{L(t_0)} = (1+z)^q; \quad z \le z_{\text{max}}, \tag{12.4}$$

where z is the redshift; and number-density evolution according to

$$\frac{\Phi(t)}{\Phi(t_0)} = (1+z)^P; \quad z \le z_{\text{max}}, \tag{12.5}$$

which could represent the effect of mergers. Some 'P' and 'Q' models (assuming an Einstein–de Sitter cosmology) are compared with the IRAS 60 μm source
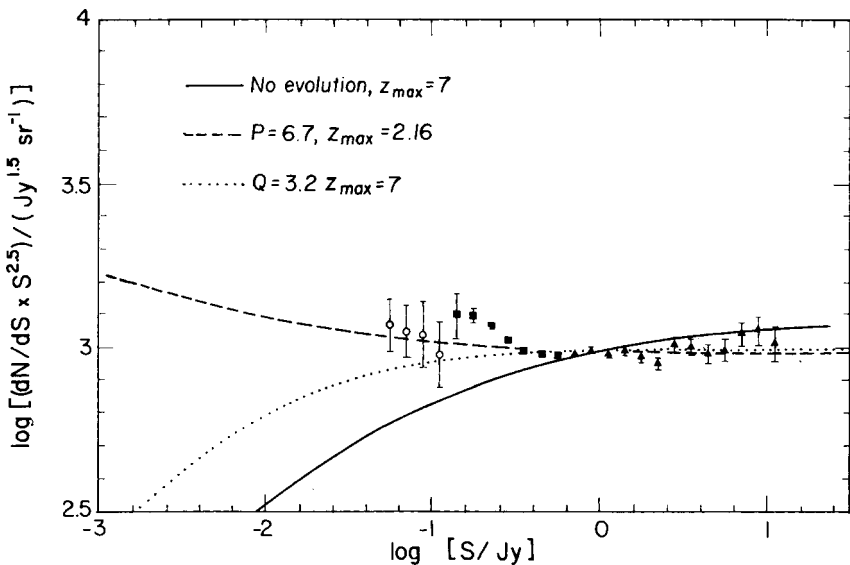
Fig. 12.2. IRAS differential source counts as a function of observed flux at 60 μm, normalized to a uniform population in Euclidean space. After Oliver, Rowan-Robinson and Saunders (1992).

counts in Fig. 12.2. ORS calculated the diffuse background resulting from all three kinds of evolution, assuming the presence of two components, normal cirrus from galactic disks (the major contributor at most wavelengths) and a warmer starburst component dominating between 60 and 120 μm, together with different values for the parameters. A 'q' model with $q = 3.15$ (a number that has been adopted for luminous quasars), $z_{max} = 5.31$, is one of a number that are compatible with the long-wavelength data in Fig. 12.1. The 'P' (number evolution) model shown in Fig. 12.2 was rejected by ORS because the resulting diffuse background was too high. They concluded that, if number-density evolution applies, then it must be cut off at $z_{max} < 2$, which could indicate a more recent peak of activity than for quasars and radio galaxies. In the optical and near infrared (1 μm), results from the Canada–France redshift survey (Lilly *et al.* 1996), which was the first major survey of cosmic star formation rates extending up to $z \simeq 1$, have been fitted to 'q' models with slightly smaller values of q between about 2 and 3 up to $z = 1$ and interpreted as resulting from a power-law decline in the star formation rate as $t^{-2.5}$ after a turn-on time of 2 to 3 Gyr.

12.3 Starbursts and metal production

Simple models of cosmic evolution expressed by formulae such as Eqs. (12.3) to (12.5) have been outdated by the discovery of large numbers of star-forming galaxies at high redshifts (from about 1.5 to 5) by the use of multi-colour photometry in deep fields to detect so-called Lyman-break galaxies (LBGs), i.e. UV-bright galaxies having star formation rates of up to several hundred $M_\odot$ per year with a sharp cut-off below the Lyman limit in the rest-frame due to their intrinsic spectra (see Fig. 12.3) combined with intervening H I clouds (mainly Lyman-limit systems) in galaxies along the line of sight – the UV or blue 'drop-out' technique (Steidel *et al.* 1996). This has been applied to the Hubble Deep Field by Madau *et al.* (1996) and to more extensive ground-based samples by Steidel, Pettini and colleagues to study cosmic star-formation rates as a function of redshift, commonly referred to as the 'Madau plot', which has been refined and extended by surveys at infrared and sub-mm wavelengths (Fig. 12.4).

Blue and UV light from stellar populations is dominated by young, massive stars which also contribute the lion's share of the *Z*-elements ('metals'). Evolutionary synthesis computations show that, between the Lyman limit (912 Å) and 2000 Å or so, the spectrum expressed as L_ν is more or less flat (Fig. 12.3). This leads to some rather simple considerations because I_ν retains its value (and flatness) when the light is redshifted (see Eq. 12.1), because the degradation in energy is simply taken up by the factor $d\nu$ on integration (Lilly & Cowie 1987).
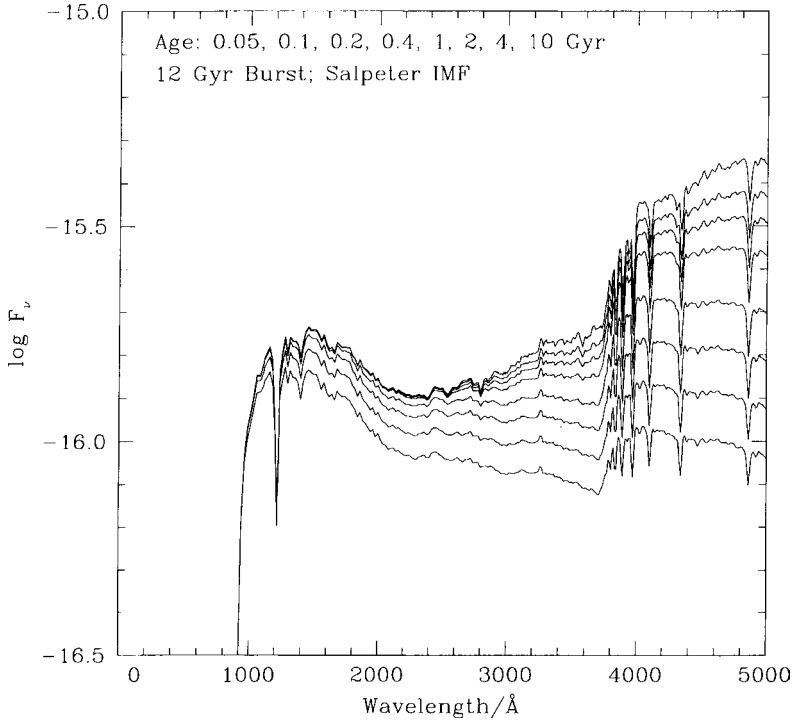
Fig. 12.3. Synthetic spectra for a region with constant star-formation rate for the ages indicated, assuming a Salpeter IMF cut-off at 75 $M_\odot$. After White (1989), based on computations by Gustavo Bruzual. With kind permission from Kluwer Academic Publishers. Courtesy Stephane Charlot.
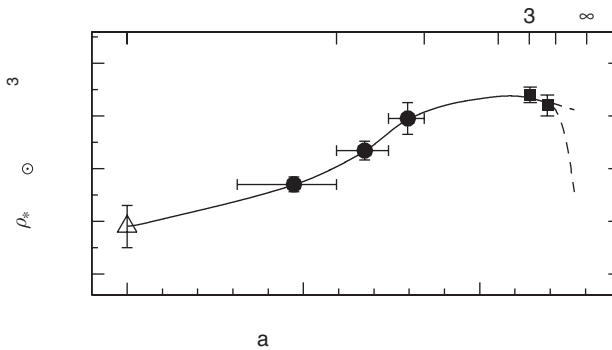
Fig. 12.4. Global co-moving star-formation rate density (assuming a Salpeter(0.1) IMF) compiled from surveys by Lilly *et al.* (1996), Connolly *et al.* (1997) and Steidel *et al.* (1999), assuming Einstein–de Sitter cosmology with $h = 0.5$. The point at zero redshift is based on an Hα survey by Gallego *et al.* (1995). After Pettini (1999). With kind permission of Springer Science and Business Media. Courtesy Max Pettini.

Furthermore, the monochromatic luminosity L_ν is related to the total luminosity (approximately) by the simple expression

$$L_\nu \simeq L/\nu_{\mathrm{Ly}} = 3 \times 10^{-16} L \ \mathrm{Hz}^{-1}. \tag{12.6}$$

When the light is dominated by massive stars, e.g. in starburst galaxies, the luminosity is related in turn to the rate of 'metal' production, since virtually all processed material is ejected in the form of 'metals' (and some helium). Thus there is a relationship between the total co-moving luminosity density, the monochromatic luminosity density (deduced from star-forming galaxy redshift surveys with appropriate corrections for absorption) in a fixed frequency bandwidth (anywhere between 912 and about 2000 Å in the rest frame) and the mass going into nucleosynthesis:

$$\rho_L(z) = \nu_{\mathrm{Ly}} \rho_{\nu\,\mathrm{UV}}(z) = \frac{1}{\epsilon} L_{\mathrm{FIR}}(z) \tag{12.7}$$

$$= 0.007 c^2 \dot{\rho}_Z(z)(1+a)/\beta \tag{12.8}$$

$$= 0.018 c^2 \dot{\rho}_Z(\mathrm{conv.}), \tag{12.9}$$

where ϵ is the fraction absorbed and re-radiated in the far IR by dust, $(1+a) \simeq 2.6$ is a correction factor to allow for the synthesis of helium in addition to 'metals' and β (probably between about 1/2 and 1) allows for the possibility of fall-back of newly synthesized material into black hole remnants in the most massive stars. Equations (12.7) and (12.9) correspond to a straight mean of Eqs. (12) and (13) of Madau *et al.* for 1500 and 2800 Å respectively; hence the designation of $\dot{\rho}_Z$ derived in this way from $\rho_{\nu\,\mathrm{UV}}(z)$ as 'conventional'. Nevertheless it is fairly robust because changes in the IMF affect both quantities about equally. The conversion to star formation rates, on the other hand, is strongly dependent on the IMF. Madau *et al.* calculated that the yield from a Salpeter(0.1) IMF is $1/42\alpha$, making

$$\dot{\rho}_*(\mathrm{conv.\ Sal}) = 42 \dot{\rho}_Z(\mathrm{conv.}) = 42 \rho_L/0.018 c^2, \tag{12.10}$$

whereas that from the Scalo (1986) IMF is about 3 times lower (see Problem 3 of Chapter 7), making the SFR density correspondingly higher. Figure 12.4 shows the SFR density as a function of lookback time and redshift from similar considerations to those of Madau *et al.*, but based on wide-field ground-based surveys and with a correction for absorption, which brings the results more into line with deductions from near-IR (Connolly *et al.* 1997) and sub-mm data (e.g. Hughes *et al.* 1998). Heavens *et al.* (2004) give the star formation history divided among galaxies of different masses.

Integration over the SFR shown in Fig. 12.4 leads to the present-day stellar density

$$\rho_s(0) = \gamma\alpha\int\dot{\rho}_*(\text{conv. Sal})dt = 3.3\,\alpha\times 10^8\,M_\odot\,\text{Mpc}^{-3}, \tag{12.11}$$

or

$$\Omega_s = 0.0043\alpha, \tag{12.12}$$

where γ (taken here as 0.4) is a correction factor corresponding to an IMF resembling Kroupa–Salpeter (see Chapter 7) (Pettini 1999). This may be compared with the result of the 2DF local survey of the galaxy infrared luminosity function, which is $\Omega_s = (0.0016 \pm 0.00024)/h$ for the IMF adopted by Kennicutt (1983), effectively similar to Kroupa–Salpeter, or $0.0029/h$ for the Salpeter(0.1) IMF (Cole *et al.* 2001). Thus stars (with the Kennicutt or Kroupa–Salpeter IMF) account for about 6 per cent of the total baryons in the Universe (Fukugita & Peebles 2004). The corresponding 'metal' density is

$$\rho_Z(0)(\text{conv.}) \simeq 2.0\times 10^7\,M_\odot\,\text{Mpc}^{-3},\ \text{ or }\Omega_Z(\text{conv.}) \simeq 1.4\times 10^{-4}. \tag{12.13}$$

12.4 Cosmic chemical evolution: observations

12.4.1 High-z absorption-line systems

Absorption lines in the spectra of quasi-stellar objects (QSOs) showing emission lines at high redshifts can be categorized into several distinct classes. The majority arise from Lyman-α absorption by clouds lying at various redshifts along the line of sight to the QSO. These lines, extending from the Ly-α emission peak of the QSO down to the Ly-α rest wavelength, are known collectively as the 'Lyman-α forest' (although they include some higher Lyman lines as well). At low column densities, the absorbing systems have very low metallicities (of order 0.01 solar or less, although none have ever been found with metals definitely absent) and could be some mixture of filaments in the cosmic large-scale structure, isolated hydrogen clouds and extended outer halos of galaxies. With increasing column density, one finds a strengthening of so-called metal-line systems with lines of Mg II and C IV, which may come from the halos of large galaxies. When the column density $N(\text{H I}) \geq 3\times 10^{17}\,\text{cm}^{-2}$, one has so-called Lyman limit systems in which the absorption edge at the Lyman limit appears in the continuum (see Fig. 4.5). For H I column densities above $2\times 10^{20}\,\text{cm}^{-2}$, the Lyman-$\alpha$ line shows broad wings due to natural damping (Fig. 12.5) and these are known as damped Lyman-α systems or DLAs.[3]

An interesting feature of damped Ly-α absorbers is that their column densities (upwards of about $1\,M_\odot\,\text{pc}^{-2}$) are comparable to those of the outer parts of the

---

[3] DLAs and other intervening absorption-line systems are also found projected against the visual afterglows of long-duration γ-ray burst sources at high redshifts.
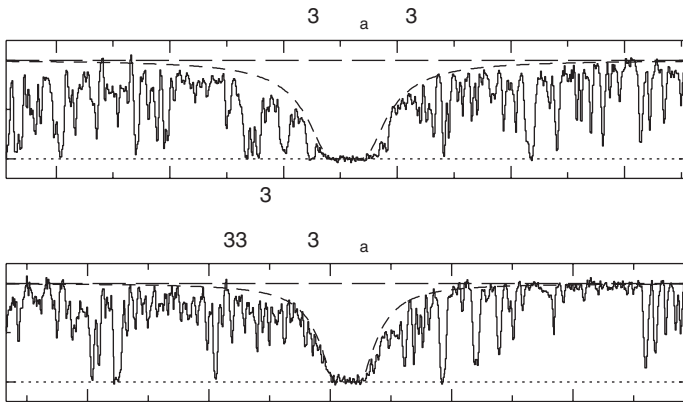
Fig. 12.5. Parts of the spectra of two QSOs (with emission redshifts 2.9 and 3.3 respectively) taken with the 4-m William Herschel Telescope on La Palma with a resolution of about $50\,\mathrm{km\,s^{-1}}$ showing Lyman-α lines with damping wings (column densities $N(\mathrm{H\,I}) \simeq 2 \times 10^{21}\,\mathrm{cm^{-2}}$ or $6\,M_\odot\,\mathrm{pc^{-2}}$ and $8 \times 10^{20}\,\mathrm{cm^{-2}}$ or $2.4\,M_\odot\,\mathrm{pc^{-2}}$ respectively). After Pettini *et al.* (1997).

disks of spiral galaxies, of which they could be precursors, in which most of the mass is still in the form of gas (Wolfe *et al.* 1986; Wolfe, Gawiser & Prochaska 2005). This idea receives some support from estimates of Ω_{HI}, defined as the co-moving density of H I absorbers (dominated by DLAs for $z \leq 5$) in units of the present-day critical density $\rho_{\mathrm{crit}} = 3H_0^2/8\pi G$ (Lanzetta *et al.* 1991). The argument is based on counts of systems with various column densities along the line of sight to many quasars in a suitable interval of redshift, and their co-moving density is given by

$$\Omega_{\mathrm{HI}} = \frac{H_0}{c}\frac{\mu m_{\mathrm{H}}}{\rho_{\mathrm{crit}}}\frac{\sum N(\mathrm{H\,I})}{\Delta X}, \qquad (12.14)$$

where ΔX is an interval of an 'absorption distance' X which is a dimensionless factor relating the proper column density as a function of redshift to the volume density for a non-evolving population that maintains its density in co-moving coordinates. If the present volume density is ρ_0, then by the definition of X the column density by mass is

$$\mu m_{\mathrm{H}} N = X\rho_0 c/H_0 = \rho_0 \int_{t(z)}^{t_0} [a(t)]^{-3}c\,dt = \rho_0 c \int_z^0 (1+z)^3\frac{dt}{dz}\,dz, \qquad (12.15)$$

where $a(t)$ is the expansion factor ($a(t_0) = 1$). Since $H_0 t = (1+z)^{-1}$ for a completely open Universe and $\frac{2}{3}(1+z)^{-3/2}$ for an Einstein–de Sitter Universe, the

corresponding absorption distances are given by

$$X(z) = \frac{1}{2}[(1+z)^2 - 1] \text{ (open), or } \frac{2}{3}[(1+z)^{3/2} - 1] \text{ (Einstein–de Sitter)}. \quad (12.16)$$

In a Λ cosmology, the corresponding formula is more complicated:

$$X(z_1) = \int_0^{z_1} (1+z)^2[(1+z)^2(1+z\Omega_M) - z(2+z)\Omega_\Lambda]^{-1/2}dz \quad (12.17)$$

(Bahcall & Peebles 1969; Péroux *et al.* 2003). Using Eqs. (12.16), Lanzetta *et al.* derived for redshifts around $z = 2.5$

$$\Omega_{HI} = 0.7 \times 10^{-3}h^{-1} \text{ for a completely open Universe} \quad (12.18)$$
$$= 1.3 \times 10^{-3}h^{-1} \text{ for an Einstein–de Sitter Universe}. \quad (12.19)$$

These and the more recent determinations shown in Fig. 12.6, based on Eq. (12.17) with matter density $\Omega_M = 0.3$, $\Omega_\Lambda = 0.7$ and $h = 0.65$, can be compared with
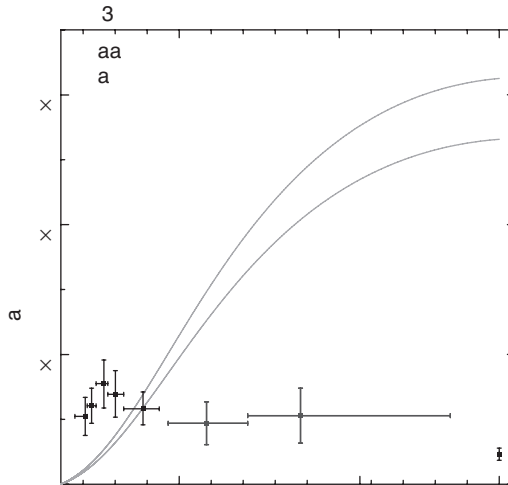
Fig. 12.6. Observable baryons in the Universe as a function of time. The curves represent the total mass density in stars (in $M_\odot \text{ Mpc}^{-3}$) from Rudnick *et al.* (2003) based on a survey of near-infrared selected galaxies in the Hubble Deep Field South, assuming a Salpeter(0.1) IMF. (For a Kennicutt (1983) IMF, the numbers would be approximately halved.) The points with error bars show the cosmic density of H I from DLAs and sub-DLAs at various redshifts, uncorrected for obscuration, while the point at bottom right shows the present-day density of H I clouds determined by Zwaan *et al.* (2005). The typical H I co-moving volume density corresponds to $\Omega_{HI} \simeq 0.7 \times 10^{-3}$ (taking $h = 0.65$). After Péroux, Dessauges-Zavatsky, D'Odorico *et al.* (2005).

the present-day mass density of galactic disks, $\Omega_{\text{disks}} \simeq 0.6 \times 10^{-3}$ (Fukugita & Peebles 2004), assuming a 'bottom-light' IMF, which agrees quite well, but the total density of stars is higher (Fig. 12.6). Thus, if DLAs are the gas reservoir for all star formation, they need to be replenished, e.g. by inflow from outside, and 'closed box' chemical evolution models cannot be applied to them (Wolfe, Gawiser & Prochaska 2005). On the other hand, Ω_{HI} could be larger if the largest column densities occur preferentially in dusty systems; these would have tended to be missed in optical surveys like SDSS because of obscuration of the background QSO (Pei & Fall 1995). Existing surveys of DLAs in front of radio-selected quasars do not provide more than marginal evidence for such an effect (Shaver *et al*. 1996; Ellison *et al*. 2001; Jorgenson *et al*. 2006), although they do not rule out factors of up to 2 or so. Tighter limits have been deduced from the relatively low amounts of dust implied by the low amount of depletion from the gas phase (Wolfe, Gawiser and Prochaska 2005). In any case, extensive measurements of H I column densities in DLAs and sub-DLAs show no clear sign of evolution over most of the time range (Fig. 12.6), although Prochaska, Herbert-Fort and Wolfe (2005) find a dip between $z = 2.0$ and 2.5.

Damped Ly-α absorbers are well suited to abundance analysis because the large column density ensures that O and N are essentially all in their neutral state while sulphur and metals are essentially all singly ionized, with column densities leading to readily measurable spectral features. Also, the degree of depletion from the gas phase by the formation of dust is lower than in the local ISM. Some typical metallicities (based on zinc which is not seriously depleted even in the local ISM) are shown in Fig. 12.7. Typically, abundances are low, with [Zn/H] ~ -1, but there is a large scatter and little sign of evolution with redshift or time, a
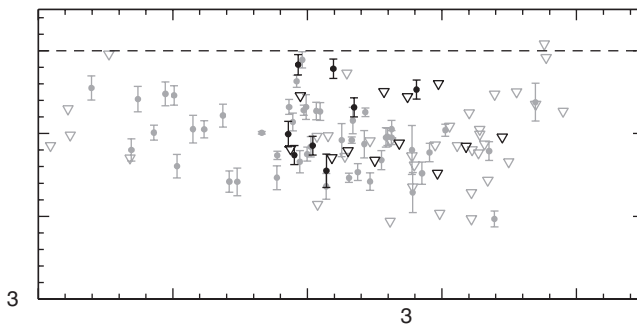
Fig. 12.7. Zn abundances in DLAs on lines of sight towards optically (faint symbols) and radio-selected (bold symbols) quasars; open triangles denote upper limits. The optically selected objects come from a compilation by Kulkarni *et al*. (2005). After Akerman *et al*. (2005).

situation reminiscent of that of the stars in the solar neighbourhood. However, surveys that include other elements besides zinc, using 10-m class telescopes, suggest an evolution in the average <[M/H]>, weighted by column density, decreasing linearly with z from -0.8 around $z \simeq 0.9$ to -1.5 around $z \simeq 4$ (Wolfe, Gawiser & Prochaska 2005; see data points in Fig. 12.14). Nevertheless, the existence of DLAs with [M/H] < -1 at redshifts below 1.8, corresponding to the 10-Gyr age of the Galactic thin disk, discourages identification of their chemical evolution exclusively with that of a galaxy like our own; alternative suggestions are that they can be progenitors of dwarf (Calura, Matteucci & Vladilo 2003) or low-surface-brightness galaxies (Jimenez, Bowen & Matteucci 1999).

Investigations of the α/Fe ratio are complicated by differential depletion of different elements on to dust; there is good evidence for an α-enhancement, in some cases showing a similar abundance pattern to Lyman-break galaxies (see next section) and ellipticals (Prochaska, Howk & Wolfe 2003), but not in others. There are significant effects involving nitrogen (see Fig. 11.7); in some cases, the N/O ratio is similar to that in local irregular and blue compact dwarfs, implying an age exceeding 0.25 to 0.5 Gyr according to Fig. 11.9, while in others it is much lower. A curious feature of DLA metallicities is an apparent anticorrelation with H I column density (Boissé *et al.* 1998; see Fig. 12.8), which could well be due to dust obscuration, although within the limited statistics of the sample optically and radio selected systems behave in much the same way. The lower bound of the correlation could easily be due to selection effects (Prantzos & Boissier 2000).
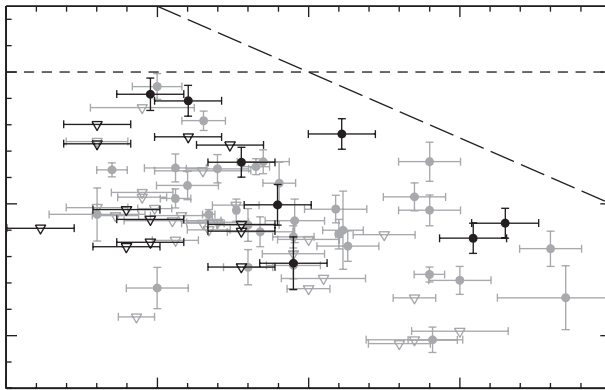
Fig. 12.8. Plot of Zn abundance in DLAs vs. H I column density, for redshifts between 1.86 and 3.45. Symbols as in Fig. 12.7. The diagonal line, corresponding to $\log N_{Zn} = 13.46$, delimits an apparent 'zone of avoidance' first noted from optically selected samples by Boissé *et al.* (1998) as modified by Prantzos and Boissier (2000). After Akerman *et al.* (2005).

The near-absence of DLAs with $\log N_{Zn} > 13.2$, corresponding to an obscuration of the order of one magnitude in the rest-frame UV, supports the existence of some obscuration and implies some biases in the H I column density distribution and perhaps in the column-density-weighted metallicity, but these cannot be very large (Akerman *et al*. 2005). The type of object that can be missed is one not shown in the figure: a system at a redshift of 0.52 towards the BL Lac object[4] AO 0235 +164, with an H I log column density of about 21.7, $Z \simeq (0.7 \pm 0.3) \, Z_\odot$ and about 1/2 to 1 magnitude of extinction in the visible (Junkkarinen *et al*. 2004).

At lower column densities, one is looking at systems where only a small fraction of the hydrogen is neutral; metal lines (e.g. C II–IV, Si II–IV) are weak and quantitative abundance estimates require an understanding of the ionizing radiation field, which may involve uncertainties of a factor of 3 or more; the O VI doublet at $\lambda\lambda$ 1032, 1037 Å, an important diagnostic, suffers from obscuration by the Ly-α forest. Existing results show a correlation with column density, with $<[O/H]> \sim -1.5$ for $N(\text{H I}) \geq 10^{15} \, \text{cm}^{-2}$ and ~ -2.5 for $10^{14.5} \leq N(\text{H I}) \leq 10^{15} \, \text{cm}^{-2}$, perhaps reflecting an increase in local pollution from nearby galaxies in denser regions (Carswell 2004). At still lower column densities, there is even more uncertainty, but metal lines have never been found to be demonstrably absent.

12.4.2 *Lyman-break galaxies and sub-mm galaxies*

The star-forming Lyman-break galaxies (LBGs) present a rather different picture of chemical evolution from that of the DLAs at the same redshifts – although some members of the two classes could be related in some way (e.g. as galactic disks to bulges) – in that they are relatively metal-rich, as evidenced from both stellar absorption lines (including the P Cygni component of C IV λ 1550) and emission lines from H II regions (using either R_{23} or the [N II]/Hα calibration which behaves rather like the [N II]/[O III] calibration shown in Fig. 3.26). Figure 12.9 displays a composite spectrum of the young stellar populations of LBGs, and Fig. 12.10 shows synthetic spectra of a particular system (cB58) suggesting a metallicity close to 0.4 solar, which agrees with a deduction from R_{23} measured with the aid of infrared array detectors (Teplitz *et al*. 2000). Other LBGs show [N II]/Hα ratios which indicate still higher abundances in some cases, approaching (or possibly even exceeding) solar (Erb *et al*. 2006). Interstellar absorption lines in cB58 are broad, indicating massive outflows, and suggest an abundance pattern differing from that found in most DLAs, with a higher overall metallicity and a clear enhancement of the Mg/Fe ratio as well as deficiency of nitrogen (also found in some DLAs), but sharing with DLAs a milder degree of depletion on to dust than

---

[4] BL Lac objects are violently variable AGNs in which the continuum is much stronger relative to emission lines than in the classical QSOs.
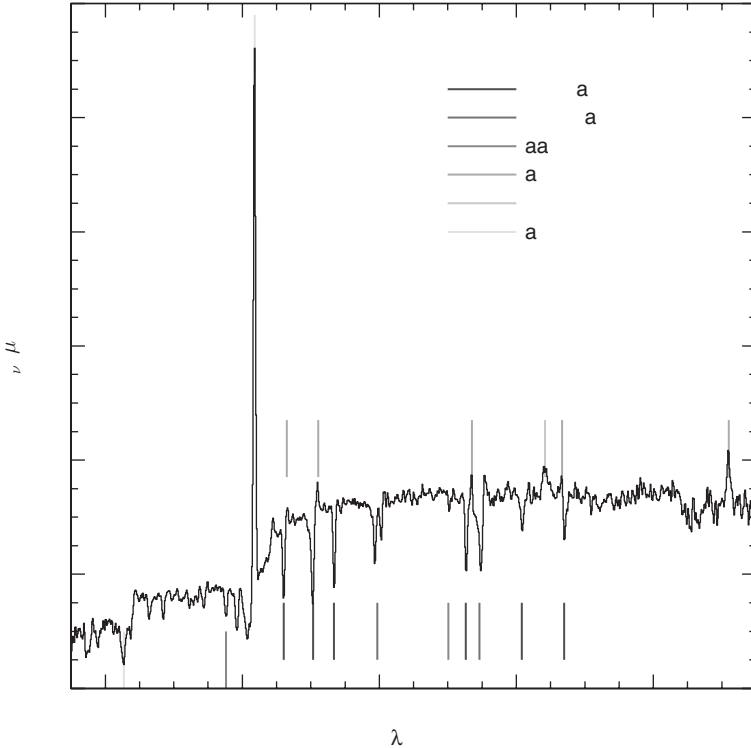
Fig. 12.9. Composite spectrum of Lyman-break galaxies showing a combination of interstellar and stellar absorption lines, P Cygni features and nebular emission lines, dominated by Lyman-α. After Shapley *et al*. (2003).

is found in the local ISM (Fig. 12.11). These features indicate a young system undergoing rapid star formation, possibly destined to become an elliptical galaxy (Pettini *et al*. 2002b).

LBGs in general display the same clustering properties as elliptical galaxies and a mass–metallicity relation similar to that of local star-forming galaxies, but shifted a factor of about 2 lower at a given stellar mass; rough estimates of the gas fractions (median 0.5, compared to 0.2 for the local sample) suggest a similar effective yield for the whole mass range, reduced by mass loss to either 1/2 or 1/4 of the true yield according as to whether a Salpeter(0.1) or a more bottom-light IMF is assumed (Erb *et al*. 2006). (See Chapter 8, Problem 8, for the relation between abundance and gas fraction.)

Sub-mm galaxies are another class of star-forming galaxies at typical redshifts around 2 found using the SCUBA detector[5] and pin-pointed from their radio

[5] Sub-mm Common User Bolometric Array on the James Clerk Maxwell Telescope (JCMT) on Hawaii.
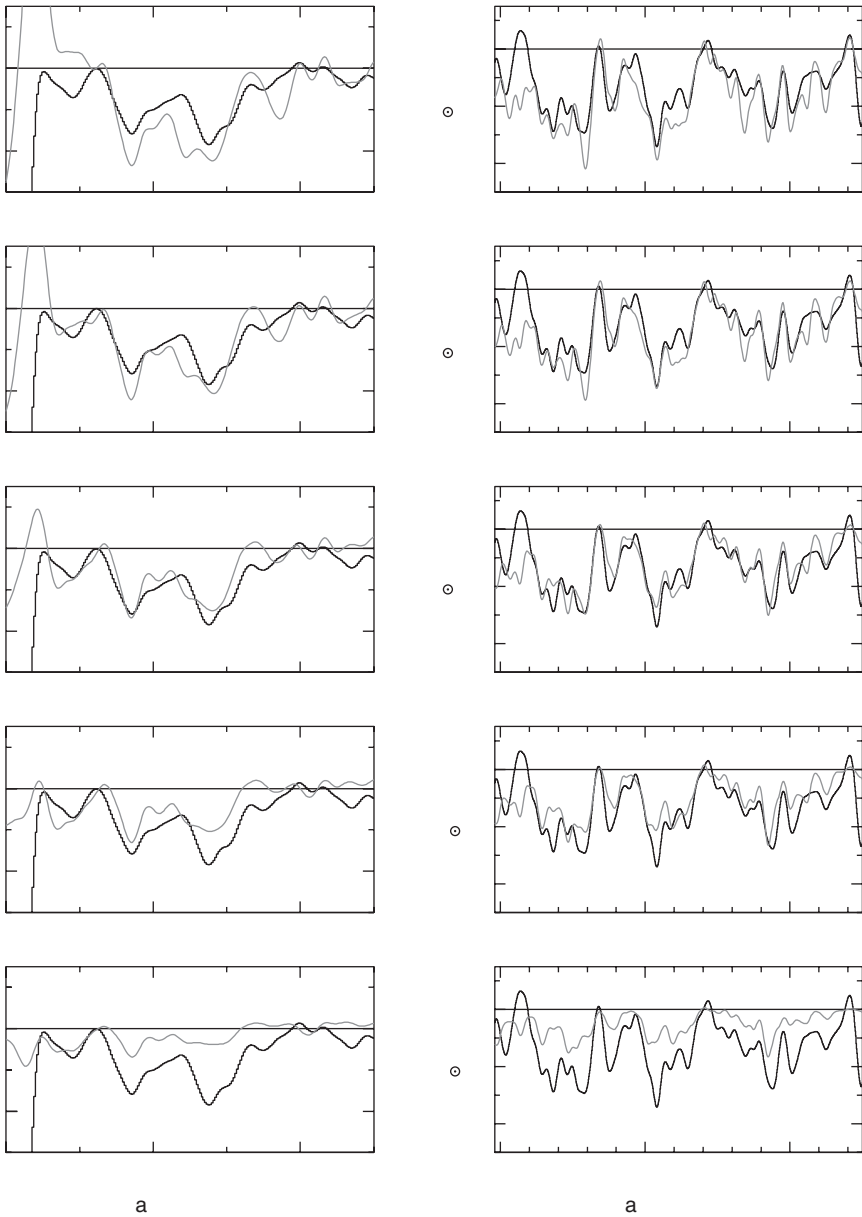
Fig. 12.10. Comparison of the observed spectrum of the gravitationally lensed LBG MS 1512-cB58 (bold), with a redshift of 2.7, with synthetic spectra calculated with *Starburst 99* together with the theoretical spectral library *WM-basic* for various metallicities (faint). The left panels show the region of the λ 1425 complex (a blend of Si, C and Fe photospheric lines), while the right panels show photospheric features of Fe III between 1900 and 2000 Å. After Rix *et al.* (2004).

aaaaa
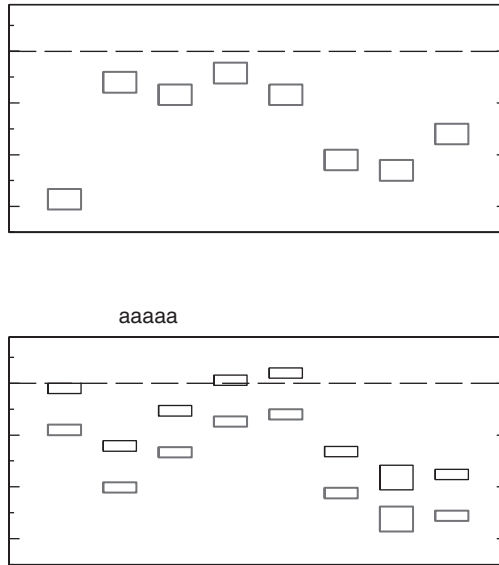
Fig. 12.11. Top panel: abundances in the interstellar medium of cB58. Lower panel: abundances of the corresponding elements in diffuse clouds of the Milky Way and the same, shifted down by 0.4 dex, to facilitate comparison with cB58. After Pettini *et al.* (2002b).
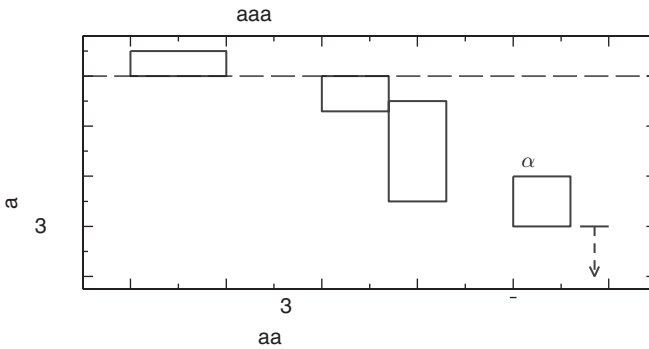
Fig. 12.12. Summary of metallicities of representative objects at redshifts around 2.5. After Pettini (2006). Courtesy Max Pettini.

emission (Smail, Ivison & Blain 1997; Ivison *et al.* 2005), in which there is strong obscuration of the optical and near infrared by dust. Typical stellar masses are large in comparison with LBGs, and emission and absorption-line spectra suggest comparably high metallicities.

Abundances of various types of object at redshifts of order 2 to 3 are summarized in Fig. 12.12, which displays a clear relation with linear scale, or perhaps

ambient density; the wide range at a given redshift or time completely swamps any hypothetical dependence on time. It is noteworthy that quasars display solar or super-solar metallicity levels at the highest redshifts ($z \simeq 6$) at which they have been observed, implying significant star formation at still higher redshifts (Hamann *et al*. 2004).

12.5 Cosmic chemical evolution: models

Pei, Fall and Hauser (1999), among others, have calculated models of 'cosmic chemical evolution' (basically evolution of a typical galaxy identified with DLAs) assuming instantaneous recycling and constant yields in the framework of an Einstein–de Sitter cosmological model with $h = 0.5$. The basic equations are similar to those of Section 7.4.2, but now expressed in terms of the mean co-moving densities of stars, Ω_s, and gas (+ dust), Ω_g, measured in units of the present-day critical density. Treating the damped Ly-α systems as galaxies that can exchange matter with their surroundings (or with other phases such as ionized gas), the analogues of Eqs. (7.31), (7.35) are, with some rearrangement,

$$\dot{\Omega}_F - \dot{\Omega}_E = \dot{\Omega}_g + \dot{\Omega}_s; \tag{12.20}$$

$$\Omega_g \dot{Z} = p\dot{\Omega}_s + (Z_F - Z)\,\dot{\Omega}_F, \tag{12.21}$$

where the dots denote differentiation with respect to cosmic time. In the scenario of Pei, Fall and Hauser, the initial conditions are

$$\Omega_g(t = 0) = \Omega_s(t = 0) = Z(t = 0) = 0, \tag{12.22}$$

so at any time

$$\Omega_F - \Omega_E = \Omega_s + \Omega_g, \tag{12.23}$$

and, taking $Z_F = 0$,

$$Z = pe^{-f(t)} \int_0^t \frac{\dot{\Omega}_s}{\Omega_g} e^{f(t')} dt', \tag{12.24}$$

where

$$f(t) \equiv \int_0^t \frac{\dot{\Omega}_F}{\Omega_g} dt'. \tag{12.25}$$

Ω_g and its derivative are deduced as a function of redshift from the distribution of H I column densities as in Eq. (12.14), with a very substantial allowance for obscuration by dust, which is calculated iteratively assuming a constant ratio of dust to heavy-element content in the ISM, $\Omega_d = 0.045 Z\Omega_g$, and different assumptions about its distribution. The co-moving star formation rate density is derived from the same data as are represented in Fig. 12.4, assuming a Salpeter(0.1) IMF

a
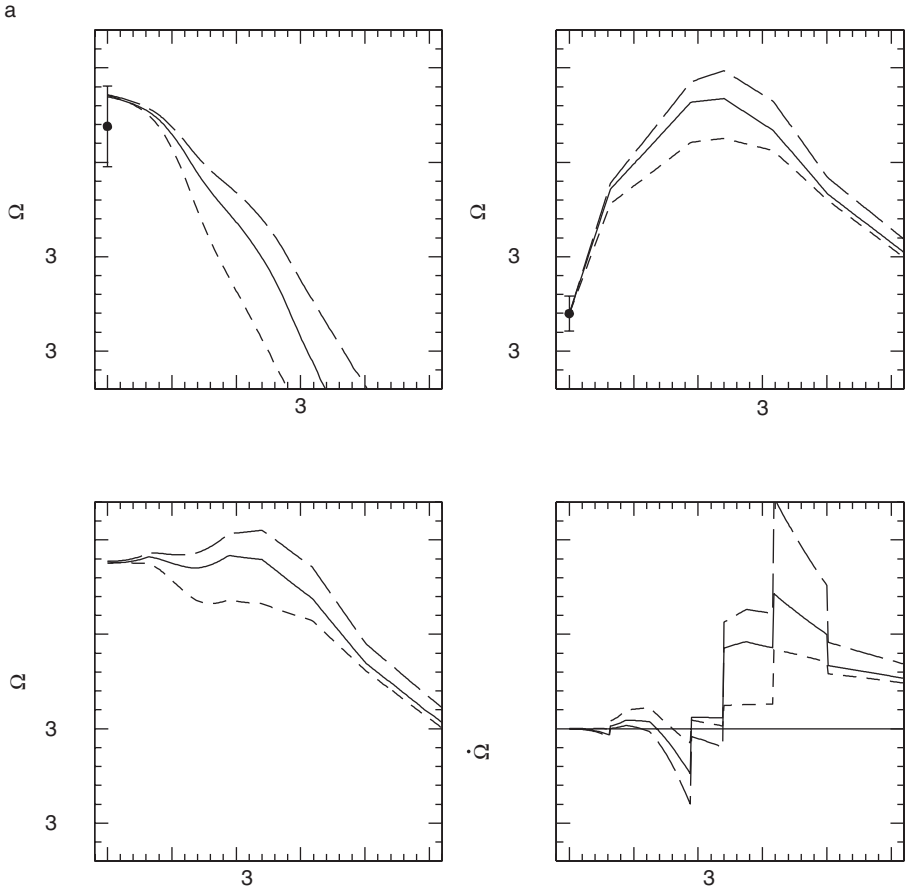
Fig. 12.13. Model evolution of stars and gas in DLAs. (a) Co-moving density of stars. (b) Co-moving density of interstellar gas. (c) Co-moving density of baryons (i.e. stars + gas). (d) Co-moving rate of baryon flow between the interstellar and intergalactic media. The data point for $\Omega_s(0)$ is an estimate from the mean blue luminosity density and M/L_B ratio of galaxies (Fukugita, Hogan & Peebles 1998). Continuous and broken curves represent preferred and maximal or minimal model solutions. After Pei, Fall and Hauser (1999).

and again with an allowance for absorption using dust models consistent with the infrared properties of nearby galaxies and the far IR extragalactic background as shown in Fig. 12.1. This combination gives $\dot{\Omega}_F - \dot{\Omega}_E$; when this is positive, representing episodes dominated by inflow (see Fig. 12.13), $\dot{\Omega}_E$ is neglected, while when it is negative, representing episodes dominated by outflow, $\dot{\Omega}_F$ is neglected, so that $f(t)$ is constant. The metallicity evolution is then calculated by numerically integrating Eq. (12.24), assuming a yield of $0.45\, Z_\odot$, chosen to give solar abundance at the present time (Fig. 12.14). There is a fairly good fit to the data
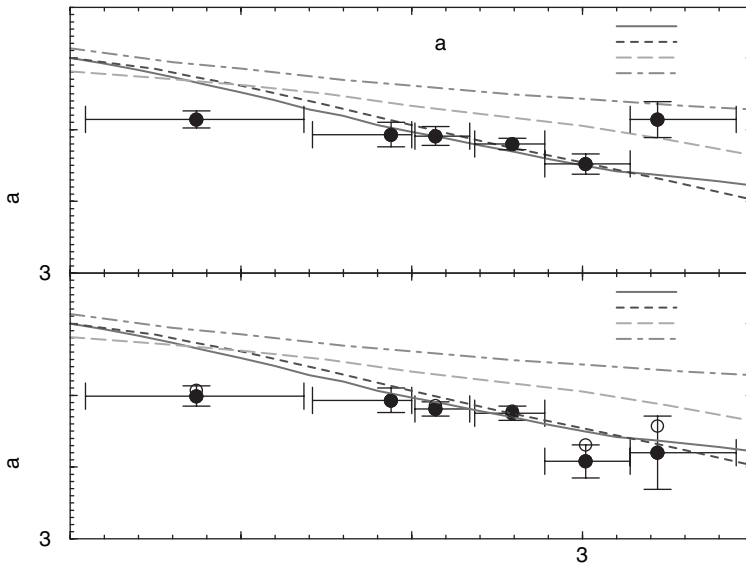
Fig. 12.14. Metallicity evolution in DLAs. Curves show predicted mean metallicity in the interstellar gas relative to solar predicted by chemical evolution models of Pei, Fall and Hauser (1999), Pei and Fall (1995), Malaney and Chaboyer (1996) and Somerville, Primack and Faber (2001) respectively. Data points giving column-density weighted metallicities based on zinc only (filled circles) or other elements (open circles) are plotted in the upper panel taking upper limits as detections and in the lower panel taking upper limits as zeros. Horizontal error bars show the redshift bins adopted. After Kulkarni *et al.* (2005).

points shown there, or to the findings of Wolfe, Gawiser and Prochaska (2005), but the LBGs seem to tell quite a different story (see Fig. 12.12), so this is at best only a partial picture of cosmic chemical evolution. The model does agree very well with the lower limits to extragalactic background light based on faint galaxy counts (Fig. 12.1). With the exception of the point at $60\,\mu$m, direct estimates of diffuse light suggest higher values, especially in the near infrared, which have inspired suggestions that these could be a signal of the earliest 'Population III' stars ever formed (Kashlinsky 2005). However, there are problems in allowing for the large foreground from zodiacal light and the results of observations of high-energy γ-rays seem to exclude a large excess above the background expected from the galaxy counts (Aharonian *et al.* 2006; Dwek, Arendt & Krennrich 2005), although a small contribution from Population III or some other exotic source could still be present (see Kashlinsky *et al.* 2007).

More light on cosmic chemical evolution in general is shed by large-scale hydrodynamical cosmological simulations (Cen & Ostriker 1999) based on an updated

Universe model; specifically $\Omega_M = 0.37$, $\Omega_b = 0.037$, $\Omega_\Lambda = 0.63$, $h = 0.7$. The key lies in the dependence of star formation rate on ambient density and temperature, roughly parameterized by the relative overdensity $\delta \equiv \rho/\langle\rho\rangle - 1$, the change in physical density from expansion being partly compensated by the drop in ambient temperature. Galaxies and clusters of stars are deemed to be formed in a cell in the computation when three criteria are satisfied (Cen & Ostriker 2000):

$$\nabla.\mathbf{v} < 0; \tag{12.26}$$

$$\text{Gas mass} > \text{Jeans mass}; \tag{12.27}$$

$$\text{Cooling time} < \text{gravitational collapse time}. \tag{12.28}$$

The result is that when δ is large, stars form rapidly, roughly as in a Schmidt Law in volume density with $n \sim 2$, until star formation is quenched by shocks and there is a saturation; conversely, when it is small, there is a much more gradual process. Figure 12.15 shows the resulting metallicity evolution with time for different δ's, assuming a yield $p = 0.02 \simeq Z_\odot$.
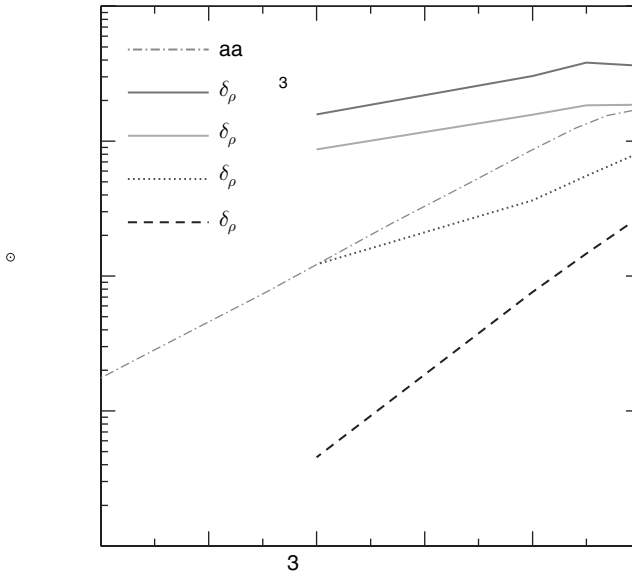
Fig. 12.15. Growth of metallicity with time in regions of differing overdensity, corresponding approximately to clusters of galaxies ($\delta = 10^3$; thick curve), DLA and Lyman-limit systems ($\delta = 10^2$; thinner curve), moderate-column-density Ly-α clouds ($\delta = 10$; dotted curve) and low-column-density Ly-α clouds ($\delta = 0$; dashed curve), The dot-dashed curve shows the global average. After Cen and Ostriker (1999). Courtesy Renyue Cen.

12.6 An inventory of baryons and metals in the Universe

There is enough information available to try to put together (not for the first time) an inventory of the smoothed-out cosmic mass density of baryons and metals in the known Universe, both now and at redshifts between 2 and 3. A proposed inventory, in units of the present-day closure density $1.5 \times 10^{11} \, (h/0.73)^2 \, M_\odot \, \mathrm{Mpc}^{-3}$ (assuming $h = 0.73$) is shown in Table 12.1, which is largely based on work by Finoguenov, Burkert and Böhringer (2003). The lower limit to present-day stellar density is in agreement with the survey by Fukugita and Peebles (2004), following earlier work by Persic and Salucci (1992) and by Fukugita, Hogan and Peebles (1998), while the upper limit allows for more bottom-heavy IMFs (e.g. Salpeter(0.1)) than adopted by Fukugita and Peebles. The mean stellar metallicity is assumed to be more-or-less solar (Phillipps & Edmunds 1996), leading to an observationally based range for the stellar contribution to Ω_Z. The second row refers to an apparently very significant – if still somewhat uncertain – population of hot intergalactic gas detected by means of its O VI absorption, which could account for as much as 1/2 of the total baryon density from cosmological nucleosynthesis and WMAP, shown in the last line; its contribution to overall metals appears to be about the same as that of stars (Finoguenov, Burkert & Böhringer 2003). The predicted total for Ω_Z, which also appears in the last line of the upper part of

Table 12.1. *Baryon and metal budgets, for $z = 0$ and $z \simeq 2.5$*

Component	Ω_b, 10^{-2}			Z, 10^{-2}	Ω_Z, 10^{-5}	
				$z = 0$		
Stars	$0.2 - 0.4$			1.2^a	$2.3 - 4.6$	— Most
O VI absorbers	$0.7 - 2.0$	— Most		0.26	$1.8 - 5.2$	— met.
Ly-α forest	$1.0 - 1.5$	— bar.		0.01	0.1	
X-r gas, clusters	0.2			0.7	$1.4 - 1.8$	
Total	$2.1 - 4.1$			0.28	$5.6 - 11.7^b$	
Predicted	3.9				$6 - 12$	
				$z = 2.5$		
Protocl. gas	0.2			0.7	1.4	
Stars (LBGs)	$0.05 - 0.1$			1.0	$0.5 - 1.0$	
ISM, dust	$0.02 - 0.04$	Most		0.8	$0.2 - 0.4$	
Ly-α forest	$1 - 5$	— bar.		0.01	$0.1 - 0.5$	
DLAs	0.25			0.1	0.25	
Total	$1.5 - 5.5$			0.1	$2.3 - 3.6$	
Predicted	3.9				$1.5 - 3.0$	

^{a}i.e. approximately solar.
$^b \Rightarrow$ yield $\equiv \Omega_Z / \Omega_{\mathrm{stars}} \simeq 0.028$.

the table, comes essentially from the 'Madau plot', updated and normalized to the present-day stellar density as in Eq. (12.13); it is not very dependent on the IMF. The upshot is that O VI absorbers could account for the bulk of 'baryonic dark matter'. Two interesting numbers come out of this table: the mean metallicity of the Universe $\langle Z \rangle \equiv \Omega_Z/\Omega_b$ is between 1.4 and 3×10^{-3}, or 0.1 to 0.2 solar (see Fig. 12.15), and the yield $p \equiv \Omega_Z/\Omega_s \simeq 0.028$, again with little sensitivity to the IMF, but much to the abundance and metallicity of the O VI absorbers. Taken at face value, it is quite consistent with a universal IMF close to Salpeter(0.1), in agreement with detailed model calculations for different sorts of galaxies in a cosmological context by Calura and Matteucci (2004).

At redshifts between 2 and 3, most baryons are in the Lyman-α forest, where the neutral hydrogen is but a tracer of a vastly greater amount of ionized gas (Rauch *et al*. 1997). There has been less certainty as to the whereabouts of the 'metals', predicted to have about 1/4 of their present-day abundance because about 1/4 of the stars were in place by a redshift of 2.5, and the metals in DLAs and the Lyman forest fall far short of this (Pettini 1999). Star-forming galaxies (LBGs) could contribute up to about 1/5 of the shortfall (Bouché, Lehnert & Péroux 2006). The contribution of dust, estimated to be substantial in the form of sub-mm galaxies by Dunne, Eales and Edmunds (2003), is restricted to under 10 per cent according to Bouché, Lehnert and Péroux (2005). Finoguenov, Burkert and Böhringer (2003) identify the remainder as belonging to gas that has later ended up in clusters of galaxies and that was already enriched by a first generation of stars before the cluster collapsed. As we mentioned in Section 11.3.5, the large amount of metals relative to the mass of associated stars requires high yields, which in turn implies a relatively top-heavy IMF for this early generation, but this does not significantly affect the overall yield from later stellar activity.

12.7 Metals in the Universe and diffuse background radiation

As was mentioned in Section 12.1, there is a relationship between metal production and diffuse background radiation, perhaps more properly referred to as extragalactic background light (EBL), shown in Fig. 12.1, since most or all of it comes from individual galaxies.

The EBL consists of three major contributions:

- Stellar radiation peaking in the visible in the rest-frame and with a redshifted component in the near IR.
- Radiation in the far IR from either cool dust associated with 'cirrus' or warm dust associated with active star formation in luminous and ultra-luminous infrared galaxies.

- Radiation from AGNs, some of which can also be reprocessed by dust, but which differs from the other two sources in being powered by gravitational rather than nuclear energy and therefore not associated with nucleosynthesis. This contribution is probably minor, however, based on the abundance of massive black holes (Madau & Pozzetti 2000), or on that of obscured hard X-ray sources (Brusa, Comastri & Vignali 2001).

Gispert, Lagache & Puget (2000) have estimated the total EBL based on observation to lie within the following limits:

$$\begin{array}{llll} \lambda \leq 6\,\mu\text{m} & 20 \text{ to } 40 & \text{nwt m}^{-2}\,\text{sterad}^{-1} \\ \lambda > 6\,\mu\text{m} & 40 \text{ to } 50 & " & " \\ \text{Total} & 60 \text{ to } 90 & " & " \end{array}$$

(The total from the model of Pei, Fall and Hauser is 55 in these units.)

We now consider how these totals relate to the abundance of helium and heavier elements in the Universe (see Songaila, Cowie & Lilly 1990; Pagel 2002). The argument is that all the heavier nuclei ever created are still here, as are the photons not absorbed by dust. Reprocessing by dust still conserves energy, however, which is only degraded by a factor of $(1 + z)$; in our simple crude approach we take this to be constant at a typical value of order 2 (see Lagache, Puget & Dole 2005). We can thus write

$$I_{\text{bol}} = 0.007\beta^{-1}\frac{c^3}{4\pi}\langle\frac{1}{1+z}\rangle\rho_b\langle Z + \Delta Y\rangle$$

$$= 7.5 \times 10^4\,\beta^{-1}\,\Omega_b\,\langle Z + \Delta Y\rangle\,\langle\frac{2}{1+z}\rangle \tag{12.29}$$

nwt m^{-2} ster^{-1}, with $\langle Z + \Delta Y\rangle = (1+a)\langle Z\rangle \simeq 2.6\langle Z\rangle$. From Table 12.1 we have the following contributions:

- Metals in stars, $\Omega_Z = (2.3 \text{ to } 4.6) \times 10^{-5}$: $I_{\text{bol}} = (4.5 \text{ to } 9)\beta^{-1}$.
- Metals in diffuse gas, $\Omega_Z = (3.3 \text{ to } 7.1) \times 10^{-5}$: $I_{\text{bol}} = (6 \text{ to } 14)\beta^{-1}$.

Together these could account for up to about 25 nwt m^{-2} ster^{-1}, perhaps mostly in the mid and far infrared. The chief component remaining (probably mostly in the visible, near IR and near UV) comes from stellar fuel consumption not resulting in the ejection of products into the ISM; these products are largely locked up in white dwarfs and the interior of red giants, where $Z + \Delta Y \simeq 1$ while $a = 0$. The co-moving density of white dwarfs and other compact remnants is about 10 per cent of the stellar density for a Salpeter(0.1) IMF, or about 0.0004 (Fukugita & Peebles 2004), leading to

- He, C, O etc. in white dwarfs, $\Omega_Z \simeq 4 \times 10^{-4}$: $I_{\text{bol}} \simeq 30$.

The result of these simple considerations is thus to account for about 55 nwt m^{-2} ster^{-1}, much the same as in the model by Pei, Fall and Hauser; it is striking to find the major contribution coming from white dwarfs. AGNs may account for another 5 or so nwt m^{-2} ster^{-1}, so that the minimal estimate of EBL is more or less accounted for by the distribution of the elements. If the true EBL intensity were closer to the maximal estimates, then there would appear to be a shortfall and one might need to search for more exotic explanations, but at the time of writing that seems less likely.

Notes to Chapter 12

Excellent introductions to cosmology, galaxy surveys, theories of structure formation and background radiation can be found in

   M. S. Longair, *Galaxy Formation*, Springer, Berlin, 1998, and

   John A. Peacock, *Cosmological Physics*, Cambridge University Press 1999.

Many aspects of background radiation at all wavelengths are discussed in

   B. Rocca-Volmerange, J. M. Deharveng and J. T. T. Van (eds.), *The Early Observable Universe from Diffuse Backgrounds*, Ed. Frontières, Gif-sur-Yvette, 1991. Infrared aspects are covered in M. Harwit and M. G. Hauser (eds.), IAU Symposium no. 204: *The Extragalactic Infrared Background and its Cosmological Implications*, 2001; by Lagache, Puget and Dole (2005) and by Kashlinsky (2005).

Problems

1. Justify Eq. (12.1).

2. If, on average, a total column density of 10^{20} H I atoms is found in the interval of redshift 2.0 to 2.5 along one line of sight by counting damped Lyman-α systems, make an estimate of Ω_{HI} for the two Universe models without cosmological constant discussed in the text.

3. Show that, in a flat Universe model with a cosmological constant, Eq. (12.17) reduces to

$$X(z_1) = \int_0^{z_1} (1 + z)^2 [\Omega_{\mathrm{M}}(1 + z)^3 + \Omega_\Lambda]^{-1/2} dz \qquad (12.30)$$

$$= \frac{2}{3\Omega_{\mathrm{M}}} [\{\Omega_{\mathrm{M}}(1 + z_1)^3 + \Omega_\Lambda\}^{1/2} - 1], \qquad (12.31)$$

where Ω_{M} is the density of matter.

Appendix 1

Some historical landmarks

1675	Measurement of the speed of light (Ole Rømer).
1687	Publication of Newton's *Principia*.
1780–1800	W. Herschel studies Galactic structure by counting stars.
1784	Messier catalogue inspires Herschel's study of 'nebulae'. Herschel later speculated that some were gaseous 'proto-stars', others unresolved stellar systems over a million light years away. He also identified 'strata of nebulae' related to the Local Supercluster of galaxies.
1803	John Dalton's Atomic hypothesis.
1814	J. Fraunhofer locates and names 'Fraunhofer lines' A...L in solar spectrum. About the same time, Herschel discovers infrared radiation from the Sun.
1816	William Prout's 'composite atoms' hypothesis.
1859–60	G. Kirchhoff and R. Bunsen discover spectral analysis and significance of Fraunhofer lines; Kirchhoff's law.
1868	J. Janssen and N. Lockyer independently discover helium from yellow emission line ('D3') in spectrum of prominence seen at eclipse.
1869	D. I. Mendeleev's Periodic Table of the elements.
1880s	Stellar spectral classification. W. Huggins discovers spectroscopic distinction between ionized gaseous nebulae (mainly emission lines) and unresolved star clusters and galaxies (mainly absorption lines). Development of statistical mechanics by Maxwell, Boltzmann *et al.*
1896	Radioactivity discovered by H. Becquerel.
1897	Electron discovered by J. J. Thomson.
1900	Planck's radiation formula.
1905	Special Relativity.

1906	Rutherford shows age of Earth is about a Gyr or more from radioactive dating.
1911	Rutherford's model of nuclear atom.
	Victor Hess discovers cosmic rays.
1913	Bohr's model of the hydrogen atom. Identification of atomic number with nuclear charge number (H. Moseley).
	Hertzsprung–Russell (HR) diagram.
1916	General Relativity.
1917	Einstein develops first relativistic cosmological model and introduces concepts of transition probabilities and stimulated emission.
	H. Shapley locates Galactic centre at centre of system of globular clusters, now thought to be 8.5 kpc away.
1919	Rutherford induces nuclear reaction $^{14}N(\alpha, p)^{17}O$.
	Aston develops mass spectrometer.
	General Relativity confirmed by eclipse observation.
1921	K. Lundmark introduces idea of a supernova, orders of magnitude brighter than an ordinary nova.
1923	M. N. Saha's ionization equation.
1924–7	M. N. Saha, R. H. Fowler, E. A. Milne and Cecilia Payne (later Payne-Gaposchkin) interpret stellar spectral sequence as temperature sequence with (mostly) constant chemical composition; crude abundances derived.
	A. S. Eddington develops theory of radiative equilibrium (building on earlier work by A. Schuster and K. Schwarzschild) and applies it to internal constitution of stars. He also pioneers physics of interstellar gas.
1925	E. Hubble uses Cepheid period–luminosity law to demonstrate M31 is an external galaxy comparable to the Milky Way.
1926	Rise of quantum mechanics.
1928	B. Lindblad and J. H. Oort discover Galactic rotation.
	Theory of α-radioactivity by quantum tunnelling (Gamow *et al.*).
	Cecilia Payne (later Payne-Gaposchkin) applies Saha's equation to the stellar spectral sequence, finding vast predominance of hydrogen and helium, but does not believe her results.
1929	H. N. Russell analyzes solar spectrum with theoretical transition probabilities and eye estimates of line intensities. Notes predominance of hydrogen (also deduced independently by Bengt Strömgren from stellar structure considerations) and otherwise similarity to meteorites rather than Earth's crust. M. Minnaert *et al.* introduce quantitative measurements of equivalent width, interpreted by the curve of growth developed by M. Minnaert, D. H. Menzel and A. Unsöld.

Hubble announces velocity–distance law.

R. Atkinson and F. Houtermans apply Gamow's theory of potential barrier penetration by quantum tunnelling to suggest how stars can release nuclear energy by synthesis of hydrogen into helium by an (unspecified) cyclic process.

1930   Neutrino hypothesis (Pauli).

1931   Discovery of deuterium (Urey), and of radio waves from the Galaxy (Jansky).

1932   Discovery of the neutron (Chadwick) and positron (Dirac, Anderson). First nuclear reaction induced in an accelerator (^{7}Li(p, α); Cockcroft and Walton). Baade and Zwicky suggest a neutron star may be created as residue of a supernova explosion.

W. H. McCrea develops models of atmospheres of A-type stars in radiative equilibrium with opacity due to H I.

1933   Atomic nucleus identified as an assemblage of protons and neutrons (Heisenberg).

1934   Russell explains spectra of carbon stars (types R, N, S) as consequence of reversal of the usual C/O ratio.

1935   Meson hypothesis (Yukawa).

1936   Compound nucleus theory (Bohr).

1938   H. Bethe and C. von Weizsäcker discover CNO cycle and pp chain. Discovery of nuclear fission (Hahn, Strassmann, Meitner, Frisch).

1939   Bengt Strömgren and A. Unsöld make quantitative analysis of solar abundances with fairly realistic model atmosphere, including H$^-$ opacity source just discovered by R. Wildt.

1942   Unsöld makes quantitative analysis of a B0 star, τ Sco, getting similar abundances to solar.

1946   F. Hoyle puts forward idea of element synthesis in supernovae. Solar ultraviolet spectrum observed in rocket flight.

1947   Discovery of π-meson (C. F. Powell).

1948   Heavy nuclei discovered in primary cosmic rays. G. Gamow, R. Alpher and R. Herman develop 'Hot Big Bang' theory and suggest all elements created by neutron captures in early Universe. W. Baade distinguishes two stellar populations.

1949   Shell model of nuclear structure.

1951   P. W. Merrill discovers Tc I lines in R And (an S star), indicating nucleosynthesis within 10^6 years or less. E. Öpik and E. E. Salpeter discover 3α reaction. J. W. Chamberlain and L. H. Aller discover that two classical 'subdwarfs' are deficient in metals by factors of order 100 relative to solar or local Galactic abundances, dispelling the idea of a universal cosmic abundance distribution.

1952   Baade revises Hubble's distance scale, so Big Bang theory not flawed by giving age of Universe less than that of the Earth.

M. Schwarzschild, A. Sandage and others pioneer theory of stellar evolution without extensive mixing and apply it to HR diagrams of globular clusters getting ages of several Gyr, comparable to the new inverse Hubble constant.

1953   Hoyle successfully predicts existence of a 7.6 MeV resonance state of the carbon-12 nucleus on grounds that otherwise little carbon would survive further processing into oxygen during stellar nucleosynthesis by helium burning, whereas in fact the C/O ratio is about 0.5.

Discovery of 'strange' particles.

1955   Salpeter introduces the Initial Mass Function for star formation.

1956   Hans Suess and H. C. Urey compile 'Cosmic Abundance Distribution' from meteorites, Sun, stars and gaseous nebulae, revealing features correlated with nuclear properties.

Experimental discovery of neutrino (Reines and Cowan).

Parity violation in weak interactions (Lee, Yang, Wu *et al.*).

1957   G. R. and E. M. Burbidge, W. A. Fowler and F. Hoyle (B^{2}FH) publish influential article describing nuclear processes which generate essentially all nuclear species by reactions in stars or interstellar medium. Similar ideas put forward by A. G. W. Cameron in a Chalk River internal report.

1958   Recoilless γ-ray emission (Mössbauer).

1962   O. J. Eggen, D. Lynden-Bell and Sandage assemble dynamical and chemical evidence for formation of the Galaxy by free-fall collapse. The issue is still debated.

S. van den Bergh identifies the 'G-dwarf problem'.

Discovery of μ neutrino.

Discovery of cosmic X-ray background and Sco X-1 point source (R. Giacconi *et al.*).

1963   Discovery of quasars (M. Schmidt *et al.*).

1964   F. Hoyle and R. J. Tayler point out significance of additional neutrinos for helium synthesis in the Big Bang model.

Solar neutrino problem identified.

Quark model of hadrons (Gell-Mann, Zweig).

1965   Discovery by A. A. Penzias and R. Wilson of microwave background, predicted by Gamow *et al.* as consequence of hot Big Bang. Their ideas of Big Bang nucleosynthesis consequently resurrected up to ^{7}Li, with significant consequences for nuclear and high-energy particle physics.

1967   Discovery of first pulsar (i.e. neutron star) announced (A. Hewish, J. Bell *et al.*).

Electroweak model (Weinberg, Salam, Glashow).

T. Gold identifies spin-down of central pulsar as energy source for Crab Nebula.

Discovery of γ-rays from Galaxy and diffuse background.

1971   Deuterium discovered in interstellar gas (Copernicus satellite) and quantitatively estimated in early Solar System, restricting baryonic density in Big Bang nucleosynthesis (BBNS) theory.

Trends in emission lines from H II regions in Scd galaxies as a function of galactocentric distance interpreted by L. Searle as a consequence of large-scale abundance gradients.

1972   L. Searle and W. L. W. Sargent identify two Zwicky blue compact galaxies as dwarf galaxies dominated by giant H II regions of low 'metallicity' but nearly normal helium abundance, supporting the existence of a universal 'floor' to helium abundance resulting from the Big Bang. Since then more such objects have been discovered, mostly in objective-prism surveys.

1975   Discovery of τ-lepton (Perl).

1979   Discovery of first gravitational lens (the double quasar 0957+561).

1982   F. and M. Spite discover Li in subdwarfs, confirming a prediction of BBNS theory.

1983   Discovery of weak bosons $W^{\pm}$ and Z^0 (Rubbia *et al.*).

1984   Estimates of primordial helium and deuterium abundance with Big Bang nucleosynthesis theory limit number of light neutrino families to 4 or less (Schramm *et al.*).

1987   Supernova 1987A tests theory of stellar nucleosynthesis. Neutrinos detected essentially as predicted.

1988   Estimates of primordial helium and deuterium with improved measurements of neutron half-life restrict number of light neutrino families to about 3. Similar, firmer result from LEP measurements at CERN of width of Z^0 resonance.

1990   COBE observations confirm black-body character of microwave background.

1992   COBE observations confirm presence of anisotropy of MWB at the 10^{-5} level.

X-ray and optical follow-up studies reveal origin of γ-ray bursts in powerful extragalactic sources ('hypernovae') at cosmological distances.

1995   Discovery of top quark at Fermilab.

1998   Super-Kamiokande light-water experiment reveals atmospheric neutrino oscillations.

1999   Observations of distant supernovae indicate expansion of the Universe accelerating.

2001   First results from SNO heavy-water experiment announced, giving definitive solution of solar neutrino problem.

2002   Balloon and WMAP satellite missions provide details of angular fluctuation spectrum of MWB, giving precise estimates of cosmological parameters.

Appendix 2

Some physical and astronomical constants

Gravitational constant	G	6.673×10^{-8}	$\mathrm{cm^3\,gm^{-1}\,s^{-2}}$
Speed of light	c	2.998×10^{10}	$\mathrm{cm\,s^{-1}}$
Reduced Planck's constant	$\hbar$	1.0546×10^{-27}	erg s
Electronic charge	e	4.803×10^{-10}	esu
	e^2	1.440	MeV fm
Electron volt	eV	1.602×10^{-12}	erg
Freq. equiv. to $1\,\mathrm{eV} = 10^8 \frac{e}{2\pi hc}$		2.418×10^{14}	$\mathrm{s^{-1}}$
Fine structure constant $e^2/(\hbar c)$	α	$1/137.036$	
Avogadro's number	N_A	6.022×10^{23}	$\mathrm{mol^{-1}}$
Atomic mass unit	amu	1.661×10^{-24}	gm
Energy equiv. of " "	$m_u c^2$	931.494	MeV
Proton mass–energy	$m_p c^2$	938.272	MeV
Neutron mass–energy	$m_n c^2$	939.565	MeV
Electron mass	m_e	9.109×10^{-28}	gm
Electron mass–energy	$m_e c^2$	0.5110	MeV
Muon mass–energy	$m_\mu c^2$	105.66	MeV
Tauon mass–energy	$m_\tau c^2$	1777	MeV
Class. electron radius $e^2/(m_e c^2)$		2.818×10^{-13}	cm
Thomson sct. x-sec. $\frac{8\pi}{3}\left(\frac{e^2}{m_e c^2}\right)^2$	σ_T	6.653×10^{-25}	$\mathrm{cm^2}$
Cl. damp. const. $2e^2\omega^2/(3m_e c^3)$	γ_cl	$8.9 \times 10^7 \left(\frac{0.5}{\lambda_{\mu\mathrm{m}}}\right)^2$	$\mathrm{s^{-1}}$
Radius of 1st Bohr orbit $\frac{h}{Zme^2}$	a_0	$0.529 \times 10^{-8}/Z$	cm
Boltzmann's constant	k	1.381×10^{-16}	$\mathrm{erg\,K^{-1}}$
	kT	$0.086\,17\,T_6$	keV
Radiation density const. $\frac{\pi^2 k^4}{15(\hbar c)^3}$	a	7.564×10^{-15}	$\mathrm{erg\,cm^{-3}\,K^{-4}}$
Eqm. photon density $\frac{2\zeta(3)}{\pi^2}\left(\frac{kT}{hc}\right)^3$	n_γ	$2.03 \times 10^{28}\,T_9^3$	$\mathrm{cm^{-3}}$

Quant. conc., protons $\left(\frac{m_p kT}{2\pi \hbar^2}\right)^{3/2}$		$5.95 \times 10^{33} \, T_9^{3/2}$	cm^{-3}
" " electrons $\left(\frac{m_e kT}{2\pi \hbar^2}\right)^{3/2}$		$2.42 \times 10^{24} \, T_6^{3/2}$	cm^{-3}
Fermi coupling constant	g_F	1.4×10^{-49}	$erg \, cm^3$
Solar mass	$M_\odot$	1.989×10^{33}	gm
Solar radius	$R_\odot$	6.96×10^{10}	cm
Solar luminosity	$L_\odot$	3.84×10^{33}	$erg \, s^{-1}$
Solar effective temperature	$T_{\mathrm{eff},\odot}$	5800	K
Solar surface gravity	$g_\odot$	2.74×10^4	$cm \, s^{-2}$
Solar mean density	$\bar{\rho}_\odot$	1.41	$gm \, cm^{-3}$
Year	yr	3.156×10^7	s
Astronomical unit	AU	1.496×10^{13}	cm
Light year	ly	9.46×10^{17}	cm
Parsec	pc	3.084×10^{18}	cm
Hubble constant	H_0	$100h$	$km \, s^{-1} \, Mpc^{-1}$
Hubble time	H_0^{-1}	$0.98 \times 10^{10} h^{-1}$	yr

Appendix 3

Time-dependent perturbation theory and transition probabilities

A3.1 The Einstein coefficients

In a celebrated paper, Einstein (1917) analyzed the nature of atomic transitions in a radiation field and pointed out that, in order to satisfy the conditions of thermal equilibrium, one has to have not only a spontaneous transition probability per unit time A_{21} from an excited state '2' to a lower state '1' and an absorption probability $B_{12} J_\nu$ from '1' to '2', but also a stimulated emission probability $B_{21} J_\nu$ from state '2' to '1'. The latter can be more usefully thought of as negative absorption, which becomes dominant in masers and lasers.[1] Relations between the coefficients are found by considering detailed balancing in thermal equilibrium

$$N_2[A_{21} + B_{21} B_\nu(T)] = N_1 B_{12} B_\nu(T) = \frac{g_1}{g_2} N_2 e^{h\nu/kT} B_{12} B_\nu(T), \qquad (A3.1)$$

where N_1, N_2 are the population numbers in the two energy states with statistical weights g_1, g_2. Hence

$$B_\nu(T) = \frac{g_2 A_{21}}{g_1 B_{12} e^{h\nu/kT} - g_2 B_{21}}. \qquad (A3.2)$$

Comparison of Eq. (A3.2) with Planck's law then gives the relations

$$g_1 B_{12} = g_2 B_{21}; \quad \frac{A_{21}}{B_{21}} = \frac{2h\nu^3}{c^2}, \qquad (A3.3)$$

which are always true because they refer to atomic constants.

To relate B_{12} to the absorption coefficient α_ν, consider a unit volume of gas bathed in a radiation field J_ν. The net rate at which energy is absorbed is then

$$(N_1 B_{12} - N_2 B_{21}) J_\nu h\nu = N_1 4\pi J_\nu \int \alpha(\Delta\nu) \, d\Delta\nu, \qquad (A3.4)$$

---

[1] Einstein defined the B coefficients in terms of radiation energy density, but following E. A. Milne it is more usual to define them in terms of the angle-averaged specific intensity $J_\nu \equiv (c/4\pi)\rho_\nu$.

where $\Delta\nu$ is the distance in frequency from the line centre. Hence

$$\alpha(\Delta\nu) = \frac{h\nu}{4\pi}\phi_{\Delta\nu}B_{12}\left(1 - \frac{N_2/g_2}{N_1/g_1}\right) \tag{A3.5}$$

where $\phi_{\Delta\nu}$ is a normalized profile function. In thermal equilibrium the factor in brackets reduces to the standard stimulated emission factor $[1 - \exp(-h\nu/kT)]$, or more generally to $[1 - \exp(-h\nu/kT_{ex})]$, where T_{ex} is an 'excitation temperature' obtained by force-fitting the two populations to a Boltzmann factor.

The corresponding result from classical electromagnetic theory is (in cgs units)

$$\int \alpha(\Delta\nu)\,d\Delta\nu = \frac{\pi e^2}{mc}. \tag{A3.6}$$

Comparison with Eq. (A3.5) then leads to the definition of a dimensionless 'oscillator strength'

$$f_{abs} = \frac{h\nu}{4\pi}B_{12}\bigg/\frac{\pi e^2}{mc} = \frac{B_{12}mch\nu}{4\pi^2 e^2} = \frac{g_2}{g_1}\frac{A_{21}}{3\gamma_{cl}} = -\frac{g_2}{g_1}f_{em}. \tag{A3.7}$$

A3.2 Time-dependent perturbation theory

In quantum mechanics, the state of an atom or nucleus is described by a complex wave function $\psi(\mathbf{r_1}, \mathbf{r_2}, \ldots, t)$ such that $\overline{\psi}\psi \equiv |\psi|^2$ is the probability density of finding particles in volume elements $d^3\mathbf{r_i}$ centred on $\mathbf{r_i}$ at time t. ψ satisfies the Schrödinger equation

$$H\psi = i\hbar\frac{\partial\psi}{\partial t} \tag{A3.8}$$

where H is the Hamiltonian operator $-(\hbar^2/2m)(\nabla_1^2 + \nabla_2^2 + \cdots) + V(\mathbf{r_1}, \mathbf{r_2}, \ldots)$.

Certain functions ψ_n are eigenfunctions of the operator H (when this is time-independent), i.e.

$$H\psi_n = E_n\psi_n \tag{A3.9}$$

where E_n is a number corresponding to a definite energy. In this case the solution of Eq. (A3.8) can be written as a product of space-dependent and time-dependent factors

$$\psi_n = u_n(\mathbf{r_1}\ldots)\,e^{-i\omega_n t}, \tag{A3.10}$$

where $\omega_n \equiv E_n/\hbar$, and $|\psi|^2$ is time-independent, i.e. the system is in a stationary state satisfying the time-independent Schrödinger equation

$$Hu_n = E_nu_n. \tag{A3.11}$$

According to the postulates of QM, any ψ representing a physical state of the system can be expressed as a linear combination of energy eigenfunctions forming an infinite orthonormal set:

$$\psi = \sum_n a_n \psi_n = \sum_n a_n u_n e^{-i\omega_n t}, \tag{A3.12}$$

$|a_n|^2$ being the probability that a measurement of the state of the system will give the result that it is in state n. If the system is 'left alone', the $|a_n|$'s are constant (strictly only true in the ground state), but if it is perturbed by altering V then they can change with time, i.e. the system undergoes a transition from one state to another. Equation (A3.8) shows that the rate of change is closely related to the energy of the interaction, and one can find an expression for the Einstein–Milne absorption and stimulated-emission coefficients from simple time-dependent perturbation theory.

Suppose that the atom (or nucleus) initially in an eigenstate '1' is subjected to a small time-dependent potential $V(t)$ on top of the unperturbed Hamiltonian H_0.[2] It is then possible to treat the coefficients a_n in Eq. (A3.12) as functions of time, with $|a_1|^2(\tau) \simeq 1$ being the probability that it is still in state '1' after a time τ and $|a_2|^2(\tau) \ll 1$ the probability that it has undergone a transition to another eigenstate '2'. Substituting in Schrödinger's equation (A3.8),

$$\sum_n [H_0 + V(t)]a_n \psi_n = i\hbar \left(\sum_n \dot{a}_n \psi_n + \sum_n a_n \dot{\psi}_n \right). \tag{A3.13}$$

The last term on the rhs cancels with $H_0 \sum_n a_n \psi_n$ by virtue of Eq. (A3.8) leaving

$$i\hbar \sum_n \dot{a}_n u_n e^{-i\omega_n t} = \sum_n V(t)a_n u_n e^{-i\omega_n t}. \tag{A3.14}$$

Multiplying through by $\overline{\psi}_2$ and integrating over space, we have

$$i\hbar \dot{a}_2 = \sum_n V_{2n}(t) \, e^{i\omega_{2n} t} a_n(t) \simeq V_{21}(t) \, e^{i\omega_{21} t} a_1(t), \tag{A3.15}$$

where $V_{2n} \equiv <u_2|V(t)|u_n>$ is a matrix element for the interaction. The first-order approximation solution to Eq. (A3.15) is

$$a_2(\tau) = \frac{1}{i\hbar} \int_0^\tau V_{21}(t) \, e^{i\omega_{21} t} dt \tag{A3.16}$$

since $a_1(t) \simeq 1$.

---

[2] In the case of electromagnetic interaction, the smallness is measured by that of the fine-structure constant $\alpha = 1/137$.

If the perturbation V_{21} is switched on suddenly at time $t = 0$ and is constant thereafter, Eq. (A3.16) can be integrated giving

$$a_2(\tau) = \frac{V_{21}}{\hbar\omega_{21}}(1 - e^{i\omega_{21}\tau}) \tag{A3.17}$$

and a transition probability

$$P_{1\to 2}(\tau) = \frac{|V_{21}|^2}{\hbar^2}\tau^2 \operatorname{sinc}^2\left(\frac{\omega_{21}\tau}{2}\right), \tag{A3.18}$$

where the function sinc x is defined as $\sin x/x$. This function is significantly large only for $|\omega_{12}\tau| \leq 2\pi$, i.e. for energy changes differing from zero by less than $2\pi\hbar/\tau$. Consequently, for transitions to a continuum which may be considered as a series of final states '2' with a density $\rho(E)$ per unit energy interval, the total transition probability is

$$P_{1\to\text{cont.}}(\tau) = \int_{E_1-2\pi h/\tau}^{E_1+2\pi h/\tau} \rho(E)\,dE\ \tau^2\frac{|V_{21}|^2}{\hbar^2}\operatorname{sinc}^2\left(\frac{\omega_{21}\tau}{2}\right). \tag{A3.19}$$

Within this narrow range of energies, $\rho(E)$ and $|V_{21}|$ can be taken as constants outside the integral leading to

$$P_{1\to\text{cont.}} = \frac{|V_{21}|^2}{\hbar^2}\rho(E)\,\tau^2\int_{E_1-2\pi h/\tau}^{E_1+2\pi h/\tau}\operatorname{sinc}^2\left(\frac{\omega_{21}\tau}{2}\right)dE. \tag{A3.20}$$

Now $dE = d(\hbar\omega) = (2\hbar/\tau)d(\omega\tau/2)$, and the variable $(\omega\tau/2)$ can be taken as going from $-\infty$ to ∞ since the contribution outside the relevant range $\pm\pi$ is negligible. Also, $\int_{-\infty}^{\infty}\operatorname{sinc}^2 x\,dx = \pi$. Hence the **Golden Rule** (see Eq. 2.92)

$$\lambda \equiv \frac{P_{1\to\text{cont.}}}{\tau} = \frac{2\pi}{\hbar}[|V_{21}|^2\rho(E)]_{E=E_1}. \tag{A3.21}$$

Suppose now that the system is subjected to an oscillating electromagnetic field with a representative Fourier component of the electric field $\mathbf{F}_0(\omega)\cos\omega t$. The predominant term in the interaction energy V is usually the electric dipole term 'E$_1$', e.g. for an electron in an atom

$$V = -e\cos\omega t\,\mathbf{F}_0(\omega).\mathbf{r} = \cos\omega t\,\mathbf{F}_0.\mathbf{p}. \tag{A3.22}$$

There are also electric quadrupole 'E$_2$' terms of order $-ex_ix_j\partial F_i/\partial x_j \sim Fpr/\lambda$ and magnetic dipole 'M$_1$' terms of order $(\mathbf{r}\times\mathbf{v}).\mathbf{B}e/c \sim Fpv/c \sim Fpr/\lambda$ since $B_0 = F_0$. These provide smaller transition probabilities by factors of the order of $(r/\lambda)^2 \sim 10^{-8}$ in the optical region. However, when the dipole vanishes, they can give rise to 'forbidden' lines indicated by square brackets, e.g. [O III]. Still higher orders of transition are sometimes significant for nuclear γ-rays.

Substituting Eq. (A3.22) for V in Eq. (A3.15), we have

$$i\hbar \dot{a}_2 = \cos \omega t \, \mathbf{F}_0(\omega).\mathbf{p}_{21} e^{i\omega_{21}t}, \tag{A3.23}$$

where $\mathbf{p}_{21} \equiv e \sum_i <2|\mathbf{r}_i|1>$ is the 2,1 matrix element of the dipole moment and the sum is carried out over all electrons (or protons) present. Equation (A3.23) leads to

$$\dot{a}_2(\omega) = \frac{1}{2i\hbar} \mathbf{F}_0(\omega).\mathbf{p}_{21}(e^{i\omega t} + e^{-i\omega t}) e^{i\omega_{21}t}, \tag{A3.24}$$

which integrates up to

$$a_2(\tau, \omega) = -\frac{i}{2\hbar} \mathbf{F}_0(\omega).\mathbf{p}_{21} \left[\frac{e^{i(\omega_{21}+\omega)\tau} - 1}{i(\omega_{21} + \omega)} + \frac{e^{i(\omega_{21}-\omega)\tau} - 1}{i(\omega_{21} - \omega)} \right]. \tag{A3.25}$$

In the neighbourhood of a resonance, $|\omega| \simeq \omega_{21}$, the two terms on the rhs of Eq. (A3.25) correspond to stimulated emission (large for $\omega \simeq \omega_{12} = -\omega_{21} < 0$) and absorption (large for $\omega \simeq \omega_{21} > 0$) respectively. In the second case we recover a relation similar to Eq. (A3.18):

$$|a_2(\tau, \omega)|^2 = \frac{|\mathbf{F}_0.\mathbf{p}_{21}|^2}{4\hbar^2} \tau^2 \, \mathrm{sinc}^2\left(\frac{\tau \Delta\omega}{2}\right). \tag{A3.26}$$

If continuous radiation is incident on the atom, Eq. (A3.26) must now be summed over all frequencies; lines are usually so narrow that J_ν can be taken as constant for $-\infty < \Delta\omega < \infty$. $|\mathbf{F}_0.\mathbf{p}_{21}|^2$ has to be expressed in terms of J_ν. To do this, note that for unpolarized isotropic radiation

$$\int_{\omega_1}^{\omega_2} J_\omega d\omega = \frac{c}{4\pi} \times \text{energy density} = \frac{c}{4\pi} \frac{3}{8\pi} \int_{\omega_1}^{\omega_2} F_0^2(\omega) d\omega, \tag{A3.27}$$

where $\frac{1}{2} F_0^2(\omega) d\omega$ is the mean squared electric field in the frequency range in any given direction, in particular that of $\mathbf{p}_{21}$.[3] Hence

$$|a_2(\tau)|^2 = \frac{8\pi^2}{3c\hbar^2} |p_{21}|^2 \, 2 J_\omega \tau \int_{-\infty}^{\infty} \mathrm{sinc}^2\left(\frac{\tau \Delta\omega}{2}\right) d\left(\frac{\tau \Delta\omega}{2}\right) \tag{A3.28}$$

$$= \frac{8\pi^2}{3c\hbar^2} |p_{21}|^2 J_\nu \tau \equiv B_{12} J_\nu \tau. \tag{A3.29}$$

Calculation of A_{21} by quantum mechanics is much more difficult, but it can be found from B_{12} using Eq. (A3.3). Taking degeneracy into account,

$$\frac{c^2}{2h\nu^3} g_2 A_{21} = g_2 B_{21} = g_1 B_{12} = \frac{8\pi^2}{3c\hbar^2} \sum_{M_1, M_2} |\mathbf{p}_{21}|^2 \equiv \frac{8\pi^2}{3c\hbar^2} S_{12}, \tag{A3.30}$$

---

[3] The total energy density is $3(\frac{1}{2} F_0^2 + \frac{1}{2} B_0^2)/8\pi = 3 F_0^2/8\pi$.

where $S_{12} \equiv S_{21}$ is called the line strength and the sum is taken over all individual (Zeeman) states of the energy levels 1 and 2. Because of the odd parity of $\mathbf{r}$, there is a selection rule that requires a change in parity between the spatial wave functions of states 1 and 2 for dipole radiation to occur; the opposite holds for 'E$_2$' and 'M$_1$'.

Finally, we can recover the classical damping constant from Eq. (A3.30) by writing

$$S_{12} = |p_{21}|^2 = e^2 \ |r|^2 = e^2 \hbar / m_e \omega \tag{A3.31}$$

for angular momentum $\hbar$, whence

$$\frac{g_2}{g_1} A_{21} = \frac{4}{\pi} \frac{\omega^3}{3c^3} \frac{e^2 \ |r|^2}{\hbar}$$

$$= \frac{4}{\pi} \frac{e^2 \omega^2}{3 m_e c^3} = \frac{2}{\pi} \gamma_{cl}. \tag{A3.32}$$

Appendix 4

Polytropic stellar models

A useful insight into the structure of nearly homogeneous stars or parts thereof can be gained from the study of so-called polytropic stellar models which depend on a combination of the principle of hydrostatic equilibrium with an assumed equation of state of the form

$$P = K\rho^{1+1/n} \tag{A4.1}$$

where n is called the polytropic index. Equation (A4.1) applies precisely to certain cases, e.g. a perfect monatomic gas in adiabatic equilibrium ($n = 3/2$), ordinary degeneracy ($n = 3/2$ again) and relativistic degeneracy ($n = 3$), and it is assumed (with $n = 3$) in Eddington's Standard Model which gives quite a good approximation to the structure of main-sequence stars. (Note that for a perfect gas, Eq. A4.1 makes $\rho \propto T^n$, which is often a good approximation in stellar interiors with $n \simeq 3$.) The following description is based on that of Clayton (1968).

In developing the theory, it is convenient to express the density as a fraction of the central density ρ_c:

$$\rho = \rho_c \phi^n; \quad P = K\rho_c^{1+1/n} \phi^{n+1}, \tag{A4.2}$$

where ϕ is some suitable dimensionless function which diminishes monotonically from its value of 1 at the centre. The equation of hydrostatic equilibrium (Eq. 5.6) then gives (with Eq. 5.7)

$$\frac{1}{r^2} \frac{d}{dr} \left(\frac{r^2}{\rho} \frac{dP}{dr} \right) = -4\pi G\rho, \tag{A4.3}$$

or

$$(n+1) K\rho_c^{1/n} \frac{1}{r^2} \frac{d}{dr} \left(r^2 \frac{d\phi}{dr} \right) = -4\pi G\rho_c \phi^n. \tag{A4.4}$$

Table A4.1. *Some constants of the*
Lane–Emden equation

n	ξ_1	$-\xi_1^2 \left(\frac{d\phi}{d\xi}\right)_{\xi_1}$	$\rho_c/\bar{\rho}$
0.0	2.45	4.90	1.00
1.5	3.65	2.71	5.99
3.0	6.90	2.02	54.2
4.5	31.8	1.74	6190

This equation is made dimensionless by introducing a unit of length. Let

$$r \equiv \xi a \equiv \xi \left[\frac{(n+1)K}{4\pi G \rho_c^{1-1/n}} \right]^{1/2}, \tag{A4.5}$$

so that Eq. (A4.4) reduces to the **Lane–Emden equation**

$$\frac{1}{\xi^2} \frac{d}{d\xi} \left(\xi^2 \frac{d\phi}{d\xi} \right) = -\phi^n. \tag{A4.6}$$

Equation (A4.6) is solved (which has to be done numerically for most values of n) using the inner boundary condition

$$\phi = 1; \quad \frac{d\phi}{d\xi} = 0, \quad \text{for } \xi = 0. \tag{A4.7}$$

For $n < 5$, ϕ vanishes at some value ξ_1 which represents the stellar surface. Some relevant quantities are given for a few polytropic indices in Table A4.1.

The stellar **radius** is

$$R = a\xi_1 = \left[\frac{(n+1)K}{4\pi G} \right]^{1/2} \rho_c^{-(n-1)/2n} \xi_1 \tag{A4.8}$$

and thus depends on both K and ρ_c (unless $n = 1$).

The **mass** is

$$M(\xi_1) = 4\pi a^3 \rho_c \int_0^{\xi_1} \xi^2 \phi^n d\xi = -4\pi a^3 \rho_c \int_0^{\xi_1} d \left(\xi^2 \frac{d\phi}{d\xi} \right) \tag{A4.9}$$

$$= -4\pi a^3 \rho_c \left(\xi^2 \frac{d\phi}{d\xi} \right)_{\xi_1} \tag{A4.10}$$

$$= -4\pi \left[\frac{(n+1)K}{4\pi G} \right]^{3/2} \rho_c^{(3-n)/2n} \left(\xi^2 \frac{d\phi}{d\xi} \right)_{\xi_1}. \tag{A4.11}$$

The **ratio of central to mean density** is given by

$$\frac{\bar\rho}{\rho_c} = \frac{3}{4\pi}\frac{M}{R^3}\frac{1}{\rho_c} = -\frac{3}{\xi_1}\left(\frac{d\phi}{d\xi}\right)_{\xi_1} \tag{A4.12}$$

from Eqs. (A4.8), (A4.11). Thus this ratio depends only on n, which can be taken as a measure of the degree of central concentration.

When $n = 3$, ρ_c obligingly cancels out in Eq. (A4.11). For the case of **relativistic degeneracy**, we have, furthermore, from Eqs. (5.46), (5.49)

$$K = \frac{\pi\hbar c}{4}(3/\pi)^{1/3}(\mu_e m_H)^{-4/3} = 1.25 \times 10^{15}\,\mu_e^{-4/3}, \tag{A4.13}$$

which with Eq. (A4.11) and $\xi^2(d\phi/d\xi)_{\xi_1}$ from Table A4.1 gives the **Chandrasekhar–Landau limiting mass for white dwarfs**

$$M_{\mathrm{Ch}} = \frac{5.83}{\mu_e^2}\,M_\odot. \tag{A4.14}$$

Another interesting application is **Eddington's Standard Model** (Eddington 1926). In this model it is assumed that gas pressure and radiation pressure contribute respective fractions β and $1 - \beta$ to the total pressure, with β constant in any one star. We then have

$$\beta P = P_{\mathrm{g}} = \frac{\rho k T}{\mu m_H}; \tag{A4.15}$$

$$(1-\beta)P = P_r = aT^4/3, \tag{A4.16}$$

whence

$$\frac{\beta^4}{1-\beta}P^3 = \frac{3}{a}\left(\frac{k\rho}{\mu m_H}\right)^4, \tag{A4.17}$$

i.e.

$$P = K\rho^{4/3}, \tag{A4.18}$$

where

$$K = \left(\frac{k}{\mu m_H}\right)^{4/3}\left(\frac{3}{a}\right)^{1/3}\left(\frac{1-\beta}{\beta^4}\right)^{1/3} = \frac{2.67\times 10^{15}}{\mu^{4/3}}\left(\frac{1-\beta}{\beta^4}\right)^{1/3}. \tag{A4.19}$$

The **mass** then follows from Eq. (A4.11)

$$M = \frac{18.3}{\mu^2}\frac{(1-\beta)^{1/2}}{\beta^2}\,M_\odot. \tag{A4.20}$$

Equation (A4.20) (Eddington's quartic equation) determines $1 - \beta$ as a function of mass. Taking $\mu \simeq 0.6$, this means that, for the Sun, $1 - \beta \simeq 4 \times 10^{-4}$, whereas for $100\,M_\odot$, $1 - \beta \simeq 0.4$.

The **central pressure** follows from Eqs. (A4.2), (A4.11), (A4.12):

$$P_{\rm c} = K\rho_{\rm c}^{4/3} = K\left(\frac{\rho_{\rm c}}{\bar{\rho}}\right)^{4/3}\left(\frac{3}{4\pi}\frac{M}{R^3}\right)^{4/3} \tag{A4.21}$$

and

$$K = \pi G\left[\frac{M}{-4\pi\xi^2(d\phi/d\xi)_{\xi_1}}\right]^{2/3}, \tag{A4.22}$$

whence

$$P_{\rm c} = \frac{1}{16\pi}\left[\left(\frac{d\phi}{d\xi}\right)_{\xi_1}\right]^{-2}\frac{GM^2}{R^4} = 1.24\times10^{17}\left(\frac{M}{M_\odot}\right)^2\left(\frac{R_\odot}{R}\right)^4 \text{ dyne cm}^{-2}. \tag{A4.23}$$

This is several hundred times the lower limit estimated in Eq. (5.9).

The **central temperature** can be deduced from the central pressure and density:

$$T_{\rm c} = \frac{\mu\beta m_{\rm H}}{k}\frac{P_{\rm c}}{\rho_{\rm c}} = \frac{\mu\beta m_{\rm H}}{k}P_{\rm c}\frac{\bar{\rho}}{\rho_{\rm c}}\left(\frac{4\pi R^3}{3M}\right) \tag{A4.24}$$

$$= 19.5\times10^6\mu\beta\left(\frac{M}{M_\odot}\right)\left(\frac{R_\odot}{R}\right) \text{ K.} \tag{A4.25}$$

The radius can be eliminated by appealing to the homology transformation (Table 5.1) from which, approximately,

$$\frac{R}{R_\odot} \simeq \left(\frac{M}{M_\odot}\right)^{2/3}, \tag{A4.26}$$

whence

$$T_{\rm c} \simeq 19.5\times10^6\mu\beta\left(\frac{M}{M_\odot}\right)^{1/3} \text{ K} \tag{A4.27}$$

for main-sequence stars with $\mu = \mu_\odot$.

Finally, the **luminosity** can be derived from the radiative transfer equation Eq. (5.21)

$$\frac{dP_{\rm r}}{dr} \equiv \frac{a}{3}\frac{dT^4}{dr} = \frac{\kappa\rho l(r)}{4\pi cr^2}. \tag{A4.28}$$

Dividing by the hydrostatic equilibrium condition Eq. (5.6),

$$\frac{dP_{\rm r}}{dP} \equiv 1 - \beta = \frac{\kappa l(r)}{4\pi cGm(r)} = \frac{L}{4\pi cGM}\eta(r)\kappa(r), \tag{A4.29}$$

where

$$\eta(r) \equiv \frac{l(r)/m(r)}{L/M}. \tag{A4.30}$$

Consequently we have for the total luminosity

$$L = \frac{4\pi c G M (1 - \beta)}{\overline{\kappa \eta}} = 1.5 \times 10^{35} \frac{(\mu\beta)^4}{\overline{\kappa \eta}} \left(\frac{M}{M_\odot} \right)^3 \text{erg s}^{-1}, \qquad (A4.31)$$

from Eq. (A4.20), where $\overline{\kappa \eta}$ represents a suitable average over the star (κ increases from about $1 \text{ cm}^2 \text{ gm}^{-1}$ in the centre of the Sun to very large values in the envelope, whereas η decreases from large values in the centre to 1 at the surface, so that the product varies by a more limited amount; strictly it should be constant in order to make β constant). Thus we need to have $\overline{\kappa \eta} \simeq 5 \text{ cm}^2 \text{ gm}^{-1}$ in order to reproduce the Sun's luminosity, which is right within a factor of a few.

See Arnett (1996) for applications of Eddington's Standard Model to more complicated situations.

Appendix 5

Dissipation and abundance gradients

Models of galaxy formation involving dissipative collapse (e.g. Larson 1974a) generically lead to a gradient in the mean stellar abundances (as well as a density gradient) caused by inflow of gas relative to stars. This can be understood analytically using the following simplified version of the 'concentration model' by Lynden-Bell (1975).

Consider star formation in a spherical galaxy of unit mass, consisting initially of gas. Stars are formed from the gas, which simultaneously contracts through the stars as a result of energy dissipation by cloud collisions etc. The abundance in the gas (assumed uniform) is still $z = \ln(1/g)$ as in the Simple model (Chapter 8), where g is the mass of gas remaining and z is in units of the yield.

Suppose that, at any time t, the mass of stars within a fixed mass coordinate m is $s(m, t)$ and that the gas is confined within a decreasing mass coordinate $m_a(t)$. We make the simplifying but reasonable assumption that, within $m_a(t)$, the radial distributions of stars and of the star formation rate are the same. Furthermore, we assume the *Ansatz*

$$m_a = g + s(m_a) = g^c \tag{A5.1}$$

where $c < 1$ is called the concentration index. To simplify the mathematics, we here take $c = 1/2$; for solutions with arbitrary c, see Lynden-Bell (1975).

With these assumptions, one can relate the rate of star formation within a fixed sphere of total mass m to the rate of consumption of gas in the system as a whole:

$$\frac{ds(m)}{dt} = -\frac{dg}{dt} \frac{s(m)}{s(m_a)} = -\frac{dg}{dt} \frac{s(m)}{g^{1/2} - g}; \quad m \le m_a(t); \tag{A5.2}$$

$$= -\frac{dg}{dt} \qquad\qquad m \ge m_a(t). \tag{A5.3}$$

These equations are easily integrated to give

$$s(m, t) = K(m)(1 - g^{1/2})^2; \quad m \le m_a = g^{1/2} = e^{-z/2}; \quad \text{(A5.4)}$$

$$= m - g; \quad m \ge m_a = g^{1/2} = e^{-z/2}. \quad \text{(A5.5)}$$

The integration constant $K(m)$ is fixed by equating (A5.4) to (A5.5) at $m = m_a(t) = [g(t)]^{1/2}$:

$$K(m) = \frac{m}{1 - m}. \quad \text{(A5.6)}$$

The mass of stars within the sphere m having metallicity less than z is then given by

$$s(m; < z) = \frac{m}{1 - m}(1 - e^{-z/2})^2; \quad m \le e^{-z/2}; \quad z \le 2 \ln \frac{1}{m}; \quad \text{(A5.7)}$$

$$= m - e^{-z}; \quad m \ge e^{-z/2}; \quad z \ge 2 \ln \frac{1}{m}. \quad \text{(A5.8)}$$

The differential distribution function of metallicities in a shell m to $m+dm$ is given by differentiating Eqs. (A5.7), (A5.8) with respect to both m and z:

$$\frac{\partial^2 s}{\partial m \, \partial z} = \frac{e^{-z/2} - e^{-z}}{(1 - m)^2}; \quad z \le 2 \ln \frac{1}{m}; \quad \text{(A5.9)}$$

$$= 0; \quad z > 2 \ln \frac{1}{m}. \quad \text{(A5.10)}$$

The mean metallicity of stars in the shell is then given by

$$\bar{z}(m \text{ to } m + dm) = \frac{\int_0^{2 \ln \frac{1}{m}} z \frac{d^2 s}{dm dz} \, dz}{\int_0^{2 \ln \frac{1}{m}} \frac{d^2 s}{dm dz} \, dz} = \frac{3 - 4m(1 - \ln m) + m^2(1 - 2 \ln m)}{(1 - m)^2}.$$

$$\text{(A5.11)}$$

The ratio in Eq. (A5.11) tends to zero for $m = 1$ and to 3 for $m = 0$, i.e. a strong abundance gradient has been built up with the mean stellar metallicity at the centre exceeding the yield by a factor of 3. See the numerical model by Larson shown in Fig. 11.13.

Appendix 6

Hints for problems

Chapter 2

1. Use Eq. (2.7).
2. ^{3}He $\frac{1}{2}^+$; ^{7}Li, ^{9}Be, ^{11}B $\frac{3}{2}^-$; ^{13}C, ^{15}N $\frac{1}{2}^-$.
4. H→He 26.73; 6.68. He→C 7.27; 0.61; ^{12}C(α, γ) 7.16; 0.45. ^{13}C(α, n) 2.22; 0.13; ^{116}Sn(n, γ) 6.95; 0.059.
5. Momenta in CM system are $\pm m\mathbf{v}$.
6. The z-component of velocity will be more than w if the total speed $v \geq w$ and $\cos\theta \geq w/v$ where θ is the angle between $\mathbf{v}$ and the z-axis. Hence

$$N(\geq w) \propto \int_w^\infty v^2 e^{-mv^2/2kT}\, dv \int_0^{\arccos w/v} \sin\theta\, d\theta \tag{A6.1}$$

$$= \int_w^\infty v^2 \left(1 - \frac{w}{v}\right) e^{-mv^2/2kT}\, dv, \tag{A6.2}$$

$$= \frac{kT}{m} \int_w^\infty e^{-mv^2/2kT}\, dv, \tag{A6.3}$$

and

$$\frac{dN}{dw} \propto e^{-mw^2/2kT}, \tag{A6.4}$$

i.e. a Gaussian distribution with variance kT/m, the same as that of $v^{-2}dN/dv$. The variance of $w_1 - w_2$ is thus $kT(1/m_1 + 1/m_2)$ and this will also be that of its projection back into 3 dimensions $|\mathbf{v_1} - \mathbf{v_2}|$.
From Eq. (2.107), the distribution function of the centre-of-mass velocity will be a Maxwellian with a mass of $m_1 + m_2$.

7. Take the starting point A at a fixed distance y_1 above the surface plane and the end-point B at a fixed distance $-y_2$ below it. The time is then $y_1 \sec i - ny_2 \sec r$, which has

to be minimized subject to the subsidiary condition that $x_A - x_B = y_1 \tan i - y_2 \tan r$ is constant. Hence

$$\delta t = y_1 \sec i \tan i \, \delta i - n y_2 \sec r \tan r \, \delta r$$

$$- A(y_1 \sec^2 i \, \delta i - y_2 \sec^2 r \, \delta r) \tag{A6.5}$$

$$= 0 \quad \forall \, \delta i, \delta r. \tag{A6.6}$$

Equating coefficients,

$$\sec i \tan i = A \sec^2 i \tag{A6.7}$$

$$n \sec r \tan r = A \sec^2 r. \tag{A6.8}$$

8.

$$S = k \ln W = k \sum_i \left[\omega_i \ln \frac{\omega_i}{\omega_i - N_i} - N_i \ln \frac{N_i}{\omega_i - N_i} \right] \tag{A6.9}$$

$$\simeq k \sum_i \left[N_i \left(1 + \frac{\tilde{E}_i - \mu}{kT} \right) \right] \tag{A6.10}$$

$$= k \sum_i \left[N_i \left(1 + \frac{p_i^2}{2mkT} + \ln(un_Q/n) \right) \right]. \tag{A6.11}$$

$\sum_i N_i p_i^2$ is just $N \times$ the average square momentum $3mkT$.

9. Electrical neutrality gives

$$n_{e^-} - n_{e^+} = 8n_O = \frac{\rho}{2m_H} = 3.0 \times 10^{26} \, \text{cm}^{-3}. \tag{A6.12}$$

The chemical potential condition gives

$$n_{e^+} n_{e^-} = 4n_Q^2 e^{-2m_e c^2/kT} = 1.9 \times 10^{53} \, \text{cm}^{-6}. \tag{A6.13}$$

Hence $n_{e^+} = 3.1 \times 10^{26} \, \text{cm}^{-3}$.

11. From Eqs. (2.56), (2.21), $E_0 = 1.7$ MeV. Since the reduced mass is $28/32 = 7/8$ of the mass of an α-particle, the laboratory energy of the α's should be $8/7 \times$ as much, i.e. 1.9 MeV.

12. For a Gaussian, say $f(E) = (1/\sigma\sqrt{2\pi}) \exp[-(E - E_0)^2/2\sigma^2]$,

$$f(E_0)/f''(E_0) = \sigma^2. \tag{A6.14}$$

Hence from Eq. (2.59),

$$\sigma = \frac{\sqrt{2}}{3} kT \tau^{1/2} \tag{A6.15}$$

and the full $1/e$ width is

$$2\sigma\sqrt{2} = 4(E_0 kT/3)^{1/2}. \tag{A6.16}$$

13. ≤ 0.42 MeV, detectable by all the reactions except the first. In case (a), the deuteron and positron have equal and opposite momentum p. The K.E. of the positron is

$$T_{e^+} = \sqrt{m_e^2 c^4 + p^2 c^2} - m_e c^2. \qquad (A6.17)$$

The K.E. of the deuteron is

$$T_d = p^2/4m_{\rm H}. \qquad (A6.18)$$

This makes $T_{e^+} = 0.42$ for $pc = 0.77$ MeV, so $T_d = 1.6 \times 10^{-4}$ MeV. In case (b), the kinetic energy of the neutrino is $pc = 0.42$ MeV, so the K.E. of the deuteron is 4.7×10^{-5} MeV.

14. In the first case, the result is obvious from Eq. (2.97). In the second case we have to go back to Eq. (2.96) with the following relations:

$$pc = \sqrt{T_e^2 + 2T_e m_e c^2}, \qquad (A6.19)$$

$$c^2 p \, dp = (T_e + m_e c^2) dT_e, \qquad (A6.20)$$

$$qc = \sqrt{(Q - T_e)^2 - m_\nu^2 c^4}, \qquad (A6.21)$$

$$c^2 q \, dq = E_\nu dE_\nu = (Q - T_e) dE_f. \qquad (A6.22)$$

Substituting in Eq. (2.96), we have

$$\frac{d\lambda}{dT_e} = \frac{d\lambda}{dp}\frac{dp}{dT_e} \propto (T_e + m_e c^2) pq E_\nu \qquad (A6.23)$$

$$\propto (T_e + m_e c^2)(Q - T_e)\sqrt{T_e^2 + 2T_e m_e c^2}\sqrt{(Q - T_e)^2 i - m_\nu^2 c^4}. \qquad (A6.24)$$

The slope of the spectrum is $d^2\lambda/dT_e^2$. Differentiating Eq. (A6.24) we get the sum of a number of terms all but one of which vanish when $(Q - T_e) = m_\nu c^2$, but the remaining term has the factor $-(Q - T_e)/\sqrt{(Q - T_e)^2 - m_\nu^2 c^4} = -\infty$.

15. From the definition of the Lorentz factor γ,

$$\frac{v}{c} = \sqrt{1 - 1/\gamma^2} \simeq 1 - \frac{1}{2\gamma^2}. \qquad (A6.25)$$

γ is 10^7 and 10^8 in the two cases and the light travel time is 3.3×10^8 yr or 10^{16} s, so the time-lags are 50 and 0.5 seconds, respectively. (The optical signal arrives many minutes later still, because of the time taken by the shock to propagate out to the surface.)

Chapter 3

1. $W_{\rm exp}/W_{\rm MEMMU} = 2/\sqrt{\pi}$.
2. 1.7×10^{19} cm^{-2}.
3. This is best done graphically, using Table 3.3 ($a = 0.001$). The data are just barely compatible with the lines being on the linear part of the curve of growth, in which case the EW of D_1 is 200 mÅ and the column density is 2.0×10^{12} cm^{-2} from Eq. (3.38). In this case, the equivalent width of D_2 could be at most about 1 Doppler width,

implying $b \geq 20 \, \text{km s}^{-1}$. The preferred doublet ratio is 0.21 dex, which corresponds to $\log(N\alpha_0\sqrt{\pi}) = 0.15$, $\log(W/\Delta\lambda_D) = 0.03$ for D_1, i.e. $b = 11 \, \text{km s}^{-1}$ and $N = 3.0 \times 10^{12} \, \text{cm}^{-2}$ from Eqs. (3.26), (3.27). The smallest doublet ratio compatible with the data is 0.12 dex, with an EW of 260 mÅ for D_1. In this case, the curve gives $\log N\alpha_0\sqrt{\pi} = 0.6$, $\log W/\Delta\lambda_D = 0.32$, $b = 6.3 \, \text{km s}^{-1}$, $N = 1.5 \times 10^{13} \, \text{cm}^{-2}$. So the final result is $\log N_{\text{cm}^{-2}} = 12.5^{+0.7}_{-0.2}$; $b \geq 6.3 \, \text{km s}^{-1}$.

4. From Fig. 3.12, the curve-of-growth shift $\log A = 0.7$. Hence from Eq. (3.58)

$$\frac{\text{Fe I}_1/g_1}{\text{H}} = 2.6 \times 10^{-7}\kappa_{0.5\,\mu\text{m}} = 5.2 \times 10^{-9} P_e \tag{A6.26}$$

from Table 3.2. Applying Saha's equation, Eq. (3.7), we get

$$\log \frac{\text{Fe}^+}{\text{H}} = -4.55. \tag{A6.27}$$

Note that iron is sufficiently ionized in the solar atmosphere that the abundance of Fe I can be neglected and its partition function (or the ground-state statistical weight g_1) and the electron pressure cancel out.

5. Equating the legend to Fig. 3.13 with Eq. (3.59),

$$0.09(I - \chi) - 0.66 = [\text{Fe}^+/\text{H}] + 0.09(I - \chi - 0.75). \tag{A6.28}$$

Hence $[\text{Fe}/\text{H}] = -0.59$.

6. Following Russell (1934), we write for the fictitious undepleted pressures $P_O = P_H(\text{O/H})$, $P_C = P_H(\text{C/H})$ of oxygen and carbon

$$P_O = p_O + p_{CO} = p_O \left(1 + \frac{p_C}{K_{CO}} \right); \tag{A6.29}$$

$$P_C = p_C + p_{CO} = p_C \left(1 + \frac{p_O}{K_{CO}} \right). \tag{A6.30}$$

Substitution of p_C from the second equation into the first, and vice versa for p_O, leads to two quadratic equations of which Eqs. (3.74) and (3.75) are the solutions.

7. From Eq. (3.67)

$$5q_{21} = 1.72 \times 10^{-7}; \quad q_{21} = 3.45 \times 10^{-8} \, \text{cm}^3 \, \text{s}^{-1}. \tag{A6.31}$$

Hence

$$n_{\text{crit}} = 2 \times 10^5 \, \text{cm}^{-3}. \tag{A6.32}$$

Chapter 4

1. Law of motion

$$\ddot{R} = \frac{1}{2}\frac{d}{dR}(\dot{R}^2) = -\frac{GM}{R^2} + \frac{1}{3}\Lambda R. \tag{A6.33}$$

Integrating,

$$3\dot{R}^2 = 8\pi G\rho R^2 + \Lambda R^2 + \text{const.} \tag{A6.34}$$

This is identical to Eq. (4.9) if the constant is identified as $-3kc^2$. If $\Lambda = 0$, then $-kc^2$ is $\dot{R}^2 - 2GM/R$, twice the total energy.

2. In adiabatic expansion,

$$T \propto \rho^{\gamma-1} \propto R^{-3(\gamma-1)}, \tag{A6.35}$$

i.e. R^{-1} for radiation and R^{-2} for a non-relativistic monatomic gas. Hence the present-day temperature is $2.73^2/1.2 \times 10^{15} = 6 \times 10^{-15}$ K.

3. Assuming $Y_P = 0.24$, the H I density is

$$n_{\mathrm{H}} = 0.76 \times 3 \times 10^{-10} \times 20.3 \, T^3 = 10^{-7}(1+z)^3 \tag{A6.36}$$

and $n_e = n_p = 0.01 n_{\mathrm{H}}$. Saha's equation then gives

$$10^{-11}(1+z)^3 = 2 \times 1.09 \times 10^{16}(1+z)^{3/2} 10^{-25110/(1+z)}, \tag{A6.37}$$

or

$$(1+z)^{3/2} = 2.2 \times 10^{27} \, 10^{-25110/(1+z)}, \tag{A6.38}$$

which holds for $z \simeq 1100$, $T \simeq 3000$ K, $n_e \simeq 1 \, \mathrm{cm}^{-3}$. Recombination time is thus of the order of 10^{12} s. From Eq. (4.25), the age of the Universe is of the order of 10^{13} s, so that there will be some minor departure from Saha equilibrium due to expansion, but the effect on the parameters deduced here is negligible (see Jones 1977).

4. Assuming $g_* = 3.36$ at that time (i.e. neutrinos effectively massless), whereas $g_* = 1$ now,

$$1 + z_{\mathrm{eq}} = \frac{1.88 \times 10^{-29} \, \Omega_m h^2 c^2}{1.68a(2.73)^4} = 2.4 \times 10^4 \, \Omega_m h^2. \tag{A6.39}$$

5.

$$\frac{\mathrm{D}}{\mathrm{H}} = \frac{3}{4} \times \frac{0.15}{1.15} \eta \, n_\gamma \times 2^{3/2} \left(\frac{2\pi \hbar^2}{m_p kT}\right)^{3/2} e^{2.224 \, \mathrm{MeV}/kT} \tag{A6.40}$$

$$= 3.0 \times 10^{-16} \, T_9^{3/2} e^{25.8/T_9} \tag{A6.41}$$

$$= 4.8 \times 10^{-5} \, (T_9 = 1), \quad 3.4 \times 10^{-10} \, (T_9 = 2). \tag{A6.42}$$

Also, the mass fraction $X_{\mathrm{D}} = 2\mathrm{D}/\mathrm{H}$ since there is not yet a significant amount of helium at this stage.

6. From Eqs. (4.23), (4.24), an extra flavour of neutrinos increases g_* by 7/4. Hence from Eq. (4.50), Y_P is increased by 0.013.

7. Use $X + Y + Z = 1$, $Y/X = 4y$.

Chapter 5

2. Taking the electrostatic energy to be $-Ze^2/d$, where $d \simeq (\rho/Am_{\mathrm{H}})^{1/3}$ is the average distance between ions, and the Fermi energy from Eq. (5.43) with $E_{\mathrm{F}} = p_{\mathrm{F}}^2/2m_e$, we have

	E.s. energy	Fermi energy	kT
Carbon white dwarf	$-150\,\mathrm{eV}$	$35\,\mathrm{keV}$	$8.75\,\mathrm{keV}$
Brown dwarf	$-125\,\mathrm{eV}$	$2.6\,\mathrm{keV}$	$0.44\,\mathrm{keV}$

The energy density from electrostatic repulsion of ions is $(Ze)^2/d = (Ze)^2(\rho/Am_\mathrm{H})^{1/3}$ per ion and $(Ze)^2(\rho/Am_\mathrm{H})^{4/3}$ per unit volume, while the density of gravitational energy is

$$-\,\Omega \simeq GM\rho/R \simeq GM\rho/(M/\rho)^{1/3} = GM^{2/3}\rho^{4/3}. \tag{A6.43}$$

Thus both energy densities have the same dependence on ρ. The critical mass is then given by

$$M_{\mathrm{plan}} \simeq \left(\frac{Z64e^2}{Gm_\mathrm{H}^2}\right)^{3/2} m_\mathrm{H}/\mu^2 \simeq 10^{-3}\,M_\odot \tag{A6.44}$$

for $Z = \mu = 1$. This is essentially just $\alpha^{3/2}$ times the Chandrasekhar mass (see Eq. 5.56).

3. From Saha's equation, $\mathrm{O}^{7+}/\mathrm{O}^{8+} = 0.63$. Lower states of ionization have lower populations, but are by no means negligible. Neglecting them nonetheless (as they will contribute some opacity), we have $\mathrm{O}^{7+}/\mathrm{O} \le 0.39$. The opacity is then

$$10^{-19} \times 0.39 Z_\mathrm{O}/A_\mathrm{O}m_\mathrm{H} \simeq 15\,\mathrm{cm}^2\,\mathrm{gm}^{-1} \gg \kappa_{\mathrm{es}}. \tag{A6.45}$$

The mean separation between ions is $(\mu m_\mathrm{H}/\rho)^{1/3} = 2.3 \times 10^{-9}\,\mathrm{cm}$, or about half the Bohr radius, so that no states of neutral hydrogen can exist.

4. Writing a monochromatic version of Eq. (3.15),

$$-\frac{dK_\nu}{\kappa_\nu \rho dz} = H_\nu \tag{A6.46}$$

and

$$-\frac{dK}{\bar{\kappa}\rho dz} = H = \int H_\nu d\nu. \tag{A6.47}$$

So

$$\frac{1}{\bar{\kappa}} = \frac{\int (1/\kappa_\nu)(dK_\nu/dz)d\nu}{dK/dz}. \tag{A6.48}$$

The Roseland formula follows by dividing top and bottom by dT/dz and taking $K_\nu = J_\nu/3 = B_\nu(T)/3$.

5. Writing

$$B_\nu(T) \propto \nu^3(e^{\nu\theta} - 1)^{-1}, \tag{A6.49}$$

where $\theta \equiv h/kT$, we have

$$\frac{dB_\nu}{d\theta} \propto \frac{\nu^4 e^{\nu\theta}}{(e^{\nu\theta} - 1)^2} \tag{A6.50}$$

and with $\kappa_\nu \propto \nu^{-3}\theta^{1/2}$

$$\frac{1}{\kappa} = \frac{\int \nu^7\theta^{-1/2}e^{\nu\theta}(e^{\nu\theta}-1)^{-2}d\nu}{\int \nu^4 e^{\nu\theta}(e^{\nu\theta}-1)^{-2}d\nu} = (kT)^{3.5}\frac{\int x^7 e^x(e^x-1)^{-2}dx}{\int x^4 e^x(e^x-1)^{-2}dx}. \tag{A6.51}$$

6. At the Eddington limit,

$$g = \frac{GM}{R^2} = \frac{\kappa\pi F}{c} = \frac{\kappa L}{4\pi R^2 c}, \tag{A6.52}$$

whence

$$\frac{L_{\text{Edd}}}{L_\odot} = \frac{4\pi cGM}{\kappa L_\odot} = 3.3 \times 10^4 \mu_e \frac{M}{M_\odot} \tag{A6.53}$$

for electron scattering opacity.

7.

$$P_c = \frac{G}{4\pi}\int \frac{m\,dm}{r^4} < \frac{G}{4\pi}\left(\frac{4\pi\rho_c}{3}\right)^{4/3}\int m^{-1/3}dm. \tag{A6.54}$$

$$\frac{1-\beta}{\beta^4} = P^3 a\left(\frac{\mu m_H}{k\rho}\right)^4 < 0.1\mu^2\left(\frac{M}{M_\odot}\right)^2 \tag{A6.55}$$

(see Eq. A4.20). With $\mu = 0.6$, the upper limits to $1-\beta$ are 0.03 ($M_\odot$), 0.56 (20 $M_\odot$), 0.67 (40 $M_\odot$). More precise, and considerably smaller, limits are derived from Eddington's quartic equation (Appendix 4).

8. -1.7.

10. If the metal abundance is $f \times$ some standard (e.g. solar), then κ/P_{ph} is replaced by $f\kappa/P_{\text{ph}}$ in Eqs. (5.63), (5.64), equivalent to replacing M by $Mf^{-1/2}$ (for $a = 1$). So in Eq. (5.65) T_{eff} is multiplied by $Z^{-0.1}$.

11. Using B to denote $(2\pi\hbar^2/m_H kT)^{3/2}$,

$$\frac{^8\text{Be}}{^4\text{He}} = \frac{n_\alpha}{2^{3/2}}Be^{x/kT}; \tag{A6.56}$$

$$\frac{^{12}\text{C}^{**}}{^8\text{Be}} = \frac{n_\alpha}{(8/3)^{3/2}}Be^{(7.275-7.654-x)/kT}; \tag{A6.57}$$

$$\frac{^{12}\text{C}^{**}}{^4\text{He}} = \left(\frac{3}{16}\right)^{3/2}\left(\frac{\rho}{4m_H}\right)^2 B^2 e^{-0.379\,\text{MeV}/kT} = 3.8 \times 10^{-29}. \tag{A6.58}$$

Hence the volume density of $^{12}\text{C}^{**}$ is

$$3.8 \times 10^{-29}(\rho/4m_H) = 0.57\,\text{cm}^{-3} \tag{A6.59}$$

and the production rate of ground-state ^{12}C is

$$0.57 \times 0.0037 \times 2.42 \times 10^{14} = 5 \times 10^{11}\,\text{cm}^{-3}\,\text{s}^{-1}. \tag{A6.60}$$

12. Equating chemical potentials,

$$Z_i[m_pc^2 + kT \ln(n_p/2n_{Q(p)})] + N_i[m_nc^2 + kT \ln(n_n/2n_{Q(n)})]$$
$$= A_i[m_ic^2 + kT \ln(n_i/u_in_{Q(i)})] \tag{A6.61}$$

and $n_i \equiv Y_i\rho/m_H$.

13. Use Eq. (5.115) with $Y_\alpha = 1/8$, $Y_p = Y_n = 1/4$. $T_9 \simeq 15$.

14.

$$\frac{dL}{dt} \propto \frac{dL}{dM_c}\frac{dM_c}{dt} \propto M_c^{16.4} \propto L^{1.86}. \tag{A6.62}$$

15. 1.9×10^{51} erg. $0.6GM^2/R = 3.2 \times 10^{50}$ erg.

Chapter 6

1. Taking $N_0 = 1$ initially, $N_0 = e^{-\sigma\tau}$ and we have

$$\frac{dN_1}{d\tau} + \sigma N_1 = \sigma e^{-\sigma\tau} N_1 = \sigma\tau e^{-\sigma\tau}; \tag{A6.63}$$

$$\frac{dN_2}{d\tau} + \sigma N_2 = \sigma^2\tau e^{-\sigma\tau} N_2 = \frac{1}{2}(\sigma\tau)^2 e^{-\sigma\tau} \dots \tag{A6.64}$$

leading to

$$N_k(\tau) = \frac{(\sigma\tau)^k}{k!}e^{-\sigma\tau}. \tag{A6.65}$$

With an exponential distribution of exposures,

$$N_k(\tau_0) = \frac{\sigma^k}{k!\tau_0}\int_0^\infty \tau^k e^{-\tau(\sigma+1/\tau_0)}d\tau \tag{A6.66}$$

$$= \frac{1}{\sigma\tau_0}\left(\frac{\sigma}{\sigma+1/\tau_0}\right)^{k+1}\frac{1}{k!}\int_0^\infty x^k e^{-x}dx \tag{A6.67}$$

$$= (\sigma\tau_0)^{-1}(1+1/\sigma\tau_0)^{-(k+1)}. \tag{A6.68}$$

2. 0.67.

3. In Eq. (2.96), $\lambda \propto \int_0^Q E^2(Q-E)^2 dE$.

Chapter 7

1. Salpeter(0.1):   2.7 to 0.13;
   Kroupa–Salpeter: 1.2 to 0.17;
   Kroupa–Scalo: 1.7 to 0.15
   (for a total mass of 1 $M_\odot$).

2.

	SFR $(M_\odot$ yr$^{-1})$	$N_{SN}(100)$ per unit mass	$N_{SN}(50)$ per unit mass	$N_{SN}(100)$ per century	Mean SN mass (10 to 100 $M_\odot$)
Salpeter(0.1)	8.5	0.0054	0.0050	4.6	25 $M_\odot$
Kroupa–Sal.	10	0.0073	0.0067	7.3	25 $M_\odot$
Kroupa–Scalo	8	0.0030	0.0029	2.4	20 $M_\odot$

3.

IMF	Oxygen yield
Salpeter(0.1)	0.015
Kroupa–Salpeter	0.020
Kroupa–Scalo	0.006

Chapter 8

1.

$$\frac{d}{dS}(gX_D) = -X_D - X_{D,E}\frac{E}{\psi} + X_{D,F}\frac{F}{\psi}. \tag{A6.69}$$

In the Simple model,

$$-g\frac{dX_D}{dg} = g\frac{dX_D}{ds} = -X_D\left(\frac{1}{\alpha} - 1\right), \tag{A6.70}$$

leading to Eq. (8.63). The remaining fractions of primordial D are 0.67 and 0.2 respectively.

2. $u = \int_0^s ds'/g$ leads to Eq. (8.65). Using Eq. (7.36) with $dg/ds = -(1+\eta)$,

$$-g\frac{dz}{dg} = \frac{1}{1+\eta}, \tag{A6.71}$$

i.e. the same as the Simple model with p divided by $(1+\eta)$.

From Eqs. (8.64), (8.65),

$$z = (1+\eta)^{-1}\ln(1/g), \tag{A6.72}$$

and from Eq. (A6.69)

$$-g\frac{dX_D}{ds} = g\frac{dX_D}{dg}(1+\eta) = X_D\left(\frac{1}{\alpha} - 1\right). \tag{A6.73}$$

Hence using Eq. (A6.72)

$$\frac{X_D}{X_{D,0}} = g^{(1/\alpha-1)/(1+\eta)} = e^{-z(1/\alpha-1)}. \tag{A6.74}$$

3. In Eq. (8.39), substitute z from Eq. (8.38) and differentiate wrt u.

4. Taking $\omega\Delta = 0.4$ (Table 8.1), $\dot{s}(u - \omega\Delta)/\dot{s}(u_{now}) = 0.87/0.75 = 1.16$ (Table 8.2). Hence $N_{Ia}/N_{II} = 0.21$.

7. In the Simple model, taking the primary yield as p_1 and the secondary yield as $p_2 z_1$, the primary abundance is

$$Z_1 \equiv p_1 z_1 = p_1 u, \tag{A6.75}$$

and the secondary abundance is

$$Z_2 = \int_0^u p_2 u' du' = \frac{1}{2} p_2 u^2, \tag{A6.76}$$

so

$$\frac{Z_2}{Z_1} = \frac{1}{2} \frac{p_2}{p_1} u = \frac{1}{2} \frac{p_2}{p_1} z_1. \tag{A6.77}$$

In the simple inflow model, the primary abundance is

$$Z_1 \equiv p_1 z_1 = \frac{1}{u} \int_0^u p_1 u' du' = \frac{1}{2} p_1 u, \tag{A6.78}$$

and the secondary abundance is

$$Z_2 = \frac{1}{2u} p_2 \int_0^u u'^2 du' = \frac{1}{6} p_2 u^2, \tag{A6.79}$$

making

$$\frac{Z_2}{Z_1} = \frac{1}{3} \frac{p_2}{p_1} u = \frac{2}{3} \frac{p_2}{p_1} z_1. \tag{A6.80}$$

Chapter 9

1. 0.52.
2. Since E is the kinetic energy, $p^2 c^2 = (E + E_0)^2 - E_0^2$.
3. Number density is $\phi/c = 2.9 \times 10^{-10} \, \text{cm}^{-3}$.
   Energy density is $0.46 \, \text{eV} \, \text{cm}^{-3}$. Mean energy is $1.6 \, \text{GeV}$.
   The rate of cosmic-ray energy production per cm^3 is thus $0.46 \, \text{eV}/10^7$ yr, or $2.4 \times 10^{-27} \, \text{erg} \, \text{s}^{-1}$. The rate of beryllium production per cm^3 is about $7 \times 10^{-29} \, \text{atoms} \, \text{s}^{-1}$, so $Q/W \simeq 0.03$ Be atoms per erg.
4. 7×10^{-12}.
5. 5.3×10^{-12}.

Chapter 10

1. 50 yr.
2.

$$k \frac{e^{\lambda_{235} t} - 1}{e^{\lambda_{238} t} - 1} = \frac{207(t)/204 - 207(0)/204}{206(t)/204 - 206(0)/204}. \tag{A6.81}$$

The slope is 0.66 compared to 0.07 for Rb–Sr.

3. Eq. (10.34) is true if, for both species, $\frac{1}{2}\lambda^2 < (t - \langle\tau\rangle)^2 > \ll 1$.
   For Solar-System ^{232}Th, ^{238}U, $\Delta - \langle\tau\rangle = 3.2$ Gyr. The error from uncertainties in $\ln K$
   is of order 10 per cent, and that from neglecting the quadratic term in Eq. (10.33) is also
   of order 10 per cent, but is systematic in the sense that the 3.2 Gyr is an overestimate by
   about that amount.
4. For $\lambda_i \Delta \gg 1$, Eq. (10.15) reduces to $1/\lambda_i \Delta$. For a stable element it reduces to $1/(1-S)$.
   The corresponding limits for Eq. (10.22) are $1/\lambda_i \Delta$ and $1/2$.

Chapter 11

2. From Eq. (7.34),

$$\frac{d}{ds}(gZ) = p(1 - \eta^*) - Z(1 + \eta + \eta^* R^*/\alpha). \tag{A6.82}$$

Also,

$$\frac{dg}{ds} = -(1 + \eta + \eta^* R^*/\alpha), \tag{A6.83}$$

leading to Eq. (11.29). $R^* = \int_{10}^{100}(m - m_{\mathrm{rem}})\phi(m)dm < 0.048$.
3. From Eq. (11.20),

$$\frac{ds}{dz} = M_e \frac{p+1}{p}(1 - e^{-z})^{1/p}. \tag{A6.84}$$

Chapter 12

1. The specific intensity is $(c/4\pi)\times$ the radiation energy density and all photons ever
   emitted are still here (in the absence of intergalactic absorption). Their energy is
   reduced by a factor of $(1+z)$, which is taken up by the $d\nu$ factor in any energy interval
   $I_\nu d\nu$, leaving I_ν unchanged.
2. From Eq. (12.16), $\Delta X = 1.62$ (open Universe) or 0.90 (Einstein–de Sitter Universe).
   Then from Eq. (12.14), $\Omega_{\mathrm{HI}} = 6.5 \times 10^{-4}h^{-1}$ or $1.2 \times 10^{-3}h^{-1}$ respectively.
3. In a flat Universe $\Omega_\Lambda + \Omega_M = 1$, so replace the bracket $(1 + Z\Omega_M)$ in Eq. (12.17) with
   $(\Omega_\Lambda + \Omega_M + Z\Omega_M)$ and expand out.

References

Aharonian, F., Akhperjanian, A. G., Bazer-Bachi, A. R. *et al.* 2006, *Nature*, **440**, 1018.

Ahmad, Q. R., Allen, R. C., Andersen, T. C. *et al.* 2002, *Phys. Rev. Lett.*, **89a**, 1301.

Akerman, C. J., Carigi, L., Nissen, P. E., Pettini, M. & Asplund, M. 2004, *A & A*, **414**, 931.

Akerman, C. J., Ellison, S. L., Pettini, M. & Steidel, C. C. 2005, *A & A*, **440**, 499.

Alcock, C., Allsman, R. A., Alves, D. R. *et al.* 2000, *Ap. J.*, **542**, 281.

Allen, C. W. 1973, *Astrophysical Quantities*, London: Athlone Press.

Allende-Prieto, C., Lambert, D. L. & Asplund, M. 2001, *Ap. J. Lett.*, **556**, L63.

Aller, L. H. & Greenstein, J. L. 1960, *Ap. J. Suppl.*, **5**, 139.

Alloin, D., Collin-Souffrin, S., Joly, M. & Vigroux, L. 1979, *A & A*, **78**, 200.

Aloisi, A., Savaglio, S., Heckman, T. M. *et al.* 2003, *Ap. J.*, **595**, 760.

Alpher, R. A., Follin, J. W. & Herman, R. C. 1953, *Phys. Rev.*, **92**, 1347.

Alpher, R. A. & Herman, R. C. 1950, *Rev. Mod. Phys.*, **22**, 153.

Amari, S., Nittler, L. R., Zinner, E., Lodders, K. & Lewis, R. S. 2001, *Ap. J.*, **559**, 463.

Anders, E. 1988, in J. F. Kerridge & M. S. Matthews (eds.), *Meteorites and the Early Solar System*, Tucson: University of Arizona Press, p. 927.

Anders, E. & Grevesse, N. 1989, *Geochim. Cosmochim. Acta*, **53**, 197.

Anders, E. & Zinner, E. 1993, *Meteoritics*, **28**, 490.

Andrievsky, S. M., Luck, R. E., Martin, P. & Lépine, J. R. D. 2004, *A & A*, **413**, 159.

Angulo, C., Arnould, M., Rayet, M. *et al.* 1999, *Nucl. Phys.,* **A656**, 3.

Arimoto, N. 1989, in J. E. Beckman & B. E. J. Pagel (eds.), *Evolutionary Phenomena in Galaxies*, Cambridge: Cambridge University Press, p. 341.

Armand, C., Milliard, B. & Deharveng, J. M. 1994, *A & A*, **284**, 12.

Arnaud, M., Rothenflug, R., Boulade, O., Vigroux, L. & Vangioni-Flam, E. 1992, *A & A*, **254**, 49.

Arnett, D. 1996, *Supernovae and Nucleosynthesis*, Princeton: Princeton University Press.

Asplund, M. 2000, *A & A*, **359**, 758.

Asplund, M., Grevesse, N. & Sauval, A. J. 2005, in T. G. Barnes III & F. N. Bash (eds.), *Cosmic Abundances as Records of Stellar Evolution and Nucleosynthesis*, ASP Conf. Series, **336**, 25.

Asplund, M., Lambert, D. L., Kipper, T. *et al.* 1999, *A & A*, **343**, 507.

Asplund, M., Nordlund, Å., Trampedach, R., Allende-Prieto, C. & Stein, R. F. 2000a, *A & A*, **359**, 729.

Asplund, M., Nordlund, Å., Trampedach, R. & Stein, R. F. 2000b, *A & A*, **359**, 743.

Atkinson, R. d'E. & Houtermans, F. G. 1929, *Zs. f. Phys.*, **54**, 656.

Aubourg, E., Bareyre, P., Bréhin, S. *et al.* 1993, *Nature*, **365**, 623.

Baade, W. 1963, *The Evolution of Stars and Galaxies*, Cambridge, Mass.: Harvard University Press; reprinted by Cambridge, Mass.: MIT Press 1975.

Badnell, N. R., Bautista, M. A., Butler, K. *et al.* 2005, *MNRAS*, **360**, 458.

Bahcall, J. N., Flynn, C. & Gould, A. 1992, *Ap. J.*, **389**, 234.

Bahcall, J. N., Huebner, W. F., Lubow, S. H., Parker, P. D. & Ulrich, R. K. 1982, *Rev. Mod. Phys.*, **54**, 767.

Bahcall, J. N. & Peebles, P. J. E. 1969, *Ap. J.*, **156**, 7.

Bahcall, J. N., Pinsonneault, M. H. & Basu, S. 2001, *Ap. J.*, **555**, 990.

Baker, J. G. & Menzel, D. H. 1938, *Ap. J.*, **88**, 52.

Balser, D. S., Bania, T. M., Rood, R. T. & Wilson, T. L. 1999, *Ap. J.*, **510**, 759.

Bania, T. M., Rood, R. T. & Balser, D. S. 2002, *Nature*, **415**, 54.

Bao, Z. Y. & Käppeler, F. 1987, *At. Data Nucl. Data Tables*, **36**, 411.

Barnes, J. E. 1995, in C. Muñoz-Tuñon & F. Sánchez (eds.), *The Formation and Evolution of Galaxies*, Cambridge: Cambridge University Press, p. 399.

Bazan, G. & Mathews, W. G. 1990, *Ap. J.*, **354**, 644.

Beer, H., Voss, F. & Winters, R. R. 1992, *Ap. J. Suppl.*, **80**, 403.

Beers, T. M., Preston, G. W. & Shectman, S. A. 1992, *Astr. J.*, **103**, 1987.

Beers, T. M. & Sommer-Larsen, J. 1995, *Ap. J. Suppl.*, **96**, 175.

Bell, A. R. 1978, *MNRAS*, **182**, 147, 443.

Belley, J. & Roy, J.-R. 1991, *Ap. J. Suppl.*, **78**, 61.

Bender, R. 1992, in B. Barbuy & A. Renzini (eds.), IAU Symp. no. 149: *The Stellar Populations of Galaxies*, Dordrecht: Kluwer, p. 267.

Bender, R., Burstein, D. & Faber, S. M. 1992, *Ap. J.*, **399**, 462.

Bender, R., Burstein, D. & Faber, S. M. 1993, *Ap. J.*, **411**, 153.

Benjamin, R. A., Skillman, E. D. & Smits, D. P. 1999, *Ap. J.*, **514**, 307.

Benjamin, R. A., Skillman, E. D. & Smits, D. P. 2002, *Ap. J.*, **569**, 288.

Bensby, T., Feltzing, S. & Lundström, I. 2003, *A & A*, **410**, 527.

Bensby, T., Feltzing, S. & Lundström, I. 2004a, *A & A*, **415**, 155.

Bensby, T., Feltzing, S. & Lundström, I. 2004b, *A & A*, **421**, 969.

Bernstein, R. A., Freedman, W. A. & Madore, B. F. 2002, *Ap. J.*, **571**, 56.

Bernstein, R. A., Freedman, W. A. & Madore, B. F. 2005, *Ap. J.*, **632**, 713.

Bessell, M. S., Sutherland, R. & Ruan, K. 1991, *Ap. J. Lett.*, **383**, L71.

Bica, E. 1988, *A & A*, **195**, 76.

Bica, E. & Alloin, D. 1986, *A & A*, **162**, 21.

Bica, E. & Alloin, D. 1987, *A & A*, **186**, 49.

Bienaimé, O., Robin, A. S. & Crézé, M. 1987, *A & A*, **180**, 94.

Binette, L., Dopita, M. A. & Tuohy, I. R. 1985, *Ap. J.*, **297**, 476.

Binney, J. & Tremaine, S. 1987, 2008, *Galactic Dynamics*, Princeton: Princeton University Press.

Birks, J. B. 1962, Rutherford at Manchester, London: Heywood.

Black, D. C. 1971, *Nature Phys. Sci.*, **234**, 148.

Blackwell, D. E., Booth, A. J., Haddock, D. J., Petford, A. D. & Leggett, S. K. 1986, *MNRAS*, **220**, 549.

Blain, A. W. & Longair, M. S. 1993, *MNRAS*, **265**, L21.

Bloemen, H., Morris, D., Knödelseder, A. *et al.* 1999, *Ap. J.*, **521**, 137.

Bloemen, H., Wijnans, R., Bennett, K. *et al.* 1994, *A & A*, **281**, L5.

Blumenthal, G. R., Faber, S. M., Primack, J. R. & Rees, M. J. 1984, *Nature*, **311**, 517.

Boesgaard, A. M. 2001, *New Astr. Rev.*, **45**, 525.

Boesgaard, A. & King, J. R. 1993, *Astr. J.*, **106**, 2309.

Boesgaard, A. & Steigman, G. 1985, *Ann. Rev. Astr. Astrophys.*, **23**, 319.

Boissé, P., Le Brun, V., Bergeron, J. & Deharveng, J. 1998, *A & A*, **333**, 841.

Boissier, S. & Prantzos, N. 1999, *MNRAS*, **307**, 857–876.

Bouché, N., Lehnert, M. D. & Péroux, C. 2005, *MNRAS*, **364**, 319.

Bouché, N., Lehnert, M. D. & Péroux, C. 2006, *MNRAS*, **367**, 16.

Bressan, A., Chiosi, C. & Fagotto, F. 1994, *Ap. J. Suppl.*, **94**, 63.

Brocato, E., Matteucci, F., Mazzitelli, I. & Tornambé, A. 1990, *Ap. J.*, **349**, 458.

Brown, G. E., Bruenn, S. W. & Wheeler, J. C. 1992, *Comments Astrophys.*, **16**, 153.

Brusa, M., Comastri, A. & Vignali, C. 2001, in D. M. Neumann & J. T. T. Van (eds.), *Clusters and galaxies in the high redshift Universe observed in X-Rays*, XXIst Moriond Astrophysics Meeting.

Bruzual, A. & Charlot, S. 1993, *Ap. J.*, **405**, 538.

Burbidge, E. M., Burbidge, G. R., Fowler, W. A. & Hoyle, F. 1957, *Rev. Mod. Phys.*, **29**, 547.

Burkert, A. & Hensler, G. 1989, in J. E. Beckman & B. E. J. Pagel (eds.), *Evolutionary Phenomena in Galaxies*, Cambridge: Cambridge University Press, p. 230.

Burkert, A., Truran, J. W. & Hensler, G. 1992, *Ap. J.*, **391**, 651.

Burstein, D., Faber, S. M., Gaskell, C. M. & Krumm, N. 1984, *Ap. J.*, **287**, 586.

Busso, M., Gallino, R. & Wasserburg, G. J. 1999, *Ann. Rev. Astr. Astrophys.*, **37**, 239.

Butcher, H. R. 1987, *Nature*, **328**, 127.

Buzzoni, A. 1989, *Ap. J. Suppl.*, **71**, 817.

Buzzoni, A., Fusi-Pecci, F., Buonanno, R. & Corsi, C. E. 1983, *A & A*, **128**, 94.

Calura, F. & Matteucci, F. 2004, *MNRAS*, **350**, 351.

Calura, F., Matteucci, F. & Vladilo, G. 2003, *MNRAS*, **340**, 59.

Cameron, A. G. W. 1957, Atomic Energy of Canada Ltd, CRL-41; *Pub. Astr. Soc. Pacific*, **69**, 201.

Cameron, A. G. W. 1982, in C. A. Barnes, D. D. Clayton & D. N. Schramm (eds.), *Essays in Nuclear Astrophysics*, Cambridge: Cambridge University Press, p. 23.

Cameron, A. G. W. 1993, in E. H. Levy, E. H. Lunine & M. Matthews (eds.), *Protostars and Planets III*, Tucson: University of Arizona Press, p. 47.

Cameron, A. G. W. & Fowler, W. A. 1971, *Ap. J.*, **164**, 111.

Caputo, F., Martínez Roger, C. & Páez, E. 1987, *A & A*, **183**, 228.

Carigi, L. 1994, *Ap. J.*, **424**, 181.

Carney, B. W., Laird, J. B., Latham, D. W. & Aguilar, L. A. 1996, *Astr. J.*, **112**, 668.

Carney, B. W., Laird, J. B., Latham, D. W. & Kurucz, R. L. 1987, *Astr. J.*, **94**, 1066.

Carney, B. W., Latham, D. W. & Laird, J. B. 1990, *Astr. J.*, **99**, 572.

Carr, B. J. & Rees, M. J. 1979, *Nature*, **278**, 605.

Carswell, R. F. 2004, in A. McWilliam & M. Rauch (eds.), *Origin and Evolution of the Elements*, Carnegie Observatories Astrophysics Series **4**, Cambridge: Cambridge University Press, p. 469.

Cassisi, S., Salaris, M. & Irwin, A. W. 2003, *Ap. J.*, **588**, 862.

Casuso, E. & Beckman, J. E. 1997, *Ap. J.*, **475**, 155.

Casuso, E. & Beckman, J. E. 2004, *A & A*, **419**, 181.

Catchpole, R., Pagel, B. E. J. & Powell, A. L. T. 1967, *MNRAS*, **136**, 403.

Caughlan, G. R. & Fowler, W. A. 1988, *At. Data Nucl. Data Tables*, **40**, 283.

Cayrel, R., Depagne, E., Spite, M. *et al.* 2004, *A & A*, **416**, 1117.

Cayrel, R. & Jugaku, J. 1963, *Ann. d'Ap.*, **26**, 495.

Cen, R. & Ostriker, J. P. 1999, *Ap. J. Lett.*, **519**, L109.

Cen, R. & Ostriker, J. P. 2000, *Ap. J.*, **538**, 83.

Chaboyer, B., Demarque, P. & Sarajedini, A. 1996, *Ap. J.*, **459**, 558.

Chamberlain, J. W. & Aller, L. H. 1951, *Ap. J.*, **114**, 52.

Chamcham, K., Pitts, E. & Tayler, R. J. 1993, *MNRAS*, **263**, 967.

Charbonnel, C. & Do Nascimento, J. D., Jr. 1998, *A & A*, **336**, 915.

Chen, B., Dobaczewski, J., Kratz, K.-L., Langanke, K., Pfeiffer, B., Thielemann, F.-K. & Vogel, P. 1995, *Phys. Lett. B*, **355**, 37.

Chengalur, J. N., Braun, R. & Burton, W. B. 1997, *A & A*, **318**, L35.

Chevalier, R. A. 1976, *Nature*, **260**, 689.

Chiappini, C., Matteucci, F., Beers, T. C. & Nomoto, K. 1999, *Ap. J.*, **515**, 226.

Chiappini, C., Matteucci, F. & Gratton, R. 1997, *Ap. J.*, **477**, 765.

Chieffi, A. & Limongi, M. 2004, *Ap. J.*, **608**, 405.

Chiosi, C. 1980, *A & A*, **83**, 206.

Christensen, T., Petersen, L. & Gammelgaard, P. 1997, *A & A*, **322**, 41.

Christy, R. F. 1966, *Ann. Rev. Astr. Astrophys.*, **4**, 353.

Ciotti, L., D'Ercole, A., Pellegrini, S. & Renzini, A. 1991, *Ap. J.*, **376**, 380.

Clarke, C. J. 1989, *MNRAS*, **238**, 283.

Clayton, D. D. 1964, *Ap. J.*, **139**, 637.

Clayton, D. D. 1968, 1984, *Principles of Stellar Evolution and Nucleosynthesis*, McGraw-Hill and University of Chicago Press, p. 556.

Clayton, D. D. 1982, *Quart. J. RAS*, **23**, 174.

Clayton, D. D. 1985a, in Arnett, W. D. & Truran, J. W. (eds.), *Nucleosynthesis: Challenges and New Developments*, Chicago: University of Chicago Press, p. 65.

Clayton, D. D. 1985b, *Ap. J.*, **285**, 411.

Clayton, D. D. 1987, *Ap. J.*, **315**, 451.

Clayton, D. D. 1988, *MNRAS*, **234**, 1.

Clayton, D. D. 2003, *Handbook of Isotopes in the Cosmos: Hydrogen to Gallium*, Cambridge: Cambridge University Press.

Clayton, D. D., Fowler, W. A., Hull, T. E. & Zimmerman, B. A. 1961, *Annals of Phys.*, **12**, 331.

Clayton, D. D. & Ward, R. A. 1974, *Ap. J.*, **193**, 397.

Clayton, D. D. & Ward, R. A. 1978, *Ap. J.*, **224**, 1000.

Clayton, R. N. 2002, *Nature*, **415**, 860.

Coc, A., Vangioni-Flam, E., Descouvemont, P., Adahchour, A. & Angulo, C. 2004, *Ap. J.*, **600**, 544.

Cohen, J. G., Christlieb, N., McWilliam, A. *et al.* 2004, *Ap. J.*, **612**, 1107.

Cole, S., Norberg, P., Baugh, C. M. *et al.* 2001, *MNRAS*, **326**, 255.

Colgate, S. A. & White, R. H. 1966, *Ap. J.*, **143**, 626.

Connolly, A. J., Szalay, A. S., Dickinson, M. *et al.* 1997, *Ap. J. Lett.*, **486**, L11.

Conti, P. S., Greenstein, J. L., Spinrad, H., Wallerstein, G. & Vardya, M. S. 1967, *Ap. J.*, **148**, 105.

Copi, C., Schramm, D. N. & Turner, M. S. 1995, *Science*, **267**, 192.

Cord, M. S., Peterson, J. D., Lojko, M. S. & Haas, R. H. 1968, *Microwave Spectral Tables V. Spectral Line Listing*, Washington: U.S. Govt. Printing Office.

Cowan, J. J., Sneden, C., Burles, S. *et al.* 2002, *Ap. J.*, **572**, 861.

Cowan, J. J., Thielemann, F.-K. & Truran, J. W. 1987, *Ap. J.*, **323**, 523.

Cowan, J. J., Thielemann, F.-K. & Truran, J. W. 1991a, *Phys. Rep.*, **208**, 267.

Cowan, J. J., Thielemann, F.-K. & Truran, J. W. 1991b, *Ann. Rev. Astr. Astrophys.*, **29**, 447.

Cowan, R. D. 1981, *The Theory of Atomic Structure and Spectra*, Berkeley: University of California Press.

Cowley, C. R. 1995, *An Introduction to Cosmochemistry*, Cambridge: Cambridge University Press.

Cox, D. P. 1972, *Ap. J.*, **178**, 143.

Cox, D. P. & Smith, B. W. 1976, *Ap. J.*, **203**, 361.

Crane, P. (ed.) 1995, *The Light Element Abundances*, Berlin: Springer-Verlag.

Crighton, N. H. M., Webb, J. K., Ortiz-Gil, A. & Fernández-Soto, A. 2004, *MNRAS*, **355**, 1042.

Cunha, K. & Lambert, D. L. 1992, *Ap. J.*, **399**, 586.

Cunha, K. & Lambert, D. L. 1994, *Ap. J.*, **426**, 170.

da Silva, L., Spite, M. & de Medeiros, J. R. (eds.) 2000, IAU Symp. no. 198: *The Light Elements and their Evolution*, ASP publ.

Dame, T. M. 1993, in S. S. Holt & F. Verter (eds.), *Back to the Galaxy*, New York: Amer. Inst. Phys. Publ., p. 267.

Davidson, K. & Kinman, T. D. 1985, *Ap. J. Suppl.*, **58**, 321.

Deharveng, L., Peña, M., Caplan, J. & Costero, R. 2000, *MNRAS*, **311**, 329.

Dekel, A. & Silk. J. 1986, *Ap. J.*, **303**, 39.

del Peloso, E. F., da Silva, L. & Porto de Mello, G. F. 2005, *A & A*, **434**, 275, 301.

Delahaye, F. & Pinsonneault, M. H. 2006, *Ap. J.*, **649**, 529.

Delbouille, L., Roland, G. & Neven, L. 1973, *Spectrophotometric Atlas of the Solar Spectrum*, Institut d'Astrophysique, Université de Liège.

Denicoló, G., Terlevich, R. & Terlevich, E. 2002, *MNRAS*, **330**, 69.

Descouvement, P., Adahchour, A., Angilo, C., Coc, A. & Vangioni-Flam, E. 2004, *At. Data and Nuclear Data Tables*, **88**, 203.

Díaz, A. & Pérez-Montero, E. 2000, *MNRAS*, **312**, 130.

Dopita, M. A. 1977, *Ap. J. Suppl.*, **33**, 437.

Dopita, M. A. 1985, *Ap. J. Lett.*, **295**, L5.

Dopita, M. A., D'Odorico, S. & Benvenuti, P. 1980, *Ap. J.*, **236**, 628.

Dopita, M. A. & Ryder, S. 1994, *Ap. J.*, **430**, 163.

Dopita, M. A. & Sutherland, R. S. 1995, *Ap. J.*, **455**, 468.

Dorman, B., Lee, Y.-W. & VandenBerg, D. 1991, *Ap. J.*, **366**, 115.

Dorman, B., VandenBerg, D. A. & Laskarides, P. G. 1989, *Ap. J.*, **343**, 750.

Drummond, J. D., Christou, J. C. & Fugate, R. Q. 1995, *Ap. J.*, **450**, 380.

Duncan, D., Lambert, D. L. & Lemke, M. 1992, *Ap. J.*, **401**, 584.

Dunne, L., Eales, S. A. & Edmunds, M. G. 2003, *MNRAS*, **341**, 589.

Dwek, E., Arendt, R. G. & Krennrich, F. 2005, *Ap. J.*, **635**, 784.

Eddington, A. S. 1926, *The Internal Constitution of the Stars*, Cambridge: Cambridge University Press.

Edmunds, M. G. 1975, *Ap. & Sp. Sci*, **32**, 483.

Edmunds, M. G. 1990, *MNRAS*, **246**, 678.

Edmunds, M. G. 1992, in M. G. Edmunds & R. J. Terlevich (eds.), *Elements and the Cosmos*, Cambridge: Cambridge University Press, p. 289.

Edmunds, M. G. & Greenhow, R. M. 1995, *MNRAS*, **272**, 241.

Edmunds, M. G., Greenhow, R. G., Johnson, D., Kluckers, V. & Vila, B. M. 1991, *MNRAS*, **251**, 33P.

Edmunds, M. G. & Pagel, B. E. J. 1978, *MNRAS*, **185**, 77P.

Edvardsson, B., Andersen, J., Gustafsson, B., Lambert, D. L., Nissen, P. E. & Tomkin, J. 1993, *A & A*, **275**, 101.

Edvardsson, B., Gustafsson, B., Johansson, S. G., Kiselman, D., Lambert, D. L., Nissen, P. E. & Gilmore, G. 1994, *A & A*, **290**, 176.

Eggen, O. J., Lynden-Bell, D. & Sandage, A. R. 1962, *Ap. J.*, **136**, 748.

Eggleton, P. P., Dearborn, D. S. P. & Lattanzio, J. C. 2006, *Science*, **314**, 1580.

Einstein, A. 1917, *Phys. Zs.*, **18**, 121.

Ellison, S. L., Yan, L., Hook, I. M., Pettini, M., Wall, J. V. & Shaver, P. 2001, *A & A*, **379**, 393.

Elmegreen, B. & Scalo, J. 2004, *Ann. Rev. Astr. Ap.*, **42**, 211.

Epstein, R. I., Lattimer, J. M. & Schramm, D. N. 1976, *Nature*, **263**, 198.

Erb, D. K., Shapley, A. E., Pettini, M. *et al.* 2006, *Ap. J.*, **644**, 813.

Faber, S. M. 1973, *Ap. J.*, **179**, 731.

Faber, S. M., Burstein, D. & Dressler, A. 1977, *Astr. J.*, **82**, 941.

Faber, S. M., Friel, E. D., Burstein, D. & Gaskell, C. M. 1985, *Ap. J. Suppl.*, **57**, 711.

Faber, S. M. & Jackson, R. E. 1976, *Ap. J.*, **204**, 668.

Faber, S. M. & Lin, D. 1983, *Ap. J. Lett.*, **266**, L17.

Faulkner, J. 2005, in D. Gough (ed.), *The Scientific Legacy of Fred Hoyle*, Cambridge: Cambridge University Press, p. 149.

Faulkner, J. & Iben, I., Jr. 1966, *Ap. J.*, **144**, 995.

Favata, F., Micela, G. & Sciortino, S. 1997, *A & A*, **323**, 998.

Fazio, A., Ashby, M. L. N., Hora, J. L. *et al.* 2004, *Ap. J. Suppl.*, **154**, 39.

Feltzing, S. & Gustafsson, B. 1994, *Ap. J.*, **423**, 68.

Feltzing, S., Holmberg, J. & Hurley, J. R. 2001, *A & A*, **377**, 911.

Ferland, G. J., Korista, K. C., Verner, D. A., Ferguson, J. W., Kingdon, J. B. & Verner, E. M. 1998, *Pub. Astr. Soc. Pacific*, **110**, 761.

Fermi, E. 1949, *Phys. Rev.*, **75**, 1169.

Fermi, E. 1954, *Ap. J.*, **119**, 1.

Ferrara, A. & Tolstoy, E. 2000, *MNRAS*, **313**, 291.

Ferreras, I., Scannapieco, E. & Silk, J. 2002, *Ap. J.*, **579**, 247.

Ferrini, F., Matteucci, F., Pardi, C. & Penco, U. 1992, *Ap. J.*, **387**, 138.

Ferrini, F., Mollá, M., Pardi, C. & Díaz, A. I. 1994, *Ap. J.*, **427**, 745.

Fields, B. D., Olive, K. A. & Schramm, D. N. 1995, *Ap. J.*, **439**, 854.

Fields, B. D. & Prodanović, T. 2005, *Ap. J.*, **623**, 877.

Fields, B. D. & Sarkar, S. 2006, *Rev. Part. Phys.*; Yao, W.-M. *et al., J. Phys.* G, **33**, 1; arXiv:astro-ph/0601514vz.

Finkbeiner, D. P., Davis, M. & Schlegel, D. J. 2000, *Ap. J.*, **544**, 81.

Finoguenov, A., Burkert, A. & Böhringer, H. 2003, *Ap. J.*, **594**, 136.

Fish, R. A. 1964, *Ap. J.*, **139**, 284.

Fisher, D., Franx, M. & Illingworth, G. D. 1996, *Ap. J.*, **459**, 110.

Fixsen, D. J., Dwek, E., Mather, J. C. *et al.* 1998, *Ap. J.*, **508**, 123.

Fleming, T. A., Liebert, J. & Green, R. F. 1986, *Ap. J.*, **308**, 176.

Flynn, C. & Fuchs, B. 1994, *MNRAS*, **270**, 471.

Flynn, C. & Morell, O. 1997, *MNRAS*, **286**, 617.

Fowler, W. A. 1987, *Quart. J. RAS*, **28**, 87.

Franceschini, A., Toffolatti, L., Mazzei, P., Danese, L. & De Zotti, G. 1991, *A & A Suppl.*, **89**, 285.

Franx, M. & Illingworth, G. 1990, *Ap. J. Lett.*, **359**, L41.

Freeman, K. C. 1990, in R. Wielen (ed.), *Dynamics and Interactions of Galaxies*, Berlin: Springer-Verlag, p. 36.

Friel, E. D., Janes, K. A., Tavarez, M. *et al.* 2002, *Astr. J.*, **124**, 2693.

Fuhrmann, K. 1998, *A & A*, **338**, 161.

Fukugita, M., Hogan, C. J. & Peebles, P. J. E. 1998, *Ap. J.*, **503**, 518.

Fukugita, M. & Kawasaki, M. 2006, *Ap. J.*, **646**, 691.

Fukugita, M. & Peebles, P. J. E. 2004, *Ap. J.*, **616**, 643.

Fulbright, J. P., McWilliam, A. & Rich, R. M. 2006, *Ap. J.*, **636**, 821.

Gallego, J., Zamorano, J., Aragón-Salamanca, A. & Rego, M. 1995, *Ap. J. Lett.*, **455**, L1.

Gallino, R. 1989, in H. R. Johnson & B. Zuckerman (eds.), *Evolution of Peculiar Red Giants*, Cambridge: Cambridge University Press, p. 176.

Gallino, R., Arlandini, C., Busso, M., Lugaro, M., Travaglio, C. *et al.* 1998, *Ap. J.*, **497**, 388.

Gamow, G. & Critchfield, C. L. 1949, *Theory of Atomic Nucleus and Nuclear Energy Sources*, Oxford: Clarendon Press, p. 273.

Garcia-López, R., Israelian, G., Rebolo, R. *et al.* 2001, *New Astr. Rev.*, **45**, 519.

Garcia-López, R., Lambert, D. L., Edvardsson, B., Gustafsson, B., Kiselman, D. & Rebolo, R. 1998, *Ap. J.*, **500**, 241.

Garnett, D. R. 1990, *Ap. J.*, **363**, 142.

Garnett, D. R. 2004, in C. Esteban, R. J. García López, A. Herrero & F. Sánchez (eds.), XIII Canary Islands Winter School on Astrophysics, *Cosmochemistry*, Cambridge: Cambridge University Press, pp. 204, 208–209, 482.

Gasson, R. E. M. & Pagel, B. E. J. 1966, *Observatory*, **86**, 196.

Geiss, J. & Gloeckler, G. 2003, in R. Kallenbach *et al.* (eds.), *Solar System History from Isotopic Signatures of Volatile Elements*, Dordrecht: Kluwer, ≡ *Space Sci. Rev.*, **106**, 3.

Geiss, J. & Reeves, H. 1972, *A & A*, **18**, 126.

Gerola, H. & Seiden, P. E. 1978, *Ap. J.*, **223**, 129.

Gilmore, G., Edvardsson, B. & Nissen, P. E. 1991, *Ap. J.*, **378**, 17.

Gilmore, G., Gustafsson, B., Edvardsson, B. & Nissen, P. E. 1992, *Nature*, **357**, 379.

Gilmore, G. & Reid, I. N. 1983, *MNRAS*, **202**, 1025.

Gilmore, G. & Wyse, R. F. G. 1985, *Astr. J.*, **90**, 2015.

Gilmore, G. & Wyse, R. F. G. 1986, *Nature*, **322**, 806.

Gilmore, G. & Wyse, R. F. G. 1991, *Ap. J. Lett.*, **367**, L55.

Gilmore, G., Wyse, R. F. G. & Jones, J. B. 1995, *Astr. J.*, **109**, 1095.

Gilmore, G., Wyse, R. F. G. & Kuijken, K. 1989, *Ann. Rev. Astr. Astrophys.*, **27**, 555.

Gispert, R., Lagache, G. & Puget, J. L. 2000, *A & A*, **360**, 1.

Gloeckler, G. & Geiss, J. 1996, *Nature*, **381**, 210.

Goldschmidt, V. M. 1954, *Geochemistry*, Oxford: Oxford University Press.

Goldstein, M. A., Fisk, L. A. & Ramaty, R. 1970, *Phys. Rev. Lett.*, **25**, 832.

Gonzalez, G., Lambert, D. L., Wallerstein, G. *et al.* 1998, *Ap. J. Suppl.*, **114**, 133.

Goodwin, S. P. & Pagel, B. E. J. 2005, *MNRAS*, **359**, 707.

Gordy, W. & Cook, R. L. 1984, *Microwave Molecular Spectra*, New York: Wiley.

Gorgas, J., Efstathiou, G. & Aragón-Salamanca, A. 1990, *MNRAS*, **245**, 217.

Goriely, S. & Arnould, M. 2001, *A & A*, **379**, 1113.

Gorjian, V., Wright, E. L. & Chary, R. R. 2000, *Ap. J.*, **536**, 550.

Goswami, J. N., Marhas, K. K. & Sahijpal, S. 2001, *Ap. J.*, **549**, 1151.

Götz, M. & Köppen, J. 1992, *A & A*, **260**, 455.

Gounelle, M., Shu, F. H., Shang, H. *et al.* 2006, *Ap. J.*, **640**, 1163.

Gratton, R., Carretta, E., Matteucci, F. & Sneden, C. 2000, *A & A*, **358**, 671.

Gray, D. F. 2005, *The Observation and Analysis of Stellar Photospheres*, 3rd edn., Cambridge: Cambridge University Press.

Grebel, E. K., Gallagher, J. S. & Harbeck, D. 2003, *Astr. J.*, **125**, 1926.

Greggio, L. & Renzini, A. 1983, *A & A*, **118**, 217.

Grenon, M. 1989, *Ap. Sp. Sci.*, **156**, 29.

Grenon, M. 1990, in B. J. Jarvis & D. M. Terndrup (eds.), *Bulges of Galaxies*, ESO Conf. & Workshop Proc. no. 5, Garching: ESO, p. 143.

Grenon, M. 1999, *Ap. Sp. Sci.*, **265**, 331.

Guiderdoni, B. & Rocca-Volmerange, B. 1987, *A & A*, **186**, 1.

Gunn, J. E. & Peterson, B. A. 1965, *Ap. J.*, **142**, 1633.

Gunn, J. E., Stryker, L. L. & Tinsley, B. M. 1981, *Ap. J.*, **249**, 48.

Gustafsson, B. 1980, in P. E. Nissen & K. Kjär (eds.), Workshop on *Methods of Abundance Determination for Stars*, Geneva: ESO.

Gustafsson, B. 1989, *Ann. Rev. Astr. Ap.*, **27**, 701.

Gustafsson, B., Karlsson, T., Olsson, E., Edvardsson, B. & Ryde, N. 1999, *A & A*, **342**, 426.

Hamann, F., Dietrich, M., Sabra, B. M. & Warner, C. 2004, in A. McWilliam & M. Rauch (eds.), *Origin and Evolution of the Elements*, Carnegie Observatories Astrophysics Series **4**, Cambridge: Cambridge University Press, p. 440.

Hamann, F. & Ferland, G. 1999, *Ann. Rev. Astr. Astrophys.*, **37**, 487.

Harris, J. & Zaritsky, D. 2004, *Astr. J.*, **127**, 1531.

Harrison, G. R. 1939, *MIT Wavelength Tables*, New York: John Wiley & Sons.

Hartwick, F. D. A. 1976, *Ap. J.*, **209**, 418.

Hartwick, F. D. A. 1987, in G. Gilmore & R. F. Carswell (eds.), *The Galaxy*, Dordrecht: Reidel, p. 281.

Harwit, M. & Hauser, M. G. (eds.) 2001. IAU Symp. no. 204, *The Extragalactic Infra-red Background and its Cosmological Implications*, Dordrecht: Kluwer.

Hauser, M. G. & Dwek, E. 2001, *Ann. Rev. Astr. Astrophys.*, **39**, 249.

Hayashi, C. 1950, *Prog. Theor. Phys.* (Japan), **5**, 224.

Hayashi, C. 1961, *Pub. Astr. Soc. Japan*, **13**, 450.

Hayashi, C. 1966, *Ann. Rev. Astr. Ap.*, **4**, 171.

Haywood, J. W., Hegyi, D. J. & Gudehus, D. H. 1992, *Ap. J.*, **392**, 172.

Haywood, M. 2001, *MNRAS*, **325**, 1365.

Haywood, M. 2002, *MNRAS*, **337**, 151.

Heasley, J. N. & Milkey, R. W. 1978, *Ap. J.*, **221**, 677.

Heavens, A., Painter, B., Jimenez, R. & Dunlop. J. 2004, *Nature*, **428**, 625.

Henry, R. B. C., Edmunds, M. G. & Köppen, J. 2000, *Ap. J.*, **541**, 660.

Henry, R. C. B. & Worthey, G. 1999, *Publ. Astr. Soc. Pacific*, **111**, 919.

Hensler, G. & Burkert, A. 1990, *Astrophys. Space Sci.*, **170**, 231, and **171**, 149.

Herzberg, G. 1945, *Molecular Spectra and Molecular Structure II: Infra-red and Raman Spectra of Polyatomic Molecules*, Princeton: Van Nostrand.

Herzberg, G. 1950, *Molecular Spectra and Molecular Structure I: Spectra of Diatomic Molecules*, Princeton: Van Nostrand.

Herzberg, G. 1966, *Molecular Spectra and Molecular Structure III: Electronic Spectra and Electronic Structure of Polyatomic Molecules*, New York: Van Nostrand.

Herzberg, G. 1971, *The Spectra and Structures of Simple Free Radicals*, Ithaca: Cornell University Press.

Higdon, J. C., Lingenfelter, R. E. & Ramaty, R. 1998, *Ap. J.*, **509**, 33.

Hill, V. 2004, in A. McWilliam & M. Rauch (eds.), *Origin and Evolution of the Elements*, Carnegie Observatories Astrophysics Series **4**, Cambridge: Cambridge University Press, p. 203.

Hill, V., Plez, B., Cayrel, R. *et al.* 2002, *A & A*, **387**, 560.

Hirata, K. S., Kajita, T., Koshiba, M. *et al.* 1988, *Phys. Rev. D*, **38**, 448.

Hobbs, L. M. 1974, *Ap. J.*, **191**, 381.

Hohenberg, C. M., Podosek, F. A. & Reynolds, J. H. 1967, *Science*, **156**, 233.

Holtzmann, J. A., Gallagher, J. S. III, Cole, A. A. *et al.* 1999, *Astr. J.*, **118**, 2262.

Holweger, H. & Müller, E. A. 1974, *Solar Phys.*, **39**, 19.

Hoppe, P. & Zinner, E. 2000, *J. Geophys. Res.*, **105**, A5, 10371.

Hoskin, M. A. 1963, *William Herschel and the Construction of the Heavens*, London: Oldbourne.

Hou, J. L., Prantzos, N. & Boissier, S. 2000, *A & A*, **362**, 921

Howard, W. M., Meyer, B. S. & Woosley. S. E. 1991, *Ap. J. Lett.*, **373**, L5.

Hoyle, F. 1946, *MNRAS*, **106**, 343.

Hoyle, F. 1953, *Ap. J.*, **118**, 512.

Hoyle, F. 1954, *Ap. J. Suppl.*, **1**, 121.

Hoyle, F. & Fowler, W. A. 1960, *Ap. J.*, **132**, 565.

Hoyle, F. & Tayler, R. J. 1964, *Nature*, **203**, 1108.

Hughes, D. H., Serjeant, S., Dunlop, J. *et al.* 1998, *Nature*, **394**, 241.

Hummer, D. G., Berrington, K. A., Eissner, W., Pradhan, A. K., Saraph, H. E. & Tully, J. A. 1993, *A & A*, **279**, 309.

Ibata, R. A., Gilmore, G. & Irwin, M. J. 1994, *Nature*, **370**, 194.

Iben, I., Jr. 1965, *Ap. J.*, **141**, 993.

Iben, I., Jr. 1967, *Ann. Rev. Astr. Astrophys.*, **5**, 571.

Iben, I., Jr. 1985, *Ap. J. Suppl.*, **58**, 661.

Iben, I., Jr. 1991, *Ap. J. Suppl.*, **76**, 55.

Iben, I., Jr. 1993, *Ap. J.*, **415**, 767.

Iben, I., Jr. & Renzini, A. 1983, *Ann. Rev. Astr. Astrophys.*, **21**, 271.

Iben, I., Jr. & Renzini, A. 1984, *Phys. Rep.*, **105**, 329.

Iben, I., Jr. & Tutukov, A. V. 1984a, *Ap. J.*, **282**, 615.

Iben, I., Jr. & Tutukov, A. V. 1984b, *Ap. J. Suppl.*, **54**, 335.

Iben, I., Jr. & Tutukov, A. V. 1987, *Ap. J.*, **313**, 727.

Iben, I., Jr., Tutukov, A. V. & Yungelson, L. R. 1996, *Ap. J.*, **456**, 750.

Ivison, R. J., Smail, I., Dunlop. J. S. *et al.* 2005, *MNRAS*, **364**, 1025.

Izotov, Y. & Thuan, T. X. 1998, *Ap. J.*, **500**, 188.

Izotov, Y. I., Thuan, T. X. & Stasinska, G. 2007, *Ap. J.*, **662**, 15.

Jedamzik, K. 2004, *Phys. Rev. D*, **70**, 063524.

Jeffrey, C. S. & Schoenberner, D. 2006, *A & A*, **459**, 885.

Jimenez, R., Bowen, D. V. & Matteucci, F. 1999, *Ap. J. Lett.*, **514**, L83.

Johnson, H. R. & Zuckerman, B. (eds.) 1989, *Evolution of Peculiar Red Giant Stars*, Cambridge: Cambridge University Press.

Jones, B. J. T. 1977, *MNRAS*, **180**, 151.

Jones, F. C. & Ellison, D. C. 1991, *Sp. Sci. Rev.*, **58**, 259.

Jørgensen, B. R. 2000, *A & A*, **363**, 947.

Jorgenson, R. A., Wolfe, A. M., Prochaska, J. X. *et al.* 2006, *Ap. J.*, **646**, 730.

Junkkarinen, V. T., Cohen, R. D., Beaver, E. A. *et al.* 2004, *Ap. J.*, **614**, 658.

Jura, M. 1989, in H. R. Johnson & B. Zuckerman (eds.), *Evolution of Peculiar Red Giant Stars*, Cambridge: Cambridge University Press, p. 348.

Käppeler, F., Beer, H. & Wisshak, K. 1989, *Rep. Prog. Phys.*, **52**, 945.

Käppeler, F., Gallino, R., Busso, M., Picchio, G. & Raiteri, C. M. 1990, *Ap. J.*, **354**, 630.

Kashlinsky, A. 2005, *Phys. Rep.*, **409**, 361.

Kashlinsky, A., Arendt, R. G., Mather, J. & Moseley, S. H. 2007, *Ap. J. Lett.*, **654**, L1.

Kauffmann, G., White, S. D. M & Guiderdoni, B. 1993, *MNRAS*, **264**, 201.

Kaye, G. W. C. & Laby, T. H. 1995, *Tables of Physical and Chemical Constants*, 16th edition, Harlow: Longman. **www.kayelaby.npl.co.uk/**.

Kelsall, T., Weiland, J. L., Franz, B. A. *et al.* 1998, *Ap. J.*, **508**, 44.

Kennicutt, R. C., Jr. 1983, *Ap. J.*, **272**, 54.

Kennicutt, R. C., Jr. 1989, *Ap. J.*, **344**, 685.

Kennicutt, R. C., Jr. 1998a, *Ann. Rev. Astr. Astrophys.*, **36**, 189.

Kennicutt, R. C., Jr. 1998b, *Ap. J.*, **498**, 541.

Kennicutt, R. C., Jr., Tamblyn, P. & Congdon, C. W. 1994, *Ap. J.*, **435**, 22.

Kewley, L. J. & Dopita, M. A. 2002, *Ap. J. Suppl.*, **142**, 35.

Kilian, J. 1992, *A & A*, **262**, 171.

King, J. 2001, *Astr. J.*, **122**, 3115.

Kingsburgh, R. L. & Barlow, M. J. 1994, *MNRAS*, **271**, 257.

Kippenhahn, R. & Weigert, A. 1990, *Stellar Structure and Evolution*, Berlin: Springer-Verlag, pp. 294, 323.

Kirkman, D., Tytler, D., Suzuki, N., O'Meara, J. M. & Lubin, D. 2003, *Ap. J. Suppl.*, **149**, 1.

Kiselman, D. & Carlsson, M. 1994, in P. Crane (ed.), *The Light Element Abundances*, Berlin: Springer-Verlag, p. 372.

Knauth, D. C., Federman, S. R. & Lambert, D. L. 2003, *Ap. J.*, **586**, 268.

Kolb, E. W. & Turner, M. S. 1990, *The Early Universe*, Harlow: Addison-Wesley Press.

Koonin, S. E., Tombrello, T. A. & Fox, G. 1974, *Nucl. Phys. A*, **220**, 221.

Köppen, J. & Arimoto, N. 1990, *A & A*, **240**, 22.

Köppen, J. & Arimoto, N. 1991, *A & A Suppl.*, **87**, 109, and *Erratum*, *A & A Suppl.*, **89**, 420.

Köppen, J. & Hensler, G. 2005, *A & A*, **434**, 531.

Kormendy, J. & Sanders, D. B. 1992, *Ap. J. Lett.*, **390**, L53.

Korn, A. J., Grundahl, F., Richard, O. *et al.* 2006, *Nature*, **442**, 657.

Kotoneva, E., Flynn, C., Chiappini, C. & Matteucci, F. 2002, *MNRAS*, **336**, 879.

Kraft, R. P. 1994, *Pub. Astr. Soc. Pacific*, **106**, 553.

Krane, K. S. 1987, *Introductory Nuclear Physics*, New York: Wiley.

Kratz, K.-L. 2001, *Nucl. Phys. A*, **688**, 308.

Kroupa, P. 2002, *Science*, **295**, 82.

Kroupa, P., Tout, C. A. & Gilmore, G. 1990, *MNRAS*, **244**, 76.

Kroupa, P. & Weidner, C. 2003, *Ap. J.*, **598**, 1076.

Kudritsky, R. F. & Hummer, D. G. 1990, *Ann. Rev. Astr. Astrophys.*, **28**, 303.

Kuhn, H. G. 1971, *Atomic Spectra*, Harlow: Longman.

Kuijken, K. & Gilmore, G. 1989, *MNRAS*, **239**, 605.

Kulkarni, S. R., Blitz, L. & Heiles, C. 1982, *Ap. J. Lett.*, **259**, L63.

Kulkarni, S. R. & Heiles, C. 1987, in D. Hollenbach & H. Thronson (eds.), *Interstellar Processes*, Dordrecht: Reidel, p. 87.

Kulkarni, V. P., Fall, S. M., Lauroesch, S. T. *et al.* 2005, *Ap. J.*, **618**, 68.

Kunth, D., Lequeux, J., Sargent, W. L. W. & Viallefond, F. 1994, *A & A*, **282**, 709.

Kunth, D. & Sargent, W. L. W. 1983, *Ap. J.*, **273**, 81.

Kurucz, R. L. 1979, *Ap. J. Suppl.*, **40**, 1.

Kurucz, R. L. 1995, Kurucz CD-ROM 23, Cambridge, Mass.: Smithsonian Astrophysical Observatory.

Kurucz, R. L. & Peytremann, E. 1975, *A Table of Semiempirical gf-Values*, Cambridge, Mass.: Smithsonian Ap. Obs. Special Rep., **362**.

Lacey, C. G. & Fall, S. M. 1985, *Ap. J.*, **290**, 154.

Lagache, G., Puget, J.-L. & Dole, H. 2005, *Ann. Rev. Astr. Astrophys.*, **43**, 727.

Laird, J. B., Rupen, M. P., Carney, B. W. & Latham, D. W. 1988, *Astr. J.*, **96**, 1908.

Lambert, D. L. 1989, in C. F. Waddington (ed.), *Cosmic Abundances of Matter*, New York: Amer. Inst. Phys., p. 168.

Lambert, D. L. 1992, *A & A Rev.*, **3**, 201.

Lambert, D. L. 2004, in C. Esteban *et al.* (eds.), *Cosmochemistry: The Melting Pot of the Elements*, Cambridge: Cambridge University Press, p. 81.

Lambert, D. L., Smith, V. V., Busso, M., Gallino, R. & Straniero, O. 1995, *Ap. J.*, **450**, 502.

Langanke, K. & Wiescher, M. 2001, *Rep. Prog. Phys.*, **64**, 1657.

Langer, N. 2004, in C. Esteban *et al.* (eds.), *Cosmochemistry: The Melting Pot of the Elements*, Cambridge: Cambridge University Press, p. 31.

Langer, N. & Henkel, C. 1995, *Sp. Sci. Rev.*, **74**, 343.

Lanzetta, K. M., Wolfe, A. M. & Turnshek, D. A. 1995, *Ap. J.*, **440**, 435.

Lanzetta, K. M., Wolfe, A. M., Turnshek, D. A., Lu, L., McMahon, R. G. & Hazard, C. 1991, *Ap. J. Suppl.*, **77**, 1.

Larsen, T. I., Sommer-Larsen, J. & Pagel, B. E. J. 2001, *MNRAS*, **323**, 555.

Larson, R. B. 1972, *Nature Phys. Sci.*, **236**, 7.

Larson, R. B. 1974a, *MNRAS*, **166**, 585.

Larson, R. B. 1974b, *MNRAS*, **169**, 229.

Larson, R. B. 1976, *MNRAS*, **176**, 31.

Larson, R. B. 1986, *MNRAS*, **218**, 409.

Larson, R. B. & Dinerstein, H. 1975, *Pub. Astr. Soc. Pacific*, **87**, 911.

Larson, R. B. & Tinsley, B. M. 1978, *Ap. J.*, **219**, 46.

Lecavelier des Etangs, A., Désert, J.-M., Kunth, D. *et al.* 2004, *A & A*, **413**, 131.

Lee, T., Papanastassiou, D. A. & Wasserburg, G. 1977, *Ap. J. Lett.*, **211**, L107.

Leitherer, C. *et al.* 1999, *Ap. J. Suppl.*, **123**, 3.

Leitherer, C. *et al.* 2001, *Ap. J.*, **550**, 724.

Lejeune, T., Cuisenier, F. & Buser, R. 1997, *A & A Suppl.*, **125**, 229.

Lejeune, T., Cuisenier, F. & Buser, R. 1998, *A & A Suppl.*, **130**, 65.

Lemoine, M., Ferlet, R. & Vidal-Madjar, A. 1994, *A & A*, **298**, 879.

Lequeux, J., Peimbert, M., Rayo, J. F., Serrano, A. & Torres-Peimbert, S. 1979, *A & A*, **80**, 155.

Levshakov, S. A., Dessauges-Sauvatsky, M., D'Odorico, S. & Molaro, P. 2002, *Ap. J.*, **565**, 696.

Lewis, J. R. & Freeman, K. C. 1989, *Astr. J.*, **97**, 139.

Lewis, R. S., Tang, M., Wacker, J. F., Anders, E. & Steel, E. 1987, *Nature*, **326**, 160.

Lilly, S. J. & Cowie, L. L. 1987, in C. G. Wynn-Williams & E. E. Becklin (eds.), *Infrared Astronomy with Arrays*, Honolulu: University of Hawaii, p. 473.

Lilly, S. J., Le Fèvre, O., Hammer, F. & Crampton, D. 1996, *Ap. J. Lett.*, **460**, L1.

Lin, D. N. C. & Pringle, J. E. 1987, *Ap. J. Lett.*, **320**, L87.

Lingenfelter, R. E., Ramaty, R. & Kozlovsky, B. 1998, *Ap. J. Lett.*, **500**, L153.

Linsky, J. L. 2003, *Sp. Sci. Rev.*, **106**, 49.

Linsky, J. L., Draine, B. T., Moos, H. W. *et al.* 2006, *Ap. J.*, **647**, 1106.

Lodders, K. 2003, *Ap. J.*, **591**, 1220.

Loewenstein, M. 2004, in A. McWilliam & M. Rauch (eds.), *Origin and Evolution of the Elements*, Carnegie Observatories Astrophysics Series, **4**, Cambridge: Cambridge University Press, p. 422.

Longair, M. S. 1998, *Galaxy Formation*, Berlin: Springer-Verlag.

Low, C. & Lynden-Bell, D. 1976, *MNRAS*, **176**, 367.

Lynden-Bell, D. 1973, in G. Contopulos, M. Hénon & D. Lynden-Bell, *Dynamical Structure and Evolution of Stellar Systems*, Geneva: Geneva Observatory, p. 132.

Lynden-Bell, D. 1975, *Vistas in Astr.*, **19**, 299.

Lynden-Bell, D. 1992, in M. G. Edmunds & R. J. Terlevich (eds.), *Elements and the Cosmos*, Cambridge: Cambridge University Press, p. 270.

Lynden-Bell, D. & Gilmore, G. (eds.) 1990, *Baryonic Dark Matter*, Dordrecht: Kluwer.

Madau, P., Ferguson, H. C., Dickinson, M. E. *et al.* 1996, *MNRAS*, **283**, 1388.

Madau, P. & Pozzetti, L. 2000, *MNRAS*, **312**, L9.

Maeder, A. 1992, *A & A*, **264**, 105.

Maeder, A. 1993, *A & A*, **268**, 833.

Maeder, A. & Meynet, G. 1987, *A & A*, **182**, 243.

Malaney, R. A. & Butler, M. N. 1993, *Ap. J. Lett.*, **407**, L73.

Malaney, R. A. & Chaboyer, B. 1996, *Ap. J.*, **462**, 57.

Malaney, R. A. & Fowler, W. A. 1988, *Ap. J.*, **333**, 14.

Malaney, R. A. & Fowler, W. A. 1989a, *Ap. J. Lett.*, **345**, L5.

Malaney, R. A. & Fowler, W. A. 1989b, *MNRAS*, **237**, 67.

Malaney, R. A., Mathews, G. J. & Dearborn, D. 1989, *Ap. J.*, **345**, 169.

Malinie, G., Hartmann, D. H. & Mathews, W. G. 1991, *Ap. J.*, **376**, 520.

Mandl, F. 1992, *Quantum Mechanics*, Chichester: J. Wiley & Sons.

Marigo, P. 2001, *A & A*, **370**, 194.

Marigo, P., Bressan, A. & Chiosi, C. 1996, *A & A*, **313**, 545.

Marigo, P., Bressan, A. & Chiosi, C. 1998, *A & A*, **331**, 564.

Martin, W. C. 1992, in P. L. Smith & W. L. Wiese (eds.), *Atomic and Molecular Data for Space Astronomy: Needs, Analysis and Availability*, Berlin: Springer-Verlag.

Mathews, G. J., Bazan, G. & Cowan, J. J. 1992, *Ap. J.*, **391**, 719.

Mathews, G. J. & Cowan, J. J. 1990, *Nature*, **345**, 491.

Mathews, G. J. & Schramm, D. N. 1988, *Ap. J. Lett.*, **324**, L67.

Mathews, W. B. & Baker, J. C. 1971, *Ap. J.*, **170**, 241.

Matsumoto, T., Matsuura, S., Murakami, H. *et al.* 2005, *Ap. J.*, **626**, 31.

Matteucci, F. 1991, in I. J. Danziger & K. Kjär (eds.), ESO/EIPC Workshop: *SN 1987A and Other Supernovae*, Garching: ESO, p. 703.

Matteucci, F. 1992, *Ap. J.*, **397**, 32.

Matteucci, F. 1994, *A & A*, **288**, 57.

Matteucci, F. 2001, *The Chemical Evolution of the Galaxy*, Dordrecht: Kluwer.

Matteucci, F., D'Antona, F. & Timmes, F. X. 1995, *A & A*, **303**, 460.

Matteucci, F. & François, P. 1989, *MNRAS*, **239**, 885.

Matteucci, F. & Greggio, L. 1986, *A & A*, **154**, 279.

Matteucci, F. & Tornambé, A. 1987, *A & A*, **185**, 51.

Matteucci, F. & Tosi, M. 1985, *MNRAS*, **217**, 391.

Mattila, K., Leinert, Ch. & Schnur, G. 1991, in B. Rocca-Volmerange, J. M. Deharveng & J. T. T. Van (eds.), *The Early Observable Universe from Diffuse Backgrounds*, Gif-sur-Yvette: Ed. Frontières, p. 133.

Mayor, M. & Vigroux, L. 1981, *A & A*, **98**, 1.

McClure, R. D., Vandenberg, D. A., Bell, R. A., Hesser, J. E. & Stetson, P. B. 1987, *Astr. J.*, **93**, 1144.

McGaugh, S. 1991, *Ap. J.*, **380**, 140.

McKee, C. F. & Ostriker, J. P. 1977, *Ap. J.*, **218**, 148.

McWilliam, A. 1997, *Ann. Rev. Astr. Astrophys.*, **35**, 503.

McWilliam, A. & Rich, R. M. 1994, *Ap. J. Suppl.*, **91**, 749.

McWilliam, A. & Rich, R. M. 2004, in A. McWilliam & M. Rauch (eds.), *Origin and Evolution of the Elements*, Carnegie Observatories Astrophysics Series **4**, Cambridge: Cambridge University Press, p. 38.

Meggers, W. F., Corliss, C. H. & Scribner, B. F. 1975, *Tables of Spectral Line Intensities*, NBS Monograph **145**, Washington: Govt. Pr. Off.

Meléndez, J. & Ramirez, I. 2004, *Ap. J. Lett.*, **615**, L33.

Meléndez, J., Shchukina, N. G., Vasiljeva, I. E. & Ramíres, I. 2006, *Ap. J.*, **642**, 1082.

Melnick, J. 1987, in T. X. Thuan, T. Montmerle & J. T. T. Van (eds.), *Starbursts and Galaxy Evolution*, Gif-sur-Yvette: Ed. Frontières, p. 215.

Melnick, J., Haydari-Malayeri, M. & Leisy, P. 1992, *A & A*, **253**, 16.

Meneguzzi, M., Audouze, J. & Reeves, H. 1971, *A & A*, **15**, 337.

Meneguzzi, M. & Reeves, H. 1975, *A & A*, **40**, 99.

Merrill, P. W. 1952, *Science*, **115**, 484.

Mestel, L. 1952, *MNRAS*, **112**, 598.

Metcalf, L., Kneib, J.-P., McBreen, B. *et al.* 2003, *A & A*, **407**, 791.

Meyer, B. S. & Schramm, D. N. 1986, *Ap. J.*, **311**, 406.

Meyer, J.-P., Drury, L. O'C. & Ellison, D. C. 1998, *Sp. Sci. Rev.*, **86**, 179.

Meylan, T., Furenlid, I., Wiggs, M. S. & Kurucz, R. L. 1993, *Ap. J. Suppl.*, **85**, 163.

Meynet, G., Maeder, A., Schaller, G., Schaerer, D. & Charbonnel, C. 1994, *A & A Suppl.*, **103**, 97.

Mezger, P. G. & Wink, J. E. 1983, in P. A. Shaver, D. Kunth & K. Kjär (eds.), *Primordial Helium*, Garching: ESO, p. 281.

Mihalas, D. 1970, *Stellar Atmospheres*, 1st edition, San Francisco: W. H. Freeman & Co.

Mihalas, D. 1978, *Stellar Atmospheres*, 2nd edition, San Francisco: W. H. Freeman & Co.

Mihalas, D. & Binney, J. 1981, *Galactic Astronomy*, San Francisco: W. H. Freeman & Co.

Miville-Deschênes, M.-A., Lagache, G. & Puget, J.-L. 2001, *A & A*, **393**, 749.

Moll, R., Schindler, S., Domainko, W. *et al.* 2007, *A & A*, **463**, 513.

Montmerle, T. 1977, *Ap. J.*, **217**, 878.

Moore, C. E. 1962, *An Ultraviolet Multiplet Table*, NBS Circ. no. 488, Washington: Nat. Bur. Stand.

Moore, C. E. 1972, *A Multiplet Table of Astrophysical Interest*, revised edn. (*RMT*), *NSRDS-NBS* **40**, Washington: Nat. Bur. Stand.

Moore, C. E., Minnaert, M. & Houtgast, J. 1966, *The Solar Spectrum 2935 Å to 8770 Å, Monograph* **61**, Washington: Nat. Bur. Stand.

Morrison, H. L., Flynn, C. & Freeman, K. C. 1990, *Astr. J.*, **100**, 1191.

Morton, D. C. 2003, *Ap. J. Suppl.*, **149**, 205.

Mould, J. R. 1978, *Ap. J.*, **220**, 434.

Mould, J. R. 1984, *Publ. Astr. Soc. Pacific*, **96**, 773.

Mushotzky, R. F., Loewenstein, M., Arnaud, K. A. *et al.* 1996, *Ap. J.*, **466**, 686.

Nagashima, M., Lacey, C. G., Baugh, C. M. & Frenk, C. S. 2005a, *MNRAS*, **358**, 1247.

Nagashima, M., Lacey, C. G., Okamoto, T., Baugh, C. M., Frenk, C. S. & Cole, S. 2005b, *MNRAS*, **363**, L31.

Nagashima, M. & Okamoto, T. 2006, *Ap. J.*, **643**, 863.

Nath, B. B., Madau, P. & Silk, J. 2006, *MNRAS*, **366**, 35.

Neese, C. & Yoss, K. 1988, *Astr. J.*, **95**, 463.

Nissen, P. E. & Edvardsson, B. 1992, *A & A*, **261**, 255.

Nissen, P. E., Edvardsson, B. & Gustafsson, B. 1985, in I. J. Danziger *et al.* (eds.), *Production and Distribution of the CNO Elements*, Garching: ESO, p. 131.

Nissen, P. E., Primas, F., Asplund, M. & Lambert, D. L. 2002, *A & A*, **390**, 235.

Nissen, P. E. & Schuster, W. J. 1991, *A & A*, **251**, 457.

Nissen, P. E. & Schuster, W. J. 1997, *A & A*, **326**, 751.

Nomoto, K. 1986, *Prog. Part. Nucl. Phys.*, **17**, 249.

Nomoto, K. & Hashimoto, M. 1988, *Phys. Rep.*, **163**, 13.

Nomoto, K. & Kondo, Y. 1991, *Ap. J. Lett.*, **367**, L19.

Nomoto, K., Thielemann, F.-K. & Yokoi, K. 1984, *Ap. J.*, **286**, 644.

Nomoto, K., Tominaga, N., Umeda, H. *et al.* 2006, *Nucl. Phys.* A, **777**, 424.

Nordström, B., Mayor, M., Andersen, J., Holmberg, F. *et al.* 2004, *A & A*, **418**, 989.

Norris, J. 1994, *Ap. J.*, **431**, 645.

Norris, J., Bessell, M. S. & Pickles, A. J. 1985, *Ap. J. Suppl.*, **58**, 463.

O'Connell, R. W. 1976, *Ap. J.*, **206**, 370.

O'Dell, C. R., Peimbert, M. & Kinman, T. D. 1964, *Ap. J.*, **140**, 119.

Olive, K. A., Steigman, G. & Skillman, E. D. 1997, *Ap. J.*, **483**, 788.

Oliver, S. J., Rowan-Robinson, M. & Saunders, W. 1992, *MNRAS*, **256**, 15P.

O'Meara, J. M., Burles, S., Prochaska, J. X. *et al.* 2006, *Ap. J. Lett.*, **649**, L61.

O'Meara, J. M., Tytler, D., Kirkman, D., Suzuki, N., Prochaska, J. X., Lubin, D. & Wolfe, A. M. 2001, *Ap. J.*, **552**, 718,

Oort, J. H. 1966, *Bull. Astr. Inst. Netherlands*, **18**, 421.

Oort, J. H. 1974, IAU Symp. no. 58, Dordrecht: Reidel, p. 375.

Öpik, E. J. 1951, *Proc. R. Irish Acad. A*, **54**, 49.

Osterbrock, D. E. 1988, *Pub. Astr. Soc. Pacific*, **100**, 412.

Osterbrock, D. E. & Ferland, G. J. 2006, *Astrophysics of Gaseous Nebulae and Active Galactic Nuclei*, Mill Valley, Cal.: University Science Books.

Ostriker, J. B. & Thuan, T. X. 1975, *Ap. J.*, **202**, 353.

Ostriker, J. B. & Tinsley, B. M. 1975, *Ap. J. Lett.*, **201**, L51.

Ott, U. 1993, *Nature*, **364**, 25.

Pagel, B. E. J. 1965, *Roy. Obs. Bull.* no. 104.

Pagel, B. E. J. 1977, in E. A. Müller (ed.), *Highlights of Astronomy*, **4**, pt II, Int. Astr. Union, p. 119.

Pagel, B. E. J. 1981, in S. M. Fall & D. Lynden-Bell (eds.), *The Structure and Evolution of Normal Galaxies*, Cambridge: Cambridge University Press, p. 211.

Pagel, B. E. J. 1989a, *Rev. Mex. Astr. Astrofis.*, **18**, 153.

Pagel, B. E. J. 1989b, in J. E. Beckman & B. E. J. Pagel (eds.), *Evolutionary Phenomena in Galaxies*, Cambridge: Cambridge University Press, p. 201.

Pagel, B. E. J. 1991, in H. Oberhummer (ed.), *Nuclei in the Cosmos*, Berlin: Springer-Verlag, p. 89.

Pagel, B. E. J. 1992a, in D. Alloin & G. Stasinska (eds.), *The Feedback of Chemical Evolution on the Stellar Content of Galaxies*, Paris: Observatoire, p. 87.

Pagel, B. E. J. 1992b, in B. Barbuy & A. Renzini (eds.), IAU Symp. 149: *The Stellar Populations of Galaxies*, Dordrecht: Kluwer, p. 133.

Pagel, B. E. J. 1993, in N. Prantzos, E. Vangioni-Flam & M. Cassé (eds.), *Origin and Evolution of the Elements*, Cambridge: Cambridge University Press, p. 496.

Pagel, B. E. J. 1994, in D. Lynden-Bell (ed.), *Cosmical Magnetism*, Dordrecht: Kluwer, p. 113.

Pagel, B. E. J. 2001, in E. Vangioni-Flam, R. Ferlet & M. Lemoine (eds.), *Cosmic Evolution*, Singapore: World Scientific, p. 223.

Pagel, B. E. J. 2002, in R. Fusco-Femiano & F. Matteucci (eds.), *Chemical Enrichment of Intracluster and Intergalactic Medium*, ASP Conf. Series, **253**, 489.

Pagel, B. E. J. 2004, in A. McWilliam & M. Rauch (eds.), *Origin and Evolution of the Elements*, Carnegie Observatories Astrophysics Series **4**, Cambridge: Cambridge University Press, pp. 482, 487.

Pagel, B. E. J. & Edmunds, M. G. 1981, *Ann. Rev. Astr. Ap.*, **19**, 77.

Pagel, B. E. J., Edmunds, M. G., Blackwell, D. E., Chun, M. S. & Smith, G. 1979, *MNRAS*, **189**, 95.

Pagel, B. E. J., Edmunds, M. G., Fosbury, R. A. E. & Webster, B. L. 1978, *MNRAS*, **184**, 569.

Pagel, B. E. J. & Patchett, B. E. 1975, *MNRAS*, **172**, 13.

Pagel, B. E. J. & Portinari, L. 1998, *MNRAS*, **298**, 747

Pagel, B. E. J., Simonson, E., Terlevich, R. J. & Edmunds, M. G. 1992, *MNRAS*, **255**, 325.

Pagel, B. E. J. & Tautvaišienė, G. 1995, *MNRAS*, **276**, 505.

Pagel, B. E. J. & Tautvaišienė, G. 1997, *MNRAS*, **288**, 108.

Pagel, B. E. J. & Tautvaišienė, G. 1998, *MNRAS*, **299**, 535.

Pagel, B. E. J., Terlevich, R. J. & Melnick, J. 1986, *Pub. Astr. Soc. Pacific*, **98**, 1005.

Pantelaki, I. & Clayton, D. D. 1987, in T. X. Thuan, T. Montmerle & J. T. T. Van (eds.), *Starbursts and Galaxy Evolution*, Gif-sur-Yvette: Ed. Frontières, p. 145.

Papovich, C., Dole, H., Egami, E. *et al.* 2004, *Ap. J. Suppl.*, **154**, 70.

Parizot, E. & Drury, L. 1999, *A & A*, **349**, 673.

Park, S., Burrows, D. N., Garmire, G. G., Nousek, J. A., Hughes, J. P. & Williams, R. M. 2003, *Ap. J.*, **586**, 210.

Parker, J. W. & Garmany, C. D. 1993, *Astr. J.*, **106**, 1471.

Partridge, R. B. & Peebles, P. J. E. 1967, *Ap. J.*, **148**, 377.

Peacock, J. A. 1999, *Cosmological Physics*, Cambridge: Cambridge University Press.

Peebles, P. J. E. 1966, *Ap. J.*, **146**, 542.

Pei, Y. C. & Fall, S. M. 1995, *Ap. J.*, **454**, 69.

Pei, Y. C., Fall, S. M. & Hauser, M. G. 1999, *Ap. J.*, **522**, 604.

Peimbert, A., Peimbert, M. & Luridiana, V. 2002, *Ap. J.*, **565**, 668.

Peimbert, M. 1967, *Ap. J.*, **150**, 825.

Peimbert, M. 1978, in Y. Terzian (ed.), IAU Symp. 76: *Planetary Nebulae, Observations and Theory*, Dordrecht: Reidel, p. 215.

Peimbert, M. 1983, in P. A. Shaver, D. Kunth & K. Kjär (eds.), *Primordial Helium*, Garching: ESO, p. 267.

Peimbert, M., Colin, P. & Sarmiento, A. 1994, in G. Tenorio-Tagle (ed.), *Violent Star Formation from 30 Doradus to QSOs*, Cambridge: Cambridge University Press, p. 79.

Peimbert, M., Luridiana, V. & Peimbert, A. 2007, *Ap. J.*, **666**, 636.

Peimbert, M. & Peimbert, A. 2006, *Rev. Mex. Astr. Astrofis.*, **26**, 163.

Peimbert, M. & Serrano, A. 1982, *MNRAS*, **198**, 563.

Peimbert, M. & Torres-Peimbert, S. 1974, *Ap. J.*, **193**, 327.

Perkins, D. H. 1982, *Introduction to High Energy Physics*, 2nd edition, Harlow: Addison-Wesley Press, p. 24.

Perkins, D. H. 1987, *Introduction to High Energy Physics*, 3rd edition, Harlow: Addison-Wesley Press.

Péroux, C., Dessauges-Zavatsky, M., D'Odorico, S. *et al.* 2005, *MNRAS*, **363**, 479.

Péroux, C., McMahon, R. G., Storrie-Lombardi, L. J. & Irwin, M. J. 2003, *MNRAS*, **346**, 1103.

Perryman, M. A. C., Lindegren, L., Kovalevsky, J. *et al.* 1995, *A & A*, **304**, 69.

Persic, M. & Salucci, P. 1992, *MNRAS*, **258**, 14P.

Persic, M., Salucci, P. & Stel, F. 1996, *MNRAS*, **281**, 27P.

Pettini, M. 1999, in J. Walsh & M. Rosa (eds.), ESO Workshop: *Chemical Evolution from Zero to High Redshift*, Berlin: Springer, p. 233.

Pettini, M. 2006, in V. LeBrun *et al.* (eds.), *The Fabulous Destiny of Galaxies: Bridging Past and Present*, Paris: Ed. Frontières, p. 319.

Pettini, M. & Bowen, B. V. 2001, *Ap. J.*, **560**, 41.

Pettini, M., Ellison, S. L., Bergeron, J. & Petitjean, P. 2002a, *A & A*, **391**, 21.

Pettini, M. & Lipman, K. 1995, *A & A*, **313**, 792.

Pettini, M. & Pagel, B. E. J. 2004, *MNRAS*, **348**, L59.

Pettini, M., Rix, S. A., Steidel, C. C., Adelberger, K. L., Hunt, M. P. & Shapley, A. E. 2002b, *Ap. J.*, **569**, 742.

Pettini, M., Smith, L. J., King, D. L. & Hunstead, R. W. 1997, *Ap. J.*, **486**, 665.

Phillipps, S. & Edmunds, M. G. 1996, *MNRAS*, **281**, 362.

Phillips, A. C. 1999, *The Physics of Stars*, Chichester: John Wiley & Sons.

Pickles, A. J. 1985, *Ap. J.*, **296**, 340.

Pilyugin, L. 2003, *A & A*, **399**, 1003.

Pilyugin, L. & Edmunds, M. G. 1996, *A & A*, **313**, 792.

Pilyugin, L. S., Thuan, T. X. & Vílchez, J. M. 2003, *A & A*, **397**, 487.

Pilyugin, L. S., Vílchez, J. M. & Contini, T. 2004, *A & A*, **425**, 849.

Pinsonneault, M. H., Walker, T. P., Naranayan, V. K. & Steigman, G. 1999, *Ap. J.*, **527**, 180.

Pipino, A. & Matteucci, F. 2004, *MNRAS*, **347**, 968.

Pipino, A., Matteucci, F., Borgani, S. & Biviano, A. 2002, *New Astr.*, **7**, 227.

Pitts, E. & Tayler, R. J. 1989, *MNRAS*, **240**, 373.

Podosek, F. A. & Swindle, T. D. 1988, in J. F. Kerridge & M. S. Matthews (eds.), *Meteorites and the Early Solar System*, Tucson: University of Arizona Press, p. 47.

Porter, R. L., Bauman, R. P., Ferland, G. J. & MacAdam, K. B. 2005, *Ap. J. Lett.*, **622**, L73.

Portinari, L. & Chiosi, C. 1999, *A & A*, **350**, 827.

Portinari, L. & Chiosi, C. 2000, *A & A*, **355**, 929.

Portinari, L., Chiosi, C. & Bressan, A. 1998, *A & A*, **334**, 505.

Pottasch, S. R. 1984, *Planetary Nebulae*, Dordrecht: Reidel.

Powell, A. L. T. 1969, *Roy. Obs. Bull.*, no. 152.

Prantzos, N. 1994, in M. Busso, R. Gallino & C. M. Raiteri (eds.), *Nuclei in the Cosmos III*, New York: Amer. Inst. Phys. Conf. Proc. no. 327, p. 531.

Prantzos, N. 2006, *A & A*, **448**, 665.

Prantzos, N. & Boissier, S. 2000, *MNRAS*, **315**, 82.

Prantzos, N., Cassé, M. & Vangioni-Flam, E. 1993, *Ap. J.*, **403**, 630.

Prantzos, N., Vangioni-Flam, E. & Chauveau, S. 1994, *A & A*, **285**, 132.

Prialnik, D. 2000, *An Introduction to the Theory of Stellar Structure and Evolution*, Cambridge: Cambridge University Press.

Prochaska, J. X., Herbert-Fort, S. & Wolfe, A. M. 2005, *Ap. J.*, **635**, 123.

Prochaska, J. X., Howk, J. C. & Wolfe, A. M 2003, *Nature*, **427**, 57.

Qian, Y.-Z. & Wasserburg, G. J. 2003, *Ap. J.*, **588**, 1099.

Rabin, D. 1982, *Ap. J.*, **261**, 85.

Raiteri, C. M., Gallino, R. & Busso, M. 1992, *Ap. J.*, **387**, 263.

Raiteri, C. M., Gallino, R., Busso, M., Neuberger, D. & Käppeler, F. 1993, *Ap. J.*, **419**, 207.

Ramaty, R., Kozlovsky, B., Lingenfelter, R. E. & Reeves, H. 1997, *Ap. J.*, **488**, 730.

Ramaty, R., Scully, S. T., Lingenfelter, R. E. & Kozlovsky, B. 2000, *Ap. J.*, **534**, 747.

Rauch, M., Miralda-Escudé, J., Sargent, W. L. W. *et al.* 1997, *Ap. J.*, **489**, 7.

Rauscher, T., Heger, A., Hoffmann, R. D. & Woosley, S. E. 2002, *Ap. J.*, **576**, 323.

Rayet, M., Arnould, M., Hashimoto, M., Prantzos, N. & Nomoto, K. 1995, *A & A*, **298**, 517.

Raymond, J. C. & Smith, B. W. 1977, *Ap. J. Suppl.*, **35**, 419.

Read, S. M. & Viola, V. E. 1984, *At. Data Nucl. Data Tables*, **31**, 359.

Recchi, S., Matteucci, F., D'Ercole, A. & Tosi, M. 2004, *A & A*, **426**, 37.

Rees, M. J. 1976, *MNRAS*, **176**, 483.

Reeves, H. 1990, in F. Sánchez, M. Collados & R. Rebolo (eds.), *Observational and Physical Cosmology*, Cambridge: Cambridge University Press, p. 73.

Reeves, H. 1991, *A & A*, **244**, 294.

Reeves, H. 2005, in G. Alecian, O. Richard & S. Vauclair (eds.), *Element Stratification in Stars, 40 years of Atomic Diffusion*, EAS Publ. Series, **17**, 15.

Reeves, H., Fowler, W. A. & Hoyle, F. 1970, *Nature*, **226**, 727.

Reeves, H. & Meyer, J.-P. 1978, *Ap. J.*, **226**, 613.

Refsdal, S. & Weigert, A. 1970, *A & A*, **6**, 426.

Reimers, D. 1975, *Mem. Soc. R. Sci. Liège*, **6**, Ser. 8, 369.

Renault, C., Guy, J., Aharonian, F. A. *et al.* 2001, *A & A*, **371**, 771.

Renzini, A., Ciotti, L. & Pellegrini, S. 1993, in I. J. Danziger, W. W. Zeilinger & K. Kjär (eds.), ESO Conference & Workshop Proc. no. 45: *Structure, Dynamics and Chemical Evolution of Elliptical Galaxies*, Garching: ESO, p. 443.

Renzini, A. & Voli, M. 1981, *A & A*, **94**, 175.

Richard, O., Michaud, G. & Richer, J. 2005, *Ap. J.*, **619**, 538.

Richer, M. G. & McCall, M. L. 1995, *Ap. J.*, **445**, 642.

Richtler, T., de Boer, K. S. & Sagar, R. 1991, ESO *Messenger*, no. 64, p. 50.

Rix, S. A., Pettini, M., Leitherer, C. *et al.* 2004, *Ap. J.*, **615**, 98.

Rocca-Volmerange, B., Deharveng, J. M. & Van J. T. T. (eds.) 1991, *The Early Observable Universe from Diffuse Backgrounds*, Gif-sur-Yvette: Ed. Frontières.

Rocha-Pinto, H. J. & Maciel, W. J. 1996, *MNRAS*, **279**, 447.

Rocha-Pinto, H. J. & Maciel, W. J. 1998, *A & A*, **339**, 791.

Rogers, F. J. & Iglesias, C. A. 1992, *Ap. J. Suppl.*, **79**, 507.

Rogerson, J. B. & York, D. G. 1973, *Ap. J. Lett.*, **196**, L95.

Rolfs, C. E. & Rodney, W. S. 1988, *Cauldrons in the Cosmos*, University of Chicago Press pp. 337, 354, 411, 509.

Rollinde, E., Vangioni-Flam, E. & Olive, K. A. 2005, *Ap. J.*, **627**, 666.

Rose, J. 1985, *Astr. J.*, **90**, 1927.

Roy, J.-R. & Kunth, D. 1995, *A & A*, **294**, 432.

Rudnick, G., Rix, H.-W., Franx, M. *et al.* 2003, *Ap. J.*, **599**, 847.

Russell, H. N. 1934, *Ap. J.*, **79**, 317.

Rutherford, E. 1929, *Nature*, **123**, 313.

Ryan, S. G. & Norris, J. 1991, *Astr. J.*, **101**, 1835.

Ryan, S. G., Norris, J. & Bessell, M. S. 1991, *Astr. J.*, **102**, 303.

Ryan, S. G., Norris, J., Bessell, M. S. & Deliyannis, C. 1992, *Ap. J.*, **388**, 184.

Rybicki, G. B. & Lightman, A. P. 1979, *Radiative Processes in Astrophysics*, New York: Wiley–Interscience.

Sackmann, I.-J. & Boothroyd, A. I. 1992, *Ap. J. Lett.*, **392**, L71.

Sackmann, I.-J. & Boothroyd, A. I. 1999, *Ap. J.*, **510**, 217.

Sadler, E. M., Rich, R. M. & Terndrup, D. M. 1996, *Astr. J.*, **112**, 171.

Salaris, M. & Cassisi, S. 2005, *Evolution of Stars and Stellar Populations*, Chichester: John Wiley & Sons.

Salpeter, E. E. 1952, *Ap. J.*, **115**, 326.

Salpeter, E. E. 1955, *Ap. J.*, **121**, 161.

Samland, M., Hensler, G. & Theis, Ch. 1997, *Ap. J.*, **476**, 544.

Sandage, A. R. 1990, *J.R.A.S. Canada*, **84**, 70.

Sandage, A. R. & Fouts, G. 1987, *Astr. J.*, **93**, 74.

Sanders, J. S. & Fabian, A. C. 2006, *MNRAS*, **371**, 1483–1496.

Sandquist, E. 2000, *MNRAS*, **313**, 571.

Sarkar, S. 1996, *Rep. Prog. Phys.*, **59**, 1493.

Savage, B. D. & Sembach, K. R. 1991, *Ap. J.*, **379**, 245.

Scalo, J. M. 1986, *Fund. Cosmic Phys.*, **11**, 1.

Scalo, J. M. 1998, in G. Gilmore & D. Howell (eds.), *The Stellar Initial Mass Function*, ASP Conf. Series, **142**, 201.

Scannapieco, E. & Broadhurst, T. 2001, *Ap. J.*, **549**, 28.

Schaller, G., Schaerer, D., Meynet, G. & Maeder, A. 1992, *A & A Suppl.*, **96**, 269.

Scheuer, P. A. G. 1965, *Nature*, **207**, 963.

Schmidt, A. A., Copetti, M. V. F., Alloin, D. & Jablonka, J. 1991, *MNRAS*, **249**, 766.

Schmidt, M. 1959, *Ap. J.*, **129**, 243.

Schmidt, M. 1963, *Ap. J.*, **137**, 758.

Schmutz, W., Leitherer, C. & Grunwald, R. B. 1992, *Pub. Astr. Soc. Pacific*, **104**, 1164.

Schönberg, M. & Chandrasekhar, S. 1942, *Ap. J.*, **96**, 161.

Schramm, D. N. 1974, *Ann. Rev. Astr. Astrophys.*, **12**, 383.

Schramm, D. N. & Wasserburg, G. J. 1970, *Ap. J.*, **162**, 57.

Searle, L. 1971, *Ap. J.*, **168**, 327.

Searle, L. & Sargent, W. L. W. 1972, *Ap. J.*, **173**, 25.

Searle, L. & Zinn, R. 1978, *Ap. J.*, **225**, 357.

Seaton, M. J. 1987, *J. Phys. B Atom. Molec. Phys.*, **20**, 6363.

Seaton, M. J. 1996, *The Opacity Project*, Vol I: *Selected Research Papers, Atomic Data Tables for He to Si*; Vol II: *Atomic Data Tables for S to Fe, Photo-ionization Cross-section Graphs*, Bristol: Inst. of Phys. Publ.

Seaton, M. J., Yan, Y., Mihalas, D. & Pradhan, A. K. 1994, *MNRAS*, **266**, 805.

Seeger, P. A., Fowler, W. A. & Clayton, D. D. 1965, *Ap. J. Suppl.*, **11**, 121.

Sellwood, J. A. & Binney, J. J. 2002, *MNRAS*, **336**, 785.

Serjeant, S., Mortier, A. M. J., Ivison, R. J. *et al.* 2004, *Ap. J. Suppl.*, **154**, 118.

Shapley, A. E., Steidel, C. C., Pettini, M. & Adelberger, K. L. 2003, *Ap. J.*, **588**, 65.

Shaver, P. A., Kunth, D. & Kjär, K. (eds.) 1983, *Primordial Helium*, Garching: ESO.

Shaver, P. A., McGee, R. X., Danks, A. C. & Pottasch, S. R. 1983, *MNRAS*, **204**, 53.

Shaver, P. A., Wall, J. V., Kellerman, K. I., Jackson, C. A. & Hawkins, M. R. S. 1996, *Nature*, **384**, 439.

Shetrone, M. D. 2004, in A. McWilliam & M. Rauch (eds.), *Origin and Evolution of the Elements*, Carnegie Observatories Astrophysics Series **4**, Cambridge: Cambridge University Press, p. 218.

Shields, G. A. 1990, *Ann. Rev. Astr. Ap.*, **28**, 303.

Shklovsky, I. S. 1964, *Astr. Zhur.*, **41**, 408.

Shvartsman, V. F. 1969, *Sov. Phys. JETP Letters*, **9**, 184.

Silk, J. & Schramm, D. N. 1992, *Ap. J. Lett.*, **393**, L9.

Skillman, E. D., Kennicutt, R. C. & Hodge, P. W. 1989, *Ap. J.*, **347**, 875.

Smail, I., Ivison, R. J. & Blain, A. W. 1997, *Ap. J.*, **490**, 5.

Smail, I., Ivison, R. J., Blain, A. W. & Kneib, J.-P. 2002, *MNRAS*, **331**, 495.

Smith, M. S., Kawano, L. H. & Malaney, R. A. 1993, *Ap. J. Suppl.*, **85**, 219.

Smith, V. V., Lambert, D. L. & Nissen, P. E. 1993, *Ap. J.*, **408**, 262.

Sneden, C., McWilliam, A., Preston, G. W., Cowan, J. J., Burris, D. L. & Armosky, B. J. 1996, *Ap. J.*, **467**, 819.

Soderblom, D. R., Duncan, D. K. & Johnson, D. R. H. 1991, *Ap. J.*, **375**, 722.

Somerville, R. S. & Primack, J. R. 1999, *MNRAS*, **310**, 1087.

Somerville, R. S., Primack, J. R. & Faber, S. M. 2001, *MNRAS*, **320**, 504.

Sommer-Larsen, J. 1991a, *MNRAS*, **249**, 368.

Sommer-Larsen, J. 1991b, *MNRAS*, **250**, 356.

Sommer-Larsen, J. & Yoshii, Y. 1990, *MNRAS*, **243**, 468.

Songaila, A., Cowie, L. L. & Lilly, S. J. 1990, *Ap. J.*, **348**, 371.

Sonneborn, G. *et al.* 2000, *Ap. J.*, **545**, 277.

Spergel, D. N., Bean, R., Doré, O. *et al.* 2007, *Ap. J. Suppl.*, **170**, 377.

Spergel, D. N., Verde, L., Peiris, H. V. *et al.* 2003, *Ap. J. Suppl.*, **148**, 175.

Spinrad, H. & Taylor, B. 1969, *Ap. J.*, **157**, 279.

Spinrad, H. & Taylor, B. 1971, *Ap. J. Suppl.*, **22**, 445.

Spite, F. & Spite, M. 1982, *Nature*, **297**, 483.

Spitzer, L., Jr. & Fitzpatrick, E. L. 1993, *Ap. J.*, **409**, 299.

Spitzer, L. & Jenkins, E. B. 1975, *Ann. Rev. Astr. Astrophys.*, **13**, 133.

Srinivisan, B. & Anders, E. 1978, *Science*, **201**, 51.

Stasinska, G. & Leitherer, C. 1996, *Ap. J. Suppl.*, **107**, 661.

Steidel, C. C., Adelberger, K. L., Giavalisco, M. *et al.* 1999, *Ap. J.*, **519**, 1.

Steidel, C. C., Giavalisco, M., Pettini, M. *et al.* 1996, *Ap. J. Lett.*, **462**, L17.

Steigman, G. 2006, *Int. J. Mod. Phys. E*, **15**, 1.

Steigman, G., Schramm, D. N. & Gunn, J. L. 1974, *Phys. Lett.*, **B 66**, 202.

Steigman, G. & Walker, T. P. 1992, *Ap. J. Lett.*, **385**, L13.

Straniero, O., Gallino, R., Busso, M. *et al.* 1995, *Ap. J. Lett.*, **440**, L85.

Strömgren, B. 1987, in G. Gilmore & R. F. Carswell (eds.), *The Galaxy*, Dordrecht: Reidel, p. 229.

Suess, H. E. & Urey, H. C. 1956, *Rev. Mod. Phys.*, **28**, 53.

Sutherland, R. S., Bicknell, G. V. & Dopita, M. A. 2003, *Ap. J.*, **591**, 238.

Sutherland, R. S. & Dopita, M. A. 1993, *Ap. J. Suppl.*, **88**, 253.

Sweigart, A. V. & Mengel, J. G. 1979, *Ap. J.*, **229**, 624.

Takahashi, K., Witti, J. & Janka, H.-Th. 1994, *A & A*, **286**, 857.

Talbot, R. J. & Arnett, W. D. 1971, *Ap. J.*, **170**, 409.

Talbot, R. J. & Arnett, W. D. 1973a, *Ap. J.*, **186**, 51.

Talbot, R. J. & Arnett, W. D. 1973b, *Ap. J.*, **186**, 69.

Talbot, R. J. & Arnett, W. D. 1975, *Ap. J.*, **197**, 551.

Tatischeff, V. & Thibaud, J.-P. 2007, *A & A*, **469**, 265.

Tayler, R. J. 1994, *The Stars: Their Structure and Evolution*, Cambridge: Cambridge University Press.

Tayler, R. J. 1995, *MNRAS*, **273**, 215.

Teplitz, H. L., McLean, I. S., Becklin, E. E. *et al.* 2000, *Ap. J.*, **533**, 65.

Terlevich, R. J., Davies, R. L., Faber, S. M. & Burstein, D. 1981, *MNRAS*, **196**, 381.

Thielemann, F.-K., Brachwitz, F., Freiburghaus, C. *et al.* 2001, *Prog. Part. Nucl. Phys.*, **46**, 5.

Thielemann, F.-K., Metzinger, J. & Klapdor, V. 1983, *A & A*, **123**, 162.

Thielemann, F.-K., Nomoto, K. & Hashimoto, M. 1996, *Ap. J.*, **460**, 408.

Thielemann, F.-K., Nomoto, K. & Yokoi, K. 1986, *A & A*, **158**, 17.

Thomas, D. 1999, *MNRAS*, **306**, 655.

Thomas, D., Greggio, L. & Bender, R. 1998, *MNRAS*, **296**, 119–149.

Thomas, D., Greggio, L. & Bender, R. 1999, *MNRAS*, **302**, 537.

Thomas, D., Maraston, C. & Bender, R. 2003, *MNRAS*, **339**, 897.

Thomas, D., Maraston, C., Bender, R. & Mendes de Oliveira, C. 2005, *Ap. J.*, **621**, 673.

Thomsen, B. & Baum, W. A. 1987, *Ap. J.*, **315**, 460.

Timmes, F. X., Woosley, S. E. & Weaver, T. A. 1995, *Ap. J. Suppl.*, **98**, 617.

Tinsley, B. M. 1968, *Ap. J.*, **151**, 547.

Tinsley, B. M. 1977, *Ap. J.*, **216**, 548.

Tinsley, B. M. 1979, *Ap. J.*, **229**, 1046.

Tinsley, B. M. 1980, *Fund. Cosmic Phys.*, **5**, 287.

Tinsley, B. M. & Larson, R. B. 1978, *Ap. J.*, **221**, 554.

Tinsley, B. M. & Larson, R. B. 1979, *MNRAS*, **186**, 503.

Tisserand, P., Le Guillou, L., Alfonso, C. *et al.* 2007, *A & A*, **469**, 387.

Toomre, A. 1977, in B. M. Tinsley & R. B. Larson (eds.), *The Evolution of Galaxies and Stellar Populations*, New Haven: Yale Obs., p. 401.

Totani, T., Yoshii, Y., Iwamuro, F., Maihara, T. & Motohara, K. 2001, *Ap. J. Lett.*, **550**, L137.

Tozzi, P., Rosati, P., Ettori, S. *et al.* 2003, *Ap. J.*, **593**, 705.

Trager, S. C. 2004 in A. McWilliam & M. Rauch (eds.), *Origin and Evolution of the Elements*, Carnegie Observatories Astrophysics Series, **4**, Cambridge: Cambridge University Press, p. 388.

Travaglio, C., Galli, D., Gallino, R., Busso, M., Ferrini, F. & Straniero, O. 1999, *Ap. J.*, **521**, 691.

Travaglio, C., Gallino, R., Busso, M. & Dalmazzo, A. 2001, *Mem. Soc. Astr. It.*, **72**, 337.

Trimble, V. 1987, *Ann. Rev. Astr. Ap.*, **25**, 425

Truran, J. W. 1981, *A & A*, **97**, 391.

Truran, J. W. & Cameron, A. G. W. 1971, *Ap. Sp. Sci.*, **14**, 179.

Tsujimoto, T. 1993, Thesis, Tokyo University.

Tsujimoto, T., Nomoto, K., Yoshii, Y., Hashimoto, M., Yanagida, S. & Thielemann, F.-K. 1995, *MNRAS*, **277**, 945.

Tsujimoto, T. & Shigeyama, T. 1998, *Ap. J. Lett.*, **508**, L151.

Tsujimoto, T., Shigeyama, T. & Yoshii, Y. 1999, *Ap. J.*, **519**, L63.

Turck-Chièze, S. & Lopez, I. 1993, *Ap. J.*, **408**, 347.

Twarog, B. 1980, *Ap. J.*, **242**, 242.

Tytler, D., O'Meara, J. M., Suzuki, N. & Lubin, D. 2000, in G. Brown, M. Kamionkowski & M. S. Turner (eds.), *David Schramm's Universe*, *Phys. Rep.*, **333-4**, 409.

Ulrich, R. K. 1973, in D. N. Schramm & W. D. Arnett (eds.), *Explosive Nucleosynthesis*, Austin: University of Texas Press, p. 139.

Uno, M., Tachibana, T. & Yamada, M. 1992, in S. Kubono & T. Kajino (eds.), *Unstable Nuclei in Astrophysics*, Singapore: World Scientific, p. 187.

Unsöld, A. 1977, *The New Cosmos*, Berlin: Springer-Verlag.

Vader, J. P. 1987, *Ap. J.*, **317**, 128.

van den Bergh, S. 1962, *Astr. J.*, **67**, 486.

van den Hoek, L. B. & Groenevegen, M. A. T. 1997, *A & A Suppl.*, **123**, 305.

van der Held, E. F. M. 1931, *Zs. Phys.*, **70**, 508.

van Wormer, L., Görres, J., Iliadis, C., Wiescher, M. & Thielemann, F.-K. 1994, *Ap. J.*, **432**, 326.

Vangioni-Flam, E., Cassé, M. & Audouze, J. 2000, *Phys. Rep.*, **333-4**, 365.

Vangioni-Flam, E., Cassé, M., Audouze, J. & Oberto, Y. 1990, *Ap. J.*, **364**, 568.

Vangioni-Flam, E., Cassé, M., Fields, B. D. & Olive, K. A. 1996, *Ap. J.*, **468**, 199.

Vidal-Madjar, A., Laurent, C., Bonnet, R. M. & York, D. G. 1977, *Ap. J.*, **211**, 91.

Vigroux, L., Chièze, J. P. & Lazareff, B. 1981, *A & A*, **98**, 119.

Vílchez, J. M. & Esteban, C. 1996, *MNRAS*, **280**, 720.

Vílchez, J. M., Pagel, B. E. J., Díaz, A. I., Terlevich, E. & Edmunds, M. G. 1988, *MNRAS*, **235**, 633.

Walker, T., Mathews, G. & Viola, V. E. 1985, *Ap. J.*, **299**, 745.

Waller, W. H., Parker, J. W. & Malamuth, E. M. 1996, in S. S. Holt & G. Sonneborn (eds.), *Cosmic Abundances*, Astr. Soc. Pacific Conf. Series, **99**, 354.

Wallerstein, G. 1962, *Ap. J. Suppl.*, **6**, 407.

Walsh, J. & Roy, J.-R. 1989, *MNRAS*, **239**, 297.

Wasserburg, G. J. 1987, *Earth & Plan. Sci. Lett.*, **86**, 129.

Wasserburg, G. J., Busso, M. & Gallino, R. 1996, *Ap. J. Lett.*, **466**, L109.

Wasserburg, G. J., Busso, M., Gallino, R. & Nollett, K. M. 2006, *Nucl. Phys.*, **A777**, 5.

Wasserburg, G. J., Busso, M., Gallino, R. & Raiteri, C. M. 1994, *Ap. J.*, **424**, 412.

Wasserburg, G. J., Gallino, R., Busso, M., Goswami, J. N. & Raiteri, C. M. 1995, *Ap. J. Lett.*, **440**, L101.

Wasserburg, G. J & Papanastassiou, D. A. 1982, in C. A. Barnes, D. D. Clayton & D. N. Schramm (eds.), *Essays in Nuclear Astrophysics*, Cambridge: Cambridge University Press, p. 77.

Wasserburg, G. J., Papanastassiou, D. A. & Sanz, H. G. 1969, *Earth & Plan. Sci. Lett.*, **7**, 33.

Wasserburg, G. J. & Qian, Y.-Z. 2000, *Ap. J. Lett.*, **529**, L21.

Weaver, T. A. & Woosley, S. E. 1993, *Phys. Rep.*, **227**, 65.

Weinberg, S. 1972, *Gravitation & Cosmology*, Chichester: John Wiley & Sons.

Weiss, A. *et al.* 2004, *Cox & Giuli's Principles of Stellar Structure*, Extended 2nd Edition, Cottenham: Cambridge Scientific Publishers.

Weiss, A., Keady, J. J. & McGee, N. H., Jr. 1990, *Atomic Data Nuclear Data Tables*, **45**, 209.

Westera, P., Lejeune, P., Buser, R. *et al.* 2002, *A & A*, **381**, 524.

Westin, J., Sneden, C., Gustafsson, B. & Cowan, J. J. 2000, *Ap. J.*, **530**, 783.

Wheeler, J. C., Sneden, C. & Truran, J. W. 1989, *Ann. Rev. Astr. Astrophys.*, **27**, 279.

Whelan, J. & Iben, I., Jr. 1973, *Ap. J.*, **186**, 1007.

Whipple, F. L. 1935, *Harvard Coll. Obs. Circ.*, **404**, 1.

White, S. D. M. 1989, in C. S. Frenk, R. S. Ellis, T. Shanks, A. Heavens & J. Peacock (eds.), *The Epoch of Galaxy Formation*, Dordrecht: Kluwer, p. 15.

White, S. D. M. & Rees, M. J. 1978, *MNRAS*, **183**, 341.

Wielen, R., Fuchs, B. & Dettbarn, C. 1996, *A & A*, **314**, 438.

Wiese, W. L., Fuhr, J. R. & Dieters, T. M. 1996, *Atomic Transition Probabilities for Carbon, Nitrogen and Oxygen: A Critical Data Compilation*, *J. Phys. Chem. Ref. Data*, Monograph 7.

Wiese, W. L. & Martin, G. A. 1980, *Wavelengths and Transition Probabilities for Atoms and Atomic Ions*, NSRDS-NBS 68, Washington, D.C.: U.S. National Bureau of Standards.

Wilson, T. L. & Rood, R. T. 1994, *Ann. Rev. Astr. Astrophys.*, **32**, 191.

Wolfe, A. M., Gawiser, E. & Prochaska, J. X. 2005, *Ann. Rev. Astr. Astrophys.*, **43**, 861.

Wolfe, A. M., Turnshek, D. A., Smith, H. E. & Cohen, R. D. 1986, *Ap. J. Suppl.*, **61**, 249.

Wood, B. E., Linsky, J. L., Hébrard, G., Williger, G. M., Moos, H. W. & Blair, W. P. 2004, *Ap. J.*, **609**, 838.

Woods, R. D. & Saxon, D. S. 1954, *Phys. Rev.*, **95**, 577.

Woosley, S. E. & Baron, E. 1992, *Ap. J.*, **391**, 228.

Woosley, S. E., Fowler, W. A., Holmes, W. A. & Zimmerman, B. A. 1978, *At. Data Nucl. Data Tables*, **22**, 371.

Woosley, S. E., Hartmann, D. H., Hoffman, R. D. & Haxton, W. C. 1990, *Ap. J.*, **356**, 272.

Woosley, S. E., Heger, A. & Weaver, T. A. 2002, *Rev. Mod. Phys.*, **74**, 1015.

Woosley, S. E. & Weaver, T. A. 1982, in C. A. Barnes, D. D. Clayton & D. N. Schramm (eds.), *Essays in Nuclear Astrophysics*, Cambridge: Cambridge University Press, p. 377.

Woosley, S. E. & Weaver, T. A. 1994, *Ap. J.*, **423**, 371.

Woosley, S. E. & Weaver, T. A. 1995, *Ap. J. Suppl.*, **101**, 181.

Woosley, S. E., Wilson, J. R., Mathews, G. J., Hoffman, R. D. & Meyer, B. S. 1994, *Ap. J.*, **433**, 229.

Worthey, G. 1994, *Ap. J. Suppl.*, **95**, 107.

Worthey, G., Dorman, B. & Jones, L. A. 1996, *Astr. J.*, **112**, 948.

Worthey, G., Faber, S. M. & Gonzales, J. J. 1992, *Ap. J.*, **398**, 69.

Wright, E. L. 2001, *Ap. J.*, **553**, 538.

Wyse, R. F. G. & Gilmore, G. 1992, *Astr. J.*, **104**, 144.

Wyse, R. F. G. & Gilmore, G. 1995, *Astr. J.*, **110**, 1071.

Wyse, R. F. G. & Silk, J. 1989, *Ap. J.*, **339**, 700.

Yang, J., Turner, M. S., Steigman, G., Schramm, D. N. & Olive, K. 1984, *Ap. J.*, **281**, 493.

Yokoi, K., Takahashi, K. & Arnould, M. 1983, *A & A*, **117**, 65.

Yoshii, Y. 1982, *Publ. Astr. Soc. Japan*, **34**, 365.

Yoshii, Y. & Arimoto, N. 1987, *A & A*, **188**, 13.

Yoshii, Y. & Takahara, F. 1988, *Ap. J.*, **326**, 1.

Zaritsky, D., Kennicutt, R. C., Jr. & Huchra, J. P. 1994, *Ap. J.*, **420**, 87.

Zinn, R. 1985, *Ap. J.*, **293**, 424.

Zoccali, M., Renzini, A., Ortolani, S. *et al.* 2003, *A & A*, **399**, 931.

Zwaan, M. A., Meyer, M., Staveley-Smith, L. *et al.* 2005, *MNRAS*, **329**, 209.

Index